CANADIAN THESES ON MICROFICHE

THESES CANADIENNES SUR MICROFICHE

NOTICE

The quality of this microfiche is heavily dependent upon the quality of the original thesis submitted for microfilming. Every effort has been made to ensure the highest quality of reproduction possible.

If pages are missing, contact the university which granted the degree.

Some pages may have indistinct print especially if the original pages were typed with a poor typewriter ribbon or if the university sent us a poor photocopy.

Previously copyrighted materials (journal articles, published tests, etc.) are not filmed.

Reproduction in full or in part of this film is governed by the Canadian Copyright Act, R.S.C. 1970, c. C-30. Please read the authorization forms which accompany this thesis.

AVIS

La qualité de cette microfiche dépend grandement de la qualité de la thèse soumise au microfilmage. Nous avons tout fait pour assurer une qualité supérieure de reproduction.

S'il manque des pages, veuillez communiquer avec l'université qui a conféré le grade.

La qualité d'impression de certaines pages peut laisser à désirer, surtout si les pages originales ont été dactylographiées à l'aide d'un ruban usé ou si l'université nous a fait parvenir une photocopie de mauvaise qualité.

Les documents qui font déjà l'objet d'un droit d'auteur (articles de revue, examens publiés, etc.) ne sont pas microfilmés.

La reproduction, même partielle, de ce microfilm est soumise à la Loi canadienne sur le droit d'auteur, SRC 1970, c. C-30. Veuillez prendre connaissance des formules d'autorisation qui accompagnent cette thèse.

THIS DISSERTATION HAS BEEN MICROFILMED EXACTLY AS RECEIVED

LA THÈSE A ÉTÉ MICROFILMÉE TELLE QUE NOUS L'AVONS REÇUE

Canada

0-315-12324-9

I✽ National Library of Canada   Bibliothèque nationale du Canada

Canadian Theses Division   Division des thèses canadiennes

Ottawa, Canada
K1A 0N4   60235

PERMISSION TO MICROFILM — AUTORISATION DE MICROFILMER

• Please print or type — Écrire en lettres moulées ou dactylographier

Full Name of Author — Nom complet de l'auteur

DONALD BRUCE GARDINER

Date of Birth — Date de naissance

MAY 19, 1957

Country of Birth — Lieu de naissance

CANADA

Permanent Address — Résidence fixe

10615 - 131 STREET
EDMONTON, ALBERTA
CANADA T5N 1Y6

Title of Thesis — Titre de la thèse

ELECTRIC AND MAGNETIC FIELD SOLUTION FOR A SHEATH
HELIX SURROUNDING A LOSSY COAXIAL ROD, WITH
APPLICATIONS TO ELECTROMAGNETIC HEATING

University — Université

UNIVERSITY OF ALBERTA

Degree for which thesis was presented — Grade pour lequel cette thèse fut présentée

MASTER OF SCIENCE IN ELECTRICAL ENGINEERING

Year this degree conferred — Année d'obtention de ce grade

1982

Name of Supervisor — Nom du directeur de thèse

DR. F.E. VERMEULEN
DR. F.S. CHUTE

Permission is hereby granted to the NATIONAL LIBRARY OF CANADA to microfilm this thesis and to lend or sell copies of the film.

The author reserves other publication rights, and neither the thesis nor extensive extracts from it may be printed or otherwise reproduced without the author's written permission.

L'autorisation est, par la présente, accordée à la BIBLIOTHÈQUE NATIONALE DU CANADA de microfilmer cette thèse et de prêter ou de vendre des exemplaires du film.

L'auteur se réserve les autres droits de publication; ni la thèse ni de longs extraits de celle-ci ne doivent être imprimés ou autrement reproduits sans l'autorisation écrite de l'auteur.

Date

OCTOBER 8, 1982

Signature

Donald Gardiner

NL-91 (4/77)

THE UNIVERSITY OF ALBERTA

ELECTRIC AND MAGNETIC FIELD SOLUTION FOR A SHEATH HELIX SURROUNDING A

LOSSY COAXIAL ROD, WITH APPLICATIONS TO ELECTROMAGNETIC HEATING

by

DONALD GARDINER

A THESIS

SUBMITTED TO THE FACULTY OF GRADUATE STUDIES AND RESEARCH

IN PARTIAL FULFILMENT OF THE REQUIREMENTS FOR THE DEGREE

OF MASTER OF SCIENCE

DEPARTMENT OF ELECTRICAL ENGINEERING

EDMONTON, ALBERTA

FALL, 1982

THE UNIVERSITY OF ALBERTA

RELEASE FORM

NAME OF AUTHOR   DONALD GARDINER

TITLE OF THESIS   ELECTRIC AND MAGNETIC FIELD SOLUTION FOR A SHEATH

HELIX SURROUNDING A LOSSY COAXIAL ROD, WITH

APPLICATIONS TO ELECTROMAGNETIC HEATING

DEGREE FOR WHICH THESIS WAS PRESENTED   MASTER OF SCIENCE

YEAR THIS DEGREE GRANTED   FALL, 1982

Permission is hereby granted to THE UNIVERSITY OF ALBERTA LIBRARY to reproduce single copies of this thesis and to lend or sell such copies for private, scholarly or scientific research purposes only.

The author reserves other publication rights, and neither the thesis nor extensive extracts from it may be printed or otherwise reproduced without the author's written permission.

(SIGNED) *Donald Gardiner*

PERMANENT ADDRESS:

10615 - 131 Street

Edmonton, Alberta, Canada.

T5N 1Y6.

DATED __September, 1982__

THE UNIVERSITY OF ALBERTA

FACULTY OF GRADUATE STUDIES AND RESEARCH

The undersigned certify that they have read, and recommend to the Faculty of Graduate Studies and Research, for acceptance, a thesis entitled ELECTRIC AND MAGNETIC FIELD SOLUTION FOR A SHEATH HELIX SURROUNDING A LOSSY COAXIAL ROD, WITH APPLICATIONS TO ELECTROMAGNETIC HEATING submitted by DONALD GARDINER in partial fulfilment of the requirements for the degree of MASTER OF SCIENCE

_____
Supervisor

Date___September, 1982___

Dedication

This thesis is dedicated to my mother.

In appreciation.

She may yet succeed in making me fat.

Abstract

The electric and magnetic field solution associated with a sheath helix surrounding a lossy coaxial rod is investigated. (The *sheath helix* is a model of the physical helix which consists of an anisotropic conducting sheet in the form of a circular cylindrical tube. At the surface of the sheet, there is infinite conductivity in the direction parallel to the windings of the physical helix, but there is zero conductivity in the direction perpendicular to this.) Three distinct regions are associated with the configuration. Region 1 consists of the lossy rod material, region 2 consists of the air gap between the surface of the lossy rod and the sheath helix surface, and region 3 consists of the air-filled region extending from the sheath helix surface radially to infinity. The configuration extends to infinity in the direction of the sheath helix axis. The electrical properties of the lossy rod are specified by a (real) permittivity ϵ, a permeability equal to that of free space, μ_0, and a conductivity, σ.

Due to the geometry of the configuration, the circular cylindrical coordinate system is used in order to obtain the field solution. It is assumed that the electromagnetic field is spatially dependent on the radial and axial coordinates but not on the angular coordinate. Equations for the electric and magnetic field components in each of the three regions are derived. Furthermore, equations which must be solved in order to calculate the radial and axial wave numbers are obtained. These wave numbers determine the spatial dependence of the electric and magnetic field components.

A direct solution of the previously mentioned equations for the wave numbers could not be obtained. It was necessary to represent the Bessel functions appearing in these equations by simpler functions in order to calculate an approximate wave numbers solution. Graphs showing the radial dependence of the electric and magnetic fields in all three regions, making use of the approximate wave numbers solution, are presented.

Equations stating the time-averaged power dissipation occurring within the lossy rod are derived. It was not possible to directly evaluate these power dissipation expressions because of the difficulty involved in solving for the radial and axial wave numbers, which appear in these equations. Two different major types of approximations were made to the power dissipation equations. The first type involved using the approximate wave numbers solution. The second type was a perturbation procedure,

making use of the electromagnetic field solution associated with two simpler configurations -- the sheath helix surrounding a perfectly conducting coaxial rod, and the sheath helix surrounding an ideal dielectric (zero conductivity) coaxial rod.

Appendices are included which are based on the empty sheath helix, the sheath helix surrounding a perfectly conducting coaxial rod, and the sheath helix surrounding an ideal dielectric coaxial rod. In each of these three appendices, the electric and magnetic field components are listed, numerically calculated values for the radial and axial wave numbers are given, and graphs showing the radial dependence of all the field components are presented.

Acknowledgment

I would like to express my appreciation to the following people and council.

Dr. F.E. Vermeulen and Dr. F.S. Chute, my two supervisors, for proposing the thesis topic, and for many helpful criticisms and suggestions made during the various drafts that the thesis went through.

Samuel Senolper's comprehensive, clearly written thesis was a source for a large amount of important background information.

Allan Hiebert, Tom Casey, and George Carmichael provided valuable assistance concerning the large amount of computer related work that was performed.

My family was a source of support and encouragement.

The Natural Sciences and Engineering Research Council of Canada provided financial support in the form of a scholarship.

Professor Max Wyman taught several mathematics courses of which I was a student. The impression that he made on me will never be forgotten.

Table of Contents

List of Tables

List of Figures

xvi

7

xvii

Glossary of Symbols

$\tilde{z}$ . . . . Take the complex conjugate of the complex number z.

$|z|$ . . . . Evaluate the magnitude of the complex number z.

$|x|$ . . . . Evaluate the absolute value of the real number x.

$\text{Re}[z]$ . . . . Calculate the real part of the complex number z.

$\text{Im}[z]$ . . . . Calculate the imaginary part of the complex number z.

a . . . . Sheath helix radius. (An average value taking into account the nonzero cross sectional area of the windings associated with the physical helix.)

b . . . . Radius of the lossy coaxial rod.

$2 z_1$ . . . . Axial length of the lossy coaxial rod element.

r, θ, z . . . . Radial; angular, circular, or azimuthal; and axial, or longitudinal; positions in the cylindrical coordinate system.

$\underline{a}_r, \underline{a}_\theta, \underline{a}_z$ . . . . . Unit vectors in cylindrical coordinates, pointing in the direction of increasing $r, \theta,$ and z, respectively.

$\underline{a}_{||}, \underline{a}_\perp$ . . . . Unit vectors which are parallel and perpendicular, respectively, to the direction of the sheath helix "windings".

t . . . . Time.

f . . . . Frequency.

$\omega = 2\pi f$ . . . . Angular frequency.

ψ . . . . Helix pitch angle.

$p = 2\pi a \tan\psi$ . . . Helix pitch distance.

$\mathcal{J}_{\parallel}$ . . . . Electrical surface current which is present at $r = a$, and which
is parallel to the direction of the sheath helix "windings".

$\underline{K}_{\parallel} =$

$\mathcal{J}_{\parallel} \cos\beta z \; \underline{a}_{\parallel}$ . . . . Vector form of the electrical surface current present at $r = a$,
showing its spatial dependence.

$\varepsilon_0, \; \mu_0$ . . . . Permittivity and permeability, respectively, of free space.

$\varepsilon, \; \mu_0, \; \sigma$ . . . . Permittivity, permeability, and conductivity, respectively, which
characterize the electrical properties of the lossy coaxial rod.

$\varepsilon_r = \varepsilon/\varepsilon_0$ . . . . . . Relative permittivity.

$\varepsilon_r^* =$

$\varepsilon_r - j \; \sigma/\omega\varepsilon_0$ . . . . Complex relative permittivity.

$ka = \omega \sqrt{\mu_0 \varepsilon_0} \; a$. Free space wave number.

$ka \cot\psi$ . . . . A variable which depends on the operating frequency and on the
sheath helix geometry -- the pitch angle and the radius.

$\eta_0 = \sqrt{\mu_0/\varepsilon_0} =$

120π . . . . Intrinsic wave impedance of free space.

$\delta = \sqrt{2/\omega\mu_0\sigma}$ . . . . . Skin depth associated with a nonmagnetic conductor.

$Z_s = \sqrt{j\omega\mu_0/\sigma} =$
$(1+j) \cdot 1/\delta\sigma \ldots$ Surface impedance associated with a good conductor $(\sigma/\omega\varepsilon_0 \gg \varepsilon_r)$, which is nonmagnetic.

$R_s = \text{Re}[Z_s] =$
$1/\delta\sigma \ldots\ldots\ldots\ldots$ Surface resistance associated with a nonmagnetic good conductor.

$I_0, I_1; K_0, K_1 \ldots$ Modified Bessel function of the first kind of orders zero and one, modified Bessel function of the second kind of orders zero and one, respectively.

$J_0, J_1; N_0, N_1 \ldots$ Bessel function of the first kind of orders zero and one, Neumann function of orders zero and one, respectively.

$\mathcal{W}(y_1, y_2) =$
$y_1 y_2' - y_1' y_2 \ldots$ Wronskian identity. (Note that the "'" means *differentiate with respect to the total argument.*)

$h_m a \ldots\ldots\ldots\ldots$ Complex-valued radial or transverse wave number associated with the sheath helix surrounding a lossy coaxial rod. ($m = 1$ refers to the rod-filled region, while $m = 2$ refers to the air-filled region.)

$\beta a \ldots\ldots\ldots\ldots$ Complex-valued axial or longitudinal wave number associated with the sheath helix surrounding a lossy coaxial rod.

$h_{mr} a, h_{mj} a;$
$\beta_r a, \beta_j a \ldots\ldots$ Real and imaginary parts, respectively, of the two preceding wave numbers.

$\mathscr{E}, \mathscr{H} \ldots\ldots$ Instantaneous (time dependent) electric and magnetic field vectors, respectively.

E_{rn}, $E_{\theta n}$, E_{zn} $\cdots$ Complex or phasor radial, angular, and axial electric field components, respectively, in region n (n = 1, 2, 3), associated with the sheath helix surrounding a lossy coaxial rod.

H_{rn}, $H_{\theta n}$, H_{zn} $\cdots$ Complex or phasor radial, angular, and axial magnetic field components, respectively, in region n (n = 1, 2, 3), associated with the sheath helix surrounding a lossy coaxial rod.

A_n, B_n, C_n, D_n $\cdots$ Arbitrary constants (with respect to the spatial coordinates) in region n (n = 1, 2, 3), which were used in order to obtain the field solution for the sheath helix surrounding a lossy coaxial rod.

$\underline{\pi}$, $\underline{\pi}^{*}$; π_z, π_z^{*} $\cdots$ Electric and magnetic Hertzian potential vectors, respectively; and the axial electric and magnetic Hertzian potential scalars, respectively.

$\underline{P} = \underline{E} \times \widetilde{\underline{H}}$ $\cdots$ Complex Poynting vector.

$P_i = 1/2 \cdot$ $Re[\oint \underline{P} \cdot \underline{dS_i}] \cdots$ Time-averaged power flow through the open surface S_i, which is perpendicular to the $\underline{a}_i$ direction. (i = r, θ, z.)

$P_{di} = \sigma/2 \cdot$ $\int |E_{i1}|^2 \, dV \cdots$ Time-averaged power dissipation occurring within the lossy coaxial rod element, as a result of the contribution associated with E_{i1}. (i = r, θ, z.)

$\varepsilon_i(r_0, z_0) \cdots$ A dimensionless ratio which compares, at some particular point (r_0, z_0) within the lossy rod element, the value of P_{di} to the power dissipation which would be obtained if the value of E_{i1} at that point was constant in magnitude at all points throughout the lossy rod element. (i = r, θ, z.)

$\beta^a a$, $h^a a$,

$\underline{E}_n{}^a$, $\underline{H}_n{}^a$ .... Axial wave number, (single) radial wave number, complex vector electric field, and complex vector magnetic field, respectively, associated with the empty sheath helix. (n = 1 and 2.)

$\beta^c a$, $h^c a$,

$\underline{E}_n{}^c$, $\underline{H}_n{}^c$ .... Axial wave number, (single) radial wave number, complex vector electric field, and complex vector magnetic field, respectively, associated with the sheath helix surrounding a perfectly conducting coaxial rod. (n = 1, 2, 3.)

$\beta^d a$, $h_m{}^d a$,

$\underline{E}_n{}^d$, $\underline{H}_n{}^d$ .... Axial wave number, radial wave number, complex vector electric field, and complex vector magnetic field, respectively, associated with the sheath helix surrounding an ideal dielectric coaxial rod. (m = 1 means that the radial wave number is associated with the rod-filled region, while m = 2 means that this wave number is associated with the air-filled region.) (n = 1, 2, 3.)

$h^d a$ .... Single wave number associated with the sheath helix surrounding an ideal dielectric coaxial rod. It is actually an approximation obtained by equating the preceding radial and axial wave numbers.

$v_p = \omega/\beta^l$ .... Axial phase velocity of traveling waves having $e^{-j\beta^l z}$ dependence on the axial coordinate. (l = a, c, d.)

$c = 1/\sqrt{\mu_0 \varepsilon_0} =$

3.00×10^8 m/s .... Velocity of light in free space.

1. Chapter 1.   Introduction

First, the subject matter is introduced and the intent of the thesis is explained. A presentation of some early work done on helical conductors is then given, followed by mention of other previous work appearing in the literature, which is pertinent to the thesis topic. A general discussion of the nature of the electromagnetic field solution on a helix is presented. Attention is then directed towards the model for which all analysis will be performed. Finally, mention is made of the purpose and general contents of the ensuing chapters and appendices, which comprise the body of this thesis.

1.1 Purpose of the Thesis

Electricity is used in a variety of different ways to generate heat for industrial, commercial, and domestic usage. One important type of electrical heating is *electromagnetic heating* or *radio frequency heating*. This refers to the process of heating a material by exposing it to electromagnetic waves in the approximate frequency range of 50 Hz to 10 GHz $(10 \times 10^9$ Hz). It is often true that no direct contact exists between the sources of the waves and the material being heated.

There are some definite advantages of the electromagnetic heating technique compared to conventional heating within an electric furnace. Two examples are that there is greater control over the specific location where heating is to occur, and that higher rates of heat transfer can be obtained (1, pp. $\underline{X}$; 2, pp. 135).

Electromagnetic heating can be divided into two groups, *induction heating* and *dielectric heating*. *Induction heating* is used with metals -- materials which are good conductors of electricity, in the approximate frequency range of 50 Hz to 100 MHz $(100 \times 10^6$ Hz). The material or work piece is placed inside a coil of wire and then exposed to time-varying electromagnetic fields, produced when the coil is excited by an alternating current. As a result of the time-varying magnetic field, electrical currents called *eddy currents* are induced in the work piece. These eddy currents heat the material. The amount of heating depends on the magnitude of the currents, the electrical resistance of the work piece, and the length of time that the work piece has been exposed to the induced currents. There is often a definite tendency for the induced currents to become concentrated near the surface of the work piece. This phenomenon

is referred to as *the skin effect*. Important applications of induction heating include melting, tempering, surface hardening, and soldering (1, pp. $\underline{XII}$; 2, pp. 3; 3, pp. 63, 115, 173).

Dielectric heating is associated with work pieces which are poor conductors of electricity, in the approximate frequency range of 100 KHz $(100 \times 10^3 \, Hz)$ to 10 GHz. Here the material to be heated may be put inside a wire coil, although it is more common to place it between two metal plates so that the arrangement becomes similar to a capacitor. Once again, heating results from induced currents produced within the work piece. Unlike induction heating, however, dielectric heating often has the property that the induced currents are uniformly distributed throughout the volume of the material. Some uses of this technique involve the drying of lumber, the setting of adhesives used in plywood, the fastening of plastic parts, and the heating of food products (3, pp. 264, 343; 4, pp. 1).

A complete and very useful understanding of electromagnetic heating would be achieved if the electric and magnetic fields interior to the work piece were known. Of course, if the material has a complicated geometry, it may be impossible, or extraordinarily difficult to devise a model so that reasonably accurate field solutions can be practically obtained from Maxwell's equations. However, if the work piece is in the form of a coaxial rod, the heating geometry is one that can be readily analyzed. Three regions are present. First is the rod, second is an air gap between the rod surface and the coil, and finally there is an air-filled region on the exterior of the coil, which, for the purposes of analysis, is considered as being of infinite extent.

Now it is possible to state the subject matter of this thesis. It is desired to develop and investigate a suitable model for the three region helix (or coil) and lossy coaxial rod configuration. The helix is excited in such a manner that an alternating electric current is present on the windings. As complete a theory as possible describing the nature of the electric and magnetic fields for a wide range of different variables is desired. Examples of these variables are the frequency of operation, the radius and pitch angle of the helix, the radius of the lossy coaxial rod (which is never greater than that of the helix), the permittivity and conductivity of the rod material, and the electrical current which is present on the helix windings. Ultimately, the power dissipation resulting from

the rod's nonzero and finite conductivity will be investigated. In short, *it is desired to develop a comprehensive theory so that electromagnetic heating of the three region helix and lossy coaxial rod configuration can be examined from the point of view of boundary value solutions to Maxwell's equations.*

One important possible application of this topic involves the in situ (in place) heating of oil sand. This requires drilling appropriate holes or tunnels so that a large coil can be placed to surround a significant volume of the oil sand formation. An alternating electrical current would be used to excite the coil. Heating will occur in a specific region of the formation. The viscosity of the oil sand in this region decreases, making it easier to recover the oil by means of a suitable gaseous or fluid driving agent. It is this application which actually provided the motivation for the thesis topic.

1.2 Discussion of Early and Related Research

It is the intention of this section to present briefly the early research done on helical conductors, and then to mention in greater detail work which is more specifically directed to the subject matter of this thesis. A much more detailed presentation of the early work is given by Sensiper (5, pp. 3-10; 6).

1.2.1 Early Work

One of the earliest investigations of helical structures was carried out by Pocklington (7). He considered the waves supported by helical wires and by the circular ring. The technique of solution was to solve the Helmholtz equation by summing an infinite number of simple solutions so that all boundary conditions were satisfied. Time-harmonic and purely imaginary exponential axial and angular dependences were used. It was correctly pointed out that for low frequencies the phase velocity is approximately that of waves traveling with the speed of light in the direction of the helical axis, while for high frequencies, it is that of these waves traveling in the direction of the helical windings. (A discussion of this behavior is presented in section B.3.) However, the nature of the functional dependences of the field components and of the wave numbers (which are associated with the spatial dependences of the fields), on the radius of the helix, the pitch angle of the helix, and the operating frequency, was not understood.

A different method of approach was used by Nicholson [8]. It consists of defining a coordinate system so that the nonzero circular cross section and the periodic nature of the helical wires are taken into account. The surface of the wires is described by holding one of the three helical coordinates constant. It is possible to express Maxwell's equations in this system and to exactly apply the boundary conditions. Unfortunately, this helical coordinate system is not orthogonal. The Helmholtz equation is not separable, and great difficulty is encountered in solving the equations. Generally severly limiting approximations must be made. Moreover, Nicholson mistakingly assumed that the coordinate system was orthogonal. The equations for resistance and inductance that he developed are of questionable accuracy.

Sollfrey [9] used the same coordinate system as Nicholson and likewise restricted attention to the empty helix. A perturbation method was employed in an attempt to solve the equations. Expansion in powers of the ratio of wire radius to the pitch distance was used. Keeping only the lower order terms yielded a wave which propagated with the velocity of light in the direction of the wire.

The first use of the *sheath helix* to represent the actual physical helix is credited to Ollendorf. (This was mentioned by Sensiper [5, pp. 4].) The sheath helix consists of an anisotropic conducting sheet. There is infinite conductivity at the sheath helix surface in the direction parallel to the windings of the physical helix, and there is zero conductivity in the direction perpendicular to this. (A more detailed discussion of the sheath helix model is presented in part 1.3.2.) Ollendorf obtained a field solution having no angular dependence.

Interesting is a comparison between the use of the sheath helix model and the approach of Nicholson and Sollfrey. The sheath helix model does not account for the nonzero wire cross section or the periodic properties of the physical helix. However, Maxwell's equations are readily solved without requiring any approximations.

1.2.2 Related Work

Little new work on the electromagnetic behavior of the helix was reported until the development of the traveling wave tube during the Second World War. Major contributions to the theory of helical conductors and traveling wave tubes were made by

Chu and Jackson (10) and by Pierce (11). Both groups employed the sheath helix to model the empty physical helix and only considered circularly symmetric (no angular dependence) field solutions. The dispersion equation was obtained. Chu and Jackson studied the quantity v_p/c, where v_p is the phase velocity and c is the velocity of light in air. (A glossary of symbols has been included near the beginning of the thesis, for convenience. However, each symbol will also be defined in the text the first time it is used.) v_p/c was plotted as a function of ka, where k is the free space wave number and a is the sheath helix radius. $(k = \omega \sqrt{\mu_0 \epsilon_0}$, where $\omega = 2\pi f$ is the angular frequency, f is the frequency, ϵ_0 is the permittivity of free space, and μ_0 is the permeability of free space.) Pierce gave a list of the electromagnetic fields and obtained the time-averaged axial power flow. The normalized radial wave number, $ka \cot\psi/ha$, where h is the radial wave number and ψ is the pitch angle, was graphed as a function of the variable $ka \cot\psi$. (The quantity $ka \cot\psi$ depends on the operating frequency and on the sheath helix geometry -- the pitch angle and the radius.) The rest of the work by the forementioned authors concentrated on effects associated with the presence of an axial electron beam, and it is not relevant to the present discussion.

Cutler (12) experimentally investigated the validity of the sheath helix model as an approximation of a physical helix. An empty copper helix with a pitch angle of about $5.0°$ was used. It was large enough in radius so that measurements could be made using probes without significantly distorting the fields. A high operating frequency was used. It was found that the electromagnetic fields cling closely to the coil and that there was no tendency for the structure to radiate. (This behavior is discussed in section B.3.) As expected, the field strengths very near the coil were significantly different than the theoretical ones. (All theoretical calculations were based on the average physical helix radius, taking into account the nonzero cross sectional area of the windings.) However, at relatively large radial distances away from the coil, the agreement was quite good. One exception was that the actual interior sheath helix region axial electric field magnitude, $|E_{z1}|$, was somewhat less than predicted. By measuring the wavelength of the standing wave pattern on the helix, the velocity of propagation associated with traveling waves was determined. There was usually very good agreement between the measured and predicted phase velocities at high frequencies, but the agreement was not as good

for low frequencies.

Cutler points out that the validity of the sheath helix model can be questioned at high frequencies, where the wavelength approaches that of the helix circumference. Here, the physical helix will have a tendency to radiate but the sheath helix model never possesses this behavior. (The fact that the sheath helix cannot act like a radiator is discussed in section B.3.) It is also mentioned that, although experimental tests were made over a wide range of frequencies and exciting conditions, the only guided wave found was the circularly symmetric one.

Harris et al. (13) made measurements of the phase velocity which characterize the fields associated with an empty physical helix, whose turns were supported by strings, and then subsequently supported by a variety of different dielectric geometries. A helix with a similar geometry to that of Cutler's was employed. When the mean radius of the physical helix was used for the sheath helix, it was found, over the frequency range of concern, that there was excellent agreement between the experimental and predicted values, when the physical helix was supported by strings. For the dielectric supported structures, it was discovered that they exhibited somewhat less dispersion than the unsupported one. Theoretical results were developed for the phase velocity associated with the sheath helix, having air in the interior region and having the infinite exterior region completely filled by dielectric material. It was concluded that at high frequencies this phase velocity was less than that of the empty sheath helix, and that there was less dispersion.

Sensiper (5, 6) provided two important advances in the understanding of helical conductors. First, he considered the field solution of the empty sheath helix, assuming an angular dependence of the form $e^{-jm\theta}$, with m an integer and θ the azimuthal or angular coordinate. In examining the resulting dispersion equation, he noted that several waves having different phase and group velocities (which are functions of frequency, sheath helix radius, and sheath helix pitch angle) can exist for each nonzero value of m. Axial power flow formulas were derived, which are valid even if several different waves are present. Sensiper also analyzed the special cases of a zero and a $\pi/2$ pitch angle, corresponding to structures he termed the "sheath ring" and the "sheath tube", respectively.

Independently, at nearly the same time, another detailed investigation of the air-filled sheath helix dispersion equation was carried out by Phillips and Malin (14, 15). Many theorems and corollaries were developed concerning the mathematical behavior of the wave number solutions, which determine the radial and axial spatial dependences of the fields, for different operating frequencies and sheath helix geometries. Special attention was paid to the circularly symmetric solution. Longitudinal and cross sectional drawings of the electric fields were made. As well, a plot of the radial dependence of the axial electric field was given. This work was more mathematically oriented than Sensiper's investigation. Its major failing is that it did not attempt to physically interpret the field properties associated with the different wave number solutions.

Sensiper's second major contribution was in the development and analysis of a new model of the physical helix. This model consists of a helix wound of a perfectly conducting wire having zero radial extension but nonzero axial extension. It is called the *tape helix*. (See Figures 1.1. Figure 1.1b shows the *developed tape helix*. This is obtained by cutting the tape helix along a plane of constant θ, looking at it from the inside, and then flattening it out.) A major advantage of the tape helix over the sheath helix is that it retains the periodic nature of the physical helix. The axial and radial wave numbers are periodic functions of the axial and angular coordinates, and all field components are expressed as an infinite sum of spatial harmonics. More specifically, it is shown that the axial wave number has the form $\beta_m = \beta_0 + 2\pi m/p$, with m an integer and p the pitch distance. In addition, the axial and angular dependence of the fields is expressed as $e^{-jm(2\pi z/p - \theta)}$. All field components are expressed as an infinite series summed over m.

To obtain the dispersion equation it is necessary to apply boundary conditions. At $r = a$, the surface of the tape helix, these are that the tangential electric field is continuous, the discontinuity in the magnetic field is related to the electrical current on the tape, the electric field tangential to the perfectly conducting tape is zero, and the electrical current may only exist on the tape. Proper application of these conditions results in a doubly infinite set of homogeneous linear simultaneous equations. In theory, these equations could be solved to obtain the eigenvalue wave number solutions. Sensiper applied approximate boundary conditions that permitted the dispersion equation

THE TAPE HELIX AND DEVELOPED TAPE HELIX

a) Tape Helix
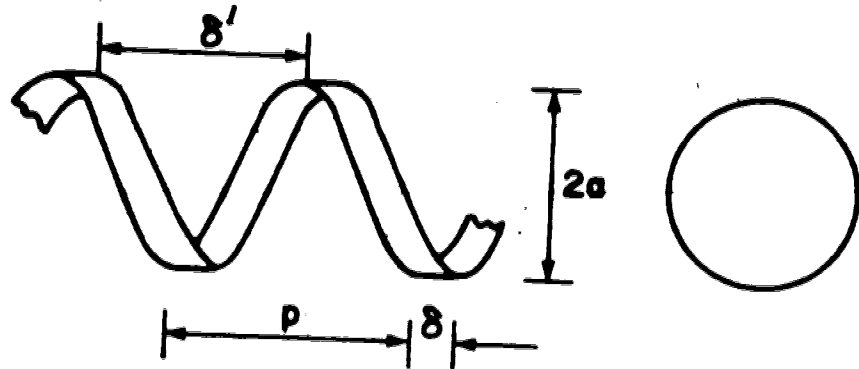
b) Developed Tape Helix

p = pitch distance ψ = pitch angle
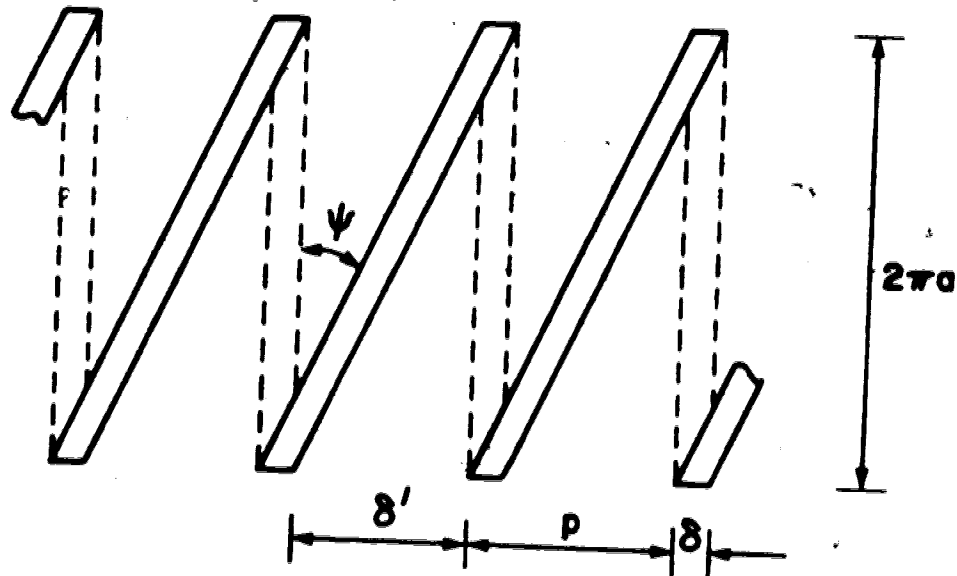
δ = tape width δ' = gap width

a = tape radius

Figures 1.1   The Tape Helix Investigated
by Sensiper (5, 6).

to be expressed in the form of a single infinite series equated to zero, which he solved using a combination of analytical, graphical, and numerical methods.

The tape helix is a more accurate model and can yield information about the nonzero wire thickness and the periodic properties of a physical helix, which the sheath helix cannot. However, the price paid for its usage is rather high. Much more difficulty in obtaining the wave number solutions for a given operating frequency and helix geometry is encountered. As well, the field expressions themselves are clumsy to manipulate and hard to interpret.

A relatively large amount of literature exists concerning the tape helix. Accounts are given in the books by Hutter (16, pp. 121-129), Watkins (17, pp. 46-55), and Collin (18, pp. 396-398). While awareness of the tape helix solution adds to one's understanding of the helical coil, the author did not make use of this solution, and hence it will not be discussed further.

Work has been done based on the sheath helix model involving geometries which are more complicated than the air-filled sheath helix. Bryant (19) considered three cases of the sheath helix plus perfectly conducting coaxial cylinders. As shown in Figure 1.2 these are:

a. Helical conductor inside the coaxial cylinder.

b. Helical conductor surrounding the coaxial cylinder.

c. Helical conductor sandwiched between two coaxial conductors.

The dispersion equation for each of the above was calculated. Graphs of $ka \cot\psi/ha$ versus ha were made.

Independently of Bryant's work, Mathers and Kino (20) investigated parts a. and b. of the above in a more comprehensive treatment. A relatively detailed procedure for obtaining the electric and magnetic field components in terms of a single undetermined constant was given, and the dispersion equation was obtained. Graphs of $ka \cot\psi/ha$ versus $ka \cot\psi$ were given, using several different cylinder radii. Mathers and Kino mentioned that the presence of the conducting cylinder acts to flatten out the dispersion curves. The phase velocity is nearly constant over a wider frequency range than it is in the case of the empty sheath helix. (This behavior is discussed in section C.2.) It is also mentioned, for the geometry in part b., that there is

SHEATH HELIX WITH INNER AND OUTER
COAXIAL PERFECTLY CONDUCTING CYLINDERS

$$0 \leq c < a < b < \infty$$

conductor

sheath helix
conductor
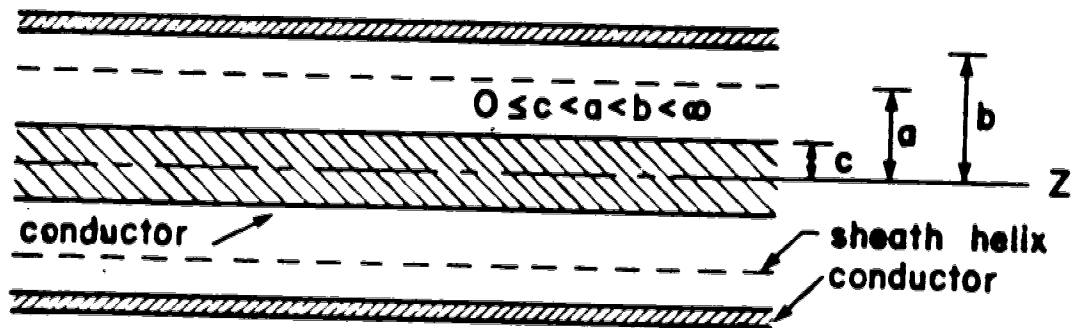
Figure 1.2   The Configuration Investigated
by Bryant (19).

11

a significantly larger radial electric field in the region between the surface of the conductor and the sheath helix surface than is the case for the empty sheath helix, assuming that both configurations have the same excitation.

In addition to the geometry with perfectly conducting coaxial cylinders, there has been research done on the sheath helix immersed in multi-dielectric media. Once again, it was assumed that the fields did not exhibit an angular dependence. Olving (21) examined the arrangement with the dielectric extending radially to infinity and extending into, or not into, the sheath helix interior region. (See Figures 1.3.) The dispersion equation was obtained for the three cases $a > b$, $a < b$, and $a = b$. For the situation when the surface of the dielectric rod touches the sheath helix surface, which occurs when $a = b$, the time-averaged axial power flow was calculated. It was shown that at high frequencies, the phase velocity normalized with respect to the velocity of light in air is

$$v_p/c = \sqrt{2/(\epsilon_r + 1)} \cdot \tan\psi, \quad \text{where} \quad \epsilon_r = \epsilon/\epsilon_0 \quad \text{is the relative}$$

permittivity of the dielectric material. Hence, one important property of the two region configuration is that the phase velocity can be greatly reduced through the proper choice of the dielectric material.

It is true that for very high frequencies, the electric and magnetic field components associated with the sheath helix are greatly attenuated over a relatively small radial distance, inward or outward away from the sheath helix surface. Here the exterior fields have a short radial extension, and so there may be little error in assuming, as Olving did, that the exterior region dielectric extends radially to infinity. However, if the physical extent of this dielectric is actually very small, or at lower frequencies, it is desirable to account for the finite dielectric size. Such an analysis was performed by Swift-Hook (22). He analyzed the configuration with three separate interfaces. (See Figures 1.4.) Exact dispersion equations for these two geometries were given in the form of determinants. Approximations to these equations were obtained by equating the radial and axial wave numbers. The approximate equations were investigated for a number of different special cases concerning the geometry and relative permittivity of the dielectric tube. A large number of graphs based on the approximate equations were made. These graphs displayed $ka \cot\psi/ha$ versus $ka \cot\psi$, and used

SHEATH HELIX EMBEDDED IN AN INFINITE DIELECTRIC MEDIUM

a)

sheath helix

dielectric interface

$(0 \leq b < a < \infty)$

b)

$(0 < a \leq b < \infty)$
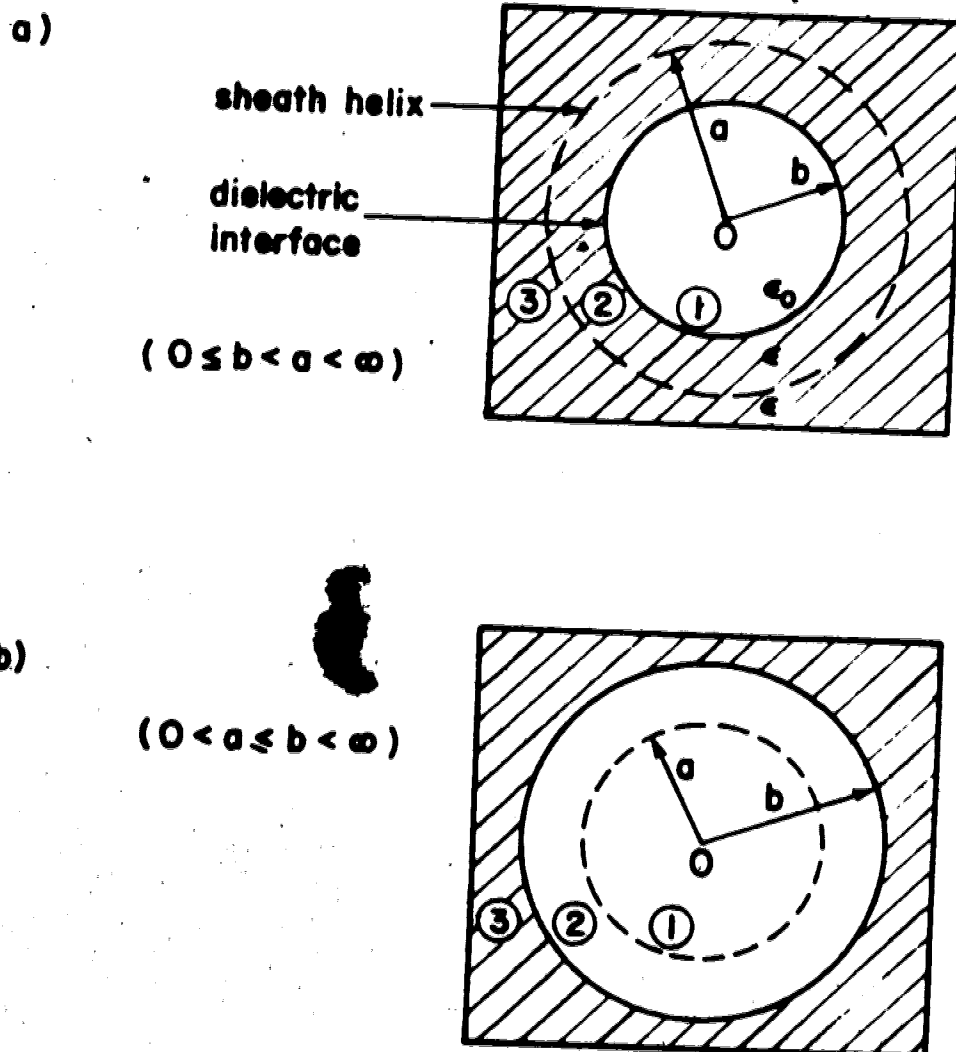
Figures 1.3   The Configurations Studied by Olving (21).

SHEATH HELIX PLUS DIELECTRIC TUBE

a) Helix contained
   inside the dielectric
   tube

   $(0 < a \leq b \leq c < \infty)$

   ④③ ② ① sheath helix
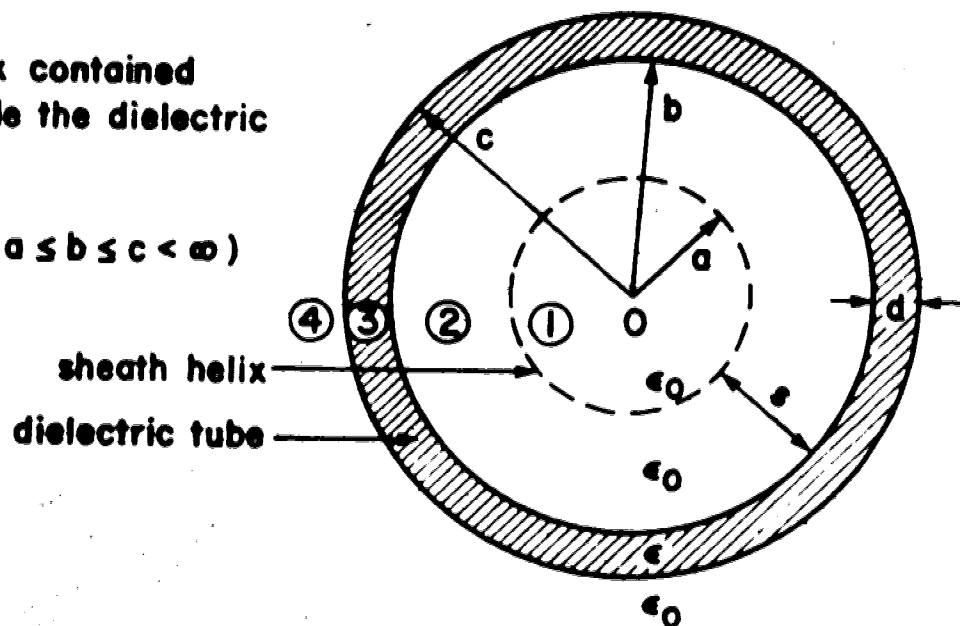
   dielectric tube

b) Helix embedded in
   the dielectric tube

   $(0 \leq b < a < c < \infty)$
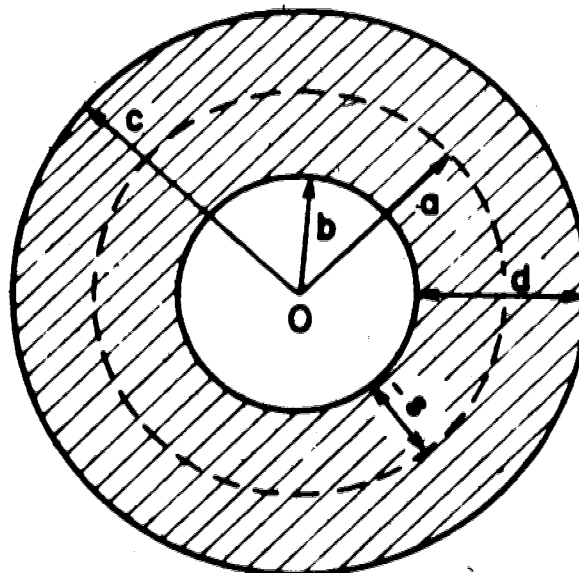
Figures 1.4   The Configurations Investigated
               by Swift-Hook (22).

ε_r, b/a, and c/a as parameters. High frequency approximations of the previous equations were developed, and the high frequency dispersion curve was examined. It was pointed out that for certain geometries of the dielectric tube, there is much less dispersion than that associated with the empty sheath helix. This is a very desirable property for microwave applications, such as the traveling wave tube.

Attention is now directed to research which is concerned with electromagentic heating. Vaughan and Williamson (23) and Baker (24) examined the three region helix and lossy coaxial rod configuration, by proposing electrical circuits to model the rod and the wire helix. The efficiency of the heating arrangement was studied, taking into account the nonzero resistance of the helical windings. These analyses are very different from that which will be followed in the thesis and so they will not be mentioned further.

An investigation of the three region helix and lossy coaxial rod based on Maxwell's equations was carried out by Brown et al. (3, pp. 27). No attempt was made to model the physical helix. Ampere's law and Faraday's law were applied to calculate a single angular electric field component and a single axial magnetic field component within the rod. These fields were only assumed to have a radial spatial dependence. Power dissipation within the lossy coaxial rod was calculated on the basis of the single electric field.

There are several limitations on the preceding analysis. First, varying the geometry of the helical coil or the radius of the lossy coaxial rod has no effect on the two field components. The analysis given in Chapter 2 of the thesis shows that this is an oversimplification. Another deficiency is that the helix will often be excited so that the electrical current present on the windings has an axial dependence, and therefore it is desirable that the field components are dependent on the axial coordinate. Finally, it will be seen in Chapter 2 and in Chapter 3 that the power dissipation results from the presence of three distinct electric field components inside the lossy coaxial rod. In Chapter 3 it is shown that if the lossy rod is a good conductor, then Brown et al. are usually justified in only considering the angular electric field to calculate the power dissipation. However, if the rod conductivity is small, the investigation performed in Chapter 3 makes it clear that the axial electric field provides a large contribution to the

power dissipation. In this case, the previously mentioned investigation must be considered as incomplete and misleading.

The only paper the author has knowledge of that made use of the sheath helix to study electromagnetic heating is that by Chute et al. (25). These authors were concerned with two regions having different electrical properties μ, ϵ, σ, where σ is the rod conductivity. One region filled the sheath helix interior and touched the sheath helix surface, while the second region started at the sheath helix surface and extended radially to infinity. It was assumed that the electric and magnetic field components did not exhibit an angular dependence. The dispersion equation was obtained and the field components were expressed in terms of the electrical current present at the sheath helix surface. Special attention was given to low operating frequencies. The power dissipations resulting from the angular and axial electric fields were calculated, and it was discovered that the latter one was usually much greater than the former. A simple electrical circuit to model the axial current flow within the region enclosed by the sheath helix was proposed. Applications for the electrical heating that takes place, such as in situ recovery of hydrocarbons from oil sand, were mentioned.

In concluding section 1.2, some past research will be mentioned, which, although not directly concerned with helical structures, still provides some useful information on this subject. Physical helices are *periodic structures*. The extensive theory on this topic is therefore of interest. A pioneering work is the book by Brillouin (26). General discussions are given by Hutter (16, pp. 73-137), Collin (18, pp. 363-430), Collin (27, pp. 368-405), Ramo et al. (28, pp. 474-479), Slater (29, pp. 169-188), and Johnson (30, pp. 244-272). In particular (18) gives a clear explanation of many periodic properties of the physical helix.

Also of interest and aiding in understanding the three region sheath helix and lossy coaxial rod configuration, is the circular cylindrical waveguide containing two coaxial dielectric regions. The circular waveguide metal surface is assumed to be perfectly conducting, and the dielectrics are assumed to be ideal (they have a zero conductivity). From a field theory point of view, this waveguide is different from the three region sheath helix structure only because the boundary conditions at the cylindrical wall force

the radial magnetic field and both the axial and angular electric fields to be zero, while the boundary conditions at the sheath helix surface are more complicated and act to couple the fields in the interior region to those in the exterior region. Early work on the circular waveguide containing two coaxial dielectrics was done by Frankel (31) and Banos et al. (32). The latter mentioned paper made an important contribution by providing a simple but effective graphical solution to obtain the wave numbers, which determine the radial and axial spatial dependences of the field components. Two examples of later work on this circular waveguide are Teasdale and Crawford (33) and Teasdale and Higgins (34).

1.3 Nature of the Desired Solution and Discussion of the Sheath Helix Model

1.3.1 Nature of the Solution for the Sheath Helix

The desired type of solution must meet the following requirements.

a. It must satisfy Maxwell's equations.

b. All boundary conditions must be satisfied. Examples of these boundary conditions are that along an interface between two regions characterized by a zero conductivity, or a nonzero but finite conductivity, the tangential electric and magnetic field components are continuous. If one region is assumed to be a perfect electrical conductor, the tangential electric fields are forced to be zero along the interface. This also means the normal magnetic fields at the interface are zero. An electrical current may be present on the surface of the perfect conductor. If this is true, the tangential magnetic fields are discontinuous according to

$$\underline{a}_n \times (\underline{H}_2 - \underline{H}_1) = \underline{K}.$$

($\underline{a}_n$ is the unit vector normal to the interface and pointing into region 2, $\underline{H}_1$ and $\underline{H}_2$ are the magnetic fields in region 1 and in region 2, respectively, evaluated at the interface, and $\underline{K}$ (A/m) is the electrical surface current present on the interface.)

c. In a source-free region, the solution must be finite, single-valued, continuous, represent a finite amount of real power transfer, and be excitable by a finite amount of energy.

d. If all sources are located within a finite distance of the chosen coordinate origin, two restrictions must be met.

1) The electric field, $\underline{E}$, and the magnetic field, $\underline{H}$, must become exponentially, or in some other manner, sufficiently small so that

$$\lim_{R \to \infty} (R \cdot \underline{E}) \quad \text{and} \quad \lim_{R \to \infty} (R \cdot \underline{H}) \quad \text{are bounded, where} \quad R$$

is the distance from the origin. Stratton (35, pp. 485) refers to this as *the condition of regularity at infinity.*

2) *The boundary condition at infinity* is satisfied. This property means that at very large distances from the sources, only outward traveling waves occur (35, pp. 486). From one point of view, this means that a matched load exists at infinity (36, pp. 712).

An electromagnetic wave which satisfies all the preceding requirements will henceforth be called a free mode field solution.

Because of the symmetry of the sheath helix, it is convenient for analysis to use the circular cylindrical coordinate system. This is defined in the usual manner, as shown in Figure 1.5a. A point in space is specified by $P(r, \theta, z)$. The unit vectors in the radial, angular or circular, and axial directions, are $\underline{a}_r$, $\underline{a}_\theta$, and $\underline{a}_z$, respectively. Electric and magnetic fields can be expressed in terms of component fields parallel to these unit vectors.

$$\underline{E} = E_r \, \underline{a}_r + E_\theta \, \underline{a}_\theta + E_z \, \underline{a}_z, \quad \text{and}$$

$$\underline{H} = H_r \, \underline{a}_r + H_\theta \, \underline{a}_\theta + H_z \, \underline{a}_z. \tag{1.1}$$

The lossy coaxial cylindrical rod is assumed to be a region which is linear, homogeneous, and isotropic. For simplicity, the rod is assumed to be nonmagnetic.

PHYSICAL HELIX AND SHEATH HELIX

a) Physical helix showing the coordinate system
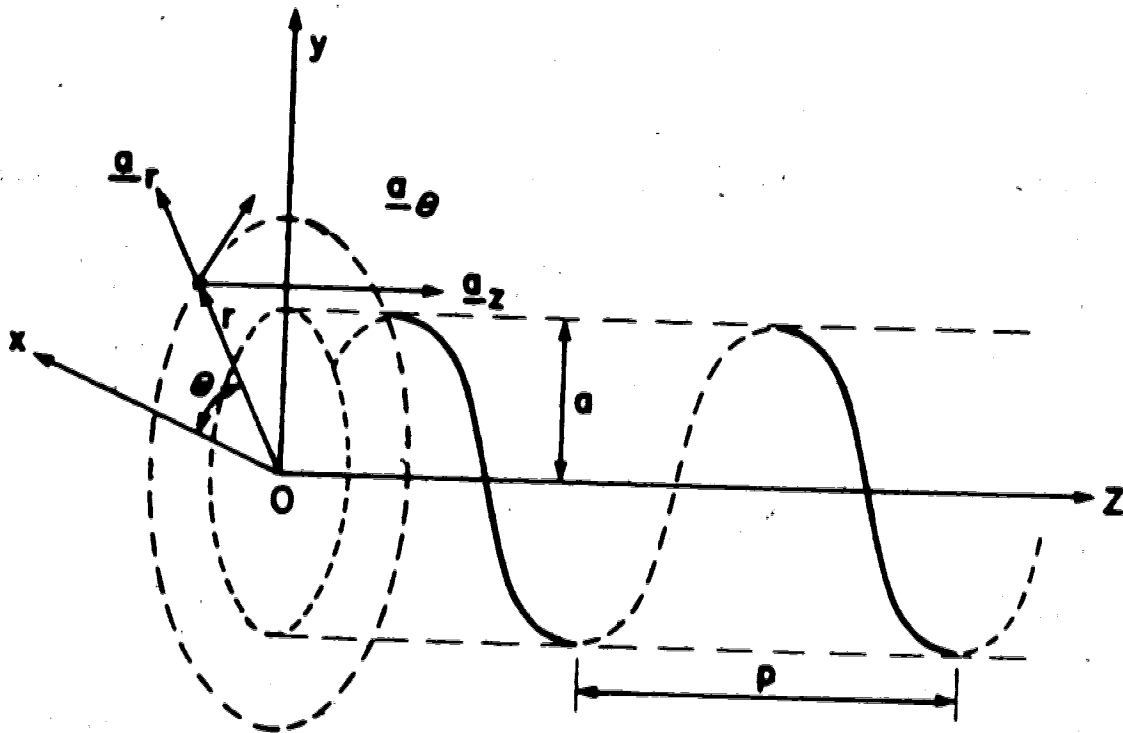
b) The developed sheath helix
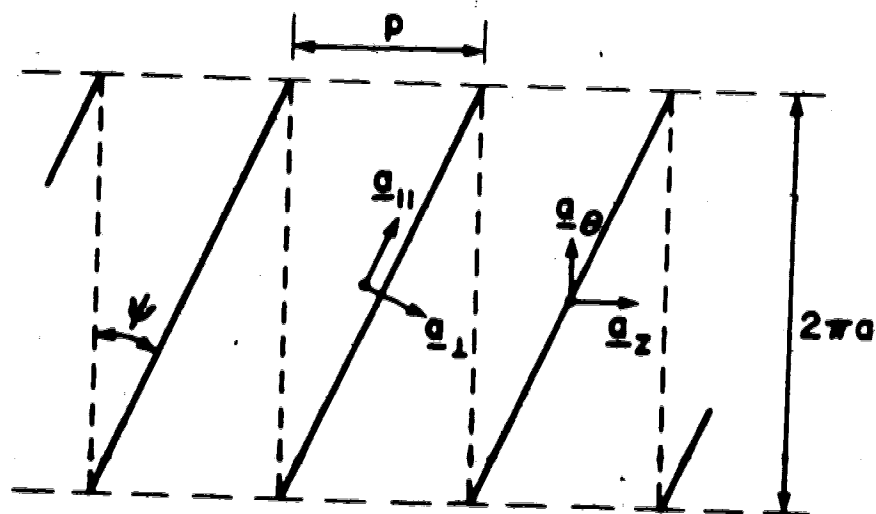
Figures 1.5   The Circular Cylindrical Coordinate
System, the Physical Helix, and the
Developed Sheath Helix.

Maxwell's equations for the *instantaneous* (time dependent) vector fields in this source-free region are well known but are repeated here for convenience.

$$\nabla \times \underline{\mathcal{E}} = - \mu_0 \frac{\partial \underline{\mathcal{H}}}{\partial t}, \qquad \nabla \times \underline{\mathcal{H}} = \epsilon \frac{\partial \underline{\mathcal{E}}}{\partial t} + \sigma \underline{\mathcal{E}},$$

$$\nabla \cdot \epsilon \underline{\mathcal{E}} = 0, \quad \text{and} \quad \nabla \cdot \mu_0 \underline{\mathcal{H}} = 0 ; \qquad (1.2)$$

where ϵ is the (real) permittivity, σ is the conductivity, $\underline{\mathcal{E}}$ is the instantaneous vector electric field, and $\underline{\mathcal{H}}$ is the instantaneous vector magnetic field. To modify these equations so that they describe an air-filled region, it is only necessary to choose $\epsilon = \epsilon_0$ and $\sigma = 0$.

A time-harmonic dependence of the form $e^{j\omega t}$, where t is time, is assumed for all the instantaneous fields. Of course, this restriction is not a severe limitation because from elementary Fourier Series theory, a wide range of time-periodic functions can be expressed as a suitable summation of such solutions. It is very useful to separate the time dependence from the instantaneous vector fields so that *complex* or *phasor* vector fields are defined.

$$\underline{\mathcal{E}}(r, \theta, z, t) = \text{Re}[\underline{E}(r, \theta, z) \cdot e^{j\omega t}] \quad \text{and}$$

$$\underline{\mathcal{H}}(r, \theta, z, t) = \text{Re}[\underline{H}(r, \theta, z) \cdot e^{j\omega t}]. \qquad (1.3)$$

$\underline{E}$ and $\underline{H}$ are the complex vector electric and magnetic fields, respectively. Equations 1.2 can be rewritten using the complex fields.

$$\nabla \times \underline{E} = - j \omega \mu_0 \underline{H}, \qquad \nabla \times \underline{H} = j \omega \epsilon \underline{E} + \sigma \underline{E},$$

$$\nabla \cdot \epsilon \underline{E} = 0, \qquad \text{and} \qquad \nabla \cdot \mu_0 \underline{H} = 0. \qquad (1.4)$$

Only the complex fields will be considered in the remainder of this thesis.

If traveling wave solutions are desired, the axial dependence of the fields is taken as $e^{-j\beta z}$, where β is referred to as the axial or longitudinal wave number. The fact that the geometrical plus electrical properties of the rod-filled region are the same for all values of z, and that the sheath helix boundary conditions are the same for all values of z, well justifies this form. Although β is independent of the spatial coordinates, it will have a complicated functional relationship dependent on the geometry of the sheath helix, on the geometry plus electrical properties of the lossy coaxial rod, and finally on the operating frequency. An important aspect of obtaining the free mode field solution is to achieve as good an understanding as possible of this functional dependence.

For standing wave solutions, the problem of the axial dependence is slightly more difficult. The choice which will be made is to have the axial dependence of E_z and H_z characterized by $\cos\beta z$. (It will later be seen that the axial dependence of the other field components is described by either $\cos\beta z$ or $\sin\beta z$.) This choice is made since it is desired that the infinite axial length sheath helix be as good a representation as possible of a finite axial length physical helix. If this finite structure is excited in a balanced manner about the mid-plane, which is taken to be $z = 0$, it is known that H_z must be characterized by a $\cos\beta z$ axial dependence so that its low frequency behavior is similar to that of the d.c. case.

It will be assumed that the field components do not exhibit an angular dependence. This choice is based on two important considerations. First, it is believed that the $m = 0$ mode is the most important for determining the electromagnetic heating which occurs within the lossy coaxial rod. Second, a complete theory of the $e^{-jm\theta}$ free mode field solution associated with the sheath helix surrounding a lossy coaxial rod is expected to be extraordinarily difficult to obtain, while not further illuminating the behavior of the electromagnetic heating occurring within the lossy rod. It is repeated here that the angularly independent solution was the only type of guided wave that Cutler was able to excite during his experimental studies of air-filled physical helices.

To complete part 1.3.1, it is mentioned that the rationalized MKS system of units will be used throughout the thesis, and that only steady state fields will be studied. Transient effects are not considered in the thesis.

1.3.2 The Sheath Helix

The physical helix may be wound in two different senses -- *positively* or *negatively*. If a particle following the windings moves in the positive z direction as θ increases, the helix is said to be *positively wound*. It will always be assumed in this thesis that the physical helix is positively wound, which means that the pitch angle satisfies $0 < \psi < 90.0°$. One can readily extend this definition to the sheath helix. (See Figures 1.5. It will later be seen in Chapter 2 that the free mode field solution is easily modified so that it corresponds to the negatively wound sheath helix. Therefore, no loss in generality occurs by restricting the pitch angle to be positive.) Keeping in mind the fact that only the circularly symmetric mode is studied and that it is desired to have the sheath helix model represent the physical helix as closely as possible, it is best to just consider relatively small pitch angles. Usually $0 < \psi \leq 10.0°$ will be used, although the free mode field solution for the sheath helix surrounding a lossy coaxial rod which is derived in Chapter 2, equations 2.65 and 2.70 - 2.88; and the Chapter 3 expressions which show the power dissipation occurring within the lossy rod, equations 3.12, 3.14, and 3.16; are actually valid for $0 < \psi < 90.0°$.

The developed sheath helix is shown in Figure 1.5b. This is a convenient way to study the geometry. It will be repeated that the developed helix is obtained by cutting the sheath helix along a plane of constant θ, looking at it from the inside, and then flattening it out. p is the pitch distance, and this is related to the sheath helix radius and the sheath helix pitch angle according to $\tan \psi = p/2\pi a$. $\underline{a}_{\parallel}$ and $\underline{a}_{\perp}$ are unit vectors parallel and perpendicular to the sheath helix "windings", respectively. These are related to the cylindrical coordinate system unit vectors according to:

$$\underline{a}_{\parallel} = \underline{a}_{\theta} \cos\psi + \underline{a}_z \sin\psi,$$

$$\underline{a}_{\perp} = -\underline{a}_{\theta} \sin\psi + \underline{a}_z \cos\psi,$$

$$(1.5)$$

$$\underline{a}_\theta = \underline{a}_\parallel \cos\psi - \underline{a}_\perp \sin\psi,$$

$$\underline{a}_z = \underline{a}_\parallel \sin\psi + \underline{a}_\perp \cos\psi, \quad \text{and} ,$$

$$\underline{a}_r \times \underline{a}_\parallel = \underline{a}_\perp .$$

(1.5)
(continued)

A physical interpretation of the sheath helix model is now presented. Consider a wire of some arbitrary cross sectional area which is wrapped around an imaginary cylinder so that it assumes a helical shape. Next, another wire is placed beside this first one and wrapped identically. This process is repeated many times. Taking the limit as the number of wires and their conductivity becomes infinitely large, with the spacing between individual wires and their cross sectional areas going to zero, the *sheath helix* is obtained. In fact, this is actually an anisotropic conducting sheet. There is infinite conductivity at the surface of the sheet in the direction parallel to the "windings", and zero conductivity in the perpendicular direction. It is important to remember that these are idealized wires and hence are very different from the physical helix windings.

In order to obtain the free mode field solution, it is necessary to satisfy the boundary conditions at the sheath helix surface. These four conditions may be stated as:

$$E_{\parallel 1}\Big|_{r=a} = 0 \quad \text{or}$$

$$E_{\theta 1}\Big|_{r=a} \cos\psi + E_{z1}\Big|_{r=a} \sin\psi = 0,$$

(1.6)

$$E_{\parallel 2}\Big|_{r=a} = 0 \quad \text{or}$$

$$E_{\theta 2}\Big|_{r=a} \cos\psi + E_{z2}\Big|_{r=a} \sin\psi = 0,$$

(1.7)

$$\left. E_{\perp 1}\right|_{r=a} = \left. E_{\perp 2}\right|_{r=a} \quad \text{or}$$

$$\tag{1.8}$$

$$\left(\left. E_{\theta 1}\right|_{r=a} - \left. E_{\theta 2}\right|_{r=a}\right)\sin\psi - \left(\left. E_{z1}\right|_{r=a} - \left. E_{z2}\right|_{r=a}\right)\cos\psi = 0,$$

and $\qquad \left. H_{\parallel 1}\right|_{r=a} = \left. H_{\parallel 2}\right|_{r=a} \qquad$ or

$$\tag{1.9}$$

$$\left(\left. H_{\theta 1}\right|_{r=a} - \left. H_{\theta 2}\right|_{r=a}\right)\cos\psi + \left(\left. H_{z1}\right|_{r=a} - \left. H_{z2}\right|_{r=a}\right)\sin\psi = 0.$$

(Note that "1" and "2" refer to the interior $(0 \leqslant r \leqslant a)$ and exterior $(a \leqslant r < \infty)$ regions, respectively, of the sheath helix.) Equations 1.6 and equations 1.7 result from the fact that $\sigma_\parallel = \infty$, where $\sigma_\parallel$ is the conductivity at the sheath helix surface in the direction parallel to the "windings". Equations 1.8 express the continuity of the tangential electric field at the sheath helix surface. Since $\sigma_\perp = 0$, where $\sigma_\perp$ is the conductivity at the sheath helix surface in the direction perpendicular to the "windings", there can only be an electrical surface current present which is parallel to the "windings". This means that at the sheath helix surface, the magnetic field parallel to the "windings" must be continuous, and this idea is expressed in equations 1.9. Later, it will be seen that equations 1.6 – 1.9 act to couple the exterior sheath helix region fields with the interior region fields, in such a manner that the free mode field solution must have axial components of both electric and magnetic fields. Transverse electric (TE) or transverse magnetic (TM) solutions cannot exist by themselves.

Two shortcomings of the sheath helix model are immediately clear. First, it does not account for the nonzero wire size of the physical helix. Second, the periodic properties of the physical helix are lost. If the physical helix is idealized as being very long, in an unbounded medium, and if it is translated in the axial direction by the pitch distance p or rotated through the angular distance θ and then translated axially by the distance $(\theta/2\pi) \cdot p$, it will be impossible to distinguish the new position from the original one. *The physical helix is, therefore, a periodic structure.* Floquet's

theorem states that for such a structure:

for a given mode of propagation at a given steady state frequency, the fields at one cross section differ from those one period away only by a complex constant. (17, pp. 2; 30, pp. 140.)

This means that the quantity βp must be periodic with a period of 2π. The sheath helix model does not predict this periodic behavior of the axial wave number.

The first mentioned deficiency is partly overcome by taking the actual physical wire radius into account to determine the value of the sheath helix radius. Also, it is expected that the physical wire size will have a significant influence on the fields only close to the physical helix windings. Insofar as the second limitation is concerned, it should be noted that the periodic effect is more significant for modes other than the circularly symmetric one. Finally, it is again mentioned that the measurements made by Cutler (12) and by Harris et al. (13) do lend support to use of the sheath helix model for the angularly independent wave.

1.4 Brief Discussion of the Chapters and Appendices that Follow

One advantage that the author has over early researchers concerns the numerical aspect of calculating the wave numbers which determine the spatial dependence of the electric and magnetic field components. This is necessary so that numerical evaluation of the fields at a particular point in space can be accomplished. Modern (1982) high speed digital computers are vastly superior to the calculating devices present in the ninteen forties or fifties. In addition, at the present time, quite extensive software programs have been developed. Good use of the computer facilities at the University of Alberta was made throughout the thesis.

A total of four chapters and five appendices comprise the thesis. The main text of the thesis following Chapter 1 is divided into two major parts. These consist of Chapter 2 and Chapter 3.

Chapter 2 is concerned with deriving and investigating the free mode field solution associated with the sheath helix surrounding a lossy coaxial rod. Approximate solutions of the wave numbers, which determine the radial and axial spatial dependences of the field components, are given. Graphs showing the approximate radial dependence

of the electric and magnetic field component magnitudes are presented.

Chapter 3 makes use of the free mode field solution discussed in the preceding chapter in order to investigate the power dissipation which occurs within the lossy coaxial rod. Exact equations for this power dissipation are developed. Unfortunately, these equations are discovered to be very difficult to numerically evaluate. In order to overcome this limitation, several different types of approximate power dissipation equations are derived and investigated.

The final chapter contained in the thesis is Chapter 4. This consists of a summary and a statement of the important conclusions obtained in the three preceding chapters.

It is possible to read Chapters 1 - 4 without referring to the appendices. However, in order to obtain as good an understanding as possible of the chapters, it is recommended that the five appendices contained in the thesis are read.

The first appendix is Appendix A. It provides a useful listing in one location of many mathematical identities and relations of Bessel functions, which are of the integral orders 0 and 1. These properties have been used many times throughout the thesis.

As has been previously mentioned in section 1.1, the objective of this thesis is to develop as comprehensive a theory as possible of the free mode field solution for the sheath helix surrounding a lossy coaxial rod, and then to investigate the power dissipation occurring within the lossy rod. Some information about this configuration will be obtained by examining other structures, which, from a field theory point of view, are not as complicated. Two configurations which immediately come to mind are to replace the lossy coaxial rod by either a perfectly conducting coaxial rod or by an ideal dielectric (zero conductivity) coaxial rod. In addition, as the radius of the lossy coaxial rod becomes much smaller than the sheath helix radius, or as its electrical properties become similar to those of air, one intuitively expects that the free mode field solution will tend to behave like that of the air-filled sheath helix. Therefore, an examination of the simplest configuration, when air completely fills the interior and exterior regions of the sheath helix, is justified.

Appendix B discusses the free mode field components and dispersion equation for the empty sheath helix. Graphs of the radial wave number solution are presented. Approximate equations which simplify calculating the radial and axial wave numbers are

given. Radial dependence graphs of all the electric and magnetic field components have been prepared.

Next comes Appendix C, which is concerned with the sheath helix surrounding a perfectly conducting coaxial rod. The free mode dispersion equation and field components are listed and discussed. Graphs of the radial wave number solution have been prepared, and approximate equations to simplify the calculation of the radial and axial wave numbers are given. The radial dependence of all the electric and magnetic field components is illustrated by using graphs.

Appendix D discusses the sheath helix surrounding an ideal dielectric coaxial rod. The free mode field solution is listed. Unfortunately, it is difficult to numerically calculate the radial and axial wave numbers solution. To overcome this problem, an approximate free mode field solution, which is obtained from the exact solution by equating the radial and axial wave numbers, is presented. The (single) wave number solution is quite extensively graphed for a wide range of operating frequencies, sheath helix geometries, ideal dielectric coaxial rod geometries, and relative permittivities of the dielectric material. Equations are developed which make it relatively easy to approximately calculate the (single) wave number solution. Graphs showing the radial dependence of the field components associated with the approximate solution are presented.

The final unit of the thesis consists of Appendix E. It contains data tables which show the electrical properties as a function of frequency for several different materials which could possibly be candidates for electromagentic heating. Graphs of the power dissipation associated with these materials are presented in part 3.2.3 of the thesis.

2. Chapter 2. Sheath Helix Surrounding a Lossy Coaxial Rod

This chapter is concerned with investigating from a field theory point of view some properties of electromagnetic waves associated with a sheath helix surrounding a centered lossy rod. The rod has a radius b, such that $0 < b < a < \infty$ is always true, and is idealized as being of infinite axial extent. Its electrical properties are described by a (real) permittivity, ϵ, a permeability equal to that of free space, μ_0, and a conductivity, σ. Free space exists in the gap between the rod surface and the sheath helix surface, and in the entire sheath helix exterior region, $a < r < \infty$. The sheath helix surrounding a lossy coaxial rod is shown in Figures 2.1.

Chute et al. (25) examined the lossy two region sheath helix configuration from the point of view of electromagnetic heating applications. They derived the field components, the dispersion equation, and the separation constant equation, assuming that a different medium was present in each of the two regions $0 \leq r \leq a$ and $a \leq r < \infty$. Each of the two media had its electrical properties characterized by some set μ, ϵ, σ. A small argument representation of the dispersion equation was given, although no attempt was made to obtain numerical solutions of the wave numbers, which determine the radial and axial spatial dependences of the field components. The power dissipation occurring within the region $0 \leq r < a$ due to the axial and angular electric fields was calculated for the special case when the two wave numbers associated with the radial spatial dependence of the fields are both small in magnitude. It was found that the axial electric field makes the dominant contribution toward the ohmic power dissipated within the sheath helix interior region, assuming that the pitch angle is small.

The previously mentioned paper is the only research conducted on the two lossy region sheath helix configuration that the author is aware of. He has no knowledge of any work performed on the three region sheath helix surrounding a lossy coaxial rod configuration.

A brief outline of the present chapter is now given. The free mode field solution for the sheath helix surrounding a lossy coaxial rod will be derived in a relatively detailed manner. All fields will be expressed in terms of the electrical current present on the sheath helix "windings". Some special limiting cases of the free mode field solution will

27

SHEATH HELIX SURROUNDING A
LOSSY COAXIAL ROD

(a) Side View

(b) End View

$$0 < b < a < \infty$$
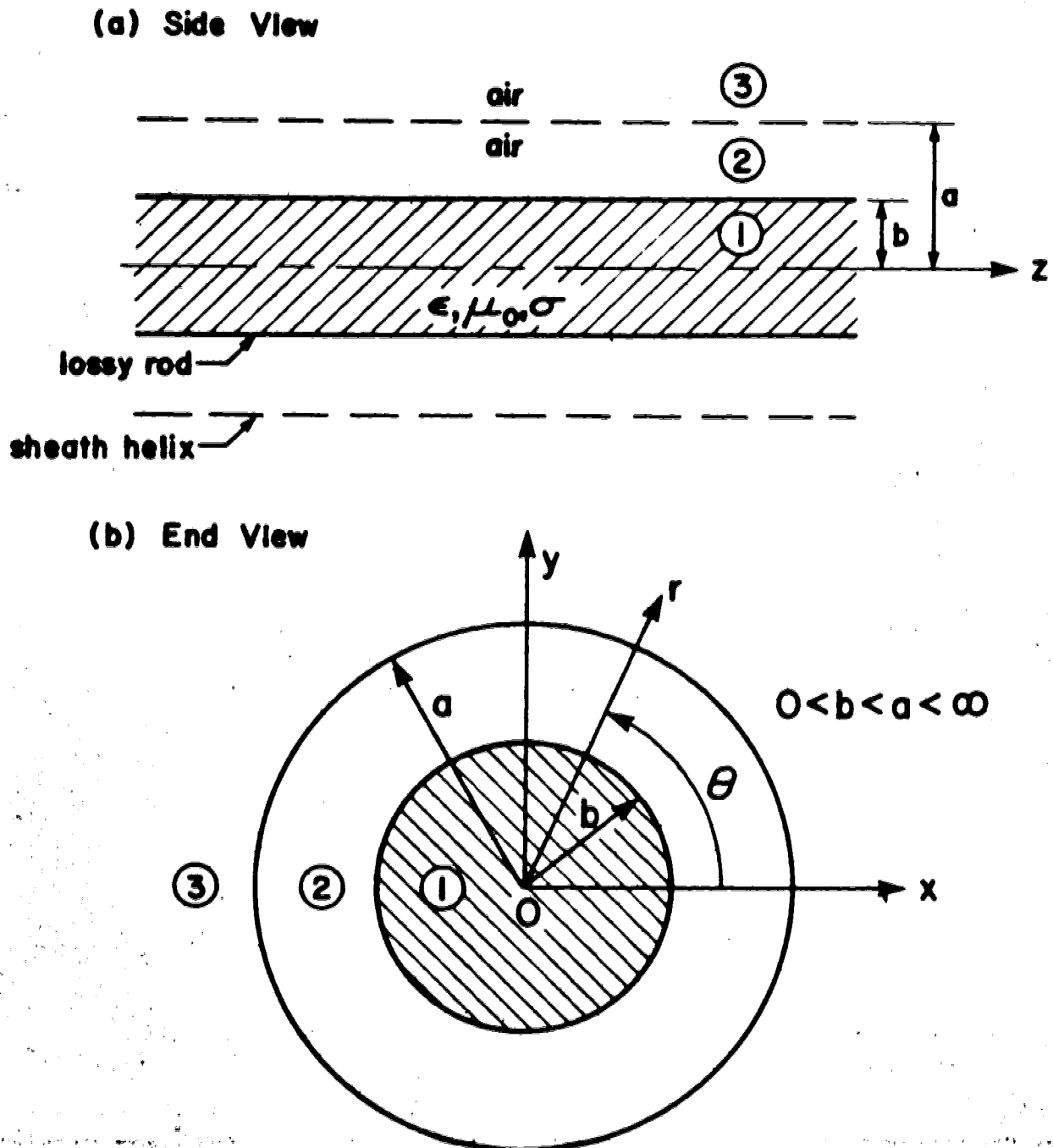
Figures 2.1   Two views of the sheath helix surrounding a lossy coaxial rod.

be studied. These are when the rod radius approaches zero, when the rod conductivity approaches zero, and when the rod conductivity approaches infinity.

It will be seen that the numerical calculation, from the dispersion equation and the separation constant equation, of the wave numbers which determine the radial and axial spatial dependences of the field components, is usually very difficult to accomplish. However, this is not true for the special cases when the magnitudes of the two radial wave numbers are either small or large. Approximations to the dispersion equation and the separation constant equation, and graphs of the radial wave number solution associated with the two air-filled regions have been made for the previously mentioned special cases. These are valid when "*the lossy rod is a good conductor*" or when "*the lossy rod is not a good conductor*". (The meanings of these two terms are later defined in section 2.3.)

Near the end of the chapter, four different sets of graphs showing the approximate radial dependence of the electric and magnetic field component magnitudes are presented. These are based on the cases when the two radial wave numbers are either small or large, for both the circumstances when "the lossy rod is a good conductor" and when "the lossy rod is not a good conductor".

2.1   Derivation and Discussion of the Free Mode Field Solution

2.1.1   Derivation of the Field Components and the Dispersion Equation

A free mode field solution must satisfy the proper form of Maxwell's equations, the appropriate boundary conditions, and all other requirements mentioned in part 1.3.1. To obtain the free mode electric and magnetic field components for the sheath helix surrounding a lossy coaxial rod, Maxwell's equations must be satisfied within the two air-filled regions and within the rod-filled region. In addition, the boundary conditions at the sheath helix surface and at the rod surface must be fulfilled. These act to couple together the fields in each of the three regions. Finally, the requirement of finiteness of the field components in a source-free region and the condition of regularity at infinity for the fields, which is discussed in part 1.3.1, must be met.

There are many different methods which can be used to obtain the electric and magnetic field components in terms of several undetermined constants, which satisfy the appropriate form of Maxwell's equations for the particular configuration of concern.

Harrington (37, pp. 129-131) expresses the electric and magnetic fields in terms of an electric vector potential and a magnetic vector potential. In a homogeneous, source-free region, these potentials satisfy the homogeneous form of the vector Helmholtz equation. Jordan and Balmain (38, pp. 257-258), and Johnson (30, pp. 116-117) use the axial electric and magnetic field components as scalar potential functions. All the other electric and magnetic field components can be calculated from these potential functions. In a homogeneous, source-free region, E_z and H_z satisfy the homogeneous form of the scalar Helmholtz equation.

The procedure which will be followed here, to obtain the free mode field solution for the sheath helix surrounding a lossy coaxial rod, is to express the field components within the air medium and within the medium consisting of the lossy rod material, using *electric and magnetic hertzian potential vector functions.* $\underline{\pi}$ is the electric hertzian potential vector and $\underline{\pi}^*$ is the magnetic hertzian potential vector. *For a cylindrical surface whose generating elements are parallel to the z axis, the total field obtained by linearly combining the partial fields due to* $\underline{\pi} = \pi_z \underline{a}_z$ *and* $\underline{\pi}^* = \pi_z^* \underline{a}_z$, *is so general that a prescribed set of boundary conditions on the surface can be satisfied* (35, pp. 351).

The rod material is assumed to be linear, homogeneous, and isotropic. Its electrical properties are characterized by a (real) permittivity, ϵ, and a nonzero and finite conductivity, σ. In addition, the permeability of free space, $\mu = \mu_0$, is used. No free electrical conduction currents or free electric charges are assumed to be present — the medium consisting of the lossy rod material is source-free. Within this medium, the scalars π_z and π_z^* satisfy the homogeneous form of the scalar Helmholtz equation.

$$\nabla^2 \pi_z + (k^2 \epsilon_r - j \omega \mu_0 \sigma) \pi_z = 0, \qquad \text{and} \qquad (2.1)$$

$$\nabla^2 \pi_z^* + (k^2 \epsilon_r - j \omega \mu_0 \sigma) \pi_z^* = 0, \qquad (2.2)$$

where $k^2 = \omega^2 \mu_0 \epsilon_0$ (35, pp. 32).

The form of these equations which is appropriate for the medium consisting of air is readily obtained by using $\epsilon_r = 1$ and $\sigma = 0$. In order that no confusion arises over the hertzian potential function solutions and the electric and magnetic field solutions associated with the lossy rod material medium, and between the air medium solutions, these latter solutions will be denoted by the symbol "$\#$".

$$\nabla^2 \pi_z\# + k^2 \pi_z\# = 0 \qquad \text{and} \qquad (2.3)$$

$$\nabla^2 \pi_z\#^* + k^2 \pi_z\#^* = 0 \qquad (2.4)$$

is the corresponding form of equations 2.1 and 2.2 which is appropriate for the air medium.

The electric and magnetic fields are expressed in terms of solutions to equations 2.1 - 2.4 according to

$$\underline{E} = \nabla \times (\nabla \times \pi_z \underline{a}_z) - j \omega \mu_0 (\nabla \times \pi_z^* \underline{a}_z), \qquad (2.5)$$

$$\underline{H} = \nabla \times [(\sigma + j \omega \epsilon) \pi_z \underline{a}_z] + \nabla \times (\nabla \times \pi_z^* \underline{a}_z), \qquad (2.6)$$

$$\underline{E}\# = \nabla \times (\nabla \times \pi_z\# \underline{a}_z) - j \omega \mu_0 (\nabla \times \pi_z\#^* \underline{a}_z), \text{ and} \qquad (2.7)$$

$$\underline{H}\# = \nabla \times (j \omega \epsilon_0 \pi_z\# \underline{a}_z) + \nabla \times \nabla \times (\pi_z\#^* \underline{a}_z). \qquad (2.8)$$

(35, pp. 32.) It was mentioned in part 1.3.1 that the desired field components will not depend on θ. This also means that the hertzian potentials are angularly independent. Making use of the curl relation and the Laplacian relation in cylindrical coordinates (for example, see 18, pp. 572), equations 2.1 - 2.8 can be rewritten in a more convenient manner.

$$\frac{1}{r} \frac{\partial}{\partial r} \left(r \frac{\partial \pi_z}{\partial r} \right) + \frac{\partial^2 \pi_z}{\partial z^2} + (k^2 \epsilon_r - j \omega \mu_0 \sigma) \pi_z = 0, \qquad (2.9)$$

$$\frac{1}{r} \frac{\partial}{\partial r} \left(r \frac{\partial \pi_z^*}{\partial r} \right) + \frac{\partial^2 \pi_z^*}{\partial z^2}$$

$$+ (k^2 \epsilon_r - j \omega \mu_0 \sigma) \pi_z^* = 0, \tag{2.10}$$

$$\frac{1}{r} \frac{\partial}{\partial r} \left(r \frac{\partial \pi_z'}{\partial r} \right) + \frac{\partial^2 \pi_z'}{\partial z^2} + k^2 \pi_z' = 0, \tag{2.11}$$

$$\frac{1}{r} \frac{\partial}{\partial r} \left(r \frac{\partial \pi_z'^*}{\partial r} \right) + \frac{\partial^2 \pi_z'^*}{\partial z^2} + k^2 \pi_z'^* = 0, \tag{2.12}$$

$$\underline{E} = \frac{\partial^2 \pi_z}{\partial z \partial r} \underline{a}_r + j \omega \mu_0 \frac{\partial \pi_z^*}{\partial r} \underline{a}_\theta - \frac{1}{r} \frac{\partial}{\partial r} \left(r \frac{\partial \pi_z}{\partial r} \right) \underline{a}_z, \tag{2.13}$$

$$\underline{H} = \frac{\partial^2 \pi_z^*}{\partial z \partial r} \underline{a}_r - (\sigma + j \omega \epsilon) \frac{\partial \pi_z}{\partial r} \underline{a}_\theta$$

$$- \frac{1}{r} \frac{\partial}{\partial r} \left(r \frac{\partial \pi_z^*}{\partial r} \right) \underline{a}_z, \tag{2.14}$$

$$\underline{E}' = \frac{\partial^2 \pi_z'}{\partial z \partial r} \underline{a}_r + j \omega \mu_0 \frac{\partial \pi_z'^*}{\partial r} \underline{a}_\theta$$

$$- \frac{1}{r} \frac{\partial}{\partial r} \left(r \frac{\partial \pi_z'}{\partial r} \right) \underline{a}_z, \quad \text{and} \tag{2.15}$$

$$\underline{H}' = \frac{\partial^2 \pi_z'^*}{\partial z \partial r} \underline{a}_r - j \omega \epsilon_0 \frac{\partial \pi_z'}{\partial r} \underline{a}_\theta$$

$$- \frac{1}{r} \frac{\partial}{\partial r} \left(r \frac{\partial \pi_z'^*}{\partial r} \right) \underline{a}_z. \tag{2.16}$$

As was mentioned in part 1.3.1, it is desired to have all the axial electric and magnetic field components characterized either by a $\cos \beta z$ or by a $\cos \beta' z$ axial dependence. Equations 2.13 – 2.16 make it clear that the hertzian potentials must have this same type of axial dependence. Therefore, the spatial dependence of the electric and magnetic hertzian potentials is

$$\pi_z(r, z) = \ell(r) \cos\beta z, \qquad (2.17)$$

$$\pi_z^*(r, z) = \ell^*(r) \cos\beta z, \qquad (2.18)$$

$$\pi_z\#(r, z) = \ell\#(r) \cos\beta\# z, \quad \text{and} \qquad (2.19)$$

$$\pi_z\#^*(r, z) = \ell\#^*(r) \cos\beta\# z. \qquad (2.20)$$

$\ell(r)$, $\ell^*(r)$, $\ell\#(r)$, and $\ell\#^*(r)$ are four unknown functions of the radial distance, which will now be determined. Substituting equations 2.17 – 2.20 into the corresponding equation of the set 2.9 – 2.12, yields

$$r^2 \frac{d^2\ell(r)}{dr^2} + r \frac{d\ell(r)}{dr} - h^2 r^2 \ell(r) = 0, \qquad (2.21)$$

$$r^2 \frac{d^2\ell^*(r)}{dr^2} + r \frac{d\ell^*(r)}{dr} - h^2 r^2 \ell^*(r) = 0, \qquad (2.22)$$

$$r^2 \frac{d^2\ell\#(r)}{dr^2} + r \frac{d\ell\#(r)}{dr} - h\#^2 r^2 \ell\#(r) = 0, \quad \text{and} \qquad (2.23)$$

$$r^2 \frac{d^2\ell\#^*(r)}{dr^2} + r \frac{d\ell\#^*(r)}{dr} - h\#^2 r^2 \ell\#^*(r) = 0. \qquad (2.24)$$

h^2 and $h\#^2$ are defined according to

$$\beta^2 = h^2 + (k^2 \epsilon_r - j \omega \mu_0 \sigma), \quad \text{and}$$
$$\qquad (2.25)$$
$$\beta\#^2 = h\#^2 + k^2.$$

Equation A.1 shows that equations 2.21 – 2.24 are the modified Bessel equations of order zero. For example,

$$\lambda(r) = A\, I_0(hr) + C\, K_0(hr),$$

where A and C are constants, is the general solution of equation 2.21. I_0 is the modified Bessel function of the first kind of order zero, while K_0 is the modified Bessel function of the second kind of order zero. Since the solutions to equations 2.21 – 2.24 are known, the solutions to equations 2.17 – 2.20 can be listed.

$$\pi_z(r, z) = [A\, I_0(hr) + C\, K_0(hr)]\cos\beta z, \qquad (2.26)$$

$$\pi_z^*(r, z) = [B\, I_0(hr) + D\, K_0(hr)]\cos\beta z, \qquad (2.27)$$

$$\pi_z\#(r, z) = [A\#\, I_0(h\#r) + C\#\, K_0(h\#r)]\cos\beta\#z, \text{ and} \quad (2.28)$$

$$\pi_z\#^*(r, z) = [B\#\, I_0(h\#r) + D\#\, K_0(h\#r)]\cos\beta\#z; \qquad (2.29)$$

where the constants A, B, C, D, $A\#$, $B\#$, $C\#$, and $D\#$ are independent of the spatial coordinates.

It is now convenient to alter the notation used on equations 2.9 – 2.16 and 2.25 – 2.29. This is done so that the field components associated with each of the two different media now refer to each of the three regions associated with the sheath helix surrounding a lossy coaxial rod. Subscripts "1", "2", and "3" will be used on the field components and on the undetermined constants. "1" refers to the rod-filled region, $0 \le r \le b$, "2" refers to the first air-filled region, $b \le r \le a$, and "3" refers to the second air-filled region, $a \le r < \infty$.

Combining equations 2.26 – 2.29 with equations 2.13 – 2.16, making use of the Bessel function relations A.5 – A.8, means that the electric and magnetic field components in each of the three regions are obtained in terms of several undetermined constants.

$$E_{r1} = -\beta h_1 [A_1 I_1(h_1 r) - C_1 K_1(h_1 r)]\sin\beta z, \qquad (2.30)$$

$$E_{\theta 1} = j\omega\mu_0 h_1 \cdot$$

$$[B_1 I_1(h_1 r) - D_1 K_1(h_1 r)]\cos\beta z, \qquad (2.31)$$

$$E_{z1} = - h_1^2 [A_1 \, I_0(h_1 r) + C_1 \, K_0(h_1 r)] \cos\beta z, \qquad (2.32)$$

$$H_{r1} = - \beta h_1 [B_1 \, I_1(h_1 r) - D_1 \, K_1(h_1 r)] \sin\beta z, \qquad (2.33)$$

$$H_{\theta 1} = - (\sigma + j \omega \epsilon) h_1 \cdot$$

$$[A_1 \, I_1(h_1 r) - C_1 \, K_1(h_1 r)] \cos\beta z, \qquad (2.34)$$

$$H_{z1} = - h_1^2 [B_1 \, I_0(h_1 r) + D_1 \, K_0(h_1 r)] \cos\beta z, \qquad (2.35)$$

$$E_{rn} = - \beta h_2 [A_n \, I_1(h_2 r) - C_n \, K_1(h_2 r)] \sin\beta z, \qquad (2.36)$$

$$E_{\theta n} = j \omega \mu_0 h_2 \cdot$$

$$[B_n \, I_1(h_2 r) - D_n \, K_1(h_2 r)] \cos\beta z, \qquad (2.37)$$

$$E_{zn} = - h_2^2 [A_n \, I_0(h_2 r) + C_n \, K_0(h_2 r)] \cos\beta z, \qquad (2.38)$$

$$H_{rn} = - \beta h_2 [B_n \, I_1(h_2 r) - D_n \, K_1(h_2 r)] \sin\beta z, \qquad (2.39)$$

$$H_{\theta n} = - j \omega \epsilon_0 h_2 \cdot$$

$$[A_n \, I_1(h_2 r) - C_n \, K_1(h_2 r)] \cos\beta z, \quad \text{and} \qquad (2.40)$$

$$H_{zn} = - h_2^2 [B_n \, I_0(h_2 r) + D_n \, K_0(h_2 r)] \cos\beta z, \qquad (2.41)$$

where n = 2 and 3.

The reader should understand why $\beta_1^2 = \beta^2$ has been used in equations 2.30 - 2.35. This anticipates the fact that the boundary conditions for the electric and magnetic fields at the lossy rod surface must be satisfied for all values of z, where $-\infty < z < \infty$. (These boundary conditions will be discussed shortly. It will be mentioned here they require that

$$E_{\theta 1}\Big|_{r=b} = E_{\theta 2}\Big|_{r=b}, \quad E_{z1}\Big|_{r=b} = E_{z2}\Big|_{r=b},$$

$$H_{\theta 1}\Big|_{r=b} = H_{\theta 2}\Big|_{r=b}, \quad \text{and} \quad H_{z1}\Big|_{r=b} = H_{z2}\Big|_{r=b}.$$

Equations 2.31, 2.32, 2.34, 2.35, 2.37, 2.38, 2.40, and 2.41 show that it is only if the square of the axial wave number associated with the lossy rod material medium equals the square of the axial wave number associated with the air medium, that it is possible to satisfy these boundary conditions.)

In equations 2.30 – 2.41, h_1 is the radial wave number associated with the rod material medium, while h_2 is the radial wave number associated with the air medium. As was previously mentioned, the axial wave number, β, is the same for both the rod material medium and for the air medium.

The separation constant equation is a modified form of equations 2.25. It is

$$\beta^2 = h_1^2 + (k^2 \epsilon_r - j \omega \mu_0 \sigma) = h_2^2 + k^2. \qquad (2.42)$$

Equation 2.42 provides a relationship between the two radial wave numbers and the axial wave number.

A total of twelve undetermined constants and three undetermined wave numbers appear in equations 2.30 – 2.41. Two of the constants associated with the rod-filled region can be immediately set to equal zero. No free electrical currents or free electric charge is present in this region. Therefore, the conditions for a free mode field solution in this source-free region, as mentioned in part 1.3.1, require that all the electric and magnetic field components be finite throughout $0 \leq r \leq b$. Equations A.28 and A.29, the small argument Bessel function representations, show that $K_0(h_1 r)$ and $K_1(h_1 r)$ are unbounded at $r = 0$. One is therefore forced to choose $C_1 = D_1 = 0$.

It will now be shown that two of the constants associated with the fields in the region $a \leqslant r < \infty$ are also required to vanish. No sources of the fields are assumed to be located at $r \to \infty$. The condition of regularity at infinity, as mentioned in part 1.3.1, can therefore be imposed. Assuming that the radial wave number h_2 is nonzero, when the radial distance is sufficiently large, it will be true that $|h_2| r \gg 1$. Now the large argument Bessel function representations are justified. Equations A.36 – A.39 show that the exponential dependence of $I_0(h_2 r)$ and $I_1(h_2 r)$ is $e^{+h_2 r}$, while that of $K_0(h_2 r)$ and $K_1(h_2 r)$ is $e^{-h_2 r}$. It will now be assumed that the real part of the complex quantity h_2 is positive. (This assumption is discussed in the next paragraph.) In order to satisfy the condition of regularity at infinity, one is forced to choose $A_3 = B_3 = 0$. At sufficiently large radial distances, all the fields exterior to the sheath helix surface will now be rapidly exponentially attenuated.

In section B.2 it is mentioned that the (single) radial wave number for the empty sheath helix, h^a, is real positive, and that the radial dependence of the exterior region fields is given by $K_0(h^a r)$ and $K_1(h^a r)$. In the limit as the lossy rod radius approaches zero, or as the electrical properties of the lossy rod approach those of air, the sheath helix surrounding a lossy coaxial rod configuration is expected to reduce to the empty sheath helix configuration. This leads to the choice $Re[h_2] > 0$, so that the radial dependence of the fields in the region $a \leqslant r < \infty$ is given by $K_0(h_2 r)$ and $K_1(h_2 r)$.

Eight undetermined constants and three undetermined wave numbers remain in equations 2.30 – 2.41. There are four boundary conditions which must be satisfied at the sheath helix surface. These are specified by equations 1.6 – 1.9. Four additional boundary conditions exist at the rod surface. They are statements of the fact that the electric and magnetic fields tangential to an interface must be continuous, whenever the conductivities of the two regions forming the interface are both finite. It was mentioned in part 1.3.1 that if the conductivity of one of the regions is assumed to be infinite, the electric fields tangential to the interface must be zero while the tangential magnetic fields are discontinuous, assuming that an electrical current is present at the surface of the interface. However, this behavior cannot occur at the lossy rod surface because the rod

conductivity has been restricted so that it cannot be infinite.) The boundary conditions at the surface of the lossy rod are

$$E_{\theta 1}\Big|_{r=b} = E_{\theta 2}\Big|_{r=b} \, , \qquad\qquad (2.43)$$

$$E_{z1}\Big|_{r=b} = E_{z2}\Big|_{r=b} \, , \qquad\qquad (2.44)$$

$$H_{\theta 1}\Big|_{r=b} = H_{\theta 2}\Big|_{r=b} \, , \text{ and} \qquad (2.45)$$

$$H_{z1}\Big|_{r=b} = H_{z2}\Big|_{r=b} \, . \qquad\qquad (2.46)$$

Requiring that equations 2.30 – 2.41, with $C_1 = D_1 = A_3 = B_3 = 0$, satisfy equations 1.6 – 1.9 and equations 2.43 – 2.46, all the field components are known in terms of a single undetermined constant plus three undetermined wave numbers, and the *dispersion equation* is obtained. The dispersion equation is sometimes called the *determinantal equation* or the *characteristic equation*. It arises because for a set of m homogeneous linear equations involving m unknowns, if a solution other than the trivial one is desired, the determinant of the coefficients of the unknowns must vanish. In short, for our purposes, the dispersion equation arises from the necessity that all eight of the undetermined constants must not each be zero. Using the previously mentioned equations and performing a large amount of algebra, which is straightforward but lengthy, seven of the constants can be expressed in terms of a single one, and the dispersion equation is obtained. A_1 is now the single undetermined constant. (A discussion of the solution to the two radial wave numbers and the axial wave number is given in part 2.1.2.)

Summary of the Fields in Terms of A_1

Region 1 ($0 \leqslant r \leqslant b$)

$$E_{r1} = -\frac{A_1}{a^2} \beta a \ h_1 a \ I_1(h_1 r) \ \sin\beta z, \qquad (2.47)$$

$$E_{\theta 1} = \frac{A_1}{a^2} (ka \ cotan\psi)^2 \ tan\psi \ \cdot$$

$$\frac{h_1 a}{h_2 a} \frac{K_1(h_2 a)}{K_0(h_2 a)} I_1(h_1 r) \ cos\beta z \ \cdot$$

$$[h_1 a \ I_0(h_1 b) \ K_1(h_2 b) \qquad (2.48)$$

$$+ (\epsilon_r - j \ \sigma/\omega\epsilon_0) \ h_2 a \ I_1(h_1 b) \ K_0(h_2 b)] \ \cdot$$

$$1/[h_1 a \ I_0(h_1 b) \ K_1(h_2 b) + h_2 a \ I_1(h_1 b) \ K_0(h_2 b)],$$

$$E_{z1} = -\frac{A_1}{a^2} (h_1 a)^2 \ I_0(h_1 r) \ cos\beta z, \qquad (2.49)$$

$$H_{r1} = j \ \frac{A_1}{a^2} \frac{ka \ cotan\psi}{120\pi} \ \beta a \ \cdot$$

$$\frac{h_1 a}{h_2 a} \frac{K_1(h_2 a)}{K_0(h_2 a)} I_1(h_1 r) \ \sin\beta z \ \cdot \qquad (2.50)$$

$$[h_1 a \ I_0(h_1 b) \ K_1(h_2 b)$$

$$+ (\epsilon_r - j \ \sigma/\omega\epsilon_0) \ h_2 a \ I_1(h_1 b) \ K_0(h_2 b)] \ \cdot$$

$$1/[h_1 a \ I_0(h_1 b) \ K_1(h_2 b) + h_2 a \ I_1(h_1 b) \ K_0(h_2 b)],$$

$$H_{\theta 1} = -j \frac{A_1}{a^2} \frac{ka \cot an\psi}{120\pi} \tan\psi \ (\epsilon_r - j \ \sigma/\omega\epsilon_0) \cdot$$

$$h_1 a \ I_1(h_1 r) \ \cos\beta z, \quad \text{and} \tag{2.51}$$

$$H_{z1} = j \frac{A_1}{a^2} \frac{ka \cot an\psi}{120\pi} \cdot$$

$$\frac{(h_1 a)^2}{h_2 a} \ \frac{K_1(h_2 a)}{K_0(h_2 a)} \ I_0(h_1 r) \ \cos\beta z \cdot$$

$$[h_1 a \ I_0(h_1 b) \ K_1(h_2 b) \tag{2.52}$$

$$+ \ (\epsilon_r - j \ \sigma/\omega\epsilon_0) \ h_2 a \ I_1(h_1 b) \ K_0(h_2 b)] \cdot$$

$$1/[h_1 a \ I_0(h_1 b) \ K_1(h_2 b) + h_2 a \ I_1(h_1 b) \ K_0(h_2 b)].$$

Region 2 $(b \leq r \leq a)$

$$E_{r2} = - \frac{A_1}{a^2} \ \beta a \ h_1 b \ \sin\beta z \cdot$$

$$[I_1(h_2 r) \cdot (h_1 a \ I_0(h_1 b) \ K_1(h_2 b)$$

$$+ \ (\epsilon_r - j \ \sigma/\omega\epsilon_0) \ h_2 a \ I_1(h_1 b) \ K_0(h_2 b)) \tag{2.53}$$

$$- \ K_1(h_2 r) \cdot (h_1 a \ I_0(h_1 b) \ I_1(h_2 b)$$

$$- \ (\epsilon_r - j \ \sigma/\omega\epsilon_0) \ h_2 a \ I_0(h_2 b) \ I_1(h_1 b))],$$

$$E_{\theta 2} = \frac{A_1}{a^2} (ka \, \cot\psi)^2 \quad \tan\psi \, \frac{h_1 b}{h_2 a} \, \frac{K_1(h_2 a)}{K_0(h_2 a)} \, \cos\beta z \, \cdot$$

$$[I_1(h_2 r) \cdot (h_1 a \, I_0(h_1 b) \, K_1(h_2 b)$$

$$+ \, h_2 a \, I_1(h_1 b) \, K_0(h_2 b))$$

$$- \, K_1(h_2 r) \cdot (h_1 a \, I_0(h_1 b) \, I_1(h_2 b) \qquad (2.54)$$

$$- \, h_2 a \, I_0(h_2 b) \, I_1(h_1 b))] \cdot$$

$$[h_1 a \, I_0(h_1 b) \, K_1(h_2 b)$$

$$+ \, (\epsilon_r - j \, \sigma/\omega\epsilon_0) \, h_2 a \, I_1(h_1 b) \, K_0(h_2 b)] \cdot$$

$$1/[h_1 a \, I_0(h_1 b) \, K_1(h_2 b) + h_2 a \, I_1(h_1 b) \, K_0(h_2 b)],$$

$$E_{z2} = - \frac{A_1}{a^2} \, h_1 b \, h_2 a \, \cos\beta z \, \cdot$$

$$[I_0(h_2 r) \cdot (h_1 a \, I_0(h_1 b) \, K_1(h_2 b)$$

$$+ \, (\epsilon_r - j \, \sigma/\omega\epsilon_0) \, h_2 a \, I_1(h_1 b) \, K_0(h_2 b)) \qquad (2.55)$$

$$+ \, K_0(h_2 r) \cdot (h_1 a \, I_0(h_1 b) \, I_1(h_2 b)$$

$$- \, (\epsilon_r - j \, \sigma/\omega\epsilon_0) \, h_2 a \, I_0(h_2 b) \, I_1(h_1 b))].$$

$$H_{r2} = j \frac{A_1}{a^2} \frac{ka \cot an\phi}{120\pi} \beta a \frac{h_1 b}{h_2 a} \frac{K_1(h_2 a)}{K_0(h_2 a)} \sin\beta z \cdot$$

$$[h_1 a \ I_0(h_1 b) \ K_1(h_2 b)$$

$$+ (\epsilon_r - j \ \sigma/\omega\epsilon_0) \ h_2 a \ I_1(h_1 b) \ K_0(h_2 b)] \cdot$$

$$(1/[h_1 a \ I_0(h_1 b) \ K_1(h_2 b) + h_2 a \ I_1(h_1 b) \ K_0(h_2 b)]) \cdot$$

$$[I_1(h_2 r) \cdot (h_1 a \ I_0(h_1 b) \ K_1(h_2 b) \hspace{2cm} (2.56)$$

$$+ h_2 a \ I_1(h_1 b) \ K_0(h_2 b))$$

$$- K_1(h_2 r) \cdot (h_1 a \ I_0(h_1 b) \ I_1(h_2 b)$$

$$- h_2 a \ I_0(h_2 b) \ I_1(h_1 b))].$$

$$H_{\theta 2} = - j \frac{A_1}{a^2} \frac{ka \cot an\phi}{120\pi} \tan\phi \ h_1 b \ \cos\beta z \cdot$$

$$[I_1(h_2 r) \cdot (h_1 a \ I_0(h_1 b) \ K_1(h_2 b)$$

$$+ (\epsilon_r - j \ \sigma/\omega\epsilon_0) \ h_2 a \ I_1(h_1 b) \ K_0(h_2 b)) \hspace{1.5cm} (2.57)$$

$$- K_1(h_2 r) \cdot (h_1 a \ I_0(h_1 b) \ I_1(h_2 b)$$

$$- (\epsilon_r - j \ \sigma/\omega\epsilon_0) \ h_2 a \ I_0(h_2 b) \ I_1(h_1 b))], \quad \text{and}$$

$$H_{z2} = j \frac{A_1}{a^2} \frac{ka \cot an\phi}{120\pi} \ h_1 b \ \frac{K_1(h_2 a)}{K_0(h_2 a)} \ \cos\beta z \cdot$$

$$[h_1 a \ I_0(h_1 b) \ K_1(h_2 b) \hspace{2cm} (2.58)$$

$$+ (\epsilon_r - j \ \sigma/\omega\epsilon_0) \ h_2 a \ I_1(h_1 b) \ K_0(h_2 b)] \cdot$$

$$(1/[h_1 a \ I_0(h_1 b) \ K_1(h_2 b) + h_2 a \ I_1(h_1 b) \ K_0(h_2 b)]) \cdot$$

$$[I_0(h_2 r) \cdot (h_1 a \ I_0(h_1 b) \ K_1(h_2 b) \qquad\qquad (2.58)$$

(continued)

$$+ h_2 a \langle I_1(h_1 b) \ K_0(h_2 b))$$

$$+ K_0(h_2 r) \cdot (h_1 a \ I_0(h_1 b) \ I_1(h_2 b)$$

$$- h_2 a \ I_0(h_2 b) \ I_1(h_1 b))].$$

Region 3 ($a \leq r < \infty$)

$$E_{r3} = \frac{A_1}{a^2} \beta a \ h_1 b \ \frac{K_1(h_2 r)}{K_0(h_2 a)} \sin\beta z \cdot$$

$$[I_0(h_2 a) \cdot (h_1 a \ I_0(h_1 b) \ K_1(h_2 b)$$

$$+ (\epsilon_r - j \ \sigma/\omega\epsilon_0) \ h_2 a \ I_1(h_1 b) \ K_0(h_2 b)) \qquad (2.59)$$

$$+ K_0(h_2 a) \cdot (h_1 a \ I_0(h_1 b) \ I_1(h_2 b)$$

$$- (\epsilon_r - j \ \sigma/\omega\epsilon_0) \ h_2 a \ I_0(h_2 b) \ I_1(h_1 b))].$$

$$E_{\theta 3} = \frac{A_1}{a^2} \tan\psi \ h_1 b \ h_2 a \ \frac{K_1(h_2 r)}{K_1(h_2 a)} \cos\beta z \cdot$$

$$[I_0(h_2 a) \cdot (h_1 a \ I_0(h_1 b) \ K_1(h_2 b) \qquad\qquad (2.60)$$

$$+ (\epsilon_r - j \ \sigma/\omega\epsilon_0) \ h_2 a \ I_1(h_1 b) \ K_0(h_2 b))$$

$$+ K_0(h_2 a) \cdot (h_1 a \ I_0(h_1 b) \ I_1(h_2 b)$$

$$- (\epsilon_r - j \ \sigma/\omega\epsilon_0) \ h_2 a \ I_0(h_2 b) \ I_1(h_1 b))].$$

$$E_{z3} = -\frac{A_1}{a^2} h_1 b\, h_2 a\, \frac{K_0(h_2 r)}{K_0(h_2 a)} \cos\beta z\, \cdot$$

$$[I_0(h_2 a) \cdot (h_1 a\, I_0(h_1 b)\, K_1(h_2 b)$$

$$+ (\epsilon_r - j\, \sigma/\omega\epsilon_0)\, h_2 a\, I_1(h_1 b)\, K_0(h_2 b)) \qquad (2.61)$$

$$+ K_0(h_2 a) \cdot (h_1 a\, I_0(h_1 b)\, I_1(h_2 b)$$

$$- (\epsilon_r - j\, \sigma/\omega\epsilon_0)\, h_2 a\, I_0(h_2 b)\, I_1(h_1 b))],$$

$$H_{r3} = j\, \frac{A_1}{a^2}\, \frac{\beta a}{120\pi}\, \frac{h_1 b\, h_2 a}{ka\, \cot an\psi}\, \frac{K_1(h_2 r)}{K_1(h_2 a)} \sin\beta z\, \cdot$$

$$[I_0(h_2 a) \cdot (h_1 a\, I_0(h_1 b)\, K_1(h_2 b)$$

$$+ (\epsilon_r - j\, \sigma/\omega\epsilon_0)\, h_2 a\, I_1(h_1 b)\, K_0(h_2 b)) \qquad (2.62)$$

$$+ K_0(h_2 a) \cdot (h_1 a\, I_0(h_1 b)\, I_1(h_2 b)$$

$$- (\epsilon_r - j\, \sigma/\omega\epsilon_0)\, h_2 a\, I_0(h_2 b)\, I_1(h_1 b))],$$

$$H_{\theta 3} = j\, \frac{A_1}{a^2}\, \frac{ka\, \cot an\psi}{120\pi}\, \tan\psi\, h_1 b\, \frac{K_1(h_2 r)}{K_0(h_2 a)} \cos\beta z\, \cdot$$

$$[I_0(h_2 a) \cdot (h_1 a\, I_0(h_1 b)\, K_1(h_2 b)$$

$$+ (\epsilon_r - j\, \sigma/\omega\epsilon_0)\, h_2 a\, I_1(h_1 b)\, K_0(h_2 b)) \qquad (2.63)$$

$$+ K_0(h_2 a) \cdot (h_1 a\, I_0(h_1 b)\, I_1(h_2 b)$$

$$- (\epsilon_r - j\, \sigma/\omega\epsilon_0)\, h_2 a\, I_0(h_2 b)\, I_1(h_1 b))], \quad \text{and}$$

$$H_{z3} = -j \frac{A_1}{a^2} \frac{1}{120\pi} \frac{h_1 b (h_2 a)^2}{ka \cot an\psi} \frac{K_0(h_2 r)}{K_1(h_2 a)} \cos\beta z \cdot$$

$$[I_0(h_2 a) \cdot (h_1 a I_0(h_1 b) K_1(h_2 b)$$

$$+ (\epsilon_r - j \sigma/\omega\epsilon_0) h_2 a I_1(h_1 b) K_0(h_2 b)) \tag{2.64}$$

$$+ K_0(h_2 a) \cdot (h_1 a I_0(h_1 b) I_1(h_2 b)$$

$$- (\epsilon_r - j \sigma/\omega\epsilon_0) h_2 a I_0(h_2 b) I_1(h_1 b))].$$

The dispersion equation which results for the sheath helix surrounding a lossy coaxial rod is the following.

Summary of the Dispersion Equation

$$(\frac{ka \cot an\psi}{h_2 a})^2 = \frac{K_0(h_2 a)}{K_1(h_2 a)} (h_1 a I_0(h_1 b) K_1(h_2 b)$$

$$+ h_2 a I_1(h_1 b) K_0(h_2 b)) \cdot (1/[h_1 a I_0(h_1 b) K_1(h_2 b)$$

$$+ (\epsilon_r - j \sigma/\omega\epsilon_0) h_2 a I_1(h_1 b) K_0(h_2 b)]) \cdot$$

$$[I_0(h_2 a) \cdot (h_1 a I_0(h_1 b) K_1(h_2 b) \tag{2.65}$$

$$+ (\epsilon_r - j \sigma/\omega\epsilon_0) h_2 a I_1(h_1 b) K_0(h_2 b))$$

$$+ K_0(h_2 a) \cdot (h_1 a I_0(h_1 b) I_1(h_2 b)$$

$$- (\epsilon_r - j \sigma/\omega\epsilon_0) h_2 a I_0(h_2 b) I_1(h_1 b))] \cdot$$

$$1/[I_1(h_2 a) \cdot (h_1 a I_0(h_1 b) K_1(h_2 b) + h_2 a I_1(h_1 b) K_0(h_2 b))$$

$$- K_1(h_2 a) \cdot (h_1 a I_0(h_1 b) I_1(h_2 b) - h_2 a I_0(h_2 b) I_1(h_1 b))].$$

where $0 < ka \cot\psi < \infty$, $0 < b/a < 1$, $\epsilon_r > 1$, and $\sigma/\omega\epsilon_0 > 0$.

In the course of carrying out the calculations to obtain equations 2.47 - 2.64, it was necessary to make use of relation A.25, which was derived from the modified Bessel function Wronskian identity, equation 2.65, which is the dispersion equation, and the equality $\sqrt{\mu_0/\epsilon_0} = 120\pi$ (Ω).

The single remaining constant which appears in equations 2.47 - 2.64, A_1, can be expressed in terms of the electrical current present on the sheath helix "windings". As was mentioned in part 1.3.1, it is assumed that the physical helix is excited in such a manner that current with no angular dependence and $\cos\beta z$ axial dependence exists on the windings. (This assumption justifies the type of angular and axial dependences used in the hertzian potentials for the sheath helix surrounding a lossy coaxial rod, equations 2.26 - 2.29.) For the sheath helix, this means that there will be an electrical surface current at $r = a$ of the type

$$\underline{K} = K_{||}\,\underline{a}_{||} = \jmath_{||}\cos\beta z\,\underline{a}_{||}, \quad \text{where} \quad \jmath_{||}\;(A/m)$$

is a constant with respect to the spatial coordinates. In part 1.3.1, the discontinuity of the magnetic field at an interface having a surface current is discussed. Applying this concept to the sheath helix surface results in

$$\underline{a}_r \times (\underline{H}_3\big|_{r=a} - \underline{H}_2\big|_{r=a}) = \underline{K}, \quad \text{or}$$

$$- (H_{z3}\big|_{r=a} - H_{z2}\big|_{r=a})\,\underline{a}_\theta$$

$$+ (H_{\theta 3}\big|_{r=a} - H_{\theta 2}\big|_{r=a})\,\underline{a}_z \qquad (2.66)$$

$$= \jmath_\theta \cos\beta z\,\underline{a}_\theta + \jmath_z \cos\beta z\,\underline{a}_z.$$

It has been assumed that the current at the sheath helix surface has components in both the angular and axial directions, with $\mathcal{J}_\theta$ and $\mathcal{J}_z$ being quantities to be determined. Combining the region 2 and region 3 angular and axial magnetic field components, which are specified by equations 2.57, 2.58, 2.63, and 2.64, with equation 2.66, making use of equation 2.65 and relation A.25 for simplification, $\mathcal{J}_\theta$ and $\mathcal{J}_z$ can be expressed in terms of the constant A_1.

$$\mathcal{J}_\theta = j \frac{A_1}{a^2} \frac{ka \, \cot an\psi}{120\pi} \frac{h_1 b}{h_2 a} \frac{1}{K_0(h_2 a)} \cdot$$

$$(h_1 a \, I_0(h_1 b) \, K_1(h_2 b) \tag{2.67}$$

$$+ \, (\epsilon_r - j \, \sigma/\omega\epsilon_0) \, h_2 a \, I_1(h_1 b) \, K_0(h_2 b)), \quad \text{and}$$

$$\mathcal{J}_z = j \frac{A_1}{a^2} \frac{ka \, \cot an\psi}{120\pi} \tan\psi \frac{h_1 b}{h_2 a} \frac{1}{K_0(h_2 a)} \cdot$$

$$(h_1 a \, I_0(h_1 b) \, K_1(h_2 b) \tag{2.68}$$

$$+ \, (\epsilon_r - j \, \sigma/\omega\epsilon_0) \, h_2 a \, I_1(h_1 b) \, K_0(h_2 b)).$$

From equations 1.5, it is possible to express $\mathcal{J}_{\parallel}$ and $\mathcal{J}_{\perp}$ in terms of $\mathcal{J}_\theta$ and $\mathcal{J}_z$. A_1 can now be related to the electrical current present on the sheath helix "windings". Combining equations 1.5 with equation 2.67 and equation 2.68 yields

$$A_1 = - j \, \mathcal{J}_{\parallel} \, a^2 \frac{120\pi}{ka \, \cot an\psi} \cos\psi \frac{h_2 a}{h_1 b} K_0(h_2 a) \cdot \tag{2.69}$$

$$1/[h_1 a \ I_0(h_1 b) \ K_1(h_2 b)$$

$$+ (\epsilon_r - j \ \sigma/\omega\epsilon_0) \ h_2 a \ I_1(h_1 b) \ K_0(h_2 b)], \quad \text{and}$$

$$\qquad\qquad\qquad\qquad\qquad\qquad\qquad\qquad (2.69)$$

$$\qquad\qquad\qquad\qquad\qquad\qquad\qquad\text{(continued)}$$

$$\mathcal{J}_\perp = 0.$$

$$($$

Since the sheath helix model was defined as having an infinite conductivity at the sheath surface in the direction parallel to the "windings" and zero conductivity in the direction perpendicular to the "windings", it follows that $\mathcal{J}_{||} \neq 0$ and $\mathcal{J}_\perp = 0$. Therefore, equations 2.69 are in good agreement with the definition of the sheath helix model, as one expects.

It is now possible to express all the field components in terms of $\mathcal{J}_{||}$. Equations 2.69 were substituted into equations 2.47 - 2.64, and equation 2.65, the dispersion equation, was used for simplification, in order to derive the following field components, equations 2.70 - 2.87.

Summary of the Final Form of the Field Components

Region 1 ($0 \leq r \leq b$)

$$E_{r1} = j \ \frac{\mathcal{J}_{||}}{b/a} \ \frac{120\pi}{ka \ \cot\psi} \ \cos\psi \ h_2 a \ \beta a \ \cdot$$

$$K_0(h_2 a) \ I_1(h_1 r) \ \sin\beta z \ \cdot \qquad\qquad (2.70)$$

$$1/[h_1 a \ I_0(h_1 b) \ K_1(h_2 b)$$

$$+ (\epsilon_r - j \ \sigma/\omega\epsilon_0) \ h_2 a \ I_1(h_1 b) \ K_0(h_2 b)],$$

$$E_{\theta 1} = -j \ \frac{\mathcal{J}_{||}}{b/a} \ 120\pi \ ka \ \cot\psi \ \sin\psi \ \cdot$$

$$K_1(h_2 a) \ I_1(h_1 r) \ \cos\beta z \ \cdot \qquad\qquad (2.71)$$

$$1/[h_1 a \ I_0(h_1 b) \ K_1(h_2 b) + h_2 a \ I_1(h_1 b) \ K_0(h_2 b)],$$

$$E_{z1} = j \frac{\partial_{H}}{b/a} \frac{120\pi}{ka \cot an\psi} \cos\psi \ h_1 a \ h_2 a \ \cdot$$

$$K_0(h_2 a) \ I_0(h_1 r) \cos\beta z \ \cdot \qquad (2.72)$$

$$1/[h_1 a \ I_0(h_1 b) \ K_1(h_2 b)$$

$$+ (\epsilon_r - j \ \sigma/\omega\epsilon_0) \ h_2 a \ I_1(h_1 b) \ K_0(h_2 b)].$$

$$H_{r1} = \frac{\partial_{H}}{b/a} \cos\psi \ \beta a \ K_1(h_2 a) \ I_1(h_1 r) \sin\beta z \ \cdot \qquad (2.73)$$

$$1/[h_1 a \ I_0(h_1 b) \ K_1(h_2 b) + h_2 a \ I_1(h_1 b) \ K_0(h_2 b)].$$

$$H_{\theta 1} = - \frac{\partial_{H}}{b/a} (\epsilon_r - j \ \sigma/\omega\epsilon_0) \sin\psi \ h_2 a \ \cdot$$

$$K_0(h_2 a) \ I_1(h_1 r) \cos\beta z \ \cdot \qquad (2.74)$$

$$1/[h_1 a \ I_0(h_1 b) \ K_1(h_2 b)$$

$$+ (\epsilon_r - j \ \sigma/\omega\epsilon_0) \ h_2 a \ I_1(h_1 b) \ K_0(h_2 b)], \quad \text{and}$$

$$H_{z1} = \frac{\partial_{H}}{b/a} \cos\psi \ h_1 a \ K_1(h_2 a) \ I_0(h_1 r) \cos\beta z \ \cdot \qquad (2.75)$$

$$1/[h_1 a \ I_0(h_1 b) \ K_1(h_2 b) + h_2 a \ I_1(h_1 b) \ K_0(h_2 b)].$$

Region 2 $(b \leq r \leq a)$

$$E_{r2} = j \, \partial_{11} \, \frac{120\pi}{ka \, \cot an\psi} \, \cos\psi \, h_2 a \, \beta \vec{a} \, \cdot$$

$$K_0(h_2 a) \, \sin\beta z \cdot [I_1(h_2 r) - K_1(h_2 r) \cdot$$

$$(h_1 a \, I_0(h_1 b) \, I_1(h_2 b) \qquad\qquad (2.76)$$

$$- (\epsilon_r - j \, \sigma/\omega\epsilon_0) \, h_2 a \, I_0(h_2 b) \, I_1(h_1 b)) \cdot$$

$$1/(h_1 a \, I_0(h_1 b) \, K_1(h_2 b)$$

$$+ (\epsilon_r - j \, \sigma/\omega\epsilon_0) \, h_2 a \, I_1(h_1 b) \, K_0(h_2 b))].$$

$$E_{\theta 2} = -j \, \partial_{11} \, 120\pi \, ka \, \cot an\psi \, \sin\psi \, \cdot$$

$$K_1(h_2 a) \, \cos\beta z \cdot [I_1(h_2 r) - K_1(h_2 r) \cdot \qquad (2.77)$$

$$(h_1 a \, I_0(h_1 b) \, I_1(h_2 b) - h_2 a \, I_0(h_2 b) \, I_1(h_1 b)) \cdot$$

$$1/(h_1 a \, I_0(h_1 b) \, K_1(h_2 b) + h_2 a \, I_1(h_1 b) \, K_0(h_2 b))].$$

$$E_{z2} = j \, \partial_{11} \, \frac{120\pi}{ka \, \cot an\psi} \, \cos\psi \, (h_2 a)^2 \cdot$$

$$K_0(h_2 a) \, \cos\beta z \cdot [I_0(h_2 r) + K_0(h_2 r) \cdot$$

$$(h_1 a \, I_0(h_1 b) \, I_1(h_2 b) \qquad\qquad (2.78)$$

$$- (\epsilon_r - j \, \sigma/\omega\epsilon_0) \, h_2 a \, I_0(h_2 b) \, I_1(h_1 b)) \cdot$$

$$1/(h_1 a \, I_0(h_1 b) \, K_1(h_2 b)$$

$$+ (\epsilon_r - j \, \sigma/\omega\epsilon_0) \, h_2 a \, I_1(h_1 b) \, K_0(h_2 b))].$$

$$H_{r2} = \sum_{II} \cos\phi \; \beta a \cdot$$

$$K_1(h_2 a) \sin\beta z \cdot [I_1(h_2 r) - K_1(h_2 r) \cdot \qquad (2.79)$$

$$(h_1 a \; I_0(h_1 b) \; I_1(h_2 b) - h_2 a \; I_0(h_2 b) \; I_1(h_1 b)) \cdot$$

$$1/(h_1 a \; I_0(h_1 b) \; K_1(h_2 b) + h_2 a \; I_1(h_1 b) \; K_0(h_2 b))].$$

$$H_{\theta 2} = - \sum_{II} \sin\phi \; h_2 a \cdot$$

$$K_0(h_2 a) \cos\beta z \cdot [I_1(h_2 r) - K_1(h_2 r) \cdot$$

$$(h_1 a \; I_0(h_1 b) \; I_1(h_2 b) \qquad (2.80)$$

$$- (\epsilon_r - j \; \sigma/\omega\epsilon_0) \; h_2 a \; I_0(h_2 b) \; I_1(h_1 b)) \cdot$$

$$1/(h_1 a \; I_0(h_1 b) \; K_1(h_2 b)$$

$$+ (\epsilon_r - j \; \sigma/\omega\epsilon_0) \; h_2 a \; I_1(h_1 b) \; K_0(h_2 b))], \quad \text{and}$$

$$H_{z2} = \sum_{II} \cos\phi \; h_2 a \cdot$$

$$K_1(h_2 a) \cos\beta z \cdot [I_0(h_2 r) + K_0(h_2 r) \cdot \qquad (2.81)$$

$$(h_1 a \; I_0(h_1 b) \; I_1(h_2 b) - h_2 a \; I_0(h_2 b) \; I_1(h_1 b)) \cdot$$

$$1/(h_1 a \; I_0(h_1 b) \; K_1(h_2 b) + h_2 a \; I_1(h_1 b) \; K_0(h_2 b))].$$

Region 3 ($a \leqslant r < \infty$)

$$E_{r3} = -j \;\rangle_{II}\; 120\pi \; ka \; \cot\phi \; \cos\phi \; \frac{\beta a}{h_2 a} \cdot \qquad (2.82)$$

$$\frac{K_1(h_2 a)}{K_0(h_2 a)} \; K_1(h_2 r) \; \sin\beta z \cdot [I_1(h_2 a) - K_1(h_2 a) \cdot$$

$$(h_1 a \; I_0(h_1 b) \; I_1(h_2 b) - h_2 a \; I_0(h_2 b) \; I_1(h_1 b)) \cdot$$

$$1/(h_1 a \; I_0(h_1 b) \; K_1(h_2 b) + h_2 a \; I_1(h_1 b) \; K_0(h_2 b))],$$

$$E_{\theta 3} = -j \;\rangle_{II}\; 120\pi \; ka \; \cot\phi \; \sin\phi \cdot$$

$$K_1(h_2 r) \; \cos\beta z \cdot [I_1(h_2 a) - K_1(h_2 a) \cdot \qquad (2.83)$$

$$(h_1 a \; I_0(h_1 b) \; I_1(h_2 b) - h_2 a \; I_0(h_2 b) \; I_1(h_1 b)) \cdot$$

$$1/(h_1 a \; I_0(h_1 b) \; K_1(h_2 b) + h_2 a \; I_1(h_1 b) \; K_0(h_2 b))],$$

$$E_{z3} = j \;\rangle_{II}\; 120\pi \; ka \; \cot\phi \; \cos\phi \cdot \qquad (2.84)$$

$$\frac{K_1(h_2 a)}{K_0(h_2 a)} \; K_0(h_2 r) \; \cos\beta z \cdot [I_1(h_2 a) - K_1(h_2 a) \cdot$$

$$(h_1 a \; I_0(h_1 b) \; I_1(h_2 b) - b_2 a \; I_0(h_2 b) \; I_1(h_1 b)) \cdot$$

$$1/(h_1 a \; I_0(h_1 b) \; K_1(h_2 b) + h_2 a \; I_1(h_1 b) \; K_0(h_2 b))],$$

$$H_{r3} = \mathcal{H}_{II} \cos\phi \ \beta a \ \cdot$$

$$K_1(h_2 r) \ \sin\beta z \ \cdot \ [I_1(h_2 a) - K_1(h_2 a) \ \cdot \qquad (2.85)$$

$$(h_1 a \ I_0(h_1 b) \ I_1(h_2 b) - h_2 a \ I_0(h_2 b) \ I_1(h_1 b)) \ \cdot$$

$$1/(h_1 a \ I_0(h_1 b) \ K_1(h_2 b) + h_2 a \ I_1(h_1 b) \ K_0(h_2 b))],$$

$$H_{\theta 3} = \mathcal{H}_{II} \ (ka \ \cot\phi)^2 \ \sin\phi \ \frac{1}{h_2 a} \ \cdot \qquad (2.86)$$

$$\frac{K_1(h_2 a)}{K_0(h_2 a)} \ K_1(h_2 r) \ \cos\beta z \ \cdot \ [I_1(h_2 a) - K_1(h_2 a) \ \cdot$$

$$(h_1 a \ I_0(h_1 b) \ I_1(h_2 b) - h_2 a \ I_0(h_2 b) \ I_1(h_1 b)) \ \cdot$$

$$1/(h_1 a \ I_0(h_1 b) \ K_1(h_2 b) + h_2 a \ I_1(h_1 b) \ K_0(h_2 b))], \ \text{and}$$

$$H_{z3} = - \ \mathcal{H}_{II} \ \cos\phi \ h_2 a \ \cdot$$

$$K_0(h_2 r) \ \cos\beta z \ \cdot \ [I_1(h_2 a) - K_1(h_2 a) \ \cdot \qquad (2.87)$$

$$(h_1 a \ I_0(h_1 b) \ I_1(h_2 b) - h_2 a \ I_0(h_2 b) \ I_1(h_1 b)) \ \cdot$$

$$1/(h_1 a \ I_0(h_1 b) \ K_1(h_2 b) + h_2 a \ I_1(h_1 b) \ K_0(h_2 b))].$$

2.1.2 Discussion of the Field Components and the Dispersion Equation

As mentioned in part 1.3.2, the field components, equations 2.70 – 2.87, are characterized by $E_{zn} \neq 0$ and $H_{zn} \neq 0$, for $n = 1, 2, 3$. Therefore, these are *hybrid* type wave solutions. Transverse electric (TE) and transverse magnetic (TM) waves cannot exist independently on the sheath helix surrounding a lossy coaxial rod configuration.

Although the field components given by equations 2.70 – 2.87 represent a standing wave with respect to the axial coordinate, they cannot be thought of as the sum of a traveling wave normally incident on a perfectly electrically conducting plane and its

reflection. No plane perpendicular to the z axis can be chosen so that all electric fields along its surface vanish. This concept has been expressed as *a traveling wave supported by the sheath helix and reflected at a plane boundary will spiral in the wrong direction* (12; 16, pp. 82).

Attention is now directed to the dispersion equation and the separation constant equation. It is convenient to rewrite equation 2.42, the separation constant equation, as

$$(\beta a)^2 = (h_1 a)^2 + (ka)^2 (\epsilon_r - j\, \sigma/\omega\epsilon_0)$$
$$= (h_2 a)^2 + (ka)^2. \qquad (2.88)$$

The dispersion equation, equation 2.65, and the separation constant equation, equation 2.88, serve to determine the two radial wave numbers, $h_1 a$ and $h_2 a$, and the axial wave number, βa. It is not difficult to state the functional dependence of the wave numbers solution on the operating frequency, the sheath helix geometry, the rod geometry, and the rod material electrical properties.

$$h_1 a = f_1(ka\, \cotan\psi,\ b/a,\ \epsilon_r,\ \sigma/\omega\epsilon_0,\ \psi), \qquad (2.89)$$

$$h_2 a = f_2(ka\, \cotan\psi,\ b/a,\ \epsilon_r,\ \sigma/\omega\epsilon_0,\ \psi),\ \text{and} \qquad (2.90)$$

$$(\beta a)^2 = f_3(ka\, \cotan\psi,\ b/a,\ \epsilon_r,\ \sigma/\omega\epsilon_0,\ \psi). \qquad (2.91)$$

The dispersion equation and the separation constant equation cannot determine the algebraic sign of the axial wave number. Therefore, they are said to specify $(\beta a)^2$ rather than βa (39, 40). (Strictly speaking, it is h_1, h_2, β^2 and not $h_1 a$, $h_2 a$, $(\beta a)^2$ which are the wave numbers solution. However, this distinction in terminology is not important. In fact, it is best to consider the latter solution because $h_1 a$ and $h_2 a$ appear as Bessel function arguments in the dispersion equation. It is then not necessary for the sheath helix radius to appear by itself as an extra variable on the right hand sides of equations 2.89 - 2.91. It is useful to think of the

radial and axial spatial dependences of the electric and magnetic field components normalized with respect to the sheath helix radius so that $h_1 r$, $h_2 r$, and βz become $h_1 a \cdot r/a$, $h_2 a \cdot r/a$, and $\beta a \cdot z/a$.)

Two properties of the dispersion equation and the separation constant equation are immediately apparent. First, the pitch angle only appears in the quantity $(ka \, \cot an\psi)^2$. Replacing ψ by $-\psi$ will therefore result in no change. This means that the wave numbers solution is independent of the positive or negative sense of the sheath helix "windings". Second, the angular frequency only appears in the quantities $(ka)^2$, $(ka \, \cot an\psi)^2$, and $\sigma/\omega\epsilon_0$. Since the quantity $\sigma/\omega\epsilon_0$ is present, the wave numbers solution will be different if the algebraic sign of the angular frequency is reversed. This is an important property. Adler (39, 40) has shown that by considering the complex electric and magnetic fields as the Fourier transform of the instantaneous time-dependent electric and magnetic fields, it follows that if $\beta^2(-\omega) = \beta^2(\omega)$, β may only be purely real or purely imaginary. Since the preceding equation is not valid for the case of a sheath helix surrounding a lossy coaxial rod, βa is allowed to be generally complex with nonzero real and imaginary parts. (Appendices B, C, and D are concerned with the empty sheath helix, the sheath helix surrounding a perfectly conducting coaxial rod, and the sheath helix surrounding an ideal dielectric coaxial rod, respectively. For each of these three configurations, the corresponding dispersion equation and separation constant equation show that $(\beta a)^2$ is not changed if ω is replaced by $-\omega$. Therefore, the previous discussion has shown that for these three configurations, the axial wave number is only allowed to be either purely real or purely imaginary.)

Information concerning the possible algebraic signs of the real and imaginary parts of the wave numbers solution can be obtained by examination of the dispersion equation, equation 2.65, the separation constant equation, equation 2.88, and the field components, equations 2.70 - 2.87. Let

$$h_1 a = h_{1r} a + j\, h_{1j} a,$$

$$_r h_2 a = h_{2r} a + j\, h_{2j} a, \text{ and} \qquad\qquad (2.92)$$

$$\beta a = \beta_r a + j\, \beta_j a,$$

where the subscript "r" denotes the real part of the complex-valued wave number and the subscript "j" denotes the imaginary part. As was previously mentioned in part 2.1.1, in order that the condition of regularity at infinity of the fields is satisfied for $r \rightarrow \infty$, it is necessary that $h_{2r} a > 0$. In addition, it has previously been said in part 2.1.2 that if a particular value of βa satisfies the dispersion equation and the separation constant equation, then $-\beta a$ must also be a valid solution. However, equations 2.70 – 2.87 show that reversing the algebraic sign of βa results in no change in the field components. Therefore, no loss in generality results from restricting $\beta_r a > 0$. Making use of the Bessel function relations A.14 and A.15, it can be shown that reversing the algebraic sign of $h_1 a$ in equations 2.65, 2.70 – 2.87 causes no change. Of course, this is also true of equation 2.88. This means that no loss in generality results from restricting $h_{1r} a > 0$. Finally, separating equation 2.88 into real and imaginary parts, shows that when the imaginary parts are equated, $\beta_j a$ and $h_{2j} a$ must have the same algebraic sign. In summary, for a free mode field solution, the wave numbers are restricted so that $h_{1r} a > 0$, $h_{2r} a > 0$, $\beta_r a > 0$, with $\beta_j a$ and $h_{2j} a$ having the same algebraic sign.

The field components and the dispersion equation are lengthy and complicated. It is desirable to make approximations to them which result in simplification. What is sometimes done in multi-dielectric region configurations is to equate the axial wave number with the radial wave numbers (22). For the sheath helix surrounding a lossy coaxial rod, this means that $h_1 a \cong h_2 a \cong \beta a \cong h a$. The necessary requirements to justify this approximation are obtained from examination of the separation constant equation. Expanding equation 2.88 and equating first the real parts and second the imaginary parts, the approximation is seen to be valid providing that

$$|(h_r a)^2 - (h_j a)^2| \gg \epsilon_r (ka)^2 \quad \text{and}$$

$$|h_r a \, h_j a| \gg (\sigma/\omega\epsilon_0)(ka)^2, \qquad (2.93)$$

$$\text{where } ha = h_r a + j \, h_j a.$$

The author spent considerable time studying the approximate form of equation 2.65, and equations 2.70 – 2.87. Unfortunately, the two inequalities listed in 2.93, especially the second one, were shown by direct numerical solution of the approximate form of the dispersion equation to be very difficult to satisfy, at least when $|h|a$ is small compared to unity. In short, although the approximate solution does provide simplification to the dispersion equation and to the field components, and is therefore highly desirable, it was found that, unfortunately, the requirements involved to justify its usage could usually not be met. No more discussion of this approximate solution will be given. Only the equations where the wave numbers $h_1 a$, $h_2 a$, and βa are assumed to be distinct values will be discussed throughout the remainder of the chapter.

2.2 Some Limiting Cases of the Free Mode Field Solution

The purpose of this section is to investigate several limiting forms of the dispersion equation, equation 2.65, the separation constant equation, equation 2.88, and the field components, equations 2.70 – 2.87. These limiting cases are when the lossy rod radius approaches zero, the lossy rod conductivity approaches zero, and the lossy rod conductivity approaches infinity. It will be seen that these special cases agree with the free mode field solution for the empty sheath helix, the sheath helix surrounding an ideal dielectric coaxial rod, and the sheath helix surrounding a perfectly conducting coaxial rod, respectively. Appendices B, C, and D discuss these three configurations. All results in these appendices were obtained completely independently of the free mode field solution for the sheath helix surrounding a lossy coaxial rod. Demonstrating that this free mode field solution correctly satisfies the three limiting cases serves as a useful check on its accuracy.

2.2.1 Limit as the Lossy Rod Radius Approaches Zero

The limit of the dispersion equation, equation 2.65, is taken as the rod radius approaches zero. It is assumed that the other geometrical variables, the operating frequency, and the electrical properties of the rod material, are all held constant during the limiting process. Making use of relations A.26 - A.29, the small argument Bessel function representations, and performing a small amount of algebra, one discovers that

$$\lim_{b \to 0^+} \left(\frac{ka \cot an\psi}{h_2 a}\right)^2 = \left(\frac{ka \cot an\psi}{h_2' a}\right)^2 \tag{2.94}$$

$$= \frac{I_0(h_2'a) \ K_0(h_2'a)}{I_1(h_2'a) \ K_1(h_2'a)} \text{, where } \lim_{b \to 0^+} h_2 a = h_2'a.$$

The correct form of the separation constant relation, equation 2.88, in this limit is

$$(\beta'a)^2 = (h_2'a)^2 + (ka)^2, \tag{2.95}$$

$$\text{where } \lim_{b \to 0^+} \beta a = \beta'a.$$

Equations 2.94 and 2.95 are the same as equation B.13, the empty sheath helix dispersion equation, and equation B.14, the empty sheath helix separation constant equation, respectively. In the limit as the lossy rod radius approaches zero, the dispersion equation and the separation constant equation become those of the empty sheath helix, as one would expect. Therefore, it is true that

$$\lim_{b \to 0^+} h_2 a = h_2'a = h^a a \text{ and}$$

$$\lim_{b \to 0^+} \beta a = \beta'a = \beta^a a, \tag{2.96}$$

where $_h{}^a{}_a$ and $_\beta{}^a{}_a$ are the radial and axial wave numbers, respectively, of the empty sheath helix.

Applying this same limit to equations 2.76 – 2.87, the field components, making use of equation 2.96, the dispersion equation, and equations A.26 – A.29, the small argument Bessel function representations, it is seen that equations B.1 – B.12, the empty sheath helix field components, result. Thus, the empty sheath helix field components are obtained by taking the limit as the rod radius approaches zero of each one of the region 2 and region 3 lossy rod configuration fields.

In summary, taking the limit of the dispersion equation, the separation constant equation, and the field components, as the lossy rod radius approaches zero, gives the corresponding equation of the empty sheath helix. The empty sheath helix is discussed in Appendix B and the analysis is carried out independently of that given in this chapter. From physical considerations, the limiting result is expected. It is a useful check on the accuracy of the free mode field solution for the sheath helix surrounding a lossy coaxial rod.

2.2.2 Limit as the Lossy Rod Conductivity Approaches Zero

Now the conductivity of the lossy rod material is made to approach zero, with all other electrical properties of the rod material, the operating frequency, the sheath helix geometry, and the rod geometry, held constant. Clearly, this means that

$$\lim_{\sigma \to 0^+} (\epsilon_r - j\, \sigma/\omega\epsilon_0) = \epsilon_r.$$

Replacing the quantity $\epsilon_r - j\, \sigma/\omega\epsilon_0$ by the quantity ϵ_r in equation 2.65, the dispersion equation, and equation 2.88, the separation constant equation, the same result as equation D.19, the dispersion equation for the ideal dielectric rod configuration, and equation D.20, the separation constant equation for the ideal dielectric rod configuration, is obtained. Taking the limit of the dispersion equation and the separation constant equation as the rod conductivity approaches zero means that the corresponding

equations for the sheath helix surrounding an ideal dielectric coaxial rod are obtained. Therefore,

$$\lim_{\sigma \to 0^+} h_1 a = h_1{}' a = h_1{}^d a, \quad \lim_{\sigma \to 0^+} h_2 a = h_2{}' a = h_2{}^d a,$$

$$\text{and} \quad \lim_{\sigma \to 0^+} \beta a = \beta' a = \beta^d a; \qquad\qquad (2.97)$$

where $h_1{}^d a$, $h_2{}^d a$, and $\beta^d a$ are the two radial wave numbers and the axial wave number, respectively, for the sheath helix surrounding an ideal dielectric coaxial rod.

In a similar manner, replacing $\epsilon_r - j \sigma/\omega\epsilon_0$ by $\epsilon_r{}'$ in equations 2.70 – 2.87, the field components, making use of equations 2.97; equations D.1 – D.18, the field components associated with the ideal dielectric rod configuration, are obtained. Taking the limit of each field component as the lossy rod conductivity approaches zero, the corresponding field component of the sheath helix surrounding an ideal dielectric coaxial rod is obtained.

A brief digression will now be made to show that equations 2.70 – 2.87, 2.65, and 2.88, which comprise the free mode field solution for a sheath helix surrounding a lossy coaxial rod, can be related to the free mode field solution for a sheath helix surrounding an ideal dielectric coaxial rod, equations D.1 – D.20. This is done by making use of the concept of *complex relative permittivity*.

Equations 1.4 list Maxwell's equations in a conducting region. It is convenient to rewrite the equation which takes the curl of $\underline{H}$ as

$$\nabla \times \underline{H} = j \omega\epsilon \underline{E} + \sigma \underline{E} = (j \omega\epsilon + \sigma) \underline{E}$$

$$= j \omega\epsilon_0 (\epsilon_r - j \sigma/\omega\epsilon_0) \underline{E}$$

or

$$\nabla \times \underline{H} = j\, \omega \varepsilon_0\, \varepsilon_r^*\, \underline{E}. \tag{2.98}$$

$\varepsilon_r^* = \varepsilon_r - j\, \sigma/\omega\varepsilon_0$ is the *complex relative permittivity*. Using the quantity ε_r in place of the quantity ε_r^*, Maxwell's equations in a conducting region can be transformed into the form of Maxwell's equations suitable for an ideal dielectric (zero conductivity) region (18, pp. 27). This has the important meaning that replacing each occurrence of ε_r^* in the equations associated with the free mode field solution for a sheath helix surrounding a lossy coaxial rod, with ε_r, must result in the correct corresponding equation of the free mode field solution for a sheath helix surrounding an ideal dielectric coaxial rod. Of course,

$$\lim_{\sigma \to 0^+} \varepsilon_r^* = \varepsilon_r,$$

and so using the concept of complex relative permittivity makes it clear that in the limit as the lossy rod conductivity approaches zero, the two free mode field solutions must be the same.

As a summary, taking the limit of the dispersion equation, the separation constant equation, and the field components, as the lossy rod conductivity approaches zero, yields the corresponding equation of the sheath helix surrounding an ideal dielectric coaxial rod. This latter mentioned configuration is studied in Appendix D and the analysis is conducted independently of that given in this chapter. In the limit as the lossy rod conductivity approaches zero, one expects from physical considerations that the free mode field solutions of the two configurations will be the same. This was indeed demonstrated to be the case. The limiting process has provided a means of checking on the accuracy of the free mode field solution for the sheath helix surrounding a lossy coaxial rod.

2.2.3 Limit as the Lossy Rod Conductivity Approaches Infinity

As a final limiting case, the conductivity of the lossy rod is made to approach infinity, with all geometrical variables, the operating frequency, and the value of ε_r, held constant. The separation constant equation, equation 2.88, makes it clear that at least one of the wave number solutions must become infinite in this limit. Using some physical insight, it is anticipated that the fields within the rod-filled region will vanish but that nonzero fields will exist in the two air-filled regions. Therefore, it will be assumed that calculating the limit as the rod conductivity approaches infinity leads to the equality

$$h_1 a = \sqrt{j \ \sigma/\omega\varepsilon_0} \ ka. \qquad (2.99)$$

(A further discussion of this choice for $h_1 a$ will be given shortly.) Taking the limit as $\sigma \to \infty$, it is clear from equation 2.99 that $|h_1|a$ becomes unbounded. Combining equations 2.88 and 2.99, it is evident that when the limit is calculated, the separation constant equation becomes

$$(\beta' a)^2 = (h_2' a)^2 + (ka)^2, \qquad (2.100)$$

$$\text{where} \quad \lim_{\sigma \to \infty} h_2 a = h_2' a \quad \text{and} \quad \lim_{\sigma \to \infty} \beta a = \beta' a,$$

and the wave number magnitudes $|h_2'|a$ and $|\beta'|a$ are finite.

For convenience, the dispersion equation, equation 2.65, is rewritten as

$$\left(\frac{ka \ \cot\alpha\psi}{h_2 a}\right)^2 \frac{K_0(h_2 a)}{K_1(h_2 a)} \cdot [I_0(h_2 a) + K_0(h_2 a) \cdot$$

$$(h_1 a \ I_0(h_1 b) \ I_1(h_2 b) \qquad (2.101)$$

$$- (\varepsilon_r - j \ \sigma/\omega\varepsilon_0) \ h_2 a \ I_0(h_2 b) \ I_1(h_1 b)) \cdot$$

$$(1/(h_1 a \ I_0(h_1 b) \ K_1(h_2 b)$$ (2.101)

(continued)

$$+ \ (\epsilon_r - j \ \sigma/\omega\epsilon_0) \ h_2 a \ I_1(h_1 b) \ K_0(h_2 b)))] \ \cdot$$

$$1/[I_1(h_2 a) - K_1(h_2 a) \ \cdot$$

$$\frac{(h_1 a \ I_0(h_1 b) \ I_1(h_2 b) - h_2 a \ I_0(h_2 b) \ I_1(h_1 b))}{(h_1 a \ I_0(h_1 b) \ K_1(h_2 b) + h_2 a \ I_1(h_1 b) \ K_0(h_2 b))}].$$

Taking the limit of equation 2.101 as $\sigma \to \infty$, using equation 2.99, and the large argument Bessel function representations, equations A.36 and A.37, one discovers that

$$\lim_{\sigma \to \infty} \left(\frac{ka \ \cot an\psi}{h_2 a}\right)^2 = \left(\frac{ka \ \cot an\psi}{h_2' a}\right)^2 = \frac{K_0(h_2' a) \ K_1(h_2' b)}{K_0(h_2' b) \ K_1(h_2' a)} \ \cdot$$

$$\frac{(I_0(h_2' a) \ K_0(h_2' b) - I_0(h_2' b) \ K_0(h_2' a))}{(I_1(h_2' a) \ K_1(h_2' b) - I_1(h_2' b) \ K_1(h_2' a))} \ \cdot$$ (2.102)

Equations 2.102 and 2.100 are the same as equations C.14 and C.15, respectively! Equations 2.102 and 2.100 agree with the dispersion equation and the separation constant equation associated with the sheath helix surrounding a perfectly conducting coaxial rod. In the limit as the lossy rod conductivity becomes infinite, it has been demonstrated that the radial wave number associated with the air medium and the axial wave number become those of the sheath helix surrounding a perfectly conducting coaxial rod. Therefore,

$$\lim_{\sigma \to \infty} h_2 a = h_2' a = h^c a \quad \text{and}$$ (2.103)

$$\lim_{\sigma \to \infty} \beta a = \beta' a = \beta^C a,$$

<div align="right">(2.103)
(continued)</div>

where h^C_a and β^C_a are the radial and axial wave numbers, respectively, for the perfectly conducting rod configuration.

Calculating this same limit of each one of equations 2.70 - 2.87, the field components, making use of equations 2.99, 2.102, 2.103, and of equations A.36 - A.39, the large argument Bessel function representations, one finds that the corresponding equations of the set C.1 - C.13, the field components for the perfectly conducting rod configuration, result! Taking the limit as the rod conductivity becomes infinite, the lossy rod configuration field components become transformed into those associated with the sheath helix surrounding a perfectly conducting coaxial rod.

A better understanding of the value chosen for $h_1 a$ can be achieved by rewriting equation 2.99 as

$$h_1 a = \sqrt{j \ \sigma / \omega \varepsilon_0} \ ka = \sqrt{j \ \omega \ \mu_0 \ \sigma} \ a.$$

In an unbounded, source-free region characterized by the electrical properties μ_0, ε, and σ, a uniform plane wave with $e^{-\gamma z}$ axial dependence has

$$\gamma = \sqrt{j \ \omega \ \mu_0 \ (\sigma + j \ \omega \ \varepsilon)}$$

as the propagation wave number. (For example, see 41, pp. 321.) In a good conductor, it is true that $\sigma >> \omega \varepsilon$ and so it is clear that $h_1 a \approx \gamma a$. Therefore, equation 2.99 represents the wave number solution associated with uniform plane wave propagation in a good conductor.

In summary, taking the limit of the separation constant equation, the dispersion equation, and the field components, as the lossy rod conductivity approaches infinity, imposing equality 2.99, means that the corresponding equation of the sheath helix surrounding a perfectly conducting coaxial rod is obtained. The perfectly conducting rod configuration is discussed in Appendix C and the analysis is carried out independently of that given in this chapter. From physical considerations, the limiting behavior is expected.

It is a useful check on the accuracy of the free mode field solution associated with the sheath helix surrounding a lossy coaxial rod.

2.3 Approximate Representations of the Dispersion Equation and Discussion of the Wave Numbers Solution

The spatial dependence of the field components explicitly appears in the modified Bessel function arguments and the trigonometric function arguments according to $h_1 a \cdot r/a$, $h_2 a \cdot r/a$, and $\beta a \cdot z/a$. In order to understand how the fields behave at different points in space, it is necessary to know the values of the two radial wave numbers and the axial wave number. Therefore, a study of the dispersion equation, equation 2.65, and the separation constant equation, equation 2.88, is well justified. It is highly desirable to obtain numerical values of the wave numbers solution using many different sets of the variables mentioned in equations 2.89 - 2.91.

Equations 2.65 and 2.88 are two simultaneous, complex-valued, nonlinear equations involving the two complex-valued unknowns $h_1 a$ and $h_2 a$. Many different iterative numerical methods are known which can be used to solve simultaneous nonlinear equations involving complex roots. Some examples of these are the Secant method, Newton's method, and Muller's method (42, pp. 74). The essential basis of these techniques is to initially guess at the roots and then use an iterative process so that the trial roots are always being modified. If the procedure works correctly, after a certain number of iterations, both the real and the imaginary parts of all the roots will converge within an acceptable error limitation to the values of the exact solutions.

Unfortunately, the direct numerical solution of equations 2.65 and 2.88 is extremely difficult to accomplish. Equation 2.65 is a very lengthy, transcendental equation involving modified Bessel functions having complex-valued arguments. In order to begin the numerical solution, it is necessary to have a computer program which can evaluate these modified Bessel functions. The program should yield accurate results, and it must be efficient so that it can be executed very rapidly. A small execution time is important in order that the cost of operating the program does not become excessively high. Taking into consideration the degree of difficulty of the dispersion equation and the nature of Bessel functions having complex-valued arguments, it is expected that

regardless of the iterative technique used, the convergence of the trial values $h_1 a$ and $h_2 a$ to their correct values will be extremely difficult to accomplish. This problem is a challenging one for the applied computer scientist. It will not be attempted here.

Although the direct solution of the dispersion equation and the separation constant equation cannot be accomplished, much useful information concerning the behavior and the numerical values of the wave numbers solution can be obtained by making approximations to equation 2.65. This involves using the small and large argument Bessel function representations to approximate all the modified Bessel functions appearing in the dispersion equation. Two major classes of approximations will be considered. These are when *the lossy rod is not a good conductor* and when *the lossy rod is a good conductor*. (The meanings of the expressions in quotation marks are later discussed in parts 2.3.1 and 2.3.2.) For these two classes of approximations, both the three region $(b < a)$ and the two region $(b = a)$ sheath helix surrounding a lossy coaxial rod configurations are considered. (The free mode field solution associated with the two region configuration can be obtained by calculating the limit as $b \to a^-$ of equation 2.65, the dispersion equation, and of equations 2.70 − 2.75 and 2.82 − 2.87, the field components. Equation 2.88, the separation constant equation, is the same for both the two and three region configurations.)

The three region configuration free mode field solution for the sheath helix surrounding a lossy coaxial rod, which consists of equations 2.65 and 2.70 − 2.88, is actually valid for all sheath helix pitch angles in the range $0 < \psi < 90.0°$. However, as was previously discussed in part 1.3.2, in order that this angularly independent free mode field solution resembles as closely as possible the solution associated with a physical helix, it is best to consider a relatively tightly wound sheath helix. Throughout the remainder of the chapter it will usually be assumed that the pitch angle is restricted to $0 < \psi \leq 10.0°$.

The discussion and the equations derived in section 2.3 will later be used in section 2.4 to make graphs of the radial dependence associated with the electric and magnetic field component magnitudes. In addition, the information presented in section 2.3 will later be used in sections 3.2 and 3.3 to investigate the power dissipation

which occurs within the lossy coaxial rod.

2.3.1 Solution of the Wave Numbers When "The Lossy Rod Is Not a Good Conductor"

2.3.1.1 Small Argument Representation

The approximation of the dispersion equation, equation 2.65, which is valid when the Bessel function arguments are small in magnitude for the case when "the lossy rod is not a good conductor" will now be investigated. *It will be assumed that the operating frequency, the sheath helix geometry, the lossy rod geometry, and the electrical properties of the lossy rod material are such that the magnitudes of the two radial wave numbers satisfy the inequalities*

$$|h_1|a < 0.10 \quad \text{and} \quad |h_2|a < 0.10. \tag{2.104}$$

Making use of the separation constant equation, equation 2.88, it is apparent that the two inequalities listed in 2.104 at least require that

$$\sqrt{\epsilon_r}\, ka < 0.10 \quad \text{and} \quad \sqrt{\sigma/\omega\epsilon_0}\, ka < 0.10. \tag{2.105}$$

The restrictions imposed in 2.104 and 2.105 serve to define what is meant by the expression "the lossy rod is not a good conductor" as it is used in sub-part 2.3.1.1 for both the two and three region sheath helix surrounding a lossy coaxial rod configurations. However, it is apparent that the rod conductivity may actually be quite large if the operating frequency is such that the radius of the sheath helix is very small compared to the free space wave length. Thus, the solution to the wave numbers which will be derived is not necessarily restricted to low loss dielectric materials but may be applied to situations where the loss tangent $(\sigma/\omega\epsilon = \sigma/\omega\epsilon_0\epsilon_r)$ of the rod material is considerably greater than unity.

Table A.1 shows that for a real positive argument x, the small argument Bessel function approximations, equations A.26 - A.29, only have a small error associated with them for $x < 0.10$. Therefore, when the inequalities listed in 2.104 are satisfied, one is well justified in using equations A.26 - A.29 to approximate the Bessel functions appearing in equation 2.65. (The single exception is that equations A.30 and A.31 must be used to approximate the quantity

$$h_1 a\ I_0(h_1 b)\ I_1(h_2 b)\ -\ h_2 a\ I_0(h_2 b)\ I_1(h_1 b)$$

because the other small argument Bessel function approximations are not sufficiently accurate.) Making these approximations, performing a relatively large amount of algebra, and carefully simplifying by eliminating less significant terms, yields

$$\left(\frac{ka\ \cot an\psi}{h_2 a}\right)^2 \simeq -2\ \log(0.891\ h_2 a)\ \cdot$$

$$\frac{[1 - (\epsilon_r - j\ \sigma/\omega\epsilon_0)\ \frac{(h_2 b)^2}{2}\ \log(b/a)]}{[1 - (\epsilon_r - j\ \sigma/\omega\epsilon_0)\ \frac{(h_2 b)^2}{2}\ \log(0.891\ h_2 b)]} \cdot \qquad (2.106)$$

Equation 2.106 is the small argument approximation of the dispersion equation, for the case when "the lossy rod is not a good conductor". It is valid for both the two and three region sheath helix surrounding a lossy coaxial rod configurations. (The correct form for the two region configuration is obtained by calculating $\lim b \rightarrow a^-$ of equation 2.106.) Note that the radial wave number $h_1 a$ does not appear in this equation. Of course, the small argument approximate values of $h_1 a$ and βa can be obtained when the small argument value of $h_2 a$ is known, by using equation 2.88, the separation constant equation. (It was previously mentioned in part 2.1.2 that the algebraic signs of the three wave numbers are chosen so that their real parts are positive.)

Taking the limit of equation 2.106 as $b \rightarrow a^-$, keeping in mind equation 2.88, yields the same small argument dispersion equation approximation and the same separation constant equation as that obtained by Chute et al. (25). (The results of this reference have been modified so that they refer to a lossy nonmagnetic rod filling the sheath helix interior region with air filling the exterior region.) This result is expected and it provides a useful check on the accuracy of equation 2.106. In addition, calculating the limit as $\sigma \rightarrow 0^+$ of equation 2.106 and performing a small amount of algebra yields equation D.48. As expected, in the limit as the lossy rod conductivity approaches zero, equation 2.106 reduces to the small argument approximation of the dispersion equation associated with the sheath helix surrounding an ideal dielectric (zero conductivity) coaxial rod. Once again, this result provides a useful check on the accuracy of equation 2.106.

In order to numerically solve equation 2.106 to obtain $h_2 a$, the equation is separated into real and imaginary parts and then these are respectively equated. Two real-valued nonlinear equations involving the two real-valued unknowns $h_{2r} a$ and $h_{2j} a$ are thus obtained. These two equations are

$$(ka \cot\psi)^2 \, [2 - (b/a)^2 \log(0.891 \, b/a \, x_m) \, \cdot$$

$$(\epsilon_r \, (x_{2r}^2 - x_{2j}^2) + 2 \, \frac{\sigma}{\omega\epsilon_0} \, x_{2r} \, x_{2j})$$

$$+ (b/a)^2 \, \theta_m \, (2 \, \epsilon_r \, x_{2r} \, x_{2j} - \frac{\sigma}{\omega\epsilon_0} \, (x_{2r}^2 - x_{2j}^2))] \quad (2.107)$$

$$= 2 \, [2 \, x_{2r} \, x_{2j} \, \theta_m - (x_{2r}^2 - x_{2j}^2) \, \log(0.891 \, x_m)] \, \cdot$$

$$[2 - (b/a)^2 \log(b/a) \, (\epsilon_r \, (x_{2r}^2 - x_{2j}^2) + 2 \, \frac{\sigma}{\omega\epsilon_0} \, x_{2r} \, x_{2j})]$$

$$- 2 \, (b/a)^2 \log(b/a) \, (2 \, \epsilon_r \, x_{2r} \, x_{2j} - \frac{\sigma}{\omega\epsilon_0} \, (x_{2r}^2 - x_{2j}^2)) \, \cdot$$

$$[\theta_m \, (x_{2r}^2 - x_{2j}^2) + 2 \, x_{2r} \, x_{2j} \log(0.891 \, x_m)] \, ,$$

and

$$(b/a)^2 (ka\ cotan\psi)^2 [\theta_m (\epsilon_r (x_{2r}^2 - x_{2j}^2) + 2 \frac{\sigma}{\omega \epsilon_0} x_{2r} x_{2j})$$

$$+ \log(0.891\ b/a\ x_m) (2 \epsilon_r x_{2r} x_{2j} - \frac{\sigma}{\omega \epsilon_0} (x_{2r}^2 - x_{2j}^2))]$$

$$= 2 ([\theta_m (x_{2r}^2 - x_{2j}^2) + 2 x_{2r} x_{2j} \log(0.891\ x_m)] \cdot \quad (2.108)$$

$$[2 - (b/a)^2 \log(b/a) (\epsilon_r (x_{2r}^2 - x_{2j}^2) + 2 \frac{\sigma}{\omega \epsilon_0} x_{2r} x_{2j})]$$

$$+ (b/a)^2 \log(b/a) (2 \epsilon_r x_{2r} x_{2j} - \frac{\sigma}{\omega \epsilon_0} (x_{2r}^2 - x_{2j}^2)) \cdot$$

$$[2 x_{2r} x_{2j} \theta_m - (x_{2r}^2 - x_{2j}^2) \log(0.891\ x_m)]).$$

The notation which is used in equations 2.107 and 2.108 is now defined.

$$x_2 = x_{2r} + j x_{2j} = x_m e^{j\theta_m}, \quad x_{2r} = h_{2r}a = Re[h_2 a],$$

$$x_{2j} = h_{2j}a = Im[h_2 a], \quad x_m = \sqrt{x_{2r}^2 + x_{2j}^2}, \quad and$$

$$\theta_m = tan^{-1}(x_{2j}/x_{2r}) .$$

In order to solve equations 2.107 and 2.108 for x_{2r} and x_{2j}, it is necessary to specify the variable set $ka\ cotan\psi$, b/a, ϵ_r, $\sigma/\omega\epsilon_0$ and to make an initial guess of x_{2r} and x_{2j}. An iterative procedure is then followed. The author made use of the IMSL (43) software program ZSCNT to numerically solve the two equations. In order that reasonably high accuracy would be obtained, the program was run using extended precision arithmetic and a large number of iterations were specified in the IMSL program. As a final check on the accuracy of the answer, the

solution h_2a was used to evaluate both sides of equation 2.106. It was ensured that the agreement for both the real parts and the imaginary parts was correct to at least three figure accuracy.

In the four graphs included in sub-part 2.3.1.1 which will shortly be discussed, based on the solution to equations 2.107 and 2.108, and in many other graphs based on the solution of these two equations that were prepared but which are not included in the thesis, it was always found that $h_{2r}a > 0$ and $h_{2i}a < 0$. As was previously mentioned in part 2.1.1, the real part of h_2a must be positive in order that the fields satisfy the condition of regularity at infinity for $r \to \infty$. In addition, when calculating the numerical solution of equations 2.107 and 2.108, it was discovered that the expression

$$(\frac{ka \ cotan\psi}{h_{2r}a})^2 \simeq -2 \ log(0.891 \ h_{2r}a) \qquad (2.109)$$

is a good approximate relation for the purpose of evaluating $h_{2r}a$. This approximation follows from equation 2.106, when further restrictions to those mentioned in inequalities 2.105 are placed on the values of ϵ_r and $\sigma/\omega\epsilon_0$. These restrictions are

$$|\epsilon_r - j \ \sigma/\omega\epsilon_0| \ \frac{|h_2b|^2}{2} \ |log(b/a)| << 1, \quad and$$

$$\qquad (2.110)$$

$$|\epsilon_r - j \ \sigma/\omega\epsilon_0| \ \frac{|h_2b|^2}{2} \ |log(0.891 \ h_2b)| << 1.$$

Clearly, equation 2.109 shows that $h_{2r}a$ is approximately dependent only on the variable $ka \ cotan\psi$. Since equations 2.109, D.49, and B.21 are the same, the small argument value of $h_{2r}a$ is similar to the small argument value of the approximate (real) radial wave number associated with the sheath helix surrounding an

ideal dielectric coaxial rod, and it is similar to the small argument value of, the (real) radial wave number associated with the empty sheath helix.

In the following four graphs, $|h_{2j}|a << h_{2r}a$ was found to be true, especially for very small $ka \, cotan\psi$ values. Since $|h_{2j}|a$ is much smaller than $h_{2r}a$, it was decided to graph the quantity h_2a directly as a function of the variables $ka \, cotan\psi$, b/a, ϵ_r, and $\sigma/\omega\epsilon_0$, rather than plotting the quantity $ka \, cotan\psi/h_2a$. This latter technique was used in Appendices B, C, D and, it was convenient when the range of values that the radial wave number assumed was not very large.

As a final remark before the graphs are specifically discussed, it will be mentioned that a data table was prepared showing the numerical values of the wave numbers solution h_1a, h_2a, and βa, associated with each one of the graphs. This table made it clear that the approximations $h_{1r}a \cong h_{2r}a$ and $h_{1j}a \cong h_{2j}a$ are usually greatly in error. It was obvious that it is not correct to equate the two radial wave numbers. Therefore, the approximate solution discussed at the end of part 2.1.2 is certainly not valid.

The following four graphs present numerical values of the solution $h_2a = h_{2r}a + j \, h_{2j}a$, based on equations 2.107 and 2.108. All the graphs have $ka \, cotan\psi$ as the abscissa. $x_{2r} = h_{2r}a$ and $-x_{2j} = -h_{2j}a$ are used as the ordinate. Each specific curve shown on any one of the graphs is associated with one specific set of the variables b/a, ϵ_r, and $\sigma/\omega\epsilon_0$. When h_2a is known, the corresponding small argument values of h_1a and βa are calculated by noting the pitch angle of the sheath helix and by using the separation constant equation, equation 2.88.

Figure 2.2 is a graph of h_2a versus $ka \, cotan\psi$ for $\epsilon_r = 10.0$, $\sigma/\omega\epsilon_0 = 10.0$, $1.00 \times 10^{-4} < ka \, cotan\psi < 0.10$, and with several different values of b/a. More specifically, $b/a = 1.00$, 0.900, 0.500, and 0.100 are used. Clearly, varying the value of b/a has no significant effect on the value of $h_{2r}a$. This behavior is expected from equation 2.109, which shows that $h_{2r}a$ is approximately only dependent on the value of $ka \, cotan\psi$. However, the value of b/a does have a great effect on the value of $h_{2j}a$. As b/a decreases,
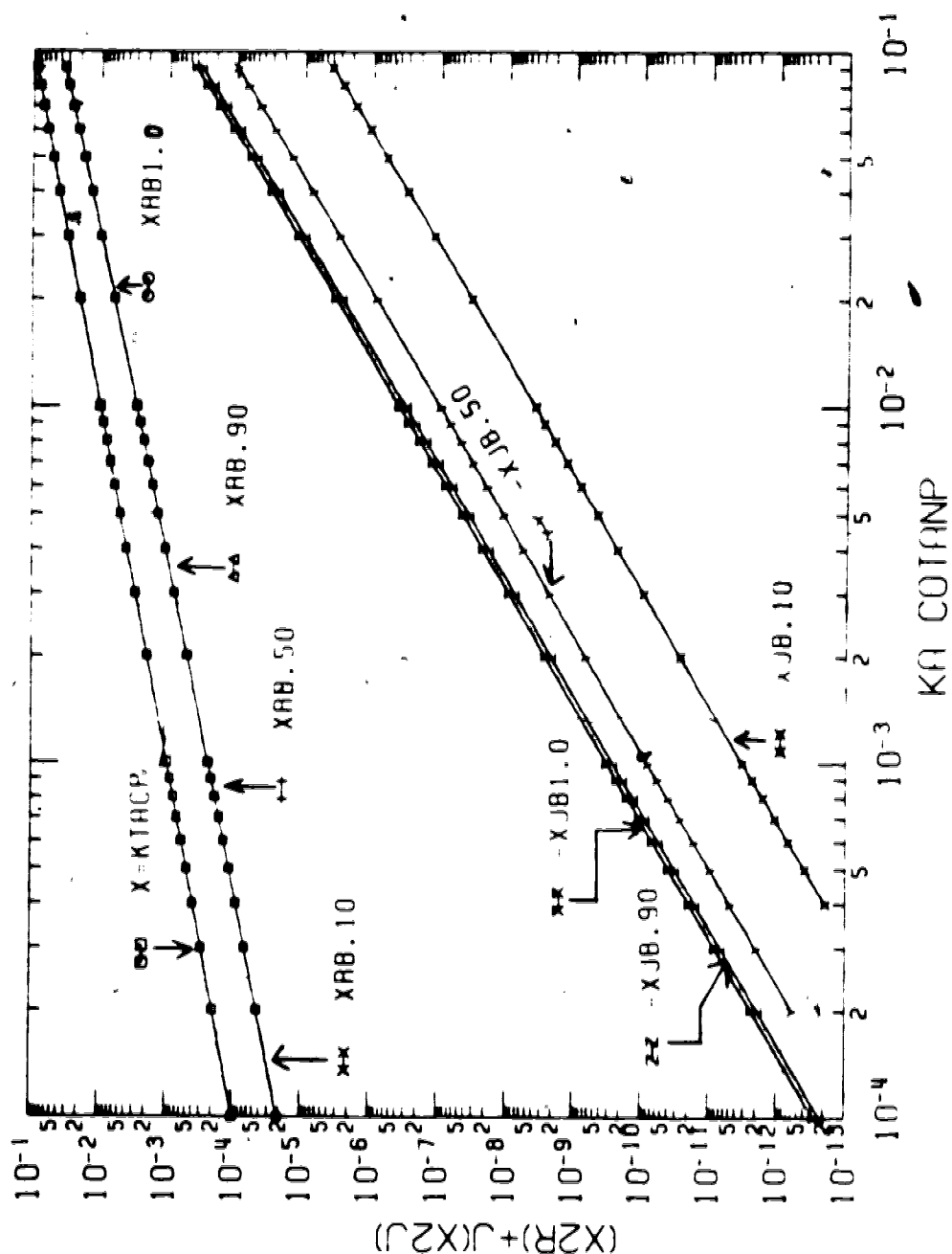
Figure 2.2   Small argument approximate solution for $h_2 a$
based on equation 2.10^{6} (the lossy rod is not a good
conductor). ϵ_r=10.0; $\sigma/\omega\epsilon_0$=10.0; b/a=1.00, 0.900, 0.500,
0.100; and 1.00×10^{-4}<ka cotanψ<0.100 are used. $h_{2r}a$ and $-h_{2j}a$
are actually shown. (Note X2=$h_{2r}a$+j$h_{2j}a$, X2R=$h_{2r}a$, X2J=$h_{2j}a$,
KA COTANP=KTACP=ka cotanψ, B/A=b/a, ER1=ϵ_r, and ER2=$\sigma/\omega\epsilon_0$.
XRB1.0 means the curve represents $h_{2r}a$ for b/a=1.00. -XJB.10
means the curve represents $-h_{2j}a$ for b/a=0.100.)

$\left|h_{2j}\right|a$ becomes smaller. Once again, this behavior is expected. In the limit as the lossy rod radius approaches zero, it was previously shown in part 2.2.1 that the radial and axial wave numbers solution become the (real) respective radial and axial wave numbers associated with the empty sheath helix. This means that in this limit, h_{2j} = 0 is required.

Figure 2.3 is a similar type of graph as Figure 2.2, with the same values of $ka\ cotan\psi$ and b/a. The two graphs are different because Figure 2.3 has much larger values of ϵ_r and $\sigma/\omega\epsilon_0$. $\epsilon_r = \sigma/\omega\epsilon_0 = 1.00\times10^3$ is used. $h_{2r}a$ is, to a good approximation, the same as for Figure 2.2. However, $h_{2j}a$ is quite different. For any value of the pair b/a and $ka\ cotan\psi$, $\left|h_{2j}\right|a$ is much larger compared to its corresponding value in Figure 2.2.

Figure 2.4 uses the values $b/a = 0.900$, $\sigma/\omega\epsilon_0 = 1.00\times10^2$, and different values of ϵ_r and $ka\ cotan\psi$. More specifically, $\epsilon_r = 1.00\times10^3$, 1.00×10^2, 10.0, 1.10 and $1.00\times10^{-4} < ka\ cotan\psi < 0.10$ are shown. It is obvious that the value of the relative permittivity has an insignificant effect on the wave number solution h_2a, except near $ka\ cotan\psi = 0.10$, when ϵ_r is large. The curves corresponding to all four different values of ϵ_r, associated with $h_{2r}a$ and with $-h_{2j}a$, are on top of each other over nearly the entire range of the $ka\ cotan\psi$ values shown.

The final graph included in sub-part 2.3.1.1 is Figure 2.5. It was prepared using $b/a = 0.900$, $\epsilon_r = 10.0$, and various values of $\sigma/\omega\epsilon_0$ and $ka\ cotan\psi$. More specifically, h_2a is evaluated for $\sigma/\omega\epsilon_0 = 1.00\times10^3$, 1.00×10^2, 10.0, 1.00×10^{-2} and $1.00\times10^{-4} < ka\ cotan\psi < 0.10$. Varying the value of $\sigma/\omega\epsilon_0$ has a negligible effect on the value of $h_{2r}a$. However, increasing this variable means that the value of $\left|h_{2j}\right|a$ definitely becomes larger. From physical considerations, one expects that the value of $\sigma/\omega\epsilon_0$ will have a great effect on the value of the imaginary part of h_2a because $h_{2j}a$ results from the fact that the rod material has a nonzero conductivity. (When the conductivity of the lossy rod approaches zero as a limit, it was demonstrated in part 2.2.2 that the free mode field solution associated with a sheath helix surrounding a lossy coaxial rod reduces to the free mode field solution associated with a sheath helix surrounding an ideal dielectric
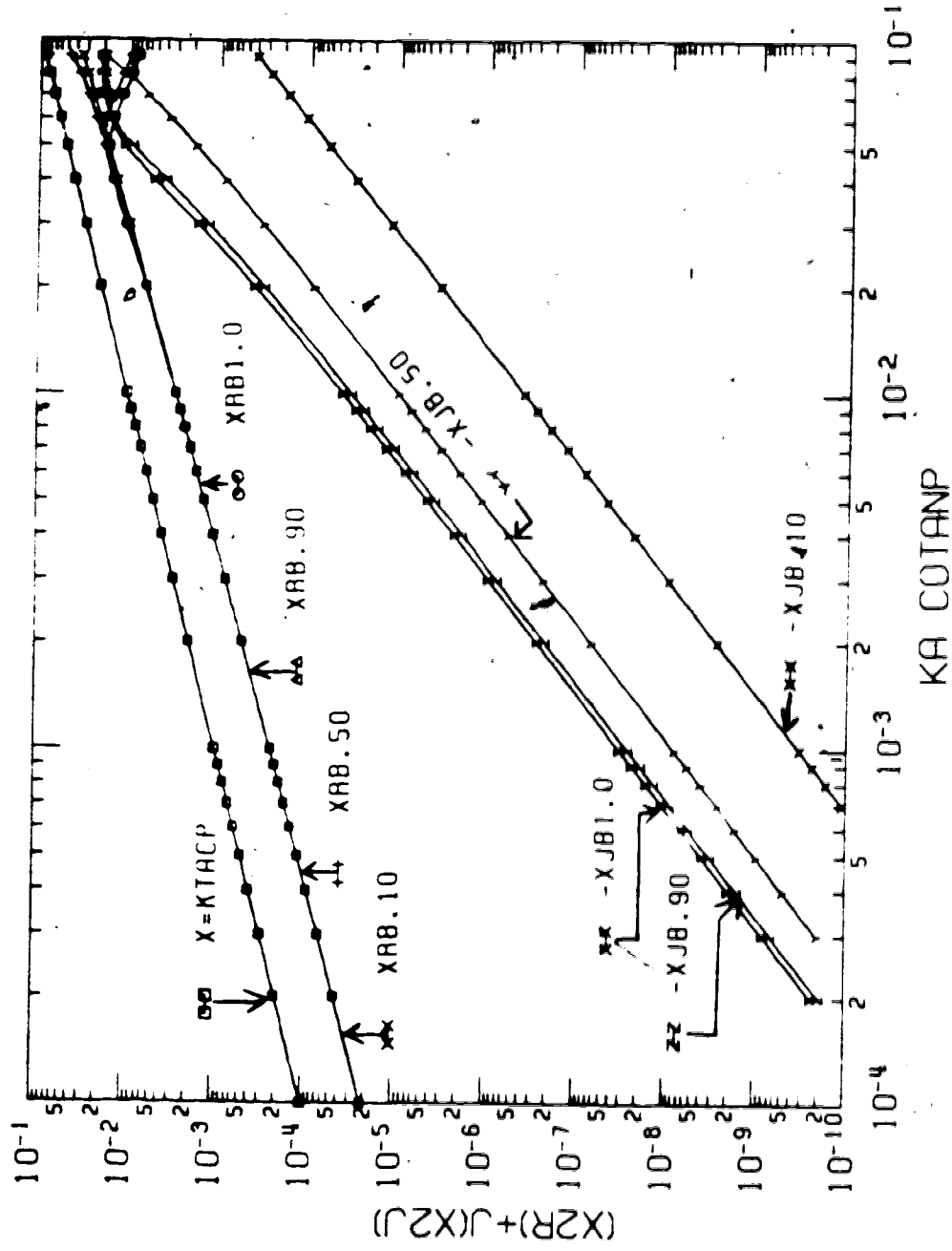
Figure 2.3   Small argument approximate solution for $h_{2}a$ based on equation 2.106 (the lossy rod is not a good conductor). $\epsilon_r=1.00\times10^3$; $\sigma/\omega\epsilon_0=1.00\times10^3$; b/a=1.00, 0.900, 0.500, 0.100; and $1.00\times10^{-4}<$ka cotan$\psi<0.100$ are used. $h_{2r}a$ and $-h_{2j}a$ are actually shown. (Note $X2=h_{2r}a+jh_{2j}a$, $X2R=h_{2r}a$, $X2J=h_{2j}a$, KA COTANP=KTACP=ka cotanψ, B/A=b/a, ER1=ϵ_r, and ER2=$\sigma/\omega\epsilon_0$. XRB1.0 means the curve represents $h_{2r}a$ for b/a=1.0 -XJB.10 means the curve represents $-h_{2j}a$ for b/a=0.100.)
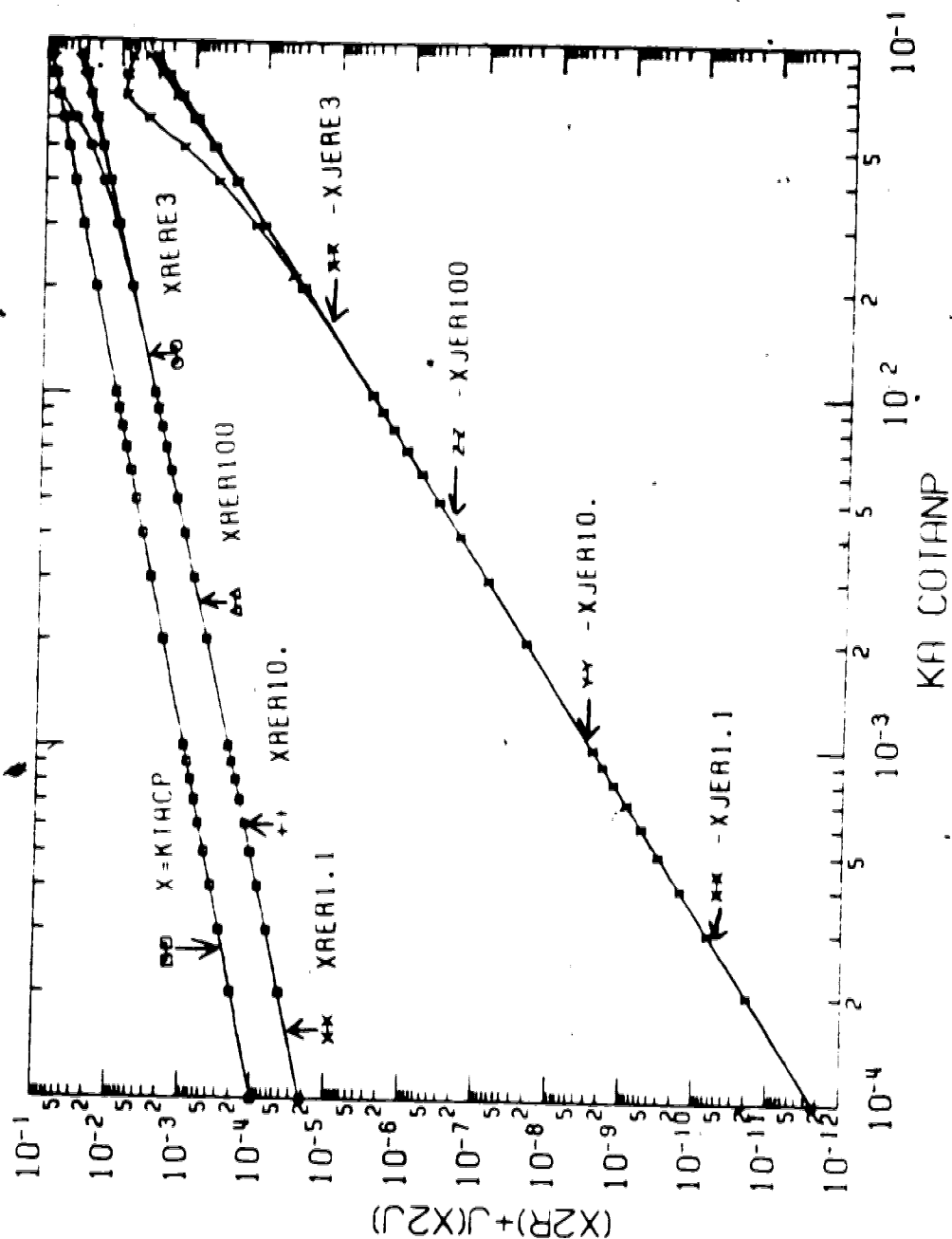
Figure 2.4   Small argument approximate solution for h_2a based on equation 2.106 (the lossy rod is not a good conductor). b/a=0.900; $\sigma/\omega\epsilon_0$=1.00x10^2; ϵ_r=1.10, 10.0, 1.00x10^2, 1.00x10^3; and 1.00x10^{-4}<ka cotanψ<0.100 are used. $h_{2r}a$ and $-h_{2j}a$ are actually shown. (Note X2=$h_{2r}a$+j$h_{2j}a$, X2R=$h_{2r}a$, X2J =$h_{2j}a$, KA COTANP=KTACP=ka cotanψ, B/A=b/a, ER1=ϵ_r, and ER2 =$\sigma/\omega\epsilon_0$. XRERE3 means the curve represents $h_{2r}a$ for ϵ_r=1.00x10^3. -XJER1.1 means the curve represents $-h_{2j}a$ for ϵ_r=1.10.)

4

Figure 2.5   Small argument approximate solution for h_2a based on equation 2.106 (the lossy rod is not a good conductor). $b/a=0.900$; $\epsilon_r=10.0$; $\sigma/\omega\epsilon_0=1.00\times10^{-2}$, 10.0, 1.00×10^2, 1.00×10^3; and $1.00\times10^{-4}<ka\ cotan\psi<0.100$ are used. $h_{2r}a$ and $-h_{2j}a$ are actually shown. (Note $X2=h_{2r}a+jh_{2j}a$, $X2R=h_{2r}a$, $X2J=h_{2j}a$, KA COTANP=KTACP=$ka\ cotan\psi$, $B/A=b/a$, $ER1=\epsilon_r$, and $ER2=\sigma/\omega\epsilon_0$. XRERE3 means the curve represents $h_{2r}a$ for $\sigma/\omega\epsilon_0=1.00\times10^3$. -XJERE-2 means the curve represents $-h_{2j}a$ for $\sigma/\omega\epsilon_0=1.00\times10^{-2}$.)

coaxial rod. In part ~~2.2.1, it is mentioned~~ that it is believed that only real-valued wave ~~numbers~~ ... associated with a sheath helix ...

2.3.3.2

The ... the dispersion equation for the case when "the lossy rod is not a good conductor" ... with both the two and three region configurations will be considered ~~in sub-part 2.3.1.2~~. First, the representation associated with the three region sheath helix surrounding a lossy coaxial rod configuration will be investigated. *It will be assumed that the operating frequency, the sheath helix geometry, the lossy rod geometry, and the lossy rod material electrical properties are such that the two radial wave numbers satisfy the inequalities*

$$|h_1|b > 1, \quad |h_2|b > 1, \quad \text{and} \quad h_{2r}a \cdot (1-b/a) > 1. \quad (2.111)$$

An equivalent statement of the preceding inequalities is

$$ka \cot\psi \cdot b/a > 1, \quad ka \cot\psi \cdot (1-b/a) > 1,$$

$$\text{and if } \epsilon_r \approx \cot^2\psi, \text{ then } \sqrt{\sigma/\omega\epsilon_0} \; ka \cdot b/a > 1. \quad (2.112)$$

(The explanation for imposing the requirements given in 2.111 and 2.112 will be provided shortly.)

Inequalities 2.111 or 2.112 define what is meant by the expression "the lossy rod is not a good conductor" as it is used in sub-part 2.3.1.2 for the three region configuration. It should be made clear that these inequalities do not place an upper limit on the values of ϵ_r and $\sigma/\omega\epsilon_0$. However, the case where the lossy rod conductivity becomes sufficiently large so that "the lossy rod is a good conductor" will be considered separately in sub-part 2.3.2.2. For the purposes of the following discussion, the conductivity is only assumed to be sufficiently large so that

inequalities 2.112 are satisfied. Indeed, provided that the variable $ka \cot a\psi$ is sufficiently large and provided that ϵ_r and $\cot^2 a\psi$ are not approximately equal,

x. Table A.3 shows [illegible] are approximated by keeping only the first term of equations A.25 - A.28 the so-called zero order large argument representations [illegible] when $|h_1|b$ and $|h_2|b$ are both greater than unity, as stipulated in inequalities 2.111, justification is provided for using the zero order large argument representations to approximate all the Bessel functions appearing in equation 2.65, the dispersion equation. For convenience, equation 2.65 is rewritten in the following manner.

$$(\frac{ka \cot a\psi}{h_2 a})^2 = \frac{I_0(h_2 a) \, K_0(h_2 a)}{I_1(h_2 a) \, K_1(h_2 a)} \cdot [1 + \frac{K_0(h_2 a)}{I_0(h_2 a)} \cdot$$

$$(h_1 a \, I_0(h_1 b) \, I_1(h_2 b)$$

$$- (\epsilon_r - j\,\sigma/\omega\epsilon_0)\, h_2 a \, I_0(h_2 b) \, I_1(h_1 b)) \cdot \qquad (2.113)$$

$$1/(h_1 a \, I_0(h_1 b) \, K_1(h_2 b)$$

$$+ (\epsilon_r - j\,\sigma/\omega\epsilon_0)\, h_2 a \, I_1(h_1 b) \, K_0(h_2 b))] \cdot$$

$$1/[1 - \frac{K_1(h_2 a)}{I_1(h_2 a)} \frac{(h_1 a \, I_0(h_1 b) \, I_1(h_2 b) - h_2 a \, I_0(h_2 b) \, I_1(h_1 b))}{(h_1 a \, I_0(h_1 b) \, K_1(h_2 b) + h_2 a \, I_1(h_1 b) \, K_0(h_2 b))}]$$

Substituting the zero order large argument Bessel function representations into equation 2.113 and performing a small amount of algebra yields

$$\left(\frac{ka\ \cot a n\psi}{h_2 a}\right)^2 \simeq \qquad\qquad (2.114)$$

$$\frac{[1 + e^{-2 h_2 a (1-b/a)} \cdot \frac{(h_1 a - (\epsilon_r - j\ \sigma/\omega\epsilon_0)h_2 a)}{(h_1 a + (\epsilon_r - j\ \sigma/\omega\epsilon_0)h_2 a)}]}{[1 - e^{-2 h_2 a (1-b/a)} \cdot \frac{(h_1 a - h_2 a)}{(h_1 a + h_2 a)}]} \cdot$$

Equation 2.114 is the large argument approximation of the dispersion equation when "the lossy rod is not a good conductor". An attempt was made to obtain numerical solutions for both $h_1 a$ and $h_2 a$ based on equations 2.114 and 2.88. Separately equating respectively the real and imaginary parts of these two equations, four real-valued equations involving the four real-valued unknowns $h_{1r} a$, $h_{1j} a$, $h_{2r} a$, and $h_{2j} a$ were obtained. The IMSL (43) software program ZSCNT was used in the attempt to solve these equations. Unfortunately, the two equations associated with the real and imaginary parts of equation 2.114 are very lengthy and complicated. Considerable difficulty was encountered in getting the trial solution of the four unknowns to converge to the correct solution. The author failed in his attempt to numerically solve equations 2.114 and 2.88.

Even though a numerical solution of $h_1 a$ and $h_2 a$ could not be achieved, expressions for the wave numbers solution can be obtained by making approximations to equation 2.114. As stipulated in inequalities 2.111, it will now be assumed that the value of $h_{2r} a$ is sufficiently large, taking into account the value of b/a, so that $h_{2r} a \cdot (1-b/a) > 1$ is true. This means that

$$1 - \left| e^{-2 h_2 a (1-b/a)} \cdot \frac{(h_1 a - h_2 a)}{(h_1 a + h_2 a)} \right| \simeq 1, \quad \text{and}$$

$$1 + \left| e^{-2 h_2 a (1-b/a)} \cdot \frac{(h_1 a - (\epsilon_r - j\ \sigma/\omega\epsilon_0)h_2 a)}{(h_1 a + (\epsilon_r - j\ \sigma/\omega\epsilon_0)h_2 a)} \right| \simeq 1.$$

Using these relations, equation 2.114 can be simplified to show that

$$h_{2r}a \cong ka \cot an\psi \quad \text{and} \quad |h_{2j}|a << ka \cot an\psi. \quad (2.115)$$

Combining these expressions for $h_2 a$ with the separation constant equation, equation 2.88, values for $h_1 a$ and βa can be obtained. (It has been assumed that the sheath helix is sufficiently tightly wound so that $\cot an^2\psi >> 1$. This will certainly be true if the pitch angle satisfies $0 < \psi \leq 10.0°$.)

$$h_{2r}a \cong \beta_r a \cong ka \cot an\psi,$$

$$|h_{2j}|a \cong |\beta_j|a << ka \cot an\psi, \quad \text{and} \quad (2.116)$$

$$h_1 a \cong ka \sqrt{(\cot an^2\psi - \epsilon_r) + j\,\sigma/\omega\epsilon_0}.$$

Equations 2.116 are the approximate large argument wave numbers solution associated with the three region configuration, when "the lossy rod is not a good conductor." Inequalities 2.112, which list the requirements necessary so that this approximate wave numbers solution is valid, can be obtained from inequalities 2.111 by making use of approximations 2.116. Note that, in agreement with the discussion previously presented in part 2.1.2, the real parts of the three wave numbers listed in 2.116 are positive. In addition, the approximation for $h_{2r}a$ is the same as that stated in equation B.20. Therefore, if the requirements listed in 2.112 are satisfied, the large argument approximation for $h_{2r}a$ is the same as the large argument approximation of the (real) radial wave number associated with the empty sheath helix.

$h_1 a$, $h_{2r}a$, and $\beta_r a$ are explicitly given in 2.116 in terms of the operating frequency, the sheath helix geometry, and the lossy rod material electrical properties. Unfortunately, an explicit solution for $h_{2j}a \cong \beta_j a$ cannot be obtained. It is the fact that the conductivity of the lossy rod is nonzero which accounts for the presence of the imaginary part of the wave numbers solution. Making use of

approximations 2.115, it is seen from equation 2.114 that the magnitude of the term containing the lossy rod conductivity,

$$\left| e^{-2\ ka\ cotan\psi(1-b/a)} \cdot \frac{(h_1 a - (\epsilon_r - j\ \sigma/\omega\epsilon_0)\ ka\ cotan\psi)}{(h_1 a + (\epsilon_r - j\ \sigma/\omega\epsilon_0)\ ka\ cotan\psi)} \right| ,$$

will rapidly become small compared to unity in an exponential fashion as the value of $ka\ cotan\psi$ increases. Therefore, as $ka\ cotan\psi$ becomes large, equation 2.114 shows that $|h_{2j}|a \cong |\epsilon_j|a$ will rapidly become small.

Attention is now directed towards deriving the approximate large argument wave numbers solution which is valid for the two region configuration. This can be obtained by substituting $b = a$ into equation 2.114. Assuming that $h_1 a \cong h_2 a$,

$$h_2 a \cong \sqrt{\frac{(\epsilon_r + 1) - j\ \sigma/\omega\epsilon_0}{2}}\ ka\ cotan\psi \qquad (2.117)$$

is obtained. Equation 2.117 can easily be shown to satisfy the inequalities given in 2.93, assuming that the sheath helix is sufficiently tightly wound so that $cotan^2\psi \gg 1$ occurs. (This is always true for $0 < \psi \leq 10.0°$.) For this special case, the approximations $h_1 a \cong h_2 a \cong \beta a$ are well justified. (This supports the approximation $h_1 a \cong h_2 a$ which was used in the derivation of equation 2.117.) Therefore, it follows from equation 2.117 that

$$\beta a \cong h_1 a \cong h_2 a \cong \sqrt{\frac{(\epsilon_r + 1) - j\ \sigma/\omega\epsilon_0}{2}}\ ka\ cotan\psi. \qquad (2.118)$$

Equations 2.118 are the approximate large argument wave numbers solution associated with the two region configuration, "when the lossy rod is not a good conductor". These equations are very convenient because both the real and the imaginary parts of the three wave numbers are explicitly expressed in terms of the operating frequency, the sheath helix geometry, and the electrical properties of the lossy rod material. Note that $h_{1r} a > 0$, $h_{2r} a > 0$, and $\beta_r a > 0$ occurs, which are the correct values of the real parts of the wave numbers, as was previously discussed in part 2.1.2. As well, $h_{2j} a < 0$ is true and so this quantity has the same algebraic sign as it did for the small argument solution which was previously discussed in sub-part 2.3.1.1.

Taking the limit of equations 2.118 as $\sigma \to 0^+$ yields equation D.54. In the limit as the conductivity of the lossy rod approaches zero, the wave numbers solution given in equations 2.118 reduces to the two region approximate large argument solution of the (real) wave number associated with the sheath helix surrounding an ideal dielectric coaxial rod. This result is expected and it provides a check on the accuracy of equations 2.118.

Equation 2.114 was used in the derivation of equations 2.118. In order that equation 2.114 with $b = a$ is justified as an approximation of the dispersion equation, it is necessary that $|h_1| a > 1$ and $|h_2| a > 1$. Furthermore, in order to obtain equations 2.118 from equation 2.117, it was assumed that the sheath helix is sufficiently tightly wound so that $\cotan^2 \psi \gg 1$. Making use of equations 2.118, it is possible to express the three preceding inequalities as

$$\left| \sqrt{\frac{(\epsilon_r + 1) - j\,\sigma/\omega\epsilon_0}{2}} \right| \quad ka\,\cotan\psi > 1,$$

$$(2.119)$$

$$\text{and} \quad \cotan^2 \psi \gg 1.$$

The requirements listed in 2.119 define what is meant by the expression "the lossy rod is not a good conductor" as it applies to the two region configuration large argument case. If these requirements are satisfied, the approximate wave numbers solution given in equations 2.118 is justified. Note that no upper limit is placed on the values of ϵ_r and $\sigma/\omega\epsilon_0$. If the value of $ka \cot\psi$ satisfies $ka \cot\psi > 1$ and if the pitch angle is sufficiently small so that $\cot^2\psi \gg 1$ is true, either $\epsilon_r \gg \sigma/\omega\epsilon_0$ or $\sigma/\omega\epsilon_0 \gg \epsilon_r$ is allowed.

2.3.2 Solution of the Wave Numbers When "The Lossy Rod Is a Good Conductor"

2.3.2.1 Small Argument Representation

Attention is now directed to the approximation of the dispersion equation which is valid when the Bessel function arguments are either small or large in magnitude, for the case when "the lossy rod is a good conductor". Both the two and three region sheath helix surrounding a lossy coaxial rod configurations will be considered. The three region configuration will be examined first. *It will be assumed that the operating frequency, the sheath helix geometry, the lossy rod geometry, and the electrical properties of the lossy rod material are such that the inequalities*

$$\sigma/\omega\epsilon_0 \gg \epsilon_r, \quad |h_1|a \cong \sqrt{j\,\sigma/\omega\epsilon_0}\,ka,$$

$$|h_1|b \cong \sqrt{\sigma/\omega\epsilon_0}\,kb > 1, \quad \text{and} \quad |h_2|a < 0.10$$

$$(2.120)$$

are satisfied.

The restrictions imposed in 2.120 serve to define what is meant by the expression "the lossy rod is a good conductor" as it is used in sub-part 2.3.2.1 for the three region sheath helix surrounding a lossy coaxial rod configuration. Note that the value selected for the radial wave number $h_1 a$ is the same as that demonstrated previously in part 2.2.3 to be the appropriate value as the lossy rod conductivity tends to infinity. It follows from this choice that equation 2.88, the separation constant equation,

approximately becomes

$$(\beta a)^2 \cong (h_2 a)^2 + (ka)^2. \qquad (2.121)$$

For convenience, equation 2.65, the dispersion equation, is written in the manner given by equation 2.101. Since $|h_2| a < 0.10$ is required from 2.120, little error is involved with using the small argument Bessel function representations, equations A.26 – A.29, to approximate all the functions of argument $h_2 a$ and $h_2 a \cdot b/a$ which appear in equation 2.101. Furthermore, since $|h_1| b > 1$ is required from 2.120, relatively little error is involved in using the zero order large argument Bessel function representations, which consist of just the first term of equations A.36 – A.39, to approximate all the functions of argument $h_1 a$ and $h_1 a \cdot b/a$ appearing in equation 2.101. Making these substitutions, employing the requirement $\sigma/\omega\varepsilon_0 \gg \varepsilon_r$ listed in 2.120, performing some algebra, and carefully simplifying by eliminating the less significant terms, yields

$$\left(\frac{ka \cot an\psi}{h_2 a}\right)^2 \cong \frac{-2\sqrt{j \ \sigma/\omega\varepsilon_0} \ ka \ \log(b/a)}{[\sqrt{j \ \sigma/\omega\varepsilon_0} \ ka \ (1-(b/a)^2) + 2 \ b/a]} \cdot$$

$$\frac{\log(0.891 \ h_2 a)}{\log(0.891 \ h_2 b)}. \qquad (2.122)$$

Equation 2.122 is the small argument approximation of the dispersion equation associated with the three region configuration, when "the lossy rod is a good conductor". It is justified when the requirements listed in 2.120 are satisfied. Taking the limit of equation 2.122 as $\sigma \to \infty$ gives the same result as equation C.21. As expected, in the limit as the lossy rod conductivity tends to infinity, equation 2.122

becomes the same as the accurate small argument approximation of the dispersion equation associated with the three region sheath helix surrounding a perfectly conducting coaxial rod configuration. This limiting result provides support for the accuracy of equation 2.122.

Equation 2.122 is numerically solved to obtain $h_2 a$ using a similar procedure to that employed previously to solve equation 2.106. Separately equating respectively the real and imaginary parts of equation 2.122 gives two real-valued equations involving the two real-valued unknowns $h_{2r} a$ and $h_{2j} a$. These are

$$
\begin{aligned}
(ka \cot\psi)^2 &\cdot [\log(0.891 \, b/a \, x_m) \cdot \\
&((1-(b/a)^2) \, ka \sqrt{\sigma/2\omega\epsilon_0} + 2 \, b/a) \\
&- \theta_m (1-(b/a)^2) \, ka \sqrt{\sigma/2\omega\epsilon_0} \,] \\
&+ 2 \, ka \sqrt{\sigma/2\omega\epsilon_0} \, \log(b/a) \cdot \\
&[(x_{2r}^2 - x_{2j}^2) \, (\log(0.891 \, x_m) - \theta_m) \\
&- 2 \, x_{2r} \, x_{2j} \, (\log(0.891 \, x_m) + \theta_m)] = 0
\end{aligned}
\tag{2.123}
$$

and

$$
\begin{aligned}
(ka \cot\psi)^2 &\cdot [\log(0.891 \, b/a \, x_m) \cdot \\
&(1-(b/a)^2) \, ka \sqrt{\sigma/2\omega\epsilon_0} \\
&+ \theta_m \cdot (2 \, b/a + (1-(b/a)^2) \, ka \sqrt{\sigma/2\omega\epsilon_0} \,)] \\
&+ 2 \, ka \sqrt{\sigma/2\omega\epsilon_0} \, \log(b/a) \cdot
\end{aligned}
\tag{2.124}
$$

$$[2 \; x_{2r} \; x_{2j} \; (\log(0.891 \; x_m) - \theta_m)$$

$$+ \; (x_{2r}^2 - x_{2j}^2) \; (\log(0.891 \; x_m) + \theta_m)] = 0.$$

The notation used in equations 2.123 and 2.124 is now defined.

$$x_{2r} = h_{2r}a, \quad x_{2j} = h_{2j}a, \quad x_m = |h_2|a = \sqrt{x_{2r}^2 + x_{2j}^2},$$

$$\text{and} \quad \theta_m = \tan^{-1}(x_{2j}/x_{2r}).$$

The IMSL (43) software program ZSCNT was used to solve equations 2.123 and 2.124 for the small argument approximate value of h_2a. In order to obtain h_2a, it is necessary to specify the variable set $ka \cot\psi$, b/a, $\sigma/\omega\epsilon_0$, and ψ. It was always ensured that the variables satisfied the requirements listed in equations 2.120.

Two graphs of the solution to equations 2.123 and 2.124 have been prepared. It was always found that $h_{2r}a > 0$ and $h_{2j}a < 0$. As was previously discussed in part 2.1.1, $\text{Re}[h_2a] > 0$ is necessary in order that the fields satisfy the condition of regularity at infinity for $r \rightarrow \infty$. $h_{2r}a$ and $-h_{2j}a$ have been plotted on the graphs. The corresponding approximate small argument value of βa is calculated when h_2a is known by using equation 2.121. Of course, the approximate value of h_1a is given in 2.120.

For both of the graphs presented in sub-part 2.3.2.1 it was discovered that the real part of h_2a is approximately given by

$$\left(\frac{ka \cot\psi}{h_{2r}a}\right)^2 \cong \frac{-2 \log(b/a)}{(1-(b/a)^2)}.$$

Clearly, equation 2.125 shows that $h_{2r}a$ is approximately dependent only on the variables $ka \cot\psi$ and b/a. This equation is the same as equation C.24, which

is the crude small argument approximation of the dispersion equation associated with the sheath helix surrounding a perfectly conducting coaxial rod.

Figure 2.6 plots $h_2 a$ versus $ka \cot an\psi$ for $1.00 \times 10^{-4} <$ $ka \cot an\psi < 0.10$, $\psi = 10.0°$, and various values of b/a and $\sigma/\omega\epsilon_0$. More specifically, $b/a = 0.100, 0.900$; and $\sigma/\omega\epsilon_0 = 1.00 \times 10^{14}$ and 1.00×10^{20} are used. (Note that the restriction $\sqrt{\sigma/\omega\epsilon_0} ka \cdot b/a > 1$ mentioned in 2.120 means that $\sigma/\omega\epsilon_0$ must be very large.) The values of b/a and $\sigma/\omega\epsilon_0$ are seen to have a great effect on $-h_{2j} a$. For a fixed value of b/a increasing $\sigma/\omega\epsilon_0$ tends to decrease $|h_{2j}| a$. This behavior is expected because it was previously shown that in the limit as $\sigma/\omega\epsilon_0$ approaches infinity, $h_{2j} = 0$ results. (In part 2.2.3 it was demonstrated that taking the limit as the lossy rod conductivity approaches infinity, the free mode field solution becomes that of a sheath helix surrounding a perfectly conducting coaxial rod. As mentioned in section C.2, it is believed that only real-valued wave numbers are permissible for the free mode field solution associated with the perfectly conducting rod configuration.)

Figure 2.7 is a graph of $h_2 a$ versus $ka \cot an\psi$ for $1.00 \times 10^{-2} <$ $ka \cot an\psi < 0.10$, $b/a = 0.900$, and $\psi = 10.0°$. Many different values of $\sigma/\omega\epsilon_0$ are used. These are $\sigma/\omega\epsilon_0 = 1.00 \times 10^8$, 1.00×10^{10}, 1.00×10^{14}, and 1.00×10^{20}. Clearly, increasing the value of $\sigma/\omega\epsilon_0$ tends to make $|h_{2j}| a$ smaller.

Attention is now directed towards deriving the small argument approximation of the dispersion equation which is valid for the two region configuration, when "the lossy rod is a good conductor". *It is assumed that the requirements listed in 2.120 are satisfied with* $b = a$. *This defines what is meant by the expression "the lossy rod is a good conductor" as it applies to the two region configuration, small argument case.*

A similar procedure to that performed at the beginning of sub-part 2.3.2.1 was carried out in order to derive the two region small argument approximation of the dispersion equation. *However, a more detailed examination showed that this approximation is actually not valid.* The small argument Bessel function representations, equations A.26 - A.29, were used to approximate all functions of
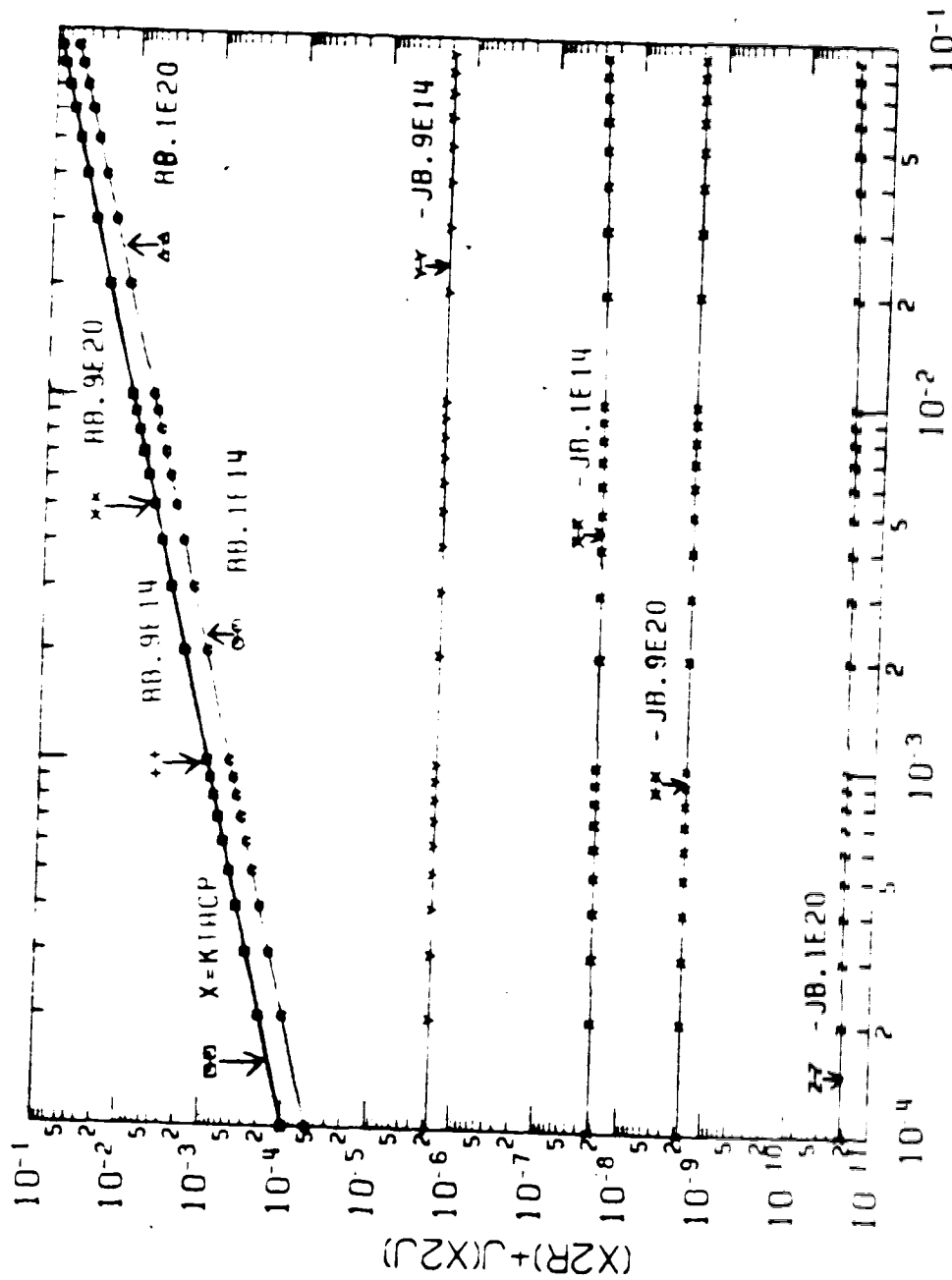
Figure 2.6   Small argument approximate solution for h_2a based on equation 2.122 (the lossy rod is a good conductor). $b/a=0.900$, 0.100; $\psi=10.0°$; $\sigma/\omega\epsilon_0=1.00\times10^{14}$, 1.00×10^{20}; and $1.00\times10^{-4}<ka$ $cotan\psi<0.100$ are used. $h_{2r}a$ and $-h_{2j}a$ are actually shown. (Note $X2=h_{2r}a+jh_{2j}a$, $X2R=h_{2r}a$, $X2J=h_{2j}a$, KA COTANP=KTACP=ka cotanψ, B/A=b/a, and ER2=$\sigma/\omega\epsilon_0$. RB.1E20 means the curve represents $h_{2r}a$ for $b/a=0.100$ and $\sigma/\omega\epsilon_0$ $=1.00\times10^{20}$. -JB.9E14 means the curve represents $-h_{2j}a$ for $b/a=0.900$ and $\sigma/\omega\epsilon_0=1.00\times10^{14}$.)
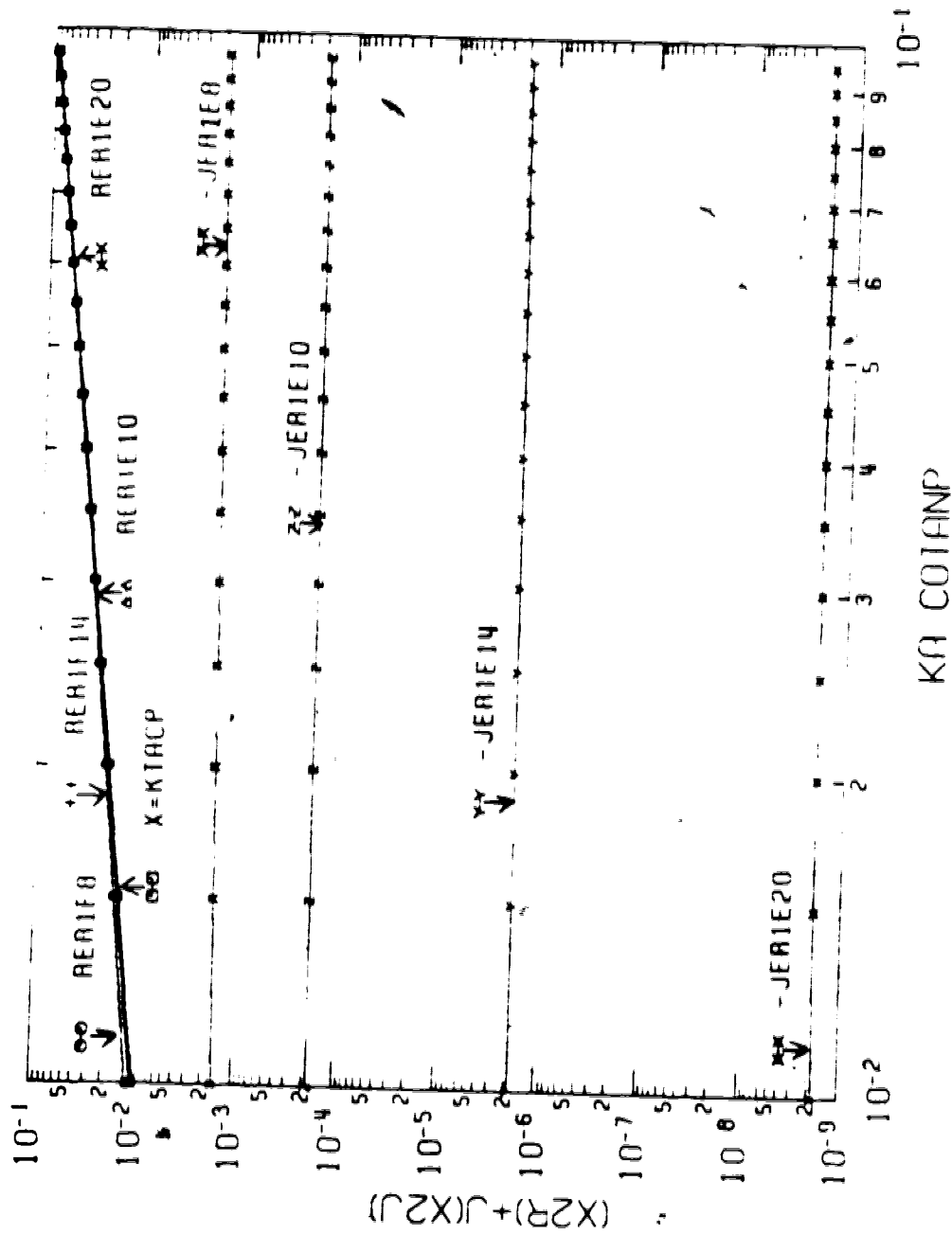
figure 2.7   Small argument approximate solution for h_2a based on equation 2.122 (the lossy rod is a good conductor). b/a=0.900; ψ=10.0°; $\sigma/\omega\epsilon_0$=1.00x10^{8}, 1.00x10^{10}, 1.00x10^{14}, 1.00x10^{20}; and 1.00x10^{-2}<ka cotanψ<0.100 are used. $h_{2r}a$ and $-h_{2j}a$ are actually shown. (Note X2=$h_{2r}a$+$jh_{2j}a$, X2R=$h_{2r}a$, X2J =$h_{2j}a$, KA COTANP=KTACP=ka cotanψ, and ER2=$\sigma/\omega\epsilon_0$. RER1E20 means the curve represents $h_{2r}a$ for $\sigma/\omega\epsilon_0$=1.00x10^{20}. -JER1E8 means the curve represents $-h_{2j}a$ for $\sigma/\omega\epsilon_0$=1.00x10^{8}.)

argument $h_2 a$ in the two region form of the angular and axial magnetic field components, which were obtained by calculating $\lim b \to a^-$ of equations 2.74, 2.75, 2.86, and 2.87. Similarly, the zero order large argument Bessel function representations, which consist of just the first term of equations A.36 – A.39, were used to approximate all functions of argument $h_1 a$ appearing in the previously mentioned magnetic field components. Making use of the requirements listed in 2.120, it was discovered that these approximate magnetic field components did not satisfy the boundary condition at the sheath helix surface given by equation 1.9. *This means that the two region configuration small argument case when "the lossy rod is a good conductor" is not a valid free mode field solution.* No attempt was made to investigate the approximate wave numbers solution because it is actually meaningless –– the field components associated with these wave numbers do not satisfy all the required boundary conditions and therefore they are rejected as an incorrect solution.

2.3.2.2 Large Argument Representation

To conclude section 2.3, the large argument representations of the dispersion equation for the case when "the lossy rod is a good conductor" associated with both the two and three region configurations will be considered. The three region sheath helix surrounding a lossy coaxial rod configuration will be considered first. *It will be assumed that the operating frequency, the sheath helix geometry, the lossy rod geometry, and the lossy rod material electrical properties are such that*

$$\sigma/\omega\epsilon_0 \gg \epsilon_r, \quad h_1 a \cong \sqrt{j\ \sigma/\omega\epsilon_0}\ ka, \quad |h_2|b > 1,$$

$$|h_1|a \cong \sqrt{\sigma/\omega\epsilon_0}\ ka \gg |h_2|a, \ \text{and} \ h_{2r}a \cdot (1-b/a) > 1. \tag{2.126}$$

(Note that equation 2.88, the separation constant equation, demonstrates that $|h_1|a \gg |h_2|a$ is required in order that $h_1 a \cong \sqrt{j\ \sigma/\omega\epsilon_0}\ ka$ is valid.) *An equivalent statement of the inequalities presented in 2.126 is*

$$\sigma/\omega\epsilon_0 >> \epsilon_r, \quad h_1 a \cong \sqrt{j\ \sigma/\omega\epsilon_0}\ ka,$$

$$ka\ \cot an\psi \cdot b/a > 1, \quad \sigma/\omega\epsilon_0 >> \cot an^2\psi, \quad and \quad (2.127)$$

$$ka\ \cot an\psi \cdot (1-b/a) > 1.$$

(The explanation concerning why the requirements listed in 2.126 and 2.127 are equivalent will be provided shortly.)

Inequalities 2.126 or 2.127 define what is meant by the expression "the lossy rod is a good conductor" as it is used for the small argument case of the three region configuration. Since $|h_1|b > 1$ and $|h_2|b > 1$ is required, relatively little error is involved in using the zero order large argument Bessel function representations to approximate the dispersion equation. Substituting just the first term of equations A.36 – A.39 in order to approximate all the Bessel functions appearing in the form of the dispersion equation given by equation 2.113, making use of all the requirements listed in 2.126, and finally employing equation 2.88, which is the separation constant equation, yields

$$h_{2r}a \cong \beta_r a \cong ka\ \cot an\psi,$$

$$|h_{2j}|a \cong |\beta_j|a << ka\ \cot an\psi, \quad and \quad (2.128)$$

$$h_{1r}a \cong h_{1j}a \cong \sqrt{\sigma/2\omega\epsilon_0}\ ka.$$

Equations 2.128 are the approximate large argument wave numbers solution associated with the three region configuration when "the lossy rod is a good conductor". They are justified when the restrictions listed in inequalities 2.126 or 2.127 are satisfied. (Note that inequalities 2.127 can be obtained from inequalities 2.126 by making use of

equations 2.128.) Interestingly, equations 2.128 can be derived from equations 2.116 when $\sigma/\omega\epsilon_0 \gg \epsilon_r$ and $\sigma/\omega\epsilon_0 \gg \cot an^2\psi$. The approximate wave numbers solution for the three region configuration large argument case when "_the lossy rod is a good conductor_" can be considered as a special case of the approximate wave numbers solution for the three region configuration large argument case when "_the lossy rod is not a good conductor_", provided that the rod conductivity is sufficiently large to satisfy the preceding two inequalities.

Finally, attention is directed towards deriving the approximate large argument wave numbers solution which is valid for the two region configuration. It is assumed that

$$b = a, \quad \sigma/\omega\epsilon_0 \gg \epsilon_r, \quad h_1 a \cong \sqrt{j\,\sigma/\omega\epsilon_0}\, ka,$$

$$|h_2|a > 1, \quad \text{and} \quad |h_1|a \cong \sqrt{\sigma/\omega\epsilon_0}\, ka \gg |h_2|a. \tag{2.129}$$

The requirements listed in 2.129 define what is meant by the expression "the lossy rod is a good conductor" as it applies to the two region configuration large argument case.

A similar procedure to that followed at the beginning of sub-part 2.3.2.2 was carried out in order to derive the two region large argument approximation of the dispersion equation. However, a more detailed investigation showed that this approximation is actually not valid. Just the first term of equations A.36 - A.39, the zero order large argument Bessel function representations, was used to approximate all the Bessel functions appearing in the two region form of the angular and axial magnetic field components, which were obtained by calculating $\lim b \to a^-$ of equations 2.74, 2.75, 2.86, and 2.87. Making use of the restrictions listed in 2.129, it was discovered that these approximate magnetic field components did not satisfy equation 1.9, which is one of the boundary conditions at the surface of the sheath helix. Therefore, the two region configuration large argument case when "the lossy rod is a good conductor" _is not a valid free mode field solution_. No attempt was made to examine the approximate wave numbers solution because it is not of any interest.

It is important to realize that the proper wave numbers solution does exist for the two region configuration large argument case, when the electrical properties of the lossy rod material are such that $\epsilon_r >> \sigma/\omega\epsilon_0$. As was previously discussed in sub-part 2.3.1.2, this means that $h_1 a \cong h_2 a$ occurs and the approximate wave numbers solution is given by equations 2.118. However, if $\epsilon_r >> \sigma/\omega\epsilon_0$, $h_1 a \cong \sqrt{j \, \sigma/\omega\epsilon_0} \; ka$ and $|h_1|a >> |h_2|a$ are all assumed, the preceding discussion has demonstrated that a free mode field solution does not exist, and so an investigation of the wave numbers solution is meaningless.

2.4 Graphs of the Radial Dependence Associated With the Magnitudes of the Approximate Fields

The field components, equations 2.70 - 2.87, are very lengthy and complicated expressions. In order to achieve an understanding of how these fields behave at different points in space, it would be useful to prepare graphs showing their radial dependence. Unfortunately, this is usually very difficult to accomplish. The reason for this originates from the hardship involved in solving the dispersion equation, equation 2.65, and the separation constant equation, equation 2.88, for an arbitrary set of the variables listed in equations 2.89 - 2.91, in order to obtain the wave numbers solution. However, it is possible to prepare radial dependence graphs which approximate the field components for certain special cases of the operating frequency, the sheath helix geometry, the lossy rod geometry, and the lossy rod material electrical properties. Previously, in section 2.3, approximate radial and axial wave numbers were calculated for both the large and small argument representations associated with the circumstances when "the lossy rod is not a good conductor", and when "the lossy rod is a good conductor". The purpose of this section is to provide some graphs of the radial dependence associated with the approximate magnitudes of the electric and magnetic field components, based on the previously mentioned approximate wave numbers solution. There are three important reasons for doing this.

1. An understanding of how the electric and magnetic fields behave at different points in space within the rod-filled region, within the air gap between the surface of the lossy rod and the sheath helix surface, and within the air-filled region exterior to

the surface of the sheath helix, will be obtained.

2. By numerically evaluating and graphing the radial dependence of the radial, angular, and axial electric fields within the rod-filled region, information concerning the time-averaged power dissipation which occurs within the lossy rod is obtained. Chapter 3 is concerned with studying this power dissipation.

3. For the operating frequency, sheath helix geometry, lossy rod geometry, and lossy rod material electrical properties which are used, it will be seen that the magnitudes of the fields associated with the lossy rod configuration are approximately similar to the absolute values of the corresponding fields associated with either the configuration studied in Appendix C or that studied in Appendix D. The configurations discussed in these two appendices are very attractive because it is relatively easy to calculate the radial and axial wave numbers, and consequently to numerically evaluate the field components. By establishing a connection between the free mode field solution associated with the sheath helix surrounding a lossy coaxial rod, and that associated with the two configurations given in Appendices C and D, the discussion given in the two appendices will aid in understanding the lossy rod configuration. Furthermore, it is important to establish this connection because Chapter 3 makes use of information given in Appendices C and D to approximately investigate the power dissipation occurring within the lossy rod.

All the electric field components, equations 2.70 - 2.72, 2.76 - 2.78, and 2.82 - 2.84, are normalized from dividing them by an electric normalizing coefficient, E_{z0}. All the magnetic field components, equations 2.73 - 2.75, 2.79 - 2.81, and 2.85 - 2.87, are normalized from dividing them by a magnetic normalizing coefficient, H_{z0}. The electric and magnetic normalizing coefficients are obtained from equations 2.78 and 2.81, respectively. They are

$$E_{z0} = E_{z2}\Big|_{\substack{z=0 \\ r=a}} = j \mathcal{D}_{II} \frac{120\pi}{ka \cot an\psi} \cos\psi \, (h_2 a)^2 \, K_0(h_2 a) \, . \qquad (2.130)$$

$$.[I_0(h_2a) \cdot (h_1a \, I_0(h_1b) \, K_1(h_2b) +$$

$$(\epsilon_r -, j \, \sigma/\omega\epsilon_0) \, h_2a \, I_1(h_1b) \, K_0(h_2b)) + K_0(h_2a) \cdot$$

$$(h_1a \, I_0(h_1b) \, I_1(h_2b) - (\epsilon_r - j \, \sigma/\omega\epsilon_0) \, h_2a \, I_0(h_2b) \, I_1(h_1b))] \cdot$$

$$1/[h_1a \, I_0(h_1b) \, K_1(h_2b) + (\epsilon_r - j \, \sigma/\omega\epsilon_0) \, h_2a \, I_1(h_1b) \, K_0(h_2b)]$$

$$\hspace{10cm}(2.130)$$

$$=j \, \partial_{11} \, \frac{120\pi \, ka \, \cot\psi \, \cos\psi \, K_1(h_2a)}{(h_1a \, I_0(h_1b) \, K_1(h_2b) + h_2a \, I_1(h_1b) \, K_0(h_2b))} \hspace{1cm} \text{(continued)}$$

$$[I_1(h_2a) \cdot (h_1a \, I_0(h_1b) \, K_1(h_2b) + h_2a \, I_1(h_1b) \, K_0(h_2b))$$

$$- K_1(h_2a) \cdot (h_1a \, I_0(h_1b) \, I_1(h_2b) - h_2a \, I_0(h_2b) \, I_1(h_1b))],$$

and

$$H_{z0} = H_{z2}\Big|_{\substack{z=0 \\ r=a}} = \partial_{11} \cos\psi \, h_2a \, K_1(h_2a) \cdot \hspace{2cm}(2.131)$$

$$[I_0(h_2a) \cdot (h_1a \, I_0(h_1b) \, K_1(h_2b) + h_2a \, I_1(h_1b) \, K_0(h_2b))$$

$$+ K_0(h_2a) \cdot (h_1a \, I_0(h_1b) \, I_1(h_2b) - h_2a \, I_0(h_2b) \, I_1(h_1b))] \cdot$$

$$1/[h_1a \, I_0(h_1b) \, K_1(h_2b) + h_2a \, I_1(h_1b) \, K_0(h_2b)].$$

Equation 2.65, the dispersion equation, was used in the derivation of equations 2.130. The normalizing coefficients associated with the two region configuration (b = a) are obtained by calculating $\lim b \to a^-$ of equations 2.130 and 2.131.

When graphs of the radial dependence of the approximate normalized field component magnitudes are presented, it is assumed that the axial coordinate is held

constant. The transverse planes are chosen so that $\cos(\beta a \cdot z/a) = \pm 1$ for the angular and axial fields. In the case of the radial fields, the transverse planes specified by $\sin(\beta a \cdot z/a) = \pm 1$ are considered.

2.4.1 "The Lossy Rod is Not a Good Conductor"

It is assumed that the operating frequency, the sheath helix geometry, the lossy rod geometry, and the lossy rod material electrical properties are such that the approximate wave numbers solution previously discussed in part 2.3.1 is justified. This solution is valid for both the three region configuration $(b < a)$ and the two region configuration $(b = a)$.

2.4.1.1 Large Argument Representation

The wave numbers solution previously given in sub-part 2.3.1.2 is employed in the normalized fields. Equations 2.116 give the approximate values of the radial and axial wave numbers for the three region configuration. To justify the usage of this solution, it is required that inequalities 2.112 are satisfied. The approximate wave numbers solution is given in equations 2.118. This approximate solution is well justified if the conditions listed in inequalities 2.119 are fulfilled.

The zero order large argument asymptotic representations, which are given by just the first term of equations A.36 – A.39, were used to approximate both the two and three region forms of the normalized fields and the normalizing coefficients. In order that these representations can be used for the region 1 $(0 \leq r \leq b)$ fields, it is required that the radial distance is sufficiently large so that $|h_1| a \cdot r/a > 1$ is true.

For the three region configuration, the approximate normalizing coefficients are calculated from equations 2.130 and 2.131 to be

$$E_{z0} \simeq j \frac{\partial_{11}}{2} 120\pi \cos\psi, \quad \text{and} \qquad (2.132)$$

$$H_{z0} \simeq \frac{\partial_{11}}{2} \cos\psi. \qquad (2.133)$$

On the other hand, for the two region configuration,

$$E_{z0} \cong j \frac{\partial_{\parallel}}{2} \frac{120\pi \cos\psi}{\sqrt{\frac{(\epsilon_r + 1) - j \, \sigma/\omega\epsilon_0}{2}}}$$

(2.134)

is the approximate electric normalizing coefficient, while the approximate magnetic normalizing coefficient is the same as that given in equation 2.133.

It was ensured that the approximate normalized fields associated with the three region configuration correctly satisfy the boundary conditions at the surface of the lossy rod, equations 2.43 - 2.46, and at the sheath helix surface, equations 1.6 - 1.9. For the two region configuration, it was ensured that the normalized fields evaluated at the surface of the sheath helix satisfied equations 1.6 - 1.9. To avoid disrupting the continuity of sub-part 2.4.1.1, the approximate normalized fields associated with both the two and three region configurations will not be listed here.

In each of the six graphs concerning the radial dependence associated with the approximate normalized field magnitudes which are presented in sub-part 2.4.1.1, it was ensured that all the requirements involved to justify using the approximate wave numbers solution given in sub-part 2.3.1.2, and that all the requirements involved to justify approximating the normalizing coefficients and the normalized field components, were satisfied. Figures 2.8 and 2.9 display the magnitude of the approximate normalized electric and magnetic field components, respectively, associated with the three region configuration, as a function of the radial distance normalized with respect to the sheath helix radius, r/a. The two vertical lines represent the surface of the lossy rod and the sheath helix surface. The operating frequency, the sheath helix geometry, the lossy rod geometry, and the lossy rod material electrical properties are specified by the variables

$ka \cot\psi = 10.0$, $b/a = 0.100$, $\epsilon_r = 100$, $\sigma/\omega\epsilon_0 = 10.0$, and $\psi = 1.00°$. The resulting approximate wave numbers solution is computed to be $h_1 a \cong 9.85 + j1.55 \times 10^{-2}$, $h_2 a \cong 10.0$, and $\beta a \cong 10.0$.

Figure 2.8 Curves of the radial dependence associated with the normalized electric field magnitudes for the large argument case, when the lossy rod is not a good conductor. The variables used are ka cotanψ = 10.0, b/a = 0.100, ϵ_r = 1.00x10^2, $\sigma/\omega\epsilon_0$ = 10.0, and ψ = 1.00°. They determine the approximate wave numbers solution $h_1 a$ = 9.85 + j1.55x10^{-2}, $h_2 a$ = βa = 10.0, and the approximate electric normalizing coefficient E_{z0} = jζ_{II} 188(V/m). (Note that ER/EZO = $|E_r/E_{z0}|$ EO/EZO = $|E_\theta/E_{z0}|$, EZ/EZO = $|E_z/E_{z0}|$, and R/A = r/a.)

Figure 2.9   Curves of the radial dependence associated
with the normalized magnetic field magnitudes for the large
argument case, when the lossy rod is not a good conductor.
The variables used are ka cotanψ = 10.0, b/a = 0.100, ϵ_r =
1.00x10^2, $\sigma/\omega\epsilon_0$ = 10.0, and ψ = 1.00°. They determine the
approximate wave numbers solution h_1a = 9.85 + j1.55x10^{-2},
h_2a = βa = 10.0, and the approximate magnetic normalizing
coefficient H_{z0} = $\S_{||}$ 0.500(A/m). (Note that HR/HZO =|H_r/H_{z0}|,
HO/HZO = |H_θ/H_{z0}|, HZ/HZO = |H_z/H_{z0}|, and R/A = r/a.)

$$E_{z0} \cong j \mathcal{B}_{11} \, 188 \ (V/m) \quad \text{and} \quad H_{z0} \cong \mathcal{B}_{11} \, 0.500 \ (A/m)$$

are the calculated values of the approximate normalizing coefficients.

Figures 2.10 and 2.11 illustrate the radial dependence of the magnitudes of the approximate normalized electric and magnetic fields, respectively, for the three region configuration. $ka \, \cot an_\psi = 10.0$, $b/a = 0.900$, $\epsilon_r = 100$, $\sigma/\omega\epsilon_0 = 10.0$, and $\psi = 1.00°$ are the variables which are used. These two graphs are a variation of Figures 2.8 and 2.9, using $b/a = 0.900$ instead of $b/a = 0.100$. The calculated approximate wave numbers solution is $h_1 a \cong 9.85 + j1.55 \times 10^{-2}$, $h_2 a \cong 10.0$, and $\beta a \cong 10.0$. The computed approximate normalizing coefficients are

$$E_{z0} \cong j \mathcal{B}_{11} \, 188 \ (V/m) \quad \text{and} \quad H_{z0} \cong \mathcal{B}_{11} \, 0.500 \ (A/m).$$

Two final graphs included in sub-part 2.4.1.1 are Figures 2.12 and 2.13. They show the radial dependence of the approximate normalized electric and magnetic field magnitudes, respectively, for the two region configuration. The variables used are $ka \, \cot an_\psi = 10.0$, $b/a = 1.00$, $\epsilon_r = 100$, $\sigma/\omega\epsilon_0 = 10.0$, and $\psi = 1.00°$. These two figures can be considered as a modification of the previous four figures, using $b/a = 1.00$ instead of $b/a = 0.100$ or $b/a = 0.900$.

$h_1 a \cong h_2 a \cong \beta a \cong 71.2 - j3.51$ are the calculated values of the approximate wave numbers.

$$E_{z0} \cong j \mathcal{B}_{11} \, (26.4 + j \, 1.31) \ (V/m) \quad \text{and} \quad H_{z0} \cong \mathcal{B}_{11} \, 0.500 \ (A/m)$$

Figure 2.10   Curves of the radial dependence associated
with the normalized electric field magnitudes for the large
argument case, when the lossy rod is not a good conductor.
The variables used are ka cotanψ = 10.0, b/a = 0.900, ϵ_r =
1.00x10^2, $\sigma/\omega\epsilon_0$ = 10.0, and ψ = 1.00°. They determine the
approximate wave numbers solution h$_1$a = 9.85 + j1.55x10^{-2},
h$_2$a = βa = 10.0, and the approximate electric normalizing
coefficient E$_{z0}$ = j β_{11} 188(V/m). (Note that ER/EZ0 = $|E_r/E_{z0}|$,
E0/EZ0 = $|E_\theta/E_{z0}|$, EZ/EZ0 = $|E_z/E_{z0}|$, and R/A = r/a.)

Figure 2.11   Curves of the radial dependence associated with the normalized magnetic field magnitudes for the large argument case, when the lossy rod is not a good conductor. The variables used are ka $\cot\psi$ = 10.0, b/a = 0.900, ϵ_r = 1.00×10^2, $\sigma/\omega\epsilon_0$ = 10.0, and ψ = 1.00°. They determine the approximate wave numbers solution $h_1 a$ = 9.85 + $j1.55\times10^{-2}$, $h_2 a$ = βa = 10.0, and the approximate magnetic normalizing coefficient H_{z0} = j|| 0.500(A/m). (Note that HR/HZO = $|H_r/H_{z0}|$, HO/HZO = $|H_\theta/H_{z0}|$, HZ/HZO = $|H_z/H_{z0}|$, and R/A = r/a.)

Figure 2.12   Curves of the radial dependence associated with the normalized electric field magnitudes for the large argument case, when the lossy rod is not a good conductor. The variables used are ka cotanψ = 10.0, b/a = 1.00, ϵ_r = 1.00x10^2, $\sigma/\omega\epsilon_0$ = 10.0, and ψ = 1.00°; They determine the approximate wave numbers solution $h_1 a = h_2 a = \beta a = 71.2 - j3.51$, and the approximate electric normalizing coefficient $E_{z0} = j \, \rangle_{11}$ (26.4 + j1.31)(V/m). (Note that ER/EZO = $|E_r/E_{z0}|$, EO/EZO = $|E_\theta/E_{z0}|$, EZ/EZO = $|E_z/E_{z0}|$, and R/A = r/a.)

Figure 2.13   Curves of the radial dependence associated
with the normalized magnetic field magnitudes for the large
argument case, when the lossy rod is not a good conductor.
The variables used a   · otanψ = 10.0, b/a = 1.00, ϵ_r =
1.00x10^2, $\sigma/\omega\epsilon_0$ = 1   , σ ψ = 1.00°. They determine the
approximate wave numb·· ·olution h_1a = h_2a = βa = 71.2 -
j3.51, and the approximate magnetic normalizing coefficient
H_{z0} = $\big)_{\text{II}}$ 0.500(A/m). (Note that HR/HZO = $|H_r/H_{z0}|$, HO/HZO =
$|H_\theta/H_{z0}|$, HZ/HZO = $|H_z/H_{z0}|$, and R/A = r/a.)

are the calculated values of the approximate normalizing coefficients.

It is clear that for the large value of $ka \ cotan\psi$ which was used in the six figures, all the electric and magnetic field components are rapidly attenuated at increasing radial distances away from the sheath helix surface. For the two region configuration, this attenuation is much greater than it is for the three region configuration. Since the variable $ka \ cotan\psi = 2\pi f \sqrt{\mu_0 \ \epsilon_0} \ cotan\psi$ is directly proportional to frequency, it can be said that at "high frequencies", which means large values of $ka \ cotan\psi$, the field components cling tightly to the sheath helix "windings". *In this circumstance, the sheath helix is said to act like a wave guiding structure.*

It is informative to compare Figures 2.8 - 2.13 with Figures D.9 - D.14. The latter mentioned set of figures is associated with the sheath helix surrounding an ideal dielectric (zero conductivity) coaxial rod. The same values of $ka \ cotan\psi$, b/a, ϵ_r, and ψ are used for both sets of figures. Keeping in mind the values of the normalizing coefficients, it is apparent that for each of the three different values of b/a which have been used, the corresponding figures of the two sets show that the magnitudes of the electric and magnetic fields associated with the lossy rod configuration are approximately similar to the absolute value of the corresponding fields associated with the ideal dielectric rod configuration.

2.4.1.2   Small Argument Representation

The wave numbers solution previously discussed in sub-part 2.3.1.1 is used in the normalized fields. Equations 2.107, 2.108, and 2.88 are numerically solved to obtain the radial and axial wave numbers, for both the two and three region configurations. In order that this approximate solution is valid, it was ensured that the restrictions listed in equations 2.104 and 2.105 are satisfied.

Equations A.26 - A.29, the small argument Bessel function representations, were used to approximate the normalized fields and the normalizing coefficients. In order that these representations could be used to approximate the normalized field components, the radial distance associated with the region 3 $(a \leqslant r < \infty)$ fields was restricted to being sufficiently small so that $|h_2|a \cdot r/a < 0.100$ is true.

The suitable approximations of equations 2.130 and 2.131, which are valid for both the two and three region configurations, are

$$E_{z0} \cong j \frac{\partial_{||}}{2} 120\pi \, ka \cot\psi \cos\psi, \quad \text{and} \qquad (2.135)$$

$$H_{z0} \cong \partial_{||} \cos\psi. \qquad (2.136)$$

All the approximate normalized fields were checked to ensure that for both the two and three region configurations, the boundary conditions associated with the surface of the lossy rod and the sheath helix surface are correctly satisfied. In order that the continuity of sub-part 2.4.1.2 is not interrupted, the normalized approximate field components will not be listed. For the six graphs illustrating the radial dependence of the approximate field component magnitudes which are presented here, it was ensured that all the restrictions required to justify obtaining the approximate wave numbers solution, approximating the normalizing coefficients, and approximating the normalized fields, were satisfied.

Figures 2.14 and 2.15 display the radial dependence of the approximate normalized electric and magnetic field magnitudes, respectively, for the three region configuration. The operating frequency, the sheath helix geometry, the lossy rod geometry, and the lossy rod material electrical properties are specified by the variables $ka \cot\psi = 5.00 \times 10^{-2}$, $b/a = 0.100$, $\epsilon_r = 100$, $\sigma/\omega\epsilon_0 = 1.00 \times 10^3$, and $\psi = 1.00°$. (Note that although $\sigma/\omega\epsilon_0 >> \epsilon_r$ is true, the requirements listed in equations 2.104 and 2.105 are satisfied. According to the definition used in sub-part 2.3.1.1, this circumstance is said to be an example of the small argument case when "the lossy rod is not a good conductor".) $h_1 a \cong 2.25 \times 10^{-2} + j1.68 \times 10^{-2}$, $h_2 a \cong 1.73 \times 10^{-2} - j6.15 \times 10^{-5}$, and $\beta a \cong 1.73 \times 10^{-2} - j6.14 \times 10^{-5}$ are the calculated approximate wave numbers solution. The approximate normalizing coefficients are obtained from equations 2.135 and 2.136.

$$E_{z0} \cong j \, \partial_{||} \, 9.43 \, (V/m) \quad \text{and} \quad H_{z0} \cong \partial_{||} \, 1.00 \, (A/m)$$
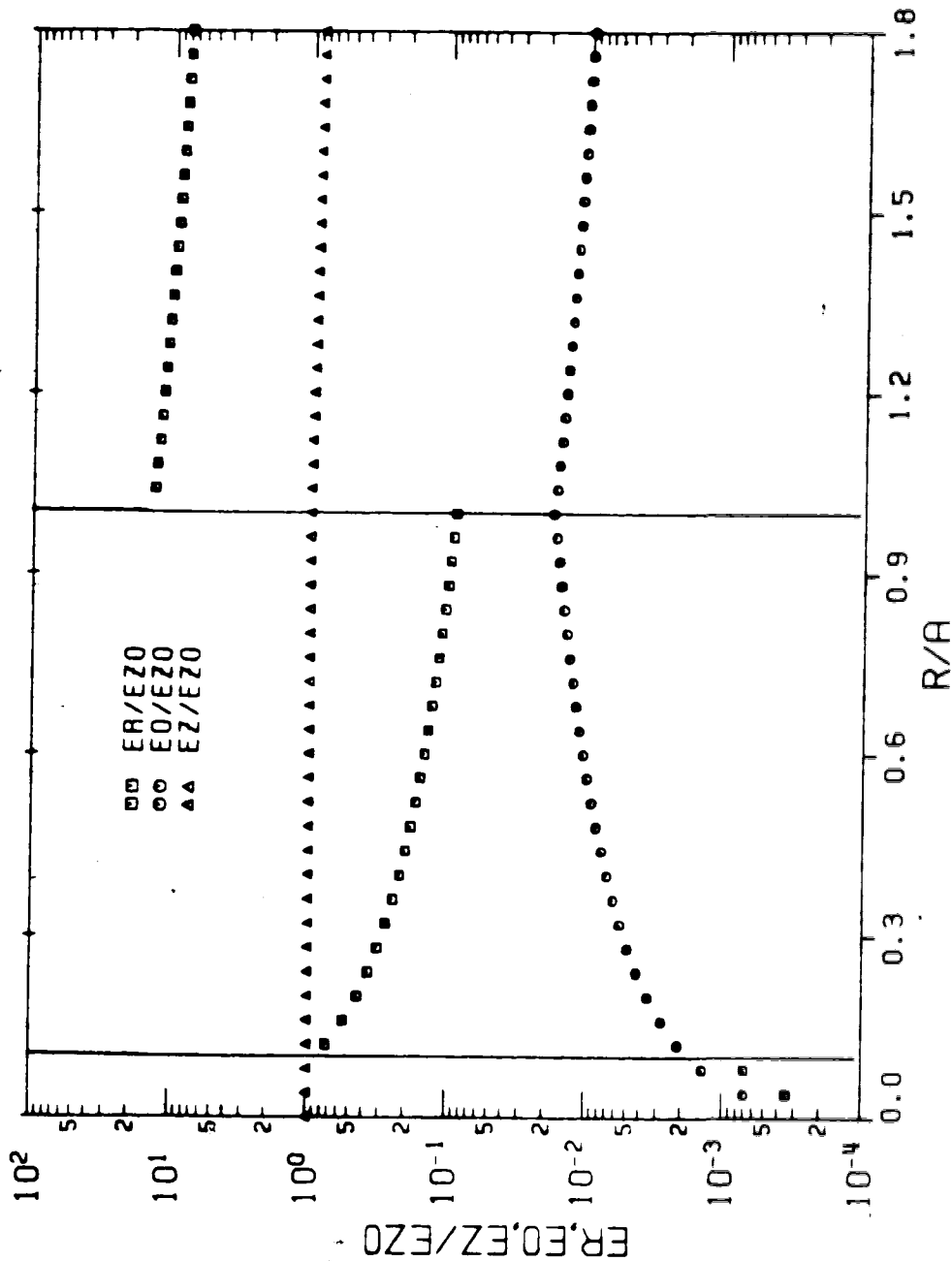
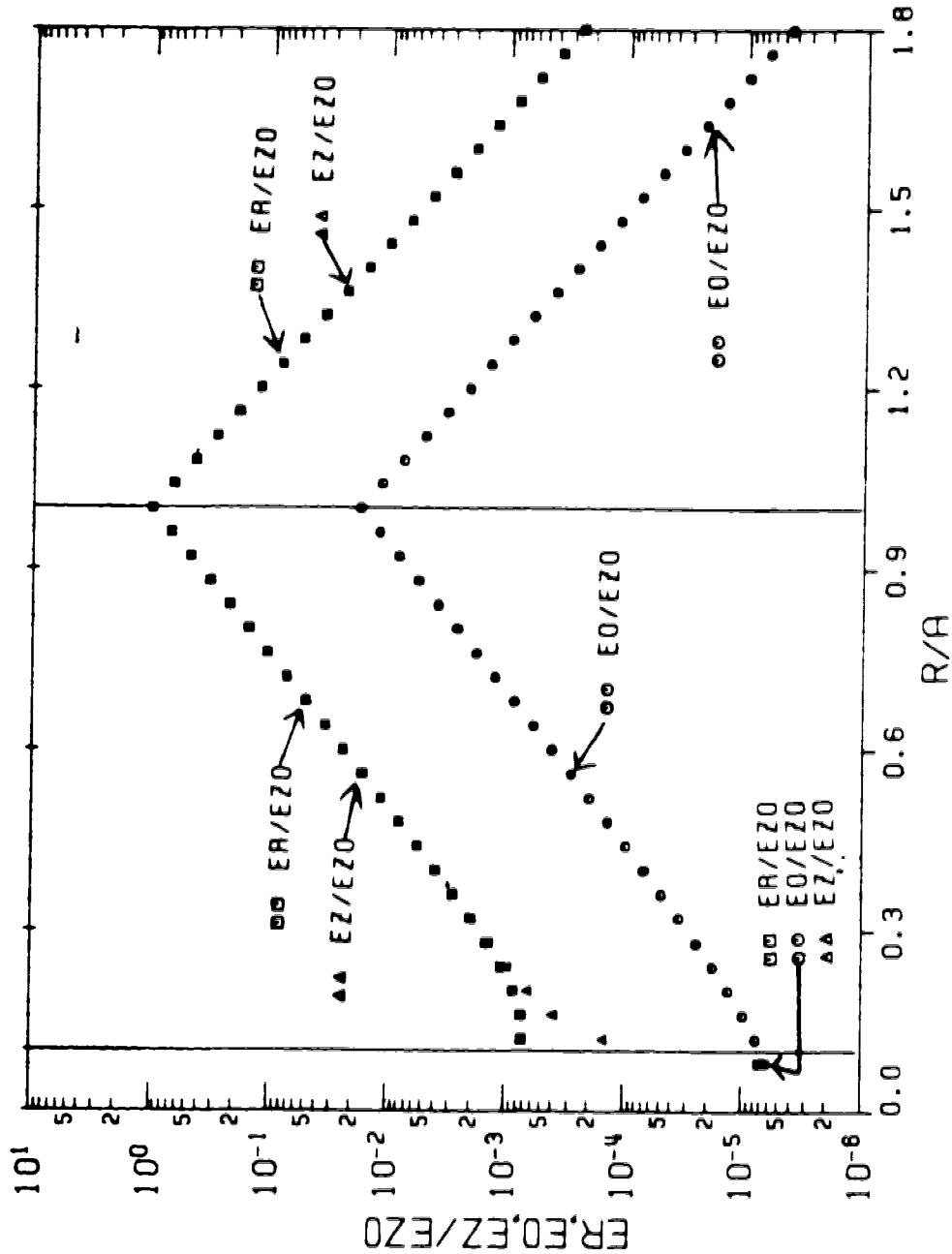RADIAL DEPENDENCE OF ELECTRIC FIELDS

Figure 2.14   Curves of the radial dependence associated with the normalized electric field magnitudes for the small argument case, when the lossy rod is not a good conductor. The variables used are $ka \cot an \psi = 5.00 \times 10^{-2}$, $b/a = 0.100$, $\epsilon_r = 1.00 \times 10^2$, $\sigma/\omega\epsilon_0 = 1.00 \times 10^3$, and $\psi = 1.00°$. They determine the approximate wave numbers solution $h_1 a = 2.25 \times 10^{-2} + j1.68 \times 10^{-2}$, $h_2 a = 1.73 \times 10^{-2} - j6.15 \times 10^{-5}$, $\beta a = 1.73 \times 10^{-2} - j6.14 \times 10^{-5}$, and the approximate electric normalizing coefficient $E_{z0} = j \beta_{11}$ 9.43(V/m). (Note that ER/EZ0=$|E_r/E_{z0}|$, EO/EZ0 = $|E_\theta/E_{z0}|$, EZ/EZ0 = $|E_z/E_{z0}|$, and R/A = r/a.)
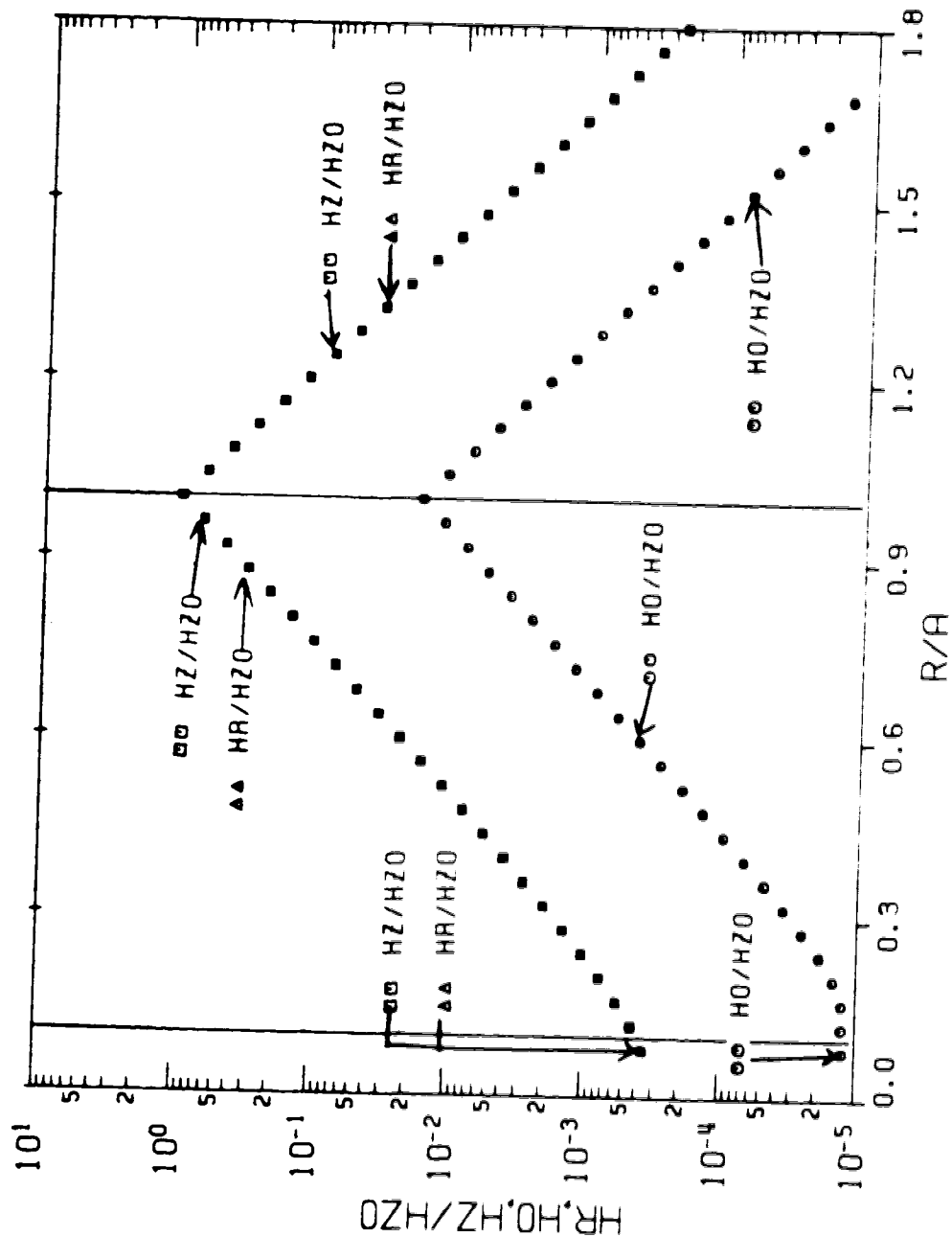
Figure 2.15   Curves of the radial dependence associated
with the normalized magnetic field magnitudes for the small
argument case, when the lossy rod is not a good conductor.
The variables used are ka cotanψ = 5.00×10^{-2}, b/a = 0.100,
ϵ_r = 1.00×10^2, $\sigma/\omega\epsilon_0$ = 1.00×10^3, and ψ = 1.00°. They determine
the approximate wave numbers solution $h_1 a$ = 2.25×10^{-2} +
$j1.68 \times 10^{-2}$, $h_2 a$ = 1.73×10^{-2} - j 6.15×10^{-5}, βa = 1.73×10^{-2} -
$j6.14 \times 10^{-5}$, and the approximate magnetic normalizing
coefficient H_{z0} = ∂_{11} 1.00(A/m). (Note that HR/HZO = $|H_r/H_{z0}|$,
HO/HZO = $|H_\theta/H_{z0}|$, HZ/HZO = $|H_z/H_{z0}|$, and R/A = r/a.)

are their computed values.

The final two graphs associated with the three region configuration are Figures 2.16 and 2.17. They show the radial dependence of the approximate normalized electric and magnetic field magnitudes, respectively. $ka \cot an\psi = 5.00 \times 10^{-2}$, $b/a = 0.900$, $\epsilon_r = 100$, $\sigma/\omega\epsilon_0 = 1.00 \times 10^3$, and $\psi = 1.00°$ are the variables which are used. Note that these graphs can be considered as a variation of Figures 2.14 and 2.15, using $b/a = 0.900$ instead of $b/a = 0.100$. The approximate radial and axial wave numbers are computed to be $h_1 a \cong 1.99 \times 10^{-2} + j1.54 \times 10^{-2}$, $h_2 a \cong 1.60 \times 10^{-2} - j4.60 \times 10^{-3}$, and $\beta a \cong 1.59 \times 10^{-2} - j4.59 \times 10^{-3}$.

$$E_{z0} \cong j \}_{||} \ 9.43 \ (V/m) \quad and \quad H_{z0} \cong \}_{||} \ 1.00 \ (A/m)$$

are the computed values of the approximate normalizing coefficients.
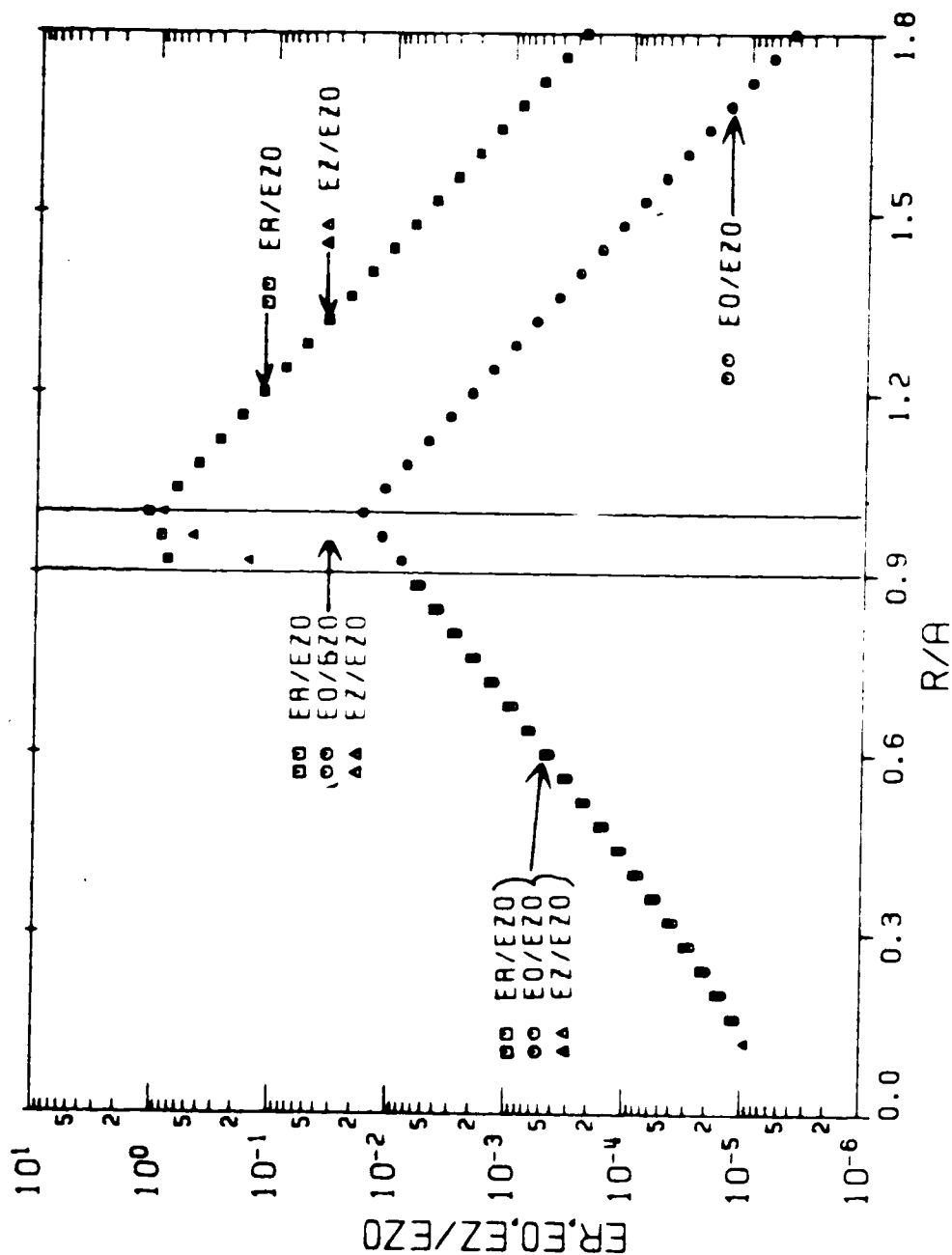
Figures 2.18 and 2.19 display the radial dependence of the approximate normalized electric and magnetic field components, respectively, for the two region configuration. The variables used are $ka \cot an\psi = 5.00 \times 10^{-2}$, $b/a = 1.00$, $\epsilon_r = 100$, $\sigma/\omega\epsilon_0 = 1.00 \times 10^3$, and $\psi = 1.00°$. These two graphs can be considered as a special case of Figures 2.14 – 2.17, using $b/a = 1.00$ instead of $b/a = 0.100$ or $b/a = 0.900$. $h_1 a \cong 1.93 \times 10^{-2} + j1.56 \times 10^{-2}$, $h_2 a \cong 1.53 \times 10^{-2} - j5.28 \times 10^{-3}$, and $\beta a \cong 1.53 \times 10^{-2} - j5.27 \times 10^{-3}$ are the calculated values of the approximate wave numbers. The approximate normalizing coefficients are calculated to be

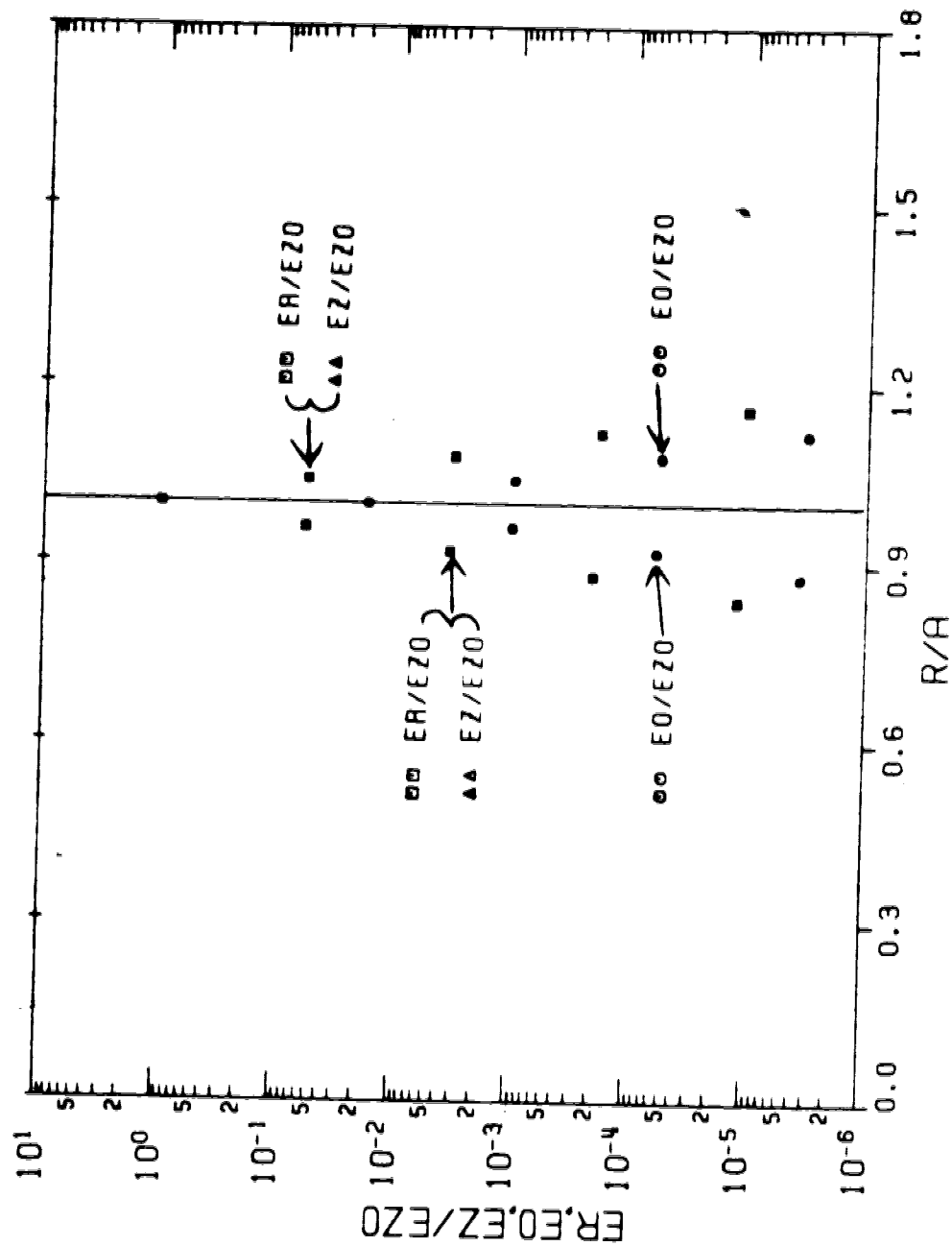$$E_{z0} \cong j \}_{||} \ 9.43 \ (V/m) \quad and \quad H_{z0} \cong \}_{||} \ 1.00 \ (A/m).$$
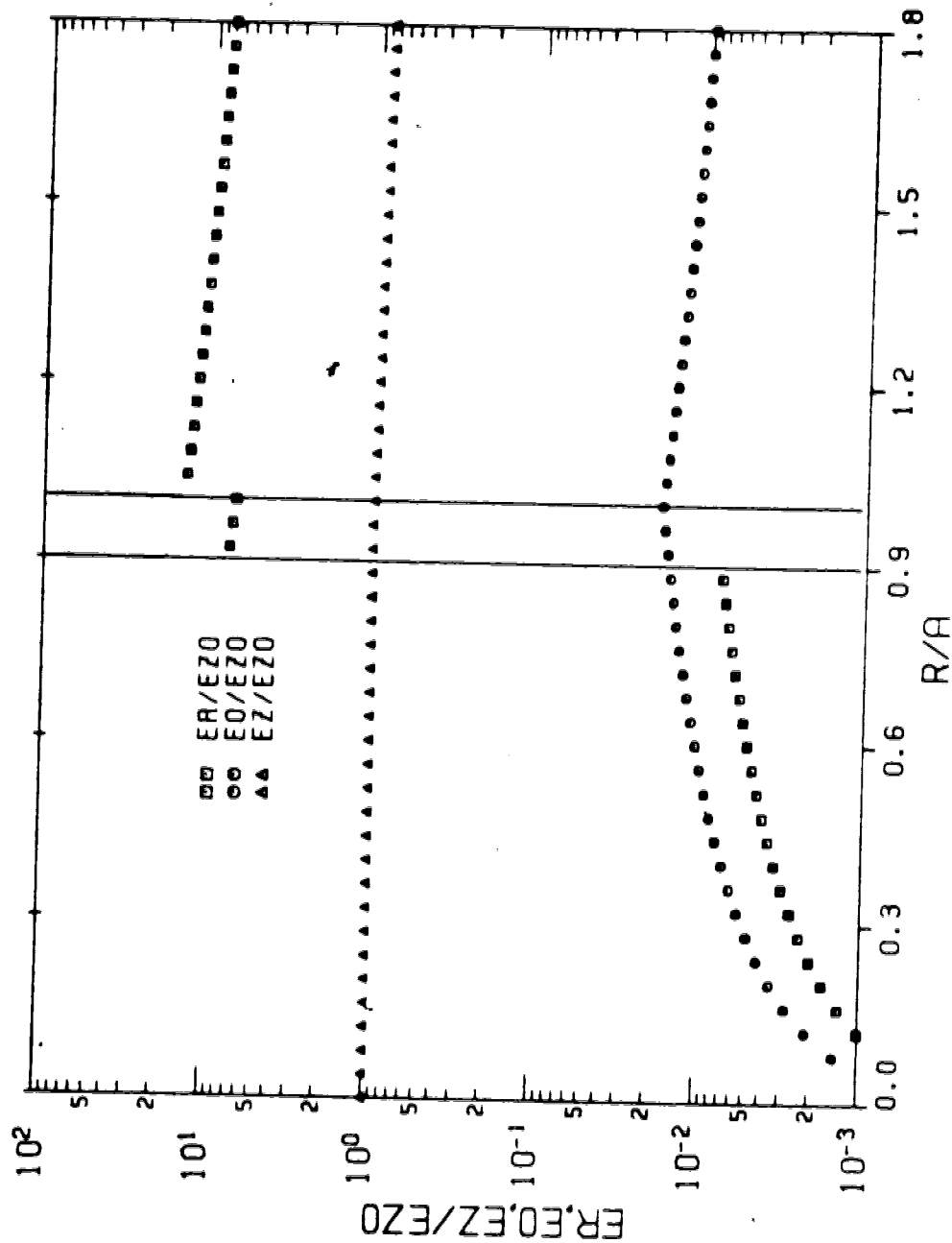
RADIAL DEPENDENCE OF ELECTRIC FIELDS

Figure 2.16   Curves of the radial dependence associated with the normalized electric field magnitudes for the small argument case, when the lossy rod is not a good conductor. The variables used are ka cotanψ = 5.00x10^{-2}, b/a = 0.900, ϵ_r = 1.00x10^2, $\sigma/\omega\epsilon_0$ = 1.00x10^3, and ϕ = 1.00°. They determine the approximate wave numbers solution h$_1$a = 1.99x10^{-2} + j 1.54x10^{-2}, h$_2$a = 1.60x10^{-2} - j 4.60x10^{-3}, βa = 1.59x10^{-2} - j 4.59x10^{-3}, and the approximate electric normalizing coefficient E$_{z0}$=j $\int_{II}$ 9.43(V/m). (Note that ER/EZO=$|E_r/E_{z0}|$, EO/EZO = $|E_\theta/E_{z0}|$, EZ/EZO = $|E_z/E_{z0}|$, and R/A = r/a.)
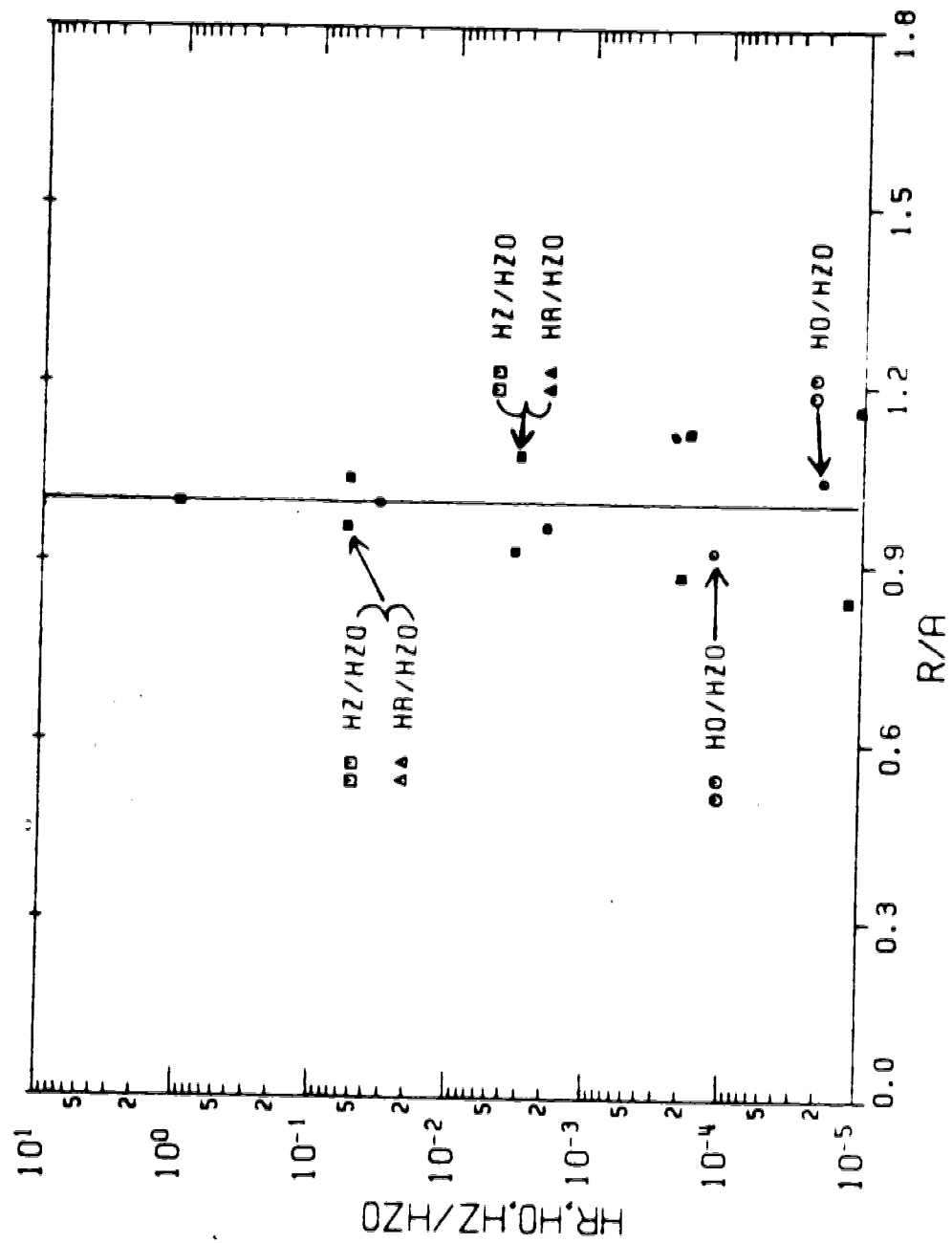
RADIAL DEPENDENCE OF MAGNETIC FIELDS

Figure 2.17   Curves of the radial dependence associated with the normalized magnetic field magnitudes for the small argument case, when the lossy rod is not a good conductor. The variables used are ka cotanψ = 5.00x10^{-2}, b/a = 0.900, ϵ_r = 1.00x10^2, $\sigma/\omega\epsilon_0$ = 1.00x10^3, and ψ = 1.00°. They determin the approximate wave numbers solution $h_1 a$ = 1.99x10^{-2} + j 1.54x10^{-2}, $h_2 a$ = 1.60x10^{-2} - j 4.60x10^{-3}, βa = 1.59x10^{-2} - j4.59x10^{-3}, and the approximate magnetic normalizing coefficient H_{z0} = $\mathcal{J}_{11}$ 1.00(A/m). (Note that HR/HZO=$|H_r/H_{z0}|$, HO/HZO = $|H_\theta/H_{z0}|$, HZ/HZO = $|H_z/H_{z0}|$, and R/A = r/a.)

Figure 2.18   Curves of the radial dependence associated with the normalized electric field magnitudes for the small argument case, when the lossy rod is not a good conductor. The variables used are ka cotanψ = 5.00x10^{-2}, b/a = 1.00, ϵ_r = 1.00x10^2, $\sigma/\omega\epsilon_0$ = 1.00x10^3, and ψ = 1.00°. They determine the approximate wave numbers solution $h_1 a$ = 1.93x10^{-2} + j1.56x10^{-2}, $h_2 a$ = 1.53x10^{-2} - j5.28x10^{-3}, βa = 1.53x10^{-2} - j5.27x10^{-3}, and the approximate electric normalizing coefficient E_{z0} = j 9.43(V/m). (Note that ER/EZ0 = $|E_r/E_{z0}|$, EO/EZ0 = $|E_\theta/E_{z0}|$, EZ/EZ0 = $|E_z/E_{z0}|$, and R/A = r/a.)

Figure 2.19 Curves of the radial dependence associated with the normalized magnetic field magnitudes for the small argument case, when the lossy rod is not a good conductor. The variables used are $ka \cot\psi = 5.00 \times 10^{-2}$, $b/a = 1.00$, $\epsilon_r = 1.00 \times 10^{2}$, $\sigma/\omega\epsilon_0 = 1.00 \times 10^{3}$, and $\psi = 1.00°$. They determine the approximate wave numbers solution $h_1 a = 1.93 \times 10^{-2} + j\,1.56 \times 10^{-2}$, $h_2 a = 1.53 \times 10^{-2} - j\,5.28 \times 10^{-3}$, $\beta a = 1.53 \times 10^{-2} - j\,5.27 \times 10^{-3}$, and the approximate magnetic normalizing coefficient $H_{z0} = $ ∥ $1.00(A/m)$. (Note that $HR/HZ0 = |H_r/H_{z0}|$, $HO/HZ0 = |H_\theta/H_{z0}|$, $HZ/HZ0 = |H_z/H_{z0}|$, and $R/A = r/a$.)

It is clear that the radial dependences of the fields shown in Figures 2.14 - 2.19 are much different from that displayed in Figures 2.8 - 2.13. The first mentioned set of graphs shows that the fields are characterized by a relatively gradual change as the radial distance is varied. The fields in region 3 decay slowly with increasing radial distance. For the small value of $ka \cot an \psi$ which is used, the field extension is large. *It can therefore be said that for "low frequencies", which means small values of* $ka \cot an \psi$, *the fields are basically unguided by the sheath helix.*

It is informative to compare Figures 2.14 -2.19 with Figures D.21 - D.26. The latter mentioned set of graphs are associated with the sheath helix surrounding an ideal dielectric coaxial rod. The same values of $ka \cot an \psi$, b/a, ε_r, and ψ are used in both sets of graphs. The magnitudes of the normalized fields associated with the lossy rod configuration are compared with the absolute value of the corresponding normalized fields associated with the ideal dielectric rod configuration, for a particular value of b/a, keeping in mind the values of the normalizing coefficients. This shows that with the exception of the region 2 radial electric field component, and of the region 1 and region 2 angular magnetic field components, the corresponding fields of the two sets of figures are similar.

Figures 2.14 and 2.15 provide a good illustration of how the electric and magnetic fields behave at the surface of the lossy rod and at the sheath helix surface. Consider the field behavior at the rod surface. Figure 2.14 shows that the angular and axial electric fields are continuous. This is simply a statement of the fact that the electric fields tangential to an interface are continuous. The figure also shows that the radial electric field is discontinuous. The explanation for this behavior is that the permittivity of the lossy rod is different than that of air, and that free electric charge is located on the rod surface. When two regions forming an interface have different permittivities, and when free electric charge is present at the interface, the normal electric field will be discontinuous at that interface.

Figure 2.15 shows that the angular and axial magnetic fields are continuous at the surface of the lossy rod. Since the conductivity of the lossy rod is finite, it cannot possess an electrical surface current. At an interface which does not possess an electrical surface current, it must be true that the tangential magnetic fields are

continuous. The figure also shows that the radial magnetic field is continuous. Since no free magnetic charge exists at $r = b$, the normal magnetic field must be continuous at the lossy rod surface.

Attention is now directed to examining the field behavior at the sheath helix surface. Figure 2.14 shows that the angular and axial electric fields are continuous at $r = a$. This is a direct consequence of the boundary conditions at the surface of the sheath helix, as is apparent from equations 1.6 - 1.8. The radial electric field is seen to be discontinuous at $r = a$. The explanation for this behavior is that free electric charge exists at the sheath helix surface.

Figure 2.15 shows that the angular and axial magnetic fields are discontinuous at the surface of the sheath helix. This is because an electrical surface current exists on the sheath helix "windings". The magnetic field tangential to an interface which possesses an electrical surface current will be discontinuous. Finally, the radial magnetic field is seen to be continuous at the sheath helix surface. Since no free magnetic charge exists at $r = a$, the normal magnetic field must be continuous at the surface of the sheath helix.

2.4.2 "The Lossy Rod is a Good Conductor"

It is now assumed that the operating frequency, the sheath helix geometry, the lossy rod geometry, and the lossy rod material electrical properties are such that the approximate wave numbers solution previously discussed in part 2.3.2 is justified. Since in part 2.3.2 it was mentioned that a free mode field solution could only be obtained for the three region configuration, the discussion of the radial dependence associated with the approximate normalized fields presented in this part will be restricted to the case of $b < a$.

2.4.2.1 Large Argument Representation

It is assumed that the restrictions listed in inequalities 2.127 are satisfied, so that the approximate wave numbers solution is given by equations 2.128. Just the first term of equations A.36 - A.39 (the zero order large argument Bessel function representations) are used to approximate the three region form of the normalized fields, and the normalizing coefficients, equations 2.130 and 2.131. When these approximations are applied to the region 1 fields, it is necessary that the radial distance is

sufficiently large so that $|h_1| a \cdot r/a > 1$ is true. It was ensured that the approximate normalized fields correctly satisfied the boundary conditions at $r = b$, equations 2.43 - 2.46, and at $r = a$, equations 1.6 - 1.9.

The approximate normalizing coefficients were computed to be

$$E_{z0_v} \cong j \frac{\partial_{II}}{2} 120\pi \cos\psi, \quad \text{and} \tag{2.137}$$

$$H_{z0} \cong \frac{\partial_{II}}{2} \cos\psi. \tag{2.138}$$

In order that the continuity of sub-part 2.4.2.1 is not interrupted, the values of the approximate normalized fields will not be listed here.

For each of the four graphs which will be examined, it was ensured that the requirements involved to justify approximating the wave numbers solution, approximating the normalizing coefficients, and approximating the normalized fields, were well justified. Figures 2.20 and 2.21 display the radial dependence of the approximate normalized electric and magnetic field magnitudes, respectively. The operating frequency, the sheath helix geometry, the lossy rod geometry, and the lossy rod material electrical properties are specified by the variables $ka \cot\psi = 10.0$, $b/a = 0.100$, $\epsilon_r = 100$, $\sigma/\omega\epsilon_0 = 1.00 \times 10^5$, and $\psi = 1.00°$. (Note that a large value of $\sigma/\omega\epsilon_0$ must be used in order to satisfy the requirement $\sigma/\omega\epsilon_0 >> \cot^2\psi$, which is mentioned in inequalities 2.127.) The approximate wave numbers are calculated to be $h_1 a \cong 39.0 + j39.0$, $h_2 a \cong 10.0$, and $\beta a \cong 10.0$. The approximate normalizing coefficients were computed from equations 2.137 and 2.138 to be

$$E_{z0} \cong j \partial_{II} 188 \text{ (V/m)} \quad \text{and} \quad H_{z0} \cong \partial_{II} 0.500 \text{ (A/m)}.$$

RADIAL DEPENDENCE OF ELECTRIC FIELDS

Figure 2.20   Curves of the radial dependence associated with the normalized electric field magnitudes for the large argument case, when the lossy rod is a good conductor. The variables used are ka cotanψ = 10.0, b/a = 0.100, ε_r = 1.00×10^2, $\sigma/\omega\varepsilon_0$ = 1.00×10^5, and ψ = 1.00°. They determine the approximate wave numbers solution $h_1 a$ = 39.0 + j39.0, $h_2 a$ = βa = 10.0, and the approximate electric normalizing coefficient, E_{z0}=j$\int_{11}$ 188(V/m). (Note that ER/EZ0=$|E_r/E_{z0}|$, EO/EZ0 = $|E_\theta/E_{z0}|$, EZ/EZ0 = $|E_z/E_{z0}|$, and R/A = r/a.)

Figure 2.21 Curves of the radial dependence associated with the normalized magnetic field magnitudes for the large argument case, when the lossy rod is a good conductor. The variables used are ka cotanψ = 10.0, b/a = 0.100, ε_r = 1.00×10^2, $\sigma/\omega\varepsilon_0$ = 1.00×10^5, and ψ = 1.00°. They determine the approximate wave numbers solution $h_1 a$ = 39.0 + j39.0, $h_2 a$ = βa = 10.0, and the approximate magnetic normalizing coefficient H_{z0} =)|| 0.500(A/m). (Note that HR/HZ0 = $|H_r/H_{z0}|$, HO/HZ0 = $|H_\theta/H_{z0}|$, HZ/HZ0 = $|H_z/H_{z0}|$, and R/A = r/a.)

Figures 2.22 and 2.23 show the radial dependence of the approximate normalized electric and magnetic field magnitudes, respectively. $ka \cot an\psi = 10.0$, $b/a = 0.900$, $\epsilon_r = 100$, $\sigma/\omega\epsilon_0 = 1.00 \times 10^5$, and $\psi = 1.00°$ are the variables which are used. These two graphs can be considered as a variation of Figures 2.20 and 2.21, with $b/a = 0.900$ instead of $b/a = 0.100$.

• $h_1 a \cong 39.0 + j39.0$, $h_2 a \cong 10.0$, and $\beta a \cong 10.0$ are the computed values of the approximate wave numbers.

$$E_{z0} \cong j \, \rbrace_{11} \, 188 \; (V/m) \quad \text{and} \quad H_{z0} \cong \rbrace_{11} \, 0.500 \; (A/m)$$

are the computed values of the approximate normalizing coefficients.

It is clear from Figures 2.20 − 2.23 that all the field components are rapidly attenuated at increasing radial distances away from the sheath helix surface. Furthermore, Figures 2.22 and 2.23 make it apparent that this attenuation is much greater for region 1 fields than it is for region 2 and region 3 fields. In fact, the radial dependence of the region 1 fields is dominated by the exponential $e^{-\sqrt{j \, \sigma/\omega\epsilon_0} \, ka \cdot b/a(1-r/b)}$. Making use of the relation

$$\sqrt{\frac{\sigma}{2\,\omega\epsilon_0}} \; kb = \sqrt{\frac{\sigma}{2\,\omega\epsilon_0}} \; \omega \; \sqrt{\mu_0 \, \epsilon_0} \; b = \frac{b}{\delta} \, , \quad \text{where} \quad \delta = \sqrt{\frac{2}{\omega\mu_0\sigma}} \tag{2.139}$$

is the *skin depth* associated with the nonmagnetic lossy rod, one can easily demonstrate that at the radial position $r = b - \delta$, the previously mentioned exponential has a magnitude of e^{-1}. Therefore, at a distance δ beneath the surface of the lossy
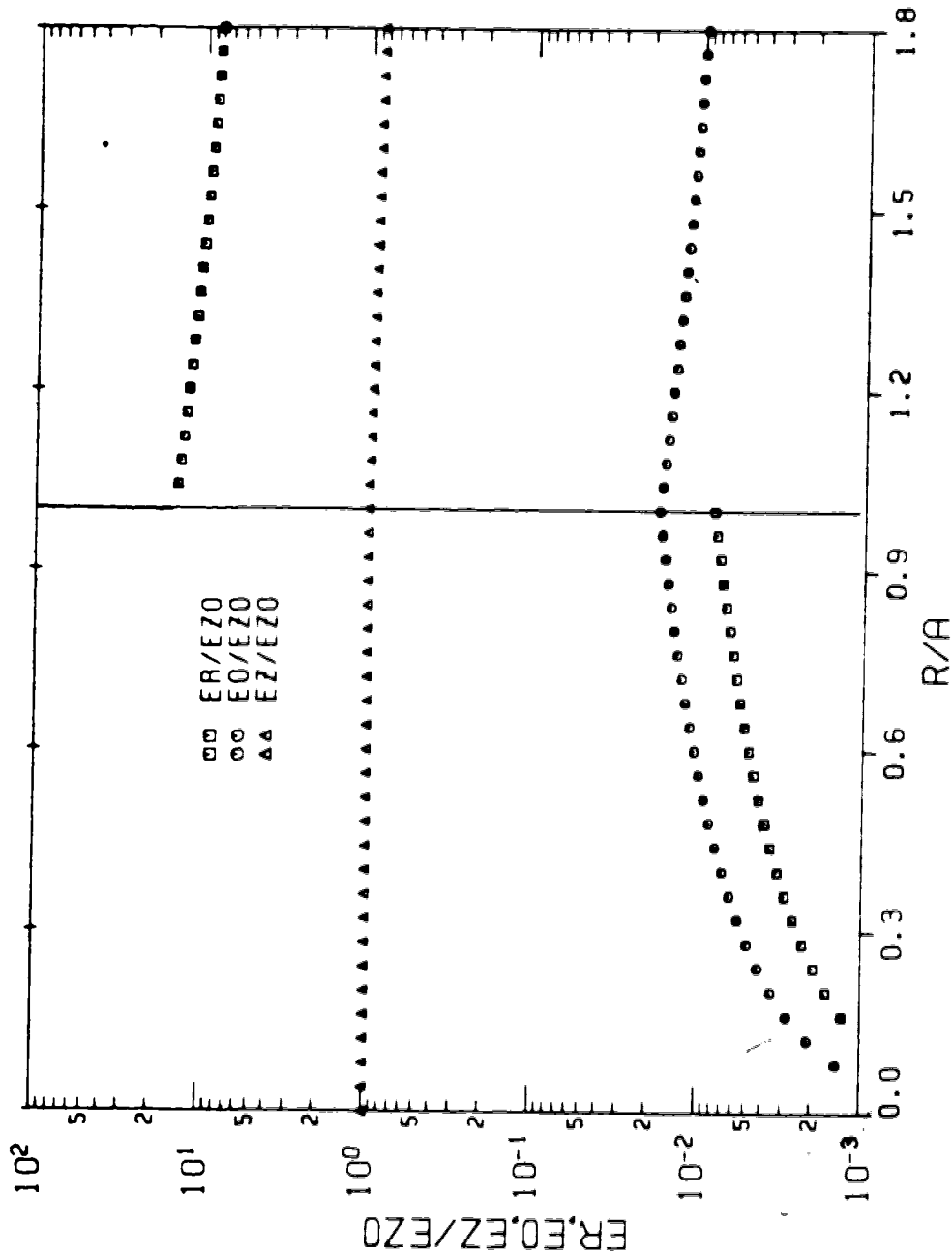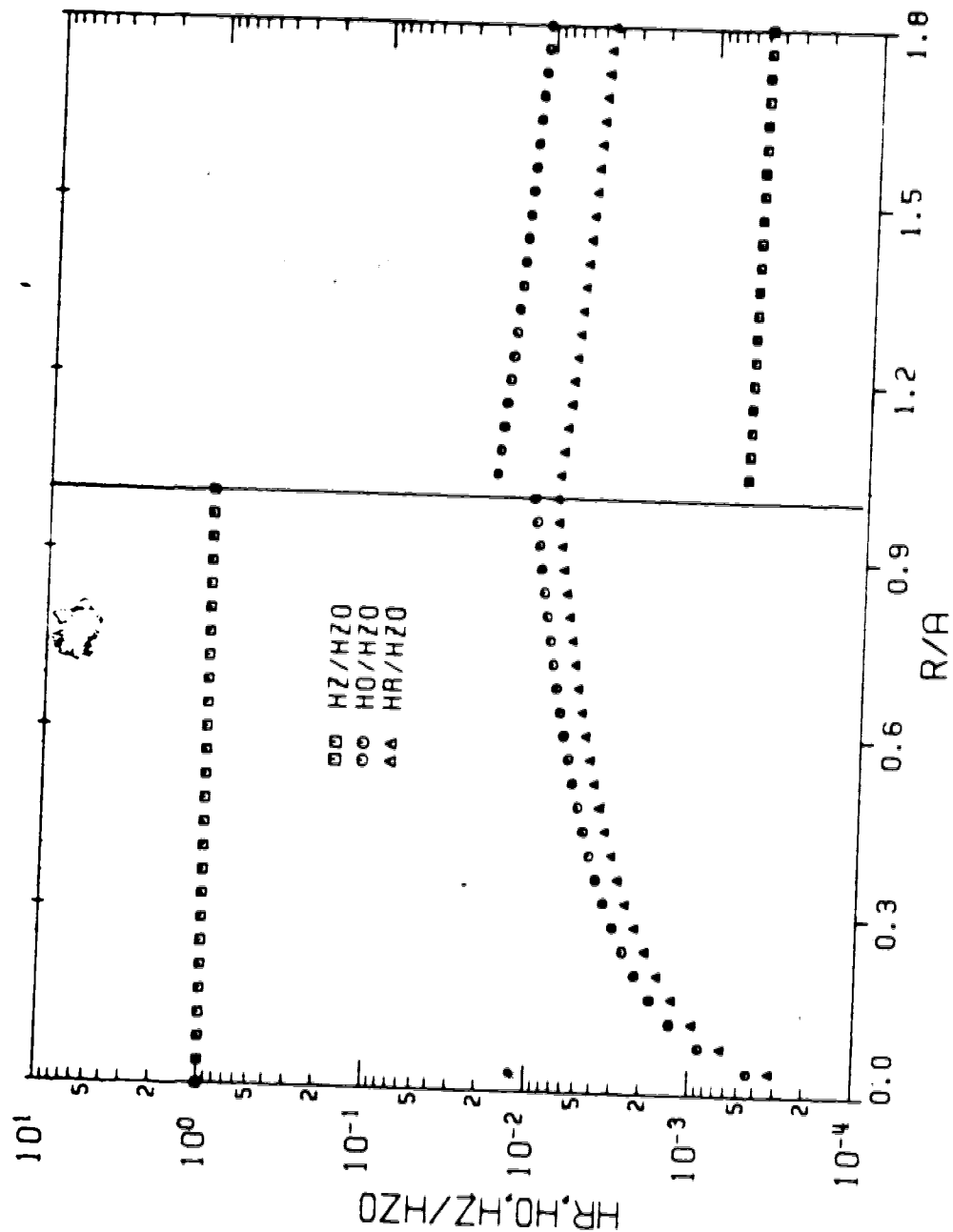
RADIAL DEPENDENCE OF ELECTRIC FIELDS

Figure 2.22   Curves of the radial dependence associated with the normalized electric field magnitudes for the large argument case, when the lossy rod is a good conductor. The variables used are ka cotanψ = 10.0, b/a = 0.900, ϵ_r = 1.00×10^2, $\sigma/\omega\epsilon_0$ = 1.00×10^5, and ψ = $1.00°$. They determine the approximate wave numbers solution h_1a = 39.0 + j39.0, h_2a = βa = 10.0, and the approximate electric normalizing coefficient E_{z0}=jβ_{11} 188(V/m). (Note that ER/EZO=$|E_r/E_{z0}|$, EO/EZO = $|E_\theta/E_{z0}|$, EZ/EZO = $|E_z/E_{z0}|$, and R/A = r/a.)

Figure 2.23 Curves of the radial dependence associated with the normalized magnetic field magnitudes for the large argument case, when the lossy rod is a good conductor. The variables used are ka cotanψ = 10.0, b/a = 0.900, ϵ_r = 1.00×10^2, $\sigma/\omega\epsilon_0$ = 1.00×10^5, and ψ = 1.00°. They determine the approximate wave numbers solution $h_1 a$ = 39.0 + j39.0, $h_2 a$ = βa = 10.0, and the approximate magnetic normalizing coefficient H_{z0} = $\mathcal{}$|| 0.500(A/m). (Note that HR/HZ0=$|H_r/H_{z0}|$, HO/HZ0 = $|H_\theta/H_{z0}|$, HZ/HZ0 = $|H_z/H_{z0}|$, and R/A = r/a.)

rod, all field components have been attenuated by the factor e^{-1} compared to their values at the lossy rod surface. This is in agreement with the definition of the term *skin depth*. (For example, see 18, pp. 36; 28, pp. 251; and 36, pp. 769.) Note that the larger the variable $\sigma/\omega\epsilon_0$ is, the more rapid is the attenuation of the region 1 fields.

Figures 2.20 – 2.23 will now be compared with Figures C.4 – C.7. The latter mentioned set of graphs is associated with the sheath helix surrounding a perfectly conducting coaxial rod. The same values of $ka \cot\psi$, b/a, and ψ are used for both sets of graphs. For the perfectly conducting rod configuration, all region 1 fields are zero. In the case of the lossy rod configuration, the region 1 fields are nonzero but they are extremely rapidly attenuated for increasing radial distances away from the rod surface. For a particular value of b/a, the two sets of graphs are examined. Keeping in mind the values of the electric and magnetic normalizing coefficients, it is seen that the magnitudes of the region 2 and region 3 fields associated with the lossy rod configuration are similar to the absolute value of the corresponding fields associated with the perfectly conducting rod configuration. The single exception occurs for region 2 fields, which are very close to the rod surface.

2.4.2.2 Small Argument Representation

The final set of graphs of the radial dependence associated with the magnitudes of the approximate normalized fields is for the small argument representation of the three region configuration, when "the lossy rod is a good conductor". It is assumed that the restrictions listed in inequalities 2.120 are satisfied, so that the wave numbers solution previously discussed in sub-part 2.3.2.1 is valid. This means that $h_1 a \cong \sqrt{j\ \sigma/\omega\epsilon_0}\ ka$, and that equation 2.122 is the approximate dispersion equation. Equation 2.122 is numerically solved to evaluate $h_2 a$, and then equation 2.121 is used to calculate βa.

The three region configuration approximate normalized fields are obtained in the following manner. All Bessel functions of argument $h_1 a$ and $h_1 a \cdot b/a$ appearing in the three region configuration normalized fields are approximated by the zero order large argument Bessel function representations, which consist of just the first term of equations A.36 – A.39. In order that this is justified, it is necessary that the radial distance associated with the region 1 fields is sufficiently large so that $|h_1|a \cdot$

$r/a = \sqrt{\sigma/\omega\epsilon_0}$ ka · r/a > 1. All Bessel functions of argument $h_2 a$ and $h_2 a$ · b/a appearing in the three region configuration normalized fields are approximated by using the small argument Bessel function representations, equations A.26 – A.29. So that these representations can be used, it is necessary that the radial distance associated with the region 3 fields is sufficiently small so that $|h_2|a$ · r/a < 0.100 is approximately true.

The normalizing coefficients, equations 2.130 and 2.131, are approximated in the manner discussed in the preceding paragraph. They are discovered to be

$$E_{z0} \cong j \frac{\partial_{||}}{2} \frac{120\pi \ ka \ cotan\psi}{\sqrt{j \ \sigma/\omega\epsilon_0} \ ka} \ cos\psi \ \cdot$$

$$[2 \ b/a + \sqrt{j \ \sigma/\omega\epsilon_0} \ ka \ (1-(b/a)^2)], \quad and \quad (2.140)$$

$$H_{z0} \cong \partial_{||} \ cos\psi. \tag{2.141}$$

It was ensured that all the normalized fields correctly satisfied the boundary conditions at the surface of the lossy rod and at the sheath helix surface. So that the continuity of sub-part 2.4.2.2 is not disrupted, the approximate normalized fields will not be listed. It will be emphasized that for the four graphs presented here, it was ensured that all the requirements necessary to justify using the approximations involved in calculating the wave numbers, the normalizing coefficients, and the normalized fields, were satisfied.

Figures 2.24 and 2.25 display the radial dependence of the normalized electric and magnetic field magnitudes, respectively. The operating frequency, the sheath helix geometry, and the lossy rod material electrical properties are specified by the variables ka cotanψ = 5.00×10^{-2}, b/a = 0.100, ϵ_r = 100, $\sigma/\omega\epsilon_0$ = 5.00×10^9, and ψ = 1.00°. (Note that a large value of $\sigma/\omega\epsilon_0$ must be used so that the previously mentioned requirement associated with the region 1 fields,

RADIAL DEPENDENCE OF ELECTRIC FIELDS

Figure 2.24 Curves of the radial dependence associated with the normalized electric field magnitudes for the small argument case, when the lossy rod is a good conductor. The variables used are ka cotanψ=5.00x10^{-2}, b/a=0.100, ϵ_r=1.00x10^2, $\sigma/\omega\epsilon_0$=5.00x10^9, and ψ=1.00°. They determine the approximate wave numbers solution h_1a=43.6 + j43.6, h_2a=βa=2.97x10^{-2} - j3.62x10^{-5}, and the approximate electric normalizing coefficient E_{z0} = jβ_{11} (9.35 - j2.16x10^{-2})(V/m). (Note that ER/EZO=$|E_r/E_{z0}|$, EO/EZO=$|E_\theta/E_{z0}|$, EZ/EZO=$|E_z/E_{z0}|$, and R/A=r/a.)

Figure 2.25 Curves of the radial dependence associated with the normalized magnetic field magnitudes for the small argument case, when the lossy rod is a good conductor. The variables used are ka cotanψ=5.00x10^{-2}, b/a=0.100, ϵ_r=1.00x10^2, $\sigma/\omega\epsilon_0$=5.00x10^9, and ψ=1.00°. They determine the approximate wave numbers solution $h_1 a$=43.6 + j43.6, $h_2 a$=βa=2.97x10^{-2} - j3.62x10^{-5}, and the approximate magnetic normalizing coefficient H_{z0}= βll 1.00(A/m). (Note that HR/HZO=$|H_r/H_{z0}|$, HO/HZO = $|H_\theta/H_{z0}|$, HZ/HZO = $|H_z/H_{z0}|$, and R/A = r/a.)

$\sqrt{\sigma/\omega\epsilon_0}$ ka · r/a > 1, is satisfied.) The approximate wave numbers solution is calculated to be $h_1 a \cong 43.6 + j43.6$, and $h_2 a \cong \beta a \cong$ $2.97 \times 10^{-2} - j3.62 \times 10^{-5}$.

$E_{z0} \cong j \mathcal{J}_{||} (9.35 - j 2.16 \times 10^{-2})$ (V/m) and $H_{z0} \cong \mathcal{J}_{||} 1.00$ (A/m)

are the calculated values of the approximate normalizing coefficients, making use of equations 2.140 and 2.141.

The final two graphs presented in sub-part 2.4.2.2 are Figures 2.26 and 2.27. These show the radial dependence of the approximate normalized electric and magnetic field magnitudes, respectively. ka cotanψ = 5.00×10^{-2}, b/a = 0.900, ϵ_r = 100, $\sigma/\omega\epsilon_0$ = 5.00×10^9, and ψ = 1.00° are the variables which are used. These two graphs can be considered as a variation of Figures 2.24 and 2.25, with b/a = 0.900 instead of b/a = 0.100. $h_1 a \cong 43.6 + j43.6$, and $h_2 a \cong \beta a \cong 5.09 \times 10^{-2} - j2.50 \times 10^{-3}$ are the computed values of the approximate wave numbers. The calculated values of the approximate normalizing coefficients are

$E_{z0} \cong j \mathcal{J}_{||} (1.99 - j 0.194)$ (V/m) and $H_{z0} \cong \mathcal{J}_{||} 1.00$ (A/m).

Figures 2.24 - 2.27 show that the region 2 and region 3 fields only change gradually as the radial distance is varied. The extension of the region 3 fields is large. However, the region 1 fields are rapidly attenuated as the radial distance decreases. More specifically, their radial dependence is dominated by the exponential

$e^{-\sqrt{j\ \sigma/\omega\epsilon_0}\ ka \cdot b/a(1-r/b)}$. This is identical to the radial dependence of the region 1 fields previously discussed in sub-part 2.4.2.1.
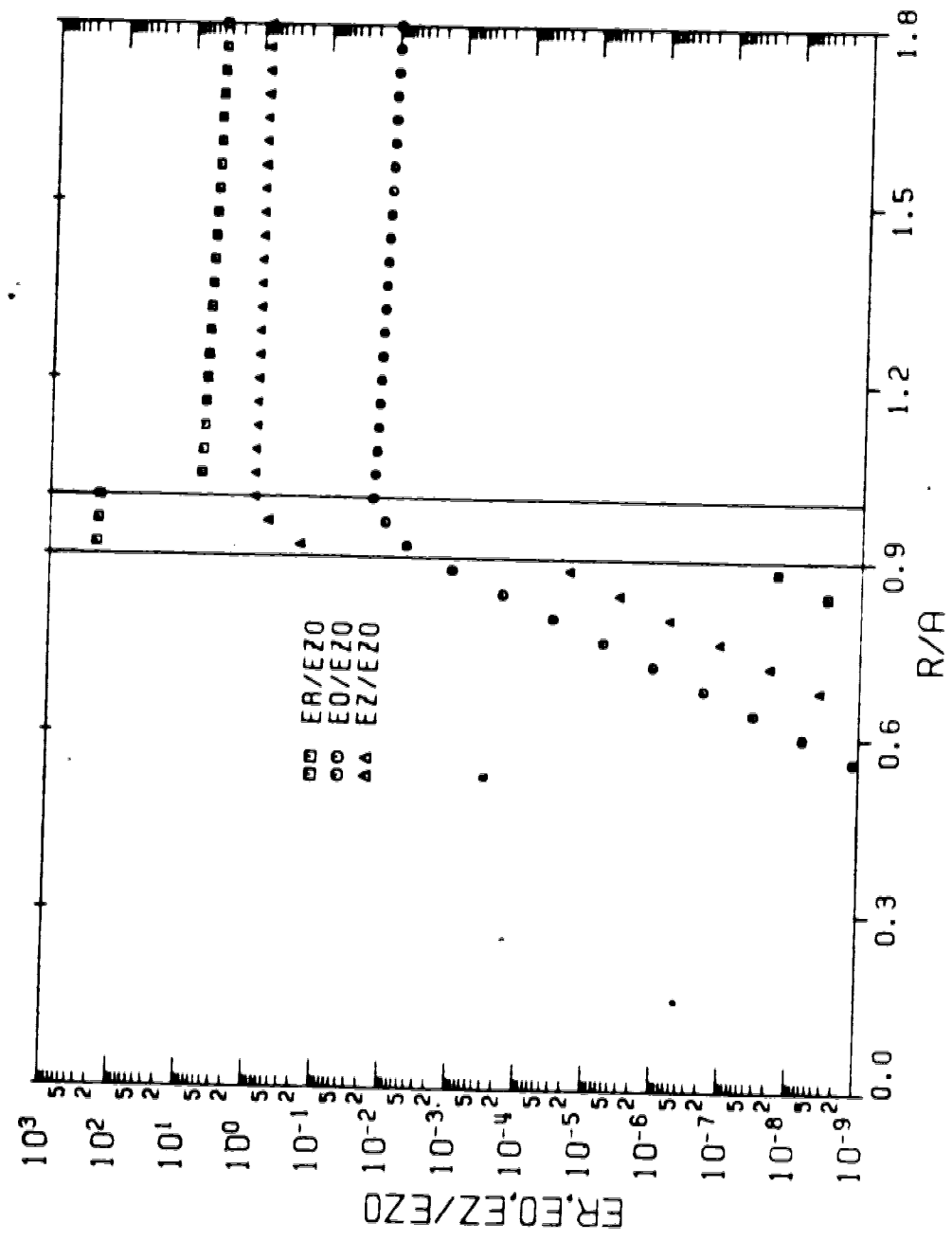
Figure 2.26 Curves of the radial dependence associated with the normalized electric field magnitudes for the small argument case, when the lossy rod is a good conductor. The variables used are $ka \cot\psi = 5.00 \times 10^{-2}$, $b/a = 0.900$, $\epsilon_r = 1.00 \times 10^2$, $\sigma/\omega\epsilon_0 = 5.00 \times 10^9$, and $\psi = 1.00°$. They determine the approximate wave numbers solution $h_1 a = 43.6 + j43.6$, $h_2 a = \beta a = 5.09 \times 10^{-2} - j2.50 \times 10^{-3}$, and the approximate electric normalizing coefficient $E_{z0} = j\mathcal{D}_{11}$ (1.99 - j0.194)(V/m). (Note that ER/EZO = $|E_r/E_{z0}|$, EO/EZO = $|E_\theta/E_{z0}|$, EZ/EZO = $|E_z/E_{z0}|$, and R/A = r/a.)
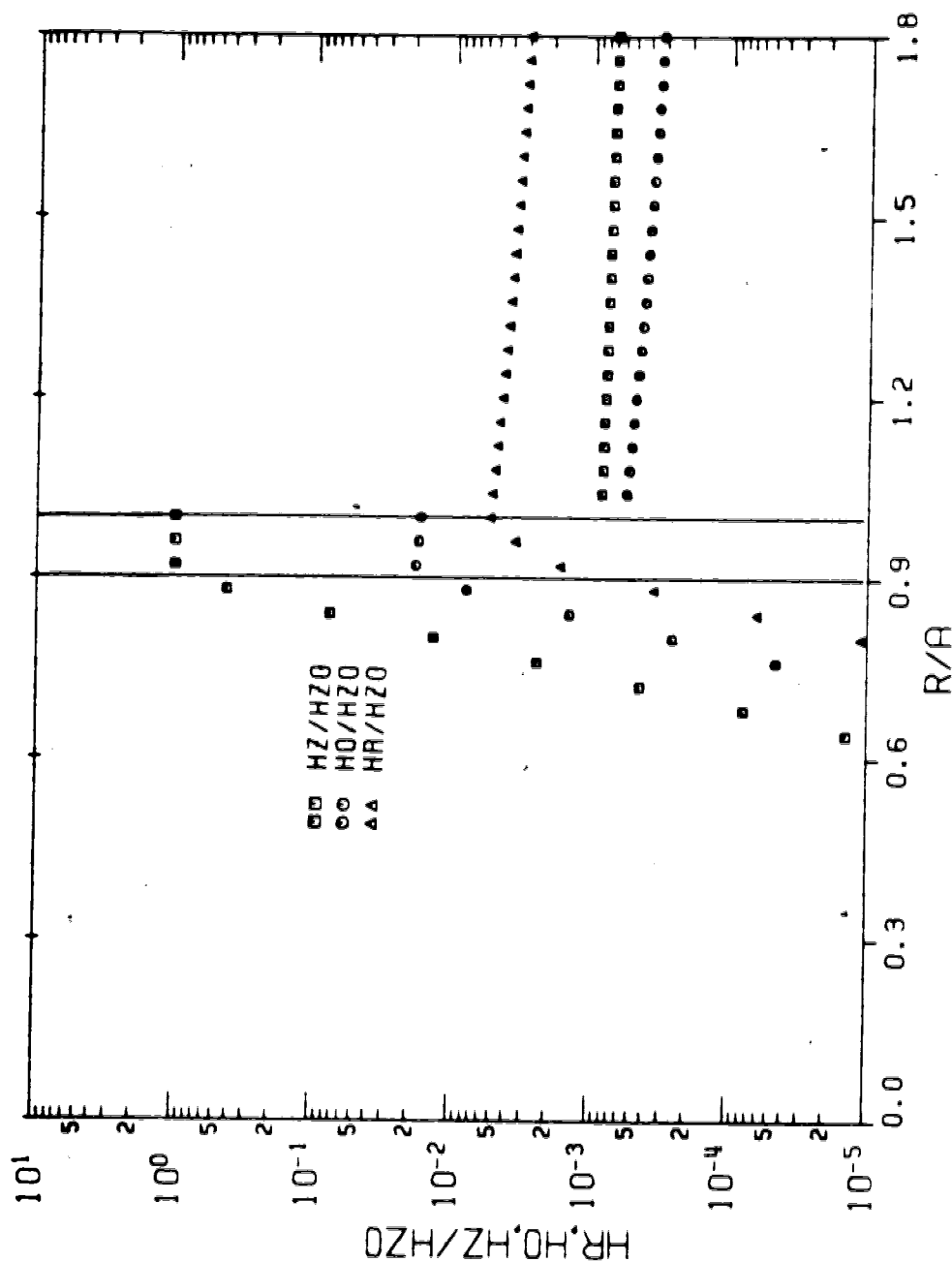
Figure 2.27   Curves of the radial dependence associated with the normalized magnetic field magnitudes for the small argument case, when the lossy rod is a good conductor. The variables used are ka cotanψ=5.00x10^{-2}, b/a=0.900, ϵ_r=1.00x10^2, $\sigma/\omega\epsilon_0$=5.00x10^9, and ψ=1.00°. They determine the approximate wave numbers solution h$_1$a=43.6 + j43.6, h$_2$a=βa=5.09x10^{-2} - j2.50x10^{-3}, and the approximate magnetic normalizing coefficient H$_{z0}$ = ∂_{II} 1.00(A/m). (Note that HR/HZO = |H$_r$/H$_{z0}$|, HO/HZO = |H$_\theta$/H$_{z0}$|, HZ/HZO = |H$_z$/H$_{z0}$|, and R/A = r/a.)

Figures 2.24 - 2.27 will now be compared with Figures C.12 - C.15. The latter mentioned set of graphs is associated with the sheath helix surrounding a perfectly conducting coaxial rod. The same values of $ka \cot an\psi$, b/a, and ψ are used in both sets of figures. Keeping in mind the values of the normalizing coefficients, it is seen that for a particular value of b/a, the magnitudes of the region 2 and region 3 fields associated with the lossy rod configuration are similar to the absolute values of the corresponding fields associated with the perfectly conducting rod configuration. All region 1 fields associated with the sheath helix surrounding a perfectly conducting coaxial rod are zero. The region 4 fields corresponding to the lossy rod configuration are rapidly attenuated as the radial distance decreases. They are only large very near to the lossy rod surface.

Figures 2.26 and 2.27 provide a good illustration of the field behavior at the surface of the lossy rod, and at the sheath helix surface. However, a relatively detailed discussion of this was previously given in sub-part 2.4.1.2 for the small argument case, when "the lossy rod is not a good conductor". A separate discussion of the field behavior at the two interfaces, for the small argument case when "the lossy rod is a good conductor", will not be presented.

2.5   Summary

The free mode field solution for the sheath helix surrounding a lossy coaxial rod has been derived. It will later be used in Chapter 3 to calculate the ohmic power dissipation occurring within the lossy rod. This solution consists of equation 2.65, the dispersion equation, equation 2.88, the separation constant equation, and equations 2.70 - 2.87, the electric and magnetic field components. The free mode field solution is valid for the three region ($b < a$) configuration. However, the appropriate solution valid for the two region ($b = a$) configuration can be obtained by calculating $\lim b \to a^-$ of the previously mentioned equations.

In theory, the dispersion equation and the separation constant equation are solved to obtain the two radial wave numbers, $h_1 a$ and $h_2 a$, and the axial wave number, βa. It is very important to calculate these three wave numbers because they determine the radial and axial spatial dependences of the electric and magnetic field

components. The wave numbers are functions of the variables listed in equations 2.89 – 2.91. By considering the dispersion equation, the separation constant equation, and the field components, it was demonstrated that the real parts of the three wave numbers are restricted to being positive. Furthermore, it was shown that the algebraic signs of the imaginary parts of $h_2 a$ and βa must be the same.

The limit of the free mode field solution associated with the sheath helix surrounding a lossy coaxial rod was taken as the lossy rod radius approaches zero, as the lossy rod conductivity approaches zero, and as the lossy rod conductivity approaches infinity. As expected, it was discovered that the free mode field solutions associated with the empty sheath helix, the sheath helix surrounding an ideal dielectric coaxial rod, and the sheath helix surrounding a perfectly conducting coaxial rod, respectively, were obtained. These three solutions are discussed in Appendices B, D, and C, respectively. All these free mode field solutions were obtained completely independently of the one studied in this chapter. Calculating the three limits provides a check on the accuracy of the free mode field solution associated with the sheath helix surrounding a lossy coaxial rod.

For the purpose of electromagnetic heating applications, the latter two limiting cases mentioned in the preceding paragraph are very important. When the lossy rod conductivity is small (but nonzero), one anticipates that the free mode field solution will approximately behave like that of the sheath helix surrounding an ideal dielectric coaxial rod. For a large (but finite) lossy rod conductivity, the free mode field solution is expected to approximate that of the sheath helix surrounding a perfectly conducting coaxial rod. The sheath helix surrounding an ideal dielectric coaxial rod and the sheath helix surrounding a perfectly conducting coaxial rod are very attractive configurations because it is much easier to numerically evaluate their radial and axial wave numbers, and consequently to numerically evaluate their field components, than it is for the configuration studied in this chapter. Approximate solutions for the power dissipation occurring within the lossy rod will be obtained in Chapter 3 for the special cases when the rod conductivity is either small or large, based on the radial and axial wave numbers solution for the previously mentioned two configurations.

Unfortunately, the direct numerical solution of the dispersion equation and the separation constant equation in order to obtain $h_1 a$, $h_2 a$, and βa for an arbitrary set of the variables listed in equations 2.89 - 2.91 is very difficult to accomplish. However, approximate solutions were obtained by using the small and large argument Bessel function representations to approximate the dispersion equation. The two major classes of approximations considered are when "the lossy rod is not a good conductor" and when "the lossy rod is a good conductor". (These two expressions are defined in section 2.3.) For the first mentioned class of approximations, small and large argument approximate wave numbers solutions were obtained for both the two and three region lossy coaxial rod configurations. In the case of the second mentioned class of approximations, small and large argument approximate wave numbers solutions could only be obtained for the three region configuration.

The field components are very lengthy and complicated expressions. In order to achieve an understanding of how these fields behave at different points in space, approximate graphs of the field component magnitudes were prepared. These made use of the approximate wave numbers solution discussed in section 2.3.

The case when "the lossy rod is not a good conductor" was examined first. For both the two and three region configurations, the field component magnitudes based on the large argument approximate wave numbers solution rapidly decayed in an exponential fashion at increasing radial distances away from the sheath helix surface. This decay was even more rapid for the two region configuration than it was for the three region configuration. *Since the field components cling tightly to the sheath helix "windings", it can be said that the sheath helix is acting like a wave guiding structure.*

The preceding graphs were compared with radial dependence graphs associated with the sheath helix surrounding an ideal dielectric coaxial rod. For the same operating frequency, sheath helix geometry, rod geometry, and rod permittivity, it was discovered that the corresponding fields in the two sets of graphs are similar. It is important to establish this connection because in Chapter 3 use is made of the information presented in Appendix D to investigate the power dissipation occurring within the lossy coaxial rod.

Two and three region configuration radial dependence graphs when "the lossy rod is not a good conductor" based on the small argument wave numbers solution were

prepared. In this circumstance, the magnitudes of the field components changed in a relatively gradual manner as the radial distance was varied. The extension of the region 3 $(a \leq r < \infty)$ field components was large. *It can therefore be said that the waves are basically unguided by the sheath helix.*

A comparison was made of the graphs mentioned in the preceding paragraph with the radial dependence graphs associated with the sheath helix surrounding an ideal dielectric coaxial rod. For the same operating frequency, sheath helix geometry, rod geometry, and rod permittivity, it was discovered that most of the corresponding field components associated with the two sets of graphs are similar. The only exceptions occurred for the region 2 $(b \leq r \leq a)$ radial electric field component, and for the region 1 $(0 \leq r \leq b)$ and region 2 angular magnetic field components.

Several different three region configuration radial dependence graphs when "the lossy rod is a good conductor" based on the large argument wave numbers solution were prepared. It was discovered that all field component magnitudes rapidly decay at increasing radial distances away from the sheath helix surface. The decay associated with the region 1 fields is even greater than that associated with the region 2 and region 3 fields.

The graphs discussed in the preceding paragraph were compared with graphs illustrating the radial dependence of the fields associated with the sheath helix surrounding a perfectly conducting coaxial rod. For the same operating frequency, sheath helix geometry, and rod geometry, it was discovered that the corresponding region 2 and region 3 fields in the two sets of graphs are usually similar. The single exception occurs for the region 2 fields which are very close to the rod surface. For the sheath helix surrounding a perfectly conducting coaxial rod, all region 1 fields are zero. In the large argument case when "the lossy rod is a good conductor", the region 1 fields are nonzero but they decay extremely rapidly at increasing radial distances away from the lossy rod surface. It is important to establish a connection between these two sets of fields because in Chapter 3 use is made of the information presented in Appendix C to investigate the power dissipation which occurs within the lossy coaxial rod.

The final set of radial dependence graphs were based on the three region configuration case when "the lossy rod is a good conductor", making use of the small

argument approximate wave numbers solution. It was discovered that the region 2 and region 3 field magnitudes exhibit a relatively gradual change as the radial distance is varied. However, the region 1 field magnitudes rapidly decay at increasing radial distances away from the lossy rod surface. These magnitudes are only large very close to the surface of the rod.

A comparison was made between the graphs discussed in the preceding paragraph and those illustrating the radial dependence of the fields associated with the sheath helix surrounding a perfectly conducting coaxial rod. For the same operating frequency, sheath helix geometry, and rod geometry, it was discovered that the corresponding region 2 and region 3 fields in the two sets of graphs are usually similar. The single exception occurred for the region 2 fields which were very close to the rod surface. All region 1 fields associated with the perfectly conducting rod configuration are zero. Although the region 1 fields associated with the lossy rod configuration are nonzero, they are extremely rapidly attenuated at increasing radial distances away from the lossy rod surface.

3. Chapter 3. Power Dissipation Occurring Within the Lossy Coaxial Rod, Which is Surrounded by a Sheath Helix

This chapter is concerned with studying the time-averaged power dissipation occurring within the lossy coaxial rod, which is surrounded by a sheath helix. Exact equations for the power dissipation will be derived. Unfortunately, the usefulness of these results is quite limited because of the difficulty involved in calculating the wave numbers h_1a, h_2a, and βa, which appear in these exact expressions.

Two major approaches have been used in order to obtain approximations of the exact power dissipation equations. The first approach involves deriving approximate power dissipation equations by restricting the magnitudes of the (complex-valued) radial wave numbers, h_1a and h_2a, so that they are either small or large. Section 2.3 previously discussed this approximate solution of the wave numbers. Note that a relatively wide range of different lossy rod material electrical properties are allowed. The lossy rod conductivity is only restricted so that the radial wave number magnitudes are either small or large.

The second approach used in this chapter involves deriving approximate power dissipation equations by placing sharp restrictions on the rod material electrical properties. Only very small or very large rod conductivities are allowed. The approximation is made of using the (real-valued) wave number solutions associated with the sheath helix surrounding an ideal dielectric coaxial rod, or the sheath helix surrounding a perfectly conducting coaxial rod. (Note that in section 2.2, it was shown that when the lossy rod conductivity approaches zero and infinity as a limit, the free mode field solution for the sheath helix surrounding a lossy coaxial rod reduces to that of the ideal dielectric coaxial rod configuration and the perfectly conducting coaxial rod configuration, respectively.) It is now not necessary to restrict the values of the wave number solutions. This means that it is possible to evaluate the approximate power dissipation equations for a wide range of operating frequencies, sheath helix geometries, and lossy coaxial rod geometries.

3.1 Derivation of the Time-Averaged Power Dissipated Within the Lossy Coaxial Rod Element Based on the Exact Electric Fields

Ohmic or *joule heating* results from the presence of electrical conduction currents, $\sigma \underline{E}$, in a region containing a medium having a nonzero and finite conductivity, σ. The total time-averaged power dissipated within the conducting region, P_d, is calculated from

$$P_d = \frac{1}{2} \int_V \sigma \cdot |\underline{E}|^2 \, dV, \qquad (3.1)$$

where the integral is evaluated over the entire conducting region volume. (For example, see 41, pp. 314.)

The purpose of this section is to derive equations stating the time-averaged power dissipation occurring within the lossy coaxial rod, which is surrounded by a sheath helix. The power dissipation is due to electrical conduction currents within the lossy coaxial rod, which originate from the presence of the radial, angular, and axial region 1 $(0 \leq r \leq b)$ electric field components. These fields are given by equations 2.70 – 2.72. For convenience, the three electric fields will be repeated here.

$$E_{r1} = j \sum_{b/a} \frac{120\pi}{ka \, \cot an\psi} \cos\psi \; h_2 a \; \beta a \; \cdot$$

$$K_0(h_2 a) \; I_1(h_1 r) \; \sin\beta z \; \cdot \qquad (3.2)$$

$$1/[h_1 a \; I_0(h_1 b) \; K_1(h_2 b)$$

$$+(\epsilon_r - j \; \sigma/\omega\epsilon_0) \; h_2 a \; I_1(h_1 b) \; K_0(h_2 b)],$$

$$E_{\theta 1} = -j \frac{\partial \mu}{\partial b/a} 120\pi \ ka \ \cotan\psi \ \sin\psi \cdot$$

$$K_1(h_2 a) \ I_1(h_1 r) \ \cos\beta z \cdot \tag{3.3}$$

$$1/[h_1 a \ I_0(h_1 b) \ K_1(h_2 b) + h_2 a \ I_1(h_1 b) \ K_0(h_2 b)], \ and$$

$$E_{z1} = j \frac{\partial \mu}{\partial b/a} \frac{120\pi}{ka \ \cotan\psi} \cos\psi \ h_1 a \ h_2 a \cdot$$

$$K_0(h_2 a) \ I_0(h_1 r) \ \cos\beta z \cdot \tag{3.4}$$

$$1/[h_1 a \ I_0(h_1 b) \ K_1(h_2 b)$$

$$+ (\epsilon_r - j \ \sigma/\omega\epsilon_0) \ h_2 a \ I_1(h_1 b) \ K_0(h_2 b)].$$

Equations 3.2 - 3.4 are region 1 fields. Therefore, their radial and axial spatial dependences are restricted to the ranges $0 \leqslant r \leqslant b$ and $-\infty < z < \infty$. The appropriate form of equation 3.1 for the lossy coaxial rod element is

$$P_d = \frac{1}{2} \int_V \sigma \ |\underline{E}_1|^2 \ dV$$

$$= \frac{\sigma}{2} \int_{z=-z_1}^{z=+z_1} \int_{\theta=0}^{\theta=2\pi} \int_{r=0}^{r=b} |\underline{E}_1|^2 \ r \ dr \ d\theta \ dz, \tag{3.5}$$

where $\underline{E}_1 = E_{r1} \ \underline{a}_r + E_{\theta 1} \ \underline{a}_\theta + E_{z1} \ \underline{a}_z$.

In actual fact, the lossy coaxial rod is assumed to extend to $z \rightarrow \pm\infty$. Equation 3.5 shows that the power dissipation is actually calculated for an *element* of the rod having the length $-z_1 \leqslant z \leqslant z_1$ $(0 < z_1 < \infty)$. Henceforth, the symbol

"P_d" is used to denote *the total time-averaged power dissipated within the lossy coaxial rod element.*

An important observation is now made. Since

$$|\underline{E}_1|^2 = \underline{E}_1 \cdot \underline{\overline{E}}_1 = |E_{r1}|^2 + |E_{\theta 1}|^2 + |E_{z1}|^2,$$

equation 3.5 shows that the total power dissipation occurring within the lossy coaxial rod element can be considered as the sum of the power dissipations resulting from the contribution due to each of the radial, angular, and axial region 1 electric field components. Hence, one can define

$$P_{dr} = \frac{\sigma}{2} \int_V |E_{r1}|^2 \, dV, \qquad (3.6)$$

$$P_{d\theta} = \frac{\sigma}{2} \int_V |E_{\theta 1}|^2 \, dV, \quad \text{and} \qquad (3.7)$$

$$P_{dz} = \frac{\sigma}{2} \int_V |E_{z1}|^2 \, dV. \qquad (3.8)$$

All integrals are evaluated over the volume mentioned in equation 3.5. P_{dr}, $P_{d\theta}$, P_{dz} are the time-averaged power dissipations occurring within the lossy coaxial rod element, resulting from electrical conduction currents associated with the region 1 radial, angular, and axial electric field components, respectively. The total time-averaged power dissipated within the lossy coaxial rod element is simply the sum of the three previously mentioned power dissipations.

$$P_d = P_{dr} + P_{d\theta} + P_{dz} \qquad (3.9)$$

The evaluation of the right hand sides of equations 3.6 - 3.8, making use of the respective field components, equations 3.2 - 3.4, is straightforward but it requires a

relatively large amount of mathematics. First, the equation for the power dissipation associated with the region 1 radial electric field component, P_{dr}, will be derived. $|E_{r1}|^2 = E_{r1} \tilde{E}_{r1}$ is calculated using equation 3.2, and then this result is substituted into equation 3.6. The following two relations are necessary to evaluate the integral which is now present.

$$\int_{z=-z_1}^{z=+z_1} |\sin\beta z|^2 \, dz = 2 \int_0^{z_1} (\sin^2\beta_r z + \sinh^2\beta_j z) \, dz$$

$$= \frac{b}{2 \, \beta_r b \, \beta_j b} [\beta_r b \, \sinh(2 \, \beta_j \, z_1) - \beta_j b \, \sin(2 \, \beta_r \, z_1)] \quad (3.10)$$

(As was previously mentioned in part 2.1.2, $\beta_r b = \text{Re}[\beta b]$ and $\beta_j b = \text{Im}[\beta b]$.)

$$\int_{r=0}^{r=b} r \, |I_1(h_1 r)|^2 \, dr = \int_0^b r \, I_1(h_1 r) \, \tilde{I}_1(h_1 r) \, dr$$

$$= \int_0^b r \, I_1(h_1 r) \, I_1(\hat{h}_1 r) \, dr = \frac{-j \, b^2}{4 \, h_{1r} b \, h_{1j} b} \cdot$$

$$[h_1 b \, I_0(h_1 b) \, I_1(\hat{h}_1 b) - \tilde{h}_1 b \, I_0(\hat{h}_1 b) \, I_1(h_1 b)] \quad (3.11)$$

It was necessary to make use of the property of analytic continuation for Bessel functions, equation A.22, the integral involving Bessel functions, equation A.51, and the recurrence relation for Bessel functions, equation A.7, in order to derive equation 3.11. (As was previously mentioned in part 2.1.2, $h_{1r} b = \text{Re}[h_1 b]$ and $h_{1j} b = \text{Im}[h_1 b]$.)

Returning to the calculation of P_{dr}, equations 3.10 and 3.11 are used to evaluate the integral appearing in equation 3.6. One finds that

$$P_{dr} = -j \frac{|A_{11}|^2}{8} \pi a^2 b \sigma \left(\frac{120\pi}{ka \cot an\psi}\right)^2 \cdot$$

$$\frac{\cos^2\psi |h_2 a|^2 |\beta a|^2 |K_0(h_2 a)|^2}{h_{1r} b \, h_{1j} b \, \beta_r b \, \beta_j b} \cdot \qquad (3.12)$$

$$\frac{[h_1 b \, I_0(h_1 b) \, I_1(\widetilde{h}_1 b) - \widetilde{h}_1 b \, I_0(\widetilde{h}_1 b) \, I_1(h_1 b)]}{|h_1 a \, I_0(h_1 b) \, K_1(h_2 b) + (\epsilon_r - j \, \sigma/\omega\epsilon_0) \, h_2 a \, I_1(h_1 b) \, K_0(h_2 b)|^2} \cdot$$

$$[\beta_r b \sinh(2 \beta_j z_1) - \beta_j b \sin(2 \beta_r z_1)].$$

This expression is the time-averaged power dissipated within the lossy coaxial rod element resulting from electrical conduction currents associated with the presence of the radial electric field component, E_{r1}. Of course, it was established in part 2.1.2 that the two radial wave numbers, $h_1 a$ and $h_2 a$, and the axial wave number, βa, are complex-valued quantities. Making use of relation A.22, which is a property of analytic continuation for Bessel functions, it is clear that

$$h_1 b \, I_0(h_1 b) \, I_1(\widetilde{h}_1 b) - \widetilde{h}_1 b \, I_0(\widetilde{h}_1 b) \, I_1(h_1 b)$$

$$= h_1 b \, I_0(h_1 b) \, I_1(\widetilde{h}_1 b) - [h_1 b \, I_0(h_1 b) \, I_1(\widetilde{h}_1 b)]^{\sim}$$

$$= j \, 2 \, Im[h_1 b \, I_0(h_1 b) \, I_1(\widetilde{h}_1 b)].$$

(Note that $[h_1 b \cdot I_0(h_1 b) \cdot I_1(\widetilde{h}_1 b)]^{\sim}$ means "take the complex conjugate of the entire quantity contained within the square brackets".) Therefore, equation 3.12 is a real-valued expression. In fact, it is clear from the integrand of equation 3.6 that this equation must be positive real.

The equation for the power dissipation associated with the region 1 angular electric field, $P_{d\theta}$, will now be derived. $|E_{\theta 1}|^2 = E_{\theta 1} \cdot \widetilde{E}_{\theta 1}$ is calculated

using equation 3.3 and then this quantity is substituted into equation 3.7. The following new relation is needed to evaluate the resulting integral.

$$\int_{z=-z_1}^{z=+z_1} |\cos\beta z|^2 \, dz = 2 \int_0^{z_1} (\cos^2\beta_r z + \sinh^2\beta_j z) \, dz$$

$$= \frac{b}{2 \beta_r b \beta_j b} [\beta_j b \sin(2 \beta_r z_1) + \beta_r b \sinh(2 \beta_j z_1)] \quad (3.13)$$

Using equations 3.13 and 3.11, the integral given in equation 3.7 is evaluated to show that

$$P_{d\theta} = -j \frac{|\overline{\beta}|^2}{8} \pi a^2 b \sigma \frac{(120\pi)^2 (ka \cot an\psi)^2}{h_{1r}b h_{1j}b \beta_r b \beta_j b} \sin^2\psi |K_1(h_2 a)|^2 \cdot$$

$$\frac{[h_1 b \, I_0(h_1 b) \, I_1(\widehat{h_1}b) - \widetilde{h_1}b \, I_0(\widetilde{h_1}b) \, I_1(h_1 b)]}{|h_1 a \, I_0(h_1 b) \, K_1(h_2 b) + h_2 a \, I_1(h_1 b) \, K_0(h_2 b)|^2} \cdot \quad (3.14)$$

$$[\beta_j b \sin(2 \beta_r z_1) + \beta_r b \sinh(2 \beta_j z_1)].$$

Equation 3.14 is *the time-averaged power dissipated within the lossy coaxial rod element resulting from electrical conduction currents associated with the presence of the angular electric field component,* $E_{\theta 1}$. Examination of the right hand side of equation 3.7 shows that it must have a positive real value.

Finally, the equation for the power dissipation associated with the region 1 axial electric field, P_{dz}, is derived. This is done by using equation 3.4 to evaluate $|E_{z1}|^2 = E_{z1} \cdot \widetilde{E}_{z1}$, and then by substituting this result into the right hand side of equation 3.8. One additional relation is needed to evaluate the integral appearing in equation 3.8. This relation is

$$\int_{r=0}^{r=b} \mathcal{P} |I_0(h_1 r)|^2 \, dr = \int_0^b r \, I_0(h_1 r) \, \tilde{I}_0(h_1 r) \, dr$$

$$= \int_0^b r \, I_0(h_1 r) \, I_0(\hat{h}_1 r) \, dr = \frac{-j \, b^2}{4 \, h_{1r} b \, h_{1j} b} \cdot \quad (3.15)$$

$$[h_1 b \, I_0(\hat{h}_1 b) \, I_1(h_1 b) - \tilde{h}_1 b \, I_0(h_1 b) \, I_1(\hat{h}_1 b)].$$

In the course of carrying out the calculations to obtain equation 3.15, it was necessary to make use of the property of analytic continuation for Bessel functions, equation A.22, the Bessel function integral, equation A.51, and the recurrence relation for Bessel functions, equation A.5. Equations 3.15 and 3.13 are used to evaluate the left hand side of equation 3.8. It follows that

$$P_{dz} = -j \, \frac{\partial_{11}^2}{8} \, \pi \, a^2 \, b \, \sigma \, \left(\frac{120\pi}{ka \, \cotan\psi}\right)^2 \cdot$$

$$\frac{\cos^2\psi \, |h_1 a|^2 \, |h_2 a|^2 \, |K_0(h_2 a)|^2}{h_{1r} b \, h_{1j} b \, \beta_r b \, \beta_j b} \cdot \quad (3.16)$$

$$\frac{[h_1 b \, I_0(\hat{h}_1 b) \, I_1(h_1 b) - \tilde{h}_1 b \, I_0(h_1 b) \, I_1(\hat{h}_1 b)]}{|h_1 a \, I_0(h_1 b) \, K_1(h_2 b) + (\epsilon_r - j \, \sigma/\omega\epsilon_0) \, h_2 a \, I_1(h_1 b) \, K_0(h_2 b)|^2} \cdot$$

$$[\beta_j b \, \sin(2 \, \beta_r \, z_1) + \beta_r b \, \sinh(2 \, \beta_j \, z_1)].$$

This expression is *the time-averaged power dissipated within the lossy coaxial rod element* resulting from electrical conduction currents associated with the presence of the axial electric field component, E_{z1}. The right hand side of equation 3.8 shows that it must be positive real in value.

The *total* time-averaged power dissipated within the lossy coaxial rod element is given by equation 3.9. It is simply the sum of equations 3.12, 3.14, and 3.16. Note that

all the power dissipation equations which have been obtained are "exact" – no approximations have been made in their derivation from the region 1 electric field components. The radial wave numbers, $h_1 a$ and $h_2 a$, and the axial wave number, βa, which appear in the power dissipation equations are obtained as solutions to the dispersion equation, equation 2.65, and the separation constant equation, equation 2.88.

It is of interest to determine how large of a contribution each of the three region 1 electric fields makes toward the total time-averaged power dissipation occurring within the lossy coaxial rod element. In particular, it is desirable to determine which electric field makes the dominant contribution. This information can be obtained by studying the ratios $P_{d\theta}/P_{dz}$ and P_{dr}/P_{dz}. From equations 3.12, 3.14, and 3.16, the following two equations are readily obtained.

$$\frac{P_{d\theta}}{P_{dz}} = \frac{(ka \cot\psi)^4 \tan^2\psi}{|h_1 a|^2 |h_2 a|^2} \frac{|K_1(h_2 a)|^2}{|K_0(h_2 a)|^2} \cdot$$

$$\frac{[h_1 b \ I_0(h_1 b) \ I_1(\widehat{h}_1 b) - \widehat{h}_1 b \ I_0(\widehat{h}_1 b) \ I_1(h_1 b)]}{[h_1 b \ I_0(\widehat{h}_1 b) \ I_1(h_1 b) - \widehat{h}_1 b \ I_0(h_1 b) \ I_1(\widehat{h}_1 b)]} \cdot \tag{3.17}$$

$$\frac{|h_1 a \ I_0(h_1 b) \ K_1(h_2 b) + (\epsilon_r - j \ \sigma/\omega\epsilon_0) \ h_2 a \ I_1(h_1 b) \ K_0(h_2 b)|^2}{|h_1 a \ I_0(h_1 b) \ K_1(h_2 b) + h_2 a \ I_1(h_1 b) \ K_0(h_2' b)|^2},$$

and

$$\frac{P_{dr}}{P_{dz}} = \frac{|\beta a|^2}{|h_1 a|^2} \frac{[h_1 b \ I_0(h_1 b) \ I_1(\widehat{h}_1 b) - \widehat{h}_1 b \ I_0(\widehat{h}_1 b) \ I_1(h_1 b)]}{[h_1 b \ I_0(\widehat{h}_1 b) \ I_1(h_1 b) - \widehat{h}_1 b \cdot I_0(h_1 b) \ I_1(\widehat{h}_1 b)]} \cdot$$

$$\frac{[\beta_r b \ \sinh(2 \ \beta_j \ z_1) - \beta_j b \ \sin(2 \ \beta_r \ z_1)]}{[\beta_r b \ \sinh(2 \ \beta_j \ z_1) + \beta_j b \ \sin(2 \ \beta_r \ z_1)]} \cdot \tag{3.18}$$

Note that equation 3.17 is independent of the lossy coaxial rod element length, $2 z_1$.

A digression will now be made to discuss the application of *Poynting's theorem in complex or phasor form* in order to investigate the power dissipation occurring within the lossy coaxial rod element. Since many clear derivations of it are available, the theorem itself will simply be listed here. (For example, see 18, pp. 31-32; 30, pp. 30-33; 36, pp. 625-628; 41, pp. 312-315; and 44, pp. 315-317.)

$$-\frac{1}{2} \oint_S (\underline{E}_1 \times \widetilde{\underline{H}}_1) \cdot \underline{dS} = \frac{1}{2} \int_V \sigma \, |\underline{E}_1|^2 \, dV$$

$$+ j \, 2 \, \omega \int_V [\frac{1}{4} \mu_0 \, |\underline{H}_1|^2 - \frac{1}{4} \epsilon_0 \, \epsilon_r \, |\underline{E}_1|^2] \, dV \qquad (3.19)$$

is the appropriate form of Poynting's theorem in complex form as applied to the lossy coaxial rod element. The closed surface of integration, S, consists of the cylindrical surface $r = b$, $-z_1 \leq z \leq z_1$, and the two endfaces $z = \pm z_1$, $0 \leq r \leq b$. Figure 3.1 illustrates the lossy coaxial rod element closed surface. Equation 3.5 shows the volume of integration, V. The region 1 electric and magnetic field components, equations 3.2 - 3.4 and equations 2.73 - 2.75, are to be used in equation 3.19. Equation 3.20 is obtained by taking the real part of both sides of equation 3.19.

$$\text{Re}[-\frac{1}{2} \oint_S (\underline{E}_1 \times \widetilde{\underline{H}}_1) \cdot \underline{dS}] = \frac{1}{2} \int_V \sigma \, |\underline{E}_1|^2 \, dV \qquad (3.20)$$

This has the important meaning that the total time-averaged power flow *into* the closed surface associated with the lossy coaxial rod element equals the total time-averaged power dissipated within the element volume. (Note that, as mentioned in section 2.1.1, the lossy coaxial rod volume is assumed to be source-free.)
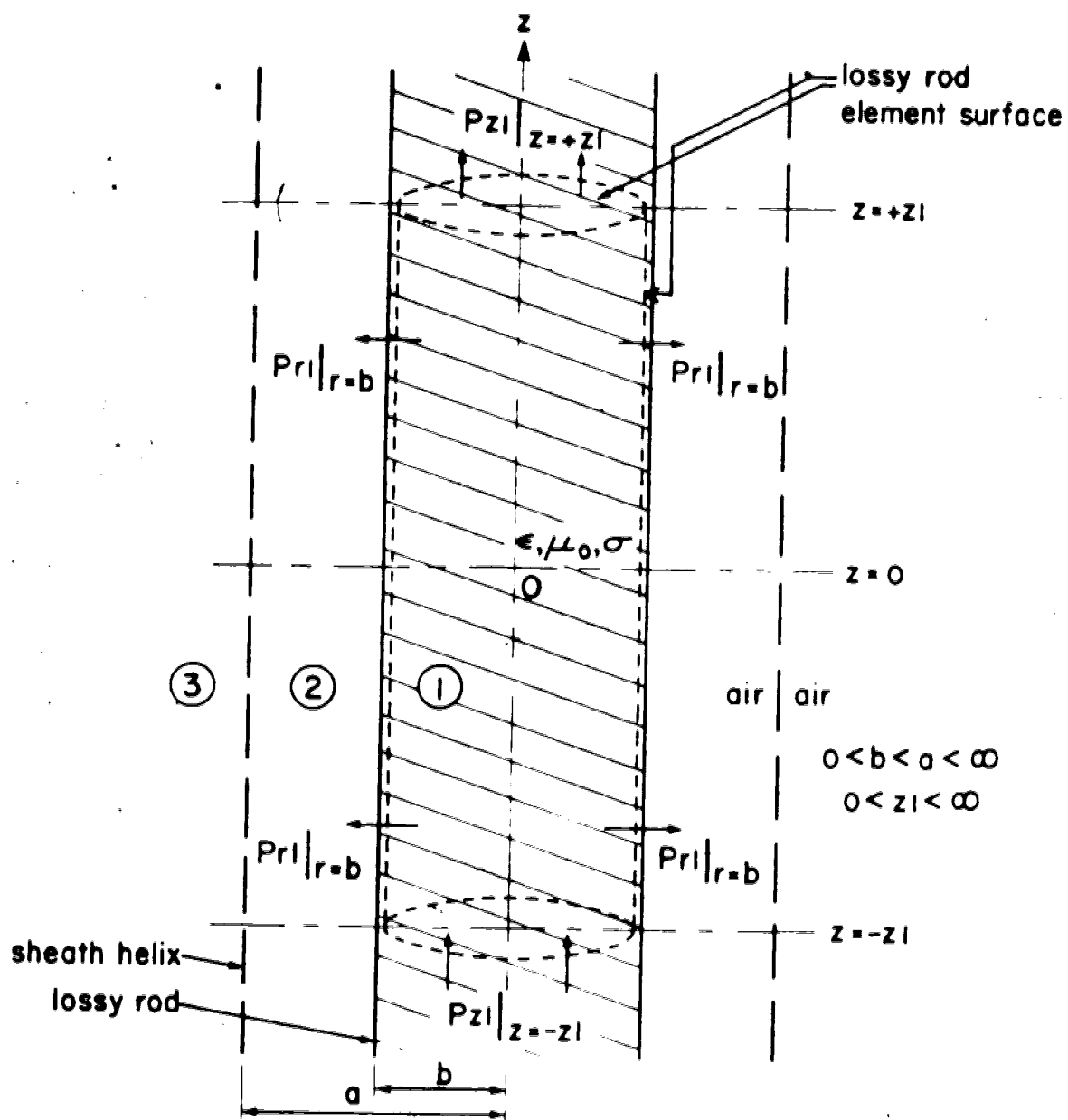
Figure 3.1   The lossy coaxial rod element of the sheath helix surrounding a lossy coaxial rod is shown. In addition, the radial and axial time-averaged power flows, $P_{r1}\big|_{r=b}$ and $P_{z1}\big|_{z=\pm z_1}$, respectively, are displayed. (Note that $z1=z_1$.)

Previously, in section 3.1, the right hand side of equation 3.20 was evaluated. It is now desired to evaluate the left hand side. In cylindrical coordinates, the complex Poynting vector associated with the region 1 fields is

$$\underline{P}_1 = \underline{E}_1 \times \widetilde{\underline{H}}_1 = (E_{\theta 1} \widetilde{H}_{z1} - E_{z1} \widetilde{H}_{\theta 1}) \, \underline{a}_r \qquad (3.21)$$

$$+ (E_{z1} \widetilde{H}_{r1} - E_{r1} \widetilde{H}_{z1}) \, \underline{a}_\theta + (E_{r1} \widetilde{H}_{\theta 1} - E_{\theta 1} \widetilde{H}_{r1}) \, \underline{a}_z .$$

Therefore,

$$Re[- \frac{1}{2} \oint_S (\underline{E}_1 \times \widetilde{\underline{H}}_1) \cdot \underline{dS}]$$

$$= - P_{r1}\big|_{r=b} + (P_{z1}\big|_{z=-z_1} - P_{z1}\big|_{z=z_1}), \text{ where} \qquad (3.22)$$

$$P_{r1}\big|_{r=b} = Re[\frac{1}{2} \int_{S_1} (\underline{E}_1 \times \widetilde{\underline{H}}_1)\big|_{r=b} \cdot \underline{a}_r \, dS_1]$$

$$= Re[\frac{1}{2} \int_{z=-z_1}^{z=+z_1} \int_{\theta=0}^{\theta=2\pi} (E_{\theta 1} \widetilde{H}_{z1} - E_{z1} \widetilde{H}_{\theta 1})\big|_{r=b} \, b \, d\theta \, dz] \qquad (3.23)$$

and

$$P_{z1}\big|_{z=\pm z_1} = Re[\frac{1}{2} \int_{S_2} (\underline{E}_1 \times \widetilde{\underline{H}}_1)\big|_{z=\pm z_1} \cdot \underline{a}_z \, dS_2]$$

$$= Re[\frac{1}{2} \int_{\theta=0}^{\theta=2\pi} \int_{r=0}^{r=b} (E_{r1} \widetilde{H}_{\theta 1} - E_{\theta 1} \widetilde{H}_{r1})\big|_{z=\pm z_1} \, r \, dr \, d\theta]. \qquad (3.24)$$

$P_{r1}\big|_{r=b}$ is the radial time-averaged power flow in the $+\ \underline{a}_r$ direction, through

the cylindrical surface associated with the lossy coaxial rod element. $P_{z1}\big|_{z=\pm z_1}$ is

the axial time-averaged power flow in the $+\ \underline{a}_z$ direction through the two endfaces associated with the element. These two power flows are clearly shown in Figure 3.1.

The procedure that the author followed to evaluate the radial and axial power flows, equations 3.23 and 3.24, respectively, will now be outlined. The field components, equations 3.2 - 3.4 and equations 2.73 - 2.75, were used. The property of analytic continuation for Bessel functions, equation A.22, was employed. The relation $Re[z] = \frac{1}{2} (z + \hat{z})$ was also used. Equations 3.13 and 3.11 were employed. Finally, the trigonometric analytic continuation properties

$$\widehat{\cos}(\beta z) = \cos(\widehat{\beta} z) \quad \text{and} \quad \widehat{\sin}(\beta z) = \sin(\widehat{\beta} z)$$

were used. All the trigonometric functions were separated into their real and imaginary parts. To minimize the disruption in the continuity of section 3.1, the values of equations 3.23 and 3.24 will not be explicitly stated here. It will be emphasized that *the author was able to demonstrate that the net radial and axial time-averaged power flow into the lossy coaxial rod element closed surface, as stated in equation 3.22, is exactly the same as the total time-averaged power dissipated within the element volume, equation 3.9.* This was accomplished by combining the two equations obtained from separately equating respectively the real and imaginary parts of the separation constant equation, equation 2.88, with equation 3.22, and performing a large amount of algebraic manipulations.

In summary, the preceding discussion has achieved two important purposes. First, it has provided another outlook for investigating the total time-averaged power dissipation occurring within the lossy coaxial rod element. Instead of regarding it from the point of view of electrical conduction currents which result in ohmic heating, the power dissipation has been considered as the net time-averaged power flow into the element closed surface. Second, the discussion has supported the validity of the

previously obtained results. The total time-averaged power dissipation, equation 3.9 (which is the sum of equations 3.12, 3.14, and 3.16), was verified to be correct from a completely different method of calculation than that which was originally used to derive it.

As was mentioned earlier in section 3.1, the two radial wave numbers and the axial wave number appearing in the power dissipation equations are obtained from the solution of the dispersion equation, equation 2.65, and the separation constant equation, equation 2.88. Unfortunately, it was previously discussed at the beginning of section 2.3 that the direct solution of equations 2.65 and 2.88 to obtain numerical values of the wave numbers solution is usually extremely difficult to accomplish. Therefore, it is not usually possible to numerically evaluate the power dissipation equations which have been obtained. However, this can be *approximately* accomplished for certain values of the radial wave numbers solution. When the magnitudes of $h_1 a$ and $h_2 a$ are either small or large, a discussion of the approximate wave numbers solution was previously given in part 2.3.1, which corresponds to the case when *"the lossy rod is not a good conductor"*, and in part 2.3.2, which corresponds to the case when the *"lossy rod is a good conductor"*. Making use of this knowledge, it is possible to derive small and large argument approximations of the power dissipation equations. This is the purpose of sections 3.2 and 3.3.

3.2   Approximate Representations of the Power Dissipation Equations When "The Lossy Coaxial Rod Is Not a Good Conductor"

Equations 3.12, 3.14, and 3.16 are the exact power dissipation equations. Approximate representations of these equations will now be derived and examined for the case when "the lossy rod is not a good conductor". (The meaning of the expression in quotation marks as it is used in part 3.2.1 is the same as it was in sub-part 2.3.1.1. This term has the same meaning as used in part 3.2.2 as it did in sub-part 2.3.1.2.)

The approximate power dissipation equations are obtained by using the small argument and large argument representations to approximate the Bessel functions appearing in the exact equations. These approximate equations will be seen to be

relatively easy to evaluate. Equally important, the effect on the app: :·'nate power dissipation equations of varying the operating frequency, the sheath helix geometry, the lossy coaxial rod element geometry, and the lossy rod electrical properties, is often readily understood.

3.2.1 Small Argument Representation

The small argument approximations of equations 3.12, 3.14, and 3.16, the exact power dissipation equations, will be obtained. To justify the usage of the small argument Bessel function representations, it is approximately necessary that the radial wave number magnitudes are restricted so that $|h_1|a < 0.100$ and $|h_2|a < 0.100$. Equations A.26 - A.29, the small argument Bessel function representations, are substituted into the three previously mentioned exact equations. (It will be mentioned that equations A.30 and A.31 were used in place of equations A.26 and A.27 to approximate the quantity

$$h_1 b \ I_0(h_1 b) \ I_1(\widehat{h_1} b) - \widehat{h_1} b \ I_0(\widehat{h_1} b) \ I_1(h_1 b)$$

because the latter mentioned two equations are not a good enough approximation.) Making the previously mentioned substitutions and performing a small amount of algebra, equations 3.25 - 3.27 are obtained.

$$P_{dr} \cong \frac{\partial_{11}^2}{32} \pi b^3 \sigma \ (\frac{120\pi}{ka \ \cot an\psi})^2 \ \cos^2\psi \ \frac{|h_2 a|^4 \ |\beta a|^2}{\beta_r a \ \beta_j a} \ .$$

$$\frac{|\log(0.891 \ h_2 a)|^2}{|1 - (\epsilon_r - j \ \sigma/\omega\epsilon_0) \ \frac{(h_2 b)^2}{2} \ \log(0.891 \ h_2 b)|^2} \ . \qquad (3.25)$$

$$[\beta_r b \ \sinh(2 \ \beta_j \ z_1) - \beta_j b \ \sin(2 \ \beta_r \ z_1)],$$

$$P_{d\theta} \cong \frac{\mu^2}{32} \pi \, b^3 \, \sigma \, (120\pi)^2 \, \frac{(ka \, \cot an\psi)^2}{\beta_r a \, \beta_j a} \, \sin^2\psi \, \cdot$$

$$[\beta_r b \, \sinh(2 \, \beta_j \, z_1) + \beta_j b \, \sin(2 \, \beta_r \, z_1)], \quad \text{and} \qquad (3.26)$$

$$P_{dz} \cong \frac{\mu^2}{4} \pi \, a^2 \, b \, \sigma \, (\frac{120\pi}{ka \, \cot an\psi})^2 \, \cos^2\psi \, \frac{|h_2 a|^4}{\beta_r a \, \beta_j a} \, \cdot$$

$$\frac{|\log(0.891 \, h_2 a)|^2}{|1 - (\varepsilon_r - j \, \sigma/\omega\varepsilon_0) \, \frac{(h_2 b)^2}{2} \, \log(0.891 \, h_2 b)|^2} \cdot \qquad (3.27)$$

$$[\beta_r b \, \sinh(2 \, \beta_j \, z_1) + \beta_j b \, \sin(2 \, \beta_r \, z_1)].$$

As a check on the accuracy of the three preceding equations, equations A.26 – A.29, the small argument Bessel function representations, were used to approximate equations 3.2 – 3.4, the region 1 electric field components. Equations 3.6 – 3.8 were then used to qalculate the approximate power dissipations. Exactly the same result as equations 3.25 – 3.27 was obtained. In summary, using the exact electric field components, integrating these to obtain the power dissipations, and then applying the small argument Bessel function representations, gives the same result as when the small argument Bessel function representations were used to approximate the electric fields, and then the integration was performed to obtain the power dissipation equations. This result is expected. It provides a check on the correctness of equations 3.25 – 3.27.

Equation 2.106 is the small argument approximation of the dispersion equation, which is valid when the lossy rod is not a good conductor. It can be used to slightly simplify equations 3.25 and 3.27.

$$P_{dr} \approx \frac{\pi^2}{128} \, \pi \, b^3 \, \sigma \, (120\pi)^2 \, (ka \, \cot\!\psi)^2 \, \frac{\cos^2\psi}{\beta_r a \, \beta_j a} \, |\beta a|^2 \, .$$

$$\frac{[\beta_r b \, \sinh(2 \, \beta_j \, z_1) - \beta_j b \, \sin(2 \, \beta_r \, z_1)]}{\left| 1 - (\epsilon_r - j \, \sigma/\omega\epsilon_0) \, \frac{(h_2 b)^2}{2} \, \log(b/a) \right|^2} , \quad \text{and} \qquad (3.28)$$

$$P_{dz} \approx \frac{\pi^2}{16} \, \pi \, a^2 \, b \, \sigma \, (120\pi)^2 \, (ka \, \cot\!\psi)^2 \, \frac{\cos^2\psi}{\beta_r a \, \beta_j a} \, .$$

$$\frac{[\beta_r b \, \sinh(2 \, \beta_j \, z_1) + \beta_j b \, \sin(2 \, \beta_r \, z_1)]}{\left| 1 - (\epsilon_r - j \, \sigma/\omega\epsilon_0) \, \frac{(h_2 b)^2}{2} \, \log(b/a) \right|^2} . \qquad (3.29)$$

Equations 3.26, 3.28, and 3.29 can be evaluated by using the wave numbers solution discussed in sub-part 2.3.1.1. This involves equation 2.106 and equation 2.88, the separation constant equation. Graphs of the radial wave number solution $h_2 a$ are given in Figures 2.2 – 2.5.

Rather than following the procedure discussed in the previous paragraph to evaluate equations 3.26, 3.28, and 3.29, the approximate power dissipation equations can be more easily understood by making some further approximations. A significant simplification is achieved by assuming that the magnitude of the axial wave number is sufficiently small for the particular normalized lossy coaxial rod element length of concern, $2 \, z_1/a$, so that $2 \, |\beta| \, z_1 = |\beta| a \cdot 2 \, z_1/a \ll 1$. This means that

$$\sin(2 \, \beta_r \, z_1) \approx 2 \, \beta_r \, z_1 - \frac{(2 \, \beta_r \, z_1)^3}{6} \quad \text{and}$$

$$\sinh(2 \, \beta_j \, z_1) \approx 2 \, \beta_j \, z_1 + \frac{(2 \, \beta_j \, z_1)^3}{6} \, .$$

One final approximation which will be made is to assume that the magnitude of the radial wave number associated with the air medium, $|h_2|a$, is sufficiently small, taking into account the normalized lossy rod radius, b/a, and the lossy rod material electrical properties, so that

$$\left| 1 - (\epsilon_r - j\, \sigma/\omega\epsilon_0)\, \frac{(h_2 b)^2}{2}\, \log(b/a) \right| \cong 1.$$

The two previously mentioned approximations were used in equations 3.26, 3.28, and 3.29. It is now possible to list the approximate small argument power dissipation equations.

$$P_{dr} \cong \frac{|I|^2}{768}\, \pi\, \sigma\, a^3\, (b/a)^4\, (120\pi)^2\, |\beta a|^4 \cdot$$

$$(ka\, \cot\!an\psi)^2\, \cos^2\!\psi\, \left(\frac{2\, z_1}{a}\right)^3, \qquad\qquad (3.30)$$

$$P_{d\theta} \cong \frac{|I|^2}{16}\, \pi\, \sigma\, a^3\, (b/a)^4\, (120\pi)^2 \cdot$$

$$(ka\, \cot\!an\psi)^2\, \sin^2\!\psi\, \frac{2\, z_1}{a}, \qquad\qquad (3.31)$$

$$P_{dz} \cong \frac{|I|^2}{8}\, \pi\, \sigma\, a^3\, (b/a)^2\, (120\pi)^2 \cdot$$

$$(ka\, \cot\!an\psi)^2\, \cos^2\!\psi\, \frac{2\, z_1}{a}, \qquad\qquad (3.32)$$

$$\frac{P_{dr}}{P_{dz}} \approx \frac{(b/a)^2}{96} |\beta a|^4 \left(\frac{2 z_1}{a}\right)^2, \quad \text{and} \tag{3.33}$$

$$\frac{P_{d\theta}}{P_{dz}} \approx \frac{1}{2} (b/a)^2 \tan^2\psi. \tag{3.34}$$

Equations 3.33 and 3.34 were obtained by simply taking the appropriate ratios of equations 3.30 - 3.32. For convenience, all the assumptions made in deriving equations 3.30 - 3.34 from the exact power dissipation equations will be gathered together and listed below.

$$|h_1'|a < 0.100, \quad |h_2|a < 0.100, \quad |\beta a| \cdot 2 z_1/a << 1,$$

$$\tag{3.35}$$

$$\text{and} \quad \left|1 - (\epsilon_r - j \ \sigma/\omega\epsilon_0) \ \frac{(h_2 b)^2}{2} \ \log(b/a)\right| \approx 1.$$

A brief digression will be made concerning the first two requirements listed in equations 3.35. Figures 2.2 - 2.5 and equation 2.109, the small argument approximate equation for calculating $h_{2r}a \approx |h_2|a$, make it clear that $|h_2|a < 0.100$ is usually true if $ka \cot\psi < 0.100$. The separation constant equation, equation 2.88, shows that when $|h_2|a < 0.100$, it is necessary that

$$\sqrt{\epsilon_r} \ ka < 0.100 \quad \text{and} \quad \sqrt{\sigma/\omega\epsilon_0} \ ka < 0.100,$$

to approximately ensure that $|h_1|a < 0.100$. In short, the requirements on the magnitudes of the two radial wave numbers, $|h_1|a < 0.100$ and $|h_2|a < 0.100$, can be approximately explicitly stated in terms of the operating frequency,

the sheath helix geometry, and the lossy rod electrical properties, according to

$$ka \cot \psi < 0.100, \quad \sqrt{\epsilon_r} \; ka < 0.100,$$

$$\text{and} \quad \sqrt{\sigma/\omega\epsilon_0} \; ka < 0.100. \tag{3.36}$$

Equations 3.30 - 3.34 are the approximate small argument power dissipation equations, when the lossy rod is not a good conductor. (The term "the lossy rod is not a good conductor" is defined as having the rod material electrical properties such that equations 3.35 and 3.36 are satisfied. This places restrictions on how large the quantities ϵ_r and $\sigma/\omega\epsilon_0$ are allowed to be. Note that $\sigma/\omega\epsilon_0 >> \epsilon_r$ *is allowed* here, which is the usual definition of the term "good conductor".) Equations 3.30 - 3.34 are valid for both the three region configuration (b < a) and for the two region configuration (b = a).

From the point of view of the electromagnetic heating of common materials, these small argument power dissipation equations are very important. For example, materials such as food stuffs, biological tissues, lumber, and oil sand, could be heated by surrounding them with a sheath helix (25). The electrical properties of these materials are such that for a wide range of operating frequencies, sheath helix geometries, and lossy coaxial rod element geometries, the restrictions given in equations 3.35 and 3.36 would be satisfied.

Equations 3.31, 3.32, and 3.34 are easy to understand because they are explicitly given in terms of the electrical current on the sheath helix "windings", the operating frequency, the sheath helix geometry, the lossy coaxial rod element geometry, and the lossy coaxial rod element electrical properties. However, in order to evaluate equations 3.30 and 3.33 it is necessary to know $|\beta| a$. The value of the magnitude of the axial wave number is approximately calculated by making use of the separation constant equation, equation 2.88, and the small argument approximate representation of the dispersion equation, equation 2.109.

$$|\beta a|^2 \simeq (\beta_r a)^2, \quad (\beta_r a)^2 \simeq (h_{2r} a)^2 + (ka)^2, \qquad (3.37)$$

where $h_{2r} a$ is approximately calculated from the relation

$$\left(\frac{ka \; cotan\psi}{h_{2r} a}\right)^2 \simeq -2 \; log(0.891 \; h_{2r} a).$$

Note that the solution for $h_2 a$ shown in Figures 2.2 – 2.5 can be used along with the separation constant equation to give a slightly more accurate value of $|\beta| a$ than that which is obtained from equations 3.37.

A discussion of the behavior of the approximate power dissipation equations as the operating frequency, sheath helix geometry, and lossy coaxial rod element geometry, are varied is now given. Decreasing only the pitch angle and the frequency of operation in such a fashion that the variable $ka \; cotan\psi = 2\pi f \sqrt{\mu_0 \epsilon_0} \; a \; cotan\psi$ remains constant, it is clear from equations 3.30 – 3.32 that $P_{d\theta}$ will be greatly reduced but P_{dr} and P_{dz} will be approximately unchanged. This behavior originates from the fact that the pitch angle appears by itself in $E_{\theta 1}$ as $sin\psi$, while in E_{r1} and E_{z1} it appears as $cos\psi$.

Making the normalized lossy coaxial rod element length, $2 z_1/a$, smaller means that P_{dr} becomes reduced more rapidly than $P_{d\theta}$ and P_{dz}. This is because E_{r1} has a $sin\beta z$ axial dependence, while $E_{\theta 1}$ and E_{z1} have a $cos\beta z$ axial dependence. (Note that, as mentioned in equations 3.35, $|\beta| a \cdot 2 z_1/a << 1$ has been assumed in the derivation of equations 3.30 – 3.34. Of course, $0 \le |\beta| z \le |\beta| z_1$ is true when the electric fields within the lossy coaxial rod element are considered. Therefore, $cos\beta z \simeq 1$ and $sin\beta z \simeq \beta z$.) Making the range of $|\beta| z$ values smaller by reducing $2 z_1/a$ clearly tends to reduce $|E_{r1}|$ but it has an insignificant effect on $|E_{\theta 1}|$ and $|E_{z1}|$. If only the lossy coaxial rod radius is reduced, just the variable b/a in equations 3.30 – 3.32 becomes smaller. It is clear that P_{dr} and $P_{d\theta}$ become smaller more rapidly than P_{dz}. The explanation for this behavior originates from the

radial dependence of the three region 1 electric fields. Equations 3.2 - 3.4, the electric field components, show that the radial dependence of E_{r1} and $E_{\theta 1}$ is given by $I_1(h_1 r)$, while that of E_{z1} is given by $I_0(h_1 r)$. As mentioned in equations 3.35, $|h_1|a < 0.100$ is true and so the small argument representations of the Bessel functions, equations A.26 and A.27, can be used to approximate $I_1(h_1 r)$ and $I_0(h_1 r)$ at all points within the lossy rod element. It is seen that E_{r1} and $E_{\theta 1}$ are directly proportional to the radial distance, while E_{z1} is independent of it. Clearly, $|E_{r1}|$ and $|E_{\theta 1}|$ are largest near the lossy rod surface. If the rod radius is decreased, the magnitudes of E_{r1} and $E_{\theta 1}$ near r = b become less while that of E_{z1} is approximately unchanged. Therefore, reducing only the lossy rod radius means that P_{dr} and $P_{d\theta}$ become small more rapidly than P_{dz}. (Figures 2.14, 2.16, and 2.18 illustrate the radial dependence of the electric fields for the small argument case, when "the lossy rod is not a good conductor". These three figures only differ because different values of the variable b/a are used. Therefore, they can be used to study how the electric fields within the lossy rod element behave as the rod radius is varied.)

Attention is now directed to determining which of the three electric fields makes the major contribution towards the total power dissipated within the lossy coaxial rod element. Assuming that the sheath helix is sufficiently tightly wound so that $0 < \psi \leq 10.0°$, it is clear from equation 3.34 that $P_{dz} >> P_{d\theta}$. Furthermore, since $|\beta|a \cdot 2 z_1/a << 1$ has been assumed in the derivation of equations 3.30 - 3.34, it follows from equation 3.33 that $P_{dz} >> P_{dr}$. Therefore, *the axial region 1 electric field provides the dominant contribution to the total power dissipation occurring within the lossy coaxial rod element, for the small argument case when "the lossy rod is not a good conductor". To a good approximation, equation 3.32 states the* total power dissipation *occurring within the lossy coaxial rod element.*

Information concerning how the total power dissipation is distributed throughout the lossy coaxial rod element volume can be obtained by examining the spatial dependence of the axial electric field component in region 1. E_{z1} has a $\cos\beta z$ axial dependence and a $I_0(h_1 r)$ radial dependence. Since $|h_1|a < 0.100$ and $|\beta|a \cdot 2 z_1/a << 1$ has been assumed, it is clear from the small argument

representations of the two previously mentioned functions that $\cos \beta z \cong 1$ and $I_0(h_1 r) \cong 1$. At all points throughout the lossy coaxial rod element, E_{z1} is approximately constant in value. This has the important meaning that *the total power dissipation is approximately distributed uniformly throughout the element volume*. A more detailed discussion of this behavior for the special case when the lossy rod material electrical properties are such that $\sigma/\omega \epsilon_0 \ll \epsilon_r$ is given later in part 3.4.3.

Chute et al. (25) mentioned the fact that for the two region configuration, where the sheath helix interior region is completely filled with a low-loss material, the total power dissipation for the situation where the wave numbers solution is small in magnitude, approximately results only from the contribution associated with the interior region axial electric field. Furthermore, it was mentioned that the total power dissipation is approximately *uniformly* distributed throughout the lossy material volume.

3.2.2 Large Argument Representation

The purpose of part 3.2.2 is to obtain large argument approximations of equations 3.12, 3.14, and 3.16, the exact power dissipation equations. Due to the nature of the radial and axial wave numbers solution, it is necessary to separately consider the two region and three region sheath helix surrounding a lossy coaxial rod configurations. This will be done in sub-parts 3.2.2.1 and 3.2.2.2.

3.2.2.1 Two Region Configuration

It is assumed that the lossy coaxial rod completely fills the interior region of the sheath helix and touches the sheath surface. Only two regions are present, the rod-filled region and the region exterior to the sheath helix.

Previously, in sub-part 2.3.1.2, the two region large argument wave numbers solution was obtained. This solution is given by equation 2.118. It is convenient to repeat this equation here.

$$h_1 a \cong h_2 a \cong \beta a \cong h a \cong \sqrt{\frac{(\epsilon_r + 1) - j\,\sigma/\omega\epsilon_0}{2}}\ ka\,\cot\alpha\psi \qquad (3.38)$$

As was mentioned in sub-part 2.3.1.2, to justify the preceding approximate wave numbers solution it is necessary that

$$|h_1|a > 1, \quad |h_2|a > 1, \quad \text{and} \quad \cotan^2\psi > 1;$$

or, equivalently, that   (3.39)

$$\left|\sqrt{\frac{(\epsilon_r+1) - j\, \sigma/\omega\epsilon_0}{2}}\right| ka \cotan\psi > 1 \quad \text{and} \quad \cotan^2\psi > 1.$$

Equation 3.38 is very useful because it shows that $h_1 a$, $h_2 a$ and βa are explicitly known in terms of the operating frequency, the sheath helix geometry, and the lossy coaxial rod material electrical properties. *Equations 3.39 define what is meant by the term "the lossy rod is not a good conductor" as it is used in sub-part 3.2.2.1.* Note that equations 3.38 and 3.39 show that either $\epsilon_r \gg \sigma/\omega\epsilon_0$ or $\sigma/\omega\epsilon_0 \gg \epsilon_r$ can occur. This is the usual meaning of the expressions "good dielectric" and "good conductor", respectively.

Taking just the first term of equations A.36 - A.39, the large argument Bessel function representations, and substituting this into equations 3.12, 3.14, and 3.16, the exact power dissipation equations, making use of the fact that $b = a$, equations 3.40 - 3.44 are obtained.

$$P_{dr} \approx -\frac{\mathcal{H}^2}{2} \frac{\pi a^3 \sigma (120\pi)^2 \cos^2\psi}{\sigma/\omega\epsilon_0 (ka \cotan\psi)^2 |(\epsilon_r + 1) - j\, \sigma/\omega\epsilon_0| h_r a}$$

$$\cdot [h_r a \sinh(2 h_j z_1) - h_j a \sin(2 h_r z_1)], \qquad (3.40)$$

$$P_{d\theta} \cong - \frac{\rangle_{11}^2}{2} \frac{\pi a^3 \sigma (120\pi)^2 \sin^2\psi}{\sigma/\omega\epsilon_0 (ka \cot an\psi)^2 |(\epsilon_r + 1) - j \sigma/\omega\epsilon_0| h_r a} \cdot$$

$$[h_r a \sinh(2 h_j z_1) + h_j a \sin(2 h_r z_1)], \qquad (3.41)$$

$$P_{dz} \cong - \frac{\rangle_{11}^2}{2} \frac{\pi a^3 \sigma (120\pi)^2 \cos^2\psi}{\sigma/\omega\epsilon_0 (ka \cot an\psi)^2 |(\epsilon_r + 1) - j \sigma/\omega\epsilon_0| h_r a} \cdot$$

$$[h_r a \sinh(2 h_j z_1) + h_j a \sin(2 h_r z_1)], \qquad (3.42)$$

$$\frac{P_{dr}}{P_{dz}} \cong \frac{[h_r a \sinh(2 h_j z_1) - h_j a \sin(2 h_r z_1)]}{[h_r a \sinh(2 h_j z_1) + h_j a \sin(2 h_r z_1)]}, \quad \text{and} \quad (3.43)$$

$$\frac{P_{d\theta}}{P_{dz}} \cong \tan^2\psi. \qquad (3.44)$$

In the course of carrying out the calculations to obtain equations 3.40 – 3.44, it was necessary to use the relation

$$h_r a \, h_j a \cong - \frac{1}{4} \frac{\sigma}{\omega\epsilon_0} (ka \cot an\psi)^2,$$

which was obtained by squaring equation 3.38 and then equating the imaginary parts. Equations 3.43 and 3.44 were derived by simply taking the appropriate ratios of equations 3.40 –3.42. Note that $h_r a = Re[ha]$ and $h_j a = Im[ha]$. ha is the (single) wave number which determines the approximate large argument radial and axial spatial dependences of the field components associated with the two region sheath helix surrounding a lossy coaxial rod configuration. To justify the large argument Bessel function approximations used to derive equations 3.40 – 3.44 from the exact/power dissipation equations, it is necessary that the requirements listed in equations 3.39 are satisfied.

Equation 3.38 makes it clear that $h_r a > 0$ and $h_j a < 0$. Employing the basic trigonometric function and hyperbolic function relations

$$\sin(-x) = -\sin x \quad \text{and} \quad \sinh(-x) = -\sinh x,$$

it is seen that equations 3.40 - 3.42 are in fact positive real in value, as they must be.

Equations 3.40 - 3.44 are the approximate large argument power dissipation equations for the two region sheath helix surrounding a lossy coaxial rod configuration, when "the lossy rod is not a good conductor." The values $h_r a$ and $h_j a$ which appear are approximately evaluated from equation 3.38.

It is possible to derive equation 3.44 without performing a detailed calculation of $P_{d\theta}$ and P_{dz}. From equation 1.6, the relation between the angular and axial electric fields in the rod-filled region at the sheath surface is

$$E_{z1}\Big|_{r=a} = -E_{\theta 1}\Big|_{r=a} \cot an\psi.$$

The radial dependence of $E_{\theta 1}$ and E_{z1} is specified by $I_0(h_1 r)$ and $I_1(h_1 r)$, respectively. When r is sufficiently large so that $|h_1| r > 1$, the zero order form of the large argument Bessel function representations, equations A.36 and A.37, are approximately valid, and they show that

$$I_0(h_1 r) \cong I_1(h_1 r) \cong \frac{e^{+h_1 r}}{\sqrt{2\pi h_1 r}}.$$

Therefore, $E_{z1} \cong -E_{\theta 1} \cdot \cot an\psi$ is valid for radial distances sufficiently close to the sheath helix surface so that $|h_1| r > 1$ is satisfied. Furthermore, the large argument Bessel function representations make it clear that $|E_{\theta 1}|$ and $|E_{z1}|$ are large near the sheath surface, but they rapidly decay as the radial distance decreases. Examination of equations 3.7 and 3.8, using the previously mentioned

relationship between $E_{\theta 1}$ and E_{z1}, shows that equation 3.44 is immediately obtained. In short, this equation is seen to be a natural consequence of the boundary conditions at the sheath helix surface and the large argument behavior of the Bessel functions.

Attention is now directed to determining how much of a contribution each of the three region 1 electric fields makes towards the total power dissipation. As was previously mentioned in equations 3.39, it is required that the sheath helix is sufficiently tightly wound so that $cotan^2 \psi \gg 1$. Therefore, it is obvious from equation 3.44 that $P_{dz} \gg P_{d\theta}$. *The contribution to the total power dissipation occurring within the lossy coaxial rod element is much greater for the region 1 axial electric field than it is for the region 1 angular electric field, which are associated with the two region large argument case, when "the lossy rod is not a good conductor".*

The relative contributions to the total power dissipation associated with E_{r1} and E_{z1} can be obtained by examining equation 3.43. From equation 3.38, keeping in mind that $\epsilon_r > 1$ and $ka \, cotan \psi > 1$, it is clear that $h_r a > 1$ is true. However, depending on the electrical properties of the lossy rod material, it is possible that $|h_j| a \cdot 2 z_1/a = -2 h_j z_1$ is either less than or greater than unity. This means that it is necessary to consider both the large argument representation $sinhx \simeq e^{+x}/2$, which is approximately valid for $x > 1$, and the small argument representation $sinhx \simeq x$, which is approximately valid for $x < 1$, in equation 3.43. These both show that $P_{dr} \simeq P_{dz}$. *The contribution to the total power dissipation occurring within the lossy coaxial rod element is approximately the same for the region 1 radial and axial electric fields, which are associated with the two region configuration large argument case, when "the lossy rod is not a good conductor".*

Information concerning how the total power dissipation is distributed within the lossy coaxial rod element volume can be obtained by examining the spatial dependence of the radial and axial region 1 electric fields. It was mentioned earlier in sub-part 3.2.2.1 in connection with the discussion of equation 3.44 that the region 1 electric field magnitudes are rapidly attenuated at decreasing radial distances away from the sheath helix surface. Figure 2.12 displays the radial dependence of the electric field

components associated with the large argument case of the two region configuration. when "the lossy rod is not a good conductor". This figure provides a good illustration of how rapidly the field magnitudes become reduced at radial distances away from the sheath helix surface. *This has the important meaning that the total power dissipation for the two region, large argument case when "the lossy rod is not a good conductor" is concentrated near the lossy rod surface, and it is very small near $r = 0$.*

3.2.2.2 Three Region Configuration

The large argument approximations of the exact power dissipation equations will be obtained for the case when "the lossy rod is not a good conductor" and for the geometry where $b < a$. It will be assumed that the restrictions on the wave numbers listed in equations 2.111 and 2.112 are satisfied so that equations 2.116 are the approximate wave numbers solution. For convenience, equations 2.111, 2.112, and 2.116 are repeated here. It is assumed that

$$|h_1|b > 1, \quad |h_2|b > 1, \quad \text{and} \quad h_{2_r}a \cdot (1 - b/a) > 1,$$

or, equivalently, that $\qquad\qquad$ (3.45)

$$ka \cotan\psi \cdot b/a > 1, \quad ka \cotan\psi \cdot (1 - b/a) > 1,$$

and if $\epsilon_r \cong \cotan^2\psi$, then $\sqrt{\sigma/\omega\epsilon_0} \, ka \cdot b/a > 1.$

It was previously shown in sub-part 2.3.1.2 that equations 3.45 lead to the following approximate wave numbers solution.

$$h_{2_r}a \cong \beta_r a \cong ka \cotan\psi,$$

$$|h_{2_j}|a \cong |\beta_j|a << ka \cotan\psi, \quad \text{and} \qquad (3.46)$$

$$h_1 a \cong ka \sqrt{(\cotan^2 \psi - \epsilon_r) + j \, \sigma/\omega\epsilon_0} .$$

$$\begin{array}{r} (3.46) \\ (\text{continued}) \end{array}$$

Substituting just the first term of the large argument Bessel function representations, equations A.36 – A.39, into the exact power dissipation equations, equations 3.12, 3.14, and 3.16, making use of the approximate wave numbers solution, equations 3.46, equations 3.47 – 3.49 are obtained.

$$P_{dr} \cong \frac{|I|^2}{4} \, \pi \, a^3 \, \sigma \, (120\pi)^2 \, \cdot$$

$$\frac{ka \cotan\psi \, \cos^2\psi \, e^{-2 \, ka \, \cotan\psi \, (1-b/a)}}{h_{1r} a \, \beta_j a \, |h_1 a + (\epsilon_r - j \, \sigma/\omega\epsilon_0) \, ka \, \cotan\psi|^2} \, \cdot \qquad (3.47)$$

$$[ka \cotan\psi \, \sinh(2 \, \beta_j \, z_1) - \beta_j a \, \sin(ka \, \cotan\psi \cdot 2 \, z_1/a)],$$

$$P_{d\theta} \cong \frac{|I|^2}{4} \, \pi \, a^3 \, \sigma \, (120\pi)^2 \, \cdot$$

$$\frac{ka \cotan\psi \, \sin^2\psi \, e^{-2 \, ka \, \cotan\psi \, (1-b/a)}}{h_{1r} a \, \beta_j a \, |h_1 a + ka \, \cotan\psi|^2} \, \cdot \qquad (3.48)$$

$$[ka \cotan\psi \, \sinh(2 \, \beta_j \, z_1) + \beta_j a \, \sin(ka \, \cotan\psi \cdot 2 \, z_1/a)],$$

and

$$P_{dz} \cong \frac{|I|^2}{4} \, \pi \, a^3 \, \sigma \, (120\pi)^2 \, \cdot \qquad (3.49)$$

$$\frac{|h_1 a|^2 \cos^2\psi \, e^{-2 \, ka \, cotan\psi \, (1-b/a)}}{ka \, cotan\psi \, h_{1r} a \, \beta_j a \, |h_1 a + (\epsilon_r - j \, \sigma/\omega\epsilon_0) \, ka \, cotan\psi|^2} \cdot$$

$$[ka \, cotan\psi \, \sinh(2 \, \beta_j \, z_1) + \beta_j \, a \, \sin(ka \, cotan\psi \cdot 2 \, z_1/a)].$$

To support the correctness of equations 3.47 − 3.49, the first term of equations A.36 − A.39 was used to approximate equations 3.2 − 3.4, the region 1 electric field components. Equations 3.6 − 3.8 were then used to calculate the power dissipations. Exactly the same results as equations 3.47 − 3.49 were obtained. As a summary, using the exact electric field components, integrating these to obtain the power dissipations, and then applying the large argument Bessel function representations, gives the same result as when the large argument Bessel function representations were used to approximate the electric fields, and then the integration was performed to obtain the power dissipation equations. This result is expected. It provides a check on the accuracy of equations 3.47 − 3.49.

Two assumptions can be made which significantly simplify equations 3.47 − 3.49. First, it will be assumed that the lossy coaxial rod element length is sufficiently large so that $2 \, z_1/a \geq 10$. It was previously mentioned in sub-part 2.3.1.2 that $|\beta_j| a$ rapidly becomes smaller as the value of $ka \, cotan\psi$ increases. The second assumption which will be made is that for the particular lossy coaxial rod element length of concern, the value of $ka \, cotan\psi$ is sufficiently large so that $|\beta_j| a$. $2 \, z_1/a << 1$. Keeping in mind the fact that equations 3.45 show that $ka \, cotan\psi > 1$, these two assumptions mean that

$$\frac{1}{\beta_j a} \cdot [ka \, cotan\psi \, \sinh(2 \, \beta_j \, z_1) \pm \beta_j a \, \sin(ka \, cotan\psi \cdot 2 \, z_1/a)]$$

$$\cong ka \, cotan\psi \cdot 2 \, z_1/a \pm \sin(ka \, cotan\psi \cdot 2 \, z_1/a)$$

$$\cong ka \, cotan\psi \cdot 2 \, z_1/a.$$

Equations 3.47 - 3.49 now become the following.

$$P_{dr} \approx \frac{|\partial_{||}|^2}{4} \pi a^3 \sigma (120\pi)^2 \, 2 \, z_1/a \cdot$$

$$\frac{(ka \, \cotan\psi)^2 \, \cos^2\psi \, e^{-2 \, ka \, \cotan\psi \, (1-b/a)}}{h_{1r}a \, |h_1 a + (\epsilon_r - j \, \sigma/\omega\epsilon_0) \, ka \, \cotan\psi|^2} , \qquad (3.50)$$

$$P_{d\theta} \approx \frac{|\partial_{||}|^2}{4} \pi a^3 \sigma (120\pi)^2 \, 2 \, z_1/a \cdot$$

$$\frac{(ka \, \cotan\psi)^2 \, \sin^2\psi \, e^{-2 \, ka \, \cotan\psi \, (1-b/a)}}{h_{1r}a \, |h_1 a + ka \, \cotan\psi|^2} , \qquad (3.51)$$

$$P_{dz} \approx \frac{|\partial_{||}|^2}{4} \pi a^3 \sigma (120\pi)^2 \, 2 \, z_1/a \cdot$$

$$\frac{|h_1 a|^2 \, \cos^2\psi \, e^{-2 \, ka \, \cotan\psi \, (1-b/a)}}{h_{1r}a \, |h_1 a + (\epsilon_r - j \, \sigma/\omega\epsilon_0) \, ka \, \cotan\psi|^2} , \qquad (3.52)$$

$$\frac{P_{dr}}{P_{dz}} \approx \frac{(ka \, \cotan\psi)^2}{|h_1 a|^2} , \quad \text{and} \qquad (3.53)$$

$$\frac{P_{d\theta}}{P_{dz}} \approx \frac{(ka \, \cotan\psi)^2}{|h_1 a|^2} \, \tan^2\psi \cdot$$

$$\frac{|h_1 a + (\epsilon_r - j \, \sigma/\omega\epsilon_0) \, ka \, \cotan\psi|^2}{|h_1 a + ka \, \cotan\psi|^2} \cdot \qquad (3.54)$$

Equations 3.53 and 3.54 were obtained by simply taking the appropriate ratios of equations 3.50 - 3.52.

For convenience, the assumptions which were used in obtaining equations 3.50 - 3.54 from the exact power dissipation equations, equations 3.12, 3.14, and 3.16, will be gathered together and listed in one location.

$$2 \ z_1/a \geq 10, \quad |\beta_j| a \cdot 2 \ z_1/a << 1, \quad ka \ \cot\psi \cdot b/a > 1,$$

$$ka \ \cot\psi \cdot (1-b/a) > 1, \quad \text{and if } \epsilon_r \cong \cot^2\psi, \qquad (3.55)$$

$$\text{then } \sqrt{\sigma/\omega\epsilon_0} \ ka \cdot b/a > 1.$$

When the restrictions listed in equations 3.55 are satisfied, the radial wave number $h_1 a$, which appears in equations 3.50 - 3.54, is approximately evaluated from equations 3.46. *Equations 3.50 - 3.54 are the approximate large argument power dissipation equations associated with the three region sheath helix surrounding a lossy coaxial rod configuration, when "the lossy rod is not a good conductor".*

The restrictions on ϵ_r and $\sigma/\omega\epsilon_0$ listed in equations 3.55 define what is meant by the term "the lossy rod is not a good conductor" as it is used in sub-part 3.2.2.2. Note that both $\epsilon_r >> \sigma/\omega\epsilon_0$ and $\sigma/\omega\epsilon_0 >> \epsilon_r$ can occur.

It is obvious from equations $3.50 - 3.52$ that increasing the value of $ka \ \cot\psi$ or decreasing the value of b/a means that the power dissipation occurring within the lossy coaxial rod element rapidly becomes small. From physical considerations, this behavior is expected. Substituting equations A.36 - A.39, the large argument Bessel function representations, into equations 2.76 - 2.78, the region 2 $(b \leq r \leq a)$ electric field components, making use of the relation $h_{2r} a \cong ka \ \cot\psi$ from equations 3.46, the radial dependence of the field components is seen to be dominated by the exponential $e^{-ka \ \cot\psi \ (1-r/a)}$. Furthermore, the boundary conditions given by equations 2.43 and 2.44 state that the radial and angular electric fields are continuous through the lossy rod surface. Evaluating equations

2.76 and 3.2, the region 2 and region 1 radial electric field components, respectively, at the lossy rod surface shows that they are discontinuous according to

$$E_{r1}\Big|_{r=b} \cdot (\epsilon_r - j\ \sigma/\omega\epsilon_0) = E_{r2}\Big|_{r=b}$$

$$\text{Clearly,}\quad \Big|E_{r1}\Big|_{r=b}\Big| < \Big|E_{r2}\Big|_{r=b}\Big|.$$

Finally, using equations A.36 - A.39 to approximate equations 3.2 - 3.4, it is seen that the magnitudes of the region 1 electric field components have a radial dependence which is dominated by $e^{-h_{1r}b(1-r/b)}$. (Note that from equations 3.45 and 3.46, it is approximately true that $h_{1r}b > 1$.) These field components exponentially decrease in magnitude as the radial distance becomes smaller. Figures 2.8 and 2.10 provide an illustration of the radial dependence associated with the region 1 and region 2 electric fields, and of their behavior at the interface $r = b$, for the three region configuration large argument case when "the lossy rod is not a good conductor".

Increasing the value of $ka\ \cot\psi$ means that the region 2 field components become more tightly held near the sheath surface. They become very small in magnitude throughout the air gap, region 2, and this is especially true near $r = b$. Keeping in mind the previously mentioned nature of the electric fields at this interface and the type of radial dependence of the region 1 fields, it is obvious that increasing the variable $ka\ \cot\psi$ will greatly reduce the electric field magnitudes throughout the rod-filled region, $0 \leq r \leq b$. In addition, reducing the variable b/a means that the lossy rod surface is moved further away from the sheath helix surface. Therefore, the electric field magnitudes in the rod-filled region will become much smaller. This provides the explanation as to why increasing the value of $ka\ \cot\psi$ or reducing the value of b/a has a great effect on making the power dissipation smaller. (Note that for the large argument two region case discussed in sub-part 3.2.2.1, the power dissipation expressions, equations 3.40 - 3.42, do not exponentially decrease when the variable

ka cotanψ increases. This is because of the fact that since the lossy rod is *touching* the sheath helix surface, the electric field magnitudes at the rod surface are always relatively large, even when the value of ka cotanψ is large. No air gap exists between the sheath helix surface and the lossy rod surface in which the electric field magnitudes are rapidly exponentially attenuated.)

The manner in which the total power dissipation is distributed throughout the lossy coaxial rod element volume is known from the previous discussion. It was mentioned that the electric field magnitudes within the rod-filled region exponentially decrease as the radial distance decreaes. Therefore, *the total power dissipation associated with the large argument case of the three region sheath helix surrounding a lossy coaxial rod configuration, when "the lossy rod is not a good conductor" is concentrated near the surface of the rod.* A more detailed discussion of the power dissipation resulting from the region 1 axial electric field for the special case when the electrical properties of the lossy rod are such that $\epsilon_r >> \sigma/\omega\epsilon_0$ is given later in part 3.4.3.

Attention is now directed towards determining how much of a contribution each of the three region 1 electric field components makes towards the total power dissipation occurring within the lossy coaxial rod element. This is achieved by examining equations 3.53 and 3.54. Making use of the approximation for $h_1 a$ given in equations 3.46, it is convenient to express equation 3.53 as

$$\frac{P_{dr}}{P_{dz}} \simeq \frac{\cotan^2\psi}{|(\cotan^2\psi - \epsilon_r) + j \, \sigma/\omega\epsilon_0|}. \tag{3.56}$$

Two natural divisions of equation 3.56 are when the lossy rod material electrical properties are such that $\sigma/\omega\epsilon_0 >> \epsilon_r$, or when $\epsilon_r >> \sigma/\omega\epsilon_0$. For the first mentioned case it is clear that $P_{dr}/P_{dz} < 1$.

A. $\sigma/\omega\epsilon_0 >> \epsilon_r$

This means that $P_{dr}/P_{dz} < 1$.

For the second mentioned case, it is best to consider three special situations.

B. $\epsilon_r >> \sigma/\omega\epsilon_0$

(a) If $\epsilon_r >> \cotan^2\psi$,   then $P_{dr}/P_{dz} << 1$.

(b) If $\cotan^2\psi >> \epsilon_r$,   it follows that $P_{dr}/P_{dz} \approx 1$.

(c) If $\epsilon_r \approx \cotan^2\psi$,   then $\sqrt{\sigma/\omega\epsilon_0}\ ka \cdot b/a > 1$ is required, in order that the requirements listed in equations 3.45 are satisfied, and it is true that $P_{dr}/P_{dz} > 1$.

Equation 3.54 shows that the ratio $P_{d\theta}/P_{dz}$ is more complicated than the ratio P_{dr}/P_{dz}. The first mentioned ratio compares the contribution to the total power dissipation occurring within the lossy coaxial rod element due to the angular region 1 electric field component, to that due to the axial region 1 electric field component. The contribution associated with the angular electric field can be regarded as ohmic heating resulting from a circumferential eddy current. Brown et al. (3, pp. 27) investigated the ohmic heating occurring within a conducting rod centered within a physical helix by assuming that only this circumferential eddy current was important. However, it will be seen later in sections 3.4 and 3.5 that, although when the lossy rod material electrical properties are characterized by $\sigma/\omega\epsilon_0 >> \epsilon_r$, the power dissipation contribution associated with $E_{\theta 1}$ usually dominates over that associated with E_{z1}, when $\epsilon_r >> \sigma/\omega\epsilon_0$ occurs, it is true that the power dissipation contribution associated with E_{z1} usually dominates over that associated with $E_{\theta 1}$. In this case, the previously mentioned discussion given by Brown et al. has to be considered as incomplete and misleading.

The ratio $P_{d\theta}/P_{dz}$ is important because it shows whether the major portion of the ohmic heating results from circumferential eddy currents or axial currents. This ratio is a complicated expression and a lengthy investigation of it has been carried out. A discussion and graphs of this quantity are given in parts 3.2.3 and 3.2.4.

3.2.3 Graphs of $P_{d\theta}/P_{dz}$

The purpose of this section is to achieve a better understanding of when the axial region 1 electric field component does or does not dominate over the angular region 1 electric field, with respect to its contribution toward the total power dissipation occurring within the lossy coaxial rod element. This will be done by plotting a series of graphs. Both the large argument and the small argument approximations of this ratio are shown on each graph. Equations 3.34 and 3.54 are used as the small and large argument approximations, respectively, of the ratio $P_{d\theta}/P_{dz}$. For convenience, these two equations will be repeated here. The small argument approximation of the ratio is

$$\frac{P_{d\theta}}{P_{dz}} \cong \frac{1}{2}(b/a)^2 \tan^2\psi, \qquad (3.57)$$

and the large argument approximation is

$$\frac{P_{d\theta}}{P_{dz}} \cong \frac{1}{|(\cotan^2\psi - \epsilon_r) + j\,\sigma/\omega\epsilon_0|} \cdot \qquad (3.58)$$

$$\frac{|\sqrt{(\cotan^2\psi - \epsilon_r) + j\,\sigma/\omega\epsilon_0} + (\epsilon_r - j\,\sigma/\omega\epsilon_0)\cotan\psi|^2}{|\sqrt{(\cotan^2\psi - \epsilon_r) + j\,\sigma/\omega\epsilon_0} + \cotan\psi|^2}.$$

Note that the solution for $h_1 a$ from equations 3.46 was substituted into equation 3.54, in order to obtain equation 3.58. It was previously mentioned in part 3.2.1 and in sub-part 3.2.2.2 that the requirements listed in equations 3.35, 3.36, and 3.55 must be met in order to justify the usage of equations 3.57 and 3.58. In all of the following graphs, it was ensured that these requirements are satisfied. (Actually, the region 1 angular and axial electric fields, equations 3.3 and 3.4, have the same type of axial dependence. This means that when the ratio $P_{d\theta}/P_{dz}$ is calculated, the quantity $2\,z_1/a$ does not appear. Therefore, the restrictions $2\,z_1/a > 10$ and $|\beta_j| a \cdot 2\,z_1/a << 1$, which are mentioned in equations 3.55, do not, in fact, have

to be satisfied.) A gap is left in the graphs where neither the small or large argument approximations of the ratio can be used.

Figures 3.2 are graphs of $P_{d\theta}/P_{dz}$ versus ka. b/a = 0.100, 0.900; ε_r = 10.0; $\sigma/\omega\varepsilon_0$ = 10.0, 1.00×10^3; ψ = 5.00°; and $1.00 \times 10^{-4} \leq$ ka < 10.0 are used. For the two curves associated with $\sigma/\omega\varepsilon_0$ = 1.00×10^3, it is seen that as ka increases, a crossover occurs from when the contribution to the total power dissipation resulting from E_{z1} dominates over that resulting from $E_{\theta1}$, to when exactly the opposite is true.

Figures 3.3 show $P_{d\theta}/P_{dz}$ versus ka for b/a = 0.900; ε_r = 10.0; $\sigma/\omega\varepsilon_0$ = 10.0, 1.00×10^3; ψ = 1.00°, 5.00°, 10.0°; and $1.00 \times 10^{-4} \leq$ ka < 10.0. The four curves, which are described by $\sigma/\omega\varepsilon_0$ = 1.00×10^3 and by $\sigma/\omega\varepsilon_0$ = 10.0, ψ = 10.0°, each have the property that, for a sufficiently large value of ka, the power dissipation contribution associated with $E_{\theta1}$ dominates over that associated with E_{z1}.

The final graphs of $P_{d\theta}/P_{dz}$ versus ka are given in Figures 3.4. b/a = 0.900; ε_r = 2.00, 1.00×10^3; $\sigma/\omega\varepsilon_0$ = 1.00×10^{-2}, 1.00×10^3; ψ = 10.0°; and $1.00 \times 10^{-4} \leq$ ka < 1.00×10^2 are used. Each of the three curves, which are associated with $\sigma/\omega\varepsilon_0$ = 1.00×10^3 and with ε_r = 1.00×10^3, $\sigma/\omega\varepsilon_0$ = 1.00×10^{-2}, show that for a sufficiently large value of ka, $E_{\theta1}$ will provide a greater contribution to the total power dissipation than E_{z1}.

Another set of graphs of the ratio $P_{d\theta}/P_{dz}$ have been prepared. These are based on the same equations that were used in Figures 3.2 - 3.4. However, the lossy coaxial rod element is now assumed to be a specific material which might be a candidate electromagnetic heating (25). Douglas Beech wood, steak meat, muscle tissue, and oil sand, are considered. For these materials, the values of ε_r and $\sigma/\omega\varepsilon_0$ depend on frequency. The electrical properties were taken from references 45, pp. 268 - 271; and 46, Figure 2. Data tables have been prepared which show the electrical properties of the materials over a wide frequency range. In order that the continuity of part 3.2.3 is not interrupted, these tables have been put in Appendix E.
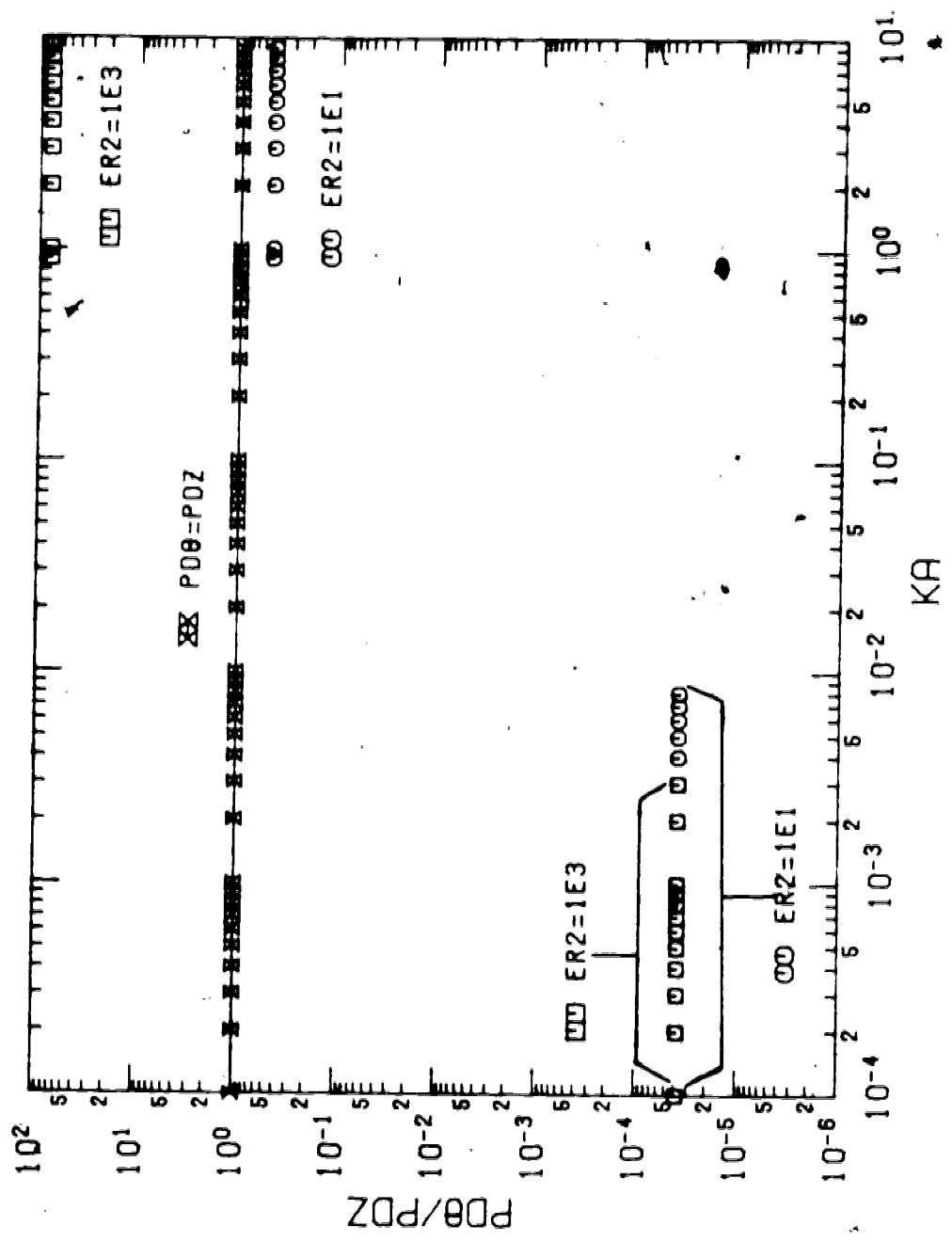
Figure 3.2a   Graph of $P_{d\theta}/P_{dz}$ versus ka, based on equations 3.57 and 3.58. Curves for b/a=0.100; ε_r=10.0; $\sigma/\omega\varepsilon_0$=10.0, 1.00x10^3; ψ=5.00°; and 1.00x10^{-4}≤ka<10.0 are shown. (Note PDθ=$P_{d\theta}$, PDZ= P_{dz}, KA=ka, and ER2= $\sigma/\omega\varepsilon_0$. ER2=1E1 means the curve represents $\sigma/\omega\varepsilon_0$=10.0.)
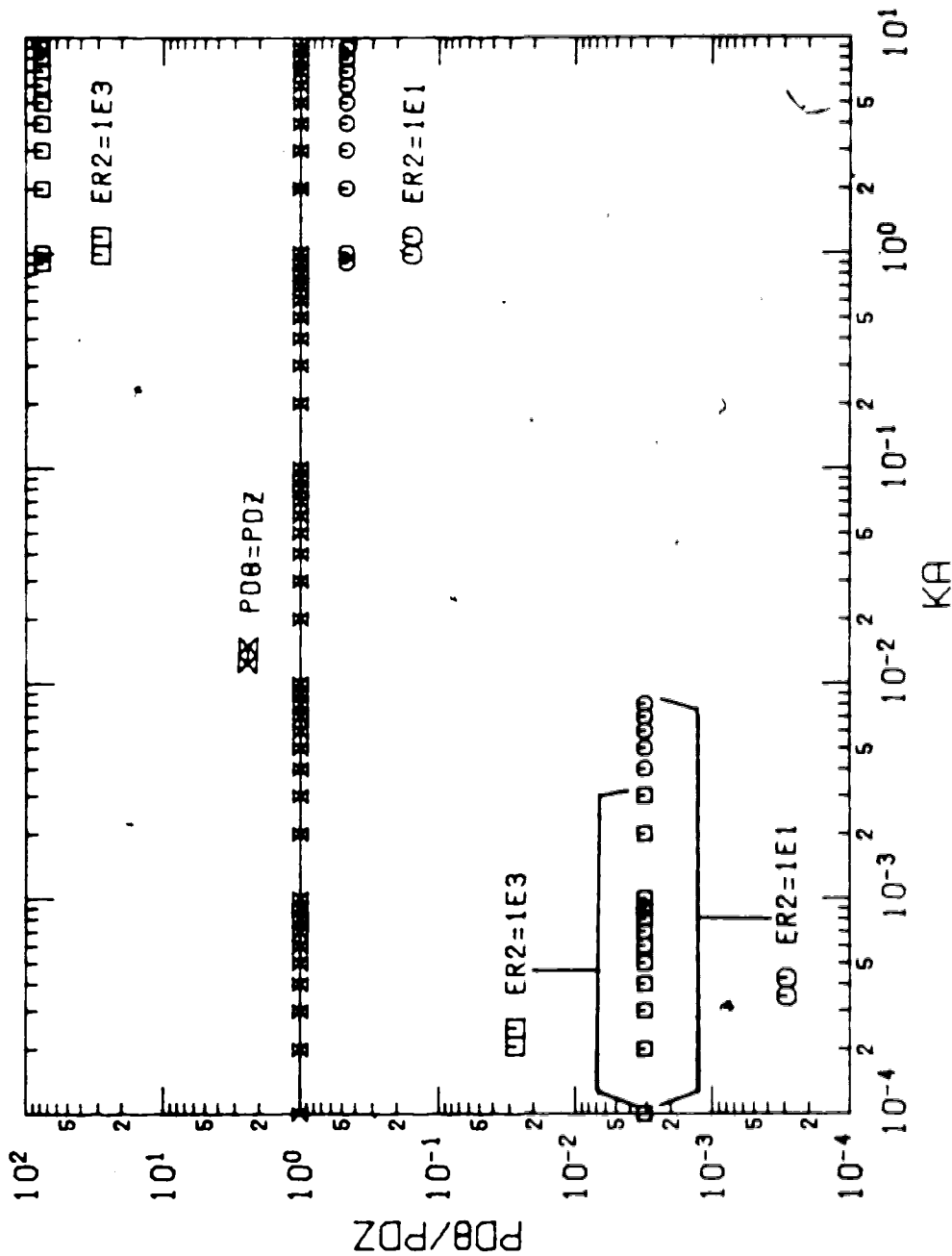
PDθ/PDZ VS. KA FOR VARIOUS ER2

Figure 3.2b   Graph of $P_{d\theta}/P_{dz}$ versus ka, based on equations 3.57 and 3.58. Curves for b/a=0.900; ϵ_r=10.0; $\sigma/\omega\epsilon_0$=10.0, 1.00x10^3; ψ=5.00°; and 1.00x10^{-4}<ka<10.0 are shown. (Note PDθ=$P_{d\theta}$, PDZ=P_{dz}, KA=ka, and ER2=$\sigma/\omega\epsilon_0$. ER2=1E3 means the curve represents $\sigma/\omega\epsilon_0$=1.00x10^3.)
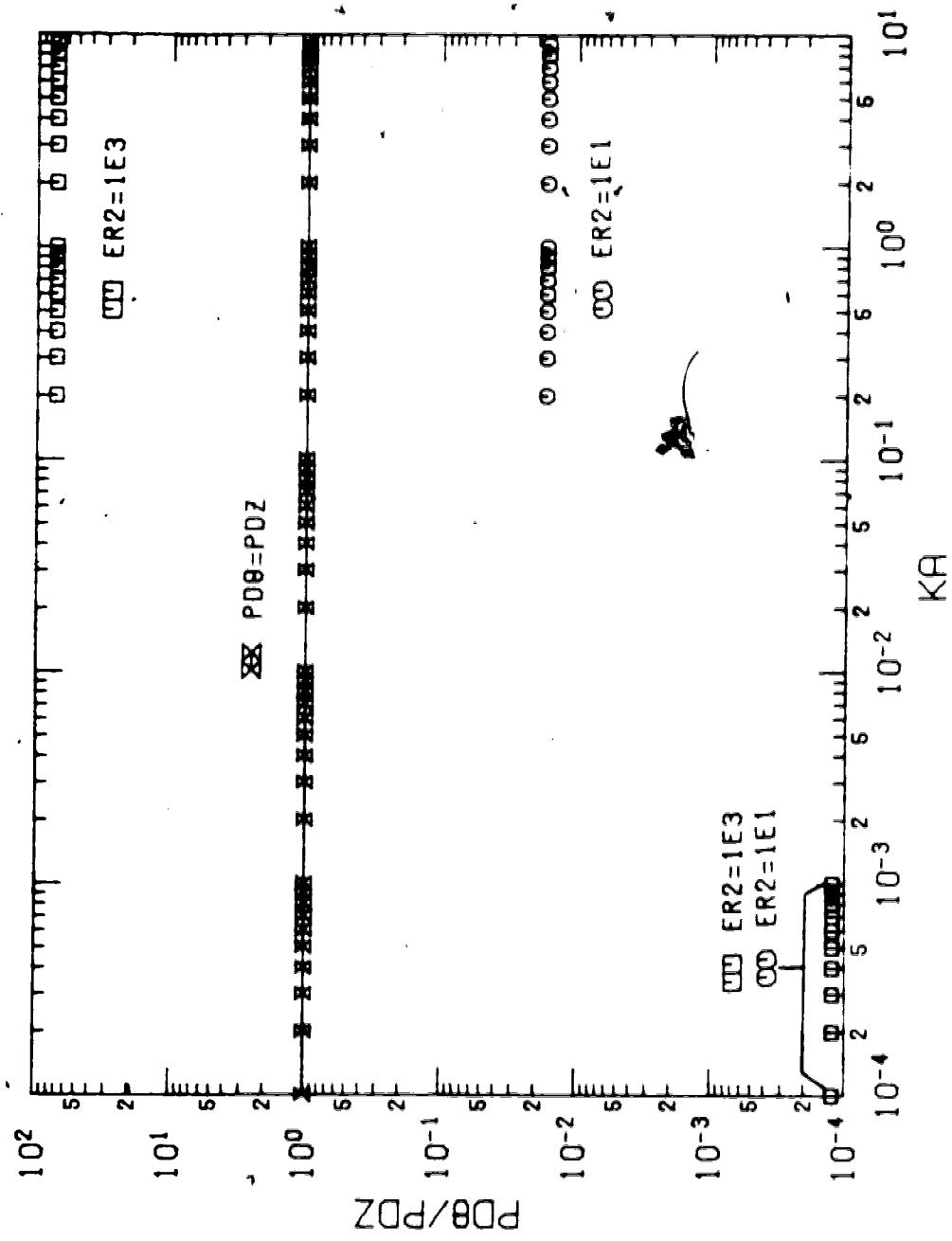
PDθ/PDZ VS. KA FOR VARIOUS ER2

Figure 3.3a   Graph of $P_{d\theta}/P_{dz}$ versus ka, based on equations 3.57 and 3.58. Curves for b/a=0.900; ϵ_r=10.0; $\sigma/\omega\epsilon_0$=10.0, 1.00x10^3; ψ=1.00°; and 1.00x10^{-4}≤ka<10.0 are shown. (Note PDθ=$P_{d\theta}$, PDZ= P_{dz}, KA=ka, and ER2=$\sigma/\omega\epsilon_0$. ER2=1E1 means the curve represents $\sigma/\omega\epsilon_0$=10.0.)
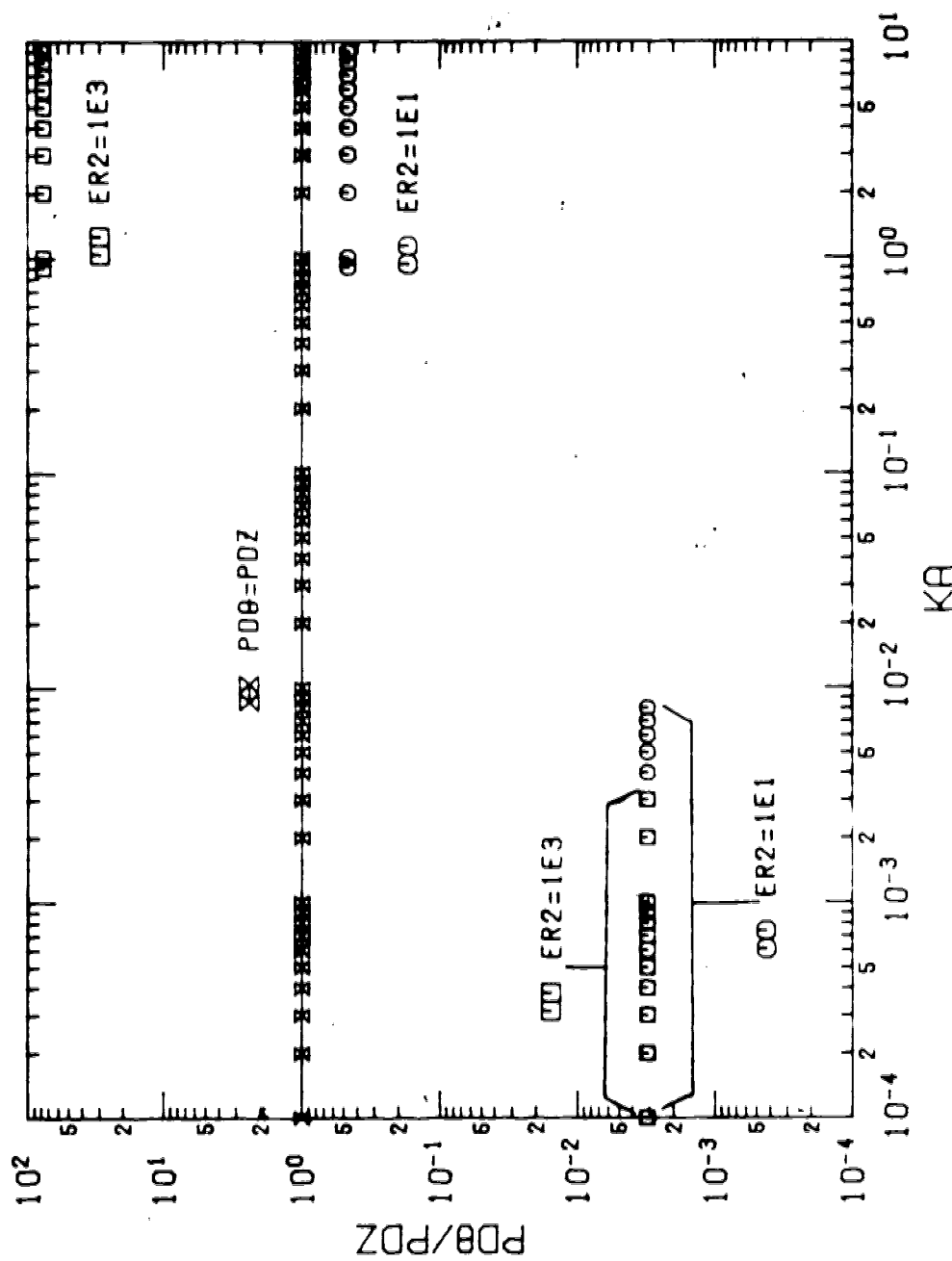
Figure 3.3b   Graph of $P_{d\theta}/P_{dz}$ versus ka, based on equations 3.57 and 3.58. Curves for b/a=0.900; ϵ_r=10.0; $\sigma/\omega\epsilon_0$=10.0, 1.00x10^3; ψ=5.00°; and 1.00x10^{-4}≤ka<10.0 are shown. (Note PDΘ=$P_{d\theta}$, PDZ=P_{dz}, KA=ka, and ER2=$\sigma/\omega\epsilon_0$. ER2=1E3 means the curve represents $\sigma/\omega\epsilon_0$=1.00x10^3.)
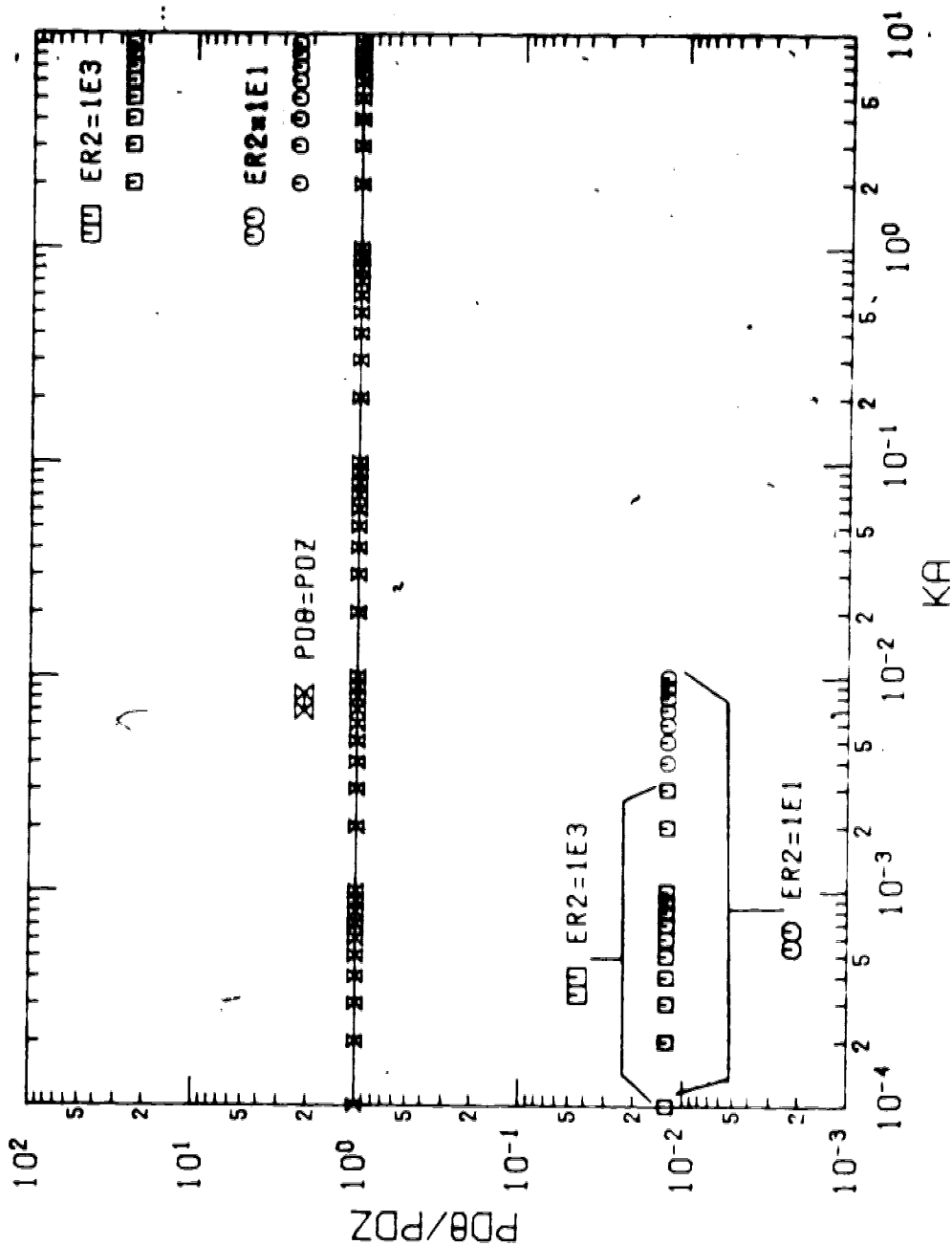
Figure 3.3c   Graph of $P_{d\theta}/P_{dz}$ versus ka, based on equations 3.57 and 3.58. Curves for b/a=0.900; ϵ_r=10.0; $\sigma/\omega\epsilon_0$=10.0, 1.00×10^3; ψ= 10.0°; and 1.00×10^{-4}<ka<10.0 are shown. (Note PDΘ=$P_{d\theta}$, PDZ= P_{dz}, KA=ka, and ER2=$\sigma/\omega\epsilon_0$. ER2=1E1 means the curve represents $\sigma/\omega\epsilon_0$=10.0.)
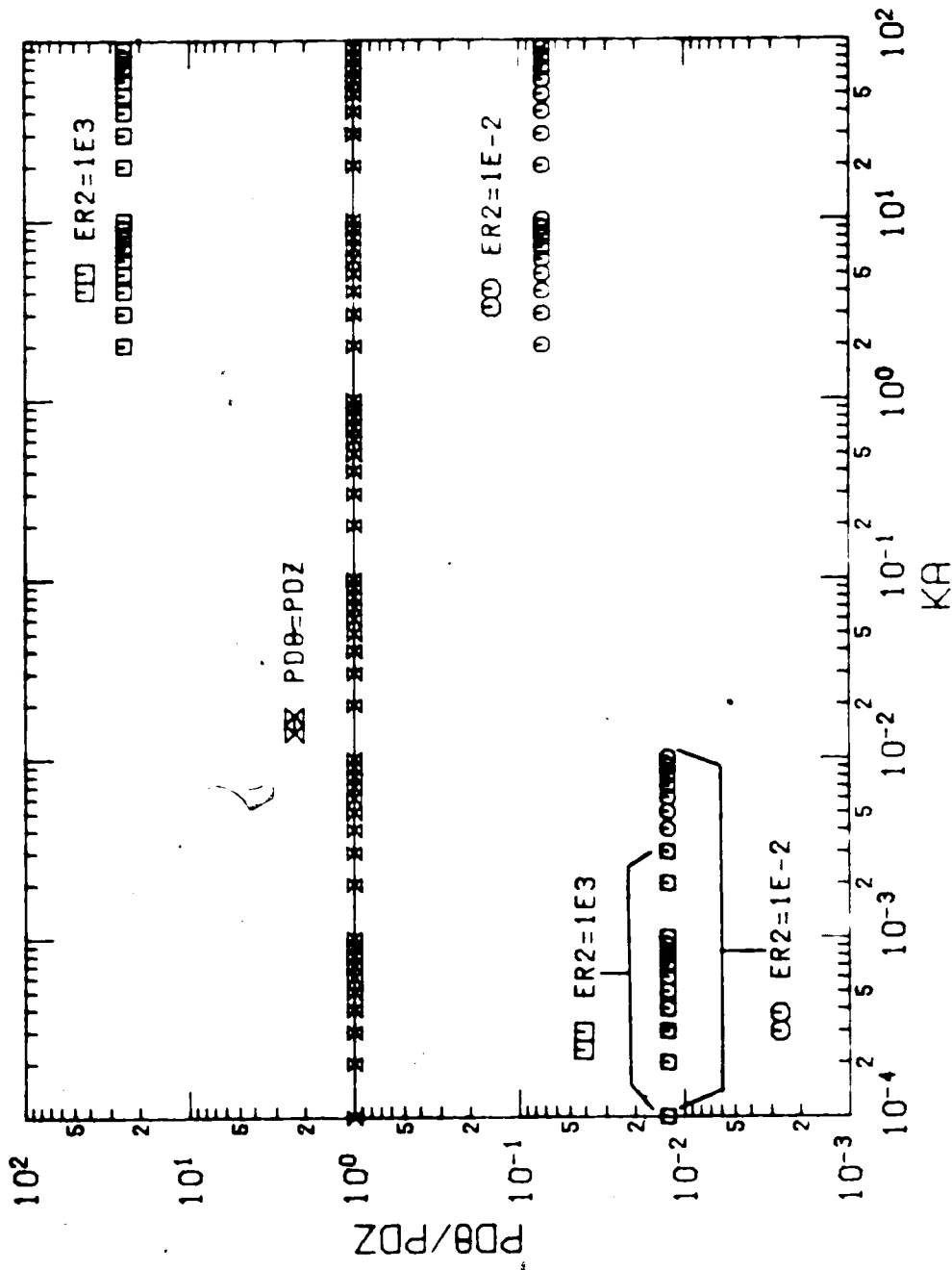
Figure 3.4a   Graph of $P_{d\theta}/P_{dz}$ versus ka, based on equations 3.57 and 3.58. Curves for b/a=0.900; ϵ_r=2.00; $\sigma/\omega\epsilon_0$=1.00x10^{-2}, 1.00x10^3; ψ=10.0°; and 1.00x10^{-4}≤ka<100.0 are given. (Note PDθ=$P_{d\theta}$, PDZ=P_{dz}, KA=ka, and ER2=$\sigma/\omega\epsilon_0$. ER2=1E3 means the curve represents $\sigma/\omega\epsilon_0$=1.00x10^3.)
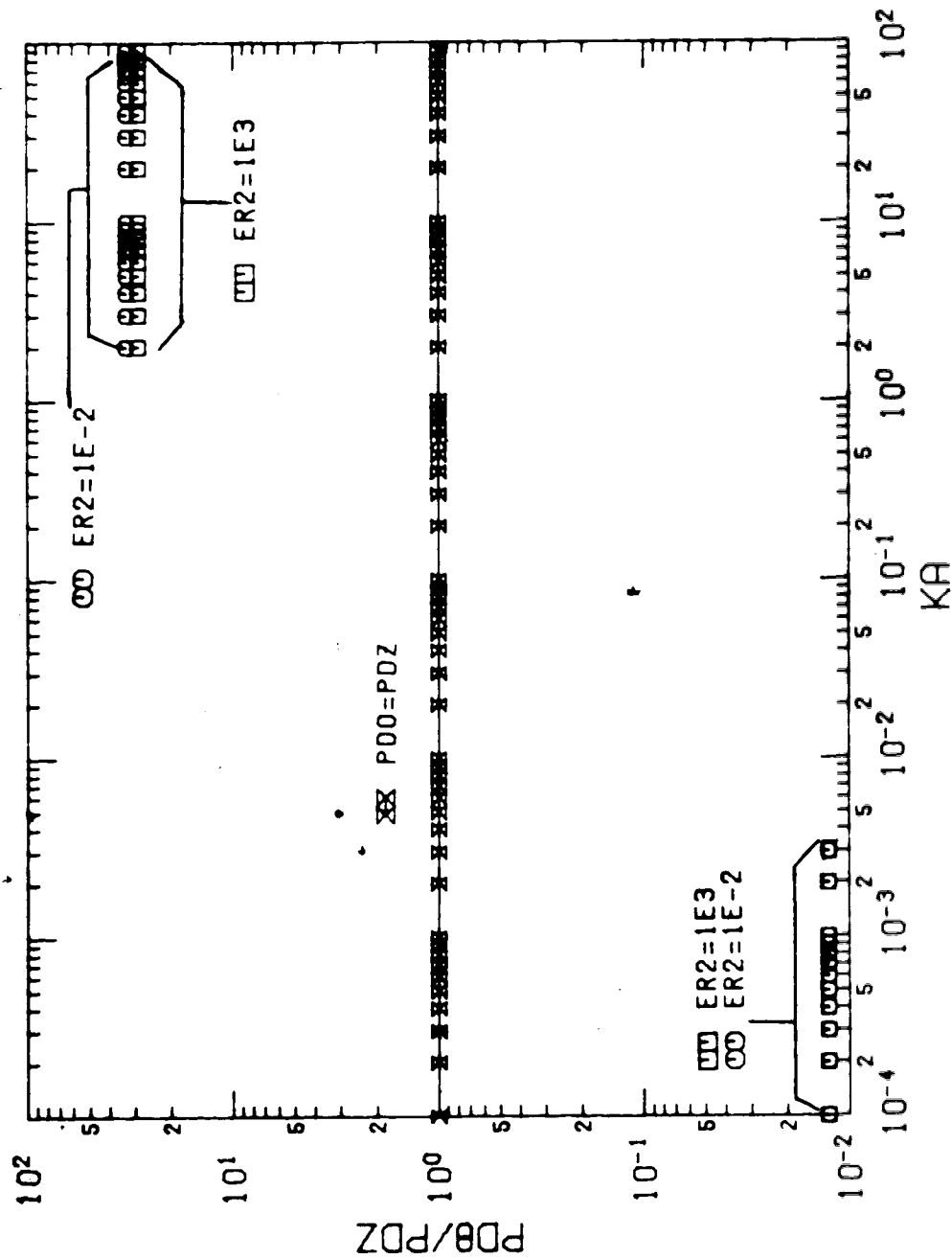
Figure 3.4b   Graph of $P_{d\theta}/P_{dz}$ versus ka, based on equations 3.57 and 3.58. Curves for b/a=0.900; ϵ_r=1.00x10^3; $\sigma/\omega\epsilon_0$=1.00x10^{-2}, 1.00x10^3; ψ= 10.0°; and 1.00x10^{-4}<ka<100.0 are given. (Note PDθ=$P_{d\theta}$, PDZ=P_{dz}, KA=ka, and ER2=$\sigma/\omega\epsilon_0$. ER2=1E-2 means the curve represents $\sigma/\omega\epsilon_0$=1.00x10^{-2}.)

Figures 3.5 are graphs of $P_{d\theta}/P_{dz}$ versus frequency for Douglas Beech wood. b/a = 0.100, 0.500, 0.900; ψ = 1.00°, 5.00°; and a = 0.100 (m) are used. Table E.1 lists the values of ϵ_r and $\sigma/\omega\epsilon_0$ as a function of frequency. The electrical properties of Douglas Beech are such that $\epsilon_r >> \sigma/\omega\epsilon_0$. For the sheath helix and lossy rod geometrical variables used in this figure, it is always true that E_{z1} provides a much larger contribution to the total power dissipation than $E_{\theta1}$.

Figures 3.6 plot $P_{d\theta}/P_{dz}$ versus frequency for a sample of steak meat. Table E.2 lists its electrical properties. The same values of b/a, a, and ψ used in Figures 3.5 are employed here. It is clear from the data table that this material is not characterized by either $\epsilon_r >> \sigma/\omega\epsilon_0$ or by $\sigma/\omega\epsilon_0 >> \epsilon_r$. The graphs show that when the pitch angle is ψ = 1.00°, for high frequencies E_{z1} makes a greater contribution to the total power dissipation than $E_{\theta1}$. However, when ψ = 5.00°, the reverse is usually true. Note that the relatively swift decrease in the ratio at high frequencies results from the fact that ϵ_r and $\sigma/\omega\epsilon_0$ are both rapidly decreasing with increasing frequency.

Figures 3.7 display $P_{d\theta}/P_{dz}$ versus frequency for a sample of muscle tissue. The electrical properties of this sample are listed in Table E.3, and the same values of b/a, a, and ψ as were used in the preceding two sets of figures are employed here. For these graphs, the only data available of the electrical properties corresponds to the large argument case of $P_{d\theta}/P_{dz}$. It is clear from the data table that $\epsilon_r >> \sigma/\omega\epsilon_0$. When ψ = 1.00°, it is seen that E_{z1} makes a larger contribution to the total power dissipation than $E_{\theta1}$. However, when ψ = 5.00°, exactly the opposite is true.

The final two figures included in part 3.2.3 are based on the sample of oil sand whose electrical properties are listed in Table E.4. Figure 3.8 uses b/a = 0.100, 0.500, 0.900; ψ = 1.00°; and a = 1.00 (m). It is apparent from the data table that $\sigma/\omega\epsilon_0 >> \epsilon_r$ is true over the frequency range for which the small argument form of $P_{d\theta}/P_{dz}$ is shown, while $\epsilon_r >> \sigma/\omega\epsilon_0$ occurs for $f \approx 1.00 \times 10^9$ (Hz). The oil sand sample exhibits a wide variety of electrical properties over the large frequency range which is considered. For most of the points shown on Figure 3.8, E_{z1} makes a larger contribution to the total power dissipation than $E_{\theta1}$.
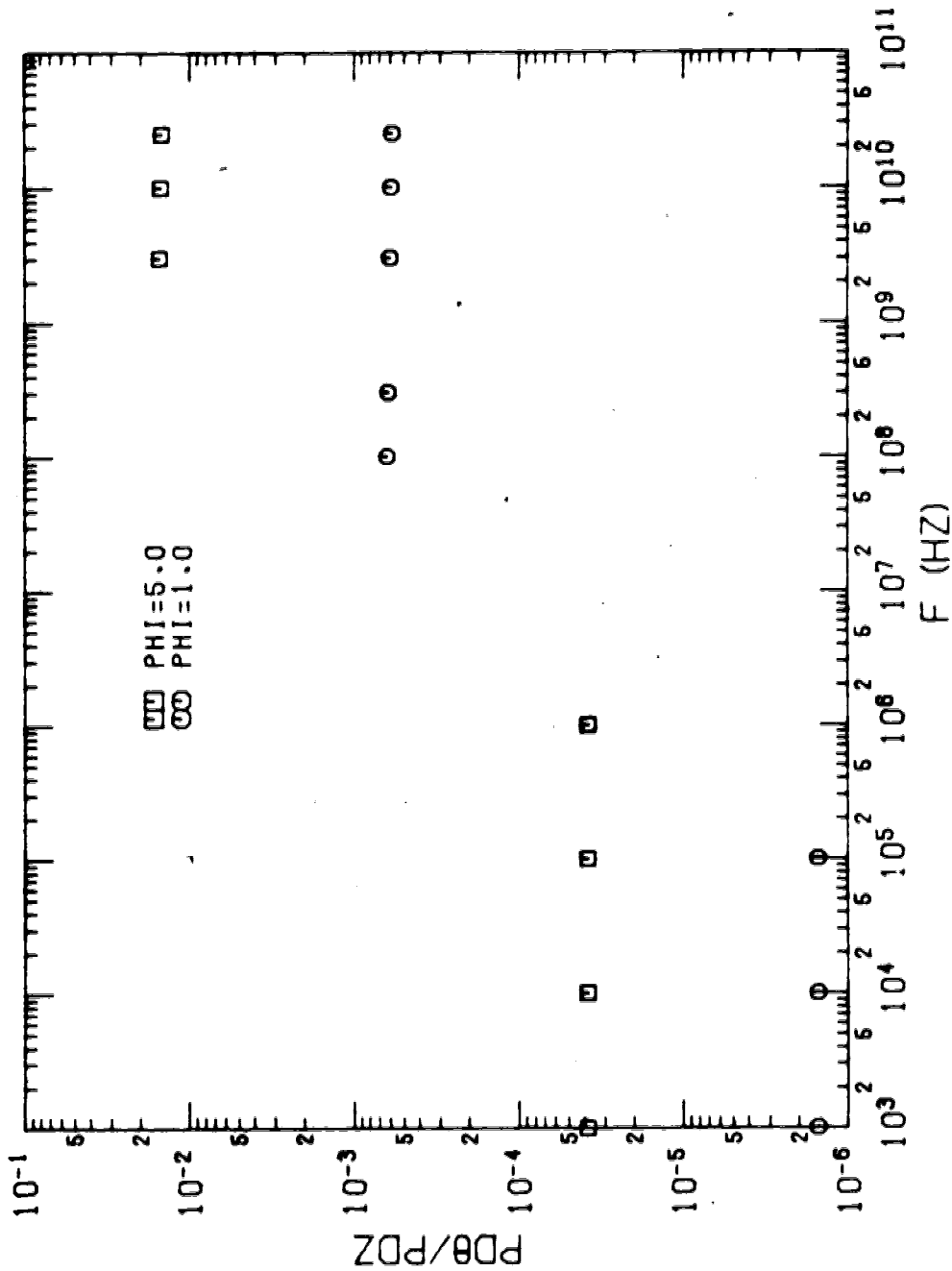
PDθ/PDZ VS. FREQUENCY FOR DOUGLAS BEECH

Figure 3.5a   Graph of $P_{d\theta}/P_{dz}$ versus frequency for Douglas Beech wood, based on equations 3.57 and 3.58. Table E.1 lists the electrical properties of this material. Curves for b/a=0.100; ψ=1.00°, 5.00°; a= 0.10 (m); and $1.00 \times 10^3 Hz \leq f < 1.00 \times 10^{11} Hz$ are shown. (Note PDθ=$P_{d\theta}$ and PDZ=P_{dz}.)

Figure 3.5b Graph of $P_{d\theta}/P_{dz}$ versus frequency for Douglas Beech wood, based on equations 3.57 and 3.58. Table E.1 lists the electrical properties of this material. Curves for b/a=0.500; ψ=1.00°, 5.00°; a= 0.10(m); and $1.00 \times 10^3 Hz \le f < 1.00 \times 10^{11} Hz$ are shown. (Note PDθ=$P_{d\theta}$ and PDZ=P_{dz}.)

PDθ/PDZ VS. FREQUENCY FOR DOUGLAS BEECH

Figure 3.5c   , Graph of $P_{d\theta}/P_{dz}$ versus frequency for Douglas Beech wood, based on equations 3.57 and 3.58. Table E.1 lists the electrical properties of this material. Curves for b/a=0.900; ψ=1.00°, 5.00°; a= 0.10 (m); and $1.00 \times 10^3 Hz \leq f < 1.00 \times 10^{11} Hz$ are shown. (Note $PD\theta = P_{d\theta}$ and $PDZ = P_{dz}$.)
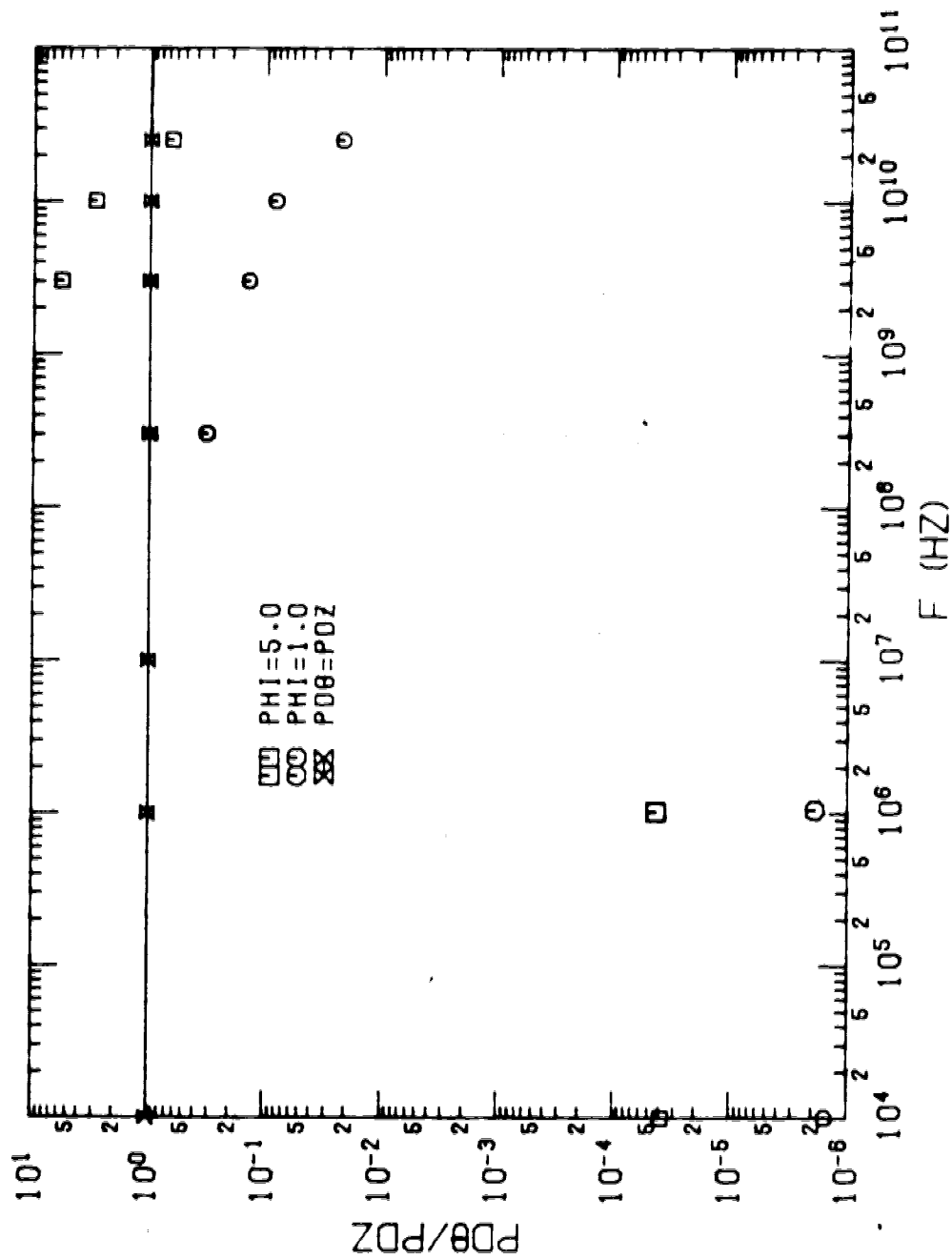
Figure 3.6a   Graph of $P_{d\theta}/P_{dz}$ versus frequency for a sample of steak meat, based on equations 3.57 and 3.58. Table E.2 presents the electrical properties of this material. Curves for b/a=0.100; ψ=1.00°, 5.00°; a=0.10 (m); and $1.00 \times 10^4 Hz \le f < 1.00 \times 10^{11} Hz$ are exhibited. (Note PDθ=$P_{d\theta}$ and PDZ=P_{dz}.)
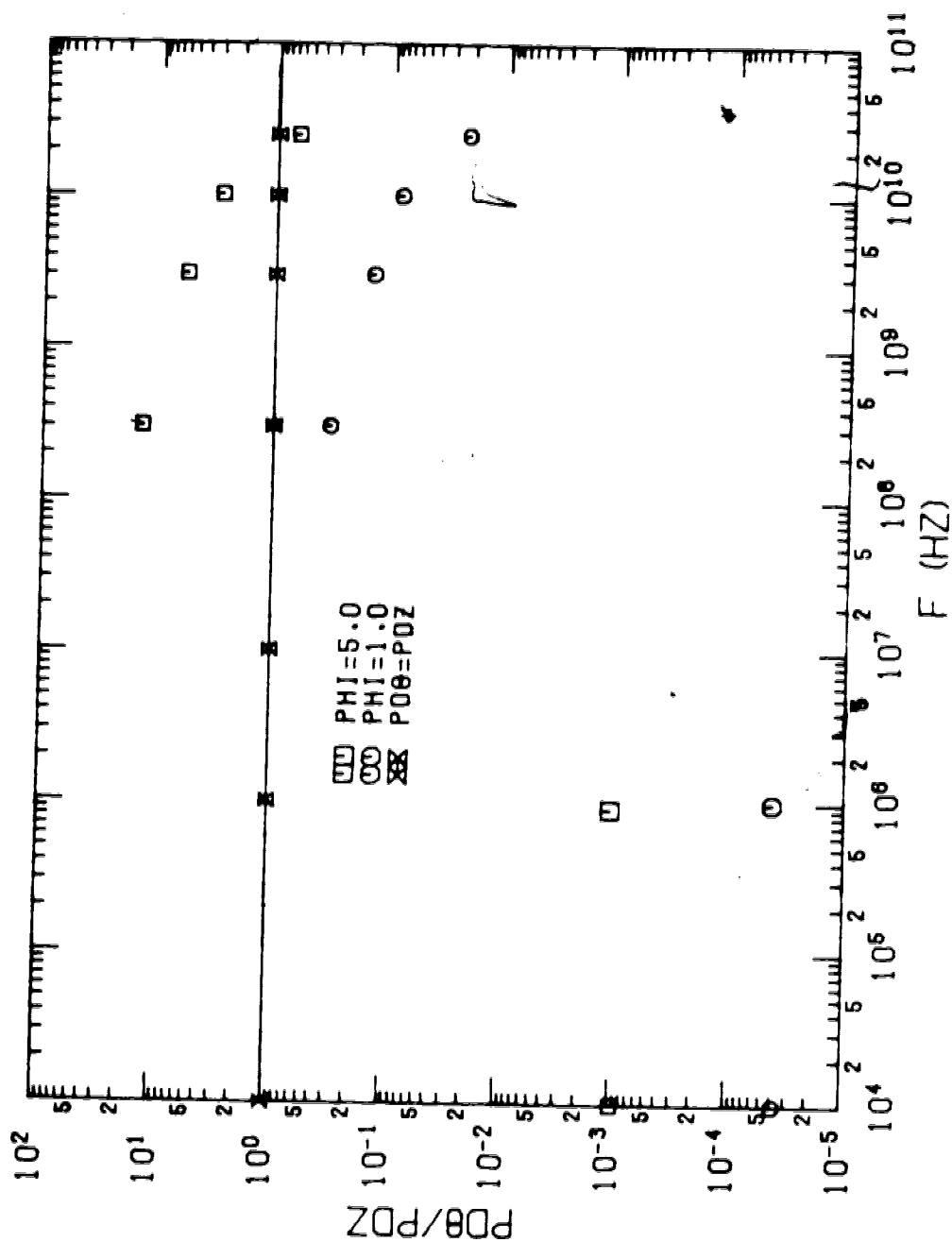
Figure 3.6b   Graph of $P_{d\theta}/P_{dz}$ versus frequency for a sample of steak meat, based on equations 3.57 and 3.58. Table E.2 presents the electrical properties of this material. Curves for $b/a=0.500$; $\psi=1.00°$, $5.00°$; $a=0.10$ (m); and $1.00\times10^4 Hz \le f < 1.00\times10^{11} Hz$ are exhibited. (Note $PD\theta=P_{d\theta}$ and $PDZ=P_{dz}$.)
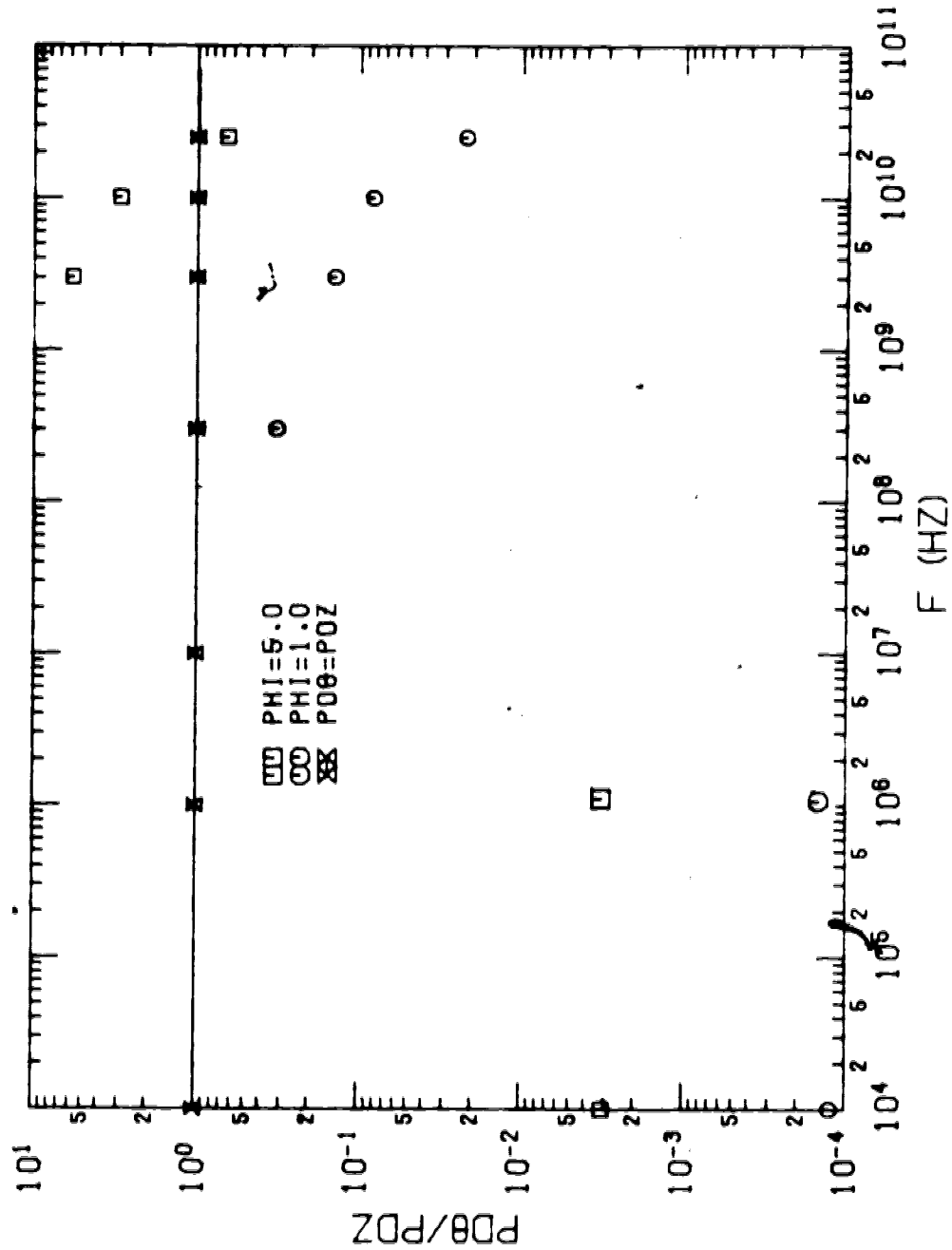
Figure 3.6c   Graph of $P_{d\theta}/P_{dz}$ versus frequency for a sample of steak meat, based on equations 3.57 and 3.58. Table E.2 presents the electrical properties of this material. Curves for b/a=0.900; ψ=1.00°, 5.00°; a=0.10 (m); and $1.00 \times 10^4 Hz \leq f < 1.00 \times 10^{11} H_z$ are exhibited. (Note $PD\theta = P_{d\theta}$ and $PDZ = P_{dz}$.)
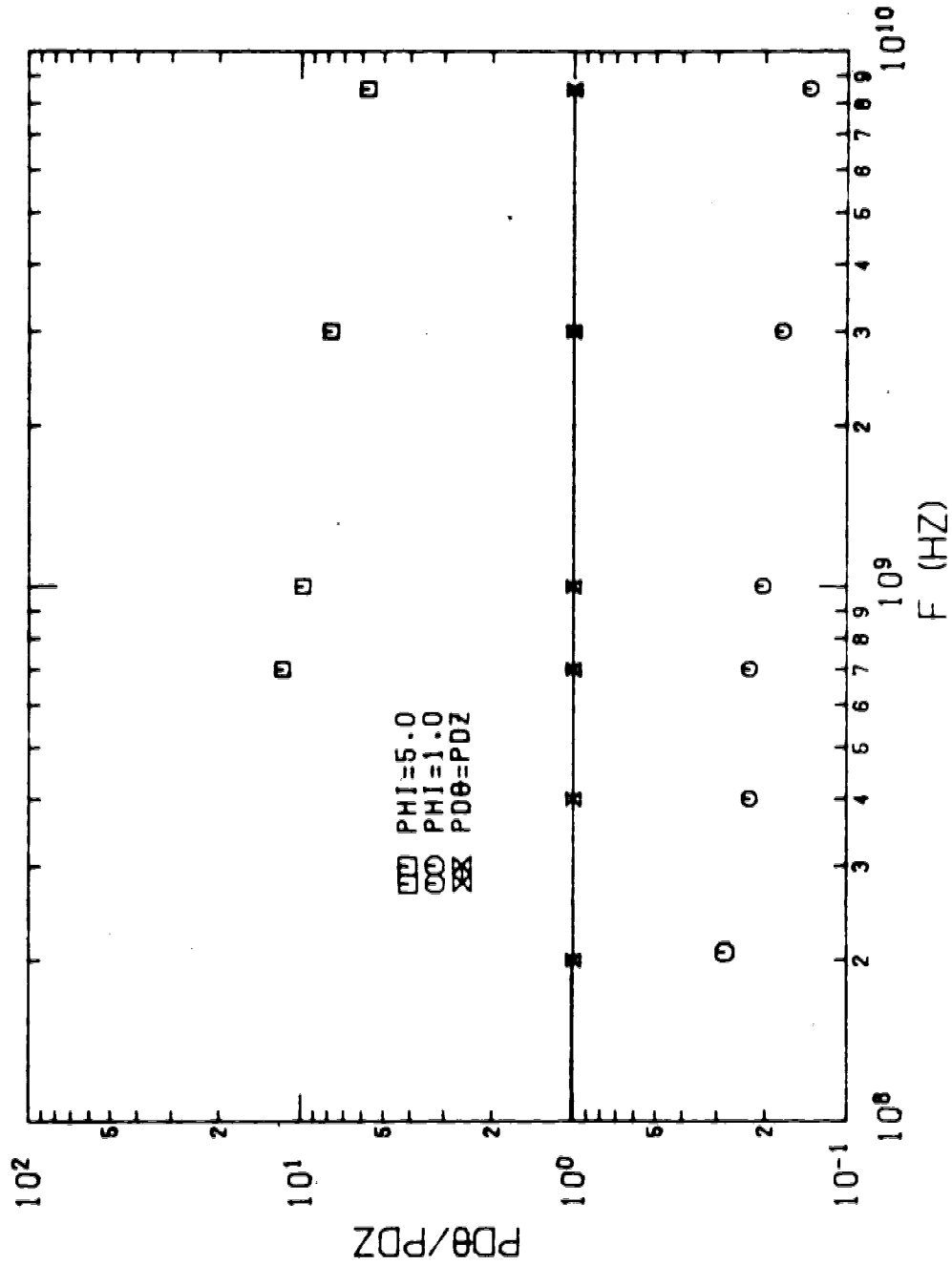
PDθ/PDZ VS. FREQUENCY FOR MUSCLE TISSUE

Figure 3.7a   Graph of $P_{d\theta}/P_{dz}$ versus frequency for a sample of muscle tissue, based on equations 3.57 and 3.58. The electrical properties of this material are listed in Table E.3. Curves for b/a=0.100; ψ=1.00°, 5.00°; a=0.10 (m); and 1.00×10^{8}Hz<f<1.00×10^{10}Hz are shown. (Note PDθ=$P_{d\theta}$ and PDZ=P_{dz}.)

PDθ/PDZ VS. FREQUENCY. FOR MUSCLE TISSUE

Figure 3.7b   Graph of $P_{d\theta}/P_{dz}$ versus frequency for a sample of muscle tissue, based on equations 3.57 and 3.58. The electrical properties of this material are listed in Table E.3. Curves for b/a=0.500; ψ=1.00°, 5.00°; a=0.10 (m); and 1.00×10^{7}Hz<f<1.00×10^{10}Hz are shown. (Note PDθ=$P_{d\theta}$ and PDZ=P_{dz}.)

Figure 3.7c   Graph of $P_{d\theta}/P_{dz}$ versus frequency for a sample of muscle tissue, based on equations 3.57 and 3.58. The electrical properties of this material are listed in Table E.3. Curves for b/a=0.900; ψ=1.00°, 5.00°; a=0.10 (m); and 1.00×10^{8}Hz<f<1.00×10^{10}Hz are shown. (Note PDθ=$P_{d\theta}$ and PDZ=P_{dz}.)

Figure 3.8   Graph of $P_{d\theta}/P_{dz}$ versus frequency for a sample of oil sand, based on equations 3.57 and 3.58. Table E.4 lists the electrical properties of the sample. Curves for b/a=0.100, 0.500, 0.900; ψ=1.00°; a=1.00 (m); and $1.00 \times 10^3 Hz < f < 1.00 \times 10^9 Hz$ are displayed. (Note PDO= $P_{d\theta}$, PDZ=P_{dz}, and B/A=b/a.)

Finally, Figure 3.9 is a similar type of graph as the previous figure, except that now $\psi = 10.0°$ is used instead of $\psi = 1.00°$. It is informative to compare these two figures. For low frequencies, the ratio $P_{d\theta}/P_{dz}$ is now much larger than it was for Figure 3.8, although it is still definitely smaller than unity. Furthermore, for large arguments, Figure 3.9 shows that $E_{\theta 1}$ makes a greater, or at least an equal, contribution to the total power dissipation, than E_{z1}. This is not true of Figure 3.8.

3.2.4 Large Argument Graphs of $P_{d\theta}/P_{dz}$

Part 3.2.3 was concerned with figures which each displayed both the small and large argument approximations of the ratio $P_{d\theta}/P_{dz}$. It is now desired to focus attention only on the large argument form of the ratio, in order to determine whether the angular region 1 electric field or the axial region 1 electric field makes the larger contribution to the total power dissipation which occurs within the lossy coaxial rod element.

It is convenient to repeat the large argument form of $P_{d\theta}/P_{dz}$, equation 3.58, here.

$$\frac{P_{d\theta}}{P_{dz}} \cong \frac{1}{|(\cotan^2\psi - \epsilon_r) + j\ \sigma/\omega\epsilon_0|} \cdot \tag{3.59}$$

$$\frac{|\sqrt{(\cotan^2\psi - \epsilon_r) + j\ \sigma/\omega\epsilon_0} + (\epsilon_r - j\ \sigma/\omega\epsilon_0)\cotan\psi|^2}{|\sqrt{(\cotan^2\psi - \epsilon_r) + j\ \sigma/\omega\epsilon_0} + \cotan\psi|^2}$$

Previously, in part 3.2.3, it was mentioned that the following requirements must be satisfied in order to justify the usage of equation 3.59.

$$ka\ \cotan\psi \cdot b/a > 1, \quad ka\ \cotan\psi \cdot (1-b/a) > 1,$$

$$\text{and if } \epsilon_r \cong \cotan^2\psi, \text{ then } \sqrt{\sigma/\omega\epsilon_0}\ ka \cdot b/a > 1. \tag{3.60}$$
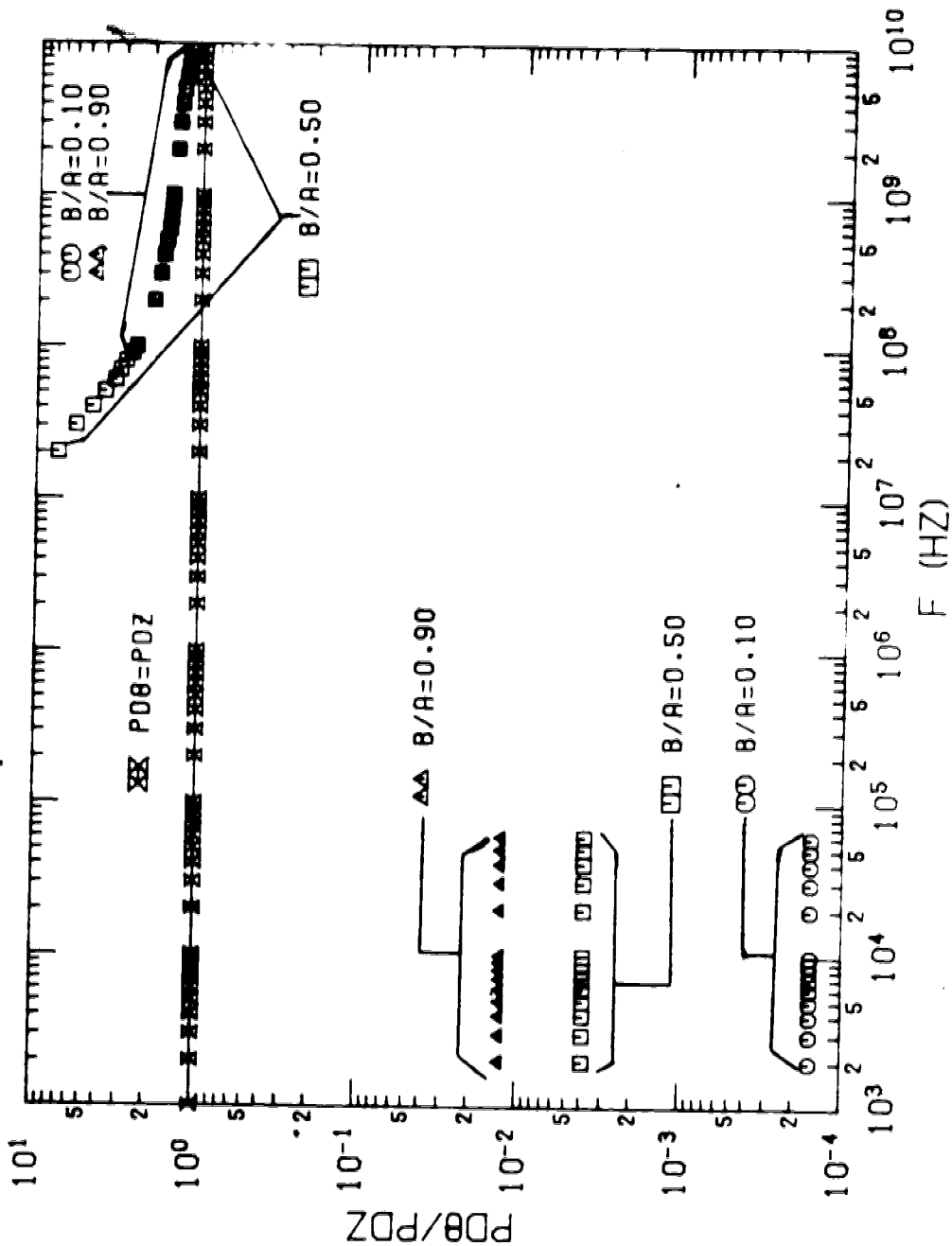
Figure 3.9   Graph of $P_{d\theta}/P_{dz}$ versus frequency for a sample of oil sand, based on equations 3.57 and 3.58. Table E.4 lists the electrical properties of the sample. Curves for b/a=0.100, 0.500, 0.900: ψ= 10.0°; a=1.00 (m); and 1.00×10^3Hz<f<1.00×10^{10}Hz are displayed. (Note $PD\theta$= $P_{d\theta}$, PDZ=P_{dz}, and B/A=b/a.)

Two ways of examining equation 3.59 are when the lossy rod material electrical properties are such that either $\varepsilon_r \gg \sigma/\omega\varepsilon_0$ or $\sigma/\omega\varepsilon_0 \gg \varepsilon_r$ is true.

A. $\varepsilon_r \gg \sigma/\omega\varepsilon_0$

Equation 3.59 simplifies to

$$\frac{P_{d\theta}}{P_{dz}} \approx \frac{1}{|\cotan^2\psi - \varepsilon_r|} \cdot$$

$$\frac{|\sqrt{\cotan^2\psi - \varepsilon_r} + \varepsilon_r \cotan\psi|^2}{|\sqrt{\cotan^2\psi - \varepsilon_r} + \cotan\psi|^2}. \qquad (3.61)$$

Two special cases of this occur, depending on the value of the relative permittivity.

(a) $\varepsilon_r \gg \cotan^2\psi$

It follows that

$$\frac{P_{d\theta}}{P_{dz}} \approx \cotan^2\psi. \qquad (3.62)$$

Clearly, $P_{d\theta} \gg P_{dz}$ occurs, assuming that the sheath helix is relatively tightly wound.

(b) $\varepsilon_r \ll \cotan^2\psi$

This means that

$$\frac{P_{d\theta}}{P_{dz}} \approx \frac{(\varepsilon_r + 1)^2}{4\cotan^2\psi}. \qquad (3.63)$$

Either $P_{d\theta} > P_{dz}$ or $P_{dz} > P_{d\theta}$ may be true.

B. $\sigma/\omega\varepsilon_0 \gg \varepsilon_r$

From equation 3.59, it follows that

$$\frac{P_{d\theta}}{P_{dz}} \cong \frac{1}{|\cotan^2\psi + j\ \sigma/\omega\varepsilon_0|} \cdot$$ (3.64)

$$\frac{|\sqrt{\cotan^2\psi + j\ \sigma/\omega\varepsilon_0} - j\ \sigma/\omega\varepsilon_0\ \cotan\psi|^2}{|\sqrt{\cotan^2\psi + j\ \sigma/\omega\varepsilon_0} + \cotan\psi|^2} \cdot$$

Once again, two special cases of the above can be considered. These depend on the value of the quantity $\sigma/\omega\varepsilon_0$.

(a) $\sigma/\omega\varepsilon_0 \gg \cotan^2\psi$

Equation 3.64 now becomes

$$\frac{P_{d\theta}}{P_{dz}} \cong \cotan^2\psi .$$ (3.65)

It is apparent that $P_{d\theta} \gg P_{dz}$, assuming that the sheath helix is relatively tightly wound.

(b) $\sigma/\omega\varepsilon_0 \ll \cotan^2\psi$

This means that

$$\frac{P_{d\theta}}{P_{dz}} \cong \frac{|1 - j\ \sigma/\omega\varepsilon_0|^2}{4\ \cotan^2\psi} .$$ (3.66)

$P_{d\theta} \ll P_{dz}$ is now true.

Two graphs of equation 3.59 have been prepared. These show the relative contribution of $E_{\theta 1}$ and E_{z1} to the total power dissipation, using many different

sets of the variables ϵ_r, $\sigma/\omega\epsilon_0$, and ψ. Of course, the values of ka $\cot an\psi$ and b/a associated with the sheath helix surrounding a lossy coaxial rod configuration must be such that the requirements listed in equations 3.60 are satisfied.

Figure 3.10 plots $P_{d\theta}/P_{dz}$ versus $\sigma/\omega\epsilon_0$. $\psi = 1.00°$, $10.0°$; $\epsilon_r = 1.1$, 100.0; and $0.100 \leq \sigma/\omega\epsilon_0 < 1.00 \times 10^6$ are used. When $\sigma/\omega\epsilon_0 >> \epsilon_r$ and $\sigma/\omega\epsilon_0 >> \cot an^2\psi$ both occur, the graph shows that equation 3.65 is correct, as one expects. The curve representing $\psi = 10.0°$ and $\epsilon_r = 100.0$ satisfies $\epsilon_r >> \sigma/\omega\epsilon_0$ and approximately satisfies $\epsilon_r >> \cot an^2\psi$, at $\sigma/\omega\epsilon_0 = 0.100$. As expected, the value of the ratio predicted by equation 3.62 is seen to be approximately correct. At $\sigma/\omega\epsilon_0 = 0.100$, the other three curves meet the requirements necessary to use equation 3.63. Indeed, their values are seen to agree well with its prediction.

Figure 3.11 is a graph of $P_{d\theta}/P_{dz}$ versus ϵ_r. $\psi = 1.00°$, $10.0°$; $\sigma/\omega\epsilon_0 = 1.00 \times 10^{-2}$, 10.0, 1.00×10^5; and $1.00 \leq \epsilon_r < 1.00 \times 10^5$ are shown. When $\sigma/\omega\epsilon_0 = 1.00 \times 10^5$, it is true that $\sigma/\omega\epsilon_0 >> \epsilon_r$, except near the top of the graph. Of course, it is also true that $\sigma/\omega\epsilon_0 >> \cot an^2\psi$. This means that the requirements necessary to use equation 3.65 are satisfied. As expected, the two curves corresponding to this value of $\sigma/\omega\epsilon_0$ agree well with this equation. At $\epsilon_r = 1.00 \times 10^5$, the other four curves satisfy both $\epsilon_r >> \sigma/\omega\epsilon_0$ and $\epsilon_r >> \cot an^2\psi$. Therefore, the usage of equation 3.62 is justified. The four curves do agree with this equation, as one expects. Consider the two curves representing $\sigma/\omega\epsilon_0 = 1.00 \times 10^{-2}$. At $\epsilon_r \simeq 1.00$, it is true that $\epsilon_r >> \sigma/\omega\epsilon_0$ and that $\epsilon_r << \cot an^2\psi$. There-fore, the requirements involved with using equation 3.63 are satisfied and indeed the curves have the value that this equation predicts. The final two curves represent $\sigma/\omega\epsilon_0 = 10.0$. At $\epsilon_r \simeq 1.00$, $\sigma/\omega\epsilon_0 >> \epsilon_r$ is true. $\sigma/\omega\epsilon_0 << \cot an^2\psi$ is correct for $\psi = 1.00°$, and it is approximately correct for $\psi = 10.0°$. The usage of equation 3.66 is justified, and the values of the two curves are seen to be in good agreement with it, as one expects.
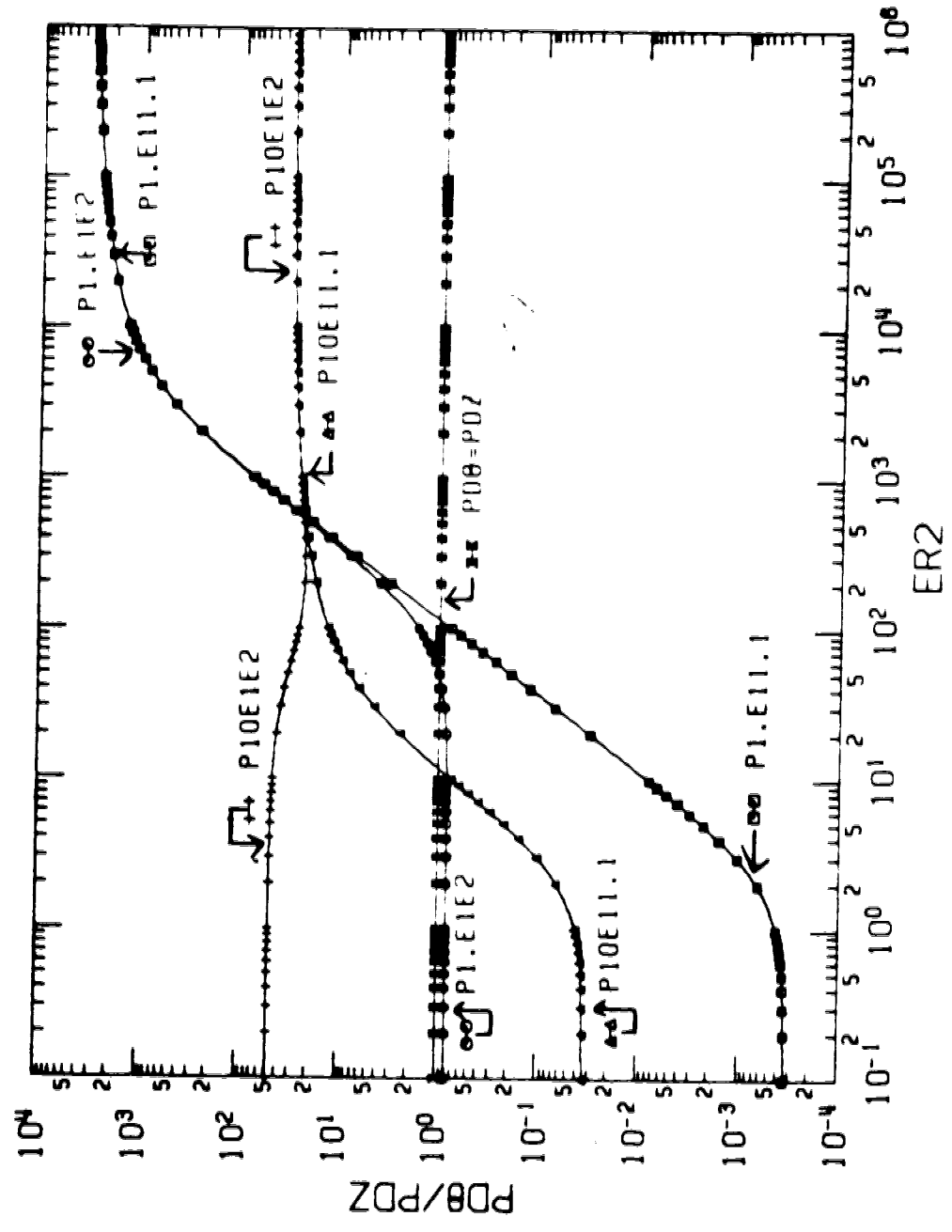
Figure 3.10 Graph of $P_{d\theta}/P_{dz}$ versus $\sigma/\omega\epsilon_0$, based on equation 3.59. Curves for $\psi=1.0°$, $10.0°$; $\epsilon_r=1.1$, $100.$; and $0.10 \leq \sigma/\omega\epsilon_0 < 1.00\times10^6$ are shown. (Note $PD\theta=P_{d\theta}$, PDZ $=P_{dz}$, $ER2=\sigma/\omega\epsilon_0$, and $ER1=\epsilon_r$. $P10E1E2$ means the curve represents $\psi=10.0°$ and $\epsilon_r=100$. $P1E11.1$ means the curve represents $\psi=1.0°$ and $\epsilon_r=1.1$.)
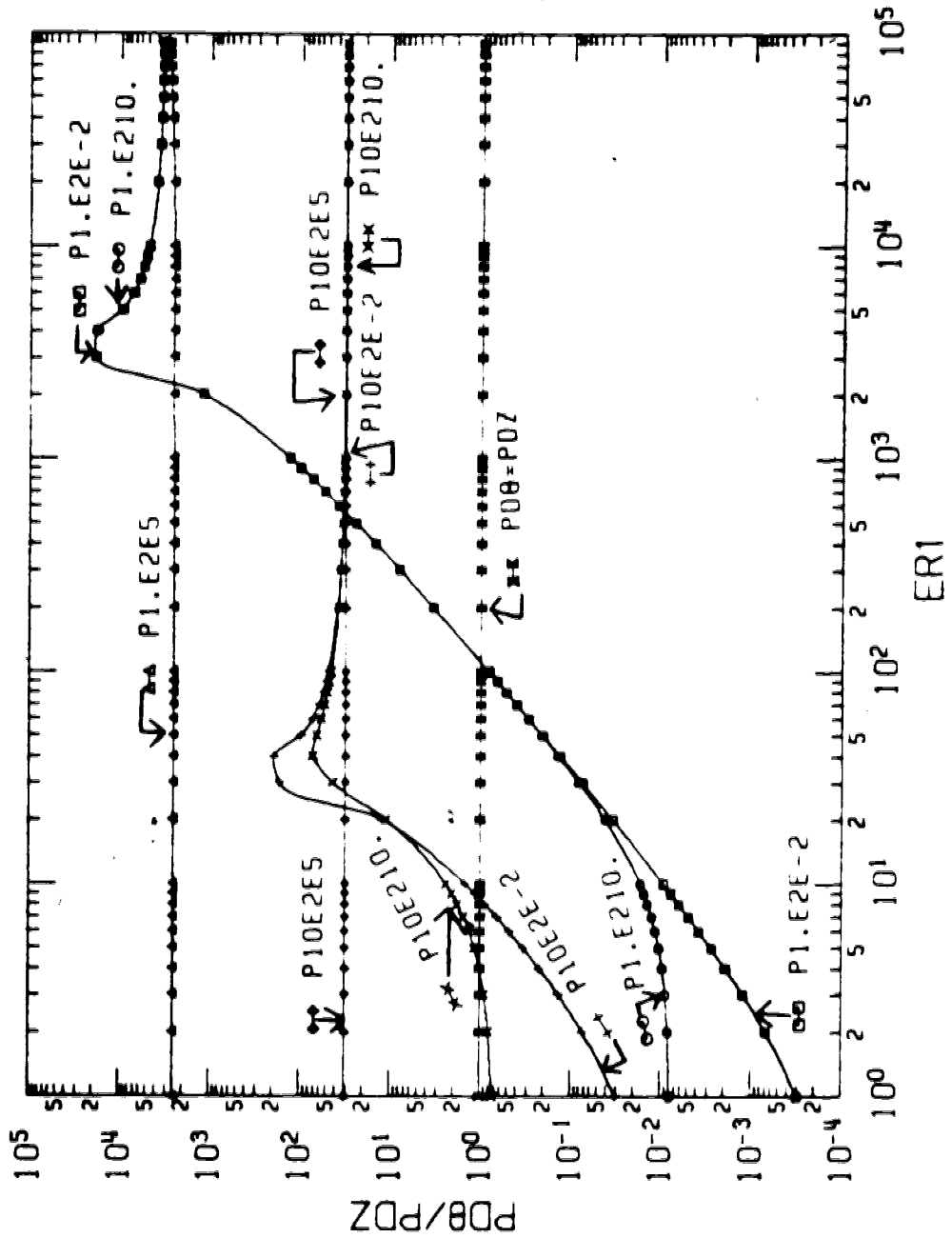
Figure 3.11   Graph of $P_{d\theta}/P_{dz}$ versus ϵ_r, based on equation 3.59. Curves for $\psi=1.0°$, 10.0°; $\sigma/\omega\epsilon_0=0.01$, 10.0, 1.00×10^5; and $1.00\leq\epsilon_r<1.00\times10^5$ are given. (Note $PD\theta=P_{d\theta}$, $PDZ=P_{dz}$, $ER1=\epsilon_r$, and $ER2=\sigma/\omega\epsilon_0$. P10E2E-2 means the curve represents $\psi=10.°$ and $\sigma/\omega\epsilon_0=0.01$. P1.E2E5 means the curve represents $\psi=1.0°$ and $\sigma/\omega\epsilon_0=1.00\times10^5$.)

3.3 Approximate Representations of the Power Dissipation Equations When "The Lossy Coaxial Rod is a Good Conductor"

The purpose of this section is to derive and investigate approximate power dissipation equations for the case when the lossy rod is a good conductor." (The meaning of the term "the lossy rod is a good conductor" as it is used in part 3.3.1 is the same as it was for sub-part 2.3.2.1. Its meaning in part 3.3.2 is the same as it was for sub-part 2.3.2.2.) Previously, in part 2.3.2, equations and graphs of the approximate radial and axial wave numbers solution were given for the sheath helix surrounding a lossy coaxial rod configuration, for the case when the lossy rod is a good conductor." This was done for the three region configuration (b < a), but not for the two region configuration (b = a). The discussion of section 3.3 will be restricted to the three region configuration.

3.3.1 Three Region Configuration Small Argument Representation

The small argument approximations of equations 3.12, 3.14, and 3.16, the exact power dissipation equations, will be obtained. The assumptions listed in equations 2.120 are made. Equations A.28 and A.29, the small argument Bessel function representations, are substituted into the exact power dissipation equations, in order to approximate all Bessel functions having $h_2 a$ and $h_2 a \cdot b/a$ as the argument. The first two terms of equations A.36 and A.37, the large argument Bessel function representations, are substituted into the exact power dissipation equations, so that all Bessel functions of argument $h_1 b$ and $\tilde{h}_1 b$ are approximated. Making these substitutions and performing some algebra, the following equations are obtained.

$$P_{dr} \approx \frac{|A_{11}|^2}{2\sqrt{2}} \frac{\pi a^3 \sigma (120\pi)^2}{(\sigma/\omega\epsilon_0)^{5/2} (ka \, \cot an\psi)^3} \cdot$$

$$\frac{|\beta a|^2 \cos^2\psi \, \cot an\psi}{\beta_r b \, \beta_j b} \frac{|\log(0.891 \, h_2 a)|^2}{|\log(0.891 \, h_2 b)|^2} \cdot \qquad (3.67)$$

$$[\beta_r b \, \sinh(2 \, \beta_j \, z_1) - \beta_j b \, \sin(2 \, \beta_r \, z_1)],$$

$$P_{d\theta} \simeq \frac{|I_1|^2}{2\sqrt{2}} \frac{\pi \ a^3 \ (b/a)^2 \ \sigma \ (120\pi)^2 \ \cos^2\psi \ \cot an\psi}{(\sigma/\omega\epsilon_0)^{3/2} \ ka \ \cot an\psi \ \beta_r b \ \beta_j b} \ . \qquad (3.68)$$

$$[\beta_r b \ \sinh(2 \ \beta_j \ z_1) + \beta_j b \ \sin(2 \ \beta_r \ z_1)], \quad \text{and}$$

$$P_{dz} \simeq \frac{|I_1|^2}{2\sqrt{2}} \frac{\pi \ a^3 \ \sigma \ (120\pi)^2}{(\sigma/\omega\epsilon_0)^{3/2} \ ka \ \cot an\psi} \ .$$

$$\frac{\sin\psi \ \cos\psi}{\beta_r b \ \beta_j b} \frac{|\log(0.891 \ h_2 a)|^2}{|\log(0.891 \ h_2 b)|^2} \ . \qquad (3.69)$$

$$[\beta_r b \ \sinh(2 \ \beta_j \ z_1) + \beta_j b \ \sin(2 \ \beta_r \ z_1)].$$

Equations 3.67 - 3.69 can be evaluated by using the approximate dispersion equation, equation 2.122, and the separation constant equation, equation 2.121, to evaluate $h_2 a$ and βa. Some numerical values of the solution for $h_2 a$ are given in Figures 2.6 and 2.7. Rather than following this procedure, however, equations 3.67 - 3.69 can be considerably simplified by assuming that the value of $|\beta| a$ is sufficiently small, taking into account the lossy coaxial rod element length, so that $|\beta| a \cdot 2 z_1/a = 2 |\beta| z_1 \ll 1$. This means that

$$\sin(2 \ \beta_r \ z_1) \simeq 2 \ \beta_r \ z_1 - \frac{(2 \ \beta_r \ z_1)^3}{6} \quad \text{and}$$

$$\sinh(2 \ \beta_j \ z_1) \simeq 2 \ \beta_j \ z_1 + \frac{(2 \ \beta_j \ z_1)^3}{6}.$$

Using these approximations in equations 3.67 - 3.69, the following equations are obtained.

$$P_{dr} \simeq \frac{|\rho_{11}|^2}{12\sqrt{2}} \frac{\pi a^3 \sigma (120\pi)^2 |\beta a|^4}{b/a (\sigma/\omega\epsilon_0)^{5/2} (ka \, \cot an\psi)^3} \cdot$$

$$\cot an\psi \, \cos^2\psi \, \frac{|\log(0.891 \, h_2 a)|^2}{|\log(0.891 \, h_2 b)|^2} \left(\frac{2 \, z_1}{a}\right)^3, \qquad (3.70)$$

$$P_{d\theta} \simeq \frac{|\rho_{11}|^2}{\sqrt{2}} \frac{\pi a^3 \, b/a \, \sigma (120\pi)^2 \cos^2\psi \, \cot an\psi}{(\sigma/\omega\epsilon_0)^{3/2} \, ka \, \cot an\psi} \frac{2 \, z_1}{a}, \qquad (3.71)$$

$$P_{dz} \lesssim \frac{|\rho_{11}|^2}{\sqrt{2}} \frac{\pi a^3 \sigma (120\pi)^2 \sin\psi \, \cos\psi}{b/a (\sigma/\omega\epsilon_0)^{3/2} \, ka \, \cot an\psi} \cdot$$

$$\frac{|\log(0.891 \, h_2 a)|^2}{|\log(0.891 \, h_2 b)|^2} \frac{2 \, z_1}{a}, \qquad (3.72)$$

$$\frac{P_{dr}}{P_{dz}} \simeq \frac{1}{12} \frac{|\beta a|^4}{\sigma/\omega\epsilon_0} \frac{\cot an^2\psi}{(ka \, \cot an\psi)^2} \left(\frac{2 \, z_1}{a}\right)^2, \quad \text{and} \qquad (3.73)$$

$$\frac{P_{d\theta}}{P_{dz}} \simeq (b/a)^2 \, \cot an^2\psi \, \frac{|\log(0.891 \, h_2 b)|^2}{|\log(0.891 \, h_2 a)|^2}. \qquad (3.74)$$

Equations 3.73 and 3.74 were obtained by taking the appropriate ratios of equations 3.70 - 3.72. For convenience, the assumptions which have been used in the derivation of equations 3.70 - 3.74 from the exact power dissipation equations will be gathered

Together and listed.

$$|\beta|a \cdot 2 z_1/a \ll 1, \quad \sigma/\omega\epsilon_0 \gg \epsilon_r, \quad h_1 a \stackrel{\sim}{=} \sqrt{j\ \sigma/\omega\epsilon_0}\ ka,$$

$$(3.75)$$

$$|h_1|b \stackrel{\sim}{=} \sqrt{\sigma/\omega\epsilon_0}\ ka \cdot b/a > 1, \quad \text{and} \quad |h_2|a < 0.100.$$

Equations 3.70 - 3.74 can be approximately numerically evaluated in the following manner. Making use of the discussion previously given in sub-part 2.3.2.1; when the requirements given in equations 3.75 are satisfied, it is approximately true that $|h_2|a \stackrel{\sim}{=} h_{2r}a$, where $h_{2r}a$ is calculated using

$$\left(\frac{ka\ \cot an\psi}{h_{2r}a}\right)^2 \stackrel{\sim}{=} \frac{-2\ \log(b/a)}{(1 - (b/a)^2)}.$$

$$(3.76)$$

Furthermore, it is true that $|\beta|a \stackrel{\sim}{=} h_{2r}a$.

Equations 3.70 - 3.74 are the approximate small argument, three region configuration, power dissipation equations, when "the lossy rod is a good conductor". (The term "the lossy rod is a good conductor" has the meaning that the electrical properties of the rod material are such that the requirements listed in equations 3.75 are satisfied.) These equations are valid for the three region sheath helix surrounding a lossy coaxial rod configuration.

The relative contribution that each of the three region 1 electric field components makes towards the total power dissipated within the lossy coaxial rod element can be understood by examining equations 3.73 and 3.74. Making use of the requirements $\sqrt{\sigma/\omega\epsilon_0} \cdot kb > 1$ and $|\beta|a \cdot 2 z_1/a \ll 1$, which are listed in equations 3.75, equation 3.73 shows that $P_{dz} \gg P_{dr}$. *For the three region, small argument representation, when "the lossy rod is a good conductor", the contribution to the total power dissipation associated with the region 1 axial electric field is much greater than that associated with the region 1 radial electric field.*

Since $|\log(0.891\ h_2 b)| = |\log(0.891\ h_2 a) + \log(b/a)| >$

$|\log(0.891\ h_2 a)|$ for $0 < b/a < 1$ and $|h_2|a < 0.100$,

equation 3.74 shows that when ψ is small, $P_{d\theta} > P_{dz}$ occurs, unless the value of b/a is very small. *Assuming that the sheath helix is tightly wound, for the three region, small argument representation, when "the lossy rod is a good conductor", the contribution to the total power dissipation associated with* $E_{\theta 1}$ *is usually greater than that associated with* E_{z1}. *The single exception to the previous statement occurs when the rod radius is much smaller than the sheath helix radius.*

To conclude part 3.3.1, it will be mentioned how the total power dissipation is distributed throughout the lossy coaxial rod element volume. Substituting just the first term of equations A.36 and A.37, the large argument Bessel function representations, into equations 3.2 - 3.4, the region 1 electric field components, making use of the relation $h_1 a \cong (1 + j) \cdot ka \cdot \sqrt{\sigma/2\omega\epsilon_0}$ from equations 3.75, it is seen that the radial dependence is dominated by the exponential

$$e^{-(1+j)\sqrt{\sigma/2\omega\epsilon_0}\ kb\ (1-r/b)}.$$ Once again making use of equations 3.75, it is known that $\sqrt{\sigma/\omega\epsilon_0} \cdot kb > 1$, and so all the electric field magnitudes are at least relatively rapidly exponentially attenuated throughout the rod-filled region, as the radial distance decreases. (Figures 2.24 and 2.26 illustrate the radial dependence of the electric field components for the three region configuration small argument case, when "the lossy rod is a good conductor".) *This has the important meaning that the total power dissipation occurring within the lossy coaxial rod element is concentrated near the surface of the rod, for the three region configuration small argument case, when "the lossy rod is a good conductor".* A further discussion of this behavior is given later in part 3.5.3.

3.3.2 Three Region Configuration Large Argument Representation

The large argument approximations of equations 3.12, 3.14, and 3.16, the exact power dissipation equations, will be obtained for the case when the lossy rod is a good conductor and for the geometry where $b < a$. It is assumed that the requirements listed in equations 2.127 are satisfied, which means that the approximate wave numbers solution is given by equations 2.128.

The first term of equations A.38, A.39, and the first two terms of equations A.36, A.37, which are the large argument Bessel function representations, are substituted into equations 3.12, 3.14, and 3.16. Equations 2.127 and 2.128 are used. Finally, two additional assumptions are made. First, it is assumed that the lossy coaxial rod element length is sufficiently large so that $2 z_1/a \geq 10$. Second, it is assumed that the value of $|\beta_j| a$ is sufficiently small for the particular element length of concern, so that $|\beta_j| a \cdot 2 z_1/a << 1$. Making the previously mentioned assumptions and substitutions, equations 3.77 - 3.81 are obtained.

$$P_{dr} \approx \frac{|J_{11}|^2}{2\sqrt{2}} \frac{\pi a^3 \sigma (120\pi)^2 \cos^2\psi \cot\psi}{(\sigma/\omega\epsilon_0)^{5/2} ka \cot\psi} \frac{2 z_1}{a} \cdot$$

$$e^{-2 ka \cot\psi (1-b/a)}, \qquad (3.77)$$

$$P_{d\theta} \approx \frac{|J_{11}|^2}{2\sqrt{2}} \frac{\pi a^3 \sigma (120\pi)^2 \cos^2\psi \cot\psi}{(\sigma/\omega\epsilon_0)^{3/2} ka \cot\psi} \frac{2 z_1}{a} \cdot$$

$$e^{-2 ka \cot\psi(1-b/a)}, \qquad (3.78)$$

$$P_{dz} \approx \frac{|J_{11}|^2}{2\sqrt{2}} \frac{\pi a^3 \sigma (120\pi)^2 \cos\psi \sin\psi}{(\sigma/\omega\epsilon_0)^{3/2} ka \cot\psi} \frac{2 z_1}{a} \cdot$$

$$e^{-2 ka \cot\psi(1-b/a)}, \qquad (3.79)$$

$$\frac{P_{dr}}{P_{dz}} \simeq \frac{cotan^2\psi}{\sigma/\omega\epsilon_0}, \quad and \tag{3.80}$$

$$\frac{P_{d\theta}}{P_{dz}} \simeq cotan^2\psi. \tag{3.81}$$

Equations 3.80 and 3.81 were obtained by taking the appropriate ratios of equations 3.77 - 3.79. It is convenient to list in one location the approximations made in deriving equations 3.77 - 3.79 from the exact power dissipation equations.

$$2\ z_1/a \geq 10, \quad |\beta_j|a \cdot 2\ z_1/a << 1, \quad \sigma/\omega\epsilon_0 >> \epsilon_r,$$

$$\sigma/\omega\epsilon_0 >> cotan^2\psi, \quad h_1 a \simeq \sqrt{j\ \sigma/\omega\epsilon_0}\ ka, \quad ka\ cotan\psi \cdot \tag{3.82}$$

$$b/a > 1, \quad and \quad ka\ cotan\psi \cdot (1 - b/a) > 1.$$

When the requirements mentioned in equations 3.82 are satisfied, it was previously mentioned in sub-part 2.3.2.2 that the following approximate wave numbers solution results.

$$h_{2r}a \simeq \beta_r a \simeq ka\ cotan\psi, \quad h_1 a \simeq \sqrt{j\ \sigma/\omega\epsilon_0}\ ka,$$

$$and \quad |h_{2j}|a \simeq |\beta_j|a << ka\ cotan\psi. \tag{3.83}$$

Equations 3.77 - 3.81 are the approximate large argument, three region configuration, power dissipation equations, for the case when "the lossy rod is a good conductor". (As it is used in part 3.3.2, the expression in quotation marks has the meaning that the electrical properties of the lossy rod satisfy the requirements listed in equations 3.82.) Assuming that the sheath helix is relatively tightly wound, equation 3.81 makes it clear that $P_{d\theta} >> P_{dz}$. Making use of equations 3.82, it is apparent from equation 3.80 that $P_{dz} >> P_{dr}$. The question concerning which of the three region 1 electric fields makes the largest contribution to the total power dissipated within the lossy coaxial rod element is easy to answer. *For the large argument case of*

the three region configuration, when "the lossy rod is a good conductor", the angular region 1 electric field makes the dominant contribution towards the total power dissipation, assuming that the sheath helix is relatively tightly wound. The total power dissipation is therefore approximately given by equation 3.78. Note that it rapidly decreases in an exponential fashion when $ka \cot an\psi$ increases or when b/a decreases. The explanation for this behavior is the same as that discussed previously in sub-part 3.2.2.2.

Substituting equations A.36 - A.39, the large argument Bessel function representations, into equation 3.3, the region 1 angular electric field, making use of the relation for $h_1 a$ from equations 3.83 and the fact that $h_1 b \sim 1$ from equations 3.82, the radial dependence of E_{z1} is seen to be similar to that discussed previously in part 3.3.1. *Therefore, for the three region configuration, large argument case, when "the lossy rod is a good conductor", the total power dissipation is concentrated near the surface of the rod.* Part 3.5.3 presents a more detailed discussion of this behavior.

To conclude part 3.3.2, the power dissipation expressions presented here will be compared to the expressions listed in sub-part 3.2.2.2. These latter mentioned equations, equations 3.50 - 3.54, are for the large argument case of the three region configuration, when "the lossy rod is not a good conductor". It will be assumed in sub-part 3.2.2.2 that the conductivity of the lossy rod is sufficiently large so that

$$\sigma/\omega\epsilon_0 \gg \epsilon_r \quad \text{and} \quad \sigma/\omega\epsilon_0 \gg \cot an^2\psi. \qquad (3.84)$$

(Note that this does not violate any of the requirements listed in equations 3.55, which were used in the derivation of equations 3.50 - 3.54 from the exact power dissipation equations.) Equations 3.84 mean that the approximate wave numbers solution listed in equations 3.46 reduce to the wave numbers solution listed in equations 3.83. The wave numbers solution associated with the three region, large argument case, when "the lossy rod is not a good conductor", has become the solution associated with the large argument, three region configuration, when "the lossy rod is a good conductor". Making use of equations 3.83, 3.84 in equations 3.50 - 3.54, and simplifying by eliminating the less significant terms, it is discovered that the corresponding equation of the set 3.77 - 3.81

is obtained. When the conductivity of the lossy rod is large enough to satisfy equations 3.84, the power dissipation equations which were previously obtained for the three region, large argument case, *when "the lossy rod is not a good conductor"*, become simplified to the equations associated with the three region, large argument case, *when "the lossy rod is a good conductor"*. This means that it is possible to consider the discussion given in part 3.3.2 as a specialized form of that given in subpart 3.2.2.2, when the conductivity of the lossy rod becomes sufficiently large. Note that demonstrating the equivalence between the two sets of equations serves as a check on the accuracy of equations 3.77 - 3.81.

3.4 Approximate Representations of the Power Dissipation Equations When the Lossy Rod is an Excellent Dielectric, Based on the Ideal Dielectric Rod Configuration Wave Number Solution

Sections 3.2 and 3.3 discussed approximate power dissipation equations. These approximate expressions were derived from the exact equations given in section 3.1, for the special cases when the magnitude of the radial wave number are either small or large, so that the Bessel functions appearing in the exact equations could be approximated by simpler functions. The electrical properties of the rod material were allowed to assume a relatively wide range of different values. They were restricted only to the extent that the radial wave number magnitudes were either sufficiently small or large to justify the usage of the small or large argument Bessel function approximations, respectively. The radial and axial wave numbers are complex-valued. Section 2.3 discusses the small argument and large argument solution of these wave numbers.

A completely different approach to that used in sections 3.2 and 3.3 will be followed in sections 3.4 and 3.5, in order to derive and discuss approximate forms of the exact power dissipation equations. It will be assumed that the conductivity of the lossy rod is either very small or very large. The approximation will be made of using the (real) radial and axial wave numbers solution, for the sheath helix surrounding an ideal dielectric coaxial rod, or for the sheath helix surrounding a perfectly conducting coaxial rod. (Recall that in the limit as the rod conductivity approaches zero, it was shown in part 2.2.2 that the free mode field solution associated with the sheath helix surrounding a

lossy coaxial rod becomes that of the sheath helix surrounding an ideal dielectric coaxial rod. Part 2.2.3 showed that in the limit as the rod conductivity approaches infinity, the free mode field solution associated with the sheath helix surrounding a lossy coaxial rod becomes that of the sheath helix surrounding a perfectly conducting coaxial rod. Therefore, one expects that when σ is very small (but nonzero) or is very large (but finite), the wave numbers solution associated with the lossy rod configuration will approximate that of the ideal dielectric rod configuration or the perfectly conducting rod configuration, respectively.)

Appendices C and D provide a relatively thorough discussion of the free mode field solution associated with the sheath helix surrounding a perfectly conducting coaxial rod and the sheath helix surrounding an ideal dielectric coaxial rod, respectively. It is shown that the solution of the dispersion equation and the separation constant equation, in order to numerically evaluate the radial and axial wave numbers, is relatively easy to accomplish. It is very attractive to use these wave numbers to derive approximate power dissipation equations. This is because these approximate equations can be numerically evaluated for a wide range of operating frequencies, sheath helix geometries, and lossy rod geometries. It is not necessary to restrict the values of these (real) radial wave numbers to be either small or large.

In summary, sections 3.4 and 3.5 will put sharp restrictions on the conductivity of the lossy rod. By using the wave numbers solution associated with Appendices D and C, it will be possible to derive and evaluate approximate power dissipation equations, without using the small and large argument Bessel function approximations. Section 3.4 is concerned with the approximate power dissipation equations for the case when the lossy rod conductivity is very small. Section 3.5 discusses the approximate expressions for the case when the lossy rod conductivity is very large.

3.4.1 Derivation of the Approximate Power Dissipation Equations

It is assumed that the lossy rod is an excellent dielectric. Approximate expressions for the power dissipation occurring within the lossy coaxial rod element will be obtained from the exact power dissipation expressions, equations 3.12, 3.14, and 3.16. Previously, in part 2.2.2, it was demonstrated that taking the limit of the radial and

axial wave numbers as the lossy rod conductivity approaches zero, the (real) radial and axial wave numbers associated with the sheath helix surrounding an ideal dielectric coaxial rod are obtained. Therefore, the following approximations are reasonable, when the lossy rod conductivity is very small.

$$\sigma / \omega \epsilon_0 \ll \epsilon_r, \quad h_{1r} a \gg |h_{1j}| a,$$

$$h_{2r} a \gg |h_{2j}| a, \quad \text{and} \quad \beta_r a \gg |\beta_j| a. \tag{3.85}$$

An additional approximation is made that the imaginary parts of the radial and axial wave numbers will tend to approach zero. This result is evaluated as a limiting case of equations 3.12, 3.14, and 3.16. During the course of evaluating these limits, it was necessary to apply L'Hopital's rule (for example, see 47, pp. 651) in order to obtain the following three results.

$$\lim_{\beta_j \to 0} \frac{[\beta_r b \sinh(2 \beta_j z_1) \pm \beta_j b \sin(2 \beta_r z_1)]}{\beta_j b}$$

$$= 2 \beta_r z_1 \pm \sin(2 \beta_r z_1), \tag{3.86}$$

$$\lim_{h_{1j} \to 0} \frac{[h_1 b \, I_0(h_1 b) \, I_1(\widehat{h}_1 b) - \widehat{h}_1 b \, I_0(\widehat{h}_1 b) \, I_1(h_1 b)]}{h_{1j} b}$$

$$= j \, 2 \, [h_{1r} b \, [I_1(h_{1r} b)]^2 - h_{1r} b \, [I_0(h_{1r} b)]^2$$

$$+ 2 \, I_0(h_{1r} b) \, I_1(h_{1r} b)], \quad \text{and} \tag{3.87}$$

$$\lim_{h_{1j} \to 0} \frac{[h_1 b \ I_0(\tilde{h}_1 b) \ I_1(h_1 b) - \tilde{h}_1 b \ I_0(h_1 b) \ I_1(\tilde{h}_1 b)]}{h_{1j} b}$$

$$= j \ 2 \ h_{1r} b \ ([I_0(h_{1r}b)]^2 - [I_1(h_{1r}b)]^2). \tag{3.88}$$

In order to evaluate equations 3.87 and 3.88, the differentiation rule

$$\frac{\partial}{\partial h_{1j}} \ I_n(h_1 b) = \frac{\partial}{\partial h_{1j}} \ I_n(h_{1r} b + j \ h_{1j} b) = j \ b \ I_n{'}(h_1 b),$$

where $n = 0, 1$ and the $"'"$ denotes differentiation with respect to the total argument, was used. Furthermore, equations A.5 and A.7, the Bessel function recurrence relations, were employed.

Calculating the limits of equations 3.12, 3.14, and 3.16, as the imaginary parts of the radial and axial wave numbers approach zero, making use of equations 3.86 – 3.88, the following three equations are obtained.

$$P_{dr} \approx \frac{|u|^2}{4} \ \pi \ a^2 \ b \ \sigma \ (\frac{120\pi}{ka \ \cot\alpha\psi})^2 \ \cos^2\psi \ \cdot$$

$$\frac{(h_{2r}a)^2 \ (\beta_r a)^2}{h_{1r}b \ \beta_r b} \ [K_0(h_{2r}a)]^2 \ (h_{1r}b \ [I_1(h_{1r}b)]^2 \tag{3.89}$$

$$- h_{1r}b \ [I_0(h_{1r}b)]^2 + 2 \ I_0(h_{1r}b) \ I_1(h_{1r}b)) \ \cdot$$

$$\frac{[2 \ \beta_r \ z_1 - \sin(2 \ \beta_r \ z_1)]}{(h_{1r}a \ I_0(h_{1r}b) \ K_1(h_{2r}b) + \epsilon_r \ h_{2r}a \ I_1(h_{1r}b) \ K_0(h_{2r}b))^2} \ ,$$

$$P_{d\theta} \simeq \frac{|I|^2}{4} \pi a^2 b \sigma (120\pi)^2 \frac{(ka \cot\alpha\psi)^2}{h_{1r}b \beta_r b} \sin^2\psi \cdot$$

$$[K_1(h_{2r}a)]^2 (h_{1r}b [I_1(h_{1r}b)]^2 \qquad\qquad (3.90)$$

$$- h_{1r}b [I_0(h_{1r}b)]^2 + 2 I_0(h_{1r}b) I_1(h_{1r}b)) \cdot$$

$$\frac{[2 \beta_r z_1 + \sin(2 \beta_r z_1)]}{(h_{1r}a I_0(h_{1r}b) K_1(h_{2r}b) + h_{2r}a I_1(h_{1r}b) K_0(h_{2r}b))^2} \quad \text{and}$$

$$P_{dz} \simeq \frac{|I|^2}{4} \pi a^2 b \sigma (\frac{120\pi}{ka \cot\alpha\psi})^2 \cos^2\psi \cdot \qquad\qquad (3.91)$$

$$\frac{(h_{1r}a)^2 (h_{2r}a)^2}{\beta_r b} [K_0(h_{2r}a)]^2 ([I_0(h_{1r}b)]^2 - [I_1(h_{1r}b)]^2) \cdot$$

$$\frac{[2 \beta_r z_1 + \sin(2 \beta_r z_1)]}{(h_{1r}a I_0(h_{1r}b) K_1(h_{2r}b) + \epsilon_r h_{2r}a I_1(h_{1r}b) K_0(h_{2r}b))^2} \cdot$$

In equations 3.89 – 3.91, the quantity $\epsilon_r - j \sigma/\omega\epsilon_0$ has been approximated as ϵ_r. In order that these equations are in a form where they can be relatively easily numerically evaluated, it is desirable to make one additional approximation. This approximation is that

$$h_{1r}a \simeq h_{2r}a \simeq \beta_r a \simeq h^d a. \qquad\qquad (3.92)$$

$h^d a$ is the (single) wave number which determines the radial and axial spatial dependences of the approximate field components for the sheath helix surrounding an ideal dielectric coaxial rod. It is discussed in section D.2.

Substituting equations 3.92 into equations 3.89 – 3.91, equations 3.93 – 3.95 are obtained.

$$P_{dr} \cong \frac{|J_1|^2}{4} \, \pi \, a^3 \, \sigma \, (\frac{120\pi}{ka \, \cot an\psi})^2 \, \cos^2\psi \, \cdot$$

$$(h^d a)^2 \, [K_0(h^d a)]^2 \, (1 - \frac{\sin(2 \, h^d \, z_1)}{2 \, h^d \, z_1}) \, \frac{2 \, z_1}{a} \, \cdot \quad (3.93)$$

$$\frac{([I_1(h^d b)]^2 - [I_0(h^d b)]^2 + \frac{2}{h^d b} I_0(h^d b) \, I_1(h^d b))}{(I_0(h^d b) \, K_1(h^d b) + \epsilon_r \, I_1(h^d b) \, K_0(h^d b))^2},$$

$$P_{d\theta} \cong \frac{|J_1|^2}{4} \, \pi \, a^3 \, (b/a)^2 \, \sigma \, (120\pi)^2 \, (ka \, \cot an\psi)^2 \, \sin^2\psi \, \cdot$$

$$[K_1(h^d a)]^2 \, (1 + \frac{\sin(2 \, h^d \, z_1)}{2 \, h^d \, z_1}) \, \frac{2 \, z_1}{a} \, \cdot \quad (3.94)$$

$$([I_1(h^d b)]^2 - [I_0(h^d b)]^2 + \frac{2}{h^d b} I_0(h^d b) \, I_1(h^d b)), \quad \text{and}$$

$$P_{dz} \cong \frac{|J_1|^2}{4} \, \pi \, a^3 \, \sigma \, (\frac{120\pi}{ka \, \cot an\psi})^2 \, \cos^2\psi \, \cdot$$

$$(h^d a)^2 \, [K_0(h^d a)]^2 \, (1 + \frac{\sin(2 \, h^d \, z_1)}{2 \, h^d \, z_1}) \, \frac{2 \, z_1}{a} \, \cdot \quad (3.95)$$

$$\frac{([I_0(h^d b)]^2 - [I_1(h^d b)]^2)}{(I_0(h^d b) \, K_1(h^d b) + \epsilon_r \, I_1(h^d b) \, K_0(h^d b))^2}.$$

Relation A.25, which was obtained from the Bessel function Wronskian identity, was used for simplification in the derivation of equation 3.94.

Equations 3.93 - 3.95 are the approximate power dissipation equations when the lossy coaxial rod is an excellent dielectric, based on the wave number solution for

the sheath helix surrounding an ideal dielectric coaxial rod. Equation D.47 lists the variables needed to determine $_h{}^d{}_a$. From equations D.47 and 3.93 – 3.95, the variables on which the approximate power dissipation expressions are dependent can be stated.

$$P_{di} = f_i(ka \cot\psi, \; b/a, \; \epsilon_r, \; \psi, \; a, \; 2\,z_1/a, \; \sigma, \; \oint_{ii}), \quad (3.96)$$

where $i = r, \theta, z$.

It is mentioned in part D.2.1 that equations D.57, D.58, and D.59 must be satisfied to justify the usage of $_h{}^d{}_a$. These equations put a limit on how large the value of ϵ_r is allowed to be, and they will be more easily satisfied for a relatively tightly wound sheath helix. The value of $_h{}^d{}_a$ is obtained for the particular set of variables $ka \cot\psi, \; b/a, \; \epsilon_r,$ by solving the dispersion equation, equation D.41. Extensive graphs of this wave number solution are given in Figures D.1 – D.8. For small or large values of $_h{}^d{}_a$, the approximate representations, equations D.49 and D.53, respectively, can be used for the solution. Once the value of $_h{}^d{}_a$ is known, equations 3.93 – 3.95 can be directly evaluated for a particular set of the variables listed in equation 3.96.

A digression will now be made to discuss an alternative procedure which was used to derive approximate power dissipation equations, when the conductivity of the lossy rod is restricted to being very small. This is actually a *perturbation method* based on the region 1 electric fields associated with the sheath helix surrounding an ideal dielectric coaxial rod. When the conductivity of the lossy rod is very small, the approximation is made of using the ideal dielectric rod configuration fields in place of the actual lossy rod configuration fields. (For example, see 3, pp. 13.)

Equations D.23 – D.25, the approximate region 1 electric fields for the ideal dielectric rod configuration, are used in the integrand of equations 3.6 – 3.8. A similar procedure to that followed in section 3.1 is used to evaluate the three integrals. In the course of carrying out these calculations, it was necessary to make use of equation A.52, a relation involving the integral of Bessel functions; and equations A.5, A.7, which

are both Bessel function recurrence relations. It is discovered that the resulting approximate power dissipations associated with the radial, angular, and axial region 1 fields are exactly the same as the corresponding expressions listed in equations 3.93 – 3.95. *The power dissipation equations, which were obtained by making approximations to the exact expressions listed in section 3.1, are the same as those obtained based on a perturbation method involving the region 1 electric field components associated with the sheath helix surrounding an ideal dielectric coaxial rod.*

This demonstration serves two important purposes. First, it supports the accuracy of equations 3.93 – 3.95. Second, it provides a new way of regarding the approximations which were made to the exact power dissipation expressions, in order to derive equations 3.93 – 3.95. These approximations can be considered as being equivalent to replacing the region 1 electric fields associated with the lossy rod configuration, with the corresponding fields associated with the ideal dielectric rod configuration.

To conclude part 3.4.1, a discussion is given concerning the overlap involving the approximate power dissipation equations listed here and those given previously for the case when "the lossy rod is not a good conductor," parts 3.2.1 and 3.2.2. Equations 3.30 – 3.32 are the two and three region, small argument, approximate power dissipation expressions, when "the lossy rod is not a good conductor." The small argument Bessel function representations, equations A.26 – A.29, are used to approximate equations 3.93 – 3.95. The single exception is in the approximation of the quantity

$$[I_1(h^d b)]^2 - [I_0(h^d b)]^2 + \frac{2}{h^d b} I_0(h^d b) I_1(h^d b),$$

where it is necessary to use the approximations given by equations A.30 and A.31. The following additional approximations are made.

$$1 - \epsilon_r \frac{(h^d b)^2}{2} \log(0.891 \, h^d b) \simeq 1, \quad h^d a \cdot 2 z_1/a \ll 1, \quad (3.97)$$

which means that $\sin(2\,h^d\,z_1) \cong 2\,h^d\,z_1 - \dfrac{(2\,h^d\,z_1)^3}{6}$, (3.97)

and $\left(\dfrac{ka\,\cot an\psi}{h^d_a}\right)^2 \cong -2\,\log(0.891\,h^d_a)$, (continued)

which is equation D.49, the crude small argument approximation of the dispersion equation.

Making the previously mentioned approximations, it is discovered that equations 3.93 - 3.95 are transformed into equations 3.30 - 3.32. When the value of h^d_a is sufficiently small, the approximate power dissipation equations based on the ideal dielectric coaxial rod configuration wave number reduce to the small argument representations of the approximate power dissipation equations, for the case when "the lossy rod is not a good conductor." This latter mentioned case was previously discussed in part 3.2.1.

Consider the two region, large argument, approximate power dissipation expressions, equations 3.40 - 3.42, which were previously discussed in sub-part 3.2.2.1. The relation $\sigma/\omega\varepsilon_0 \cdot (ka\,\cot an\psi)^2 \cong -4\,h_r a\,h_j a$ is used, which is obtained by squaring equation 3.38 and then equating the imaginary parts. Furthermore, it is assumed that the conductivity of the lossy rod is sufficiently small so that $\sigma/\omega\varepsilon_0 \ll \varepsilon_r$. From equation 3.38, this means that $h_r a \gg |h_j|a$. Finally, the limit of equations 3.40 - 3.42 is taken as the imaginary part of the (single) wave number solution approaches zero. The following relation is used.

$$\lim_{h_j \to 0} \frac{[h_r a\,\sinh(2\,h_j\,z_1) \pm h_j a\,\sin(2\,h_r\,z_1)]}{h_j a}$$

$$= h_r a\,\frac{2\,z_1}{a} \pm \sin(2\,h_r\,z_1) \cong h_r a\,\frac{2\,z_1}{a}.$$

Attention is now directed to equations 3.93 - 3.95, for the special case when $b = a$. Just the first term of equations A.38, A.39, and the first two terms of equations A.36, A.37, the large argument Bessel function representations, are used to approximate equations 3.93 - 3.95. To justify usage of these representations, it is necessary that $_h{}^d_a > 1$. The approximate two region, large argument dispersion equation, equation D.54, is used. Finally, it is assumed that

$$2\, z_1/a \geq 10, \text{ which means that } 1 \pm \frac{\sin(2\, h^d\, z_1)}{2\, h^d\, z_1} \cong 1. \quad (3.98)$$

Making use of the restrictions and assumptions mentioned in the preceding two paragraphs, it is discovered that equations 3.93 - 3.95 equal the corresponding equation of the set 3.40 - 3.42. When the wave number $_h{}^d_a$ is assumed to be sufficiently large in the equations considered in part 3.4.1, and when the value of the lossy rod conductivity associated with the equations considered in sub-part 3.2.2.1 becomes sufficiently small, the two sets of approximate power dissipation equations agree with each other.

Finally, the three region, large argument, approximate power dissipation expressions, equations 3.50 - 3.52, which were previously discussed in sub-part 3.2.2.2, are considered. It is assumed that the conductivity of the lossy rod is sufficiently small so that $\sigma/\omega\epsilon_0 << \epsilon_r$. Furthermore, it is assumed that the sheath helix is sufficiently tightly wound so that $\cotan^2\psi >> \epsilon_r$. From equations 3.46, this means that $|h_1|a \cong h_{1r}a \cong ka\cotan\psi$.

Equations 3.93 - 3.95 are now investigated. Just the first term of equations A.38, A.39, and the first two terms of equations A.36, A.37, are used to approximate the previously mentioned expressions. To justify using the large argument Bessel function representations, it is necessary that $_h{}^d_b > 1$. The assumption listed in equation 3.98 is used. Finally, the three region, large argument approximation of the

dispersion equation, equation D.53, is used.

When the restrictions and assumptions mentioned in the previous two paragraphs are made, it is discovered that equations 3.93 - 3.95 agree with the corresponding expression of equations 3.50 - 3.52. For a sufficiently large value of $h^d{}_a$, the approximate power dissipation expressions given in part 3.4.1 become the same as the approximate expressions given in sub-part 3.2.2.2, provided that for the latter mentioned equations, the conductivity of the lossy rod is assumed to be sufficiently small.

In summary, a discussion has been given of the overlap between the approximate power dissipation equations given in part 3.4.1 and those given in part 3.2.1, sub-part 3.2.2.1, and sub-part 3.2.2.2. It was discovered that if the value of $h^d{}_a$ is assumed to be sufficiently small or sufficiently large, and if the value of the lossy rod conductivity is assumed to be sufficiently small, then the approximate power dissipation equations based on the wave number solution for the ideal dielectric coaxial rod configuration, become the approximate small and large argument power dissipation equations, respectively, for the case when "the lossy rod is not a good conductor". This result is expected. It provides a check on the accuracy of the previously mentioned equations.

3.4.2 Graphs of P_{dr}/P_{dz} and $P_{d\theta}/P_{dz}$

It is desirable to know how much of a contribution towards the total power dissipation is associated with each of the three electric fields present in the rod-filled region. In particular, knowing which electric field provides the dominant contribution is useful. This means that the total power dissipation occurring within the lossy coaxial rod element is approximately given by a single equation of the set 3.93 - 3.95. The total power dissipation can be studied more easily now than it could if all three of the previously mentioned equations had to be considered.

The contribution that each of the radial, angular, and axial region 1 electric field components makes towards the total power dissipation is obtained by examining the ratios P_{dr}/P_{dz} and $P_{d\theta}/P_{dz}$. These ratios are easily obtained from the power dissipation expressions, equations 3.93 - 3.95.

$$\frac{P_{dr}}{P_{dz}} = \frac{([I_1(h^d b)]^2 - [I_0(h^d b)]^2 + \frac{2}{h^d b} I_0(h^d b) I_1(h^d b))}{([I_0(h^d b)]^2 - [I_1(h^d b)]^2)} \cdot$$

$$\cdot \frac{(2 h^d z_1 - \sin(2 h^d z_1))}{(2 h^d z_1 + \sin(2 h^d z_1))}, \quad \text{and} \tag{3.99}$$

$$\frac{P_{d\theta}}{P_{dz}} = (\frac{ka \text{ cotan}\psi}{h^d a})^4 (h^d b)^2 \tan^2\psi \frac{[K_1(h^d a)]^2}{[K_0(h^d a)]^2} \cdot \tag{3.100}$$

$$\frac{([I_1(h^d b)]^2 - [I_0(h^d b)]^2 + \frac{2}{h^d b} I_0(h^d b) I_1(h^d b))}{([I_0(h^d b)]^2 - [I_1(h^d b)]^2)} \cdot$$

$$(I_0(h^d b) K_1(h^d b) + \epsilon_r I_1(h^d b) K_0(h^d b))^2.$$

Equations 3.99 and 3.100 are the power dissipation ratios, when the lossy rod is an excellent dielectric, based on the ideal dielectric rod configuration wave number solution. Making use of equation D.47, which lists the variables on which the wave number $h^d a$ is dependent, the functional dependences of the previous two equations can be stated.

$$\frac{P_{dr}}{P_{dz}} = f(ka\ cotan\psi,\ b/a,\ \epsilon_r,\ 2\ z_1/a),\quad and$$

$$\frac{P_{d\theta}}{P_{dz}} = g(ka\ cotan\psi,\ b/a,\ \epsilon_r,\ \psi). \tag{3.101}$$

Equations 3.99 and 3.100 are more easily understood if approximate forms of them are derived. These approximations are valid when the Bessel function arguments are either small or large. First, the small argument representations are considered. Equations A.30 and A.31 are used to approximate the quantity

$$[I_1(h^d b)]^2 - [I_0(h^d b)]^2 + \frac{2}{h^d b}\ I_0(h^d b)\ I_1(h^d b).$$

Equations A.26 - A.29 are used to approximate all the other Bessel functions appearing in equations 3.99 and 3.100. To justify the usage of these small argument Bessel function representations, it is necessary that $h^d a < 0.100$. One discovers that

$$\frac{P_{dr}}{P_{dz}} \simeq \frac{(b/a)^2}{96}\ (h^d a)^2\ (2\ h^d\ z_1)^2,\quad and \tag{3.102}$$

$$\frac{P_{d\theta}}{P_{dz}} \simeq \frac{(b/a)^2}{2}\ tan^2\psi \tag{3.103}$$

are the small argument forms of equations 3.99 and 3.100, for the three region (b < a) configuration. When performing the calculations required to obtain equation 3.103, equation D.49, the small argument approximate dispersion equation, was used. Furthermore, it was assumed that the value of $h^d a \cdot b/a$ is sufficiently small for the particular value of ϵ_r which is specified, so that

$$1 - \epsilon_r \frac{(h^d b)^2}{2} \log(0.891\ h^d b) \cong 1.$$

In order to obtain equation 3.102, it was assumed that the value of $_h d_a$ is sufficiently small for the specified value of the lossy coaxial rod element length normalized with respect to the sheath helix radius, $2\ z_1/a$, so that

$$2\ h^d\ z_1 = h^d a \cdot 2\ z_1/a \ll 1.$$

Therefore, $\sin(2\ h^d\ z_1) \cong 2\ h^d\ z_1 - \frac{(2\ h^d\ z_1)^3}{6}$.

The value of $_h d_a$, which appears in equation 3.102, is approximately evaluated using the small argument form of the dispersion equation, equation D.49.

The special case of the power dissipation ratios associated with the two region configuration (b = a) can be obtained by simply taking the limit as $b \to a^-$ of equations 3.102 and 3.103. Equation D.49 shows that for a particular value of $ka\ \cot an\psi$, the wave number solution $_h d_a$, which appears in equation 3.102, is the same for both the two and three region configurations.

The large argument representations of equations 3.99 and 3.100 are now considered. The first two terms of equations A.36 and A.37 are used to approximate the expression

$$\frac{[I_1(h^d b)]^2 - [I_0(h^d b)]^2 + \frac{2}{h^d b} I_0(h^d b)\ I_1(h^d b)}{[I_0(h^d b)]^2 - [I_1(h^d b)]^2}.$$

Just the first term of equations A.36 - A.39 is used to represent all the other Bessel functions appearing in equation 3.100. To justify usage of these large-argument Bessel function approximations, it is necessary that $h^d b > 1$. It follows that

$$\frac{\dot{P}_{dr}}{P_{dz}} \cong 1, \quad \text{and} \tag{3.104}$$

$$\frac{P_{d\theta}}{P_{dz}} \cong \frac{1}{4} (\epsilon_r + 1)^2 \tan^2 \psi. \tag{3.105}$$

are the large argument representations of the power dissipation ratios, for the three region configuration.

It was necessary to assume that $_h d_a \cong k a \cot an \psi$ when the derivation of equation 3.105 was performed. This assumption is just a statement of the three region, large argument, approximate dispersion equation, equation D.53. In part D.2.1, it is mentioned that equation D.53 is approximately valid when $k a \cot an \psi \cdot$ $(1-b/a) > 1$. During the calculations followed to obtain equation 3.104, it was assumed that $2 z_1/a \geq 10$.

The special case of the two region, large argument, power dissipation ratios is now considered. These are obtained from equations 3.99 and 3.100 by using a similar procedure to that followed to derive equations 3.104 and 3.105. However, the two region, large argument, approximate dispersion equation, equation D.54, is used, instead of the three region, large argument equation, equation D.53. It is discovered that

$$\frac{P_{dr}}{P_{dz}} \cong 1, \quad \text{and} \tag{3.106}$$

$$\frac{P_{d\theta}}{P_{dz}} \cong \tan^2 \psi \tag{3.107}$$

are the large argument approximate power dissipation ratios, for the two region configuration. Note that equations 3.106 and 3.104 are identical, but equations 3.107

and 3.105 are different.

The ratios $P_{d\theta}/P_{dz}$ and P_{dr}/P_{dz} have been visually represented as graphs for some typical sets of the variables mentioned in equations 3.101. These graphs were obtained by first solving the dispersion equation, equation D.41, for the specified values of $ka \cot an\psi$, b/a, ϵ_r, in order to obtain $_h{}^d{}_a$. Equations 3.99 and 3.100 are then directly numerically evaluated. A single graph based on each of equations 3.99 and 3.100 has been prepared. For these two graphs, it was always ensured that equations D.57 and D.59 are satisfied, so that the usage of $_h{}^d{}_a$ as the single wave number determining the radial and axial spatial dependences of the ideal dielectric rod configuration field components is justified. (This is discussed in part D.2.1.)

Figure 3.12 is a graph of $P_{d\theta}/P_{dz}$ versus ka. $\psi = 0.100°$, $1.00°$; $b/a = 0.100$, 0.900; $\epsilon_r = 2.00$, 1.00×10^2; and $1.00 \times 10^{-4} < ka < 10.0$ are used. (Note that quite small values of the pitch angle were used in order to satisfy equation D.59.) Equations 3.103 and 3.105 are seen to be in good agreement with the curves for very small and large values of ka, respectively. For very small values of ka (or, equivalently, small values of $ka \cot an\psi$), it is clear that $P_{dz} >> P_{d\theta}$. In addition, when ka is large (or, equivalently, $ka \cot an\psi$ is large), $P_{dz} > P_{d\theta}$ is usually true. This is apparent from equation 3.105, keeping in mind that $4 \epsilon_r \tan^2\psi < 1$ must be true, since this is just a statement of equation D.57. Only if ϵ_r is very large and ψ is small will it be possible to satisfy the previously mentioned inequality, and also satisfy the inequality $\frac{1}{4}(\epsilon_r+1)^2 \cdot \tan^2\psi > 1$. Except for this special case of the large argument form of the ratio $P_{d\theta}/P_{dz}$, equations 3.103, 3.105, 3.107, and Figure 3.12 show that for both the two and three region configurations, the contribution to the total power dissipation associated with the region 1 axial electric field is usually much larger than that associated with the region 1 angular electric field.

Figure 3.13 shows several different curves of the ratio P_{dr}/P_{dz}, plotted versus ka. $2 z_1/a = 10.0$; $\psi = 0.100°$, $1.00°$; $b/a = 0.100$, 0.900; $\epsilon_r = 2.00$, 1.00×10^2; and $1.00 \times 10^{-4} < ka < 10.0$ are used. When ka is small or large, equations 3.102 and 3.104, respectively, are seen to be in good agreement with the curves. Equations 3.102, 3.104, 3.106, and Figure 3.13
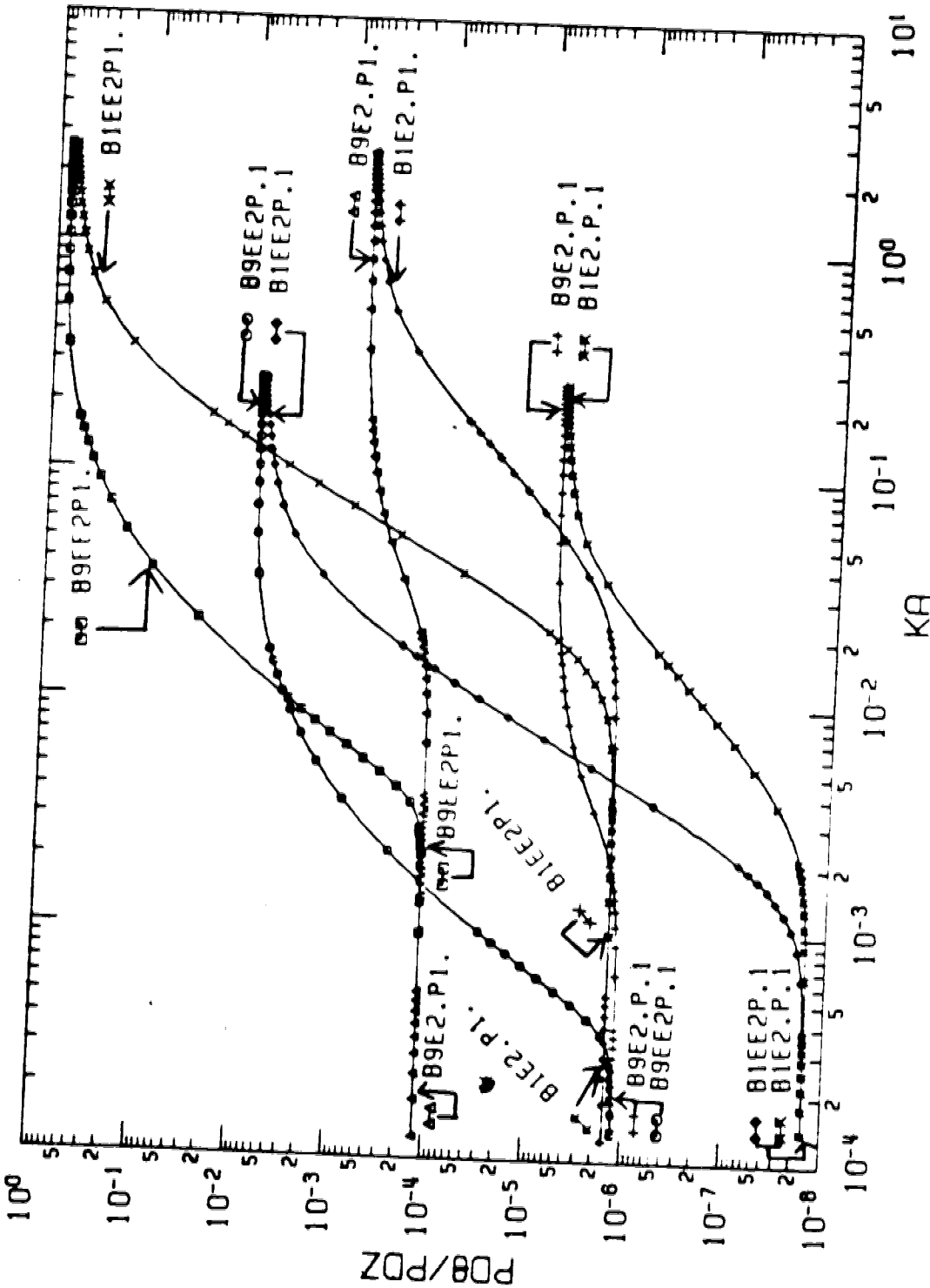
PLOT OF PDθ/PDZ VS. KA

Figure 3.12 Graph of $P_{d\theta}/P_{dz}$ versus ka, based on equation 3.100. The lossy rod is an excellent dielectric. Curves for b/a=0.10, 0.90; ψ=0.10°, 1.0°; ϵ_r=2.0, 100.0; and 1.00×10^{-4}<ka<10.0 are shown. (Note PDθ=$P_{d\theta}$, PDZ=P_{dz}, and KA=ka. B1E2.P.1 means the curve represents b/a=0.10, ϵ_r=2.0, and ψ=0.10°. B9EE2P1. means the curve represents b/a=0.90, ϵ_r=100.0, and ψ=1.0°.)
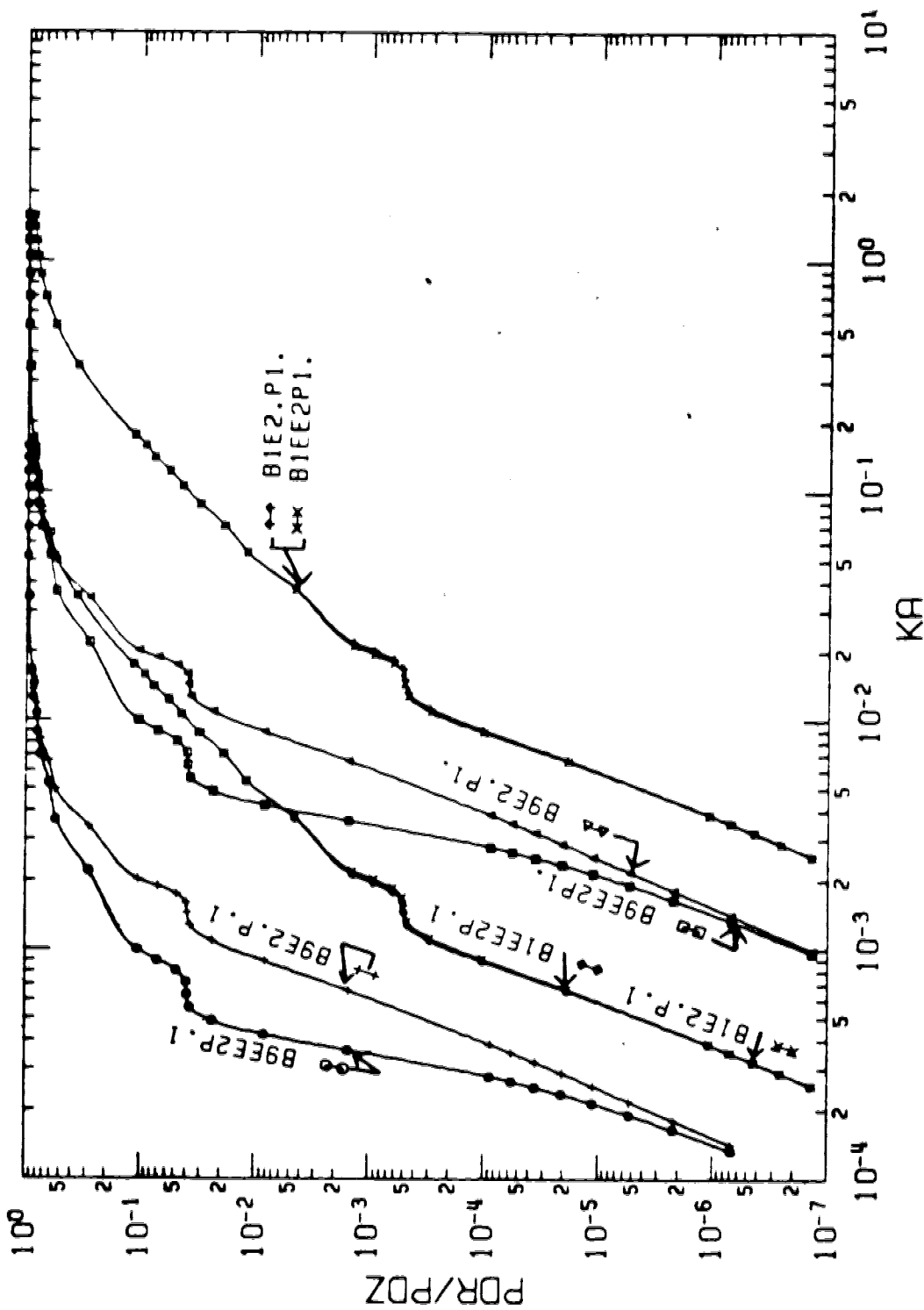
PLOT OF PDR/PDZ VS. KA

Figure 3.13 Graph of P_{dr}/P_{dz} versus ka, based on equation 3.99. The lossy rod is an excellent dielectric. Curves for b/a=0.10, 0.90; ψ=0.10°, 1.0°; ϵ_r=2.0, 100.0; 2 z_1/a=10.0; and 1.00×10^{-4}<ka<10.0 are shown. (Note PDR=P_{dr}, PDZ=P_{dz}, and KA=ka. B1E2.P.1 means the curve represents b/a=0.10, ϵ_r=2.0, and ψ=0.10°. B9EE2P1. means the curve represents b/a=0.90, ϵ_r=100.0, and ψ=1.00°.)

show that when the value of ka is very small (which means that $ka \cot an\psi$ is small), $P_{dz} >> P_{dr}$ occurs. On the other hand, when ka is large (which means that $ka \cot an\psi$ is large), P_{dr} and P_{dz} are, to a good approximation, equal in value. The preceding two sentences are valid for both the two region and three region configurations.

In summary, the previous discussion has assumed that the sheath helix is tightly wound and it is has shown that for small values of $ka \cot an\psi$ (which also means that $h^d{}_a$ is small) $P_{dr}/P_{dz} << 1$ and $P_{d\theta}/P_{dz} << 1$ occurs. When $ka \cot an\psi$ is large (which means that $h^d{}_a$ is large), the region 1 axial electric field usually contributes significantly more to the total power dissipation than the region 1 angular electric field. However, in this situation, the region 1 radial electric field makes a contribution equally as large as that of the axial electric field.

For both the two region and three region configurations, when the lossy rod is an excellent dielectric, so that the ideal dielectric coaxial rod configuration wave number solution can be used, the contribution to the total power dissipation associated with the region 1 axial electric field is usually much larger than that associated with the region 1 radial and angular electric fields. One exception to the previous sentence occurs when the value of $ka \cot an\psi$ is large. In this situation, the region 1 radial and axial electric fields each contribute nearly half of the total power dissipation, for both the two region and three region configurations.

3.4.3 Graphs of the Spatial Distribution of the Power Dissipation, Based on E_{z1}

The preceding part, part 3.4.2, has shown that the contribution to the total power dissipation associated with the region 1 axial electric field is much greater than the contribution associated with the region 1 radial and angular electric fields, for small values of $h^d{}_a$, assuming that the sheath helix is relatively tightly wound. For large values of $h^d{}_a$, the power dissipation contributions associated with the region 1 axial and radial electric fields are equal, and they are usually much larger than that associated with the region 1 angular electric field.

An understanding of how the total ohmic heating is distributed at different points within the lossy coaxial rod element can be achieved by following the procedure

suggested by Brown et al. (3, pp. 13). This involves defining the dimensionless ratio ξ_z, which is a function of the radial and axial spatial position.

$$\xi_z(r_0, z_0) = \frac{\frac{\sigma}{2} \int_V |E_{z1}\#|^2 \, dV}{\frac{\sigma}{2} \int_V |E_{z1}|^2 \, dV} = \frac{\frac{\sigma}{2} |E_{z1}\#|^2 \int_V dV}{P_{dz}}$$

$$= \frac{\frac{\sigma}{2} \pi b^2 \, 2 \, z_1 \, |E_{z1}\#|^2}{P_{dz}} \qquad (3.108)$$

The volume of integration is taken as the lossy coaxial rod element volume. P_{dz}, as given by equation 3.95, is the contribution to the power dissipation associated with the region 1 axial electric field. $|E_{z1}\#|$ is the magnitude of the region 1 axial electric field for the case when the lossy rod is an excellent dielectric, based on the ideal dielectric coaxial rod configuration wave number solution, evaluated at a particular point (r_0, z_0) within the lossy coaxial rod element. Furthermore, this electric field is now assumed to be constant in magnitude throughout the lossy coaxial rod element volume, which means that it can be taken outside of the integral sign, as was done in equations 3.108.

Whenever ξ_z is greater than unity at a particular point, the meaning is that if the axial electric field which exists at that point had the same value at all points throughout the lossy coaxial rod element volume, the associated power dissipation would be greater than P_{dz}. Therefore, studying the value of ξ_z at several different points gives information concerning the spatial distribution associated with the power dissipation or the ohmic heating, which arises from the contribution associated with E_{z1}. When this contribution is much larger than that associated with the two other region 1 electric fields, ξ_z approximately represents the spatial distribution of *the total power dissipation occuring within the lossy coaxial rod element.*

In order to evaluate equations 3.108, it is necessary to obtain $E_{z1}\#$. This is done from the (exact) axial region 1 electric field component, as given by equation 3.4, by making the approximations listed in equations 3.85 and 3.92. It is discovered that

$$E_{z1}\#(r_0, z_0) = j \frac{\partial H}{b/a} \frac{120\pi}{ka \cot an\psi} \cos\psi \, h^d a \cdot \quad (3.109)$$

$$\frac{K_0(h^d a) \, I_0(h^d r_0) \, \cos(h^d z_0)}{(I_0(h^d b) \, K_1(h^d b) + \epsilon_r \, I_1(h^d b) \, K_0(h^d b))}$$

is the region 1 axial electric field associated with the case when the lossy rod is an excellent dielectric, based on the ideal dielectric coaxial rod configuration wave number solution, $h^d a$. (Note that equation 3.109 is the same as equation D.25. Applying the approximations listed in equations 3.85 and 3.92 to the (exact) region 1 electric field components associated with the lossy coaxial rod configuration, the electric fields associated with the ideal dielectric coaxial rod configuration are obtained. This is an expected result. It was previously mentioned in part 3.4.1 that the approximate power dissipation expressions, equations 3.93 - 3.95, could be obtained by using a perturbation procedure based on the ideal dielectric coaxial rod configuration region 1 electric fields.)

Equations 3.95 and 3.109 are used to evaluate equation 3.108. It is easily shown that

$$\xi_z(r_0, z_0) = \frac{2 \, [I_0(h^d r_0)]^2}{([I_0(h^d b)]^2 - [I_1(h^d b)]^2)} \cdot$$

$$\frac{\cos^2(h^d z_0)}{(1 + \frac{\sin(2 \, h^d z_1)}{2 \, h^d z_1})} \cdot \quad (3.110)$$

Making use of equation D.47, which lists the variables on which the wave number $_h{}^d{}_a$ is dependent, the nonspatial functional dependence of ξ_z is

$$\xi_z = f(ka \; cotan\psi, \; b/a, \; \epsilon_r, \; 2 \; z_1/a). \qquad (3.111)$$

ξ_z has been visually represented, to show the spatial distribution of the power dissipation associated with the region 1 axial electric field, using several different sets of the variables mentioned in equation 3.111. $\xi_z(r_0, 0)$ was plotted versus r_0/b to show the radial dependence occurring at the transverse plane $z_0 = 0$. $\xi_z(b, z_0)$ was plotted versus z_0/z_1 to show the axial dependence occurring at the lossy rod surface. The numerical solution was achieved by first solving equation D.41, the dispersion equation associated with the ideal dielectric coaxial rod configuration, for the specified values of the variables $ka \; cotan\psi$, b/a, ϵ_r, in order to obtain $_h{}^d{}_a$. Equation 3.110 was then directly evaluated.

The six figures presented here are each chacterized by $b/a = 0.100, 0.500, 0.900$; $\epsilon_r = 10.0$; $2 \; z_1/a = 10.0$; and a particular value of $ka \; cotan\psi$. (Note that the pitch angle does not have to be explicitly specified. However, it must be sufficiently small so that equations D.57 and D.59 are satisfied in order that the usage of the wave number $_h{}^d{}_a$ is justified. As an example, $\psi = 1.00°$ could be used in these figures.)

Figure 3.14 illustrates $\xi_z(r_0, 0)$ versus r_0/b, for $0 \leq r_0/b \leq 1$ and $ka \; cotan\psi = 10.0$. Clearly, when $b/a = 0.900$, the ohmic heating is large at the lossy rod surface, and it decays rapidly as the value of r_0/b decreases. However, when $b/a = 0.100$, the ohmic heating is smaller at $r_0 = b$, and it exhibits only a slow change as the normalized radial position, r_0/b, is varied.

Figure 3.15 displays $\xi_z(b, z_0)$ versus z_0/z_1, for $0 \leq z_0/z_1 \leq 0.20$ and $ka \; cotan\psi = 10.0$. Each of the three curves shows that the ohmic heating is distributed very nonuniformly along the lossy coaxial rod element surface. It is large at some points but it is small just a short axial distance away. The maximum value of ξ_z tends to increase as the value of b/a increases.
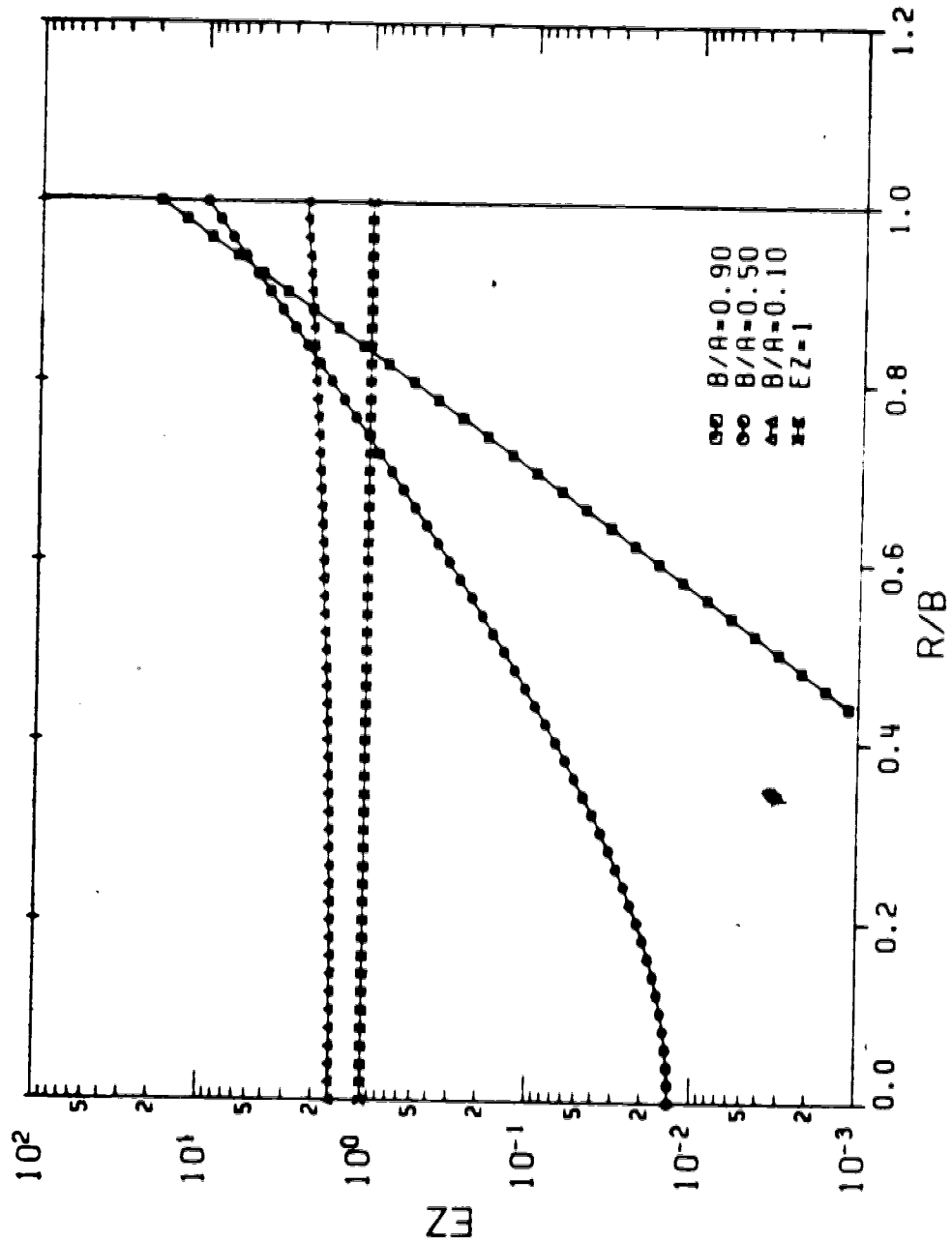
PLOT OF EZ VS. R/B FOR Z=0 WHEN KA CP=10.0

Figure 3.14   Graph of ξ_z versus r_0/b for $z_0=0$, based on equation 3.110. The lossy rod is an excellent dielectric Curves for $b/a=0.10$, 0.50, 0.90; $\epsilon_r=10.0$; $2\ z_1/a=10.0$; ka cotan$\psi=10.0$; and $0.0\leq r_0/b\leq1.00$ are shown. The line $\xi_z=1.00$ is presented. (Note EZ=ξ_z, R/B=r_0/b, Z=z_0, KA CP=ka cotanψ, and B/A=b/a.)
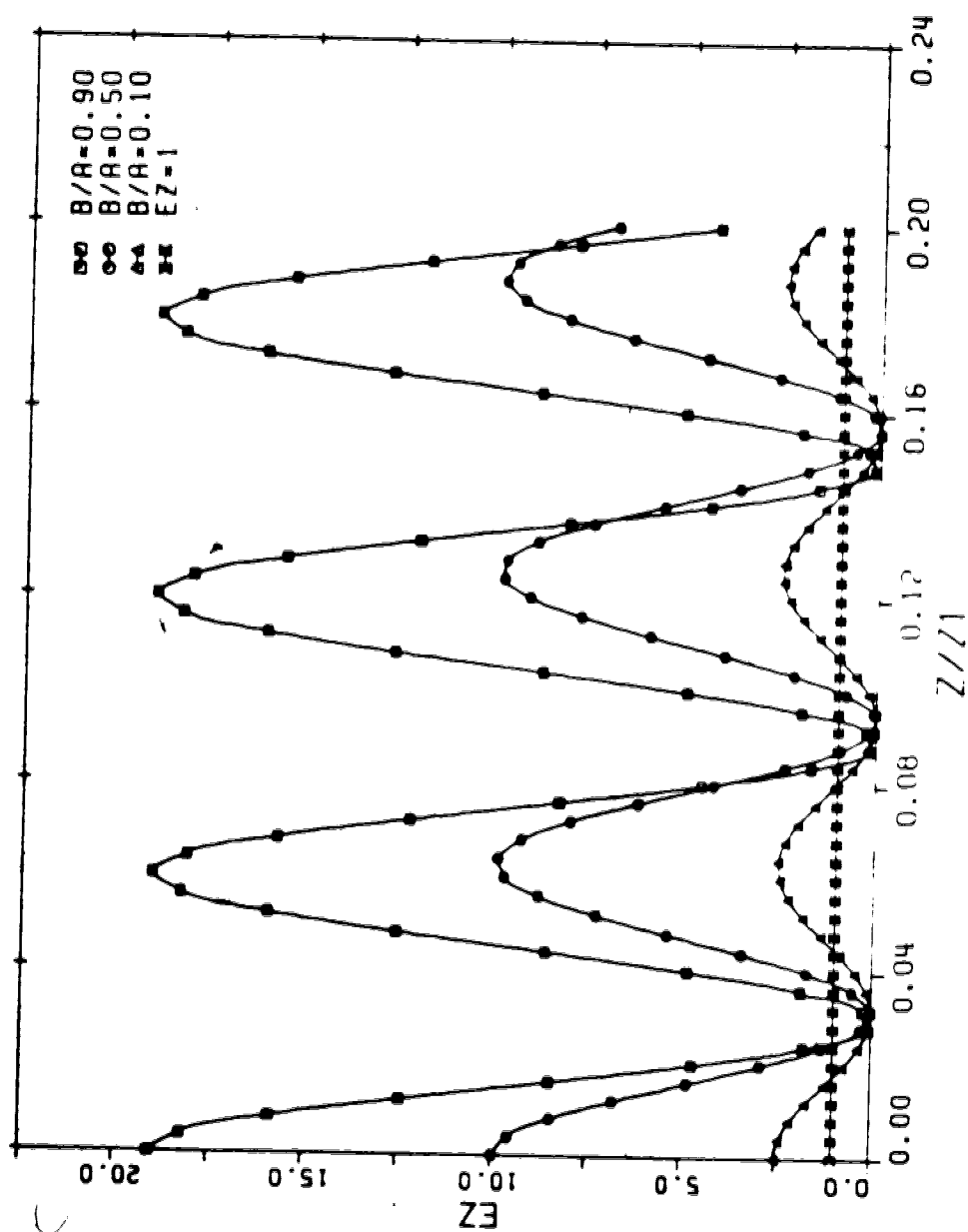
Figure 3.15 Graph of ξ_z versus z_0/z_1 for $r_0 = b$, based on equation 3.110. The lossy rod is an excellent dielectric. Curves for $b/a = 0.10$, 0.50, 0.90; $\epsilon_r = 10.0$; $2\, z_1/a = 10.0$; ka cotan$\psi = 10.0$; and $0.0 \leqslant z_0/z_1 \leqslant 0.20$ are given. The line $\xi_z = 1.00$ is shown. (Note $EZ = \xi_z$, $R = r_0$, $Z/Z1 = z_0/z_1$, KA CP $= $ ka cotanψ, and $B/A = b/a$.)

The next two graphs are based on $ka \cot an\psi = 0.500$. Figure 3.16 displays $\xi_z(r_0, 0)$ versus r_0/b for $0 \le r_0/b \le 1$. It is obvious that the ohmic heating is approximately uniform throughout the transverse plane $z_0 = 0$, for a particular value of b/a. Furthermore, the value of b/a does not have a very strong effect on the ohmic heating.

The other graph of the previously mentioned set, Figure 3.17, shows $\xi_z(b, z_0)$ versus z_0/z_1 for $0 \le z_0/z_1 \le 1.00$. At $z_0 = 0$, the ohmic heating is large but it becomes small near the endfaces of the lossy coaxial rod element. Once again, the value of b/a does not have a great effect on the ohmic heating.

Finally, two graphs were prepared using $ka \cot an\psi = 1.00 \times 10^{-2}$. Figure 3.18 displays $\xi_z(r_0, 0)$ versus r_0/b for $0 \le r_0/b \le 1$. $\xi_z = 1$ is now true for $b/a = 0.100, 0.500, 0.900$, and for all values of r_0/b. This has the meaning that the ohmic heating occurs uniformly within the lossy coaxial rod element, at the plane $z_0 = 0$.

Figure 3.19 is the second graph of the previously mentioned set. It illustrates $\xi_z(b, z_0)$ versus z_0/z_1 for $0 \le z_0/z_1 \le 1$. Once again, $\xi_z = 1$ occurs. This is true for all three values of b/a and for all values of z_0/z_1. Taken together, Figures 3.18 and 3.19 show that the ohmic heating is uniformly distributed at all points within the lossy coaxial rod element.

It has been previously mentioned at the beginning of part 3.4.3 and in part 3.4.2, that for large values of $ka \cot an\psi$ (which also means large values of $h^d a$), the region 1 radial electric field makes the same contribution to the total power dissipation as the region 1 axial electric field, and both of these are usually much larger than the contribution associated with the region 1 angular electric field. Although to a good approximation, Figures 3.16 – 3.19 represent the spatial distribution of *the total power dissipation occurring within the lossy coaxial rod element*, this is not necessarily true of Figures 3.14 and 3.15, because the power dissipation contribution associated with the region 1 radial electric field has been neglected.

A similar procedure to that followed at the beginning of part 3.4.3 was used, in order to calculate $\xi_r(r_0, z_0)$. Equation 3.93, the approximate power dissipation
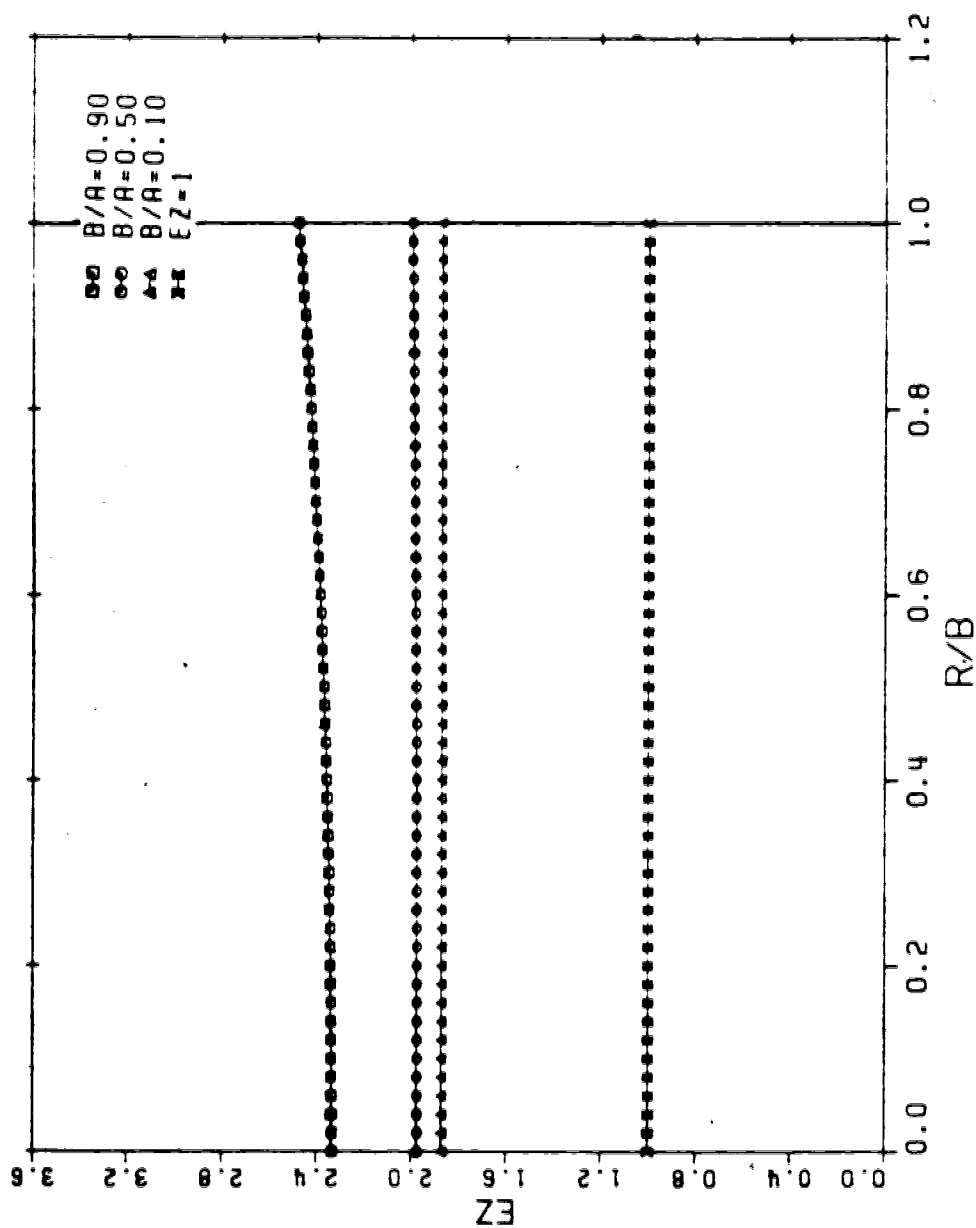
Figure 3.16   Graph of ξ_z versus r_0/b for $z_0=0$, based on equation 3.110. The lossy rod is an excellent dielectric. Curves for $b/a=0.10$, 0.50, 0.90; $\epsilon_r=10.0$; $2\ z_1/a=10.0$; ka cotan$\psi=0.50$; and $0.0 \leqslant r_0/b \leqslant 1.00$ are shown. The line $\xi_z=1.00$ is given. (Note $EZ=\xi_z$, $R/B=r_0/b$, $Z=z_0$, KA CP $=$ka cotanψ, and $B/A=b/a$.)
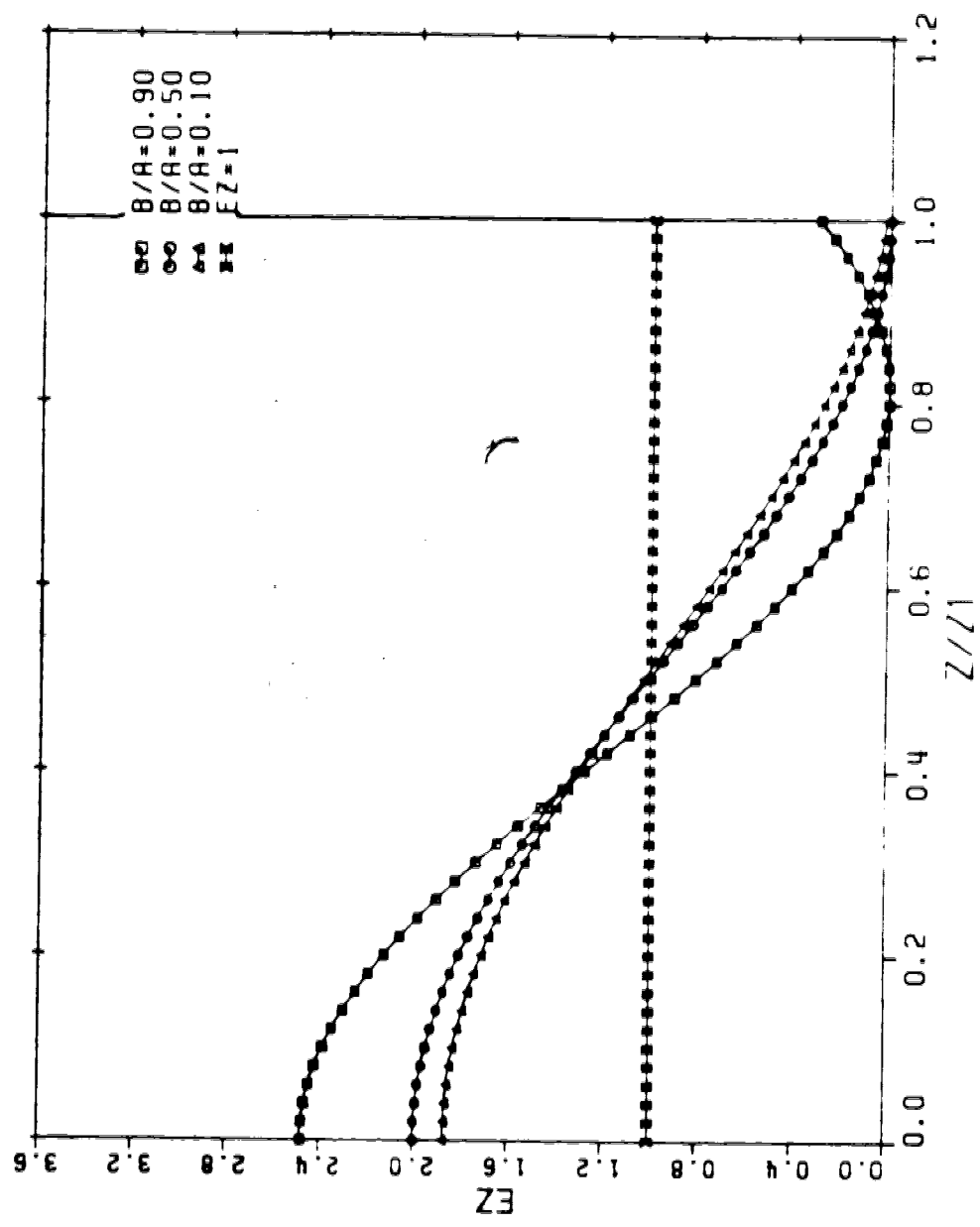
Figure 3.17   Graph of ξ_z versus z_0/z_1 for $r_0 = b$, based on equation 3.110. The lossy rod is an excellent dielectric Curves for $b/a = 0.10$, 0.50, 0.90; $\epsilon_r = 10.0$; $2 z_1/a = 10.0$; ka cotan$\psi = 0.50$; and $0.0 \leq z_0/z_1 \leq 1.00$ are given. The line $\xi_z = 1.00$ is shown. (Note EZ$=\xi_z$, R$=r_0$, Z/Z1$=z_0/z_1$, KA CP $=$ka cotanψ, and B/A$=$b/a.)
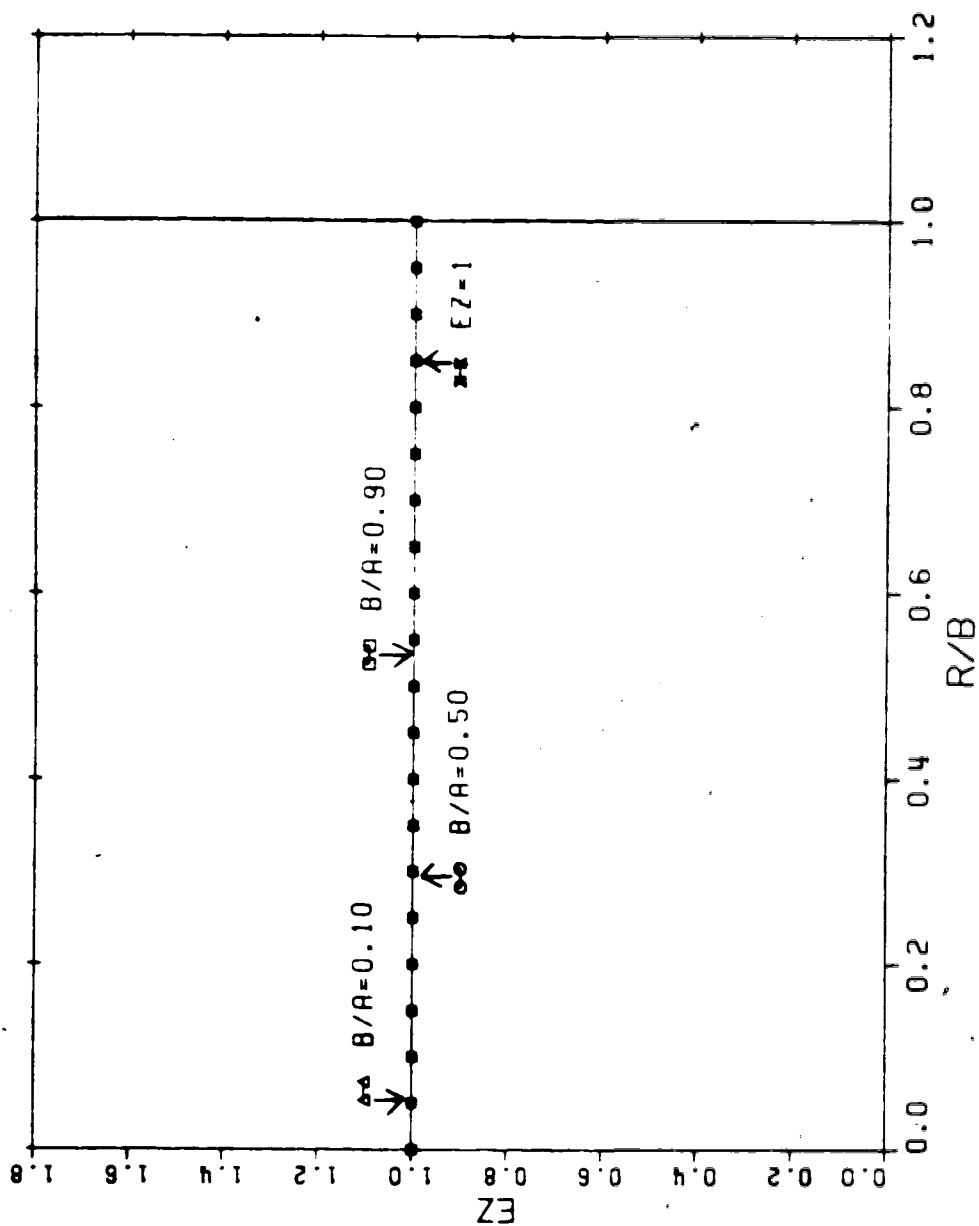
PLOT OF EZ VS. R/B FOR Z=0 WHEN KA CP=1.00E-2

Figure 3.18   Graph of ξ_z versus r_0/b for $z_0 = 0$, based on equation 3.110. The lossy rod is an excellent dielectric. Curves for $b/a = 0.10$, 0.50, 0.90; $\epsilon_r = 10.0$; 2 $z_1/a = 10.0$; ka cotan$\psi = 1.00 \times 10^{-2}$; and $0.0 < r_0/b \leqslant 1.00$ are shown. The line $\xi_z = 1.00$ is presented. (Note $EZ = \xi_z$, $R/B = r_0/b$, $Z = z_0$, KA CP = ka cotanψ, and B/A = b/a.)
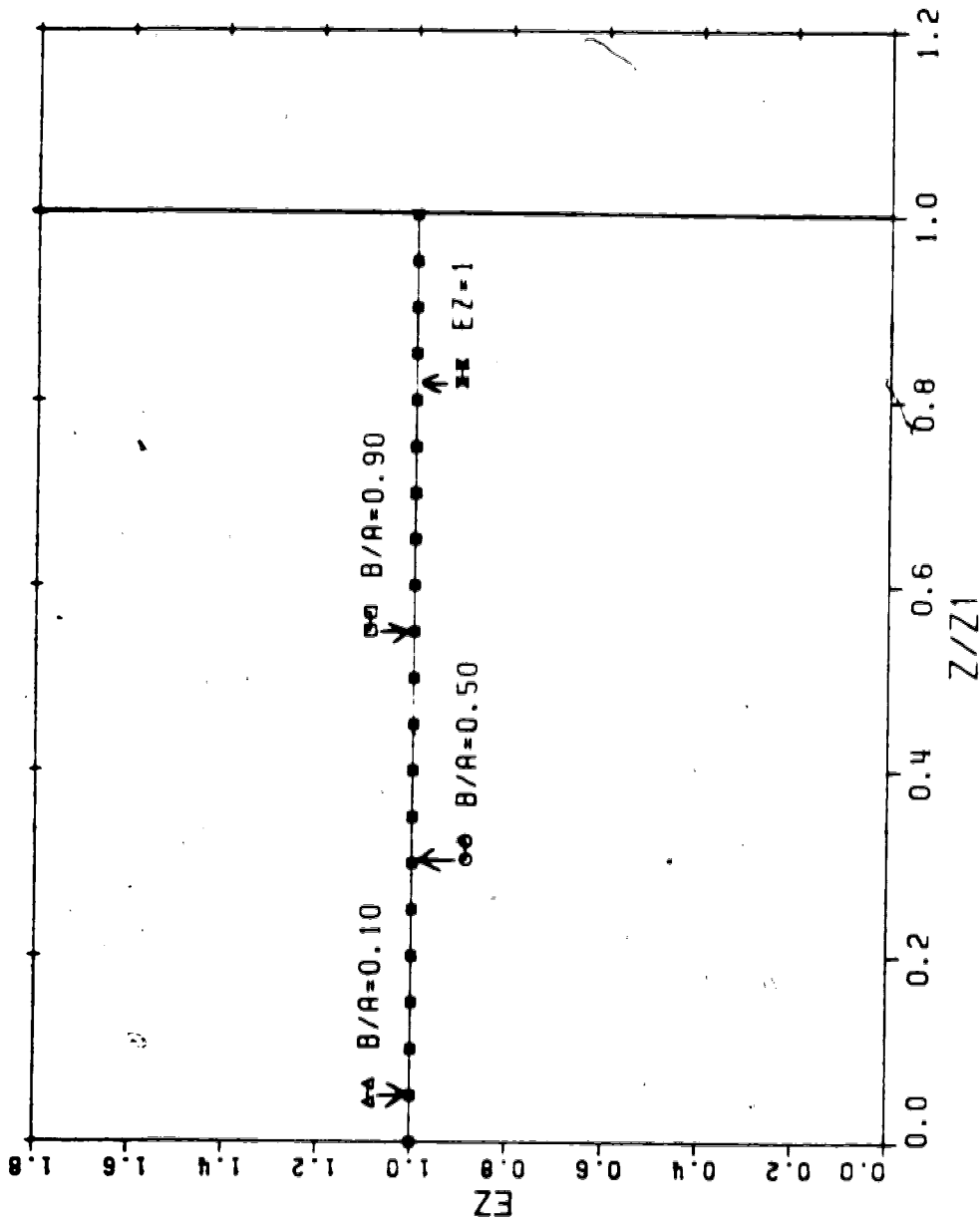
PLOT OF EZ VS. Z/Z1 FOR R=B WHEN KA CP=1.00E-2

Figure 3.19   Graph of ξ_z versus z_0/z_1 for r_0=b, based on equation 3.110. The lossy rod is an excellent dielectric. Curves for b/a=0.10, 0.50, 0.90; ϵ_r=10.0; 2 z_1/a=10.0; ka cotanψ=1.00x10^{-2}; and $0.0 \le z_0/z_1 \le 1.00$ are given. The line ξ_z=1.00 is shown. (Note EZ=ξ_z, R=r_0, Z/Z1=z_0/z_1, KA CP=ka cotanψ, and B/A=b/a.)

associated with the region 1 radial electric field, for the case when the lossy rod is an excellent dielectric, and equation D.23, the region 1 radial electric field associated with the ideal dielectric coaxial rod configuration, were used in the denominator and numerator, respectively, of equation 3.108. Assuming that $h^d r_0 > 1$, $h^d a$. $2 z_1/a \geq 10$, and using equations A.36 and A.37, the large argument Bessel .function representations, it was discovered that

$$\xi_r(r_0, z_0) \cong 2 h^d b \frac{e^{-2 h^d b (1-r_0/b)}}{r_0/b} \sin^2(h^d z_0). \quad (3.112)$$

The same approximations mentioned in the previous sentence were made to equation 3.110. This resulted in

$$\xi_z(r_0, z_0) \cong 2 h^d b \frac{e^{-2 h^d b (1-r_0/b)}}{r_0/b} \cos^2(h^d z_0). \quad (3.113)$$

The value of $h^d b = h^d a \cdot b/a$ appearing in the previous two equations is approximately evaluated for the two and three region configurations by using the large argument approximations of the dispersion equation, equations D.54 and D.53, respectively.

In short, examination of equations 3.112 and 3.113 is necessary to obtain an understanding of the spatial distribution associated with the total power dissipation, when the value of $k a$ $\cot a n \psi$ is large. Note that the approximation for ξ_r only differs from that for ξ_z because it has a $\sin^2(h^d z_0)$ type of axial dependence instead of $\cos^2(h^d z_0)$. This means that the total power dissipation occurring within the lossy coaxial rod element is concentrated near the surface of the rod, and it rapidly becomes small as the value of r_0/b decreases, as shown in Figure 3.14. Since the region 1 radial and axial fields each contribute nearly one half to the total power dissipation, the spatial distribution of the total power dissipation is approximately given

simply by the sum of equations 3.112 and 3.113. Making use of the trigonometric identity $\cos^2 x + \sin^2 x = 1$, it is seen that the total power dissipation is approximately constant over the entire axial length of the lossy coaxial rod element. Figure 3.15 does not accurately represent the spatial dependence of *the total power dissipation* on the axial position.

In summary, the approximate spatial distribution associated with the *total power dissipation* has been examined. *For large values of* $ka \cot an \psi$ *(which also means large values of* $h^d a$ *)*, *the power dissipation is large near the rod surface and it rapidly decreases as the radial distance becomes smaller. It is approximately constant for a fixed value of* r_0/b, *as the axial distance is varied. On the other hand, for small values of* $ka \cot an \psi$ *(which also means small values of* $h^d a$ *)*, *the power dissipation is approximately distributed uniformly throughout the entire lossy coaxial rod element volume.*

3.5 Approximate Representations of the Power Dissipation Equations When the Lossy Rod Is an Excellent Conductor, Based on the Perfectly Conducting Rod Configuration Wave Number Solution

The final section of this chapter is concerned with investigating the power dissipation occurring within the lossy coaxial rod element, when the lossy rod is an excellent conductor. A similar format to that of section 3.4 is followed. The approximation is made of using the radial wave number and the axial wave number associated with the sheath helix surrounding a perfectly conducting coaxial rod. As explained in section C.2, the free mode field solution discussed in Appendix C for the perfectly conducting coaxial rod configuration is not valid for the special case when the perfectly conducting rod surface touches the sheath helix surface. Therefore, the discussion in section 3.5 will be restricted to the three region configuration (b < a).

3.5.1 Derivation of the Approximate Power Dissipation Equations

Representations of the exact power dissipation expressions, equations 3.12, 3.14, and 3.16, will now be derived which are approximately correct when the lossy rod is an excellent conductor. More specifically, the conductivity is assumed to be sufficiently large so that the following approximations are valid.

$$\sigma/\omega\epsilon_0 \gg \epsilon_r, \quad h_1 a \cong \sqrt{j\ \sigma/\omega\epsilon_0}\ ka,$$

$$|h_1|a \gg |h_2|a, \quad \text{and} \quad |h_1|b \cong \sqrt{\sigma/\omega\epsilon_0}\ kb > 1. \tag{3.114}$$

(Note that from the separation constant equation, equation 2.88, the restriction $|h_1|a \gg |h_2|a$ is required to justify using $h_1 a \cong \sqrt{j\ \sigma/\omega\epsilon_0} \cdot ka$. $|h_1|b > 1$ is restricted in order that the large argument Bessel function representations, equations A.36 and A.37, can be used to approximate equations 3.12, 3.14, and 3.16, as will shortly be done.)

Two other assumptions are made which result in a significant simplification. These are

$$|h_1 a\ K_1(h_2 b) + h_2 a\ K_0(h_2 b)| \cong |h_1|a\ |K_1(h_2 b)|$$

$$\cong \sqrt{\sigma/\omega\epsilon_0}\ ka\ |K_1(h_2 b)|, \quad \text{and} \tag{3.115}$$

$$|h_1 a\ K_1(h_2 b) + (\epsilon_r - j\ \sigma/\omega\epsilon_0)\ h_2 a\ K_0(h_2 b)|$$

$$\cong \sigma/\omega\epsilon_0\ |h_2|a\ |K_0(h_2 b)|. \tag{3.116}$$

Making use of assumptions 3.114 - 3.116, keeping just the first term of the large argument Bessel function representations, equations A.36 and A.37, in order to approximate all Bessel functions with arguments $h_1 b$ and $\tilde{h}_1 b$, and performing a

small amount of algebra, equations 3.12, 3.14, and 3.16 are transformed into the following equations.

$$P_{dr} \cong |J_{11}|^2 \frac{\pi}{2\sqrt{2}} \frac{1}{b/a} \frac{a}{\sigma\sqrt{\sigma/\omega\epsilon_0}} \frac{(h^c a)^2}{ka \cot an\psi} \cos\psi \sin\psi \cdot$$

$$\frac{[K_0(h^c a)]^2}{[K_0(h^c b)]^2} (1 - \frac{\sin(2 h^c z_1)}{2 h^c z_1}) \frac{2 z_1}{a}, \qquad (3.117)$$

$$P_{d\theta} \cong |J_{11}|^2 \frac{\pi}{2\sqrt{2}} \frac{120\pi a^2}{\sqrt{\sigma/\omega\epsilon_0}} \frac{\cos^2\psi}{b/a} \cdot$$

$$\frac{[K_1(h^c a)]^2}{[K_1(h^c b)]^2} (1 + \frac{\sin(2 h^c z_1)}{2 h^c z_1}) \frac{2 z_1}{a}, \text{ and } \qquad (3.118)$$

$$P_{dz} \cong |J_{11}|^2 \frac{\pi}{2\sqrt{2}} \frac{120\pi a^2}{\sqrt{\sigma/\omega\epsilon_0}} \frac{\sin^2\psi}{b/a} \cdot$$

$$\frac{[K_0(h^c a)]^2}{[K_0(h^c b)]^2} (1 + \frac{\sin(2 h^c z_1)}{2 h^c z_1}) \frac{2 z_1}{a}. \qquad (3.119)$$

It is now assumed in equations 3.117 - 3.119 that the imaginary parts of $h_2 a$ and βa are much smaller in absolute value than their real parts. Furthermore, it is assumed that the real parts of these wave numbers are similar to the corresponding (real) wave numbers for the sheath helix surrounding a perfectly conducting coaxial rod. A summary of these assumptions is given below.

$$h_2 a = h_{2r} a + j h_{2j} a, \quad |h_{2j}| a << h_{2r} a, \qquad (3.120)$$

$$h_{2r}a \cong h^C a, \quad \beta a = \beta_r a + j \beta_j a,$$

$$|\beta_j| a \ll \beta_r a, \quad \text{and} \quad \beta_r a \cong \beta^C a,$$

where $h^C a$ and $\beta^C a$ are the radial and axial wave numbers, respectively, for the perfectly conducting coaxial rod configuration.

Next, it is assumed that the imaginary parts of $h_2 a$ and βa approach zero. L'Hopital's rule is used to evaluate

$$\lim_{\beta_j \to 0} \frac{[\beta_r b \sinh(2 \beta_j z_1) \pm \beta_j b \sin(2 \beta_r z_1)]}{\beta_j b}$$

$$= \beta_r 2 z_1 \pm \sin(2 \beta_r z_1).$$

Finally, the approximation $\beta^C a \cong h^C a$ is used. This is discussed in section C.2, and it is usually well justified for a relatively tightly wound sheath helix. It requires that equation C.30 is satisfied.

Applying the assumptions and approximations discussed in the previous three paragraphs to equations 3.117 – 3.119, equations 3.121 – 3.123 are obtained.

$$P_{dr} \cong |I|^2 \frac{\pi}{2\sqrt{2}} \frac{1}{b/a} \frac{a}{\sigma \sqrt{\sigma/\omega\epsilon_0}} \frac{(h^C a)^2}{ka \cot an\psi} \cos\psi \sin\psi \cdot$$

$$\frac{[K_0(h^C a)]^2}{[K_0(h^C b)]^2} \left(1 - \frac{\sin(2 h^C z_1)}{2 h^C z_1}\right) \frac{2 z_1}{a}, \qquad (3.121)$$

$$P_{d\theta} \cong |\mathfrak{H}_{11}|^2 \frac{\pi}{2\sqrt{2}} \frac{120\pi \, a^2}{\sqrt{\sigma/\omega\epsilon_0}} \frac{\cos^2\psi}{b/a} \cdot$$

$$\frac{[K_1(h^Ca)]^2}{[K_1(h^Cb)]^2} \left(1 + \frac{\sin(2\,h^C z_1)}{2\,h^C z_1}\right) \frac{2\,z_1}{a}, \quad \text{and} \quad (3.122)$$

$$P_{dz} \cong |\mathfrak{H}_{11}|^2 \frac{\pi}{2\sqrt{2}} \frac{120\pi \, a^2}{\sqrt{\sigma/\omega\epsilon_0}} \frac{\sin^2\psi}{b/a} \cdot$$

$$\frac{[K_0(h^Ca)]^2}{[K_0(h^Cb)]^2} \left(1 + \frac{\sin(2\,h^C z_1)}{2\,h^C z_1}\right) \frac{2\,z_1}{a}. \qquad (3.123)$$

Equations 3.121 - 3.123 are the approximate power dissipation equations for the case when the lossy coaxial rod is an excellent conductor, based on the wave number solution for the sheath helix surrounding a perfectly conducting coaxial rod. Keeping in mind equation C.19, which lists the variables on which the wave number h^Ca is dependent, the functional dependences of the three types of power dissipation contributions can be stated.

$$P_{di} = f_i(ka \cot an\psi, \, b/a, \, \psi, \, a, \, 2\,z_1/a, \, \sigma/\omega\epsilon_0, \, \sigma, \, \mathfrak{H}_{11}),$$

where $i = r, \theta, z$. $\qquad (3.124)$

The wave number h^Ca is obtained by solving the dispersion equation, equation C.14, for a given set of the variables listed in equation C.19. Graphs of this wave number solution are shown in Figures C.1 - C.3. For small and large values of h^Ca, equations C.24 and C.28, respectively, can be used to obtain an approximate wave number solution. When h^Ca is known, equations 3.121 - 3.123 can be directly evaluated for a particular set of the variables listed in equation 3.124.

A digression will be now be made to discuss an investigation of the power dissipation occurring within the lossy coaxial rod element, making use of the concept of *surface resistance* and the magnetic fields associated with *the perfectly conducting coaxial rod configuration*. This procedure can be regarded as a perturbation method, based on the fields associated with the sheath helix surrounding a perfectly conducting coaxial rod. The (time-averaged) power dissipation is

$$P_d\# = \frac{R_s}{2} \int_S |\underline{H}_t{}^c|^2 \, dS$$

$$= \frac{R_s}{2} \int_S (|H_{\theta 2}{}^c|^2 + |H_{z2}{}^c|^2) \, dS. \qquad (3.125)$$

$R_s = \mathrm{Re}[Z_s]$ is the surface resistance associated with the nonmagnetic lossy rod.

$$Z_s = \sqrt{\frac{j \, \omega \, \mu_0}{\sigma}} = (1 + j) \frac{1}{\sigma} \sqrt{\frac{\omega \, \mu_0 \, \sigma}{2}} = \frac{(1 + j)}{\sigma \, \delta} \text{ is the}$$

surface impedance, where $\delta = \sqrt{\dfrac{2}{\omega \, \mu_0 \, \sigma}}$ is the skin depth.

(For example, see 38, pp. 153 - 155; 44, pp. 356 - 360; 48, pp. 263 - 269; and 49, pp. 331 - 335.) $\underline{H}_t{}^c = H_{\theta 2}{}^c \, \underline{a}_\theta + H_{z2}{}^c \, \underline{a}_z$ is the magnetic field tangential to the coaxial rod surface, *assuming that it is perfectly conducting*. $H_{\theta 2}{}^c$ and $H_{z2}{}^c$ are given by equations C.6 and C.7, respectively. The surface of integration, S, consists of the lossy coaxial rod element cylindrical surface, which is specified by $r = b$, $-z_1 \leqslant z \leqslant z_1$.

Equations 3.125 are actually an approximation of the left hand side of equation 3.20, which is a form of Poynting's energy theorem. This can be understood by examining the integrand in the left hand side of equation 3.20.

$$(\underline{E}_1 \times \widetilde{\underline{H}}_1)\Big|_{r=b} \cdot \underline{a}_r = (E_{\theta 1} \widetilde{H}_{z1} - E_{z1} \widetilde{H}_{\theta 1})\Big|_{r=b}$$

$$= - Z_s (|H_{\theta 1}|^2 + |H_{z1}|^2)\Big|_{r=b} = - Z_s (|H_{\theta 2}|^2 + |H_{z2}|^2)\Big|_{r=b} \qquad (3.126)$$

since the region 1 and region 2 magnetic fields tangential to the lossy rod surface are continuous at $r = b$. (See equations 2.45 and 2.46.)

$$Z_s = - \frac{E_{\theta 1}\Big|_{r=b}}{H_{z1}\Big|_{r=b}} = \frac{E_{z1}\Big|_{r=b}}{H_{\theta 1}\Big|_{r=b}}$$

is the surface impedance. Next, the approximation is made in equations 3.126 of using the magnetic fields for the perfectly conducting coaxial rod configuration, $H_{\theta 2}{}^C$ and $H_{z2}{}^C$, in place of the magnetic fields associated with the lossy coaxial rod configuration, $H_{\theta 2}$ and H_{z2}, respectively. Finally, the closed surface of integration mentioned in equation 3.20 is taken as the cylindrical rod element surface. The power flow through the area consisting of the two element endfaces, which are specified by $z = \pm z_1$, $0 \le r \le b$, is neglected. This is justified when the conductivity of the lossy rod is very large, because the skin depth is much smaller than the rod radius. The region 1 electric and magnetic field magnitudes are only large very close to the surface of the lossy rod.

Making use of the discussion given in the preceding paragraph, it is seen that the left hand side of equation 3.20 approximately simplifies to equations 3.125. In summary, the perturbation type of procedure used to investigate the power dissipation occurring within the lossy coaxial rod element, based on the magnetic fields associated with the perfectly conducting coaxial rod configuration and the concept of surface resistance, is actually an approximation of Poynting's energy theorem.

Attention is now directed to the simple task of evaluating equations 3.125. It is convenient to rewrite these equations as

$$P_d\text{\#} = \frac{R_s}{2} \int_S (|H_{\theta 2}{}^c|^2 + |H_{z2}{}^c|^2) \, dS$$

$$= \frac{R_s}{2} \int_{\theta=0}^{\theta=2\pi} \int_{z=-z_1}^{z=+z_1} (|H_{\theta 2}{}^c|^2 + |H_{z2}{}^c|^2)\Big|_{r=b} \, dz \, b \, d\theta, \quad \text{or}$$

$$P_d\text{\#} = \frac{R_s}{2} \, 2\,\pi\,b \int_{-z_1}^{+z_1} (|H_{\theta 2}{}^c|^2 + |H_{z2}{}^c|^2)\Big|_{r=b} \, dz. \quad (3.127)$$

Making use of the values of $H_{\theta 2}{}^c$ and $H_{z2}{}^c$ from equations C.6 and C.7, respectively, and the value of R_s mentioned after equations 3.125, and making the approximation $\beta^c{}_a \hat{=} h^c{}_a$, it can be shown that equation 3.127 is just the sum of equations 3.122 and 3.123. Taking the ratio of equations 3.121, 3.122, and of equations 3.121, 3.123, it is clear that P_{dr} is smaller by the factor $1/\sigma$ than $P_{d\theta}$ and P_{dz}. Therefore, since the rod conductivity has been assumed to be very large, *the total power dissipation* is, to a good approximation, given only by the sum of equations 3.122 and 3.123. This means that *using the concept of surface impedance and the magnetic fields associated with the perfectly conducting coaxial rod configuration, the same total power dissipation was calculated as that given near the beginning of part 3.5.1, which was obtained directly by making approximations to the exact power dissipation equations listed in section 3.1.*

The preceding discussion serves three purposes. First, it provides a check on the accuracy of the approximate power dissipation expressions, equations 3.121 - 3.123. Second, a better understanding of the meaning of the assumptions made during the derivation of these approximate power dissipation expressions is achieved. Third, an alternative interpretation of the nature of the power dissipation is obtained. Instead of saying that the power dissipation results from ohmic heating associated with the presence of electrical currents flowing within the lossy coaxial rod element, the power dissipation is considered from the point of view of the time-averaged power flow

through the cylindrical surface of the lossy coaxial rod element.

To conclude part 3.5.1, a discussion will be given of the overlap which occurs between equations 3.121 - 3.123, the approximate power dissipation equations for the case when the lossy rod is an excellent conductor, based on the perfectly conducting coaxial rod configuration wave number solution, and equations 3.70 - 3.72, 3.77 - 3.79, the approximate power dissipation equations when "the lossy rod is a good conductor", as discussed in section 3.3.

First, equations 3.121 - 3.123 and equations 3.70 - 3.72, the small argument approximate power dissipation equations for the case when "the lossy rod is a good conductor", are considered. For the first mentioned set of equations, it is assumed that $h^C a < 0.100$ and $h^C a \cdot 2 z_1 / a << 1$. Equations A.28 and A.29, the small argument Bessel function representations, are applied. Finally, equation C.24, the small argument approximation of the dispersion equation, is used. Keeping in mind the approximations listed in equations 3.76, it can be shown that the corresponding equations of the sets 3.121 - 3.123 and 3.70 - 3.72 are equal. When the value of $h^C a$ is sufficiently small, the approximate power dissipation equations for the case when the lossy rod is an excellent conductor, based on the perfectly conducting coaxial rod configuration wave number solution, become the same as the small argument approximate power dissipation equations for the case when "the lossy rod is a good conductor", which were previously discussed in part 3.3.1.

Finally, equations 3.121 - 3.123 and equations 3.77 - 3.79, the large argument approximate power dissipation equations for the case when "the lossy rod is a good conductor", are examined. Consider equations 3.121 - 3.123. It is assumed that $h^C b = h^C a \cdot b/a > 1$, and that $2 z_1 / a \geq 10$. Equation C.28, the large argument approximate dispersion equation, is used. The large argument Bessel function representations, equations A.38 and A.39, are applied. Making these approximations and performing some algebra, equations 3.121 - 3.123 are transformed into the corresponding equation of the set 3.77 - 3.79. If the values of $h^C a$ and $2 z_1 / a$ are sufficiently large, the approximate power dissipation equations for the case when the lossy rod is an excellent conductor, based on the perfectly conducting coaxial rod configuration wave number solution, become the same as the large argument

approximate power dissipation equations for the case when the lossy rod is a good conductor," which were previously discussed in part 3.3.2.

In summary, it has been shown that when the values of $h^c a$ and $2 z_1/a$ are sufficiently small or large, the approximate power dissipation equations given in part 3.5.1 become those given in parts 3.3.1 and 3.3.2, respectively. This overlap is an expected result. It supports the accuracy of the approximate power dissipation equations listed in the three previously mentioned parts of Chapter 3.

3.5.2 Graphs of P_{dr}/P_{dz} and $P_{d\theta}/P_{dz}$

In order to achieve a better understanding of the power dissipation which occurs within the lossy coaxial rod element, for the case when the lossy rod is an excellent conductor, making use of the perfectly conducting coaxial rod configuration wave number solution, it is desirable to know how much of a contribution to the total power dissipation is associated with each of the three region 1 electric fields. It is especially important to determine which electric field makes the dominant contribution. This means that the total power dissipation can be investigated by considering just a single equation of the set 3.121 - 3.123. In order to obtain this information, it is necessary to study the ratios P_{dr}/P_{dz} and $P_{d\theta}/P_{dz}$. Equations 3.128 and 3.129 are obtained simply by taking the appropriate ratios of equations 3.121 - 3.123.

$$\frac{P_{dr}}{P_{dz}} = \frac{1}{\sigma/\omega\epsilon_0} \frac{(h^c a)^2}{(ka\, \cotan\psi)^2} \cotan^2\psi \cdot$$

$$\frac{[1 - \dfrac{\sin(2\, h^c\, z_1)}{2\, h^c\, z_1}]}{[1 + \dfrac{\sin(2\, h^c\, z_1)}{2\, h^c\, z_1}]}, \quad \text{and} \tag{3.128}$$

$$\frac{P_{d\theta}}{P_{dz}} = \cotan^2\psi \; \frac{[K_1(h^Ca)]^2}{[K_1(h^Cb)]^2} \; \frac{[K_0(h^Cb)]^2}{[K_0(h^Ca)]^2}. \qquad (3.129)$$

Equations 3.128 and 3.129 are the power dissipation ratios, when the lossy rod is an excellent conductor, based on the perfectly conducting coaxial rod configuration wave number solution. Equation C.19 lists the variables on which the wave number h^Ca is dependent. Keeping this in mind, it is possible to state the functional dependences of equations 3.128 and 3.129.

$$\frac{P_{dr}}{P_{dz}} = f(ka \; \cotan\psi, \; b/a, \; \psi, \; \sigma/\omega\varepsilon_0, \; 2 \; z_1/a), \quad \text{and}$$

$$\frac{P_{d\theta}}{P_{dz}} = g(ka \; \cotan\psi, \; b/a, \; \psi). \qquad (3.130)$$

It is important to realize that the requirements listed in equations 3.114 – 3.116, and in equation 3.120, must be satisfied to justify the usage of equations 3.128 and 3.129.

Equations 3.128 and 3.129 can be more easily understood by using approximations of the trigonometric and Bessel functions, which are valid for certain values of the arguments. First, the small argument approximations are considered. Restricting $h^Ca < 0.100$ so that the small argument Bessel function representations, equations A.28 and A.29, are well justified, and substituting these into equation 3.129, it follows that

$$\frac{P_{d\theta}}{P_{dz}} \approx (b/a)^2 \; \cotan^2\psi \; \frac{[\log(0.891 \; h^Cb)]^2}{[\log(0.891 \; h^Ca)]^2}. \qquad (3.131)$$

If the value of b/a is not too small, taking into consideration the value of h^Ca,

$$\log(0.891\ h^c b) = \log(0.891\ h^c a) + \log(b/a) \cong \log(0.891\ h^c a).$$

Therefore, equation 3.131 approximately simplifies to

$$\frac{P_{d\theta}}{P_{dz}} \cong (b/a)^2 \cot an^2 \psi. \tag{3.132}$$

If the values of $h^c a$ and $2\ z_1/a$ are sufficiently small so that

$$2\ h^c\ z_1 = h^c a \cdot 2\ z_1/a << 1,$$

$$\sin(2\ h^c\ z_1) \cong 2\ h^c\ z_1 - \frac{(2\ h^c\ z_1)^3}{6}$$

can be used. In addition, the small argument approximation of the dispersion equation, equation C.24, is employed. As mentioned in section C.2, this is valid for $h^c a <$ 0.100 if b/a is not too small, and it tends to be more accurate for a fixed value of b/a when $h^c a$ becomes very small. Making the two previously mentioned approximations in equation 3.128,

$$\frac{P_{dr}}{P_{dz}} \cong \frac{1}{48} \left(\frac{2\ z_1}{a}\right)^2 \frac{1}{\sigma/\omega\epsilon_0} (ka\ \cot an\psi)^2 \cot an^2 \psi \cdot$$

$$\frac{(1 - (b/a)^2)^2}{(\log(b/a))^2} \tag{3.133}$$

is obtained. Equations 3.132 and 3.133 are very convenient because the two ratios are explicitly given in terms of the operating frequency, the sheath helix geometry, the lossy coaxial rod element geometry, and the lossy rod conductivity.

The large argument approximations of equations 3.128 and 3.129 are now obtained. Just the first term of equations A.38 and A.39 is substituted into equation 3.129. To justify using these large argument Bessel function representations, it is necessary that $_h c_b > 1$. The large argument approximation of the dispersion equation, equation C.28, is used in equation 3.128. Finally, the assumption $2 z_1 / a \geq 10$ is used in equation 3.128. The following two equations are easily obtained.

$$\frac{P_{dr}}{P_{dz}} \simeq \frac{1}{\sigma / \omega \varepsilon_0} \cot a n^2 \psi_a, \quad \text{and} \qquad (3.134)$$

$$\frac{P_{d\theta}}{P_{dz}} \simeq \cot a n^2 \psi. \qquad (3.135)$$

A graph for each of equations 3.128 and 3.129 has been prepared. It was necessary to first solve equation C.14, the dispersion equation, for the specified values of $k a \cot a n_\psi$ and b/a, in order to obtain $_h c_a$. Equations 3.128 and 3.129 were then directly evaluated.

Figure 3.20 is a graph of the ratio $P_{d\theta} / P_{dz}$, as given by equation 3.129. $\psi = 1.00°$, $10.0°$; $b/a = 0.100, 0.500, 0.900$; and $1.00 \times 10^{-7} < k a < 10.0$ are used. (Note that as mentioned in equations 3.130, the value of $\sigma / \omega \varepsilon_0$ does not have to be explicitly specified. However, the lossy rod conductivity must be sufficiently large so that the requirements listed in equations equations 3.114 - 3.116, and in equation 3.120, are satisfied.) Equations 3.132 and 3.135 are seen to be in good agreement with the curves, for small and large values of $k a$, respectively. It is clear from this figure that $P_{d\theta} >> P_{dz}$ is usually true.

Figure 3.21 is a graph of P_{dr} / P_{dz}, based on equation 3.128. $\psi = 1.00°$, $10.0°$; $b/a = 0.100, 0.900$; $\sigma / \omega \varepsilon_0 = 1.00 \times 10^{10}$, 1.00×10^{15}; $2 z_1 / a = 10.0$; and $1.00 \times 10^{-3} < k a < 1.00$ are used. (Note that a large value of $\sigma / \omega \varepsilon_0$ must be used to ensure that $\sqrt{\sigma / \omega \varepsilon_0} \cdot k a \cdot b/a > 1$. This requirement is mentioned in equations 3.114.) It is apparent that equation 3.134 is in good agreement with the curves when the value of $k a$ is
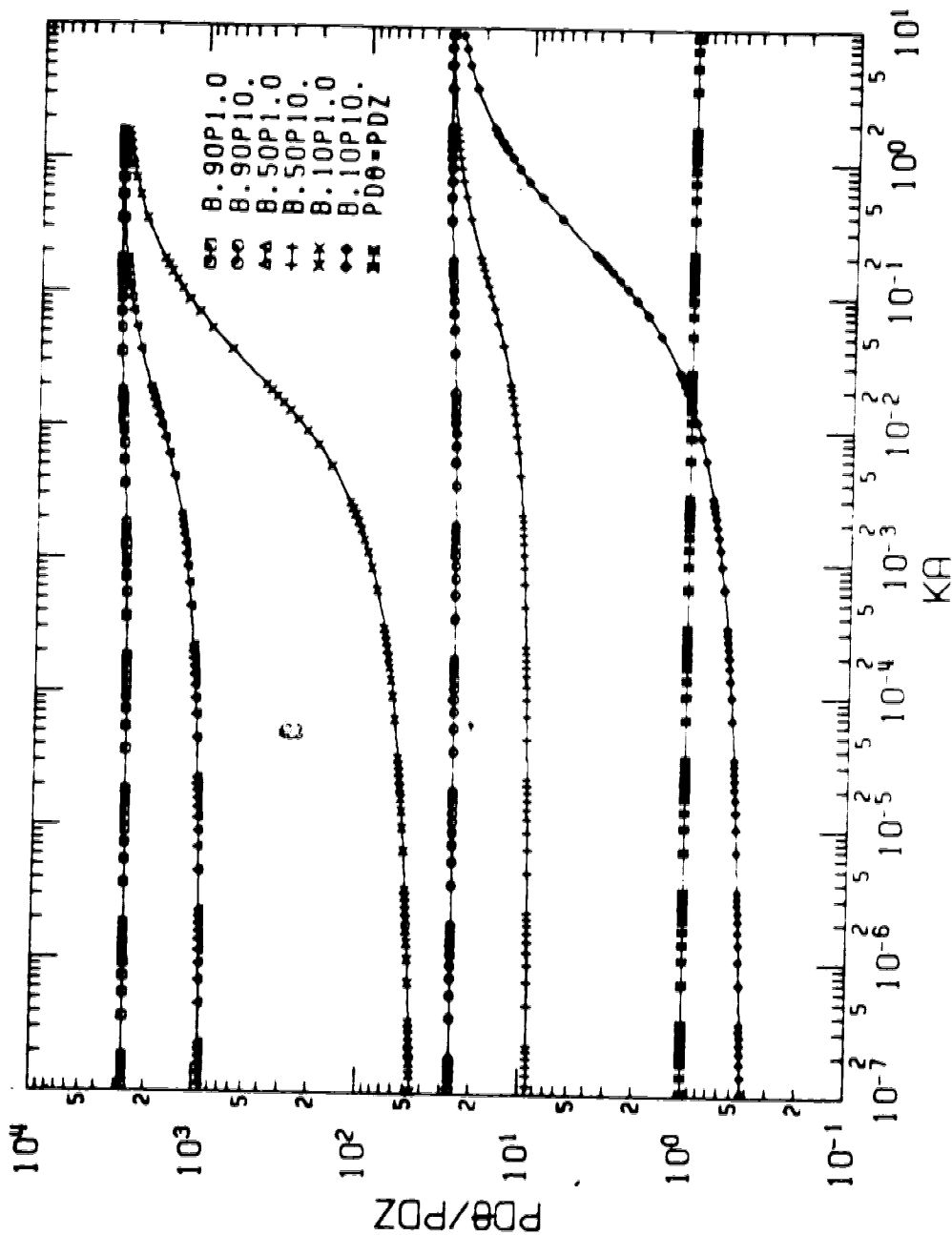
Figure 3.20   Graph of $P_{d\theta}/P_{dz}$ versus ka, based on equation 3.129. The lossy rod is an excellent conductor. Curves for b/a=0.10, 0.50, 0.90; ψ=1.0°, 10.0°; and 1.00×10^{-7}<ka<10.0 are shown. (Note PDΘ=$P_{d\theta}$, PDZ=P_{dz}, and KA=ka. B.10P10. means the curve represents b/a =0.10 and ψ=10.0°. B.90P1.0 means the curve represents b/a=0.90 and ψ=1.0°.)
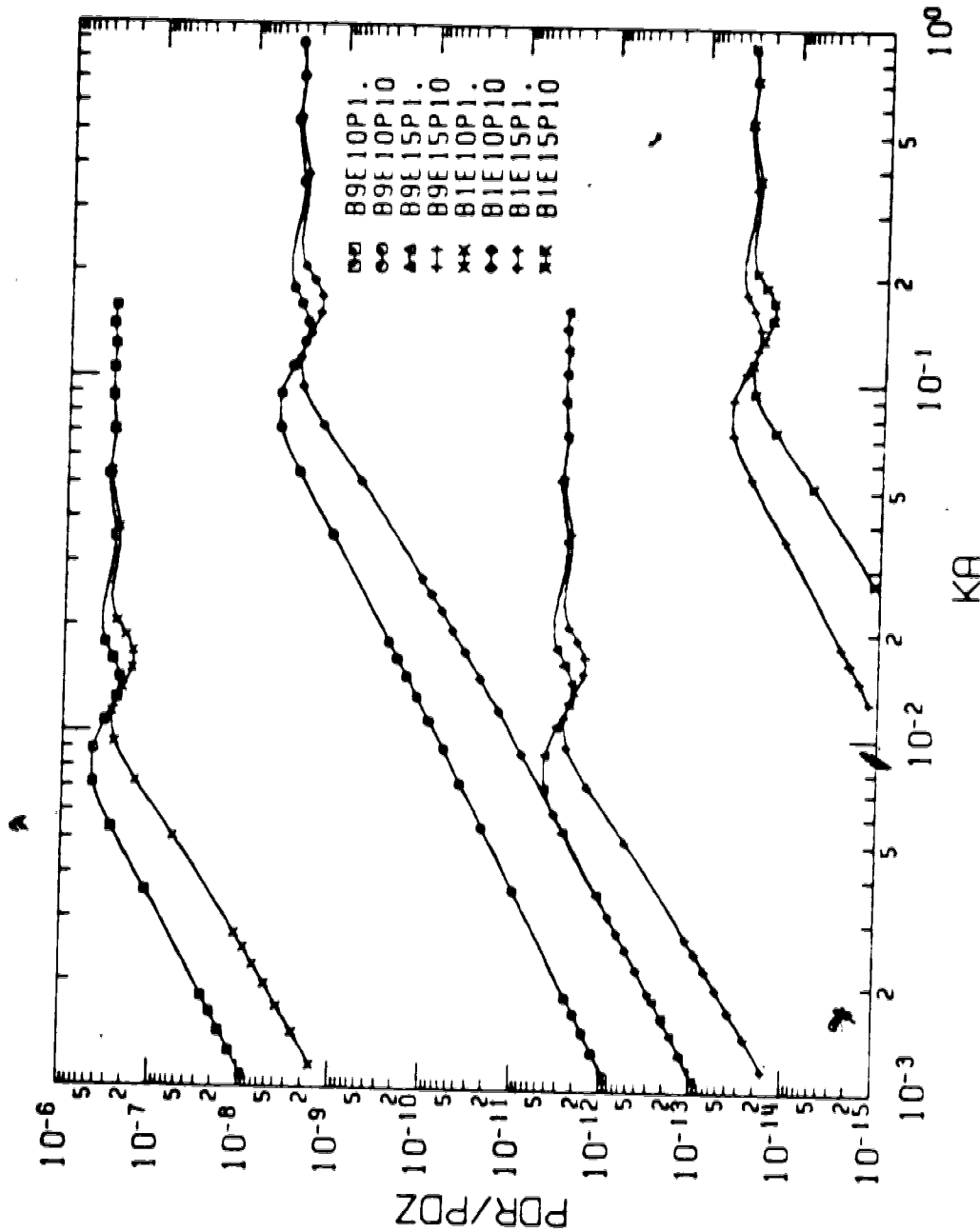
Figure 3.21   Graph of P_{dr}/P_{dz} versus ka, based on equation 3.128. The lossy rod is an excellent conductor. Curves for b/a=0.10, 0.90; ψ=1.0°, 10.0°; $\sigma/\omega\epsilon_0$ =1.00x10^{10}, 1.00x10^{15}; 2 z_1/a=10.0; and 1.00x10^{-3}<ka<1.0 are displayed. (Note PDR=P_{dr}, PDZ=P_{dz}, and KA=ka. B1E15P10 means the curve represents b/a=0.10, $\sigma/\omega\epsilon_0$ =1.00x10^{15}, and ψ=10.0°. B9E10P1. means the curve represents b/a=0.90,$\sigma/\omega\epsilon_0$=1.00x10^{10}, and ψ=1.0°.)

large. For small values of ka, there is reasonably good agreement between the curves and the prediction of equation 3.133. More specifically, there is just a few percent error at $ka = 1.00 \times 10^{-3}$ when $b/a = 0.900$, but there is about fifty percent error at $ka = 1.00 \times 10^{-3}$ when $b/a = 0.100$. The large error results from using equation C.24 in the derivation of equation 3.133. Equation C.24, the small argument approximation of the dispersion equation, will only be highly accurate for values of b/a as small as 0.100, for values of $ka \cot \psi$ less than those used here. It is obvious from the figure that $P_{dz} >> P_{dr}$ is true.

In summary, graphs of the power dissipation ratios $P_{d\theta}/P_{dz}$ and P_{dr}/P_{dz} have been presented, assuming that the sheath helix is relatively tightly wound, using different operating frequencies, sheath helix geometries, lossy coaxial rod element geometries, and lossy rod conductivities. It has been clearly shown that $P_{d\theta} >> P_{dz}$ and $P_{dz} >> P_{dr}$ are almost always true. *This has the important meaning that for the case when the lossy rod is an excellent conductor, making use of the wave number solution for the perfectly conducting coaxial rod configuration, the contribution to the total power dissipation associated with the region 1 angular electric field is usually much greater than that associated with the other two region 1 electric fields. Therefore, to a good approximation, the total power dissipation occurring within the lossy coaxial rod element is given by equation 3.122.*

3.5.3 Graphs of the Spatial Distribution of the Power Dissipation, Based on $E_{\theta 1}$

The preceding part, part 3.5.2, has shown that the contribution to the total power dissipation associated with the region 1 angular electric field is usually much greater than that associated with the region 1 radial and axial electric fields, when the sheath helix is relatively tightly wound. Therefore, an understanding of the spatial distribution of the total ohmic heating occurring within the lossy coaxial rod element can be achieved by repeating the same procedure previously followed in part 3.4.3, using $E_{\theta 1}$ as the electric field component.

The dimensionless ratio ξ_θ is defined as

$$\xi_\theta(r_0, z_0) = \frac{\frac{\sigma}{2} \int_V |E_{\theta 1}\#|^2 \; dV}{\frac{\sigma}{2} \int_V |E_{\theta 1}|^2 \; dV} = \frac{\frac{\sigma}{2} |E_{\theta 1}\#|^2 \int_V dV}{P_{d\theta}}$$

$$= \frac{\frac{\sigma}{2} \pi b^2 \; 2 \; z_1 \; |E_{\theta 1}\#|^2}{P_{d\theta}}. \qquad (3.136)$$

The volume of integration in equations 3.136 is the entire lossy coaxial rod element volume. $P_{d\theta}$ is specified by equation 3.122. $|E_{\theta 1}\#|$ is the magnitude of the region 1 angular electric field component evaluated at the particular point within the lossy coaxial rod element specified by (r_0, z_0). Futhermore, this magnitude is then assumed to be constant at all points throughout the element volume. Therefore, as shown in equations 3.136, it can be taken outside of the integral sign.

The value of ξ_θ has the same meaning as the value of ξ_z, which was previously discussed in part 3.4.3. Studying ξ_θ at several different points (r_0, z_0) gives information concerning the spatial distribution of the ohmic heating, which arises from the contribution to the total power dissipation associated with $E_{\theta 1}$. However, as was discussed in part 3.5.2, this contribution is, to a good approximation, equal to the total power dissipation. Therefore, equations 3.136 approximately show the spatial distribution throughout the lossy coaxial rod element of *the total power dissipation*.

In order to evaluate equations 3.136, the approximations listed in equations 3.114 and 3.115, as well as the approximations $\beta a \simeq h_2 a \simeq h^c a$, are used in the expression for the region 1 angular electric field, equation 3.3. It follows that

$$|E_{\theta 1}\#(r_0, z_0)|^2 = \frac{|I|^2}{(b/a)^2} \frac{(120\pi)^2 \cos^2\psi}{\sigma/\omega\epsilon_0} \frac{[K_1(h^c a)]^2}{[K_1(h^c b)]^2} \cdot$$

$$\frac{|I_1(\sqrt{j \; \sigma/\omega\epsilon_0} \; k \; r_0)|^2}{|I_1(\sqrt{j \; \sigma/\omega\epsilon_0} \; k \; b)|^2} \cos^2(h^c z_0). \qquad (3.137)$$

Substituting equations 3.122 and 3.137 into equations 3.136,

$$\xi_\theta(r_0, z_0) = \sqrt{\frac{2\ \sigma}{\omega\epsilon_0}}\ \ kb\ \ \frac{|I_1(\ \sqrt{j\ \sigma/\omega\epsilon_0}\ \ k\ \ r_0)|^2}{|I_1(\ \sqrt{j\ \sigma/\omega\epsilon_0}\ \ k\ \ b)|^2} \ \cdot$$

$$\frac{\cos^2(h^c\ z_0)}{[1 + \dfrac{\sin(2\ h^c\ z_1)}{2\ h^c\ z_1}]} \qquad\qquad (3.138)$$

is obtained. If the radial distance of concern is sufficiently large so that $\sqrt{\sigma/\omega\epsilon_0}$ $\cdot$ $kb \cdot r_0/b > 1$, just the first term of equation A.37, the large argument Bessel function representation, can be used to approximate equation 3.138. It follows that

$$\xi_\theta(r_0, z_0) \approx \sqrt{\frac{2\ \sigma}{\omega\epsilon_0}}\ kb\ \ \frac{e^{-\sqrt{2\ \sigma/\omega\epsilon_0}\ kb\ (1-r_0/b)}}{r_0/b}$$

$$\frac{\cos^2(h^c\ z_0)}{[1 + \dfrac{\sin(2\ h^c\ z_1)}{2\ h^c\ z_1}]} \ \cdot \qquad\qquad (3.139)$$

Keeping in mind equation C.19, which lists the variables on which $h^c a$ is dependent, the nonspatial functional dependence of equation 3.139 is

$$\xi_\theta = f(ka\ cotan\psi,\ b/a,\ \psi,\ \sigma/\omega\epsilon_0,\ 2\ z_1/a). \qquad (3.140)$$

To achieve a better understanding of equation 3.139, it has been graphed using several different sets of the variables mentioned in equation 3.140. Two different types of figures were used to show the spatial distribution of the power dissipation. First, $\xi_\theta(r_0, 0)$ was plotted for different values of r_0/b, to show the radial

dependence occurring at the transverse plane $z_0 = 0$. Second, $\xi_\theta(b, z_0)$ was plotted versus z_0/z_1 to show the axial dependence occurring at the lossy rod surface. Numerical calculation of equation 3.139 was achieved by first solving equation C.14, the dispersion equation, for the specified values of $ka \cot an \psi$ and b/a, in order to obtain $h^c a$. Equation 3.139 was then directly evaluated.

The six figures which follow are each characterized by $b/a = 0.100, 0.500, 0.900$; $\psi = 1.00°$; $\sigma/\omega\epsilon_0 = 1.00 \times 10^{12}$; $2 z_1/a = 10.0$; and a particular value of $ka \cot an \psi$. (Note that the value of $\sigma/\omega\epsilon_0$ was chosen sufficiently large so that the requirement $\sqrt{\sigma/\omega\epsilon_0} \cdot kb \cdot r_0/b > 1$, which is mentioned after equation 3.138, is always satisfied.)

Figure 3.22 shows $\xi_\theta(r_0, 0)$ versus r_0/b for $0.9995 \leqslant r_0/b \leqslant 1.0000$, and for $ka \cot an \psi = 10.0$. All three curves make it immediately clear that the value of ξ_θ is very large at $r_0 = b$ but it decays extremely rapidly as the value of r_0/b decreases. This means that the ohmic heating is very strongly concentrated near the lossy rod surface. It can be seen that the larger the value of b/a, the larger is the value of ξ_θ at $r_0 = b$, and the more rapidly it decays as the value of r_0/b is decreased.

Figure 3.23 displays $\xi_\theta(b, z_0)$ versus z_0/z_1 for $0 \leqslant z_0/z_1 \leqslant 0.20$ and the same value of $ka \cot an \psi$ as was used previously. All the curves show that the ohmic heating at the lossy coaxial rod element surface is very large at certain axial positions but it is small just a short distance away from these positions. The distribution of the power dissipation as a function of the axial distance is very nonuniform.

Next, Figure 3.24 graphs $\xi_\theta(r_0, 0)$ for $0.990 < r_0/b \leqslant 1.000$, and it is associated with $ka \cot an \psi = 0.500$. Similar behavior to Figure 3.22 occurs. However, the fact that the value of $ka \cot an \psi$ used here is smaller than that used in Figure 3.22 means that the value of ξ_θ at $r_0 = b$, although large, is not as big as that of the previously mentioned figure. In addition, although the rate at which ξ_θ becomes smaller for decreasing values of r_0/b is very rapid, it is not as great as that exhibited in Figure 3.22.
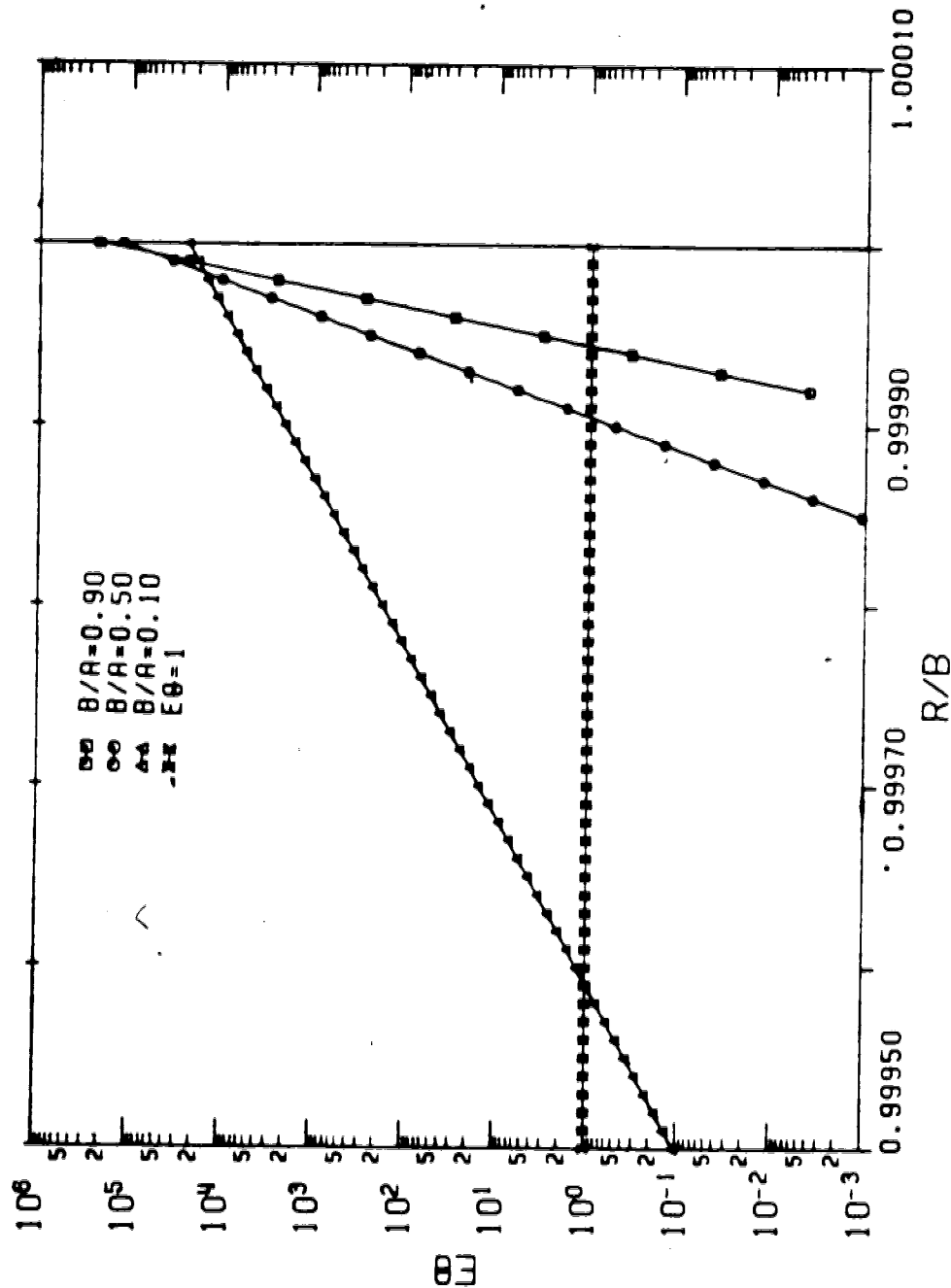
PLOT OF Eθ VS. R/B FOR Z=0 WHEN KA CP=10.0

Figure 3.22   Graph of ξ_θ versus r_0/b for $z_0=0$, based
on equation 3.139. The lossy rod is an excellent conductor.
Curves for b/a=0.10, 0.50, 0.90; $\psi=1.0°$; $\sigma/\omega\epsilon_0=1.00\times10^{12}$;
2 $z_1/a=10.0$; ka cotan$\psi=10.0$; and $0.9995 < r_0/b < 1.0000$ are
shown. The line $\xi_\theta=1.00$ is also given. (Note Eθ=ξ_θ, R/B
=r_0/b, Z=z_0, KA CP=ka cotanψ, and B/A=b/a.)
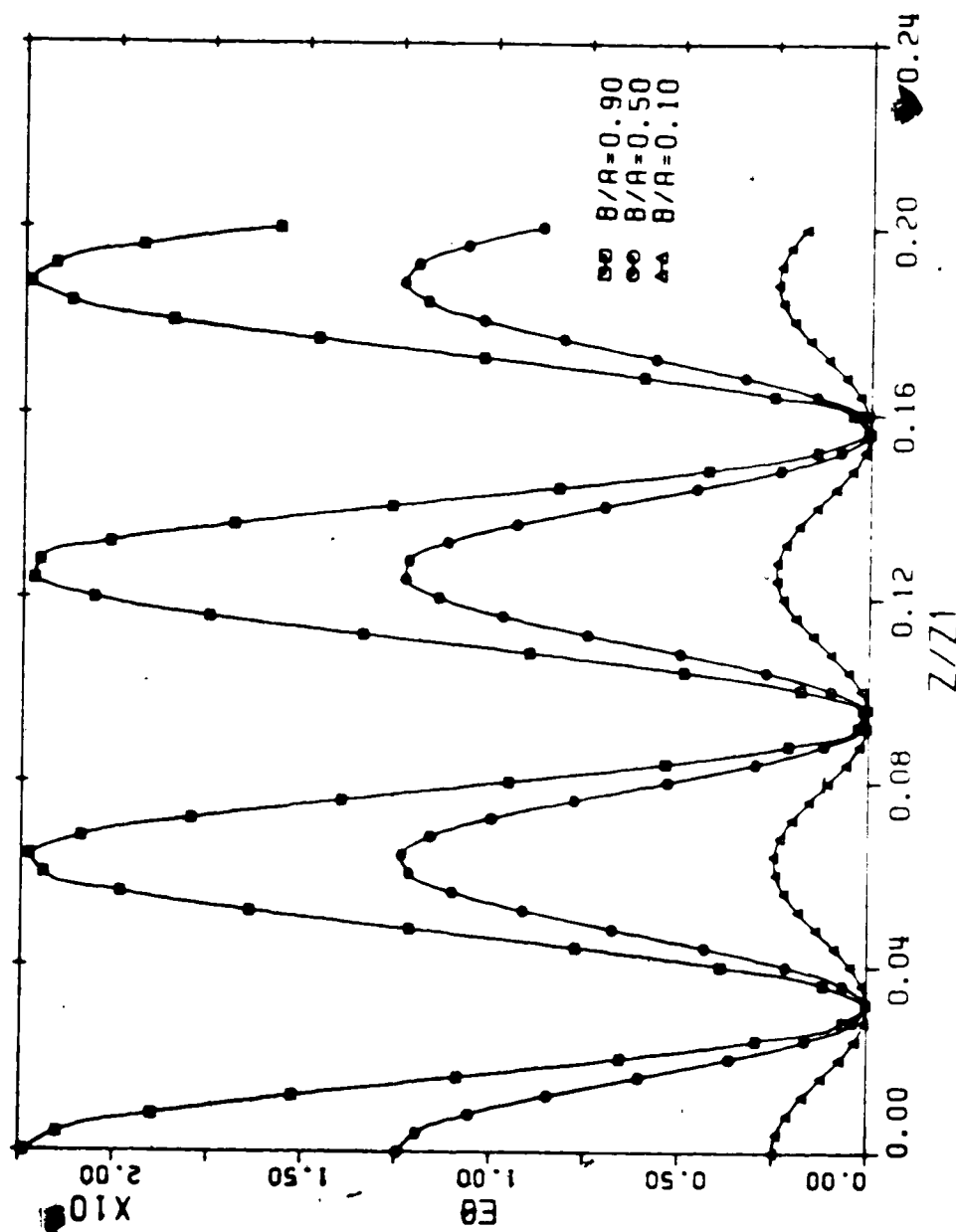
Figure 3.23   Graph of ξ_θ versus z_0/z_1 for $r_0=b$, based on equation 3.139. The lossy rod is an excellent conductor. Curves for $b/a=0.10$, 0.50, 0.90; $\psi=1.0°$; $\sigma/\omega\epsilon_0=1.00\times10^{12}$; 2 $z_1/a=10.0$; ka $\cot\psi=10.0$; and $0.0 \leq z_0/z_1 \leq 0.20$ are displayed. (Note $E_\theta=\xi_\theta$, $R=r_0$, $Z/Z1=z_0/z_1$, KA CP $=ka$ $\cot\psi$, and $B/A=b/a$.)
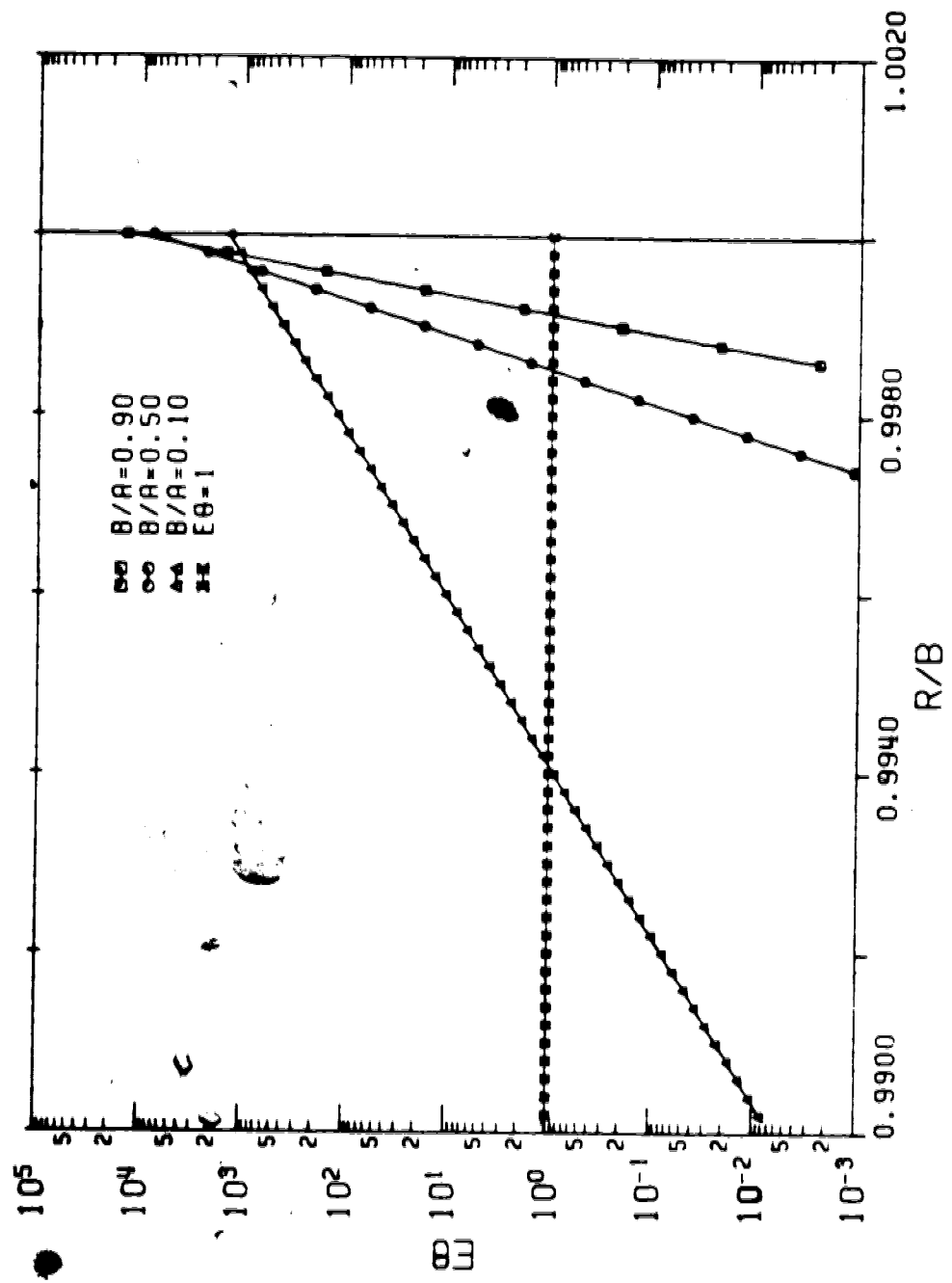
Figure 3.24   Graph of ξ_θ versus r_0/b for $z_0=0$, based on equation 3.139. The lossy rod is an excellent conductor. Curves for $b/a=0.10$, 0.50, 0.90; $\psi=1.0°$; $\sigma/\omega\epsilon_0=1.00\times10^{12}$; $2 z_1/a=10.0$; $ka\,\cot\psi=0.50$; and $0.99<r_0/b\leq1.00$ are shown. The line $\xi_\theta=1.00$ is also displayed. (Note $E\theta=\xi_\theta$, $R/B=r_0/b$, $Z=z_0$, KA CP$=ka\,\cot\psi$, and B/A$=b/a$.)

Figure 3.25 displays $\xi_\theta(b, z_0)$ using $0 \leq z_0/z_1 \leq 1.00$, and it corresponds to $ka\,cotan\psi = 0.500$. At $z_0 = 0$, the ohmic heating is large. It exhibits a relatively slow variation as the axial position changes, and it becomes small about halfway between the plane $z_0 = 0$ and the two endfaces of the lossy coaxial rod element.

Figure 3.26 graphs $\xi_\theta(r_0, 0)$ for $0.90 \leq r_0/b \leq 1.00$, and it uses $ka\,cotan\psi = 1.00\times10^{-2}$. Similar behavior to Figures 3.22 and 3.24 is exhibited. The differences are that since the quantity $ka\,cotan\psi$ is now smaller than it was for the two previously mentioned figures, the value of ξ_θ at $r_0 = b$ is less, although it is still large, and the rate of decrease associated with ξ_θ as r_0/b becomes smaller is less, although it is still rapid.

The final graph, Figure 3.27, shows $\xi_\theta(b, z_0)$ for $0 \leq z_0/z_1 \leq 1.00$, and it is associated with $ka\,cotan\psi = 1.00\times10^{-2}$. The ohmic heating which now occurs at the rod surface is seen to be constant over the entire lossy coaxial rod element length. This behavior is greatly different than that of Figure 3.23, which has a large value of $ka\,cotan\psi$ associated with it.

In summary, when the lossy coaxial rod element is an excellent conductor, the (total) ohmic heating is very large near the surface of the rod, but it extremely rapidly decreases moving radially inwards toward the center of the rod. When the value of $ka\,cotan\psi$ is large (which means that $_hc_a$ is large), the ohmic heating is very large at $r_0 = b$ and $z_0 = 0$. It changes rapidly in value along the rod surface as the axial distance is varied. On the other hand, when the value of $ka\,cotan\psi$ is small (which means that $_hc_a$ is small) the ohmic heating is large at $r_0 = b$ and $z_0 = 0$, although it is much smaller than for the previously mentioned case. It is now constant along the rod surface, for all the values $-z_1 \leq z_0 \leq z_1$.
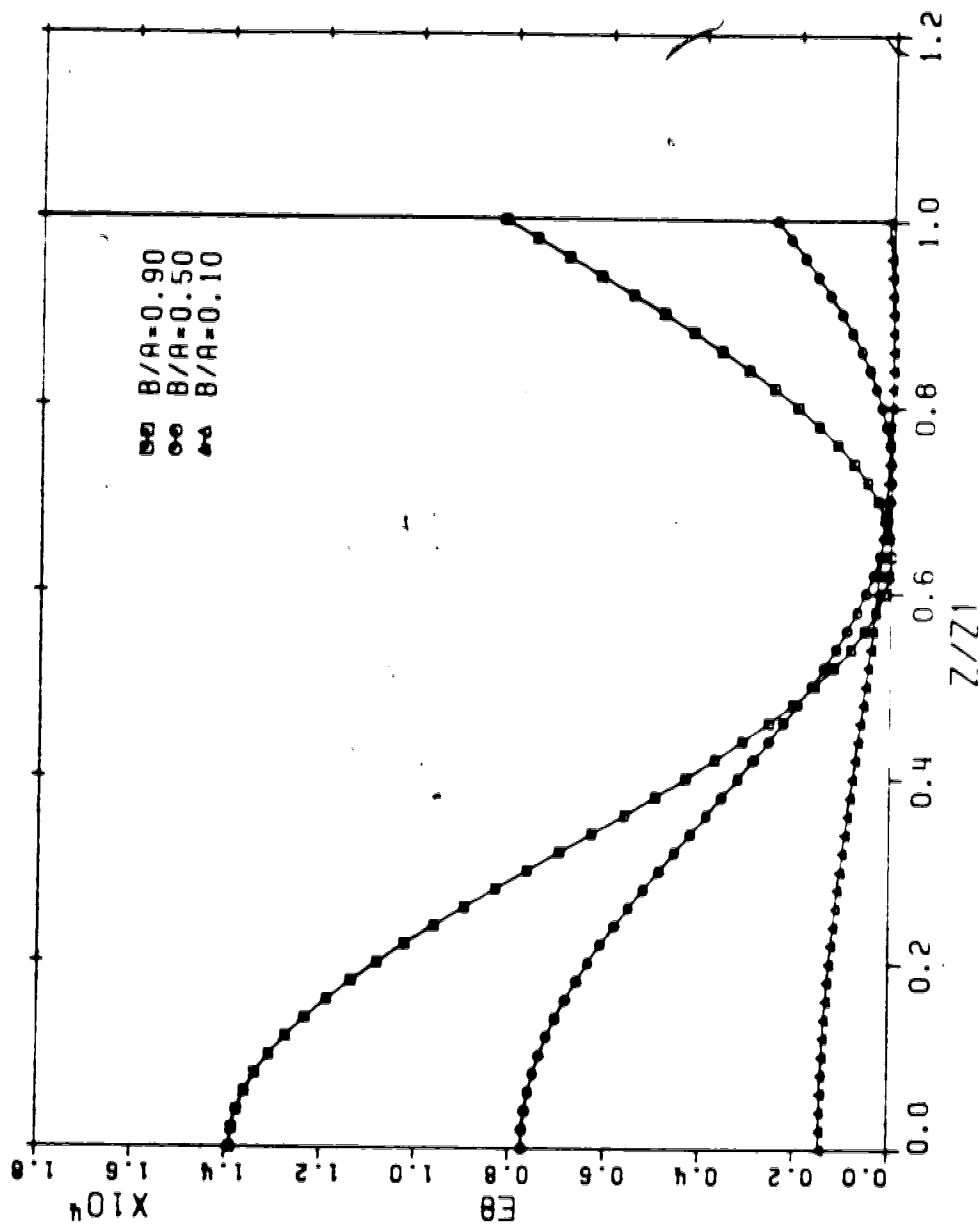
Figure 3.25 Graph of ξ_θ versus z_0/z_1 for $r_0 = b$, based on equation 3.139. The lossy rod is an excellent conductor. Curves for $b/a = 0.10$, 0.50, 0.90; $\psi = 1.0°$; $\sigma/\omega\epsilon_0 = 1.00 \times 10^{12}$; $2z_1/a = 10.0$; ka cotan$\psi = 0.50$; and $0.0 \leq z_0/z_1 \leq 1.00$ are given. (Note $E\theta = \xi_\theta$, $R = r_0$, $Z/Z1 = z_0/z_1$, KA CP = ka cotanψ, and $B/A = b/a$.)
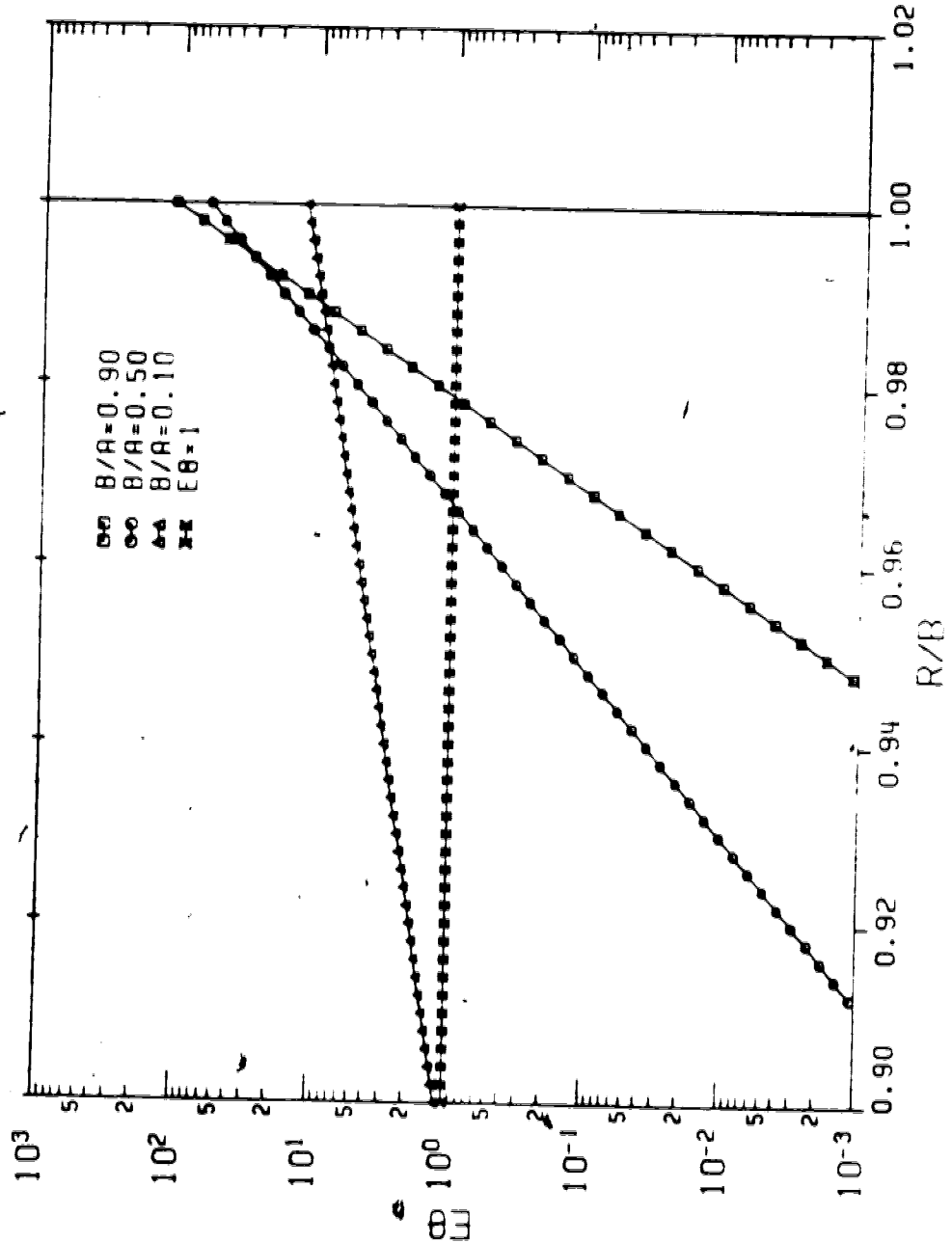
Figure 3.26   Graph of ξ_θ versus r_0/b for $z_0=0$, based on equation 3.139. The lossy rod is an excellent conductor. Curves for $b/a=0.10$, 0.50, 0.90; $\psi=1.0°$; $\sigma/\omega\epsilon_0=1.00\times10^{12}$; $2 z_1/a=10.0$; ka $\cot\psi=1.00\times10^{-2}$; and $0.90\leq r_0/b\leq1.00$ are shown. The line $\xi_\theta=1.00$ is also given. (Note $E\theta=\xi_\theta$, R/B $=r_0/b$, $Z=z_0$, KA CP$=ka$ $\cot\psi$, and B/A$=b/a$.)
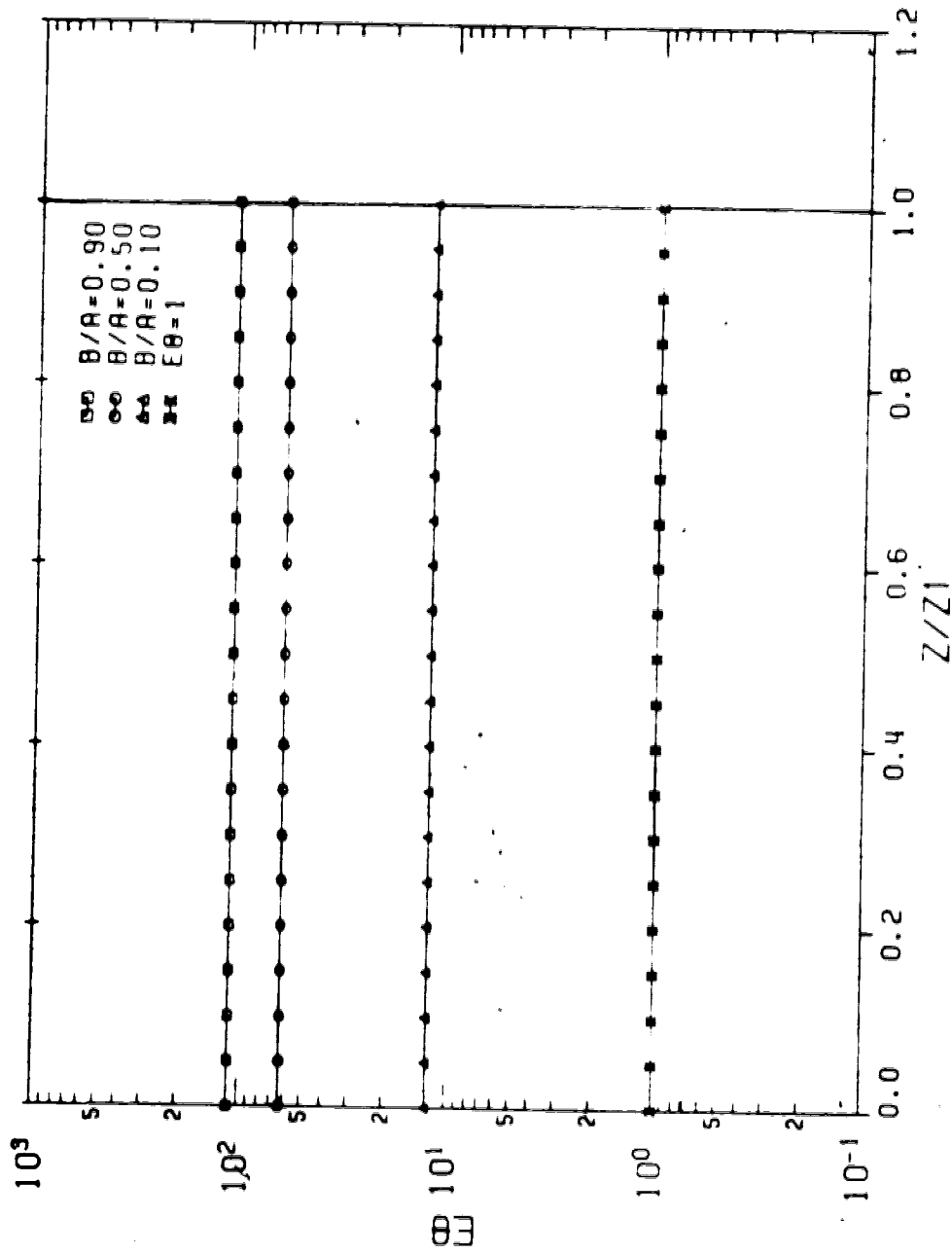
PLOT OF EΘ VS. Z/Z1 FOR R=B WHEN KA CP=1.00E-2

Figure 3.27   Graph of ξ_θ versus z_0/z_1 for $r_0 = b$, based on equation 3.139. The lossy rod is an excellent conductor. Curves for $b/a = 0.10$, 0.50, 0.90; $\psi = 1.0°$; $\sigma/\omega\epsilon_0 = 1.00 \times 10^{12}$; $2 z_1/a = 10.0$; ka cotan$\psi = 1.00 \times 10^{-2}$; and $0.0 \leq z_0/z_1 \leq 1.00$ are given. The line $\xi_\theta = 1.00$ is also shown. (Note E$\theta = \xi_\theta$, R=r_0, Z/Z1=z_0/z_1, KA CP=ka cotanψ, and B/A=b/a.)

3.6 Summary

This chapter is concerned with studying the time-averaged power dissipation occurring within the lossy coaxial rod element, which is surrounded by a sheath helix. (The lossy coaxial rod element is described by $0 \leq r \leq b$, $-z_1 \leq z \leq z_1$, where $0 < z_1 < \infty$.) Exact power dissipation equations were derived. (The term "exact" means that the field components of part 2.1.1 were used and that no approximations were made to these fields during the calculation of the power dissipation expressions.) Poynting's theorem for complex fields was applied to the lossy coaxial rod element. Both sides of the equation stating this theorem were evaluated, and it was demonstrated that the theorem is correctly satisfied. This provides a check on the accuracy of the exact power dissipation equations. It also shows that the total power dissipation occurring within the lossy coaxial rod element could be considered either from the point of view of electrical currents flowing within the lossy rod which result in ohmic heating, or from the point of view of the net radial and axial time-averaged power flow which pass through the closed surface defining the element volume.

Although exact power dissipation equations have been derived, it is usually extremely difficult to calculate the wave numbers $h_1 a$, $h_2 a$, and βa which appear in these equations. In order to achieve a good understanding of the power dissipation occurring within the lossy coaxial rod element, it is necessary to develop approximations to the exact power dissipation equations.

One type of approximate power dissipation equations, which were derived from the exact equations, are valid for the case when "the lossy rod is not a good conductor". (The term "the lossy rod is not a good conductor" as used here has the same meaning that it did in part 2.3.1.) These approximate equations make use of the approximate small and large argument wave numbers solution discussed in part 2.3.1. Two region configuration $(b = a)$ and three region configuration $(b < a)$ small and large argument approximate power dissipation equations were derived.

Assuming that the sheath helix is relatively tightly wound (as an example, $0 < \psi \leq 10.0°$), for the small argument case, both the two and three region configurations have the property that the region 1 $(0 \leq r \leq b)$ axial electric field provides a much larger contribution to the total power dissipation occurring within

the lossy coaxial rod element than the region 1 radial and angular electric fields. For the large argument case of the two region configuration, the region 1 radial and axial electric fields approximately make an equal contribution to the total power dissipation. This contribution is much larger than that associated with the region 1 angular electric field. Finally, the large argument case of the three region configuration is more difficult. Usually, the power dissipation contribution associated with the region 1 axial electric field is greater than that associated with the region 1 radial electric field. The contribution associated with the region 1 angular electric field may or may not be greater than that associated with the region 1 axial electric field, depending on the electrical properties of the lossy rod and the pitch angle of the sheath helix.

To help understand the circumstances under which either the angular or axial region 1 electric field makes the larger power dissipation contribution, two sets of graphs of the ratio $P_{d\theta}/P_{dz}$ were prepared. The first set displayed both the small and large argument approximations of the ratio on the same graph. A gap was left in the middle, where neither of these approximations was justified. The second set of graphs showed only the large argument approximation of $P_{d\theta}/P_{dz}$.

Another type of approximate power dissipation equations were derived from the exact equations, for the case when "the lossy rod is a good conductor", making use of the approximate small and large argument wave numbers solution discussed in part 2.3.2. (The term "the lossy rod is a good conductor" as used here has the same meaning that it did in part 2.3.2.) Only the three region configuration was considered because approximate wave number solutions for the two region configuration were not obtained in part 2.3.2.

For the small argument circumstance, the contribution to the total power dissipation associated with the region 1 axial electric field is much greater than that associated with the region 1 radial electric field. In addition, the contribution associated with the region 1 angular electric field is usually greater than that associated with the region 1 axial electric field. When the large argument case was investigated, it was seen that the contribution to the total power dissipation associated with the region 1 angular electric field is much greater than that associated with the region 1 radial and axial electric fields.

Another set of approximate power dissipation equations was derived from the exact equations by assuming that the lossy rod is an excellent dielectric. This makes use of the wave number solution associated with the sheath helix surrounding an ideal dielectric coaxial rod, $_h d_a$. The conductivity of the lossy rod is restricted to being very small. However, it is not necessary to restrict the value of $_h d_a$. The approximate equations are useful because they can be evaluated over a wide range of operating frequencies, sheath helix geometries, and lossy coaxial rod element geometries.

As a check on the accuracy of these approximate power dissipation equations, the region 1 electric fields associated with the ideal dielectric coaxial rod configuration were used to develop a set of approximate equations. It was discovered that these equations are identical to those obtained by making approximations to the exact power dissipation equations. Therefore, the approximate power dissipation equations for the case when the lossy rod is an excellent dielectric can be considered as a *perturbation solution*, based on the ideal dielectric coaxial rod fields.

A discussion was given of the overlap associated with these power dissipation equations and the equations for the case when "the lossy rod is not a good conductor". Roughly speaking, if the conductivity of the lossy rod is assumed to be sufficiently small for the second mentioned set of equations, and if the value of $_h d_a$ is assumed to be sufficiently small or large for the first set, the two sets of equations were discovered to be equal. This is an expected result. It provides a check on the accuracy of these two sets of equations.

Graphs of P_{dr}/P_{dz} and $P_{d\theta}/P_{dz}$ were prepared. For both the two and three region configurations, it was discovered that for small values of $ka \cot an\psi$, the contribution to the total power dissipation associated with the region 1 axial electric field is much greater than that of the region 1 radial and angular electric fields. On the other hand, for large values of $ka \cot an\psi$, both the two and three region configurations showed that the contribution associated with the region 1 axial and radial electric fields is equal, and that this is usually much greater than the contribution associated with the region 1 angular electric field.

The spatial distribution of the total power dissipation occurring within the lossy coaxial rod element was examined. It was found that for large values of $ka \cot \psi$, the power dissipation is large near the surface of the rod and it rapidly decreases moving radially inwards toward the center of the rod. It is approximately constant with respect to the axial position over the entire length of the element. When the value of $ka \cot \psi$ is small, the power dissipation is uniformly distributed at all points throughout the lossy coaxial rod element volume.

The final set of approximate power dissipation equations discussed in the chapter were derived from the exact equations for the case when the lossy rod is an excellent conductor. The wave number solution for the sheath helix surrounding a perfectly conducting coaxial rod, $h^c a$, is used. Only the three region configuration is considered. (In Appendix C it is mentioned that the free mode field solution associated with the two region configuration is not of interest.) The approximate power dissipation equations are convenient because they can be evaluated over a wide range of operating frequencies, sheath helix geometries, and lossy coaxial rod element geometries.

In order to check on the accuracy of these approximate power dissipation equations, a perturbation procedure was performed, making use of the concept of surface resistance and the region 2 $(b \leq r \leq a)$ magnetic fields associated with the perfectly conducting coaxial rod configuration. It was discovered that approximately the same total power dissipation was calculated from this procedure as that obtained by making approximations to the exact power dissipation equations.

The overlap associated with these power dissipation equations and the equations for the case when "the lossy rod is a good conductor", was discussed. Roughly speaking, it was discovered that if the value of $h^c a$ is sufficiently small or large for the first mentioned set of equations, and if the lossy rod conductivity is sufficiently large in the second set, the two sets of equations are equal. This result is expected. It provides a check on the accuracy of the two sets of equations.

Graphs of P_{dr}/P_{dz} and $P_{d\theta}/P_{dz}$ were prepared. Assuming that the sheath helix is relatively tightly wound, it was discovered that the contribution to the total power dissipation associated with the region 1 angular electric field is usually much greater than that associated with the region 1 radial and axial electric fields.

The spatial distribution of the total power dissipation occurring within the lossy coaxial rod element was examined. For large values of $ka \ cotan\psi$, the power dissipation is very large near the surface of the lossy rod, and it very rapidly decreases moving radially inwards toward the center of the rod. Furthermore, the power dissipation is very nonuniformly distributed over the axial length of the element. For small values of $ka \ cotan\psi$, the power dissipation is large at the lossy rod surface and it rapidly decreases as the radial distance becomes smaller. It is uniformly distributed over the axial length of the element.

4. Chapter 4. Summary and Conclusions

The purpose of the thesis is to derive and investigate the free mode field solution associated with a sheath helix surrounding a lossy coaxial rod, and then to examine the time-averaged power dissipation which occurs within the lossy rod. Equations for the exact electric and magnetic field components, and for the exact total power dissipation within the lossy rod, are derived in Chapters 2 and 3. (The *total power dissipation*, results from contributions associated with the presence inside the lossy rod of the radial, angular, and axial electric field components.) It was not possible to solve the exact dispersion and separation constant equations, in order to numerically evaluate the two radial wave numbers and the axial wave number. As a result, the exact electric and magnetic field components, and the exact power dissipation, could not be numerically evaluated.

In order to obtain numerical values for the field components and for the power dissipation, it is necessary to make approximations. Four distinct major classes of approximations are made. (Although the exact equations derived for the fields and power dissipation are valid for all pitch angles in the range $0 < \psi < 90.0°$, it is usually assumed that the sheath helix is relatively tightly wound, for example $0 < \psi \leq 10.0°$, when the approximate equations are considered.)

The first two classes of approximations are concerned with the cases when "*the lossy rod is not a good conductor*" and when "*the lossy rod is a good conductor*". (The meanings of the two expressions in quotation marks are defined in part 2.3.1 and in part 2.3.2, respectively.) Within these two classes of approximations, the magnitudes of the two radial wave numbers are restricted to being either small or large. This means that all the Bessel functions appearing in the dispersion equation, the electric and magnetic field components, and the power dissipation equations, can be approximated by replacing them with their small and large argument representations. With this approximation, it is possible to solve the dispersion equation and the separation constant equation to calculate approximate radial and, axial wave numbers. These wave numbers can then be used to approximately evaluate the electric and magnetic field components, and the power dissipation. Unfortunately, the resulting solutions are only valid for certain ranges of the operating frequency and for certain geometries of the sheath helix and lossy

266

coaxial rod configuration.

The second two classes of approximations are concerned with the cases when *the lossy rod is an excellent dielectric*, and when *the lossy rod is an excellent conductor*. For these cases, the radial and axial wave numbers solution associated with the ideal dielectric (zero conductivity) coaxial rod configuration, and the perfectly conducting coaxial rod configuration, respectively, are used in order to obtain numerical values for the field components and to investigate the power dissipation occurring within the lossy rod. It is now not necessary to make any approximations to the Bessel functions which appear in the field components and in the power dissipation equations. The solution is valid over a wide range of operating frequencies and for many different goemetries of the sheath helix and lossy coaxial rod configuration. However, sharp restrictions are placed on the electrical properties of the lossy rod.

For the four classes of approximations, it is possible to determine how much of a contribution towards the total power dissipation is associated with each of the three electric field components present within the lossy rod. Furthermore it is possible to determine how the total power dissipation is distributed spatially throughout the lossy rod volume.

The discussion presented in Chapter 2 and in Chapter 3 considers a relatively wide range of different cases. It is recognized that for the purposes of actual electromagnetic heating applications, some of these cases are of more academic interest than practical interest. In order to provide an illustration of the conclusions which can be reached using the information presented in Chapters 2 and 3, a brief discussion will be given of two important practical applications of electromagnetic heating involving a cylindrical rod of lossy material centered inside of a physical helix.

For both of these practical applications, the following variables are used. It is assumed that the length of the physical helix (which is the same as that of the lossy rod) is ten times as great as the radius of the physical helix. This is done so that the effects of fringing associated with the finite length physical structure are insignificant near the mid-plane, which is chosen as the transverse plane $z = 0$. Furthermore, in order that the sheath helix model is well justified as a representation of the physical helix, it is

assumed that the physical helix is tightly wound with a wire of small cross sectional area. A pitch angle of $1.00°$ is used. It is assumed that the physical helix has a radius of 0.100 m. Therefore, the length of the physical helix is 1.00 m and it consists of 91 turns of wire in total. Next, it is assumed that the radius of the lossy rod is 0.090 m. Finally, an operating frequency of 1.00×10^4 Hz is employed.

For the first practical application of electromagnetic heating, it is assumed that the lossy rod consists of a sample of Douglas Beech Wood whose conductivity and permittivity are listed in Table E.1. The electrical properties of this sample are such that it can be considered as an example of the small argument case, when "the lossy rod is not a good conductor". Thus, from the information presented in sub-parts 2.3.1.1 and 2.4.1.2, the electric field components in all three regions can be numerically evaluated and so their behavior at different points in space is known.

The axial electric field within the lossy rod does not change as the radial distance is varied. (When the radial dependence of the electric fields is discussed, it is assumed that the axial position is held constant.) However, the radial and angular electric fields within the lossy rod are directly proportional to the radial distance. *At all radial positions within the Douglas Beech Wood rod, the magnitude of the axial electric field is much greater than that of the radial and angular electric fields.*

The axial electric field within the air gap between the lossy rod surface and the physical helix windings is constant with respect to changes in the radial distance. The radial and angular electric fields within the air gap change relatively gradually as the radial distance is varied. In the air-filled region just outside of the physical helix windings, all the electric fields are slowly reduced in magnitude as the radial distance increases. More specifically, the axial electric field has a logarithmic radial dependence while the radial and angular electric fields are proportional to the inverse of the radial distance. One exception to the behavior mentioned in the two preceding sentences occurs at very large distances away from the physical helix windings. All of the electric field components are now rapidly exponentially attenuated as the radial distance increases.

Consider now the axial dependence of the electric field components. (It is assumed that the radial position is held constant.) Within the lossy rod, as well as in the air gap region and in the air-filled region outside of the physical helix windings, the

angular and axial electric fields are constant as the axial distance is varied. However, the radial electric fields increase linearly in magnitude as the axial distance from the transverse plane $z = 0$ increases.

Attention is now directed towards examining the time-averaged power dissipation which occurs within the Douglas Beech Wood rod volume. Since the power dissipation is calculated by integrating the square of the electric field components throughout the rod-filled region -- as shown in equations 3.6 - 3.8 -- the power dissipation contribution associated with the axial electric field component is much larger than the contribution associated with the radial and angular electric field components. Since, as has been previously mentioned in this chapter, the axial electric field component is constant at all points throughout the lossy rod volume, the total power dissipation within the Douglas Beech Wood rod is uniformly distributed. The total power dissipation is approximately given by equation 3.32.

Finally, it is of interest to discuss how the total power dissipation within the lossy rod behaves when relatively small changes are made to the variables which were initially specified. These variables consist of the terminal current associated with the physical helix windings, the physical helix pitch angle, the physical helix radius, the lossy rod radius, the length of the physical helix (which equals that of the lossy rod), and the operating frequency. (The electrical current present at the two terminals of the physical helix windings is i_0 (A). It is related to the electrical surface current present on the sheath helix "windings", $\jmath_{11}$ (A/m), according to

$$ i_0 = \jmath_{11} \; p \; \cos\psi = \jmath_{11} \; 2\pi a \; \sin\psi. $$

p is the pitch distance -- the axial distance between two successive windings, a is the helix radius, and ψ is the helix pitch angle. See Figure 1.5b.) When one particular variable is altered, it is assumed that all other variables are held constant.

Doubling the terminal current means that the total power dissipation increases four times. Reducing the helix pitch angle by a factor of two means that the total power dissipation increases sixteen times. Varying the helix radius has approximately no effect

on the total power dissipation. If the lossy rod radius is reduced by a factor of two, the total power dissipation decreases by a factor of four. Doubling the length of the helix means that the total power dissipation is doubled. Finally, reducing the operating frequency by a factor of two means that the total power dissipation decreases by a factor of four.

If just the contribution to the total power dissipation associated with the angular electric field had been considered -- which is the type of analysis performed by Brown et al. (3, pp. 27) -- a different value for the total power dissipation would have been obtained. Furthermore, its functional dependence would be different than that discussed in the preceding paragraph. One important achievement of the thesis is the recognition that the total power dissipation within the Douglas Beech Wood rod is approximately given by the contribution associated with the axial electric field and not by the contribution associated with the angular electric field.

The second practical application of eletromagnetic heating assumes that the lossy rod consists of a sample of aluminum with $\epsilon_r \cong 1$ and $\sigma = 3.54 \times 10^7$ S/m. Here the electrical properties are such that this is an example of the small argument representation, for the case when "the lossy rod is a good conductor". The same physical helix geometry, terminal current of the physical helix windings, and lossy rod geometry, used in the first practical example of electromagnetic heating are employed here.

Assuming that the axial position is held constant, all of the electric field components within the rod-filled region are rapidly exponentially attenuated as the radial distance decreases. *In the rod-filled region, the angular electric field component is much larger in magnitude than the radial and axial electric field components, except at radial distances very close to the center of the aluminum rod.* Electric field components in the air gap, and in the air-filled region outside of the physical helix windings, vary relatively gradually as the radial distance is changed. There are, however, two exceptions to the preceding statement. Inside the air gap, near the surface of the lossy rod, the magnitudes of the angular and axial electric field components decrease rapidly while the magnitude of the radial electric field component increases rapidly, as the

radial distance becomes smaller. At large distances from the physical helix windings, the electric fields are rapidly exponentially attenuated as the radial distance increases.

At a fixed radial position within the lossy rod, the air-gap region, and the air filled region outside of the physical helix windings, the angular and axial electric fields remain the same when the axial coordinate is varied. However, in all three regions, the magnitudes of the radial electric fields increase linearly as the axial distance from thé transverse mid-plane $z = 0$ becomes larger.

Since the angular electric field has a magnitude much greater than that of the radial and axial electric fields at most points throughout the lossy rod volume, the power dissipation contribution associated with the angular electric field dominates over that associated with the other two electric fields. (In fact, the total power dissipation is approximately given by equation 3.71.) Since the magnitude of the angular electric field within the lossy rod is rapidly attenuated as the radial distance decreases (for a fixed axial position) but is constant as the axial distance is varied (for a fixed radial position), the total power dissipation is strongly concentrated near the surface of the aluminum rod and it is uniformly distributed over the axial length of the rod.

Attention is now directed towards investigating the behavior of the total power dissipation when relatively small changes are made to the initially specified variables. It is assumed that all other variables are held constant when a particular variable is altered. When the terminal electrical current associated with the physical helix windings is doubled, the total power dissipation increases four times. If the pitch angle of the physical helix windings is reduced by a factor of two, the total power dissipation increases by a factor of four. Decreasing the radius of the aluminum rod by a factor of two means that the total power dissipation becomes half of its original value. If the radius of the physical helix doubles, the total power dissipation is reduced by a factor of four. Doubling the length of the physical helix means that the total power dissipation doubles. Finally, increasing the frequency of operation four times means that the total power dissipation doubles.

For this practical application involving the aluminum rod, the contribution to the total power dissipation within the rod associated with the angular electric field is much greater than that associated with the axial or radial electric fields. Therefore, the

assumption made by Brown et al. (3, pp. 27) in only considering the angular electric field for calculating the total power dissipation is well justified here.

While only two practical numerical examples have been cited, the free mode field solution and the power, dissipation derived and discussed in this thesis can be used to give important information concerning the field distribution and the power dissipation for many other practical cases of interest. This information is invaluable in the design and use of induction coils for the purpose of electromagnetic heating. Potential applications occur in many disciplines, ranging from biomedical applications to the food and construction industries, and resource recovery operations.

Bibliography and References

1. Lozinskii,M., "Industrial Applications of Induction Heating", (Pergamon Press, New York, 1969).

2. Osborn,H.(JR), Brace,P., Johnson,W., Cable,J., and Eagan,T., "Induction Heating (a series of five educational lectures presented to members of the ASM during the 27th National Metal Congress and Exposition)", American Society for Metals, Cleveland, Ohio, 1946.

3. Brown,G., Hoyler,C., and Bierwirth,R., "Theory and Application of Radio Frequency Heating", (D. Van Nostrand, New York, 1947).

4. Pound,J., "Radio Frequency Heating in the Timber Industry", (Second Edition, Halstead Press [a division of John Wiley and Sons], New York, 1973).

5. Sensiper,S., "Electromagnetic Wave Propagation on Helical Conductors", D.Sc. Thesis, Massachusetts Institute of Technology (M.I.T. University), May, 1951.

6. Sensiper,S., "Electromagnetic Wave Propagation on Helical Structures (A Review and Summary of Recent Progress)", *Proc. I.R.E.*, vol. 43, pp. 149, 1955.

7. Pocklington,H.C., "Electrical Oscillations in Wires", *Proc. Camb. Phil. Soc.*, vol. 9, pp. 324, 1897.

8. Nicholson,J.W., "Resistance and Inductance of a Helical Conductor", *Phil. Mag.*, vol. 19, pp. 77, 1910.

9. Sollfrey,W., "Wave Propagation on Helical Wires", *J. Appl. Phys.*, vol. 22, pp. 905, 1951.

10. Chu,L.J. and Jackson,D., "Field Theory of Traveling Wave Tubes", M.I.T. University, Research Laboratory of Electronics (R.L.E.) Report No. 38, 1947.

11. Pierce,J.R., "Traveling Wave Tubes", (D. Van Nostrand, New York, 1950).

12. Cutler,C.C., "Experimental Determination of Helical Wave Properties", *Proc. I.R.E.*, vol. 36, pp. 230, 1948.

13. Harris,L., Johnson,A., Karp,L., and Smullin,L., "Some Measurements of Phase Velocity Along a Helix with Dielectric Supports", M.I.T. University, R.L.E. Report No. 93, 1949.

14. Phillips,R.S. and Malin,H., "A Helical Wave Guide, Part 2", Research Report 170-3 of the N.Y.U. Mathematics Research Group (New York University, Washington Square College, New York, New York, 1947).

15. Phillips,R.S. and Malin,H., "Investigation of the Exceptional Modes: n=±1, ±2", Research Report 170-7 of the N.Y.U. Mathematics Research Group (Addendum to

Research Report 170-3), 1948.

16. Hutter,R., "Beam and Wave Electronics for Microwave Tubes", (D. Van Nostrand, New York, 1960).

17. Watkins,D., "Topics in Electromagnetic Theory", (John Wiley and Sons, New York, 1958).

18. Collin,R., "Foundations for Microwave Engineering", (McGraw-Hill, New York, 1966).

19. Bryant,J.H., "Some Wave Properties of Helical Conductors", *J. Electrical Communications*, vol. 31, pp. 50, 1954.

20. Mathers,G. and Kino,G., "Some Properties of a Sheath Helix with a Center Conductor or External Shield", Stanford University, R.L.E. Report No. 65, 1953.

21. Olving,S., "Electromagnetic Wave Propagation on Helical Conductors Embedded in a Dielectric Medium", Chalmers University of Technology, R.L.E. Report No. 33, Gothenberg, Sweden, 1955.

22. Swift-Hook,D.T., "Dispersion Curves for a Helix in a Glass Tube", *Proc. I.E.E. (London)*, vol. 105b, Sup. No. 11, pp. 747, 1958.

23. Vaughan,J. and Williamson,J., "Design of Induction Heating Coils for Cylindrical Nonmagnetic Loads", *Trans. A.I.E.E.* part 2, vol. 64, pp. 587, 1945.

24. Baker,R., "Design and Calculation of Induction Heating Coils", *Trans. A.I.E.E.* part 2, vol. 76, pp. 31, 1957.

25. Chute,S., Vermeulen,F., and Cervenan,M., "On the Electromagnetic Heating of Low Loss Materials using Induction Coils", *Can. Elec. Eng. J.*, vol. 6, pp. 20, 1981.

26. Brillouin,L., "Wave Propagation in Periodic Structures", (McGraw-Hill, New York, 1946).

27. Collin,R., "Field Theory of Guided Waves", (McGraw-Hill, New York, 1960).

28. Ramo,S., Whinnery,J., and Van Duzer,T., "Fields and Waves in Communication Electronics", (John Wiley and Sons, New York, 1965).

29. Slater,J., "Microwave Electronics", (D. Van Nostrand, New York, 1950).

30. Johnson,C.C., "Field and Wave Electrodynamics", (McGraw-Hill, New York, 1966).

31. Frankel,S., "TM_{11} Mode in Circular Wave Guides with Two Coaxial Dielectrics", *J. Appl. Phys.*, vol. 18, pp. 650, 1947.

32. Banos,A., Saxon,D., and Gruen,H., "Propagation Characteristics in a Coaxial Structure with Two Dielectrics", *J. Appl. Phys.*, vol. 22, pp. 117, 1951.

33. Teasdale,R.D. and Crawford,G.N., "Cut off Frequency for Circular Waveguides Containing Two Coaxial Dielectrics", *Proc. National Electronics Conference (USA)*, vol. 8, pp. 296, 1952.

34. Teasdale,R.D. and Higgins,T.J., "Electromagnetic Waves in a Circular Waveguide Containing Two Coaxial Media", *Proc. National Electronics Conference (USA)*, vol. 5, pp. 427, 1949.

35. Stratton,J.A., "Electromagnetic Theory", (McGraw-Hill, New York, 1941).

36. Magid,L.M., "Electromagnetic Fields, Energy, and Waves", (John Wiley and Sons, New York, 1972).

37. Harrington,R.F., "Time-Harmonic Electromagnetic Fields", (McGraw-Hill, New York, 1961).

38. Jordan,E. and Balmain,K., "Electromagnetic Waves and Radiating Systems", (Prentice-Hall, Englewood Cliffs, New Jersey, 1968).

39. Adler,R.B., "Waves on Inhomogeneous Cylindrical Structures", *Proc. I.R.E.*, vol. 40, pp. 339, 1952.

40. Adler,R.B., "Properties of Guided Waves on Inhomogeneous Cylindrical Structures", M.I.T. University, R.L.E. Report No. 102, 1949.

41. Paris,D. and Hurd,F., "Basic Electromagnetic Theory", (McGraw-Hill, New York, 1969).

42. Conte,S. and Boor,C., "Numerical Analysis -- an Algorithmic Approach", (Third Edition, McGraw-Hill, New York, 1980).

43. "International Mathematical and Statistical Library (IMSL)", Edition 8, IMSL, Inc., Sixth Floor, NBC Building, 7500 Bellaire Boulevard, Houston, Texas, 77036, USA, 1980.

44. Plonsey,R. and Collin,R., "Principles and Applications of Electromagnetic Fields", (McGraw-Hill, New York, 1961).

45. Puschner, H., "Heating with Microwaves", (Philips Technical Library, New York, 1966).

46. Vermeulen,F., Chute,S., and Cervenan, M., "Physical Modelling of the Electromagnetic Heating of Oil Sand and other Earth-Type and Biological Materials", Can. Elec. Eng. J., vol. 4, pp. 19, 1979.

47. Thomas,G.B., "Calculus and Analytic Geometry", (Fourth Edition, Addison-Wesley, Reading, Massachusetts, 1968).

48. Seshadri, S., "Fundamentals of Transmission Lines and Electromagnetic Fields", (Addison-Wesley, Reading, Massachusetts, 1971).

49. Neff, H., "Basic Electromagnetic Fields," (Harper and Row, New York, 1981).

50. Abromowitz, M., and Stegun, I., "Handbook of Mathematical Functions", (Dover Publications, New York, 1965).

51. Watson, G.N., "A Treatise on the Theory of Bessel Functions", (Second Edition, Cambridge University Press, Cambridge, England, 1966).

52. Kreider, D., Kuller, R., Ostberg, D., and Perkins, F. "An Introduction to Linear Analysis", (Addison-Wesley, Reading, Massachusetts, 1966).

53. Tranter, J., "Bessel Functions with some Physical Applications", (English Universities Press, London, 1968).

54. Bowman, F., "Introduction to Bessel Functions", (Dover Publications, New York, 1958).

55. Wylie, C.R., "Differential Equations", (McGraw-Hill, New York, 1979).

A. Appendix A. The Modified Bessel Functions

The purpose of this appendix is to collect in one convenient location the many mathematical identities and properties of Bessel functions, which have been used throughout Chapters 2 and 3, and in Appendices B, C, and D. References used are 50, pp. 355-389; 51; 52, Chapter 15; 53; 54; and 55, pp. 306-333. It is definitely not the intention to prove or derive the following properties. Interested readers are directed to the references.

An explanation of the symbols which are used is now given. z, λ, and α are complex numbers, x is a real positive number, "$\simeq$" means "is approximately equal to", "$/$" means "differentiate with respect to the total argument", and "$\sim$" means "take the complex conjugate". Only Bessel functions of integral orders q where $q = 0$ or 1, are used since just these integral order functions are of concern in the thesis. Many results presented here are actually valid for a much wider class of orders.

A.1 Differential Equation, Recurrence Properties, Relation with other Bessel Functions, Analytic Continuation, and Wronskian Identity

The modified Bessel equation of order q is

$$z^2 \frac{d^2 y}{dz^2} + z \frac{dy}{dz} - (\lambda^2 z^2 + q^2)y = 0. \qquad (A.1)$$

Employing the power series method of Frobenius, taking into consideration the fact that the roots of the indicial equation differ by an integer, yields two linearly independent solutions (55, pp. 306-333). These are I_q, the modified Bessel function of the first kind of order q, and K_q, the modified Bessel function of the second kind of order q. Hence

$$y = C I_q(\lambda z) + D K_q(\lambda z), \tag{A.2}$$

where

$$I_q(\lambda z) = \sum_{k=0}^{\infty} \frac{(\lambda z)^{2k+q}}{2^{2k+q} k! (k+q)!}, \quad \text{and} \tag{A.3}$$

$$K_q(\lambda z) = \frac{\pi}{2} \cdot \lim_{\nu \to q} \left[\frac{I_{-\nu}(\lambda z) - I_{\nu}(\lambda z)}{\sin(\nu\pi)} \right]. \tag{A.4}$$

For real positive arguments, I_q and K_q are plotted in Figure A.1.

I_q and K_q do not obey the same recurrence relations. These are

$$I_0'(z) = I_1(z), \tag{A.5}$$

$$K_0'(z) = -K_1(z), \tag{A.6}$$

$$I_1'(z) = I_0(z) - \frac{1}{z} I_1(z), \quad \text{and} \tag{A.7}$$

$$K_1'(z) = -K_0(z) - \frac{1}{z} K_1(z). \tag{A.8}$$

The modified Bessel functions are related to the Bessel functions of the first and second kinds.

$$I_0(z) = J_0(jz), \tag{A.9}$$

$$I_1(z) = -j J_1(jz), \tag{A.10}$$

$$K_0(z) = j \frac{\pi}{2} (J_0(jz) + j N_0(jz)), \quad \text{and} \tag{A.11}$$

$$K_1(z) = -\frac{\pi}{2} (J_1(jz) + j N_1(jz)); \tag{A.12}$$
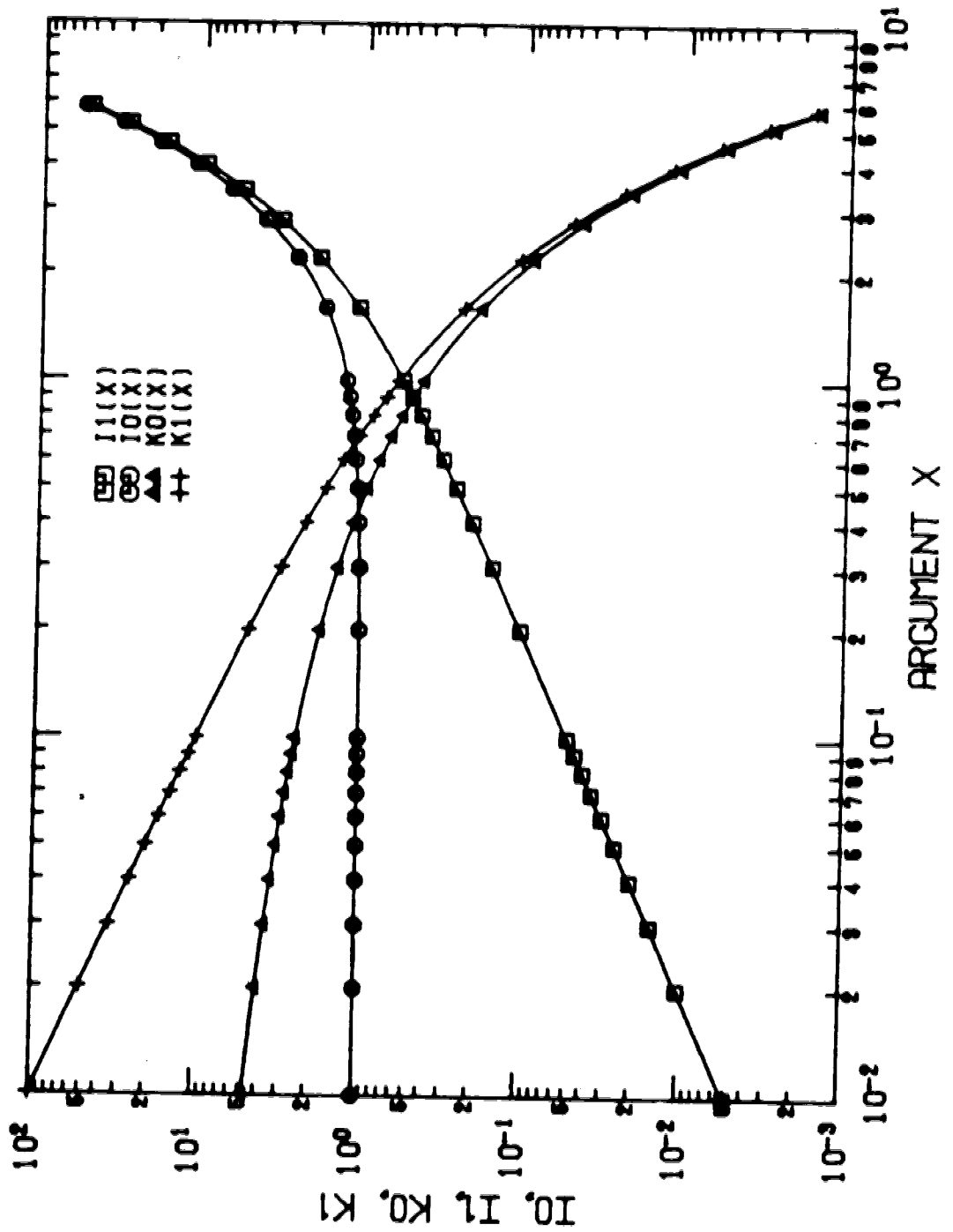
Figure A.1   Graphs of the Bessel functions I_0, I_1, K_0, and K_1 for real positive arguments. (Note $I0 = I_0$, $I1 = I_1$, $K0 = K_0$, and $K1 = K_1$.)

where J_q is the Bessel function of the first kind of order q, and N_q is the Bessel function of the second kind (or the Neumann function) of order q. $J_q(\lambda z)$ and $N_q(\lambda z)$ are two linearly independent solutions of the Bessel equation

$$z^2 \frac{d^2 y}{dz^2} + z \frac{dy}{dz} + (\lambda^2 z^2 - q^2)y = 0.$$

These two solutions satisfy the Wronskian identity

$$W(J_q(z), N_q(z)) = J_q(z) N_q'(z) - J_q'(z) N_q(z)$$

$$= \frac{2}{\pi z}. \tag{A.13}$$

Modified Bessel functions formed by a change in the algebraic sign of the argument are related to the original functions according to

$$I_0(-z) = I_0(z), \tag{A.14}$$

$$I_1(-z) = - I_1(z), \tag{A.15}$$

$$K_0(-z) = K_0(z) - j \pi I_0(z), \quad \text{and} \tag{A.16}$$

$$K_1(-z) = - K_1(z) - j \pi I_1(z). \tag{A.17}$$

It is convenient to express equations A.9 - A.12 in another manner. This is done using equations A.14 - A.17.

$$I_0(jz) = J_0(z), \tag{A.18}$$

$$I_1(jz) = j \, J_1(z), \tag{A.19}$$

$$K_0(jz) = -\frac{\pi}{2} \, (N_0(z) + j \, J_0(z)), \quad \text{and} \tag{A.20}$$

$$K_1(jz) = -\frac{\pi}{2} \, (J_1(z) - j \, N_1(z)). \tag{A.21}$$

Taking the complex conjugate of the modified Bessel functions results in

$$\widetilde{I}_q(z) = I_q(\widetilde{z}), \quad \text{and} \tag{A.22}$$

$$\widetilde{K}_q(z) = K_q(\widetilde{z}). \tag{A.23}$$

This is a property of analytic continuation.

The Wronskian identity is

$$W(I_q(z), K_q(z)) = I_q(z) \, K_q'(z) - I_q'(z) \, K_q(z)$$

$$= -\frac{1}{z}. \tag{A.24}$$

It is very useful to combine equation A.24 with equations A.5 and A.6, when $q = 0$, with the result that

$$I_0(z) \, K_1(z) + I_1(z) \, K_0(z) = \frac{1}{z}. \tag{A.25}$$

The preceding formula was used many times throughout the thesis.

A.2 Small and Large Argument Approximations of the Bessel Functions

One can obtain the small argument representations of the modified Bessel functions by only keeping the most significant term in the infinite series expansions, equations A.3 and A.4.

$$I_0(z) \cong 1, \tag{A.26}$$

$$I_1(z) \cong \frac{z}{2}, \tag{A.27}$$

$$K_0(z) \cong -\log(0.891\ z), \quad \text{and} \tag{A.28}$$

$$K_1(z) \cong \frac{1}{z}, \tag{A.29}$$

are the small argument approximations of the modified Bessel functions. Table A.1 is a list of the percent error associated with the exact functions compared to equations A.26 - A.29, for real positive arguments. Clearly, for $0 < x \leq 0.10$, the error involved with using the approximate equations is very small, about one percent or less.

Sometimes, such as when two nearly equal quantities are being subtracted, it is necessary to use more accurate small argument approximations. In particular, if the first two terms in the infinite series expansion for I_q are kept, there results

$$I_0(z) \cong 1 + \frac{z^2}{4}, \quad \text{and} \tag{A.30}$$

$$I_1(z) \cong \frac{z}{2} + \frac{z^3}{16}. \tag{A.31}$$

In a similar fashion, small argument representations of the Bessel functions of the first and second kind can be obtained from their infinite series representations [50, pp. 360].

$$J_0(z) \cong 1, \tag{A.32}$$

Table A.1   Percentage error associated with the
small argument representations of the Bessel functions
I_0, I_1, K_0, and K_1, based on equations A.26 - A.29.
(Note $I0=I_0$, $I1=I_1$, $K0=K_0$, $K1=K_1$, and SM means the
small argument approximation.)

X	IO(X)	SM IO(X)	%ERROR SM IO(X)
0.1000E-03	1.000	1.000	0.2500E-06
0.4000E-03	1.000	1.000	0.4000E-05
0.7000E-03	1.000	1.000	0.1225E-04
0.1000E-02	1.000	1.000	0.2500E-04
0.4000E-02	1.000	1.000	0.4000E-03
0.7000E-02	1.000	1.000	0.1225E-02
0.1000E-01	1.000	1.000	0.2500E-02
0.4000E-01	1.000	1.000	0.3999E-01
0.7000E-01	1.001	1.000	0.1224
0.1000	1.003	1.000	0.2495
0.4000	1.040	1.000	3.883
0.7000	1.126	1.000	11.21
1.000	1.266	1.000	21.02
4.000	11.30	1.000	91.15
7.000	168.6	1.000	99.41

X	I1(X)	SM I1(X)	%ERROR SM I1(X)
0.1000E-03	0.5000E-04	0.5000E-04	0.1250E-06
0.4000E-03	0.2000E-03	0.2000E-03	0.2000E-05
0.7000E-03	0.3500E-03	0.3500E-03	0.6125E-05
0.1000E-02	0.5000E-03	0.5000E-03	0.1250E-04
0.4000E-02	0.2000E-02	0.2000E-02	0.2000E-03
0.7000E-02	0.3500E-02	0.3500E-02	0.6125E-03
0.1000E-01	0.5000E-02	0.5000E-02	0.1250E-02
0.4000E-01	0.2000E-01	0.2000E-01	0.2000E-01
0.7000E-01	0.3502E-01	0.3500E-01	0.6122E-01
0.1000	0.5006E-01	0.5000E-01	0.1249
0.4000	0.2040	0.2000	1.974
0.7000	0.3719	0.3500	5.884
1.000	0.5652	0.5000	11.53
4.000	9.759	2.000	79.51
7.000	156.0	3.500	97.76

Table A.1 (continued)

X	KO(X)	SM KO(X)	%ERROR SM KO(X)
0.1000E-03	9.326	9.326	0.5583E-02
0.4000E-03	7.940	7.939	0.6562E-02
0.7000E-03	7.380	7.380	0.7069E-02
0.1000E-02	7.024	7.023	0.7442E-02
0.4000E-02	5.637	5.637	0.9707E-02
0.7000E-02	5.078	5.077	0.1172E-01
0.1000E-01	4.721	4.721	0.1406E-01
0.4000E-01	3.337	3.334	0.6758E-01
0.7000E-01	2.780	2.775	0.1852
0.1000	2.427	2.418	0.3738
0.4000	1.115	1.032	7.432
0.7000	0.6605	0.4721	28.53
1.000	0.4210	0.1154	72.59
4.000	0.1116E-01	-1.271	0.1149E+05
7.000	0.4248E-03	-1.830	0.4310E+06

X	K1(X)	SM K1(X)	%ERROR SM K1(X)
0.1000E-03	0.1000E+05	0.1000E+05	-0.4913E-05
0.4000E-03	2500.	2500.	-0.6752E-04
0.7000E-03	1429.	1429.	-0.1931E-03
0.1000E-02	1000.	1000.	-0.3762E-03
0.4000E-02	250.0	250.0	-0.4910E-02
0.7000E-02	142.8	142.9	-0.1367E-01
0.1000E-01	99.97	100.0	-0.2611E-01
0.4000E-01	24.92	25.00	-0.3078
0.7000E-01	14.17	14.29	-0.8095
0.1000	9.854	10.00	-1.483
0.4000	2.184	2.500	-14.45
0.7000	1.050	1.429	-36.02
1.000	0.6019	1.000	-66.14
4.000	0.1248E-01	0.2500	-1903.
7.000	0.4542E-03	0.1429	-0.3135E+05

$$J_1(z) \approx \frac{z}{2},$$

(A.33)

$$N_0(z) \approx \frac{2}{\pi} \log(0.891\ z), \cdot \text{and}$$

(A.34)

$$N_1(z) \approx -\frac{2}{\pi z}.$$

(A.35)

The asymptotic representations valid for large arguments are known in the form of an infinite series. Keeping the first three terms of the series for the modified Bessel functions, the asymptotic representations are

$$I_0(z) \approx \frac{e^z}{\sqrt{2\pi z}} [1 + \frac{0.125}{z} + \frac{0.0703}{z^2}],$$

(A.36)

$$I_1(z) \approx \frac{e^z}{\sqrt{2\pi z}} [1 - \frac{0.375}{z} - \frac{0.117}{z^2}],$$

(A.37)

$$K_0(z) \approx \sqrt{\frac{\pi}{2z}}\ e^{-z} [1 - \frac{0.125}{z} + \frac{0.0703}{z^2}], \text{ and}$$

(A.38)

$$K_1(z) \approx \sqrt{\frac{\pi}{2z}}\ e^{-z} [1 + \frac{0.375}{z} - \frac{0.117}{z^2}].$$

(A.39)

Table A.2 compares equations A.36 - A.39, first keeping only the initial term and then keeping only the first two terms, with the exact values. (When only the first term of the series is kept, the resulting representation is called the *zero order large argument approximation*.) Real positive arguments are used in the table. If only the first term is kept, the error associated with using the approximation is large at $x = 1$. However, it rapidly decreases with increasing values of x, and the error is only a few percent for $x > 10$. When the first two terms of equations A.36 - A.39 are kept, Table A.2 shows that the error involved in using the approximation is about one percent or less for $x > 4$. In fact, the error associated with using these approximations for values of x

Table A.2   Percentage error associated with the large argument representations of the Bessel functions I_0, I_1, K_0, and K_1, based on equations A.36 - A.39. Errors for the approximations using only the first term of the series, and the first two terms of the series, are given. (Note $I0=I_0$, $I1=I_1$, $K0=K_0$, and $K1=K_1$. AS0 I0 means only the first term of equation A.36 is used to approximate I_0. AS1 K1 means the first two terms of equation A.39 are used to approximate K_1.)

X	IO(X)	AS0 IO(X)	AS1 IO(X)
0.1000	1.003	1.394	3.137
0.4000	1.040	0.9410	1.235
0.7000	1.126	0.9602	1.132
1.000	1.266	1.084	1.220
4.000	11.30	10.89	11.23
7.000	168.6	165.4	168.3
10.00	2816.	2779.	2814.
40.00	0.1489E+17	0.1485E+17	0.1489E+17
70.00	0.1202E+30	0.1199E+30	0.1202E+30
100.0	0.1074E+43	0.1072E+43	0.1074E+43
120.0	0.4755E+51	0.4750E+51	0.4755E+51
140.0	0.2135E+60	0.2133E+60	0.2135E+60

X	%ERROR AS0 IO(X)	%ERROR AS1 IO(X)
0.1000	-39.08	-212.9
0.4000	9.553	-18.71
0.7000	14.75	-0.4772
1.000	14.35	3.639
4.000	3.638	0.6268
7.000	1.920	0.1687
10.00	1.312	0.7815E-01
40.00	0.3161	0.4616E-02
70.00	0.1798	0.1571E-02
100.0	0.1257	0.8266E-03
120.0	0.1047	0.6090E-03
140.0	0.8968E-01	0.4780E-03

X	I1(X)	AS0 I1(X)	AS1 I1(X)
0.1000	0.5006E-01	1.394	-3.834
0.4000	0.2040	0.9410	0.5881E-01
0.7000	0.3719	0.9602	0.4458
1.000	0.5652	1.084	0.6778
4.000	9.759	10.89	0.6778
7.00u	156.0	165.4	156.5
10.00	2671.	2779.	2675.
40.00	0.1471E+17	0.1485E+17	0.1471E+17
70.00	0.1193E+30	0.1199E+30	0.1193E+30
100.0	0.1068E+43	0.1072E+43	0.1068E+43
120.0	0.4735E+51	0.4750E+51	0.4735E+51
140.0	0.2128E+60	0.2133E+60	0.2128E+60

Table A.2 (continued)

X	%ERROR AS0 I1(X)	%ERROR AS1 I1(X)
0.1000	-2685.	7759.
0.4000	-361.2	71.17
0.7000	-158.2	-19.88
1.000	-91.88	-19.93
4.000	-11.59	-1.130
7.000	-5.971	-0.2943
10.00	-4.036	-0.1344
40.00	-0.9539	-0.7445E-02
70.00	-0.5409	-0.2318E-02
100.0	-0.3775	-0.1070E-02
120.0	-0.3142	-0.7055E-03
140.0	-0.2691	-0.4864E-03

X	K0(X)	AS0 K0(X)	AS1 K0(X)
0.1000	2.427	3.586	-0.8965
0.4000	1.115	1.328	0.9132
0.7000	0.6605	0.7439	0.6110
1.000	0.4210	0.4611	0.4034
4.000	0.1116E-01	0.1148E-01	0.1112E-01
7.000	0.4248E-03	0.4320E-03	0.4243E-03
0.00	0.1778E-04	0.1799E-04	0.1777E-04
40.00	0.8393E-18	0.8419E-18	0.8393E-18
70.00	0.5945E-31	0.5955E-31	0.5945E-31
100.0	0.4657E-44	0.4662E-44	0.4657E-44
120.0	0.8764E-53	0.8773E-53	0.8764E-53
140.0	0.1673E-61	0.1674E-61	0.1673E-61

X	%ERROR AS0 K0(X)	%ERROR AS1 K0(X)
0.1000	-47.76	136.9
0.4000	-19.18	18.06
0.7000	-12.62	7.490
1.000	-9.511	4.178
4.000	-2.849	0.3648
7.000	-1.688	0.1278
10.00	-1.200	0.6458E-01
40.00	-0.3093	0.4181E-02
70.00	-0.1776	0.1300E-02
100.0	-0.1246	0.5799E-03
120.0	-0.1039	0.3677E-03
140.0	-0.8913E-01	0.2395E-03

Table A.2 (continued)

X	K1(X)	AS0 K1(X)	AS1 K1(X)
0.1000	9.854	3.586	17.03
0.4000	2.184	1.328	2.574
0.7000	1.050	0.7439	1.142
1.000	0.6019	0.4611	0.6340
4.000	0.1248E-01	0.1148E-01	0.1255E-01
7.000	0.4542E-03	0.4320E-03	0.4551E-03
10.00	0.1865E-04	0.1799E-04	0.1867E-04
40.00	0.8497E-18	0.8419E-18	0.8498E-18
70.00	0.5987E-31	0.5955E-31	0.5987E-31
100.0	0.4680E-44	0.4662E-44	0.4680E-44
120.0	0.8800E-53	0.8773E-53	0.8800E-53
140.0	0.1679E-61	0.1674E-61	0.1679E-61

X	%ERROR AS0 K1(X)	%ERROR AS1 K1(X)
0.1000	63.61	-72.87
0.4000	39.19	-17.82
0.7000	29.17	-8.770
1.000	23.40	-5.327
4.000	8.058	-0.5621
7.000	4.891	-0.2037
10.00	3.514	-0.1045
40.00	0.9216	-0.7220E-02
70.00	0.5304	-0.2467E-02
100.0	0.3723	-0.1274E-02
120.0	0.3106	-0.9223E-03
140.0	0.2664	-0.7095E-03

as little as unity is relatively small.

The large argument asymptotic representations of the Bessel functions of the first and second kinds are listed.

$$J_0(z) \approx \sqrt{\frac{2}{\pi z}} \left[\cos(z - \frac{\pi}{4}) + \frac{1}{8z} \sin(z - \frac{\pi}{4}) \right], \qquad (A.40)$$

$$J_1(z) \approx \sqrt{\frac{2}{\pi z}} \left[\sin(z - \frac{\pi}{4}) + \frac{3}{8z} \cos(z - \frac{\pi}{4}) \right], \qquad (A.41)$$

$$N_0(z) \approx \sqrt{\frac{2}{\pi z}} \left[\sin(z - \frac{\pi}{4}) - \frac{1}{8z} \cos(z - \frac{\pi}{4}) \right], \text{ and} \qquad (A.42)$$

$$N_1(z) \approx \sqrt{\frac{2}{\pi z}} \left[-\cos(z - \frac{\pi}{4}) + \frac{3}{8z} \sin(z - \frac{\pi}{4}) \right]. \qquad (A.43)$$

Limiting cases, as the argument of the modified Bessel functions becomes very small or very large, can be readily obtained by making use of equations A.26 - A.29 and equations A.36 - A.39. For x approaching zero,

$$\lim_{x \to 0^+} I_0(x) = 1, \qquad (A.44)$$

$$\lim_{x \to 0^+} I_1(x) = 0, \quad \text{and} \qquad (A.45)$$

$$\lim_{x \to 0^+} K_0(x) = \lim_{x \to 0^+} K_1(x) = \infty. \qquad (A.46)$$

On the other hand, as x becomes very large,

$$\lim_{x \to \infty} I_0(x) = \lim_{x \to \infty} I_1(x) = \infty, \text{ and} \qquad (A.47)$$

$$\lim_{x \to \infty} K_0(x) = \lim_{x \to \infty} K_1(x) = 0. \qquad (A.48)$$

If the argument is restricted to being real and positive, the behavior of the modified Bessel functions is quite easily understood. I_0 and I_1 are strictly increasing positive functions, while K_0 and K_1 are strictly decreasing positive functions. Figure A.1 provides an illustration of this behavior. From equations A.26 – A.29, and A.36 – A.39, the following inequalities can be inferred.

$$0 < I_1(x) < I_0(x) < \infty, \text{ and} \tag{A.49}$$

$$0 < K_0(x) < K_1(x) < \infty; \tag{A.50}$$

where $0 < x < \infty$.

A.3 Integrals Involving Bessel Functions

The first mentioned two equations are equally valid if I_q and I_q' are replaced by K_q and K_q', respectively.

$$\int I_q(\lambda x) \, I_q(\alpha x) \, x \, dx = \frac{x}{\lambda^2 - \alpha^2}$$

$$[\lambda \, I_q(\alpha x) \, I_q'(\lambda x) - \alpha \, I_q(\lambda x) \, I_q'(\alpha x)], \text{ and} \tag{A.51}$$

$$\int [I_q(\lambda x)]^2 \, x \, dx = \frac{x^2}{2} \cdot$$

$$[(1 + \frac{q^2}{(\lambda x)^2}) \, [I_q(\lambda x)]^2 - [I_q'(\lambda x)]^2]. \tag{A.52}$$

In the final two equations, the integrand involves the modified Bessel functions of both the first and second kinds.

$$\int I_q(\lambda x) \; K_q(\alpha x) \; x \; dx = \frac{x}{\lambda^2 - \alpha^2} \cdot$$

$$[\lambda \; K_q(\alpha x) \; I_q'(\lambda x) - \alpha \; I_q(\lambda x) \; K_q'(\alpha x)], \text{ and} \qquad (A.53)$$

$$\int I_q(\lambda x) \; K_q(\lambda x) \; x \; dx = \frac{x^2}{2} \cdot$$

$$[(1 + \frac{q^2}{(\lambda x)^2}) \; I_q(\lambda x) \; K_q(\lambda x) - I_q'(\lambda x) \; K_q'(\lambda x)]. \qquad (A.54)$$

B. Appendix B. The Empty Sheath Helix

When air fills both the interior and exterior regions, the simplest possible sheath helix structure results. It can be considered as a special case of the sheath helix surrounding a lossy coaxial rod. This is true when the lossy rod radius becomes much smaller than the sheath helix radius, or when the electrical properties of the lossy rod become similar to those of air.

Considerable past work has been done on the empty sheath helix. Chu and Jackson (10), and Pierce (11) are two examples where research was performed in connection with applications to traveling wave tubes. Sensiper (5; 6) performed a very comprehensive study on this configuration, although most of the labor was directed to waves having angular dependence.

B.1 List of the Field Components and the Dispersion Equation

It is not the intention of this section to show the derivation of the dispersion equation and of the free mode field components. Interested readers are directed to Sensiper's thesis (5, pp. 22-27). An electrical current of the form

$$\underline{K} = \partial_{\shortparallel} \cos\beta^a z \; \underline{a}_{\shortparallel} \, ,$$

where $\partial_{\shortparallel}(A/m)$ is a constant with respect to the spatial coordinates, is assumed to be present on the sheath helix "windings". (See Figure 1.5b. This displays the developed sheath helix.)

Summary of the Field Components

Region 1 ($0 \le r \le a$)

$$E_{r1}{}^a = j \, \partial_{\shortparallel} \, \frac{120\pi}{ka \, \cot a n \psi} \, \cos\psi \; \beta^a a \; h^a a \; \cdot$$

$$K_0(h^a a) \; I_1(h^a r) \; \sin\beta^a z, \qquad \qquad (B.1)$$

295

$$E_{\theta 1}^{a} = -j \, \mathcal{G}_{||} \, 120\pi \, ka \, \cot\psi \, \cdot$$

$$\sin\psi \, K_1(h^a a) \, I_1(h^a r) \, \cos\beta^a z, \tag{B.2}$$

$$E_{z1}^{a} = j \, \mathcal{G}_{||} \, \frac{120\pi}{ka \, \cot\psi} \, \cos\psi \, (h^a a)^2 \cdot$$

$$K_0(h^a a) \, I_0(h^a r) \, \cos\beta^a z, \tag{B.3}$$

$$H_{r1}^{a} = \mathcal{G}_{||} \, \cos\psi \, \beta^a a \, K_1(h^a a) \, I_1(h^a r) \, \sin\beta^a z, \tag{B.4}$$

$$H_{\theta 1}^{a} = -\mathcal{G}_{||} \, \sin\psi \, h^a a \, K_0(h^a a) \, I_1(h^a r) \, \cos\beta^a z, \text{ and} \tag{B.5}$$

$$H_{z1}^{a} = \mathcal{G}_{||} \, \cos\psi \, h^a a \, K_1(h^a a) \, I_0(h^a r) \, \cos\beta^a z. \tag{B.6}$$

Region 2 $(a \leqslant r < \infty)$

$$E_{r2}^{a} = -j \, \mathcal{G}_{||} \, \frac{120\pi}{ka \, \cot\psi} \, \cos\psi \, \beta^a a \, h^a a \, \cdot$$

$$I_0(h^a a) \, K_1(h^a r) \, \sin\beta^a z, \tag{B.7}$$

$$E_{\theta 2}^{a} = -j \, \mathcal{G}_{||} \, 120\pi \, ka \, \cot\psi \, \cdot$$

$$\sin\psi \, I_1(h^a a) \, K_1(h^a r) \, \cos\beta^a z, \tag{B.8}$$

$$E_{z2}^{a} = j \, \mathcal{G}_{||} \, \frac{120\pi}{ka \, \cot\psi} \, \cos\psi \, (h^a a)^2 \cdot$$

$$I_0(h^a a) \, K_0(h^a r) \, \cos\beta^a z, \tag{B.9}$$

$$H_{r2}{}^a = \mathcal{J}_{11} \cos\psi \; \beta^a a \; I_1(h^a a) \; K_1(h^a r) \; \sin\beta^a z, \tag{B.10}$$

$$H_{\theta 2}{}^a = \mathcal{J}_{11} \sin\psi \; h^a a \; I_0(h^a a) \; K_1(h^a r) \; \cos\beta^a z, \quad \text{and} \tag{B.11}$$

$$H_{z2}{}^a = -\mathcal{J}_{11} \cos\psi \; h^a a \; I_1(h^a a) \; K_0(h^a r) \; \cos\beta^a z. \tag{B.12}$$

Summary of the Dispersion Equation

$$\left(\frac{ka \; \cot an}{h^a a}\right)^2 = \frac{I_0(h^a a) \; K_0(h^a a)}{I_1(h^a a) \; K_1(h^a a)} \tag{B.13}$$

Along with the *separation constant equation,*

$$h^a a = + \sqrt{(\beta^a a)^2 - (ka)^2}, \tag{B.14}$$

equation B.13 is used to calculate the radial wave number $h^a a$, and the axial wave number, $\beta^a a$.

Equations B.1 - B.14 comprise the free mode field solution of the empty sheath helix. The superscript " a " is used on all the electric and magnetic field components, and on the radial and axial wave numbers, so it is obvious that they are associated with the air-filled sheath helix, and not with any of the other configurations which have been studied in the thesis. The operating frequency and the sheath helix geometry are specified by two variables, $ka \; \cot an\psi = \omega \sqrt{\mu_0 \epsilon_0} \; a \; \cot an\psi$ and ψ. $0 < ka \; \cot an\psi < \infty$ and $0 < \psi < 90.0°$ are the allowed values of these variables. Throughout the remainder of this appendix, it will usually be

assumed that the sheath helix is sufficiently tightly wound so that $0 < \psi \leq 10.0°$.

Equations B.1 - B.14 agree with the angularly independent form of the field solution given by Sensiper (5, pp. 25-27). The dispersion equation, equation B.13, was mentioned in references 10; 11, pp. 231; 16, pp. 78; 17, pp. 43; 18, pp. 395; 27, pp. 404; 28, pp. 469; and 30, pp. 259.

It is convenient to consider the wave numbers solution of the dispersion equation and the separation constant equation as h^a_a and $(\beta^a_a)^2$, rather than as h^a and $(\beta^a)^2$, respectively. The advantage of this is that the sheath helix radius does not appear by itself as a variable, it only appears in the quantities $(ka)^2$ and $(ka \cot\psi)^2$. In equations B.1 - B.12, the spatial dependences of the field components are now regarded as being normalized with respect to the sheath helix radius so that h^a_r and β^a_z become $h^a_a \cdot r/a$ and $\beta^a_a \cdot z/a$, respectively.

B.2 Discussion of the Dispersion Equation and Graphs of the Radial Wave Number Solution

Attention is now directed to equations B.13 and B.14, the dispersion equation and the separation constant equation, respectively. Since the pitch angle and the angular frequency appear only as $(ka)^2$ and $(ka \cot\psi)^2$, it is clear that these equations are even functions of ψ and ω. The wave numbers solution h^a_a and $(\beta^a_a)^2$ do not depend on the positive or negative sense of the sheath helix "windings", or on the algebraic sign of the frequency. (As was previously mentioned in part 2.1.2, the dispersion equation along with the separation constant equation cannot determine the algebraic sign of the axial wave number. They are said to determine $(\beta^a_a)^2$ rather than β^a_a.) The concept that

$$(\beta^a(-\omega) \ a)^2 = (\beta^a(+\omega) \ a)^2$$

$$(B.15)$$

is very important in showing that the radial and axial wave numbers cannot be generally complex, with nonzero real and imaginary parts (5, pp. 232; 39; 40). A detailed investigation of the possible values $h^a{}_a$ and $_\beta{}^a{}_a$ which may satisfy the dispersion equation and the separation constant equation, shows that only *real wave numbers* such that

$$0 < h^a{}_a < \infty \quad \text{and} \quad (\beta^a{}_a)^2 > (ka)^2, \tag{B.16}$$

are permissible to obtain the free mode field solution. (Equations A.14 - A.17, A.18 - A.21, and A.24 can be used to evaluate the right hand side of equation B.13 and show that negative real or purely imaginary values of $h^a{}_a$ are not possible. A relatively thorough discussion of this is given in 5, pp. 231.)

It is clear from equations B.13 and B.14 what variables the radial wave number and the square of the axial wave number depend on.

$$h^a{}_a = f(ka \; \cot an\psi) \quad \text{and} \tag{B.17}$$

$$(\beta^a{}_a)^2 = g(ka \; \cot an\psi, \; \psi). \tag{B.18}$$

So that a better understanding of the behavior of the radial and axial wave number solutions, for different operating frequencies and sheath helix geometries, is obtained, and to facilitate computation of these wave numbers, it is very useful to develop approximations of equation B.13. First, the approximation valid when the radial wave number is large will be considered. Keeping all three terms of equations A.36 - A.39, substituting into the right hand side of equation B·13, and performing a small amount of algebra, yields

$$\left(\frac{ka \; \cot an\psi}{h^a{}_a}\right)^2 \simeq 1 + \frac{0.50}{(h^a{}_a)^2}. \tag{B.19}$$

Equation B.19 is the *accurate large argument approximation of the dispersion equation.*

Keeping only the first term of equations A.36 - A.39 (which is the zero order asymptotic representation), and repeating the previous procedure, results in

$$\frac{ka \; cotan\psi}{h^a_a} \cong 1.$$

(B.20)

Equation B.20 is the *crude large argument approximation of the dispersion equation.* Note that this equation is very convenient because the radial wave number is explicitly given in terms of the operating frequency, the sheath helix radius, and the sheath helix pitch angle.

A data table (which will not be presented here) was prepared to compare the right hand side of equation B.13 with that of equations B.19 and B.20. It demonstrated that for values of $ka \; cotan\psi$ as small as $\hat{1}$, the maximum error associated with equation B.19 is two percent, while that associated with equation B.20 is twenty percent. As $ka \; cotan\psi$ increases, the error very rapidly decreases, and for $ka \; cotan\psi > 5$, it is less than one percent for both equations B.19 and B.20.

Substituting equations A.26 - A.29 into the right hand side of equation B.13, it is seen that for small values of the radial wave number,

$$(\frac{ka \; cotan\psi}{h^a_a})^2 \cong -2 \; log(0.891 \; h^a a).$$

(B.21)

This is the *small argument representation of the dispersion equation.*

Another data table was prepared which compared the right hand sides of equations B.13 and B.21. It was discovered that for values of $ka \; cotan\psi$ as large as 0.10, the maximum error is about 0.20 percent, while for $ka \; cotan\psi$ as large as 0.50, it is about 7 percent. The error involved with using the small argument representation of the dispersion equation decreased as the value of $ka \; cotan\psi$ became smaller.

Equations B.19 - B.21 show that for very large $ka \cot\psi$, $h^a{}_a \cong ka \cot\psi$, while for very small $ka \cot\psi$, $h^a{}_a \ll ka \cot\psi$. The right hand side of equation B.13 is a strictly decreasing positive function, which, for $h^a{}_a$ close to zero, has a large value and a large negative slope, but which approaches unity from the upperside with a zero slope as $h^a{}_a$ becomes large. Therefore, it is always true that

$$0 < h^a{}_a < ka \cot\psi < \infty . \tag{B.22}$$

A useful approximation which simplifies calculating the field components is to equate the absolute value of the axial wave number with the radial wave number. Equation B.14 is rewritten as

$$|\beta^a|a = \sqrt{(h^a{}_a)^2 + (ka)^2} = h^a{}_a \sqrt{1 + \left(\frac{ka}{h^a{}_a}\right)^2} . \tag{B.23}$$

Using the Binomial theorem (47, pp. 737) to expand the square root as an infinite series, and keeping only the first two terms of the series, yields

$$|\beta^a|a \cong h^a{}_a \left[1 + \frac{1}{2} \left(\frac{ka}{h^a{}_a}\right)^2\right]. \tag{B.24}$$

The approximation $|\beta^a|a \cong h^a{}_a$ is valid within about ten percent error if

$$\frac{1}{2} \left(\frac{ka}{h^a{}_a}\right)^2 < 0.10 \quad \text{or} \quad \left. \frac{ka}{h^a{}_a}\right|_{max} = \sqrt{0.20} \cong 0.50. \tag{B.25}$$

Hence, if

$$h^a{}_a > 2 ka \qquad (B.26)$$

is satisfied, $|\beta^a|_a \cong h^a{}_a$ is an approximation which is accurate within the previously mentioned error limitation.

Inequality B.26 is now examined, using the approximations of the dispersion equation which were previously stated. Equation B.20, the crude large argument representation of the dispersion equation, shows that when $ka \ \cot an\psi$ is large, the inequality is clearly satisfied for all pitch angles in the range $0 < \psi \lesssim 10.0°$. From equation B.21, the small argument representation of the dispersion equation,

$$ka \cong \tan\psi \ h^a{}_a \sqrt{-2 \ \log(0.891 \ h^a{}_a)} \ . \qquad (B.27)$$

Therefore, inequality B.26 becomes

$$2 \ \tan\psi \sqrt{-2 \ \log(0.891 \ h^a{}_a)} < 1 . \qquad (B.28)$$

It is apparent that inequality B.28 is most easily satisfied if the sheath helix is very tightly wound. As an example, if $\psi = 10.0°$, the inequality is satisfied for values of $h^a{}_a$ as small as $h^a{}_a = 2.0 \times 10^{-2}$. (Making use of equation B.21, this value of $h^a{}_a$ corresponds to $ka \ \cot an\psi = 5.7 \times 10^{-2}$.) If $\psi = 5.0°$, then the inequality is satisfied for values of $h^a{}_a$ as small as $h^a{}_a = 9.0 \times 10^{-8}$. (This value of $h^a{}_a$ corresponds to $ka \ \cot an\psi = 5.1 \times 10^{-7}$.) One concludes that inequality B.28 will be satisfied down to very small values of the variable $ka \ \cot an\psi$, if the pitch angle is small. However, as $ka \ \cot an\psi \rightarrow 0^+$, inequalities B.22 demonstrate it must be true that $h^a{}_a \rightarrow 0^+$. Therefore, for any (fixed) value of the pitch angle, regardless of how small, when the variable $ka \ \cot an\psi$ becomes sufficiently small, inequality B.28 will not be

satisfied.

In summary, the approximation $|\beta^a|a \simeq h^a a$ is valid over a wide range of $ka\,\cot an\psi$ values. For a tightly wound sheath helix, it is always valid for large $ka\,\cot an\psi$ ($ka\,\cot an\psi > 1$), and it is justified until $ka\,\cot an\psi$ becomes very small ($ka\,\cot an\psi \ll 1$). However, it is never correct in the limit as $ka\,\cot an\psi$ approaches zero.

One can obtain numerical solutions to equation B.13, the dispersion equation, in a very straightforward manner. The method is to first choose a value of $h^a a$ and then calculate by direct evaluation of Bessel functions, the corresponding value of $ka\,\cot an\psi$. It is now pretended that the value of $ka\,\cot an\psi$ was originally specified, and that this determined the value of $h^a a$. So that better accuracy in reading the graph is obtained, it is helpful to shrink the ordinate axis scale by plotting the quantity $ka\,\cot an/h^a a$ versus the variable that depends on the operating frequency and the sheath helix geometry, $ka\,\cot an\psi$, rather than directly plotting $h^a a$ versus $ka\,\cot an\psi$. For a desired value of $ka\,\cot an\psi$, the corresponding value of $h^a a$ is easily obtained from this graph. Interestingly, since

$$ka\,\cot an\psi/h^a a = \frac{1}{h^a a} \cdot ka\,\cot an\psi, \qquad (B.29)$$

lines of constant $h^a a$ on the graph are straight lines through the origin, having the slope $1/h^a a$.

Using the approximation $|\beta^a|a \simeq h^a a$, it follows that

$$\frac{ka\,\cot an\psi}{h^a a} \simeq \frac{ka\,\cot an\psi}{|\beta^a|a}$$

$$= \frac{\omega}{|\beta^a|}\sqrt{\mu_0\,\epsilon_0}\,\cot an\psi = \frac{v_p}{c}\cot an\psi. \qquad (B.30)$$

Therefore, the graph of $ka \ cotan\psi/h^a a$ versus $ka \ cotan\psi$ is proportional to a graph of the phase velocity normalized with respect to the speed of light in air, as a function of frequency. (The phase velocity is associated with traveling waves having $e^{-j \ \beta^a z}$ axial dependence.) The previously discussed method of presenting the radial wave number solution can be regarded as a type of *dispersion curve*.

Figures B.1 and B.2 were computed directly from equation B.13 by first choosing several different values of $h^a a$, calculating $ka \ cotan\psi/h^a a$ at each point by evaluating the right hand side of the equation, performing the multiplication $h^a a$. $ka \ cotan\psi/h^a a$ in order to obtain $ka \ cotan\psi$, and finally pretending that $ka \ cotan\psi$ was originally specified and that this determined the quantity $ka \ cotan\psi/h^a a$. Software program routines from the IMSL library (43) were used to evaluate the Bessel functions, and the graphs were prepared by the Amdahl V/8 computer at the University of Alberta.

Figure B.1 is a linear graph of $ka \ cotan\psi/h^a a$ versus $ka \ cotan\psi$. Several different lines of constant $h^a a$ values are shown. In addition, the large argument asymptote $ka \ cotan\psi/h^a a = 1$ is presented.

Figure B.2 is a semilogarithmic graph, having the same abscissa and ordinate as the previous figure. Many decade ranges of $ka \ cotan\psi$ values are shown. The asymptote $ka \ cotan\psi/h^a a = 1$ is given.

B.3 Discussion and Graphs of the Field Components

Some properties of the field components will now be mentioned. Replacing $\beta^a a$ by $-\beta^a a$ in equations B.1 – B.12, the field components, in equation B.13, the dispersion equation, and in equation B.14, the separation constant equation, results in no change. Therefore, no loss in generality occurs from restricting $\beta^a > 0$. Decreasing the pitch angle in such a fashion that the variable $ka \ cotan\psi$ remains constant (keeping in mind equation B.17, which gives the functional dependence of $h^a a$), will greatly decrease the magnitude of the angular electric and magnetic fields, because they have an explicit $sin\psi$ dependence. However, to a good approximation, the other field components are not affected. The previous two sentences have assumed that the sheath helix is sufficiently tightly wound so that $cos\psi \cong 1$ and $\beta^a a \cong h^a a$.
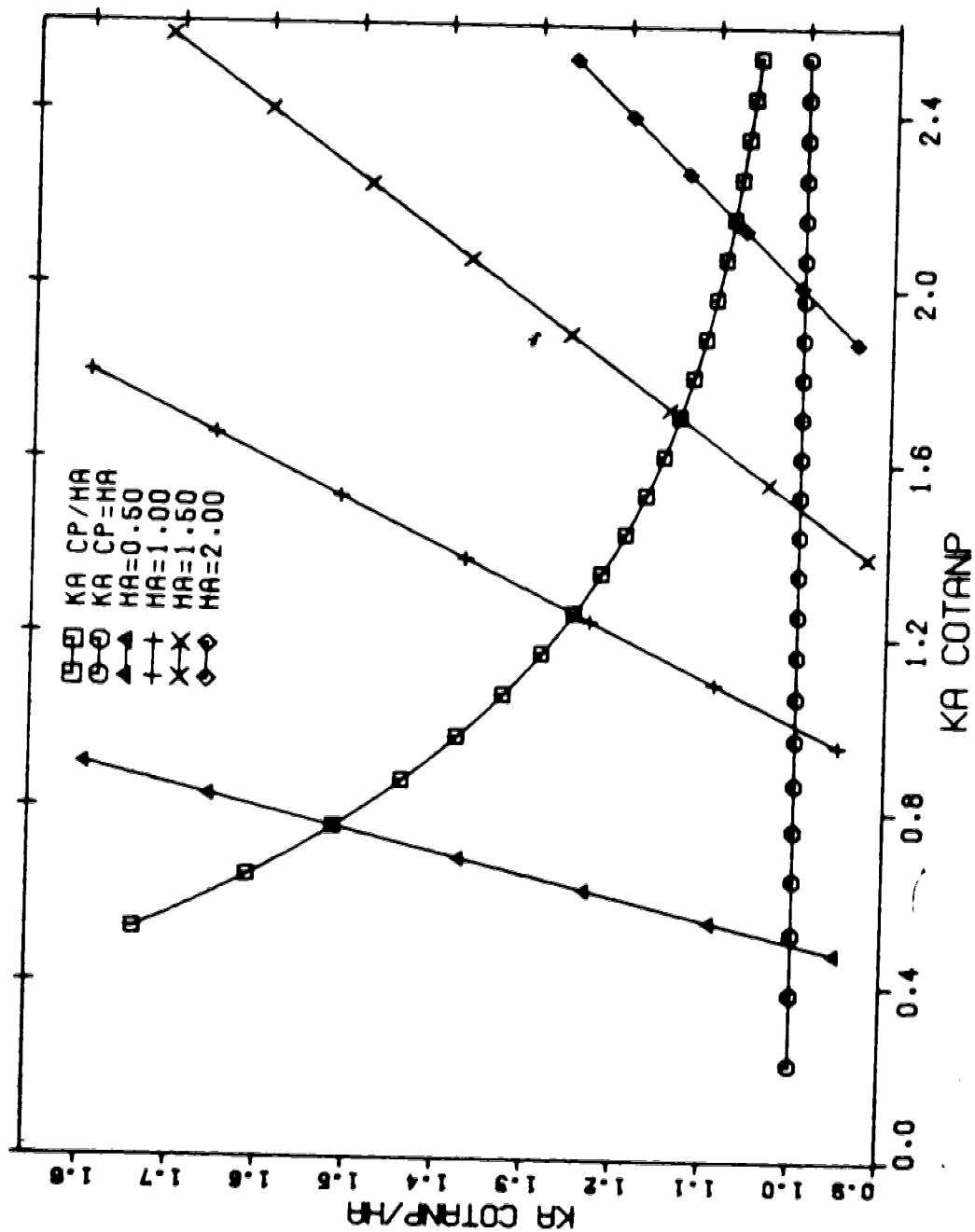
Figure B.T Graph of ka cotanψ/h^{a}a versus ka cotanψ based on equation B.13. Several lines of constant h^{a}a are shown, and so is the asymptote ka cotanψ/h^{a}a = 1.0. (Note that HA=h^{a}a and KA COTANP=KA CP=ka cotanψ.)
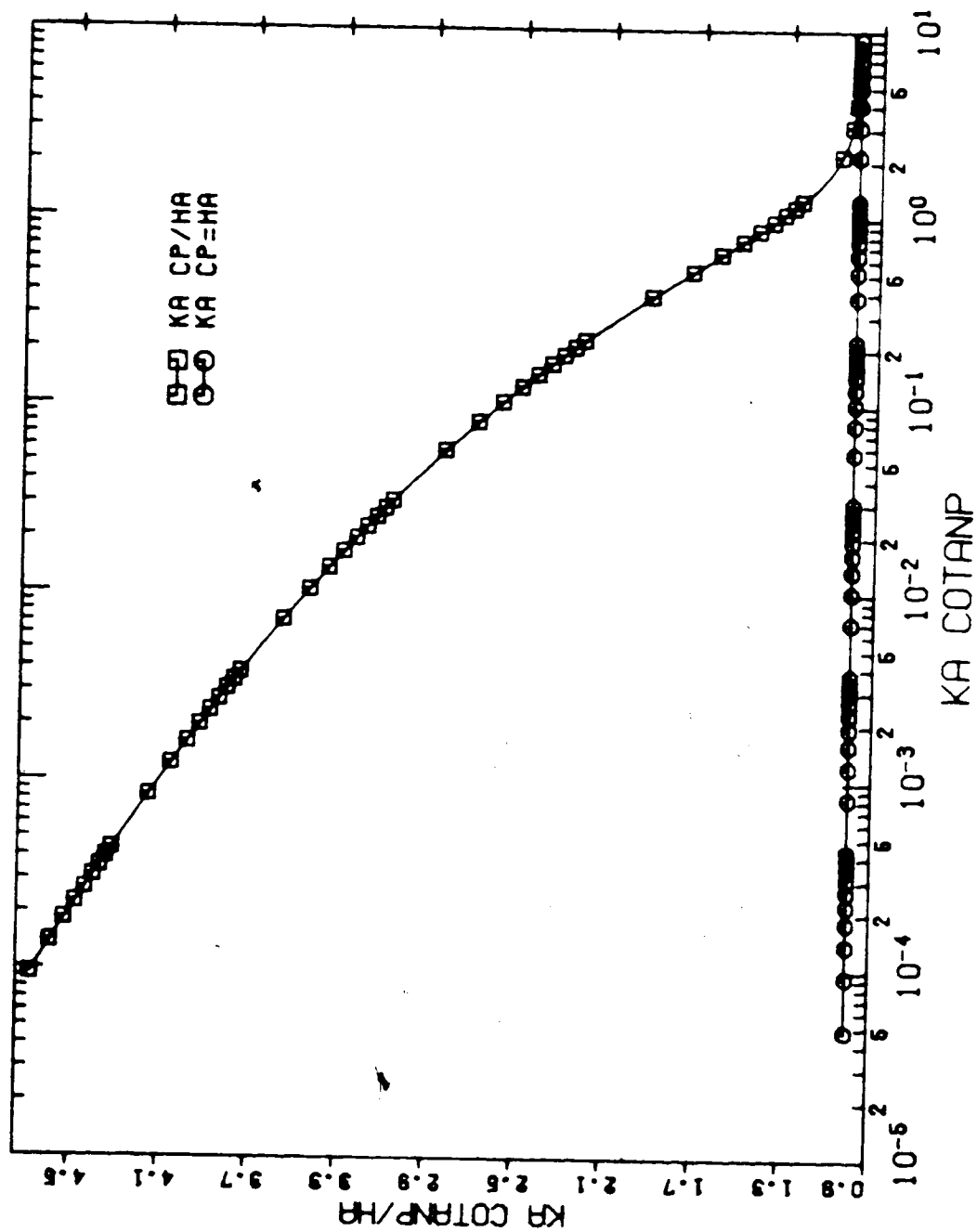
Figure B.2   Graph of ka cotanψ/h^{a}a versus ka cotanψ based on equation B.13. The asymptote ka cotanψ/h^{a}a = 1.0 is shown. (Note that HA=h^{a}a and KA COTANP=KA CP=ka cotanψ.)

(See equation B.26. This states the requirement necessary so that the axial and radial wave number can be equated.) If this is true, it is apparent that the field components have the following approximate functional dependences on the operating frequency, the sheath helix geometry, and the sheath helix "windings'" current.

$$E_{\theta n}{}^{a} = L_n(\beta_{II}, ka \cot an\psi, \psi),$$ (B.31)

$$H_{\theta n}{}^{a} = S_n(\beta_{II}, ka \cot an\psi, \psi),$$ (B.32)

$$E_{rn}{}^{a} = Q_n(\beta_{II}, ka \cot an\psi),$$ (B.33)

$$E_{zn}{}^{a} = U_n(\beta_{II}, ka \cot an\psi),$$ (B.34)

$$H_{rn}{}^{a} = V_n(\beta_{II}, ka \cot an\psi), \quad and$$ (B.35)

$$H_{zn}{}^{a} = W_n(\beta_{II}, ka \cot an\psi);$$ (B.36)

where $n = 1, 2$.

Since the interior sheath helix region fields' radial dependence is characterized by either $I_0(h^a r)$ or $I_1(h^a r)$, while that of the exterior region fields is either $K_0(h^a r)$ or $K_1(h^a r)$, with all the Bessel function arguments being real positive, it is true that for one particular operating frequency and for one particular sheath helix geometry (which means that $h^a a$ has one particular value), the interior region field magnitudes always increase as the radial distance increases, while the exterior region field magnitudes always get smaller with increasing r. (See Figure A.1. This shows graphs of I_0, I_1, K_0, and K_1, for real positive arguments.) All field magnitudes attain a maximum value at $r = a$, the sheath helix surface.

For values of $ka \cot an\psi$ sufficiently large so that $ka \cot an\psi > 1$, equation B.20 and Figures B.1, B.2 show it is true that $h^a a \simeq ka \cot an\psi$.

Table A.2 demonstrates that for this value of $h^a a > 1$, the large argument Bessel function representations, equations A.36 - A.39, have a relatively small error associated with their usage. Substituting equations A.36 - A.39 into equations B.1 - B.12, it is seen that all the electric and magnetic field components rapidly decay about the sheath helix surface in an exponential fashion, according to

$$e^{-ka \cot an\psi(1-r/a)} \quad \text{for interior region fields, or}$$

$$e^{-ka \cot an\psi(r/a-1)} \quad \text{for exterior region fields.}$$

$$(B.37)$$

(The single exception to this behavior occurs at points in the sheath helix interior region where the radial distance is sufficiently small for the particular value of $h^a a > 1$, so that $h^a a \cdot r/a < 1$ is true. Table A.2 makes it clear that a large error is involved with using the approximations given by equations A.36 - A.39, when the arguments of the Bessel functions are smaller than unity.)

Attention is now directed to the radial dependence of the field components for small values of $ka \cot an\psi$. When $ka \cot an\psi < 0.10$ occurs, it must be true that $h^a a < 0.10$. (See equation B.22 and Figures B.1, B.2.) Table A.1 shows that for this argument, very little error is involved in using the small argument Bessel function representations, equations A.26 - A.29. Substituting these equations into equations B.1 - B.12, it is apparent that the approximate radial dependence of the field components is

$$E_{r1}{}^a \simeq h^a r, \quad E_{\theta 1}{}^a \simeq h^a r, \quad E_{z1}{}^a \simeq 1,$$

$$H_{r1}{}^a \simeq h^a r, \quad H_{\theta 1}{}^a \simeq h^a r, \quad H_{z1}{}^a \simeq 1,$$

$$(B.38)$$

$$E_{r2}{}^a \simeq \frac{1}{h^a r}, \quad E_{\theta 2}{}^a \simeq \frac{1}{h^a r}, \quad E_{z2}{}^a \simeq \log(0.891 \ h^a r),$$

$$H_{r2}{}^a \simeq \frac{1}{h^a r}, \quad H_{\theta 2}{}^a \simeq \frac{1}{h^a r}, \quad \text{and} \quad H_{z2}{}^a \simeq \log(0.891 \ h^a r).$$

(For the fields in the sheath helix exterior region, when the radial distance is sufficiently large for the particular value of $h^a a < 0.10$, it will be true that $h^a a \cdot r/a >> 0.10$. Table A.1 makes it apparent that a great error is associated with using equations A.26 - A.29 when the argument is this large. For this special case, the radial dependence of the sheath helix exterior region fields given by equations B.38 is not correct.)

In summary, for large values of $ka \cot an\psi$ (which could be considered to mean high frequencies since $ka \cot an\psi = 2\pi f \sqrt{\mu_0 \epsilon_0} \, a \cot an\psi$), the fields cling very closely to the sheath helix "windings". The sheath helix is now acting like a *waveguiding* structure. On the other hand, for small values of $ka \cot an\psi$ (which could be considered to mean low frequencies), the fields in the exterior region have a large radial extension. The waves associated with the sheath helix are now largely *unguided*.

The fact that the field components cling closely to the sheath helix surface for high frequencies is in agreement with the experimental work that Cutler (12) performed on a physical helix. This was previously mentioned in part 1.2.2.

Attention is now directed to examining the phase velocity of the traveling wave form of the field components. These are characterized by having $e^{-j\beta^a z}$ axial dependence. They can be easily obtained from the standing wave fields, equations B.1 - B.12, by using the identities

$$\cos\beta^a z = \frac{e^{+j\beta^a z} + e^{-j\beta^a z}}{2} \quad \text{and}$$

$$\sin\beta^a z = \frac{e^{+j\beta^a z} - e^{-j\beta^a z}}{2j} ,$$

(B.39)

multiplying by two, and by keeping only the $e^{-j\beta^a z}$ term.

The phase velocity normalized with respect to the speed of light in air, is

$$\frac{v_p}{c} = \frac{\omega}{\beta^a} \sqrt{\mu_0 \epsilon_0} = \frac{ka}{\beta^a a} . \qquad (B.40)$$

For large values of $ka \cot\psi$, equation B.20 and Figures B.1, B.2 show that $h^a a \cong ka \cot\psi$. It follows from equation B.14 that

$$\beta^a a = \sqrt{(h^a a)^2 + (ka)^2} \cong ka \csc\psi. \qquad (B.41)$$

Substitution of equation B.41 into equation B.40 yields

$$\frac{v_p}{c} \cong \sin\psi. \qquad (B.42)$$

This can be interpreted as describing a wave traveling with the speed of light in the direction of the sheath helix "windings". (See Figure 1.5b. It displays the developed sheath helix.) From the discussion presented earlier in section B.3, this is the expected behavior of a guided wave.

For very small values of $ka \cot\psi$, $h^a a$ will be very small. (This is apparent from equation B.22 and from Figures B.1, B.2.) Equation B.21 makes it clear that $h^a a \ll ka \cot\psi$. Furthermore, for any fixed value of the pitch angle, if $ka \cot\psi$ is sufficiently small, it will be true that the radial wave number is such that $h^a a \ll ka$. Equation B.14 shows that $\beta^a a \cong ka$, and it follows from equation B.40 that

$$\frac{v_p}{c} \cong 1. \qquad (B.43)$$

The phase velocity now describes a wave traveling in the axial direction with the speed

of light. This is the expected behavior when the sheath helix does not act to guide the wave.

Equations B.42 and B.43 are in agreement with the theoretical investigation of helical wires at high and low frequencies, respectively, performed by Pocklington (7). This was previously discussed in part 1.2.1.

In general, the phase velocity is between the limits specified by equations B.42 and B.43.

$$ \sin\psi \; < \; \frac{v_p}{c} \; < \; 1 \qquad\qquad (B.44) $$

A brief mention will now be given of the power flow that is associated with the air-filled sheath helix. The time-averaged power flow in the axial and radial directions can be calculated by integration of the Poynting vector over the appropriate surfaces, as was previously explained in section 3. 1. Rather than repeating this procedure here, only the results of the author's calculations will be discussed. Through any transverse plane of constant $z = z_0$ $(-\infty < z_0 < \infty)$ which extends to infinity in the radial direction, the time-averaged power flow associated with the fields given by equations B.1 — B.12 is zero. In fact, this result is also true for any area of the transverse plane. Considering traveling waves characterized by $e^{-j\beta^a z}$ axial dependence, Sensiper (5, pp. 59) has shown that the time-averaged axial power is nonzero but it is independent of the position of the transverse plane $z = z_0$ through which it is calculated.

The time-averaged power flow based on equations B.1 – B.12 and calculated through a cylindrical wall of radius $r = r_0$ $(0 < r_0 < \infty)$ was discovered to be zero. Therefore, *the empty sheath helix cannot act like a radiator.* This property was noted by Cutler (12). A discussion of his investigation was previously given in part 1.2.2.

In order to help understand the behavior of the field components at different points in space, several graphs of their radial dependence have been prepared. All the electric field components, equations B.1 – B.3 and B.7 – B.9, were normalized from dividing them by an electric normalizing coefficient, $E_{z0}{}^a$. All the magnetic fields,

equations B.4 - B.6 and B.10 - B.12, were normalized from dividing them by a magnetic normalizing coefficient, $H_{z0}{}^a$. The electric and magnetic normalizing coefficients are defined as

$$E_{z0}{}^a = E_{z1}{}^a \Big|_{\substack{z=0 \\ r=a}} = j \, \mathcal{Y}_{11} \, \frac{120\pi}{ka \, \cot\psi} \, \cos\psi \, \cdot$$

$$(h^a a)^2 \, I_0(h^a a) \, K_0(h^a a)$$

$$= j \, \mathcal{Y}_{11} \, 120\pi \, ka \, \cot\psi \, \cos\psi \, I_1(h^a a) \, K_1(h^a a), \quad \text{and} \qquad (B.45)$$

$$H_{z0}{}^a = H_{z1}{}^a \Big|_{\substack{z=0 \\ r=a}} = \mathcal{Y}_{11} \, \cos\psi \, h^a a \, I_0(h^a a) \, K_1(h^a a). \qquad (B.46)$$

(The dispersion equation, equation B.13, was used in the derivation of equations B.45.)

Only the radial dependence of the normalized fields has been graphed. It is assumed that the axial coordinate is held constant. The transverse planes specified by $z = 0$ and by $\beta^a a \cdot z/a = \pm 2n\pi$ $(n = 1, 2, 3, ...)$ are considered for the angular and axial field components. This means that $\cos\beta^a z = +1$. On the other hand, for the radial field components, the transverse planes $\beta^a a \cdot z/a = (4n + 1) \frac{\pi}{2}$ and $\beta^a a \cdot z/a = -(4n + 1) \frac{3\pi}{2}$ $(n = 0, 1, 2, ...)$ are used. It is now true that $\sin\beta^a z = +1$.

Three different types of graphs have been prepared. The first set represents the "high frequency" case. This term means that the value of $ka \, \cot\psi$ is chosen sufficiently large so that the corresponding value of $h^a a$, which results as a solution of the dispersion equation, is such that little error is involved in using the large argument Bessel function representations. Equations A.36 - A.39 can be used to approximate the dispersion equation, the normalizing coefficients, and the normalized field components.

The second set of graphs represents the "mid frequency" case. Here the variable $ka \, \cot\psi$ is chosen so that considerable error is involved with using equations A.26 - A.29, or equations A.36 - A.39. The small or large argument Bessel function

representations cannot be used to approximate the dispersion equation, the normalizing coefficients, and the normalized fields.

Finally, the third set of graphs represents the "low frequency" case. $ka \ cotan\psi$ is chosen sufficiently small so that little error is involved in using the small argument Bessel function representations. Equations A.26 - A.29 can be used to approximate the dispersion equation, the normalizing coefficients, and the normalized fields.

The method of solution which is used to obtain the graphs will now be explained. For the specified value of the variable $ka \ cotan\psi$, equation B.13 is solved to obtain the radial wave number, $h^a{}_a$. (Actually, as was discussed in section B.2, the dispersion equation is solved by first specifying $h^a{}_a$ and then by calculating the corresponding value of $ka \ cotan\psi$.) Making use of the specified value of the pitch angle and the value of $ka \ cotan\psi$, equation B.14 is solved to obtain the axial wave number, $\beta^a{}_a$. Next, equations B.45 and B.46 are evaluated to obtain the normalizing coefficients. Finally, the normalized field components are calculated for many different values of the radial distance normalized with respect to the sheath helix radius,

r/a. All the Bessel functions were directly evaluated by making use of software program routines from the IMSL (43) library. It will be emphasized that the six graphs of the field components' radial dependence presented here are "exact" - no approximations have been made to the dispersion equation, the separation constant equation, the normalizing coefficients, and the normalized fields.

Figures B.3 and B.4 show the absolute value of the normalized electric and magnetic field components, respectively, as a function of r/a. The vertical line represents the sheath helix surface. In both the interior and exterior sheath helix regions, the algebraic sign of each normalized field is given. The sheath helix goemetry and the operating frequency are specified according to the variables $ka \ cotan\psi =$ 10.0 and $\psi = 1.00°$. This is an example of the "high frequency" case. $h^a{}_a = 10.0$ and $\beta^a{}_a = 10.0$ are the calculated values of the wave numbers. (Note that the value of $h^a{}_a$ is in good agreement with equation B.20, as one expects.)

Figure B.3   Curves of the radial dependence associated with the normalized electric fields. The variables used are ka cotanψ=10.0 and ψ=1.00°. They determine the wave numbers, $h^a a$ = 10.0 and $\beta^a a$ = 10.0, and the electric normalizing coefficient, $E_{z0}{}^a$ = j β_{11} 188 (V/m). (Note that ER/EZO = $E_r{}^a/E_{z0}{}^a$, EO/EZO = $E_\theta{}^a/E_{z0}{}^a$, EZ/EZO = $E_z{}^a/E_{z0}{}^a$, and R/A = r/a.)
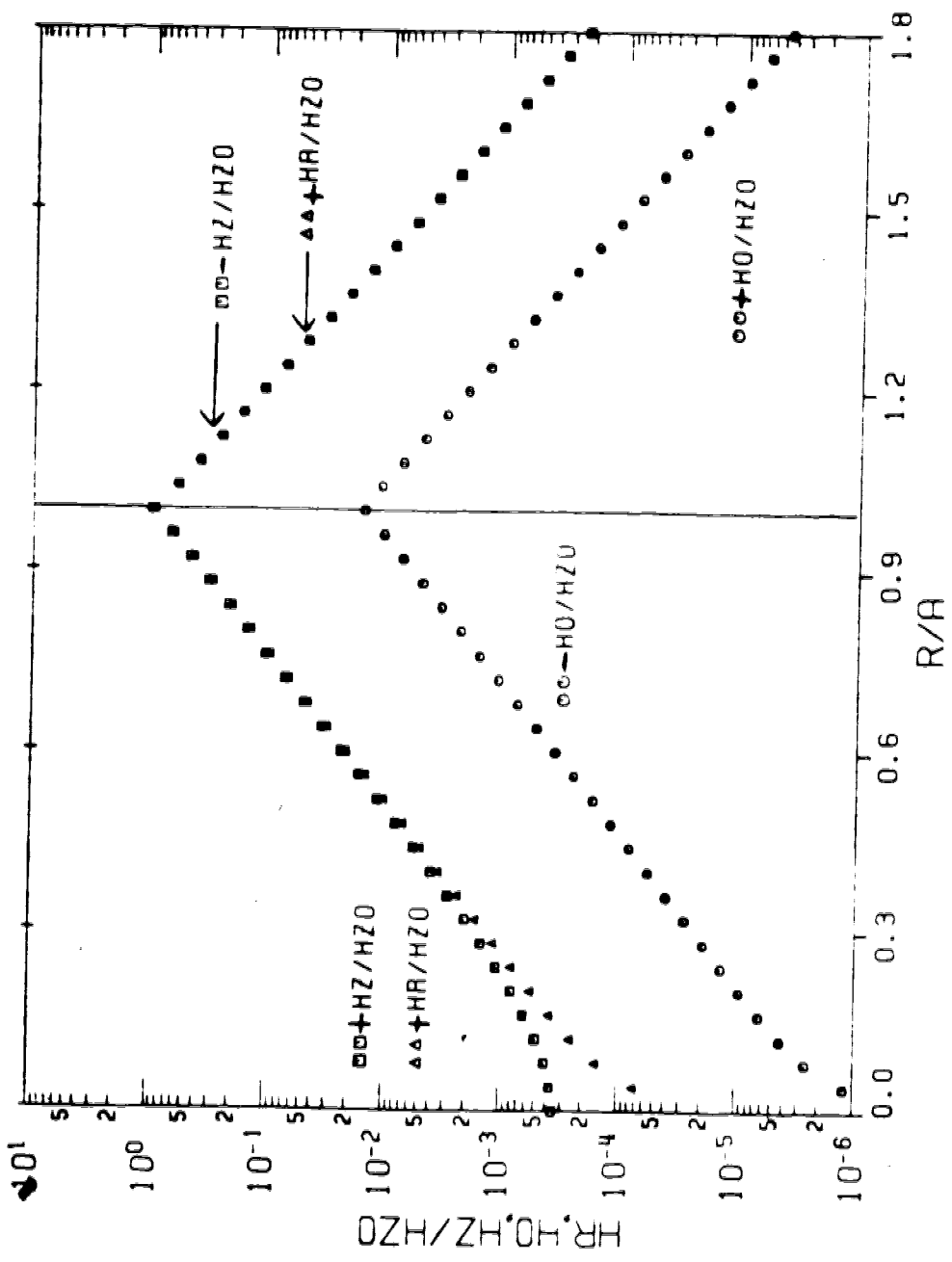
Figure B.4   Curves of the radial dependence associated
with the normalized magnetic fields. The variables used
are ka cotanψ=10.0 and ψ=1.00°. They determine the wave
numbers, $h^a a$ = 10.0 and $\beta^a a$ = 10.0, and the magnetic
normalizing coefficient, H_{z0}^a = 0.525 (A/m). (Note
that HR/HZO = H_r^a/H_{z0}^a, HO/HZO = H_θ^a/H_{z0}^a, HZ/HZO =
H_z^a/H_{z0}^a, and R/A = r/a.)

$$E_{z0}{}^a = j \mathcal{J}_{11} \ 188 \ (V/m) \quad \text{and} \quad H_{z0}{}^a = \mathcal{J}_{11} \ 0.525 \ (A/m)$$

are the calculated values of the normalizing coefficients.

It is apparent that all the field components are rapidly attenuated at increasing radial distances away from the sheath helix surface. The radial dependence of the fields is approximately given by equations B.37. Since the fields cling tightly to the sheath helix "windings", the sheath helix is said to act like a *waveguiding structure*.

Figures B.5 and B.6 show the radial dependence of the normalized electric and magnetic fields, respectively, for the "mid frequency" case. $ka \cot \psi = 1.00$ and $\psi = 1.00°$ are used. $h^a a = 0.734$ and $\beta^a a = 0.734$ are the calculated values of the wave numbers. The values of the normalizing coefficients are calculated to be

$$E_{z0}{}^a = j \mathcal{J}_{11} \ 145 \ (V/m) \quad \text{and} \quad H_{z0}{}^a = \mathcal{J}_{11} \ 0.820 \ (A/m)$$

Note that both the interior region and the exterior region fields change much more gradually as the radial distance is varied, compared to the behavior exhibited in Figures B.3 and B.4.

The final two graphs included in this appendix are Figures B.7 and B.8. These represent the radial dependence of the normalized electric and magnetic fields for the "low frequency" case. $ka \cot \psi = 5.00 \times 10^{-2}$ and $\psi = 1.00°$ are chosen. The wave number solutions are calculated to be $h^a a = 1.73 \times 10^{-2}$ and $\beta^a a = 1.74 \times 10^{-2}$. (As expected, the value of $h^a a$ approximately agrees with that predicted by equation B.21.)

$$E_{z0}{}^a = j \mathcal{J}_{11} \ 9.44 \ (V/m) \quad \text{and} \quad H_{z0}{}^a = \mathcal{J}_{11} \ 1.00 \ (A/m)$$

are the computed values of the normalizing coefficients. The radial dependences of the fields are approximately given by equations B.38. It is apparent that the sheath helix
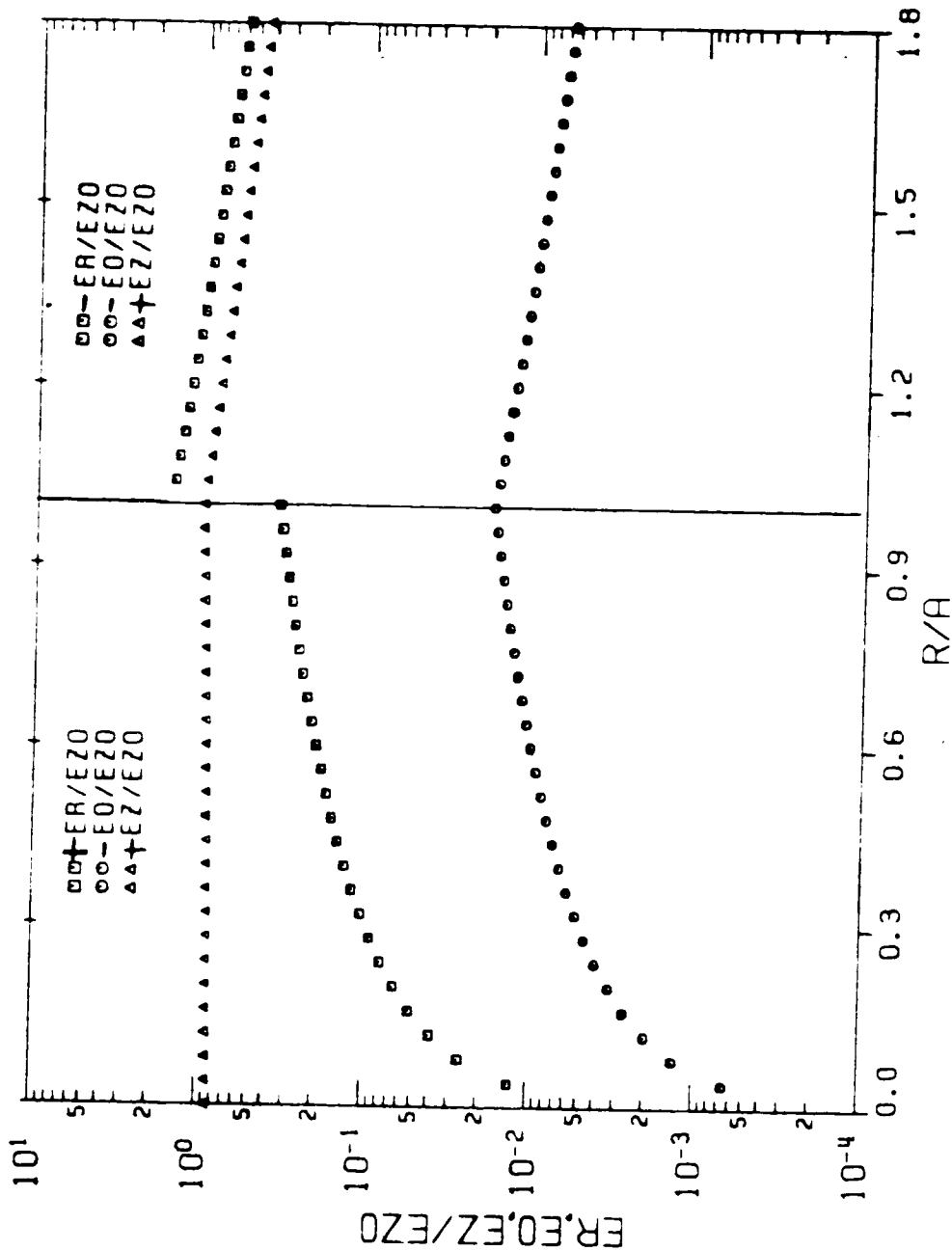
RADIAL DEPENDENCE OF ELECTRIC FIELDS

Figure B.5   Curves of the radial dependence associated with the normalized electric fields. The variables used are ka cotanψ=1.00 and ψ=1.00°. They determine the wave numbers, $h^a a$ = 0.734 and $\beta^a a$ = 0.734, and the electric normalizing coefficient, E_{z0}^a = j ϑ_{11} 145 (V/m). (Note that ER/EZO = E_r^a/E_{z0}^a, EO/EZO = E_θ^a/E_{z0}^a, EZ/EZO = E_z^a/E_{z0}^a, and R/A = r/a.)
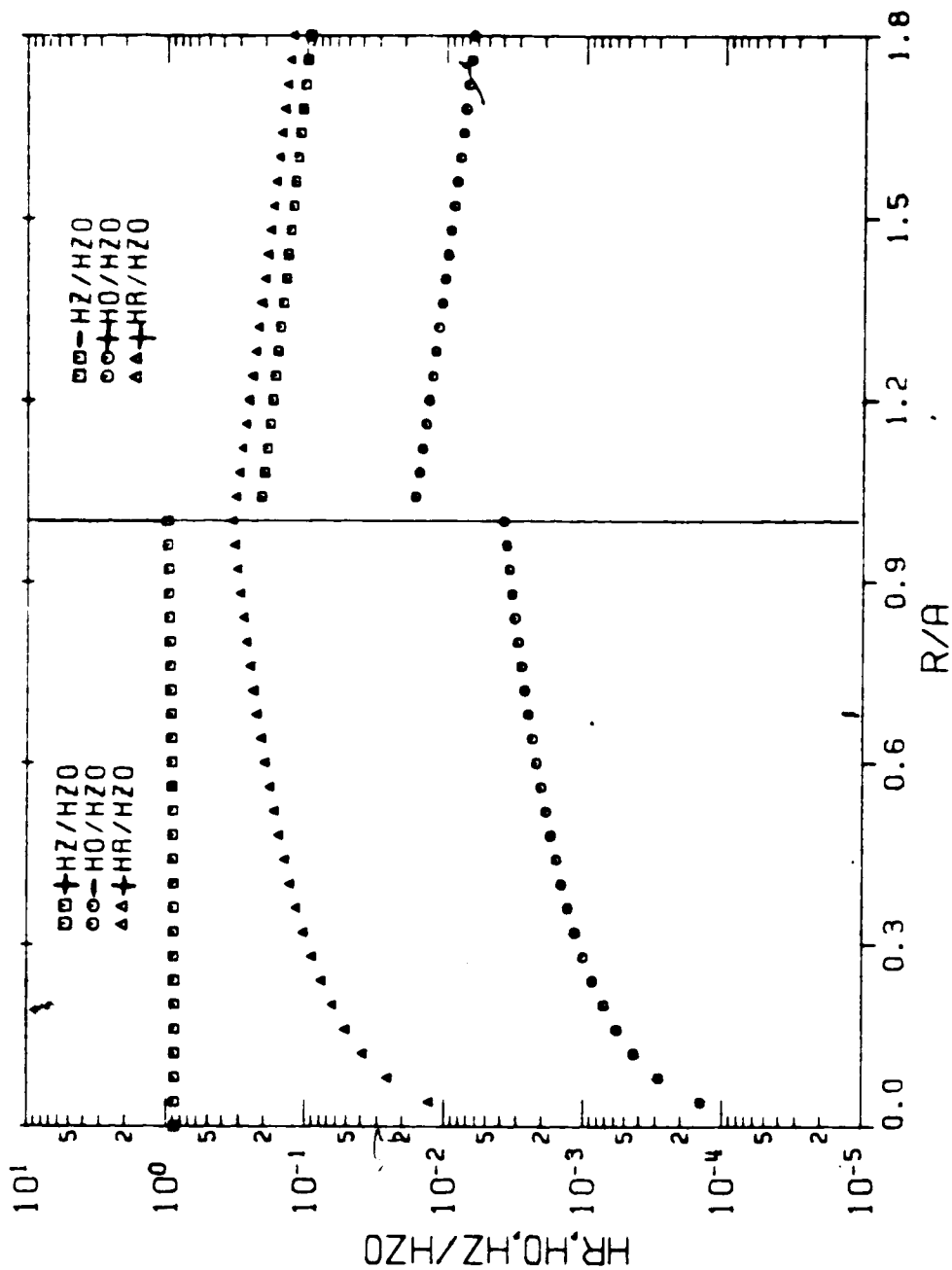
Figure B.6   Curves of the radial dependence associated
with the normalized magnetic fields. The variables used
are ka cotanψ=1.00 and ψ=1.00°. They determine the wave
numbers, $h^a a$ = 0.734 and $\beta^a a$ = 0.734, and the magnetic
normalizing coefficient, $H_{z0}{}^a$ = $\vartheta_{||}$ 0.820 (A/m). (Note
that HR/HZO = $H_r{}^a/H_{z0}{}^a$, HO/HZO = $H_\theta{}^a/H_{z0}{}^a$, HZ/HZO =
$H_z{}^a/H_{z0}{}^a$, and R/A = r/a.)
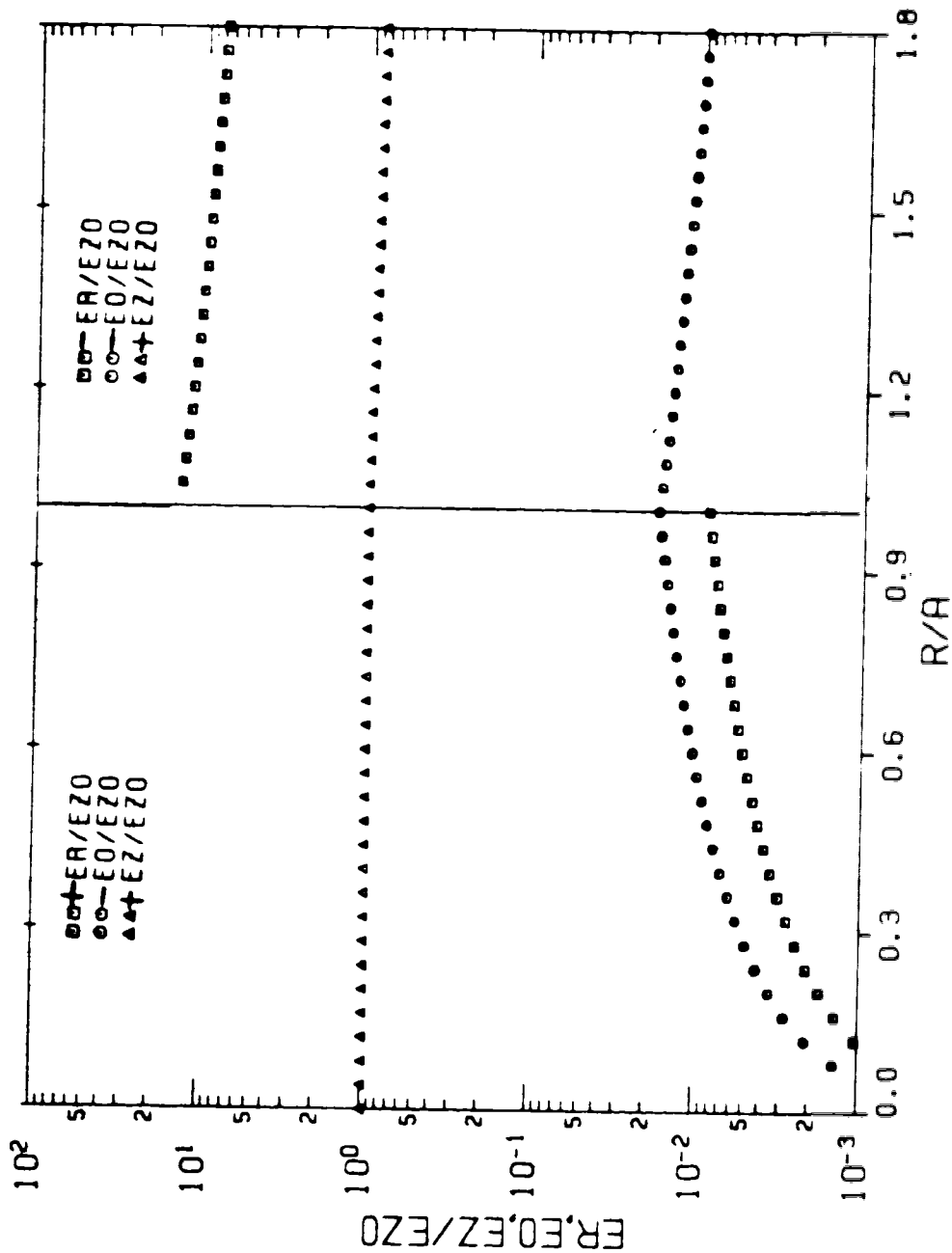
Figure B.7 Curves of the radial dependence associated with the normalized electric fields. The variables used are ka cotanψ=5.00x10^{-2} and ψ=1.00°. They determine the wave numbers, h^{a}a=1.73x10^{-2} and β^aa=1.74x10^{-2}, and the electric normalizing coefficient, $E_{z0}{}^a$ = j ϑ_{11} 9.44 (V/m). (Note that ER/EZO = $E_r{}^a/E_{z0}{}^a$, EO/EZO = $E_\theta{}^a/E_{z0}{}^a$, EZ/EZO = $E_z{}^a/E_{z0}{}^a$, and R/A = r/a.)
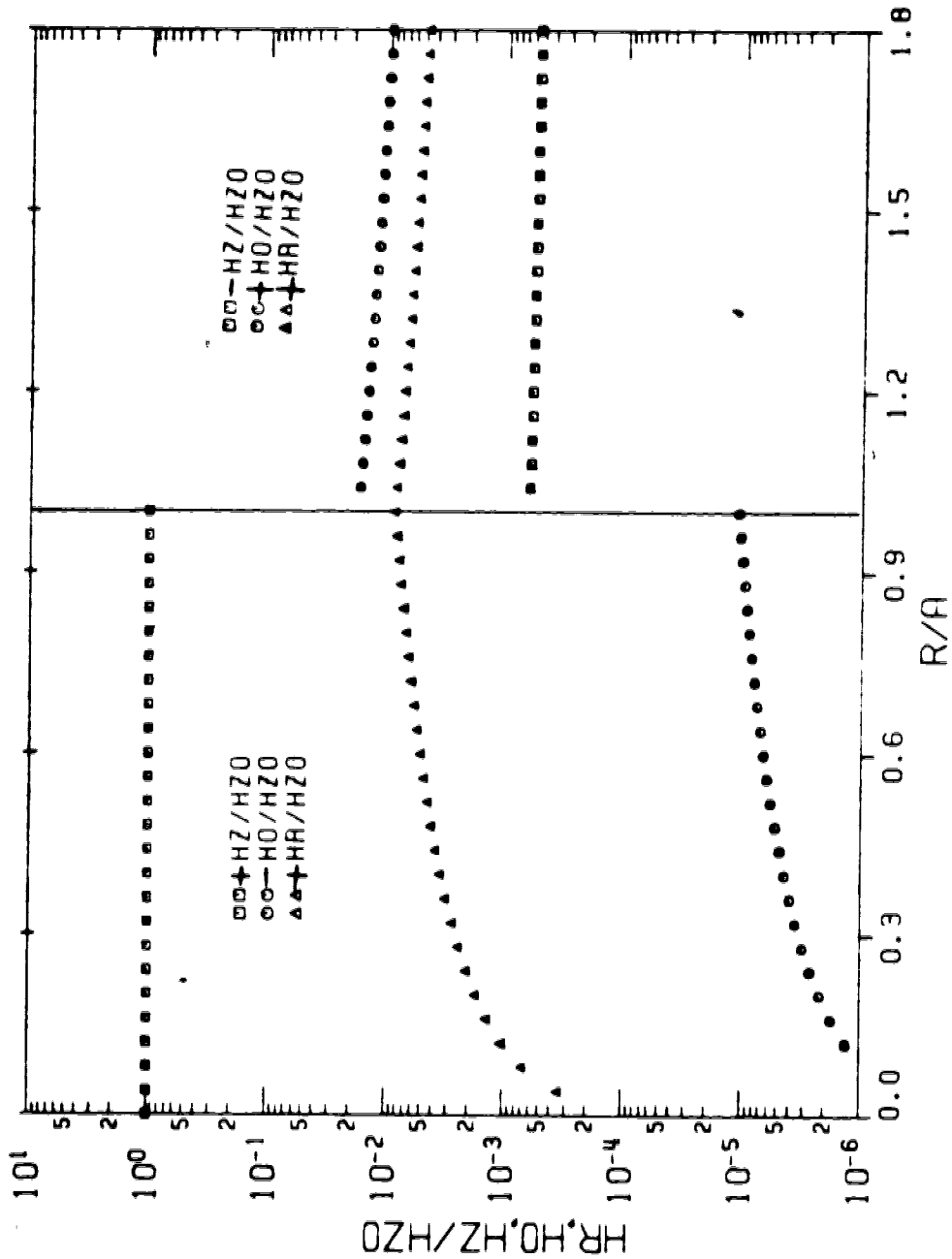
Figure B.8   Curves of the radial dependence associated with the normalized magnetic fields. The variables used are ka cotan $=5.00 \times 10^{-2}$ and $\psi = 1.00°$. They determine the wave numbers, $h^a a = 1.73 \times 10^{-2}$ and $\beta^a a = 1.74 \times 10^{-2}$, and the magnetic normalizing coefficient, $H_{z0}{}^a = \}_{||} 1.00$ (A/m). (Note that HR/HZO $= H_r{}^a/H_{z0}{}^a$, HO/HZO $= H_\theta{}^a/H_{z0}{}^a$, HZ/HZO $= H_z{}^a/H_{z0}{}^a$, and R/A $= r/a$.)

exterior region electric and magnetic field magnitudes decay slowly with increasing radial distance. The field extension is large. Therefore, it can be said that *the fields are basically unguided by the sheath helix.*

To conclude the discussion of the radial dependence graphs of the normalized fields, attention is directed to the field behavior at the sheath helix surface. Figure B.7 makes it clear that $E_\theta{}^a/E_{z0}{}^a$ and $E_z{}^a/E_{z0}{}^a$ are continuous at $r = a$. This is simply a statement of the boundary condition that the electric field tangential to an interface is continuous. Indeed, the continuity of the region 1 and region 2 angular electric fields, and of the region 1 and region 2 axial electric fields, at $r = a$, can easily be shown from equations 1.6 - 1.8 to be a necessary consequence of the sheath helix surface boundary conditions.

Figure B.7 shows that the normalized radial electric field is discontinuous at $r = a$. The physical explanation for this behavior is that the discontinuity results from the presence of free electric charge located at the sheath helix surface.

Directing attention to the normalized magnetic fields, Figure B.8 makes it apparent that the radial electric field is continuous at the sheath helix surface. From physical considerations, this must be true because free magnetic charge does not exist at $r = a$. It is also apparent from the figure that $H_\theta{}^a/H_{z0}{}^a$ and $H_z{}^a/H_{z0}{}^a$ are discontinuous at $r = a$. This is because there is an electrical surface current present on the sheath helix "windings". At an interface which possesses an electrical surface current, the tangential magnetic fields must be discontinuous.

C. Appendix C. Sheath Helix Surrounding a Perfectly Conducting Coaxial Rod

The configuration of concern in this appendix consists of a perfectly conducting circular cylindrical rod, having a radius b, which is centered inside a sheath helix. It is always assumed that $0 < b < a < \infty$, where, of course, a is the radius of the sheath helix. (See Figure 1.5b. It displays the developed sheath helix.) This configuration can be regarded as a limiting case of the sheath helix surrounding a lossy coaxial rod, when the conductivity of the lossy rod becomes very large.

Bryant (19), and Mathers and Kino (20), previously investigated this structure. Bryant only briefly examined it. He obtained the dispersion equation and made a single graph of the quantity $ka \cot\psi / h^C a$ versus $h^C a$, where $h^C a$ is the radial wave number, and $ka \cot\psi = \omega \sqrt{\mu_0 \epsilon_0}\, a \cot\psi$. b/a, the rod radius normalized with respect to the sheath helix radius, was a parameter of the graphs.

Mathers and Kino performed a more detailed study. All field components in terms of a single undetermined constant were listed. In addition to obtaining the dispersion equation, approximations of it were given which are valid for small or large values of the variable $ka \cot\psi$. Graphs of $ka \cot\psi / h^C a$ versus $ka \cot\psi$ were made for different normalized rod radii. It was mentioned that these curves are flatter than those of the empty sheath helix, and that this is especially true when b/a is nearly unity.

C.1 List of the Field Components and the Dispersion Equation

To obtain the free mode field solution, it is necessary to apply boundary conditions. In addition to the four boundary conditions at the sheath helix surface, equations 1.6 – 1.9, there are also the boundary conditions that the tangential electric fields vanish at the perfectly conducting rod surface. (Note this will also mean that the normal magnetic field at the rod surface is zero.) Since the rod is a perfect conductor, all electromagnetic fields in the region $0 \leq r < b$ must be zero. The same type of electrical current discussed in section B.1 is assumed to be present on the sheath helix "windings". A brief derivation of the following results is given by Mathers and Kino (20).

Summary of the Field Components

Region 1 $(0 \leq r \leq b)$

$$E_{r1}{}^C = E_{\theta 1}{}^C = E_{z1}{}^C = H_{r1}{}^C = H_{\theta 1}{}^C = H_{z1}{}^C = 0. \qquad (C.1)$$

Region 2 $(b \leq r \leq a)$

$$E_{r2}{}^C = j \mathcal{J}_{II} \frac{120\pi}{ka \cot a n \psi} \beta^C a \, h^C a \, \cos\psi \, \frac{K_0(h^C a)}{K_0(h^C b)} \cdot$$

$$(K_0(h^C b) \, I_1(h^C r) + I_0(h^C b) \, K_1(h^C r)) \, \sin\beta^C z, \qquad (C.2)$$

$$E_{\theta 2}{}^C = -j \mathcal{J}_{II} \, 120\pi \, ka \cot a n \psi \, \sin\psi \, \frac{K_1(h^C a)}{K_1(h^C b)} \cdot$$

$$(K_1(h^C b) \, I_1(h^C r) - I_1(h^C b) \, K_1(h^C r)) \, \cos\beta^C z, \qquad (C.3)$$

$$E_{z2}{}^C = j \mathcal{J}_{II} \frac{120\pi}{ka \cot a n \psi} (h^C a)^2 \cos\psi \, \frac{K_0(h^C a)}{K_0(h^C b)} \cdot$$

$$(K_0(h^C b) \, I_0(h^C r) - I_0(h^C b) \, K_0(h^C r)) \, \cos\beta^C z, \qquad (C.4)$$

$$H_{r2}{}^C = \mathcal{J}_{II} \, \beta^C a \, \cos\psi \, \frac{K_1(h^C a)}{K_1(h^C b)} \cdot$$

$$(K_1(h^C b) \, I_1(h^C r) - I_1(h^C b) \, K_1(h^C r)) \, \sin\beta^C z. \qquad (C.5)$$

$$H_{\theta 2}{}^c = -\oint_{11} h^c a \sin\psi \; \frac{K_0(h^c a)}{K_0(h^c b)} \cdot$$

$$\text{(C.6)}$$

$$(K_0(h^c b)\, I_1(h^c r) + I_0(h^c b)\, K_1(h^c r))\, \cos\beta^c z, \text{ and}$$

$$H_{z2}{}^c = \oint_{11} h^c a \cos\psi \; \frac{K_1(h^c a)}{K_1(h^c b)} \cdot$$

$$\text{(C.7)}$$

$$(K_1(h^c b)\, I_0(h^c r) + I_1(h^c b)\, K_0(h^c r))\, \cos\beta^c z.$$

Region 3 ($a \leq r < \infty$)

$$E_{r3}{}^c = -j \oint_{11} \frac{120\pi}{ka \cot\psi} \, \beta^c a \, h^c a \cos\psi \cdot \tag{C.8}$$

$$(I_0(h^c a)\, K_0(h^c b) - I_0(h^c b)\, K_0(h^c a))\, \frac{K_1(h^c r)}{K_0(h^c b)} \, \sin\beta^c z,$$

$$E_{\theta 3}{}^c = -j \oint_{11} 120\pi \, ka \cot\psi \, \sin\psi \cdot \tag{C.9}$$

$$(I_1(h^c a)\, K_1(h^c b) - I_1(h^c b)\, K_1(h^c a))\, \frac{K_1(h^c r)}{K_1(h^c b)} \, \cos\beta^c z,$$

$$E_{z3}{}^c = j \oint_{11} \frac{120\pi}{ka \cot\psi} \, (h^c a)^2 \cos\psi \cdot \tag{C.10}$$

$$(I_0(h^c a)\, K_0(h^c b) - I_0(h^c b)\, K_0(h^c a))\, \frac{K_0(h^c r)}{K_0(h^c b)} \, \cos\beta^c z,$$

$$H_{r3}{}^c = \oint_{11} \beta^c a \cos\psi \, (I_1(h^c a)\, K_1(h^c b) - I_1(h^c b)\, K_1(h^c a))$$

$$\frac{K_1(h^c r)}{K_1(h^c b)} \, \sin\beta^c z, \tag{C.11}$$

r

325

$$H_{\theta 3}{}^{c} = \int_{II} h^{c}a \, \sin\psi \, (I_0(h^c a) \, K_0(h^c b) - I_0(h^c b) \, K_0(h^c a))$$

$$\frac{K_1(h^c r)}{K_0(h^c b)} \cos \beta^c z, \text{ and} \tag{C.12}$$

$$H_{z3}{}^{c} = -\int_{II} h^{c}a \, \cos\psi \, (I_1(h^c a) \, K_1(h^c b) - I_1(h^c b) \, K_1(h^c a))$$

$$\frac{K_0(h^c r)}{K_1(h^c b)} \cos \beta^c z. \tag{C.13}$$

Summary of the Dispersion Equation

$$\left(\frac{ka \, \cot an\psi}{h^c a}\right)^2 = \frac{K_0(h^c a) \, K_1(h^c b)}{K_0(h^c b) \, K_1(h^c a)} \cdot$$

$$\frac{(I_0(h^c a) \, K_0(h^c b) - I_0(h^c b) \, K_0(h^c a))}{(I_1(h^c a) \, K_1(h^c b) - I_1(h^c b) \, K_1(h^c a))} \tag{C.14}$$

The separation constant equation, which relates the axial wave number, $\beta^c a$, to the radial wave number, $h^c a$, is

$$h^c a = +\sqrt{(\beta^c a)^2 - (ka)^2} . \tag{C.15}$$

Equations C.14 and C.15 are used to calculate the radial and axial wave numbers.

Equations C.1 - C.15 comprise the free mode field solution of the sheath helix surrounding a perfectly conducting coaxial rod. The superscript " c " is used on all the electric and magnetic field components, and on the radial and axial wave numbers, so it is obvious that they are associated with the perfectly conducting coaxial rod

configuration, and not with any of the other configurations which have been studied in the thesis. The operating frequency, the perfectly conducting rod geometry, and the sheath helix geometry, are specified by the variables $ka \cot\psi$, b/a, and ψ. $0 < ka \cot\psi < \infty$, $0 < b/a < 1$, and $0 < \psi < 90.0°$ are the values of these variables which are acceptable for a free mode field solution. Throughout the remainder of this appendix, it will usually be assumed that the sheath helix is sufficiently tightly wound so that $0 < \psi \leq 10.0°$.

As was previously discussed in section B.1 in connection with the empty sheath helix, it is convenient to regard the radial and axial wave numbers solution as $h^C a$ and $\beta^C a$, rather than as h^C and β^C, respectively. The quantity $h^C b$ in equations C.2 - C.14 is now thought of as $h^C a \cdot b/a$. In addition, the spatial dependences of all field components are considered as normalized with respect to the sheath helix radius, so that $h^C r$ and $\beta^C z$ become $h^C a \cdot r/a$ and $\beta^C a \cdot z/a$, respectively.

To complete this section, it is mentioned that E_{r3}^C, E_{z3}^C, $H_{\theta 3}^C$ as given in equations 14 by Mathers and Kino (20) are incorrect. These field components do not satisfy the boundary conditions at the sheath helix surface, equations 1.6 - 1.9. Otherwise, equations C.1 - C.13 agree with their results. Equation C.14, the dispersion equation, is the same as equation 15 of Mathers and Kino, and equation 5 of Bryant (19).

C.2 Investigation of the Dispersion Equation and Graphs of the Radial Wave Number Solution

As was true of the empty sheath helix, the dispersion equation and the separation constant equation, equations C.14 and C.15, respectively, are even functions of both the angular frequency, ω, and the pitch angle, ψ. Therefore, the comments made at the beginning of section B.2 also apply here.

Two limiting cases of the perfectly conducting rod geometry are when its radius decreases until it approaches zero, and when its radius increases until it approaches that of the sheath helix. Assuming that the variables $ka \cot\psi$ and a are held constant and taking the limit as $b \to 0^+$ of equation C.14, making use of the small argument Bessel function representations, equations A.26 - A.29, it can be shown that

equation B.13 is obtained. As expected, in the limit when the rod radius approaches zero, the dispersion equation is transformed into the empty sheath helix dispersion equation. Since the separation constant equations for the sheath helix surrounding a perfectly conducting coaxial rod and for the empty sheath helix, equations C.15 and B.14, respectively, have an identical form, the previous sentence means that

$$\lim_{b\to0^+} h^c a = h^a a \quad \text{and} \quad \lim_{b\to0^+} (\beta^c a)^2 = (\beta^a a)^2, \quad (C.16)$$

where $h^a a$ and $\beta^a a$ are the radial and axial wave numbers of the empty sheath helix, respectively. In addition, taking this same limit of equations C.2 - C.13, assuming that the variables $ka\cot\psi$, ψ, a, and $\gamma_{||}$ are held constant, and making use of relations A.26 - A.29 and C.16, it can be demonstrated that equations B.1 - B.12 are obtained. Taking the limit as the rod radius approaches zero of each field component in region 2 and in region 3 gives the corresponding empty sheath helix field component, as one would expect. In summary, *in the limit as the rod radius approaches zero, the free mode field solution associated with the sheath helix surrounding a perfectly conducting coaxial rod is correctly transformed into that associated with the empty sheath helix.*

Attention is now directed toward investigating the limit when the radius of the perfectly conducting rod increases so that the rod surface touches the sheath helix surface. The limit as $b\to a^-$ of the dispersion equation is calculated, assuming that the variables $ka\cot\psi$ and a are held constant. L' Hopital's rule (47, pp. 651) is needed to evaluate the resulting indeterminate form, and the Bessel function recurrence relations A.5 - A.8 are used. It can be demonstrated that

$$\lim_{b\to a^-} \left(\frac{ka\cot\psi}{h^c a}\right)^2 = \left(\frac{ka\cot\psi}{h^{c*} a}\right)^2 = 1,$$

$$(C.17)$$

where $\lim_{b\to a^-} h^c a = h^{c*} a.$

If this same limit is taken of the field components, it is discovered that they all become zero in the regions $0 \leq r < a$ and $a < r < \infty$.

When the rod completely fills the sheath helix interior region so that its surface touches the sheath helix surface, there is infinite conductivity in all directions on the surface at $r = a$. This means that all properties of the sheath helix have been lost. (See part 1.3.2 for a discussion of the sheath helix.) In fact, there is actually a perfectly conducting rod in an unbounded air-filled region. It is known that the only nontrivial field solution, so that at least one of the field components is nonzero, results when $h^C = 0$ (35, pp. 527). Only E_{r3}^C and $H_{\theta 3}^C$ do not vanish. These are characterized by a $1/r$ type of radial dependence, and a $\sin \beta^C z$ or $\cos \beta^C z$ axial dependence, respectively, where $(\beta^C a)^2 = (ka)^2 = \omega^2 \mu_0 \epsilon_0 a^2$. Stratton (35, pp. 527) has said that a perfectly conducting rod in space only has an unguided wave associated with it.

For a sheath helix surrounding a perfectly conducting coaxial rod, the problem of determining the values of $h^C a$ and $\beta^C a$ which may possibly result in a free mode field solution is more difficult than was true of the empty sheath helix. If negative real or purely imaginary values of $h^C a$ are substituted into the right hand side of equation C.14, and the Bessel function relations, equations A.14 – A.21 are used, a very lengthy expression occurs. It appears to be necessary to use the small and large argument approximations of the Bessel functions, equations A.26 – A.29 and A.32 – A.43, to see if the two sides of the dispersion equation can possibly be equated. A relatively thorough investigation of this was carried out. In addition, the special case of $h^C = 0$ was considered. ($h^C a$ complex valued with nonzero real and imaginary parts cannot possibly result in a free mode field solution. The previous statement is known to be true by applying the same reasoning as was previously discussed at the beginning of section B.2.) Just the conclusion of this investigation will be mentioned. It is believed that only *real wave numbers* such that

$$0 < h^C a < \infty \quad \text{and} \quad (\beta^C a)^2 > (ka)^2 \qquad (C.18)$$

are acceptable for a free mode field solution. Note that when $h^c{}_a$ is real positive, the Bessel function inequalities A.49 and A.50 can be used to demonstrate that the right hand side of equation C.14 is real and positive. Of course, the left hand side is also positive real, and so it is possible to equate the two sides. Therefore, a solution to the dispersion equation does exist for the values of the wave numbers given in equations C.18.

It is clear from equations C.14 and C.15 what variables the radial and axial wave numbers depend on.

$$h^c{}_a = f(ka \ cotan\psi, \ b/a) \quad and \qquad (C.19)$$

$$(\beta^c a)^2 =' g(ka \ cotan\psi, \ b/a, \ \psi). \qquad (C.20)$$

As was true of the empty sheath helix, it is highly desirable to develop approximations of the dispersion equation, in order that the radial and axial wave numbers solution is more easily calculated, and so that their behavior for different frequencies of operation, perfectly conducting rod geometries, and sheath helix geometries, is more easily understood. First, the approximation which is valid when the radial wave number is small will be considered. Substituting equations A.26 – A.29, the small argument Bessel function representations, into the right hand side of equation C.14, and performing a small amount of algebra, yields

$$(\frac{ka \ cotan\psi}{h^c{}_a})^2 \ \simeq \ \frac{log(0.891 \ h^c a)}{log(0.891 \ h^c b)} \cdot \frac{(-2 \ log(b/a))}{(1 - (b/a)^2)}. \qquad (C.21)$$

Equation C.21 is the accurate small argument approximation of the dispersion equation. Of course, $(\beta^c{}_a)^2$ is calculated from equation C.21 by making use of the separation constant equation, equation C.15. Reassuringly, calculating the limit of equation C.21 as $b \to 0$, assuming that the variables $ka \ cotan\psi$ and a are held constant, correctly results in equation B.21, which is the small argument approximation of the empty sheath helix dispersion equation.

Assuming that the variable b/a is fixed and taking the limit of equation C.21 as $ka \cot an\psi$ approaches zero, realizing this also means that $h^C a$ approaches zero, yields

$$\lim_{ka \cot an\psi \to 0^+} (\frac{ka \cot an\psi}{h^C a})^2 = (\frac{ka \cot an\psi}{h^{C*} a})^2$$

$$= \frac{(-2 \log(b/a))}{(1 - (b/a)^2)} , \qquad (C.22)$$

$$\text{where} \qquad \lim_{ka \cot an\psi \to 0^+} h^C a = h^{C*} a.$$

The result given by equation C.22 was previously mentioned by Mathers and Kino (20). It is actually an approximation of equation C.21 which is valid when $h^C a << b/a$, since

$$\frac{\log(0.891\ h^C a)}{\log(0.891\ h^C b)} = \frac{\log(0.891\ h^C a)}{(\log(0.891\ h^C a) + \log(b/a))} \qquad (C.23)$$

$$\cong 1, \quad \text{if} \quad |\log(0.891\ h^C a)| >> |\log(b/a)|.$$

$$(\frac{ka \cot an\psi}{h^C a})^2 \cong \phi(b/a) = \frac{(-2 \log(b/a))}{(1 - (b/a)^2)} . \qquad (C.24)$$

Equation C.24 is the crude small argument approximation of the dispersion equation. It is much more convenient than equation C.21 because it is possible to express $h^C a$ explicitly as a function of the operating frequency, the sheath helix geometry, and the perfectly conducting rod geometry. $\phi(b/a)$ is a strictly decreasing positive function. It has a large value and a large negative slope for b/a close to zero, and it approaches unity form the upperside as b/a becomes close to

1.

For the empty sheath helix, the small argument representation of the dispersion equation, equation B.21, shows that

$$\lim_{ka \ cotan\psi \to 0^+} \left(\frac{ka \ cotan\psi}{h^a a}\right)^2 = \infty . \qquad (C.25)$$

Comparsion of equations C.22 and C.25 makes it clear that when the variable $ka \ cotan\psi$ becomes sufficiently small, the radial and axial wave numbers solution associated with the sheath helix surrounding a perfectly conducting coaxial rod is very different than that associated with the empty sheath helix.

A data table, which will not be presented here, was prepared which compared the right hand side of equations C.21 and C.24, with that of equation C.14, for a wide range of values of the variables $ka \ cotan\psi$ and b/a. It was discovered that the error associated with equation C.21 is about one percent or less for $ka \ cotan\psi <$ 0.100, and that it is about ten percent or less for $ka \ cotan\psi < 0.500$. The error associated with equation C.24 is small when b/a is nearly unity, but it may be very large when b/a is small. For example, it is about two percent or less when $b/a = 0.900$, for $ka \ cotan\psi < 0.100$. However, when $b/a = 0.100$, it is as high as thirty five percent over the same range of $ka \ cotan\psi$ values. Equations C.21 and C.24 both have the property that for a fixed value of b/a, the error decreases as the value of $ka \ cotan\psi$ becomes smaller. Furthermore, for a fixed value of $ka \ cotan\psi$, the error increases as the value of b/a becomes smaller.

In summary, equation C.21 will be sufficiently accurate for most applications so that it can be used to calculate the radial and axial wave numbers when $ka \ cotan\psi < 0.10$. This is true for any value of b/a, which, of course, must be in the range $0 < b/a < 1$. Equation C.24 can be used with little error to approximate the wave numbers solution over the previously mentioned range of $ka \ cotan\psi$ values, when the value of b/a is close to unity. However, when b/a is much smaller than unity, this approximation is significantly in error, except when

the value of $ka \cot an\psi$ is very, very small.

To obtain the approximations of the dispersion equation, which are justified when the radial wave number is large, it is helpful to rewrite equation C.14 in the form

$$\left(\frac{ka \cot an\psi}{h^C a}\right)^2 = \frac{I_0(h^C a) \, K_0(h^C a)}{I_1(h^C a) \, K_1(h^C a)} \cdot$$

$$\frac{\left[1 - \frac{I_0(h^C b) \, K_0(h^C a)}{I_0(h^C a) \, K_0(h^C b)}\right]}{\left[1 - \frac{I_1(h^C b) \, K_1(h^C a)}{I_1(h^C a) \, K_1(h^C b)}\right]}$$

$$(C.26)$$

Keeping three terms of equations A.36 – A.39, the large argument Bessel function representations, and substituting into the unbracketed expression on the right hand side of equation C.26, while only using the first two terms and substituting into the pair of bracketed expressions, gives

$$\left(\frac{ka \cot an\psi}{h^C a}\right)^2 = \left(1 + \frac{0.50}{(h^C a)^2}\right) \cdot$$

$$\frac{\left[1 - e^{-2 \, h^C a(1-b/a)} \cdot \frac{[h^C b + 0.125(1-b/a)]}{[h^C b - 0.125(1-b/a)]}\right]}{\left[1 - e^{-2 \, h^C a(1-b/a)} \cdot \frac{[h^C b - 0.375(1-b/a)]}{[h^C b + 0.375(1-b/a)]}\right]} \cdot$$

$$(C.27)$$

Equation C.27 is the accurate large argument approximation of the dispersion equation. Of course, for a particular approximate solution $h^C a$ of equation C.27, the corresponding approximate value of $\pm \beta^C a$ is calculated by making use of equation C.15, the separation constant equation.

If it is assumed that $h^c a$ is sufficiently large so that $h^c a \cdot (1-b/a) >> 1$, equation C.27 becomes considerably simplified to

$$\frac{ka\ cotan\psi}{h^c a} \simeq 1. \qquad (C.28)$$

Equation C.28 is the crude large argument approximation of the dispersion equation. Mathers and Kino (20) previously mentioned this result. Equation C.28 is very convenient because the radial wave number is explicitly given as a function of the operating frequency and the sheath helix geometry. It is important to realize that this equation is the same as equation B.20. Since the separation constant equations, equations C.15 and B.14, are identical, it is true for large values of $ka\ cotan\psi$ that the radial and axial wave numbers solution for the sheath helix surrounding a perfectly conducting coaxial rod is similar to that associated with the empty sheath helix.

In all the numerical calculations of the radial wave number that the author performed, which were based on equation C.14, it was discovered that

$$1 < \frac{ka\ cotan\psi}{h^c a} < \frac{ka\ cotan\psi}{h^a a} < \infty. \qquad (C.29)$$

(A discussion of this numerical solution will be given shortly.) This is a statement of the fact that the dispersion curve associated with the sheath helix surrounding a perfectly conducting coaxial rod is flatter than that of the empty sheath helix. Therefore, the approximation $h^c a \simeq ka\ cotan\psi$ is always better than the approximation $h^a a \simeq ka\ cotan\psi$. From the discussion given in section B.2 concerning equation B.20, it must be true that equation C.28 is an approximation of equation C.14, which is accurate to less than twenty percent error for $ka\ cotan\psi > 1$, and to less than one percent error for $ka\ cotan\psi > 5$, for all values of b/a, $0 < b/a < 1$.

In fact, the previously mentioned error limitations are correct but they cannot be justified on the basis of developing large argument approximations of the dispersion equation. For some fixed value of $ka \cot\psi$, where $ka \cot\psi > 1$, using $h^c a \overset{\sim}{=} ka \cot\psi$ means that if b/a is sufficiently small, it will be true that $h^c a \cdot b/a << 1$. The large argument asymptotic representations of the Bessel functions are not valid for arguments much less than unity, and so equation C.28 cannot be justified. (See Table A.2. This shows the error involved in using the large argument Bessel function representations.) In order to support the usage of $h^c a \overset{\frown}{=} ka \cot\psi$ for $ka \cot\psi \overset{\frown}{=} 1$ and $b/a << 1$, it is necessary to say that this approximation must be a better one than that of the empty sheath helix, and then examine the error involved with it for the empty sheath helix configuration.

A data table was prepared which compared the right hand sides of equations C.27 and C.28, with the right hand side of equation C.14, for many different values of $ka \cot\psi$ and b/a. For the two approximations, increasing $ka \cot\psi$ for a fixed value of b/a, and increasing b/a for a fixed value of $ka \cot\psi$, both tended to reduce the error. Equation C.27 was discovered to usually be much more accurate than equation C.28. However, as previously discussed, equation C.28 is itself quite accurate, and its simplicity means that it is clearly preferable to equation C.27.

In summary, equation C.28 is the crude large argument representation of the dispersion equation. It is valid to less than twenty percent error for $ka \cot\psi > 1$ and for all values of b/a, $0 < b/a < 1$. Although the error is relatively great at $ka \cot\psi = 1$, it rapidly decreases as this variable becomes larger.

As was true of the empty sheath helix, the approximation of equating the absolute value of the axial wave number to the radial wave number, $|\beta^c| a \overset{\frown}{=} h^c a$, results in simplification because it is not necessary to have the pitch angle appearing by itself as a variable, in order to calculate the axial wave number. The functional dependences of both the axial and radial wave numbers are now given by equation C.19. Using a similar procedure to that previously followed in section B.2, and making use of equation Cr28, it is clear that for a sheath helix sufficiently tightly wound so that $0 < \psi \overset{<}{_\sim} 10.0°$, the approximation is certainly correct for large values of $ka \cot\psi$

$(ka\ cotan\psi > 1)$. Equation C.24 shows, as a worst case, in order that the approximation be valid within about ten percent error for small values of $ka\ cotan\psi$ ($ka\ cotan\psi \ll 1$), the requirement is

$$2\ tan\psi \sqrt{\frac{-2\ log(b/a)}{(1 - (b/a)^2)}} < 1 . \qquad (C.30)$$

Even for b/a as small as 1.0×10^{-2} and ψ as large as $10°$, the inequality is satisfied. Unlike the empty sheath helix, equating the axial and radial wave numbers is often valid even when the variable $ka\ cotan\psi$ approaches zero. Of course, in the limit when both $ka\ cotan\psi$ and b/a become very small, inequality C.30 will not be satisfied. The wave number solutions are now similar to those of the empty sheath helix.

In summary, the approximation $|\beta^c|a \simeq h^c a$ is justified to about ten percent error or less, assuming that the pitch angle satisfies $0 < \psi \le 10.0°$, over the entire range $0 < ka\ cotan\psi < \infty$, for most b/a values. The single exception occurs for small values of $ka\ cotan\psi$, when the rod radius is much less than the sheath helix radius, so that, for the particular pitch angle of concern, inequality C.30 is not satisfied.

Attention is now directed to the numerical solution of equation C.14, the dispersion equation, in order to calculate the radial wave number. The variable $ka\ cotan\psi$ only appears in the left hand side of the equation. In a similar fashion to that mentioned near the end of section B.2, the quantity $ka\ cotan\psi/h^c a$ is calculated. However, it is now necessary to specify the variable b/a, in addition to specifying the value of $ka\ cotan\psi$.

The following three figures were obtained from direct calculation of equation C.14, making use of the IMSL (43) software program routines to evaluate the Bessel functions. Figure C.1 is a linear graph of $ka\ cotan\psi/h^c a$ versus $ka\ cotan\psi$. Each curve is associated with one particular value of b/a. $b/a = 0$, 0.100, 0.300, 0.500, 0.700, and 0.900 are used. The curve representing $b/a = 0$ is
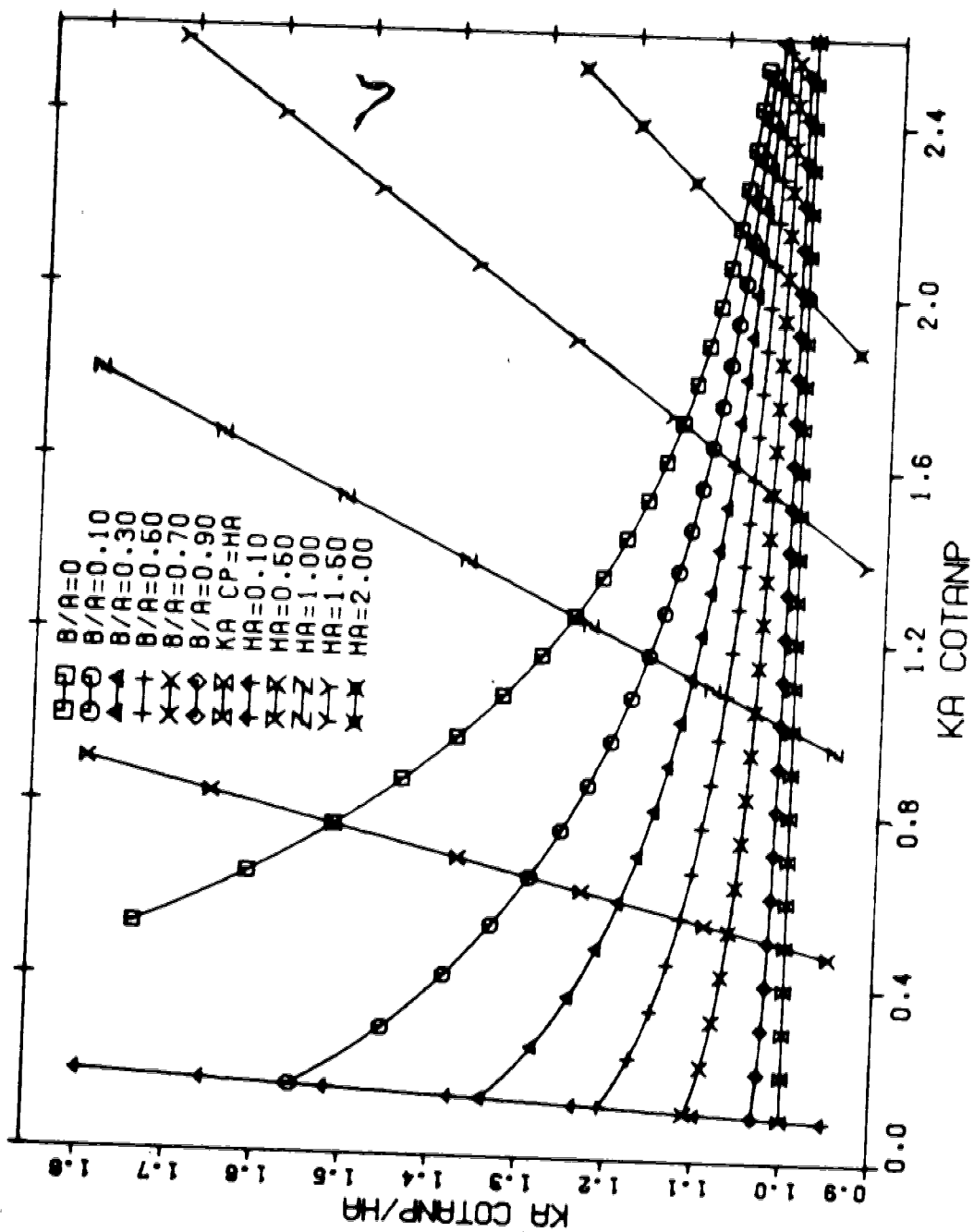
PLOT OF KA COTANP/HA VS. KA COTANP

Figure C.1   Graph of ka cotanψ/h^{C}a versus ka cotanψ based on equation C.14. Curves for b/a = 0.100, 0.300, 0.500, 0.700, and 0.900 are given. The curve for b/a = 0 is based on the dispersion equation for the empty sheath helix, equation B.13. Several lines of constant h^{C}a are shown, and so is the asymptote ka cotanψ/h^{C}a = 1.0. (Note that HA=h^{C}a, KA COTANP=KA CP=ka cotanψ, and B/A=b/a.)

based on the dispersion equation for the empty sheath helix, equation B.13. Several different lines of constant $h^c a$ are displayed, and so is the asymptote $ka \, cotan\psi/h^c a = 1.0$. Note that this figure is in agreement with equation C.29. The dispersion curve for the 'sheath helix surrounding a perfectly conducting coaxial rod is flatter than that for the empty sheath helix, especially when the value of b/a is nearly unity.

Figure C.2 is a semilogarithmic graph, with the same abscissa and ordinate as the previous figure. $b/a = 0.100, 0.300, 0.500, 0.700,$ and 0.900 are used. Many decade ranges of $ka \, cotan\psi$ values are displayed. The asymptote $ka \, cotan\psi/h^c a = 1.0$ is given.

Figures C.1 and C.2 both demonstrate that the large argument representations of the dispersion equation, equations C.27 and C.28, are approximately correct when $ka \, cotan\psi > 1$ is true. Furthermore, Figure C.2 is in good agreement with the accurate small argument representation of the dispersion equation, equation C.21, when $ka \, cotan\psi << 1$. However, in order that little error is involved with the usage of the crude small argument representation of the dispersion equation, equation C.24, for the case when $b/a = 0.100$, it is seen to be necessary that the value of $ka \, cotan\psi$ is very, very small. More specifically, so that less than 10% error occurs, it is necessary that $ka \, cotan\psi < 1.00 \times 10^{-5}$.

It is informative to compare Figures C.2 and B.2. The latter mentioned figure is a semilogarithmic graph of the dispersion curve for the empty sheath helix. Clearly, for large values of $ka \, cotan\psi$ $(ka \, cotan\psi > 1)$, the radial wave number ' solution associated with the sheath helix surrounding a perfectly conducting coaxial rod is very similar to that for the empty sheath helix. However, when the variable $ka \, cotan\psi$ is small $(ka \, cotan\psi << 1)$, the radial wave number solution is certainly different for the two configurations. It is clear that the value of b/a has a great effect on the solution $h^c a$ for small values of $ka \, cotan\psi$.

The final computer generated graph included in section C.2 is Figure C.3. This is a three dimensional plot of the quantity $ka \, cotan\psi/h^c a$ as a function of both the variable $ka \, cotan\psi$ and the variable b/a. It indicates in a qualitative manner the functional dependences of $ka \, cotan\psi/h^c a$ on its two variables. When the rod
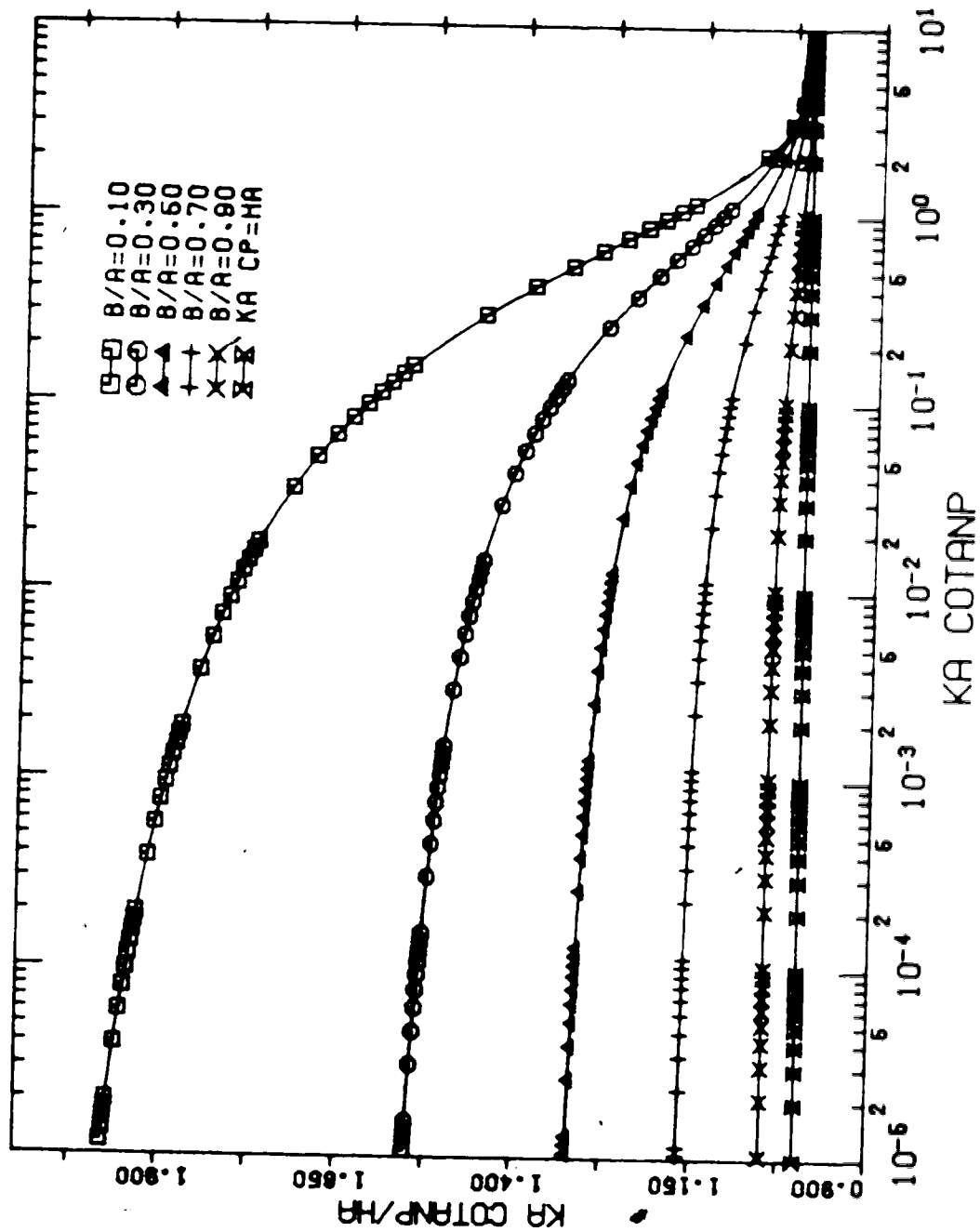
Figure C.2   Graph of ka cotanψ/h^{C}a versus ka cotanψ based on equation C.14. Curves for b/a = 0.100, 0.300, 0.500, 0.700, and 0.900 are shown, and so is the asymptote ka cotanψ/h^{C}a = 1.0. (Note that HA = h^{C}a, KA COTANP = KA CP = ka cotanψ, and B/A = b/a.)
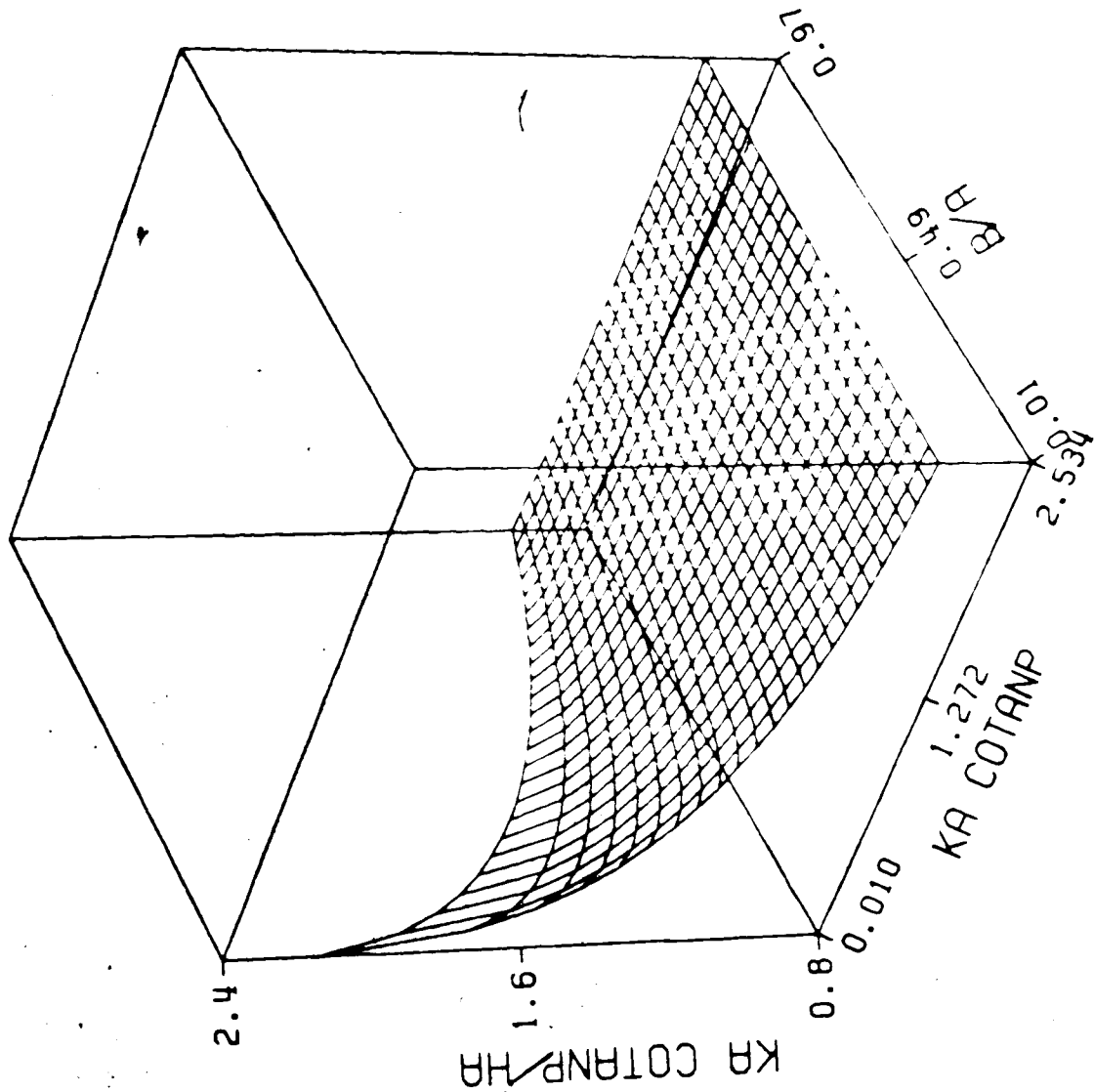
Figure C.3   Three dimensional graph of ka cotanψ/h^{c}a versus both ka cotanψ and b/a. The graph is based on equation C.14. (Note that HA = h^{c}a, KA COTANP = ka cotanψ, and B/A = b/a.)

radius is much smaller than that of the sheath helix, the dependence on $ka \cot \psi$ is similar to that of the empty sheath helix. On the other hand, when b/a approaches unity, it is seen that $ka \cot \psi / h^C a \cong 1$. For a fixed value of $ka \cot \psi$, increasing b/a tends to make $ka \cot \psi / h^C a$ smaller, or equivalently, $h^C a$ larger. This effect is more pronounced for small values of $ka \cot \psi$.

C.3 Discussion and Graphs of the Field Components

The final section of this appendix consists of an investigation of equations C.1 – C.13. Replacing $\beta^C a$ by $-\beta^C a$ in the field components results in no change. This property is also true of equation C.15. Since the dispersion equation, the separation constant equation, and the field components are not affected when the algebraic sign of the axial wave number is reversed, no loss in generality results from restricting $\beta^C a > 0$.

The pitch angle appears by itself in the angular field components as $\sin \psi$, while in the radial and axial field components, it appears by itself as $\cos \psi$. It is assumed that the sheath helix is sufficiently tightly wound so that $\cos \psi \cong 1$ and $\beta^C a \cong h^C a$. (As was previously mentioned in section C.2, equation C.30 states the requirement which must be satisfied for a relatively tightly wound sheath helix, in order that the axial wave number can be equated with the radial wave number.) Since $\beta^C a \cong h^C a$ is assumed, equation C.19 lists the variables on which both the radial and axial wave numbers are dependent. Decreasing the pitch angle in such a fashion that the variable $ka \cot \psi$ remains constant, keeping in mind equation C.19, the magnitudes of the angular fields are seen to be greatly reduced, but no significant change occurs to the radial and axial fields.

Making use of equation C.19 and of the assumptions $\cos \psi \cong 1$ and $\beta^C a \cong h^C a$, it is a simple matter to state the approximate functional dependences of the region 2 and region 3 field components on the operating frequency, the perfectly conducting coaxial rod geometry, the sheath helix geometry, and the sheath helix "windings'" current.

$$E_{\theta n}{}^{c} = L_n(\text{⟩}_{II}, \ ka \ \cot an\psi, \ b \angle a, \ \psi), \qquad (C.31)$$

$$H_{\theta n}{}^{c} = S_n(\text{⟩}_{II}, \ ka \ \cot an\psi, \ b/a, \ \psi), \qquad (C.32)$$

$$E_{rn}{}^{c} = Q_n(\text{⟩}_{II}, \ ka \ \cot an\psi, \ b/a), \qquad (C.33)$$

$$E_{zn}{}^{c} = U_n(\text{⟩}_{II}, \ ka \ \cot an\psi, \ b/a), \qquad (C.34)$$

$$H_{rn}{}^{c} = V_n(\text{⟩}_{II}, \ ka \ \cot an\psi, \ b/a), \ \text{and} \qquad (C.35)$$

$$H_{zn}{}^{c} = W_n(\text{⟩}_{II}, \ ka \ \cot an\psi, \ b/a); \qquad (C.36)$$

where $n = 2, \ 3$.

Region 3 fields have a radial dependence described by either $K_0(h^c r)$ or $K_1(h^c r)$, while the radial dependence of region 2 fields is a linear combination of either $I_0(h^c r)$ and $K_0(h^c r)$, or of $I_1(h^c r)$ and $K_1(h^c r)$. As was previously mentioned in section C.2, it is believed that the radial wave number must be real positive in order to obtain a free mode field solution, and so all the arguments of these Bessel functions are real positive. For one particular operating frequency, perfectly conducting coaxial rod geometry, and sheath helix geometry (which means that $h^c a$ has one particular value), as the normalized radial distance r/a increases, it must be true that the magnitude of a region 3 field always decreases, while the magnitude of a region 2 field may either increase or decrease. (See Figure A.1. This is a graph of I_0, I_1, K_0, and K_1 for real positive arguments.)

For small values of $ka \ \cot an\psi$, so that $0 < ka \ \cot an\psi < 0.100$, equation C.29 and Figure C.2 show that $0 < h^c a < 0.100$ occurs. Furthermore, the discussion previously given in section B.2 for the empty sheath helix makes it apparent that for this range of $ka \ \cot an\psi$ values, $0 < h^a a < 0.100$ occurs. The small argument Bessel function representations are therefore well justified to approximate the fields for the sheath helix surrounding a perfectly

conducting coaxial rod, equations C.1 - C.13, and to approximate the empty sheath helix fields, equations B.1 - B.12. (See Table A.1. Note that in order to use the small argument Bessel function representations for the fields in the region exterior to the sheath helix, the radial distance must be limited in extent so that approximately $h^c{}_a \cdot r/a <$ 0.100 and $h^a{}_a \cdot r/a < 0.100$ is true.)

The author made use of equations A.26 - A.29 to develop small argument approximations of equations C.2 - C.13, and of equations B.1 - B.12. A comparison of the two sets of equations shows that $H_{z2}{}^c \cong H_{z1}{}^a$, while the other corresponding interior and exterior region sheath helix fields are quite different, for b/a clearly distinct from zero. Therefore, for small values of $ka \cot an\psi$, most of the fields of the sheath helix surrounding a perfectly conducting coaxial rod are usually very different from the corresponding fields of the empty sheath helix.

For large values of $ka \cot an\psi$, so that at least $ka \cot an\psi > 1$, equation C.28 and Figures C.1, C.2 show that $h^c{}_a \cong ka \cot an\psi$. In addition, it was previously discussed in section B.2 that for this range of $ka \cot an\psi$ values, the radial wave number for the empty sheath helix is $h^a{}_a \cong ka \cot an\psi$. The author made use of equations A.36 - A.39, keeping just the first term, to develop large argument Bessel function representations of equations B.1 - B.12 and C.2 - C.13. (See Table A.2. Note it is approximately required that the radial distance associated with the empty sheath helix and the radius of the perfectly conducting coaxial rod are both sufficiently large so that $h^a{}_a \cdot r/a > 1$ and $h^c{}_a \cdot b/a > 1$, in order that usage of the large argument representations of the Bessel functions to approximate the field components is justified.) Comparison of the field components in the two sets shows that if the value of $ka \cot an\psi$ is sufficiently large so that

$ka \cot an\psi \cdot (1-b/a) > 1$ and $ka \cot an\psi \cdot b/a > 1$, then, near r = a, the corresponding fields in the two sets are very similar. Since all field components are rapidly exponentially attenuated about the sheath helix surface according to

$$e^{-ka \cot an\psi(1-r/a)}$$ for interior region fields, and

$$e^{-ka \cot an\psi(r/a-1)}$$ for exterior region fields, $\qquad$ (C.37)

the field magnitudes near $r = a$ are certainly the largest. (For the empty sheath helix this behavior of the fields was previously discussed in section B.3.) Therefore, for sufficiently large values of $ka \cot\psi$, the dominant fields of the sheath helix surrounding a perfectly conducting coaxial rod are similar to the corresponding ones of the empty sheath helix.

A crude summary of the previous two paragraphs is now presented. *For large values of* $ka \cot\psi$ *(which could be considered to mean high frequencies since* $ka \cot\psi = 2\pi f \sqrt{\mu_0 \epsilon_0}\, a \cot\psi$*), the field components associated with the sheath helix surrounding a perfectly conducting coaxial rod do not "see" the rod. However, when the value of* $ka \cot\psi$ *is small (which could be considered to mean low frequencies), the field components do "see" the rod.*

Equations C.2 - C.13 are lengthy and complicated expressions. In order to help understand how the field components behave at different points in space, several graphs of their radial dependence have been prepared. The electric field components were normalized from dividing them by an electric normalizing coefficient, $E_{z0}{}^c$, and the magnetic field components were normalized from dividing them by a magnetic normalizing coefficient, $H_{z0}{}^c$. These normalizing coefficients are defined as

$$E_{z0}{}^c = E_{z2}{}^c \Big|_{\substack{z=0 \\ r=a}} = j\, \mathcal{Y}_{II}\, \frac{120\pi}{ka \cot\psi}\, (h^c a)^2\, \cos\psi\, \frac{K_0(h^c a)}{K_0(h^c b)} \cdot$$

$$(I_0(h^c a)\, K_0(h^c b) - I_0(h^c b)\, K_0(h^c a)) \tag{C.38}$$

$$= j\, \mathcal{Y}_{II}\, 120\pi\, ka \cot\psi\, \cos\psi\, \frac{K_1(h^c a)}{K_1(h^c b)} \cdot$$

$$(I_1(h^c a)\, K_1(h^c b) - I_1(h^c b)\, K_1(h^c a)),\quad \text{and}$$

$$H_{z0}{}^c = H_{z2}{}^c \Big|_{\substack{z=0 \\ r=a}} = \mathcal{Y}_{II}\, h^c a\, \cos\psi\, \frac{K_1(h^c a)}{K_1(h^c b)} \cdot$$

$$\tag{C.39}$$

$$(I_0(h^c a)\, K_1(h^c b) + I_1(h^c b)\, K_0(h^c a)).$$

When the radial dependence graphs were prepared, it was assumed that the axial coordinate is held constant. These transverse planes were chosen so that

$$\cos(\beta^c a \cdot z/a) = +1$$ for the angular and axial fields, and so that

$$\sin(\beta^c a \cdot z/a) = +1$$ for the radial fields.

Three different types of graphs are presented. These represent the "high frequency", "mid frequency", and "low frequency" cases. (The meanings of the terms in quotation marks is the same as it was when these expressions were previously used in section B.3.)

The radial dependence graphs are only concerned with the three region configuration $(b < a)$. The special case of the two region configuration $(b = a)$ is not considered. This is because the latter mentioned configuration has a free mode field solution completely different from that of the three region configuration. As was previously mentioned in section C.2, in the special case of $b = a$, all properties of the sheath helix are lost. Therefore, this special case is not of interest and will not be considered here.

In order to obtain the radial dependence graphs, the following procedure was used. For the specified values of the variables $ka \cot an\psi$ and b/a, equation C.14 is solved to obtain the radial wave number, $h^c a$. (Actually, as was previously mentioned in section C.2, the method used to solve the dispersion equation is to first specify the quantities $h^c a$ and b/a, and then to directly calculate the corresponding value of $ka \cot an\psi$.) Noting the value of the sheath helix pitch angle and the value of $ka \cot an\psi$, equation C.15 is solved to obtain the axial wave number, $\beta^c a$. Next, equations C.38 and C.39 are calculated to obtain the electric and magnetic normalizing coefficients. Finally, the normalized field components are evaluated for several different values of the radial distance normalized with respect to the sheath helix radius, r/a. The IMSL (43) software program library was used to evaluate the Bessel functions. All twelve graphs of the normalized fields' radial dependence presented here are "exact" – no approximations have been made to the dispersion equation, the separation constant equation, the normalizing coefficients, and the normalized fields.

Figures C.4 and C.5 show the absolute value of the normalized electric and magnetic field components, respectively, as a function of r/a. The two vertical lines
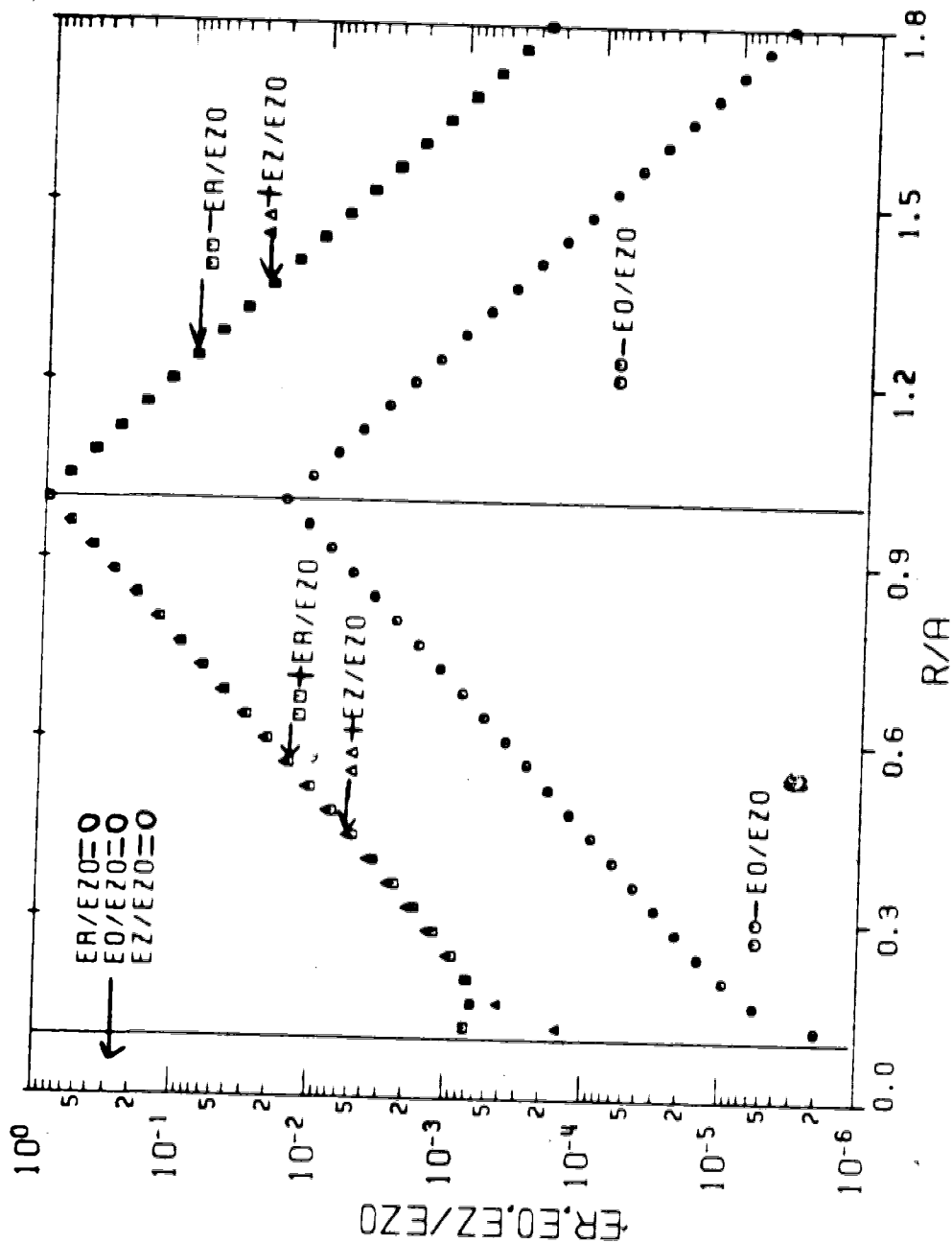
Figure C.4   Curves of the radial dependence associated with the normalized electric fields. The variables used are ka cotanψ = 10.0, b/a = 0.100, and ψ = 1.00°. They determine the wave numbers, $h^c a$=10.0 and $\beta^c a$=10.0, and the electric normalizing coefficient, E_{z0}^{c} = J ∂_{11} 188 (V/m). (Note that ER/EZO = E_r^c/E_{z0}^c, EO/EZO = E_θ^c/E_{z0}^c, EZ/EZO = E_z^c/E_{z0}^c, and R/A = r/a.)
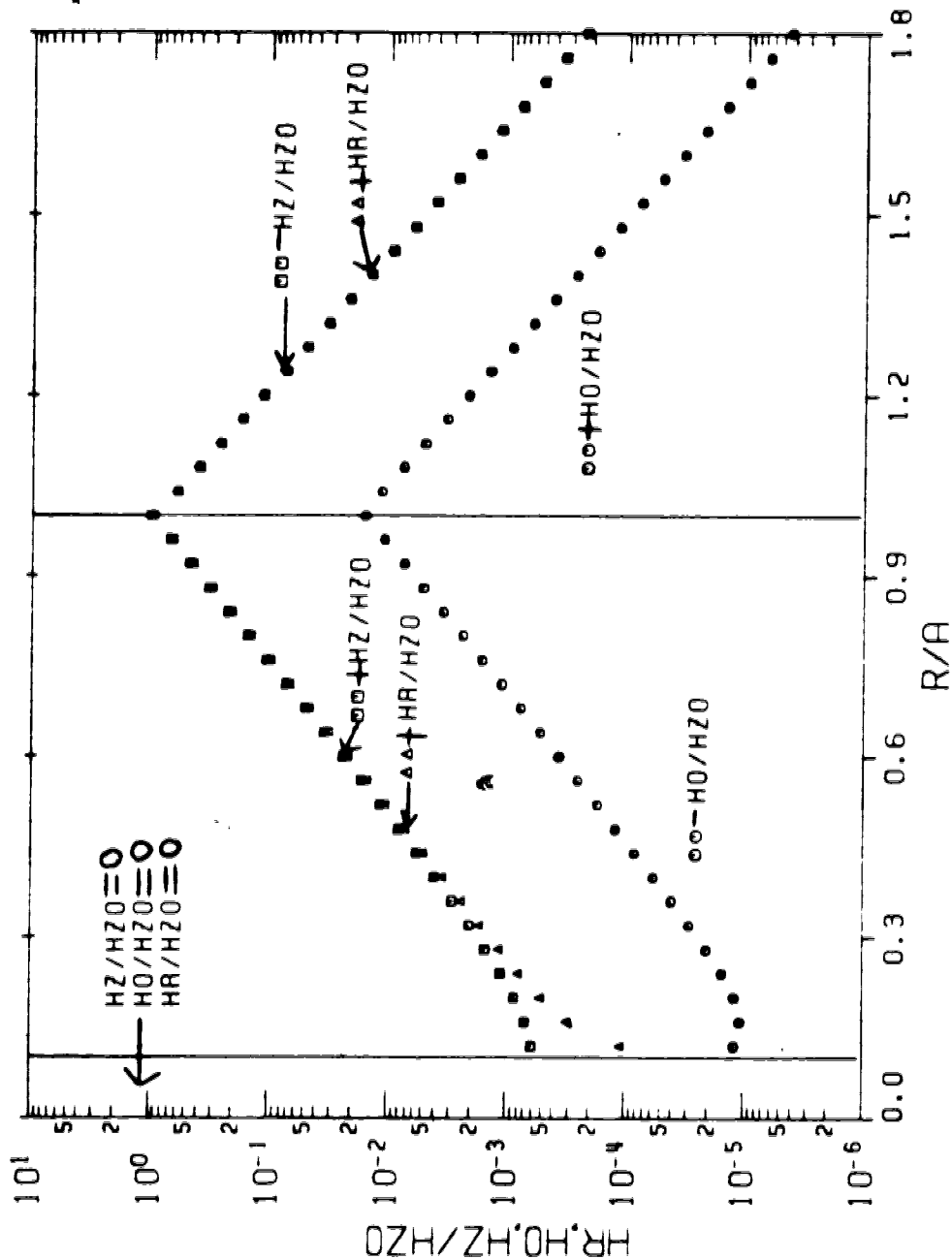
Figure C.5   Curves of the radial dependence associated with the normalized magnetic fields. The variables used are ka cotanψ = 10.0, b/a = 0.100, and ψ = 1.00°. They determine the wave numbers, $h^c a$=10.0 and $\beta^c a$=10.0, and the magnetic normalizing coefficient, H_{z0}^c = ∂_{11} 0.525 (A/m). (Note that HR/HZO = H_r^c/H_{z0}^c, HO/HZO = H_θ^c/H_{z0}^c, HZ/HZ0 = H_z^c/H_{z0}^c, and R/A = r/a.)

represent the surface of the perfectly conducting coaxial rod and the sheath helix surface. In region 2 and in region 3, the algebraic sign of each (real valued) normalized field component is indicated. The operating frequency, the rod geometry, and the sheath helix geometry, are specified by the variables $ka \cot an\psi = 10.0$, $b/a = 0.100$, and $\psi = 1.00°$. This is an example of the "high frequency" case. $h^C a = 10.0$ and $\beta^C a = 10.0$ are the calculated values of the wave numbers.

$$E_{z0}^{C} = j \,\}_{||}\, 188 \ (V/m) \quad \text{and} \quad H_{z0}^{C} = \,\}_{||}\, 0.525 \ (A/m)$$

are the calculated values of the normalizing coefficients.

Two additional graphs representing the "high frequency" case are Figures C.6 and C.7. $ka \cot an\psi = 10.0$, $b/a = 0.900$, and $\psi = 1.00°$ are the variables associated with these graphs. Figures C.6 and C.7 are actually a variation of Figures C.4 and C.5, respectively, using $b/a = 0.900$ instead of $b/a = 0.100$. The calculated wave numbers for the first mentioned two graphs are $h^C a = 10.0$ and $\beta^C a = 10.0$, and the calculated normalizing coefficients are

$$E_{z0}^{C} = j \,\}_{||}\, 163 \ (V/m) \quad \text{and} \quad H_{z0}^{C} = \,\}_{||}\, 0.589 \ (A/m).$$

The value of $h^C a$ associated with the four previously mentioned figures is in good agreement with the large argument approximations of the dispersion equation, equations C.27 and C.28, as one expects. These graphs show that all field components are rapidly attenuated at increasing radial distances away from the sheath helix surface. In fact, comparison of them with Figures B.3 and B.4, keeping in mind the values of all normalizing coefficients and that the same $ka \cot an\psi$ and ψ values are used, shows that near $r = a$, the "high frequency" fields for the configuration studied in this appendix are similar to the corresponding fields of the empty sheath helix configuration. This is expected behavior and it was discussed earlier in section C.3.
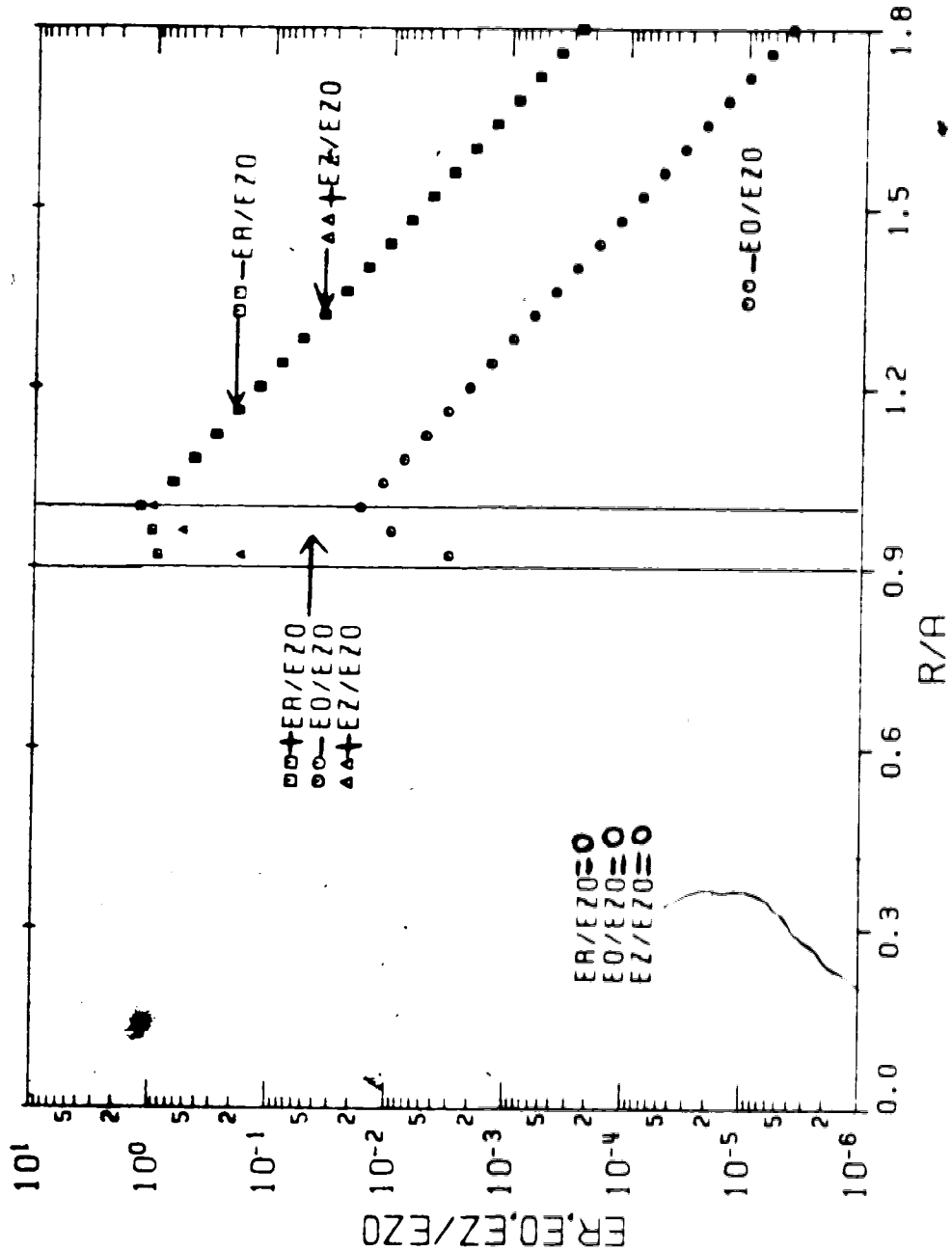
RADIAL DEPENDENCE OF ELECTRIC FIELDS

Figure C.6   Curves of the radial dependence associated
with the normalized electric fields. The variables used
are $ka \cot\psi = 10.0$, $b/a = 0.900$, and $\psi = 1.00°$. They
determine the wave numbers, $h^c a = 10.0$ and $\beta^c a = 10.0$,
and the electric normalizing coefficient, $E_{z0}^c = j$ 163
(V/m). (Note that $ER/EZO = E_r^c/E_{z0}^c$, $EO/EZO = E_\theta^c/E_{z0}^c$,
$EZ/EZO = E_z^c/E_{z0}^c$, and $R/A = r/a$.)
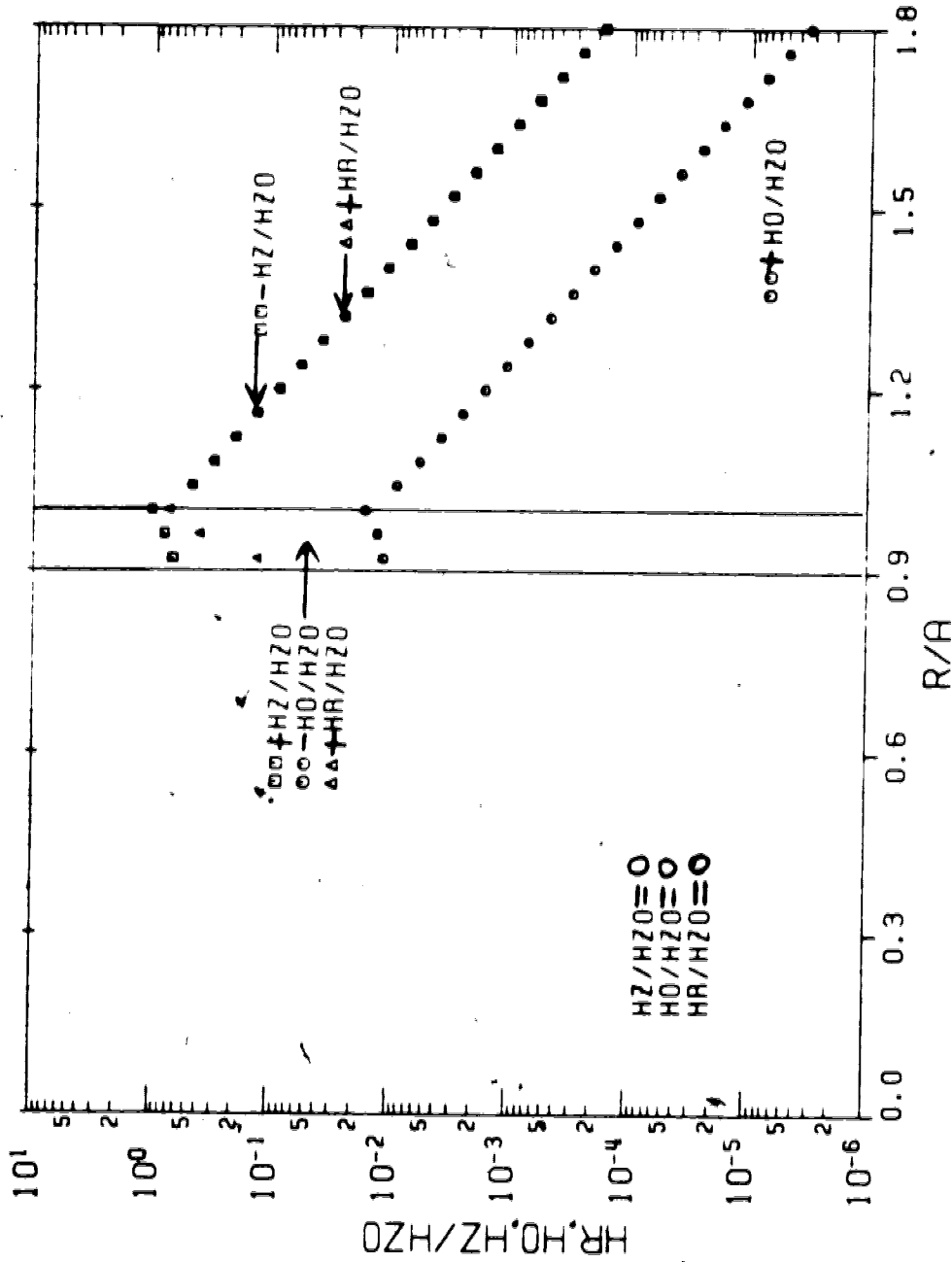
Figure C.7   Curves of the radial dependence associated with the normalized magnetic fields. The variables used are ka cotan$_\psi$ = 10.0, b/a = 0.900, and ψ = 1.00°. They determine the wave numbers, $h^c a$ = 10.0 and $\beta^c a$ = 10.0, and the magnetic normalizing coefficient, $H_{z0}^c = \mathcal{Y}_{II}$ 0.589 (A/m). (Note that HR/HZO = H_r^c/H_{z0}^c, HO/HZO = H_θ^c/H_{z0}^c, HZ/HZO = H_z^c/H_{z0}^c, and R/A = r/a.)

Figures C.8 and C.9 display the radial dependence of the normalized electric and magnetic fields, respectively, for the "mid frequency" case. $ka \cot an\psi = 1.00$, $b/a = 0.100$, and $\psi = 1.00°$ are the variables which are used. The wave numbers are calculated to be $h^C a = 0.830$ and $\beta^C a = 0.830$, while the computed normalizing coefficients are

$$E_{z0}^C = j \oint_{||} 137 \ (V/m) \quad \text{and} \quad H_{z0}^C = \oint_{||} 0.799 \ (A/m).$$

The final two examples of the electric and magnetic fields' radial dependence for the "mid frequency" case are Figures C.10 and C.11, respectively. The variables used are $ka \cot an\psi = 1.00$, $b/a = 0.900$, and $\psi = 1.00°$. Since the same values of $ka \cot an\psi$ and ψ are used, these graphs can be considered as a variation of Figures C.8 and C.9, using $b/a = 0.900$ instead of $b/a = 0.100$. For Figures C.10 and C.11, $h^C a = 0.985$ and $\beta^C a = 0.985$ are the computed values of the wave numbers.

$$E_{z0}^C = j \oint_{||} 33.5 \ (V/m) \quad \text{and} \quad H_{z0}^C = \oint_{||} 0.939 \ (A/m)$$

are the calculated values of the normalizing coefficients.

Figures C.12 and C.13 illustrate the radial dependence of the normalized electric and magnetic fields, respectively, for the "low frequency" case. $ka \cot an\psi = 5.00 \times 10^{-2}$, $b/a = 0.100$, and $\psi = 1.00°$ are used. These variables determine the wave numbers $h^C a = 2.95 \times 10^{-2}$ and $\beta^C a = 2.95 \times 10^{-2}$, and the normalizing coefficients

$$E_{z0}^C = j \oint_{||} 9.29 \ (V/m) \quad \text{and} \quad H_{z0}^C = \oint_{||} 0.998 \ (A/m).$$
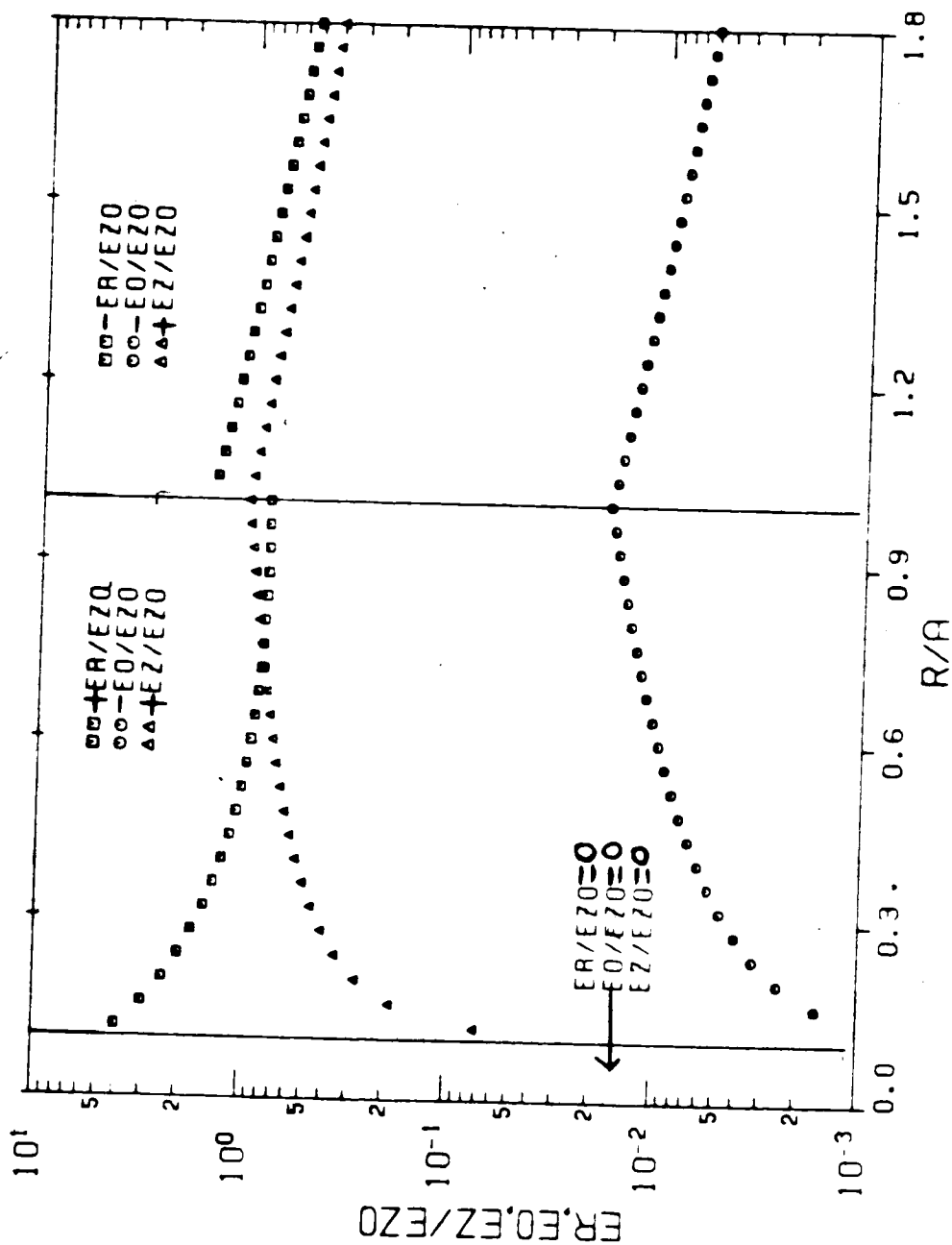
Figure C.8   Curves of the radial dependence associated
with the normalized electric fields. The variables used
are ka cotanψ =1.00, b/a = 0.100, and ψ = 1.00°. They
determine the wave numbers, $h^c a$ = 0.830 and $\beta^c a$ = 0.830,
and the electric normalizing coefficient, $E_{z0}{}^c$ = j9₁₁ 137
(V/m). (Note that ER/EZO = $E_r{}^c/E_{z0}{}^c$, EO/EZO = $E_\theta{}^c/E_{z0}{}^c$,
EZ/EZO = $E_z{}^c/E_{z0}{}^c$, and R/A = r/a.)
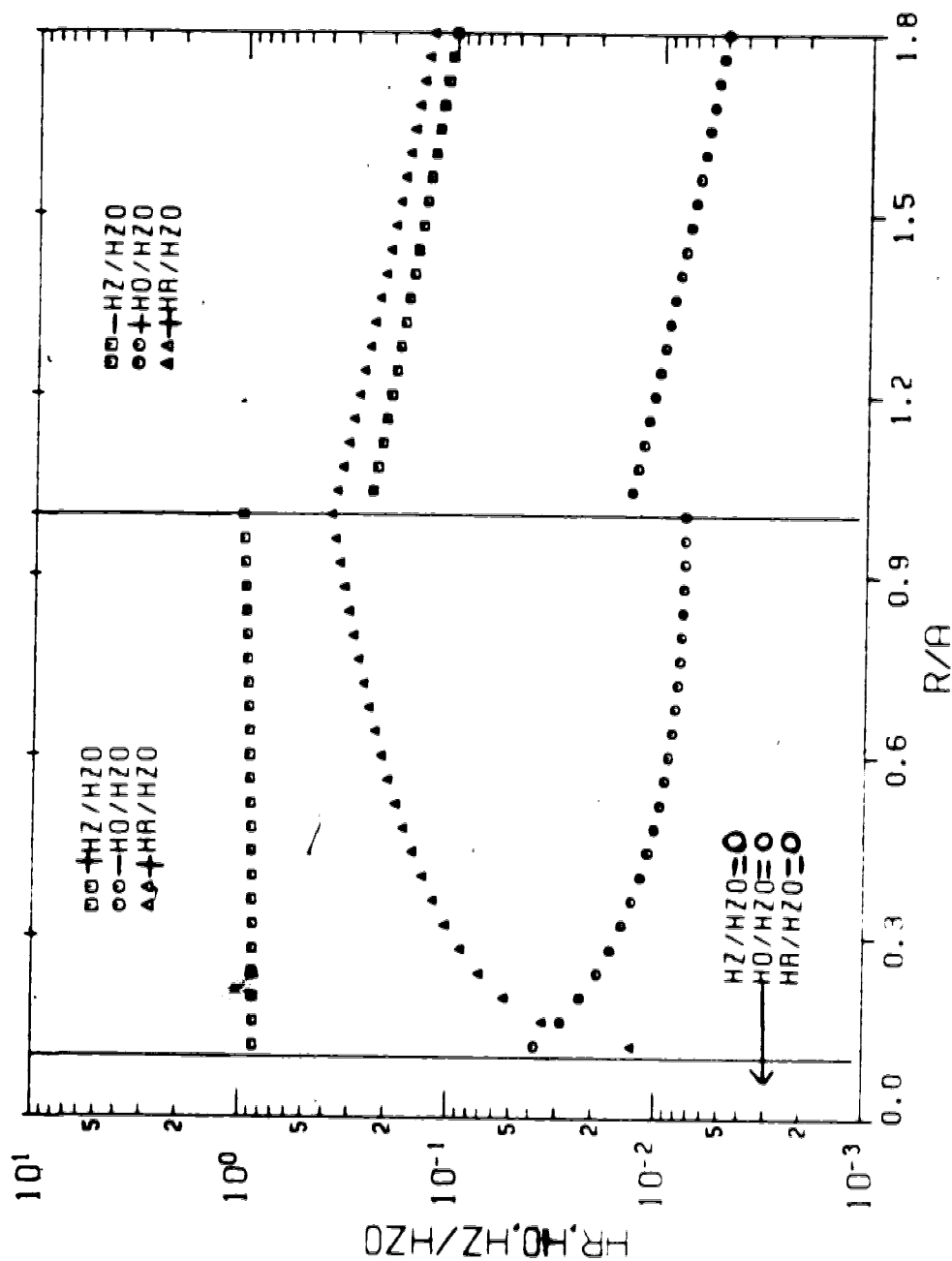
Figure C.9   Curves of the radial dependence associated with the normalized magnetic fields. The variables used are ka cotanψ = 1.00, b/a = 0.800, and ψ = 1.00°. They determine the wave numbers, $h^c a$ = 0.830 and $\beta^c a$ = 0.830, and the magnetic normalizing coefficient, H_{z0}^c = 0.799 (A/m). (Note that HR/HZO = H_r^c/H_{z0}^c, HO/HZO = H_θ^c/H_{z0}^c, HZ/HZO = H_z^c/H_{z0}^c, and R/A = r/a.)

Figure C.10   Curves of the radial dependence associated with the normalized electric fields. The variables used are ka cotanψ = 1.00, b/a = 0.900, and ψ = 1.00°. They determine the wave numbers, $h^c a$ = 0.985 and $\beta^c a$ = 0.985, and the electric normalizing coefficient, E_{z0}^c = J β_{11} 33.5 (V/m). (Note that ER/EZO = E_r^c/E_{z0}^c, EO/EZO = E_θ^c/E_{z0}^c, EZ/EZO = E_z^c/E_{z0}^c, and R/A = r/a.)

Figure C.11   Curves of the radial dependence associated with the normalized magnetic fields. The variables used are ka cotanψ = 1.00, b/a = 0.900, and ψ = 1.00°. They determine the wave numbers, $h^c a$ = 0.985 and $\beta^c a$ = 0.985, and the magnetic normalizing coefficient, H_{z0}^c = ⎰₌₁₁ 0.939 (A/m). (Note that HR/HZO = H_r^c/H_{z0}^c, HO/HZO = H_θ^c/H_{z0}^c, HZ/HZO = H_z^c/H_{z0}^c, and R/A = r/a.)
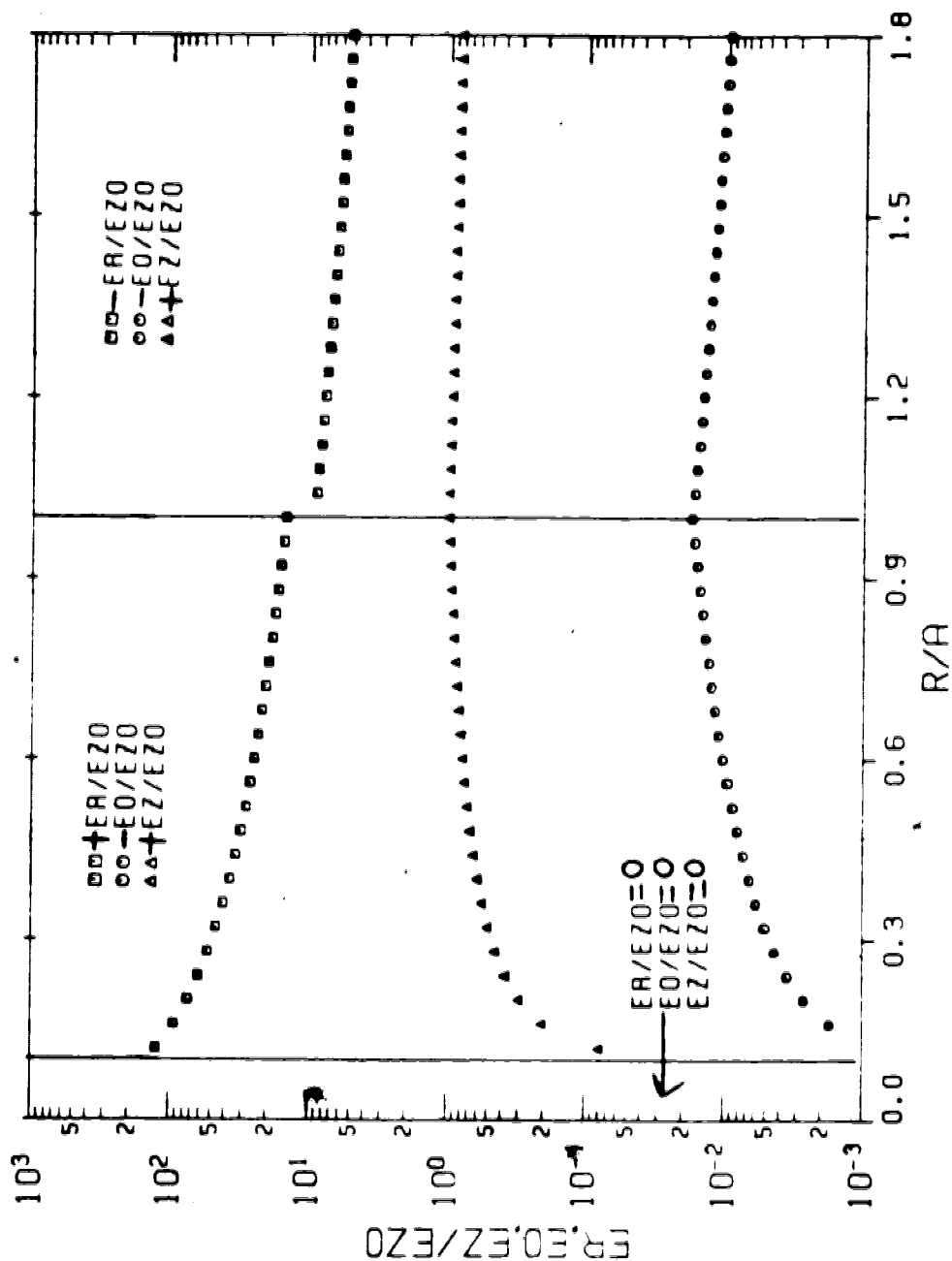
Figure C.12   Curves of the radial dependence associated with the normalized electric fields. The variables used are ka cotanψ=5.00x10⁻², b/a=0.100, and ψ=1.00°. They determine the wave numbers, $h^c a$ = 2.95x10⁻² and $_\beta{}^c a$ = 2.95x10⁻², and the electric normalizing coefficient, $E_{z0}{}^c$ = j $\bigg\}_{\parallel}$ 9.29 (V/m). (Note that ER/EZO = $E_r{}^c/E_{z0}{}^c$, EO/EZO = $E_\theta{}^c/E_{z0}{}^c$, EZ/EZO = $E_z{}^c/E_{z0}{}^c$, and R/A = r/a.)
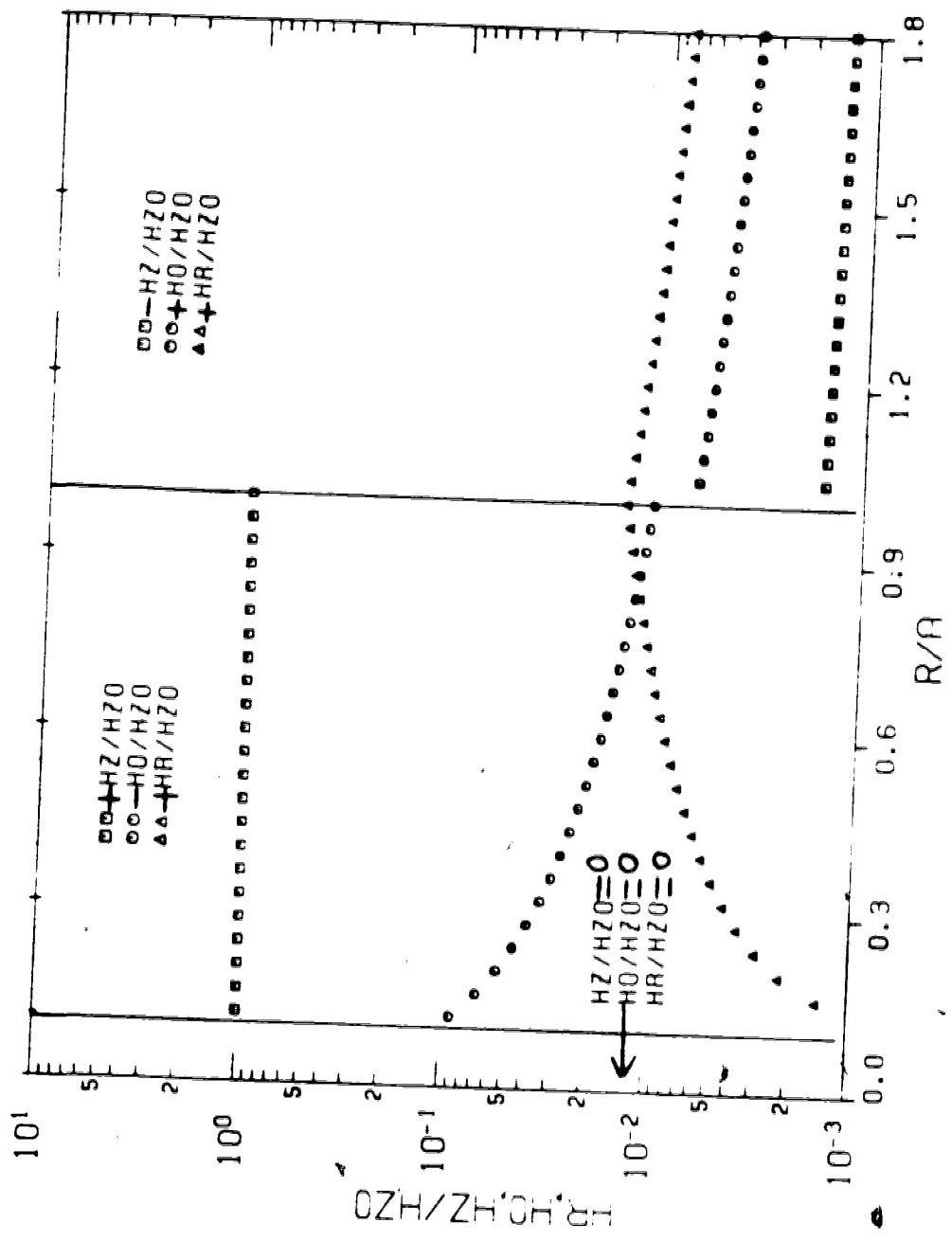
Figure C.13   Curves of the radial dependence associated with the normalized magnetic fields. The variables used are ka cotanψ=5.00x10^{-2}, b/a=0.100, and ψ=1.00°. They determine the wave numbers, h^{c}a = 2.95x10^{-2} and β^ca = 2.95x10^{-2}, and the magnetic normalizing coefficient, $H_{z0}{}^c$ = ∂_{11} 1.00 (A/m). (Note that HR/HZO = $H_r{}^c/H_{z0}{}^c$, HO/HZO = $H_\theta{}^c/H_{z0}{}^c$, HZ/HZO = $H_z{}^c/H_{z0}{}^c$, and R/A = r/a.)

Figures C.14 and C.15 are the final two examples of the electric and magnetic fields' radial dependence, respectively, associated with the "low frequency" case. The variables employed are $ka \cot an \psi = 5.00 \times 10^{-2}$, $b/a = 0.900$, and $\psi = 1.00°$. Since the same values of $ka \cot an \psi$ and ψ are used in Figures C.12 – C.15, Figures C.14 and C.15 can be considered as a special case of Figures C.12 and C.13, respectively, using $b/a = 0.900$ instead of $b/a = 0.100$. For Figures C.14 and C.15, $h^c a = 4.82 \times 10^{-2}$ and $\beta^c a = 4.82 \times 10^{-2}$ are the calculated values of the wave numbers, while

$$E_{z0}{}^c = j \bigg\}_{||} 1.79 \ (V/m) \quad and \quad H_{z0}{}^c = \bigg\}_{||} 0.999 \ (A/m)$$

are the calculated values of the normalizing coefficients.

As expected, the value of $h^c a$ associated with the previously mentioned four figures is approximately given by equations C.21 and C.24, the small argument representations of the dispersion equation. More specifically, there is less than one percent error involved in using equation C.21. There is two percent error involved with using equation C.24 when $b/a = 0.900$, and twenty one percent error when $b/a = 0.100$. For the case when $b/a = 0.100$, it is necessary that the value of $ka \cot an \psi$ is much less than 5.00×10^{-2}, in order that only a small percentage error occurs with using equation C.24 to approximate $h^c a$.

Comparing Figures C.14 and C.15 with Figures B.7 and B.8, respectively, keeping in mind the values of all normalizing coefficients and the fact, that the same values of $ka \cot an \psi$ and ψ are used, it is clear that the "low frequency" fields associated with the configuration studied in this appendix are usually different from the corresponding empty sheath helix fields. The single exception is that $H_{z2}{}^c \cong H_{z1}{}^a$, in the region $b \leq r \leq a$. This behavior is expected and it was discussed earlier in section C.3.

Figures C.14 and C.15 provide a good illustration of how the electric and magnetic fields behave at the sheath helix surface. However, this behavior was previously discussed in section B.3 and so it will not be mentioned further here. Figures C.12 and
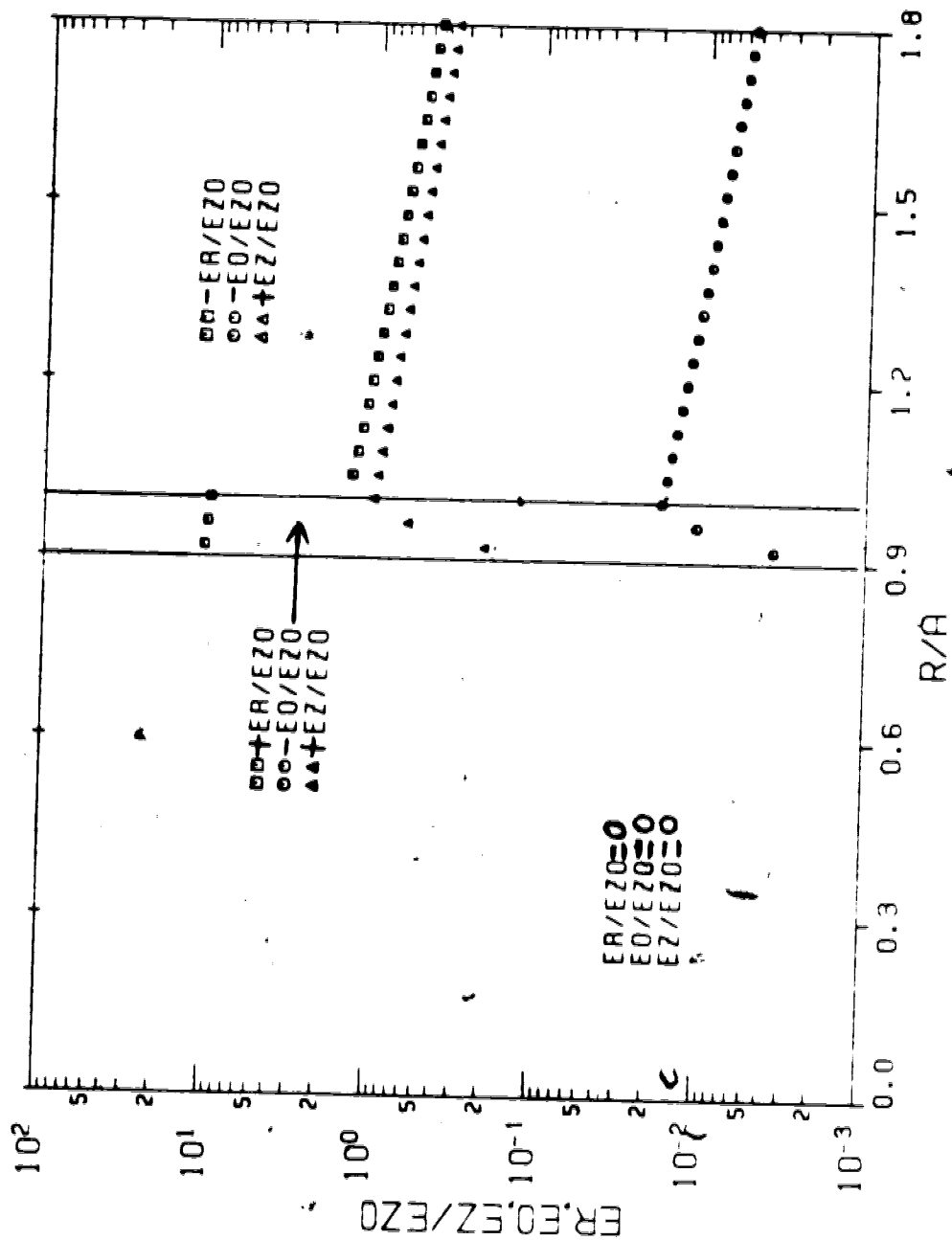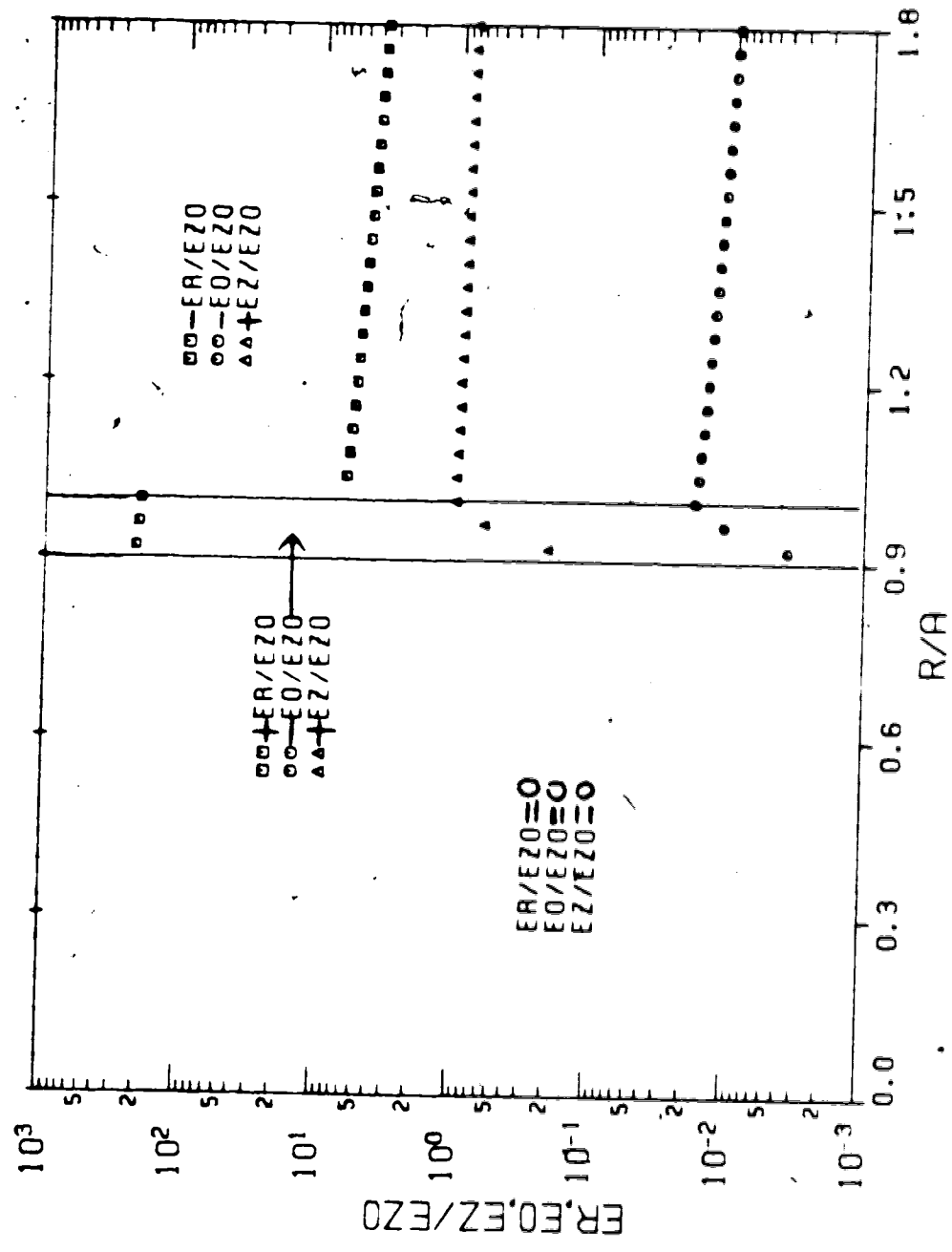
Figure C.14   Curves of the radial dependence associated with the normalized electric fields. The variables used are ka cotanψ=5.00x10^{-2}, b/a=0.900, and ψ=1.00°. They determine the wave numbers, h^{c}a = 4.82x10^{-2} and β^ca = 4.82x10^{-2}, and the electric normalizing coefficient, E_{z0}^c = j$\delta_{||}$ 1.79 (V/m). (Note that ER/EZO = E_r^c/E_{z0}^c, EO/EZO = E_θ^c/E_{z0}^c, EZ/EZO = E_z^c/E_{z0}^c, and R/A = r/a.)
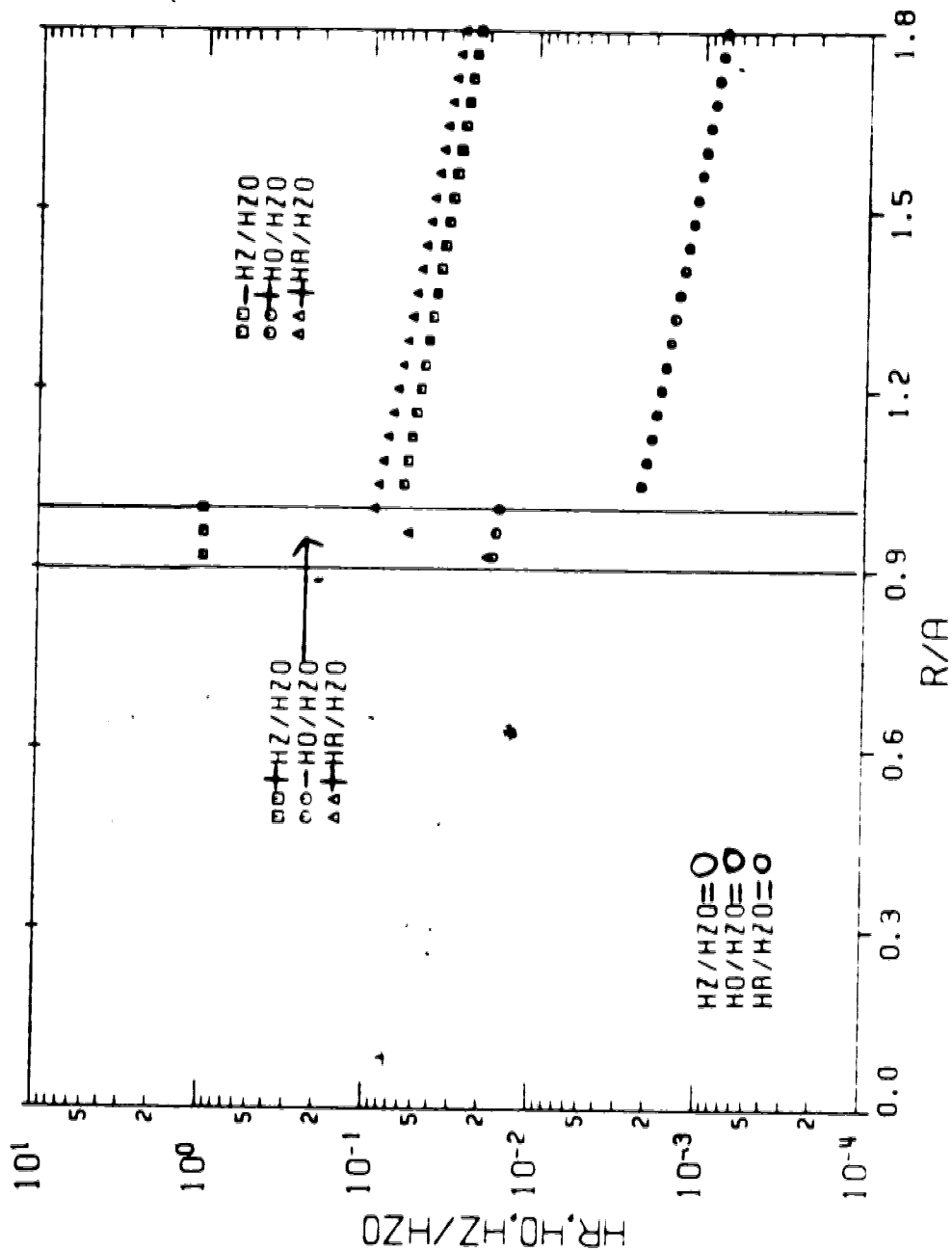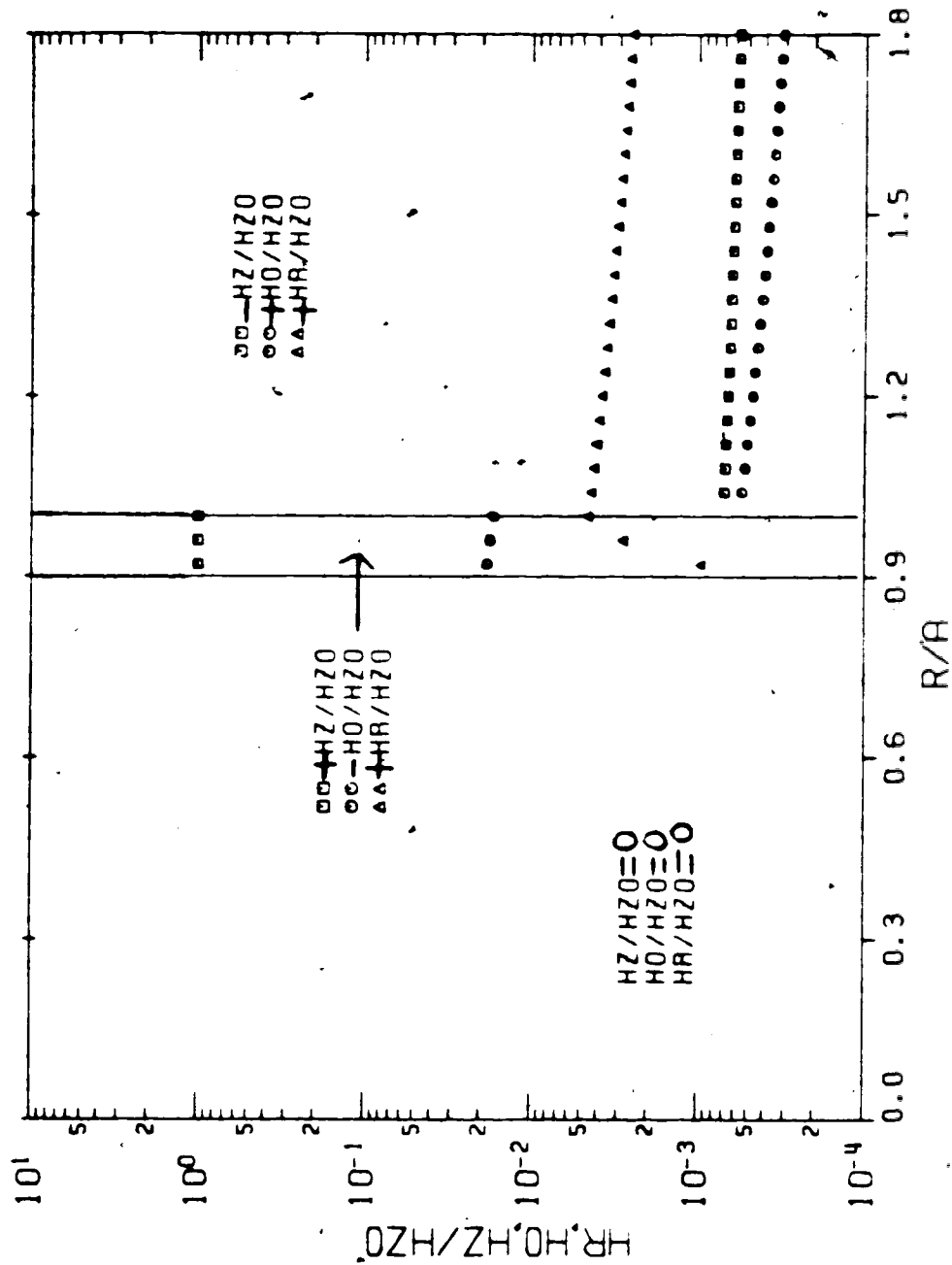
Figure C.15   Curves of the radial dependence associated with the normalized magnetic fields. The variables used are ka cotanψ=5.00x10^{-2}, b/a=0.900, and ψ=1.00°. They determine the wave numbers, h^{c}a = 4.82x10^{-2} and β^ca = 4.82x10^{-2}, and the magnetic normalizing coefficient, H$_{z0}^c$ =$\}$II 1.00 (A/m). (Note that HR/HZO = H$_r^c$/H$_{z0}^c$, HO/HZO = H$_\theta^c$/H$_{z0}^c$, HZ/HZO = H$_z^c$/H$_{z0}^c$, and R/A = r/a.)

C.13 illustrate the behavior of the fields at the surface of the perfectly conducting coaxial rod. Figure C.12 shows that $E_{\theta 2}{}^{c}/E_{z0}{}^{c}$ and $E_{z2}{}^{c}/E_{z0}{}^{c}$ become zero at $r = b$. This is simply a statement of the fact that the electric fields tangential to a perfectly conducting interface are zero. However, the radial electric field is nonzero at $r = b$. This is because free electric charge is present at the perfectly conducting rod surface.

Directing attention to the magnetic fields, Figure C.13 shows that $H_{r2}{}^{c}/H_{z0}{}^{c}$ is zero at $r = b$. The radial magnetic field cannot be discontinuous at the surface of the perfectly conducting rod because free magnetic charge does not exist at this surface. Finally, the figure makes it clear that the angular and axial mangetic fields are nonzero at $r = b$. This is because an electrical surface current is present on the perfectly conducting rod surface, and so the magnetic fields tangential to this surface are discontinuous.

D.   Appendix D.   Sheath Helix Surrounding an Ideal Dielectric Coaxial Rod

Inside the sheath helix is a coaxial rod made of an ideal dielectric material, which means that it has a zero conductivity. The rod radius, b, is restricted so that $0 <$ $b < a < \infty$ is always true, where, of course, a is the radius of the sheath helix. This configuration can be considered as a limiting case of the sheath helix surrounding a lossy coaxial rod, when the rod conductivity becomes very small.

Past research on configurations related to the sheath helix surrounding an ideal dielectric coaxial rod was conducted by Olving (21) and Swift-Hook (22). As Figure 1.3a shows, Olving considered the mirror-image of the geometry investigated in this appendix, when the dielectric material fills the entire exterior region and comes inside the sheath helix. The angularly independent field components in terms of a single undetermined constant were obtained, and so was the dispersion equation. An approximate equation was derived from the original dispersion equation by equating the two radial wave numbers with the axial wave number. The two region configuration, where the dielectric is only present at $a \leq r < \infty$, was studied as a limiting case of the previous results.

Swift-Hook actually studied a four region geometry. However, when the radius c approaches infinity, Figure 1.4b reduces to what Olving studied. It was assumed that the field components do not possess an angular dependence. The radial wave numbers in all four regions were equated to the axial wave number, in order to obtain the dispersion equation. From the limit as $b \to a^-$ and $c \to \infty$, the dispersion equation for the two region configuration was obtained. (See Figure 1.4b.) For this geometry, the quantity $ka \, \cot an\psi / h^d{}_a$ was plotted versus $ka \, \cot an\psi$, where $h^d{}_a$ is the (single) wave number which determines the radial and axial spatial dependences of the field components, and where $ka \, \cot an\psi = \omega \sqrt{\mu_0 \, \epsilon_0} \, a \, \cot an\psi$. These graphs were given using several different values of the dielectric material relative permittivity, ϵ_r, where $\epsilon_r = \epsilon / \epsilon_0$. The phenomenon of *negative dispersion* was discussed for the geometry where the dielectric material does not touch the sheath helix surface. (*Negative dispersion* refers to the behavior when the phase velocity associated with traveling waves increases as the frequency of operation increases.)

D.1 List of the Exact Field Components and the Exact Dispersion Equation

A brief derivation of the field components and the dispersion equation for the previously mentioned mirror-image geometry to that of concern in this appendix is given by Olving (2¹). However, a better understanding of how the equations listed in this section are derived can be obtained from Chapter 2 of the thesis. If the (real) relative permittivity ϵ_r is used in place of the quantity $\epsilon_r - j \; \sigma / \omega \epsilon_0$, the free mode field solution previously given in part 2.1.1 is exactly the same as that for the sheath helix surrounding an ideal dielectric coaxial rod. In order that the field expressions associated with the ideal dielectric coaxial rod configuration are all located in this appendix, justification is provided for repeating the appropriate form of the previously mentioned equations here. (Note that the term "exact" is used to distinguish this free mode field solution from the one which will later be discussed in section D.2.)

Summary of the Exact Field Components

Region 1 (0 ≤ r ≤ b)

$$E_{r1}^d = j \frac{\lambda_u}{b/a} \frac{120\pi}{ka \; \cot an\psi} \cos\psi \; h_2^{\;d}a \; \beta^d a \cdot \qquad (D.1)$$

$$\frac{K_0(h_2^{\;d}a) \; I_1(h_1^{\;d}r) \; \sin\beta^d z}{(h_1^{\;d}a \; I_0(h_1^{\;d}b) \; K_1(h_2^{\;d}b) + \epsilon_r \; h_2^{\;d}a \; I_1(h_1^{\;d}b) \; K_0(h_2^{\;d}b))} \; ,$$

$$E_{\theta 1}^d = -j \frac{\lambda_{11}}{b/a} 120\pi \; ka \; \cot an\psi \; \sin\psi \cdot \qquad (D.2)$$

$$\frac{K_1(h_2^{\;d}a) \; I_1(h_1^{\;d}r) \; \cos\beta^d z}{(h_1^{\;d}a \; I_0(h_1^{\;d}b) \; K_1(h_2^{\;d}b) + h_2^{\;d}a \; I_1(h_1^{\;d}b) \; K_0(h_2^{\;d}b))} \; ,$$

$$E_{z1}^d = j \frac{\lambda_{11}}{b/a} \frac{120\pi}{ka \; \cot an\psi} \cos\psi \; h_1^{\;d}a \; h_2^{\;d}a \cdot \qquad (D.3)$$

$$\frac{K_0(h_2^{\;d}a) \; I_0(h_1^{\;d}r) \; \cos\beta^d z}{(h_1^{\;d}a \; I_0(h_1^{\;d}b) \; K_1(h_2^{\;d}b) + \epsilon_r \; h_2^{\;d}a \; I_1(h_1^{\;d}b) \; K_0(h_2^{\;d}b))} \; ,$$

$$H_{r1}{}^d = \frac{\partial \| }{b/a} \cos\psi \ \beta^d a \cdot \tag{D.4}$$

$$\frac{K_1(h_2{}^d a) \ I_1(h_1{}^d r) \ \sin\beta^d z}{(h_1{}^d a / I_0(h_1{}^d b) \ K_1(h_2{}^d b) + h_2{}^d a \ I_1(h_1{}^d b) \ K_0(h_2{}^d b))} \cdot$$

$$H_{\theta 1}{}^d = - \frac{\partial \| }{b/a} \epsilon_r \ \sin\psi \ h_2{}^d a \cdot \tag{D.5}$$

$$\frac{K_0(h_2{}^d a) \ I_1(h_1{}^d r) \ \cos\beta^d z}{(h_1{}^d a \ I_0(h_1{}^d b) \ K_1(h_2{}^d b) + \epsilon_r \ h_2{}^d a \ I_1(h_1{}^d b) \ K_0(h_2{}^d b))} \cdot$$

$$\text{and} \quad H_{z1}{}^d = \frac{\partial \| }{b/a} \cos\psi \ h_1{}^d a \cdot \tag{D.6}$$

$$\frac{K_1(h_2{}^d a) \ I_0(h_1{}^d r) \ \cos\beta^d z}{(h_1{}^d a \ I_0(h_1{}^d b) \ K_1(h_2{}^d b) + h_2{}^d a \ I_1(h_1{}^d b) \ K_0(h_2{}^d b))}$$

Region 2 (b≤r≤a)

$$E_{r2}{}^d = j \partial \| \frac{120\pi}{ka \ \cot\psi} \cos\psi \ h_2{}^d a \ \beta^d a \cdot \tag{D.7}$$

$$K_0(h_2{}^d a) \ \sin\beta^d z \ [I_1(h_2{}^d r) - K_1(h_2{}^d r) \cdot$$

$$\frac{(h_1{}^d a \ I_0(h_1{}^d b) \ I_1(h_2{}^d b) - \epsilon_r \ h_2{}^d a \ I_0(h_2{}^d b) \ I_1(h_1{}^d b))}{(h_1{}^d a \ I_0(h_1{}^d b) \ K_1(h_2{}^d b) + \epsilon_r \ h_2{}^d a \ I_1(h_1{}^d b) \ K_0(h_2{}^d b))}] \cdot$$

$$E_{\theta 2}{}^d = -j \partial \| \ 120\pi \ ka \ \cot\psi \ \sin\psi \cdot \tag{D.8}$$

$$K_1(h_2{}^d a) \ \cos\beta^d z \ [I_1(h_2{}^d r) - K_1(h_2{}^d r) \cdot$$

$$\frac{(h_1{}^d a \ I_0(h_1{}^d b) \ I_1(h_2{}^d b) - h_2{}^d a \ I_0(h_2{}^d b) \ I_1(h_1{}^d b))}{(h_1{}^d a \ I_0(h_1{}^d b) \ K_1(h_2{}^d b) + h_2{}^d a \ I_1(h_1{}^d b) \ K_0(h_2{}^d b))}] \cdot$$

$$E_{z2}^d = j \, \partial_{11} \frac{120\pi}{ka \cot\psi} \cdot \cos\psi \, (h_2^d a)^2 \cdot \tag{D.9}$$

$$K_0(h_2^d a) \cos\beta^d z \, [I_0(h_2^d r) + K_0(h_2^d r) \cdot$$

$$\frac{(h_1^d a \, I_0(h_1^d b) \, I_1(h_2^d b) - \epsilon_r h_2^d a \, I_0(h_2^d b) \, I_1(h_1^d b))}{(h_1^d a \, I_0(h_1^d b) \, K_1(h_2^d b) + \epsilon_r h_2^d a \, I_1(h_1^d b) \, K_0(h_2^d b))}] \cdot$$

$$H_{r2}^d = \partial_{11} \cos\psi \, \beta^d a \cdot \tag{D.10}$$

$$K_1(h_2^d a) \sin\beta^d z \, [I_1(h_2^d r) - K_1(h_2^d r) \cdot$$

$$\frac{(h_1^d a \, I_0(h_1^d b) \, I_1(h_2^d b) - h_2^d a \, I_0(h_2^d b) \, I_1(h_1^d b))}{(h_1^d a \, I_0(h_1^d b) \, K_1(h_2^d b) + h_2^d a \, I_1(h_1^d b) \, K_0(h_2^d b))}] \cdot$$

$$H_{\theta 2}^d = -\partial_{11} \sin\psi \, h_2^d a \cdot \tag{D.11}$$

$$K_0(h_2^d a) \cos\beta^d z \, [I_1(h_2^d r) - K_1(h_2^d r) \cdot$$

$$\frac{(h_1^d a \, I_0(h_1^d b) \, I_1(h_2^d b) - \epsilon_r h_2^d a \, I_0(h_2^d b) \, I_1(h_1^d b))}{(h_1^d a \, I_0(h_1^d b) \, K_1(h_2^d b) + \epsilon_r h_2^d a \, I_1(h_1^d b) \, K_0(h_2^d b))}] \cdot$$

$$\text{and} \quad H_{z2}^d = \partial_{11} \cos\psi \, h_2^d a \cdot \tag{D.12}$$

$$K_1(h_2^d a) \cos\beta^d z \, [I_0(h_2^d r) + K_0(h_2^d r) \cdot$$

$$\frac{(h_1^d a \, I_0(h_1^d b) \, I_1(h_2^d b) - h_2^d a \, I_0(h_2^d b) \, I_1(h_1^d b))}{(h_1^d a \, I_0(h_1^d b) \, K_1(h_2^d b) + h_2^d a \, I_1(h_1^d b) \, K_0(h_2^d b))}] \cdot$$

Region 3 $(a \leqslant r < \infty)$

$$E_{r3}^d = -j \, \partial_{11} \, 120\pi \, ka \cot\psi \, \cos\psi \, \frac{\beta^d a}{h_2^d a} \cdot \tag{D.13}$$

$$\frac{K_1(h_2{}^d a)}{K_0(h_2{}^d a)} \, K_1(h_2{}^d r) \, \sin\beta^d z \, [I_1(h_2{}^d a) - K_1(h_2{}^d a) \cdot \tag{D.13}$$
<div align="right">(continued)</div>

$$\frac{(h_1{}^d a \, I_0(h_1{}^d b) \, I_1(h_2{}^d b) - h_2{}^d a \, I_0(h_2{}^d b) \, I_1(h_1{}^d b))}{(h_1{}^d a \, I_0(h_1{}^d b) \, K_1(h_2{}^d b) + h_2{}^d a \, I_1(h_1{}^d b) \, K_0(h_2{}^d b))}] \, ,$$

$$E_{\theta 3}{}^d = -j \, \mathcal{G}_{||} \, 120\pi \, ka \, \cot\psi \, \sin\psi \cdot \tag{D.14}$$

$$K_1(h_2{}^d r) \, \cos\beta^d z \, [I_1(h_2{}^d a) - K_1(h_2{}^d a) \cdot$$

$$\frac{(h_1{}^d a \, I_0(h_1{}^d b) \, I_1(h_2{}^d b) - h_2{}^d a \, I_0(h_2{}^d b) \, I_1(h_1{}^d b))}{(h_1{}^d a \, I_0(h_1{}^d b) \, K_1(h_2{}^d b) + h_2{}^d a \, I_1(h_1{}^d b) \, K_0(h_2{}^d b))}] \, ,$$

$$E_{z3}{}^d = j \, \mathcal{G}_{||} \, 120\pi \, ka \, \cot\psi \, \cos\psi \cdot \tag{D.15}$$

$$\frac{K_1(h_2{}^d a)}{K_0(h_2{}^d a)} \, K_0(h_2{}^d r) \, \cos\beta^d z \, [I_1(h_2{}^d a) - K_1(h_2{}^d a) \cdot$$

$$\frac{(h_1{}^d a \, I_0(h_1{}^d b) \, I_1(h_2{}^d b) - h_2{}^d a \, I_0(h_2{}^d b) \, I_1(h_1{}^d b))}{(h_1{}^d a \, I_0(h_1{}^d b) \, K_1(h_2{}^d b) + h_2{}^d a \, I_1(h_1{}^d b) \, K_0(h_2{}^d b))}] \, ,$$

$$H_{r3}{}^d = \mathcal{G}_{||} \, \cos\psi \, \beta^d a \cdot \tag{D.16}$$

$$K_1(h_2{}^d r) \, \sin\beta^d z \, [I_1(h_2{}^d a) - K_1(h_2{}^d a) \cdot$$

$$\frac{(h_1{}^d a \, I_0(h_1{}^d b) \, I_1(h_2{}^d b) - h_2{}^d a \, I_0(h_2{}^d b) \, I_1(h_1{}^d b))}{(h_1{}^d a \, I_0(h_1{}^d b) \, K_1(h_2{}^d b) + h_2{}^d a \, I_1(h_1{}^d b) \, K_0(h_2{}^d b))}] \, ,$$

$$H_{\theta 3}{}^d = \mathcal{G}_{||} \, (ka \, \cot\psi)^2 \, \sin\psi \, \frac{1}{h_2{}^d a} \cdot \tag{D.17}$$

$$\frac{K_1(h_2{}^d a)}{K_0(h_2{}^d a)} \, K_1(h_2{}^d r) \, \cos\beta^d z \, [I_1(h_2{}^d a) - K_1(h_2{}^d a) \cdot$$

$$\frac{(h_1{}^d a \, I_0(h_1{}^d b) \, I_1(h_2{}^d b) - h_2{}^d a \, I_0(h_2{}^d b) \, I_1(h_1{}^d b))}{(h_1{}^d a \, I_0(h_1{}^d b) \, K_1(h_2{}^d b) + h_2{}^d a \, I_1(h_1{}^d b) \, K_0(h_2{}^d b))}] \cdot$$

and $H_{z3}{}^d = -\int_{11} \cos\psi \, h_2{}^d a \cdot$ (D.18)

$$K_0(h_2{}^d r) \, \cos\beta^d z \, [I_1(h_2{}^d a) - K_1(h_2{}^d a) \cdot$$

$$\frac{(h_1{}^d a \, I_0(h_1{}^d b) \, I_1(h_2{}^d b) - h_2{}^d a \, I_0(h_2{}^d b) \, I_1(h_1{}^d b))}{(h_1{}^d a \, I_0(h_1{}^d b) \, K_1(h_2{}^d b) + h_2{}^d a \, I_1(h_1{}^d b) \, K_0(h_2{}^d b))}] \cdot$$

Summary of the Exact Dispersion Equation

$$\left(\frac{ka \, \cotan\psi}{h_2{}^d a}\right)^2 = \frac{K_0(h_2{}^d a)}{K_1(h_2{}^d a)} \cdot$$ (D.19)

$$\frac{(h_1{}^d a \, I_0(h_1{}^d b) \, K_1(h_2{}^d b) + h_2{}^d a \, I_1(h_1{}^d b) \, K_0(h_2{}^d b))}{(h_1{}^d a \, I_0(h_1{}^d b) \, K_1(h_2{}^d b) + \epsilon_r h_2{}^d a \, I_1(h_1{}^d b) \, K_0(h_2{}^d b))} \cdot$$

$$[I_0(h_2{}^d a) \cdot (h_1{}^d a \, I_0(h_1{}^d b) \, K_1(h_2{}^d b) +$$

$$\epsilon_r h_2{}^d a \, I_1(h_1{}^d b) \, K_0(h_2{}^d b)) + K_0(h_2{}^d a) \cdot$$

$$(h_1{}^d a \, I_0(h_1{}^d b) \, I_1(h_2{}^d b) - \epsilon_r h_2{}^d a \, I_0(h_2{}^d b) \, I_1(h_1{}^d b))] \cdot$$

$$1/[I_1(h_2{}^d a) \cdot (h_1{}^d a \, I_0(h_1{}^d b) \, K_1(h_2{}^d b) +$$

$$h_2{}^d a \, I_1(h_1{}^d b) \, K_0(h_2{}^d b)) - K_1(h_2{}^d a) \cdot$$

$$(h_1{}^d a \, I_0(h_1{}^d b) \, I_1(h_2{}^d b) - h_2{}^d a \, I_0(h_2{}^d b) \, I_1(h_1{}^d b))]$$

The exact separation constant equation provides a relation between the two radial wave numbers, $h_1{}^d a$ and $h_2{}^d a$, and the axial wave number, $\beta{}^d a$. It is

$$(\beta{}^d a)^2 = (h_1{}^d a)^2 + \epsilon_r (ka)^2 = (h_2{}^d a)^2 + (ka)^2. \qquad (D.20)$$

(Note that $(ka)^2 = \omega^2 \mu_0 \epsilon_0 a^2 = (2\pi f)^2 \mu_0 \epsilon_0 a^2$.) Equations D.19 and D.20, the exact dispersion equation and the exact separation constant equation, respectively, are used to solve for the wave numbers $h_1{}^d a$, $h_2{}^d a$, and $\beta{}^d a$.

Equations D.1 - D.20 comprise the exact free mode field solution for the sheath helix surrounding an ideal dielectric coaxial rod. Both radial wave numbers, the axial wave number, and all the electric and magnetic field components are given the superscript " d " so it is clear that they are associated with the sheath helix surrounding an ideal dielectric coaxial rod, and not with any of the other configurations which have been studied in the thesis.

As has been previously mentioned in part 2.1.2, the dispersion equation and the separation constant equation cannot determine the algebraic sign of the axial wave number. Furthermore, if $-\beta{}^d a$ is used in place of $\beta{}^d a$ in the field components, equations D.1 - D.18, no change results. Replacing $h_1{}^d a$ by $-h_1{}^d a$ in equations D.1 - D.20, making use of the Bessel function relations A.14 and A.15, it is discovered that no change has taken place. These properties of the radial and axial wave numbers mean that if $h_1{}^d$ and $\beta{}^d$ are assumed to be real and nonzero, restricting $h_1{}^d a > 0$ and $\beta{}^d a > 0$ results in no loss in generality.

A special case of the configuration studied in this appendix occurs when the rod radius increases so that the surface of the rod touches the sheath helix "windings". Since the conductivity of the rod is zero, the usual four boundary conditions given by equations 1.6 - 1.9 apply at the sheath helix surface. The proper dispersion equation for this geometry can be obtained by taking $\lim b \to a^-$ of equation D.19, assuming that the variables $ka \cot\psi$, ψ, ϵ_r, a are all held constant. This yields

$$\lim_{b \to a^-} \left(\frac{ka \cot\psi}{h_2{}^d a}\right)^2 = \left(\frac{ka \cot\psi}{h_2{}^{d*} a}\right)^2 \qquad (D.21)$$

$$= \frac{I_0(h_1^{d*}a) \, K_0(h_2^{d*}a)}{I_1(h_1^{d*}a) \, K_{1}(h_2^{d*}a)} \cdot \frac{h_1^{d*}a}{h_2^{d*}a} \cdot \qquad \qquad \text{(D.21)}$$

$$\frac{(h_1^{d*}a \, I_0(h_1^{d*}a) \, K_1(h_2^{d*}a) + h_2^{d*}a \, I_1(h_1^{d*}a) \, K_0(h_2^{d*}a))}{(h_1^{d*}a \, I_0(h_1^{d*}a) \, K_1(h_2^{d*}a) + \epsilon_r \, h_2^{d*}a \, I_1(h_1^{d*}a) \, K_0(h_2^{d*}a))} ,$$

where $\lim_{b \to a^-} h_n^{d}a = h_n^{d*}a$, for $n = 1, 2$.

Here the subscript " 1 " refers to the sheath helix interior region, $0 \leq r \leq a$, while " 2 " refers to the exterior region, $a < r < \infty$. Equation D.20 is the correct form of the separation constant equation for this two region geometry. If modifications are made to equation D.21 so that it refers to the dielectric material completely filling the exterior sheath helix region with air in the interior region, it is exactly the same as the two region dispersion equation given by Olving (21). Equation D.19 was modified in a similar manner and an attempt was made to transform it into the three region dispersion equation which Olving obtained. Unfortunately, Olving's equation was expressed in such an unusual manner that, despite performing a large amount of algebra, the author was not able to demonstrate that it is the same as the modified form of equation D.19.

In summary, by suitably changing equations D.19 and D.21 so that they are valid for the geometries studied by Olving, it was possible to show that the two region configuration (b = a) dispersion equation exactly agreed with his corresponding equation, but it is not clear if the three region configuration (b < a) dispersion equation agrees with his corresponding result. To reassure the reader, equations D.1 – D.20 do satisfy all the conditions associated with free mode fields, as was previously discussed in part 1.3.1, including the boundary conditions at the two interfaces, r = b, and r = a. Equations D.1 – D.20 are claimed to be the correct free mode field solution for the three region configuration sheath helix surrounding an ideal dielectric coaxial rod.

D.2 The Approximate Field Components and the Approximate Dispersion Equation

The exact field components and the exact dispersion equation, which are given by equations D.1 - D.19, are very lengthy and complicated. One intuitively expects that it will be very difficult to numerically or graphically solve equations D.19 and D.20, the exact dispersion equation and the exact separation constant equation, respectively, in order to determine the wave numbers $h_1{}^d a$, $h_2{}^d a$, and $\beta{}^d a$. What is sometimes done in multi-dielectric geometries is to make an approximation which provides simplification. This is done by equating the radial wave number associated with region 1 $(0 \leqslant r \leqslant b)$, $h_1{}^d a$, and the axial wave number, $\beta{}^d a$, with the radial wave number associated with region 2 $(b \leqslant r \leqslant a)$ and with region 3 $(a \leqslant r < \infty)$, $h_2{}^d a$. (For example, see (22).)

$$h_1{}^d a \cong h^d a, \text{ and } \beta{}^d a \cong h^d a, \text{ where } h_2{}^d a = h^d a. \qquad (D.22)$$

The subscript " 2 " will no longer be used on the wave number solution since it is not necessary to distinguish between two different radial wave numbers. (Note that if just the exact separation constant equation was considered, $h^d a \cong \pm h_1{}^d a \cong \pm \beta{}^d a$ would have to be used. However, no loss in generality results from only using the positive algebraic signs, as was previously mentioned in section D.1.) Obviously, equation D.20 shows in order that the approximations given in equations D.22 are justified, it is necessary that $h^d a \gg \sqrt{\epsilon_r} k a$. A more detailed discussion of the requirements necessary to justify using the approximation will be presented later in part D.2.1.

The following field components and dispersion equation are obtained from substituting equations D.22 into equations D.1 - D.19, and making use of the Bessel function property, relation A.25, to provide simplification. Strictly speaking, this should be called the *approximate free mode field solution for the sheath helix surrounding an ideal dielectric coaxial rod*. However, throughout the remainder of this appendix, only this approximate solution will be considered. Therefore, it is convenient to refer to these equations simply as the *field components* and the *dispersion equation*.

/

Summary of the Field Components

Region 1 $(0 \leq r \leq b)$

$$E_{r1}{}^d = j \frac{\partial_{11}}{b/a} \frac{120\pi}{ka \cot an\psi} \cos\phi \; h^d a \; \cdot \tag{D.23}$$

$$\frac{K_0(h^d a) \; I_1(h^d r) \; \sin(h^d z)}{(I_0(h^d b) \; K_1(h^d b) + \epsilon_r \; I_1(h^d b) \; K_0(h^d b))} \; ,$$

$$E_{\theta 1}{}^d = -j \, \partial_{11} \, 120\pi \, ka \cot an\psi \, \sin\psi \; \cdot \tag{D.24}$$

$$K_1(h^d a) \; I_1(h^d r) \; \cos(h^d z) \; ,$$

$$E_{z1}{}^d = j \frac{\partial_{11}}{b/a} \frac{120\pi}{ka \cot an\psi} \cos\psi \; h^d a \; \cdot \tag{D.25}$$

$$\frac{K_0(h^d a) \; I_0(h^d r) \; \cos(h^d z)}{(I_0(h^d b) \; K_1(h^d b) + \epsilon_r \; I_1(h^d b) \; K_0(h^d b))} \; ,$$

$$H_{r1}{}^d = \partial_{11} \cos\phi \; h^d a \; K_1(h^d a) \; I_1(h^d r) \; \sin(h^d z) \; , \tag{D.26}$$

$$H_{\theta 1}{}^d = - \frac{\partial_{11}}{b/a} \; \cdot \tag{D.27}$$

$$\frac{\epsilon_r \; \sin\psi \; K_0(h^d a) \; I_1(h^d r) \; \cos(h^d z)}{(I_0(h^d b) \; K_1(h^d b) + \epsilon_r \; I_1(h^d b) \; K_0(h^d b))} \; , \text{ and}$$

$$H_{z1}{}^d = \partial_{11} \cos\phi \; h^d a \; K_1(h^d a) \; I_0(h^d r) \; \cos(h^d z) \; . \tag{D.28}$$

Region 2 (b≤r≤a)

$$E_{r2}^d = j \oint_{II} \frac{120\pi}{ka \cot an\psi} \cos\psi \, (h^d a)^2 \, K_0(h^d a) \, \sin(h^d z) \cdot \quad (D.29)$$

$$\left[I_1(h^d r) + \frac{(\epsilon_r - 1) \, I_0(h^d b) \, I_1(h^d b) \, K_1(h^d r)}{(I_0(h^d b) \, K_1(h^d b) + \epsilon_r \, I_1(h^d b) \, K_0(h^d b))} \right] .$$

$$E_{\theta 2}^d = -j \oint_{II} 120\pi \, ka \, \cot an\psi \, \sin\psi \cdot \quad (D.30)$$

$$K_1(h^d a) \, I_1(h^d r) \, \cos(h^d z) .$$

$$E_{z2}^d = j \oint_{II} \frac{120\pi}{ka \cot an\psi} \cos\psi \, (h^d a)^2 \, K_0(h^d a) \, \cos(h^d z) \cdot \quad (D.31)$$

$$\left[I_0(h^d r) - \frac{(\epsilon_r - 1) \, I_0(h^d b) \, I_1(h^d b) \, K_0(h^d r)}{(I_0(h^d b) \, K_1(h^d b) + \epsilon_r \, I_1(h^d b) \, K_0(h^d b))} \right] ,$$

$$H_{r2}^d = \oint_{II} \cos\psi \, h^d a \, K_1(h^d a) \, I_1(h^d r) \, \sin(h^d z) , \quad (D.32)$$

$$H_{\theta 2}^d = -\oint_{II} \sin\psi \, h^d a \, K_0(h^d a) \, \cos(h^d z) \cdot \quad (D.33)$$

$$\left[I_1(h^d r) + \frac{(\epsilon_r - 1) \, I_0(h^d b) \, I_1(h^d b) \, K_1(h^d r)}{(I_0(h^d b) \, K_1(h^d b) + \epsilon_r \, I_1(h^d b) \, K_0(h^d b))} \right] , \text{ and}$$

$$H_{z2}^d = \oint_{II} \cos\psi \, h^d a \, K_1(h^d a) \, I_0(h^d r) \, \cos(h^d z) . \quad (D.34)$$

Region 3 (a≤r<∞)

$$E_{r3}^d = -j \oint_{II} 120\pi \, ka \, \cot an\psi \, \cos\psi \cdot \quad (D.35)$$

$$I_1(h^d a) \, \frac{K_1(h^d a)}{K_0(h^d a)} \, K_1(h^d r) \, \sin(h^d z) ,$$

$$E_{\theta 3}{}^d = -j \, \mathcal{J}_{\parallel} \, 120\pi \, ka \, \cot\!an\psi \, \sin\psi \cdot \tag{D.36}$$

$$I_1(h^d a) \, K_1(h^d r) \, \cos(h^d z) \ ,$$

$$E_{z3}{}^d = j \, \mathcal{J}_{\parallel} \, 120\pi \, ka \, \cot\!an\psi \, \cos\psi \cdot \tag{D.37}$$

$$I_1(h^d a) \, \frac{K_1(h^d a)}{K_0(h^d a)} \, K_0(h^d r) \, \cos(h^d z) \ ,$$

$$H_{r3}{}^d = \mathcal{J}_{\parallel} \, \cos\psi \, h^d a \cdot \tag{D.38}$$

$$I_1(h^d a) \, K_1(h^d r) \, \sin(h^d z) \ ,$$

$$H_{\theta 3}{}^d = \mathcal{J}_{\parallel} \, (ka \, \cot\!an\psi)^2 \, \sin\psi \, \frac{1}{h^d a} \cdot \tag{D.39}$$

$$I_1(h^d a) \, \frac{K_1(h^d a)}{K_0(h^d a)} \, K_1(h^d r) \, \cos(h^d z) \ , \text{ and}$$

$$H_{z3}{}^d = - \mathcal{J}_{\parallel} \, \cos\psi \, h^d a \cdot \tag{D.40}$$

$$I_1(h^d a) \, K_0(h^d r) \, \cos(h^d z) \ .$$

Summary of the Dispersion Equation

$$\left(\frac{ka \, \cot\!an\psi}{h^d a}\right)^2 = \frac{I_0(h^d a) \, K_0(h^d a)}{I_1(h^d a) \, K_1(h^d a)} \ . \tag{D.41}$$

$$\left[1 - \frac{I_0(h^d b)}{I_0(h^d a)} \, \frac{(\epsilon_r - 1) \, I_1(h^d b) \, K_0(h^d a)}{(I_0(h^d b) \, K_1(h^d b) + \epsilon_r \, I_1(h^d b) \, K_0(h^d b))}\right]$$

Equations D.23 - D.41 comprise the free mode field solution of the sheath helix surrounding an ideal dielectric coaxial rod. The operating frequency, the ideal dielectric rod geometry, the dielectric rod material permittivity, and the sheath helix geometry are specified by the variables $ka \cot an\psi$, b/a, ϵ_r, and ψ.

$0 < ka \cot an\psi < \infty$, $0 < b/a < 1$, $\epsilon_r > 1$, and $0 < \psi < 90.0°$ are the values of these variables which are acceptable for a free mode field solution. Throughout the remainder of this appendix, it will usually be assumed that the sheath helix is sufficiently wound so that the pitch angle is restricted to $0 < \psi \le 10.0°$.

Equation D.41, the dispersion equation, is solved in order to obtain $_h d_a$, the (single) wave number which determines the radial and axial spatial dependences of the field components. (As was previously discussed in section B.1 in connection with the empty sheath helix, it is convenient to consider the wave number solution as $_h d_a$ rather than as $_h d$. The quantity $_h d_b$ appearing in equations D.23 - D.41 is considered as $_h d_a \cdot b/a$. Furthermore, the radial and axial spatial dependences of the field components are considered to be normalized with respect to the sheath helix radius so that $_h d_r$ and $_h d_z$ become $_h d_a \cdot r/a$ and $_h d_a \cdot z/a$, respectively.) Modifying equation D.41 so that it is valid when dielectric material fills the region $b \le r < \infty$ and air fills the region $0 \le r \le b$, it is discovered to be identical with what Swift-Hook (22) gave for the previously mentioned geometry.

The free mode field solution for the two region configuration (which is characterized by the dielectric rod filling the interior sheath helix region, $0 \le r \le a$, with air filling the exterior region, $a \le r < \infty$) can be obtained by taking the limit as b approaches a of equations D.23 - D.28, and D.35 - D.41. In particular, the dispersion equation for this geometry is obtained from equation D.41, and it is discovered to be

$$\lim_{b \to a^-} \left(\frac{ka \cot an\psi}{_h d_a}\right)^2 = \left(\frac{ka \cot an\psi}{_h d^*_a}\right)^2 \qquad (D.42)$$

$$. = \frac{I_0(h^{d*}a) \; K_0(h^{d*}a)}{I_1(h^{d*}a) \; K_1(h^{d*}a)} \cdot \frac{1}{h^{d*}a} \cdot$$

<div style="text-align:right">(D.42)
(continued)</div>

$$\frac{1}{(I_0(h^{d*}a) \; K_1(h^{d*}a) + \epsilon_r \; I_1(h^{d*}a) \; K_0(h^{d*}a))} \cdot$$

where $\lim_{b \to a^-} h^d a = h^{d*}a$.

The Bessel function property, relation A.25, was used to simplify this limit. (Note that equation D.42 can be directly obtained from equation D.21 by using $h_1^{d*}a = h_2^{d*}a = h^{d*}a$ and relation A.25.) Modifying equation D.42 so that it describes the geometry with dielectric in the region $a \le r < \infty$ and air in the region $0 \le r \le a$, it agrees with the dispersion equation for the corresponding geometry given by Swift-Hook (22).

D.2.1 Discussion of the Dispersion Equation and Graphs of the Wave Number Solution

Equation D.41, the dispersion equation for the three region geometry (b < a), is not altered if ψ is replaced by $-\psi$, or if ω is replaced by $-\omega$. Therefore, the same comments made at the beginning of section B.2 are valid here.

Two special limiting cases of the three region geometry are of interest. First, the ideal dielectric rod radius is made to approach zero. Assuming that the variables $ka \cot\psi$, ϵ_r, and a are held constant and calculating $\lim b \to 0^+$ of equation D.41, making use of the small argument Bessel function representations, equations A.26 - A.29, it is discovered that equation B.13 is obtained. In the limit as the rod radius decreases until it approaches zero, the dispersion equation becomes that of the empty sheath helix, as one expects. Therefore, it is true that

$$\lim_{b \to 0^+} h^d{}_a = h^a{}_a, \qquad (D.43)$$

where $h^a{}_a$ is the radial wave number associated with the empty sheath helix. It is now assumed that the variables $ka \ cotan\psi$, ϵ_r, ψ, a, and β_{II} are held constant. Taking this same limit of equations D.29 - D.40, which represent the field components in region 2 ($b \leq r \leq a$) and in region 3 ($a \leq r < \infty$), it is discovered that the corresponding fields for the empty sheath helix, equations B.1 - B.12, are obtained. In the course of calculating this limit, equations A.26 - A.29 and equation D.43 were used. Furthermore, the approximation associated with the empty sheath helix of equating the axial wave number with the radial wave number was used. (This was previously discussed in section B.2.) Finally, equation B.13 was used to simplify some of the limiting expressions of the field components. In summary, *in the limit as the rod radius approaches zero, the free mode field solution associated with the sheath helix surrounding an ideal dielectric coaxial rod is correctly transformed into that associated with the empty sheath helix.*

The second special limiting case occurs when the relative permittivity of the ideal dielectric coaxial rod decreases until it approaches unity. Assuming that the variables $ka \ cotan\psi$ and b/a are held constant, and evaluating $\lim_{\epsilon_r \to 1^+}$ of equation D.41, it is readily apparent that equation B.13 is obtained. As one expects, in the limit as the rod relative permittivity decreases until it approaches unity, the dispersion equation for the empty sheath helix results. This means that

$$\lim_{\epsilon_r \to 1^+} h^d{}_a = h^a{}_a. \qquad (D.44)$$

In addition, if this limit is taken of the field components in regions 1 and 2, equations D.23 - D.34, it is discovered that the corresponding fields in the two regions are the same, and that these equal the corresponding interior sheath helix region field components associated with the empty sheath helix, equations B.1 - B.6. Evaluating this

same limit of the region 3 fields, equations D.35 - D.40, the corresponding exterior sheath helix region field components associated with the empty sheath helix, equations B.7 - B.12, are obtained. In the course of carrying out these calculations, equations B.13 and D.44, and the Bessel function property, relation A.25, were all used for simplification. Furthermore, for the empty sheath helix field components, the approximation of equating the axial wave number with the radial wave number was made. In summary, *in the limit as the relative permittivity characterizing the dielectric rod approaches unity, the free mode field solution associated with the sheath helix surrounding an ideal dielectric coaxial rod is correctly transformed into that associated with the empty sheath helix.*

Attention is now directed to the values of $h^d{}_a$ which may possibly satisfy the dispersion equation. Since the angular frequency only appears in equation D.41 in the form $(ka \cot an\psi)^2 = \omega^2 \mu_0 \epsilon_0 a^2 \cot an^2\psi$, it is obvious that reversing the algebraic sign of ω will not produce any change in the dispersion equation. As was previously explained at the beginning of section B.2, the fact that $(h^d{}_{(-\omega)} a)^2 =$

$(h^d{}_{(+\omega)} a)^2$ means that $h^d{}_a$ is not allowed to be generally complex with nonzero real and imaginary parts. This information was easily obtained. However, a lengthy investigation was performed to see if negative real or purely imaginary values of $h^d{}_a$ are allowed. The details of this investigation will only briefly be mentioned here. It was necessary to make use of equations A.13 - A.21, A.24, A.26 - A.29, and A.32 - A.43 to see if the two sides of equation D.41 could possibly be equated. Since the small and large argument approximations of the Bessel functions are used, which are not valid for all possible arguments, this analysis cannot claim to be rigorous. The conclusion reached was that it is not believed to be possible to satisfy the dispersion equation using these values of $h^d{}_a$.

Finally, $h^d{}_a$ was assumed to be real positive. This possibility will now be discussed in detail. Examine the part of equation D.41 within the square brackets. Making use of the fact that $I_0(x)$ is a strictly increasing positive function, while $K_0(x)$ is a strictly decreasing positive function, where $0 < x < \infty$, means that

$$0 \ < \ \frac{I_0(h^d a \cdot b/a)}{I_0(h^d a)} \ < \ 1, \ \text{and}$$

<div align="right">(D.45)</div>

$$(\epsilon_r - 1) \ I_1(h^d b) \ K_0(h^d a) \ < \ \epsilon_r \ I_1(h^d b) \ K_0(h^d a \cdot b/a) \ . \ .$$

(See Figure A.1. This is a graph of I_0, I_1, K_0, and K_1 for real positive arguments.) Relations A.49 and A.50, and Figure A.1 make it clear that $I_1(x)$ and $K_1(x)$ are also positive functions. It follows that

$$0 \ < \ [1 - \frac{I_0(h^d b)}{I_0(h^d a)} \ .$$

<div align="right">(D.46)</div>

$$\frac{(\epsilon_r - 1) \ I_1(h^d b) \ K_0(h^d a)}{(I_0(h^d b) \ K_1(h^d b) + \epsilon_r \ I_1(h^d b) \ K_0(h^d b))}] \ < \ 1.$$

which means that the right hand side of equation D.41 is real positive. Obviously, the left hand side is also real positive. Therefore, a solution for $h^d a$ will exist because it is possible to equate the two sides of the dispersion equation.

In summary, it is believed that only $0 < h^d a < \infty$ may satisfy the dispersion equation. *Only real positive values of the wave number $h^d a$ are acceptable for a free mode field solution.*

Equation D.41 makes apparent the functional dependence of the wave number solution on variables describing the operating frequency, the geometry of the sheath helix, the geometry of the ideal dielectric coaxial rod, and the type of dielectric material.

$$h^d a = f(ka \cot\psi, \ b/a, \ \epsilon_r) \qquad (D.47)$$

It is highly desirable to obtain approximations of the dispersion equation, in order that the wave number solution $h^d{}_a$ is more easily calculated, and so that the behavior of $h^d{}_a$ for different operating frequencies, ideal dielectric rod geometries, rod permittivies, and sheath helix geometries, is more easily understood. These approximations are valid when the Bessel function arguments which appear in the dispersion equation are either small or large. First, the small argument approximations will be examined. Substituting equations A.26 – A.29, the small argument Bessel function representations, into the right hand side of equation D.41, yields

$$\left(\frac{ka\ \cotan\psi}{h^d{}_a}\right)^2 \cong -2\ \log(0.891\ h^d a) \cdot$$

$$\left[1 + \frac{(\epsilon_r - 1)\ (h^d b)^2\ \log(0.891\ h^d a)}{(2 - \epsilon_r\ (h^d b)^2\ \log(0.891\ h^d b))}\right] \cdot$$

$$(D.48)$$

Equation D.48 is the accurate small argument approximation of the dispersion equation. Reassuringly, calculating the limit of equation D.48 as $b \to 0^+$, assuming that the variables $ka\ \cotan\psi$, ϵ_r, and a are held constant, correctly results in equation B.21, which is the small argument approximation of the empty sheath helix dispersion equation. The result given in the previous sentence is also obtained if the limit as the dielectric rod relative permittivity approaches unity is calculated. Note that the correct form for the two region configuration (b = a) is found simply by calculating $\lim b \to a^-$ of equation D.48.

If the value of $h^d{}_a$ becomes sufficiently small for the specified values of b/a and ϵ_r, so that $(h^d b)^2 \cdot (\epsilon_r - 1) << 1$ occurs, equation D.48 approximately reduces to

$$\left(\frac{ka\ \cotan\psi}{h^d{}_a}\right)^2 \cong -2\ \log(0.891\ h^d a). \qquad (D.49)$$

Equation D.49 is the crude small argument approximation of the dispersion equation. It is valid for both the three region $(b < a)$ and the two region $(b = a)$ configurations. Note that this is the same equation as the small argument representation of the empty sheath helix dispersion equation, equation B.211 This has the important meaning that when $h^d{}_a$ becomes sufficiently small, to a good approximation it will have the same value as the radial wave number of the empty sheath helix, for the corresponding value of $ka\ cotan\psi$. Here the presence of the ideal dielectric coaxial rod has an insignificant effect on the wave number solution.

A data table was prepared which compared the right hand sides of the approximations D.48 and D.49, to the right hand side of the actual dispersion equation, equation D.41. A wide range of values of the variables given by equation D.47 was used. The important results of these calculations will be mentioned but the data table itself will not be presented. Equation D.49 tends to be least accurate when $b/a \simeq 1$ and $\epsilon_r >> 1$. Both equations D.48 and D.49 became less accurate as $ka\ cotan\psi$ became large. Equation D.48 was accurate to less than 10% error for $1 < \epsilon_r \lesssim 1.0 \times 10^3$, $0 < b/a < 1$, and values of $ka\ cotan\psi$ as large as 0.10, while the error associated with equation D.49 was sometimes much greater than this. Even for values of ϵ_r as large as 1.0×10^3 and values of b/a as large as 1, equation D.49 had a maximum error of about 1% if $ka\ cotan\psi$ was restricted so that $ka\ cotan\psi < 1.0 \times 10^{-2}$.

In short, equation D.48 has a higher accuracy than equation D.49, for values of $ka\ cotan\psi$ near 0.10, when ϵ_r and b/a are both large. However, even for the worst case error, which occurs for $b/a \simeq 1$ and $\epsilon_r >> 1$, equation D.49 will have a maximum error of only a few percent if $ka\ cotan\psi$ is restricted so that $ka\ cotan\psi < 1.0 \times 10^{-2}$ or $ka\ cotan\psi < 1.0 \times 10^{-3}$. Under these circumstances, the wave number solution, $h^d{}_a$, is, to a good approximation, for the same value of $ka\ cotan\psi$, equal to $h^a{}_a$, the radial wave number of the empty sheath helix.

Attention is now directed to the approximations of the dispersion equation which are valid when the Bessel function arguments are large. Substituting equations A.36 – A.39, the large argument Bessel function representations, into the right hand side of

equation D.41, using three terms of the Bessel function representations in the quantity next to the " = " but just the first term for the quantity within the square brackets, yields

$$\left(\frac{ka\ cotan\psi}{h^d a}\right)^2 \cong \left(1 + \frac{0.50}{(h^d a)^2}\right) \cdot$$

$$\left[1 - e^{-2\ h^d a\ (1-b/a)} \cdot \frac{(\epsilon_r - 1)}{(\epsilon_r + 1)}\right]. \tag{D.50}$$

Equation D.50 is the accurate large argument approximation of the dispersion equation.

Since $0 < (\epsilon_r - 1)/(\epsilon_r + 1) < 1$ for $\epsilon_r > 1$, it is clear that when $h^d a$ is sufficiently large for the specified value of b/a so that $h^d a \cdot (1-b/a) > 1$,

$$1 - e^{-2\ h^d a\ (1-b/a)} \cdot \frac{(\epsilon_r - 1)}{(\epsilon_r + 1)} \cong 1. \tag{D.51}$$

will be true. Of course, the preceding inequality at least means that $h^d a > 1$, and so it is true that

$$1 + \frac{0.50}{(h^d a)^2} \cong 1. \tag{D.52}$$

Equations D.51 and D.52 mean that equation D.50 can be approximated as

$$\frac{ka\ cotan\psi}{h^d a} \cong 1. \tag{D.53}$$

Equation D.53 is the crude large argument approximation of the dispersion equation, which is valid for the three region (b < a) *configuration.* It is the same as equation B.20, the large argument representation of the dispersion equation associated with the empty sheath helix! Therefore, for the three region sheath helix surrounding an ideal dielectric coaxial rod configuration, when h^d_a is sufficiently large its value is, to a good approximation, the same as the radial wave number solution associated with the empty sheath helix, and is in fact approximately the same as the variable $ka \cot\psi$. Once again, the presence of the ideal dielectric coaxial rod has no significant effect on the wave number solution.

Taking the limit of equation D.50 as the rod radius increases so that the rod surface touches the sheath helix surface, assuming that $h^d_a > 1$, yields

$$\lim_{b\to a^-} \left(\frac{ka\cot\psi}{h^d_a} \right) = \frac{ka\cot\psi}{h^{d*}_a} \simeq \sqrt{\frac{2}{(\epsilon_r+1)}} \ , \tag{D.54}$$

$$\text{where} \quad \lim_{b\to a^-} h^d_a = h^{d*}_a .$$

Equation D.54 is the two region (b = a) *configuration large argument approximation of the dispersion equation.* It was given by Olving (21) as the large argument approximation of the dispersion equation for the configuration with dielectric material filling the region $a \le r < \infty$ and air filling the region $0 \le r \le a$. It was also mentioned by Swift-Hook (22) whenever the dielectric tube came in contact with the sheath helix surface. This occurs for a = b in Figure 1.4a and for a = c in Figure 1.4b. Equations D.53 and D.54 make it clear that there is a major difference in the solution of the wave number when its value becomes large, for the configuration where the ideal dielectric rod completely fills the region $0 \le r \le a$, compared to the configuration where a gap exists between the rod surface and the sheath helix surface.

Numerical calculations were performed to compare the right hand sides of equations D.50 and D.53, with that of the the actual dispersion equation, equation D.41.

A wide range of different values of the variables $ka \cot an\psi$, b/a, and ϵ_r were used. It was found that equation D.53 tended to have the greatest error for large values of b/a, when $\epsilon_r >> 1$. (Of course, $b/a < 1$ is always assumed.) Both equations D.50 and D.53 became more accurate as the value of $ka \cot an\psi$ increased. If the restriction $ka \cot an\psi \cdot (1-b/a) > 1$ was imposed, it was discovered that equation D.53 had a maximum error of about 10% for large values of b/a. Just restricting $ka \cot an\psi > 1$, for a wide range of b/a and ϵ_r values, gave about 10% maximum error for equation D.50.

It was previously shown in part D.2.1 that as a limiting case, when the value of b/a becomes sufficiently small, the wave number solution becomes that of the empty sheath helix, regardless of the value of ϵ_r. This reasoning gives an unexpected bonus to the validity of equation D.53. Numerical calculations showed that when $b/a << 1$, the equation resulted in about 20% maximum error for values of $ka \cot an\psi$ as small as unity, and the error rapidly decreased as $ka \cot an\psi$ became larger. This is similar to the error which was previously found in section B.2, using equation B.20 to approximate the radial wave number for the empty sheath helix. When $b/a << 1$ occurs and $ka \cot an\psi \simeq 1$, equation D.53 predicts that $h^d_a \cdot b/a << 1$ will occur. The large argument representations of the Bessel functions of argument $h^d_a \cdot b/a$, which were used in equation D.41 to obtain equation D.53, are not expected to be valid. (See Table A.2.) In fact, equation D.53 can be used when $b/a << 1$, as a result of the knowledge that the value of h^d_a is similar to the radial wave number of the empty sheath helix.

In summary, restricting $ka \cot an\psi \cdot (1-b/a) > 1$ means that the error involved in equation D.53 is about 20% maximum for $b/a \rightarrow 1^-$, and about 10% maximum for $b/a << 1$ for values of $ka \cot an\psi$ as small as 1. Equation D.50 is accurate to a maximum error of about 10% for values of $ka \cot an\psi$ as small as 1. For both equations, increasing $ka \cot an\psi$ tends to rapidly reduce the error. Since in equation D.53 the wave number solution is explicitly expressed in terms of the operating frequency and the sheath helix geometry, equation D.53 is is much more convenient than equation D.50.

A sufficient understanding has now been obtained to show when the approximations

$$h_1{}^d{}_a \cong {}_\beta{}^d{}_a \cong , h_2{}^d{}_a = h^d{}_a \qquad (D.55)$$

made on *the exact field solution*, which is given in section D.1, in order to obtain the solution given in section D.2, are justified. From the separation constant equation, equation D.20, and from the discussion previously given in section B.2, it is known that the approximations are valid to within about 10% error if

$$h^d{}_a > 2 \sqrt{\epsilon_r} \, ka. \qquad (D.56)$$

For the three region configuration, when $h^d{}_a$ is sufficiently large so that equation D.53 is valid, inequality D.56 becomes

$$2 \sqrt{\epsilon_r} \, \tan\psi < 1. \qquad (D.57)$$

If the sheath helix is tightly wound, this inequality will be satisified, unless the value of ϵ_r is very large.

Considering the two region configuration, when $h^d{}_a$ is sufficiently large so that equation D.54 is valid, inequality D.56 will be satisfied if

$$2 \sqrt{2} \, \tan\psi < 1 \qquad (D.58)$$

is true. For a sheath helix sufficiently tightly wound so that $0 < \psi \leqslant 10.0°$, this inequality will certainly be satisfied.

On the other hand, assuming that h^d_a is sufficiently small so that equation D.49 is valid, inequality D.56 becomes

$$\tan\psi \sqrt{-8\ \epsilon_r\ \log(0.891\ h^d_a)}\ <\ 1. \qquad (D.59)$$

Inequality D.59 is valid for both the two and three region configurations. It is a more severe restriction than that specified by the two preceding inequalities. In order that inequality D.59 is satisfied, it is necessary that ψ must be quite small, if the value of ϵ_r is large, or if the value of h^d_a is small. For example, if it is desired to have h^d_a as small as 1.0×10^{-3} (which, from equation D.49, corresponds to $ka\ \cot\psi = 3.8 \times 10^{-3}$), and if $\epsilon_r = 1.0 \times 10^3$, the largest acceptable value of the pitch angle is $\psi = 0.25°$. However, if the relative permittivity is smaller, it is permissible to use larger values of ψ and much smaller values of h^d_a. As an example, if $\epsilon_r = 10.0$ and $\psi = 1.0°$, inequality D.59 is still satisfied for values of h^d_a as small as 1.6×10^{-18} (corresponding to $ka\ \cot\psi = 1.5 \times 10^{-17}$). Note that for a fixed value of ϵ_r and for a fixed value of ψ, regardless of how small this pitch angle is, in the limit as $ka\ \cot\psi$ approaches zero, equation D.49 shows that h^d_a must also approach zero, which means that inequality D.59 cannot be satisfied.

In summary, a discussion has been given of the approximations listed in equation D.55, which were applied to the *exact* free mode field solution, equations D.1 – D.20, in order to obtain the solution given by equations D.23 – D.41. For large values of $ka\ \cot\psi$, the approximations are always valid for the two region configuration if the pitch angle satisfies $0 < \psi \leq 10.0°$, and they are valid for the three region configuration if ψ is small and ϵ_r is not extremely large. When $ka\ \cot\psi$ is small, the approximations are valid for both the two and three region configurations, if ψ is small and ϵ_r is not extremely large. However, in the limit as $ka\ \cot\psi$ approaches zero, the approximations are certainly not correct.

Numerical solutions to the wave number h^d_a have been calculated from equation D.41. As was true of the empty sheath helix, the variable $ka \cot an\psi$ only appears on the left hand side of the dispersion equation. The same procedure for calculating the quantity $ka \cot an\psi/h^d_a$ versus $ka \cot an\psi$ as was previously discussed in section B.2 is used. except that it is now necessary to specify the variables b/a and ϵ_r, in addition to specifying the variable $ka \cot an\psi$.

The following eight figures were obtained from direct calculation of equation D.41, making use of the IMSL (43) software program routines to evaluate the Bessel functions appearing in the dispersion equation. Figure D.1 is a linear plot of $ka \cot an\psi/h^d_a$ versus $ka \cot an\psi$. The variables used are $b/a = 0, 0.500,$ $0.900;$ $\epsilon_r = 5.00,$ and 10.0. Each curve is associated with one particular value of the pair $(b/a, \epsilon_r)$. (Note that the curve for $b/a = 0$ is based on the dispersion equation for the empty sheath helix, equation B.13.) Several different lines of constant h^d_a are displayed. and so is the asymptote $ka \cot an\psi/h^d_a = 1.0$.

Figure D.1 exhibits a behavior which never occurred for the empty sheath helix, or for the sheath helix surrounding a perfectly conducting coaxial rod. For some curves, a minimum value of $ka \cot an\psi/h^d_a$ less than unity occurs in the mid-region of $ka \cot an\psi$ values. Since

$$\frac{ka \cot an\psi}{h^d_a} \approx \frac{ka \cot an\psi}{|\beta^d|a} = \frac{\omega}{|\beta^d|}\sqrt{\mu_0 \epsilon_0} \cot an\psi$$

$$\qquad\qquad (D.60)$$

$$= \frac{v_p}{c} \cot an\psi,$$

graphing the quantity $ka \cot an\psi/h^d_a$ versus $ka \cot an\psi$ is proportional to graphing the phase velocity associated with traveling waves having $e^{-j\beta^d z}$ axial dependence, normalized with respect to the velocity of light in air, as a function of frequency. Whenever the phase velocity increases with increasing frequency, which
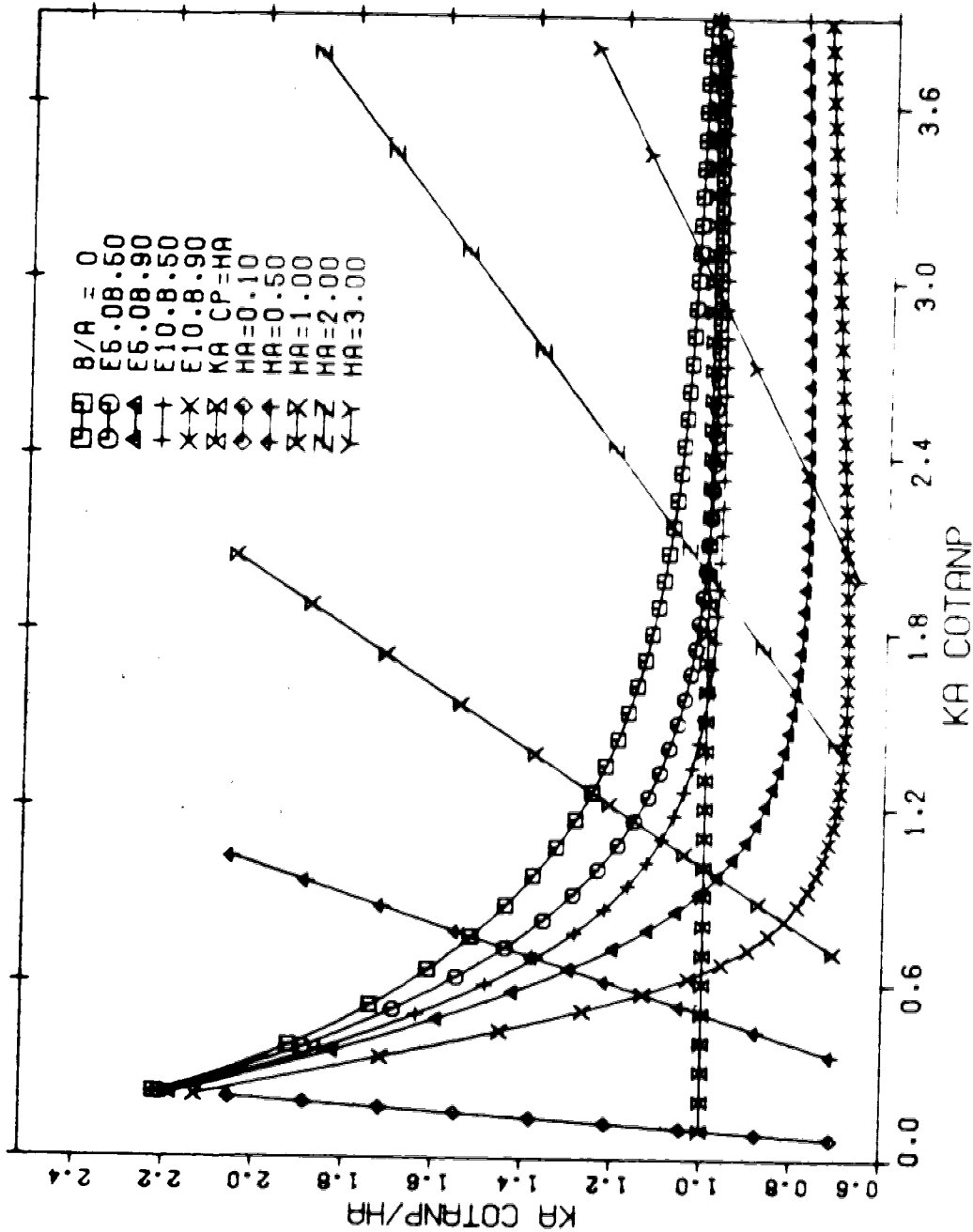
PLOT OF KA COTANP/HA VS. KA COTANP

Figure D.1   Graph of ka cotanψ/h^{d}a versus ka cotanψ based on equation D.41. Curves for b/a = 0, 0.500, 0.900; and ϵ_r = 5.00, 10.0 are given. The curve for b/a = 0 is based on the dispersion equation for the empty sheath helix, equation B.13. Several lines of constant h^{d}a are shown, and so is the asymptote ka cotanψ/h^{d}a = 1.00.

(Note that HA = h^{d}a and KA COTANP = ka cotanψ. E5.0B.90 means that the curve represents ϵ_r = 5.00 and b/a = 0.900.)

means that the curves have a positive slope, *negative dispersion* is said to occur.

Equation D.50 can be used to understand the phenomenon of negative dispersion. The first bracketed quantity on the right hand side is always greater than unity, while the second bracketed quantity is always less than unity. If it happens that this second quantity is sufficiently small, it will be true that $ka\ cotan\psi/h^d_a << 1$ occurs. However, as h^d_a becomes large, which occurs when $ka\ cotan\psi$ is large, the exponential term rapidly becomes small and so the first bracketed quantity dominates the behavior. Therefore, it is always true for sufficiently large values of $ka\ cotan\psi$, that the quantity $ka\ cotan\psi/h^d_a$ approaches unity from above. This means that the region of negative dispersion has a finite extent. Swift-Hook (22) has previously discussed the phenomenon of negative dispersion for the configurations shown in Figures 1.4.

It is apparent from Figure D.1 that negative dispersion is most pronounced when the values of b/a and ε_r are both large. If at least one of b/a, ε_r is sufficiently small, this behavior does not occur.

Figure D.2 is a semilogarithmic graph of $ka\ cotan\psi/h^d_a$ versus $ka\ cotan\psi$, for the fixed value $b/a = 0.100$, and for many different relative permittivities. $\varepsilon_r = 1.00,\ 5.00,\ 10.0,\ 1.00\times10^2$, and 1.00×10^3 are used. (The curve based on $\varepsilon_r = 1.00$ is the same as the solution associated with the empty sheath helix, based on equation B.13.) Many different decade ranges of $ka\ cotan\psi$ values are shown. Note that for the small value of b/a which is used, negative dispersion does not occur. In addition, it is clear that the value of the relative permittivity has little effect on h^d_a. As an example, the graphs for $\varepsilon_r = 1.00,\ 5.00$, and 10.0 are on top of each other. For large or small values of $ka\ cotan\psi$, all the curves are in good agreement with the empty sheath helix dispersion curve. As a final remark, in order that the approximations given in equations D.55 are justified for all values of h^d_a given in the figure, it is necessary that inequalities D.57 and D.59 are satisfied. This is the most difficult to accomplish when $\varepsilon_r = 1.00\times10^3$ and $ka\ cotan\psi = 1.00\times10^{-3}$. It can be demonstrated that the largest acceptable value of the pitch angle is $\psi = 0.25°$, in order that the wave number solution h^d_a given in Figure D.2 is always justified as an approximation of the exact solution given in section D.1.
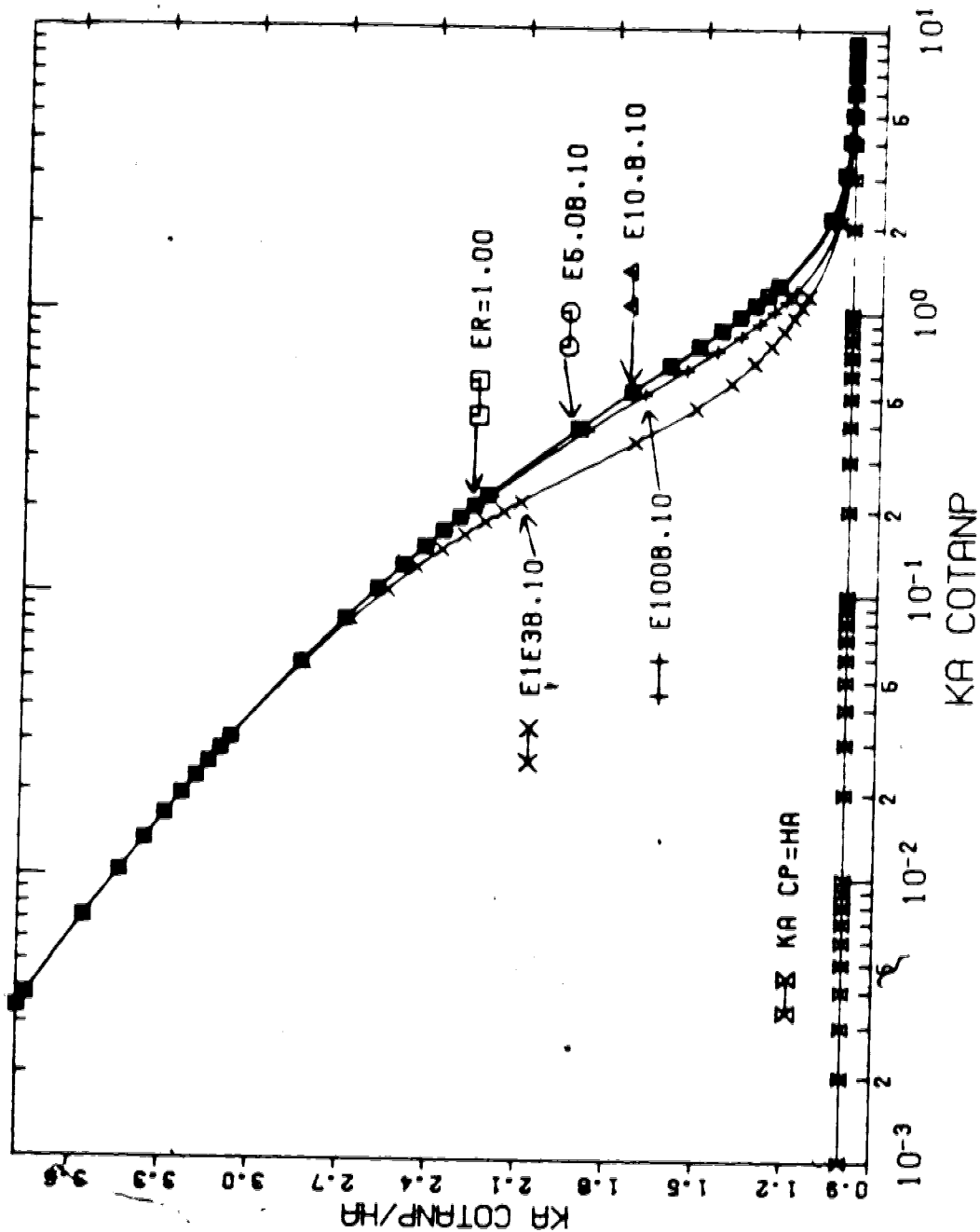
PLOT OF KA COTANP/HA VS. KA COTANP

Figure D.2   Graph of ka cotanψ/h^{d}a versus ka cotanψ
based on equation D.41. Curves for b/a = 0.100 and
ϵ_r = 1.00, 5.00, 10.0, 1.00x10^2, and 1.00x10^3 are shown.
The asymptote ka cotanψ/h^{d}a = 1.00 is given. (The curve
for ϵ_r = 1.00 is the same as the solution associated with
the empty sheath helix, based on equation B.13. Note that
HA = h^{d}a and KA COTANP = ka cotanψ. E1E3B.10 means that
the curve represents ϵ_r = 1.00x10^3 and b/a = 0.100.)

Figure D.3 is a semilogarithmic graph with the same abscissa and ordinate as the previous figure. b/a = 0.900 with the same values of the relative permittivity given in Figure D.2 are used. For the large value of b/a which is employed, the negative dispersion is very apparent, except for the curve based on ϵ_r = 1.00. It is more pronounced for large values of ϵ_r. However, for sufficiently large or small values of ka cotanψ, all the curves are in good agreement with the dispersion curve for the empty sheath helix.

Figure D.4 is a semilogarithmic graph of ka cotanψ/h^d_a versus ka cotanψ, based on the two region configuration. b/a = 1.00 with the same values of ϵ_r used in Figures D.2 and D.3 are employed. The asymptotes based on equation D.54, which are valid for large values of ka cotanψ, are plotted. Note that negative dispersion does not occur for the two region configuration. Clearly, for large values of ka cotanψ, the behavior of the curves is very different from that of the configuration where a gap exists between the dielectric rod surface and the surface of the sheath helix. However, for small values of ka cotanψ, the wave number solution h^d_a is similar for both the two and three region geometries. In fact, it is similar to the radial wave number solution associated with the empty sheath helix.

A rather small value of the relative permittivity, ϵ_r = 5.00, and a wide range of different b/a values, is illustrated by the semilogarithmic graph of ka cotanψ/h^d_a versus ka cotanψ, which is presented in Figure D.5. b/a = 0, 0.100, 0.300, 0.500, 0.700, 0.900, and 1.00 are used. Note that when the rod radius is much smaller than the sheath helix radius, varying the value of b/a has an insignificant effect on h^d_a. For example, the graphs for b/a = 0 and b/a = 0.100 are on top of each other.

In Figure D.6, the same set of b/a values just considered is employed, but now the ideal dielectric rod is characterized by a much larger relative permittivity, ϵ_r = 1.00×10^3. Clearly, the effect of varying b/a on h^d_a is greater than was true of the preceding figure. In addition, for the three region configuration, the negative dispersion is more pronounced compared to Figure D.5.

A qualitative description of the behavior shown in Figures D.2 - D.6 will now be given. For the three region configuration, when the rod radius is much smaller than the
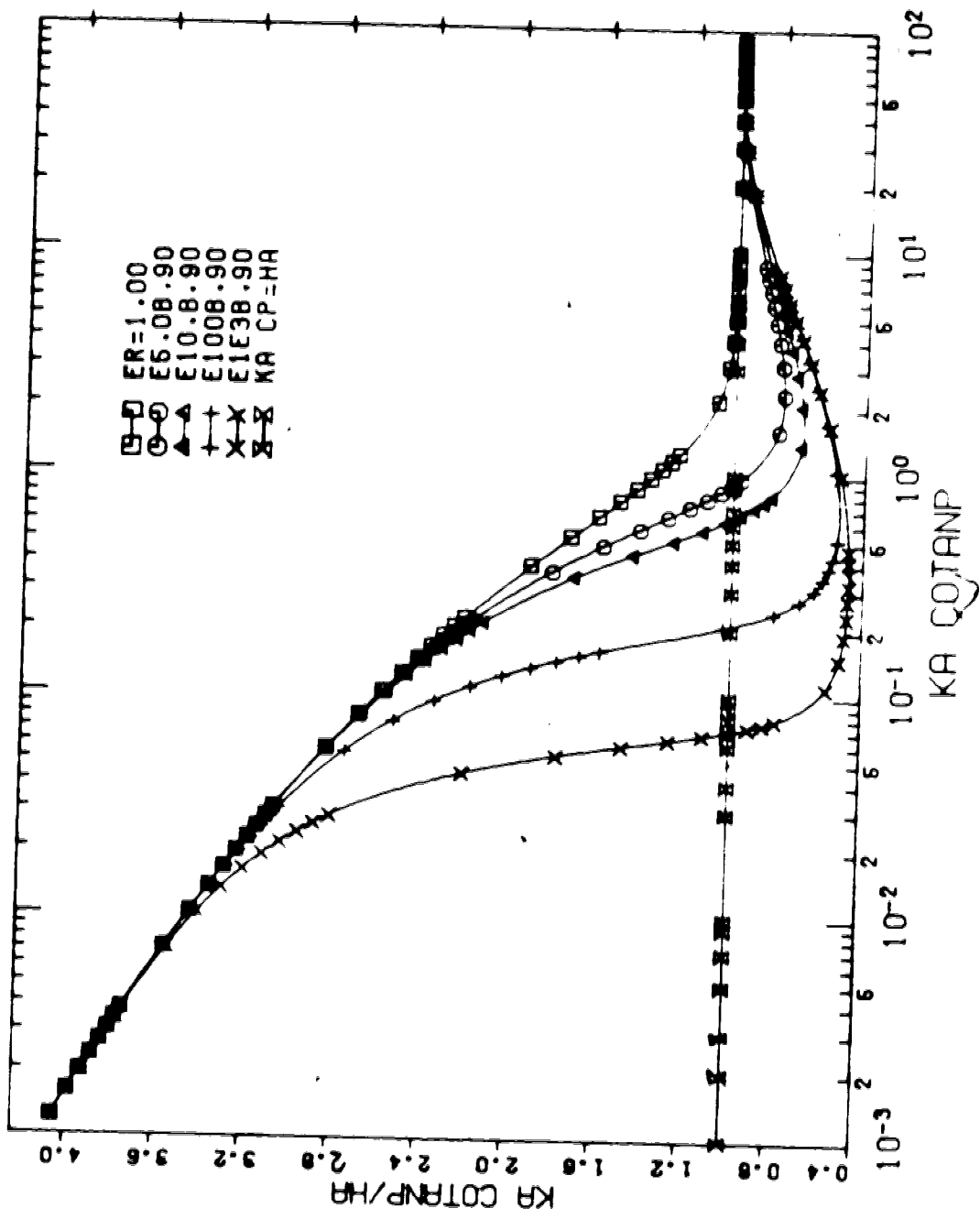
Figure D.3   Graph of ka cotanψ/h^{d}a versus ka cotanψ based on equation D.41. Curves for b/a = 0.900 and ϵ_r = 1.00, 5.00, 10.0, 1.00x10^2, and 1.00x10^3 are shown. The asymptote ka cotanψ/h^{d}a = 1.00 is given. (The curve for ϵ_r = 1.00 is the same as the solution associated with the empty sheath helix, based on equation B.13. Note that HA = h^{d}a and KA COTANP = ka cotanψ. E1E3B.90 means that the curve represents ϵ_r = 1.00x10^3 and b/a = 0.900.)
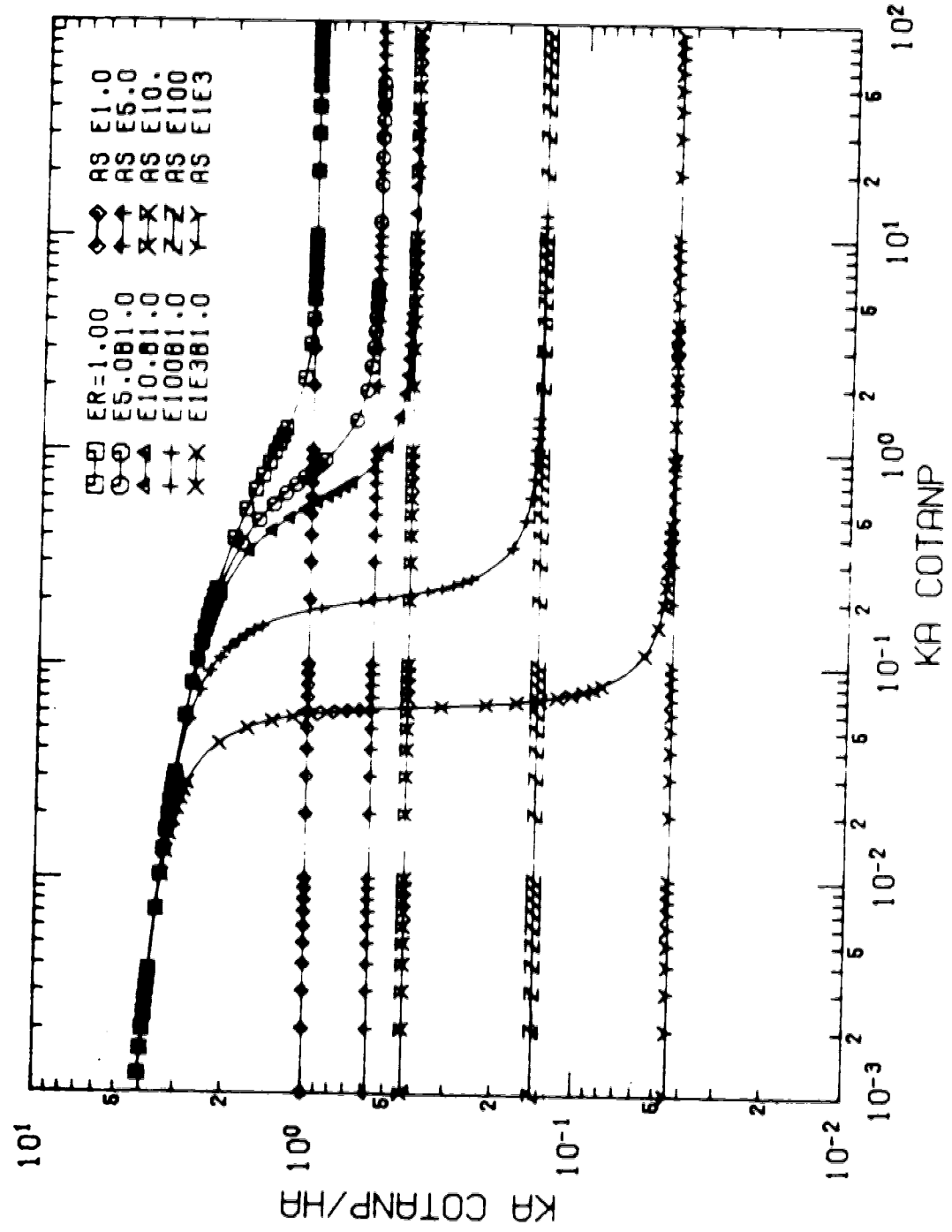
Figure D.4   Graph of ka cotanψ/h^{d}a versus ka cotanψ
based on equation D.41. Curves for b/a = 1.00 and ϵ_r =
1.00, 5.00, 10.0, 1.00x10^2, and 1.00x10^3 are shown. The
two region configuration asymptotes based on equation D.5 4
are shown for each particular value of ϵ_r. (Note that HA =
h^{d}a and KA COTANP = ka cotanψ. E1E3B1.0 means that the curve
represents ϵ_r = 1.00x10^3 and b/a = 1.00. AS E100 means
that the asymptote was calculated using ϵ_r = 1.00x10^2.)
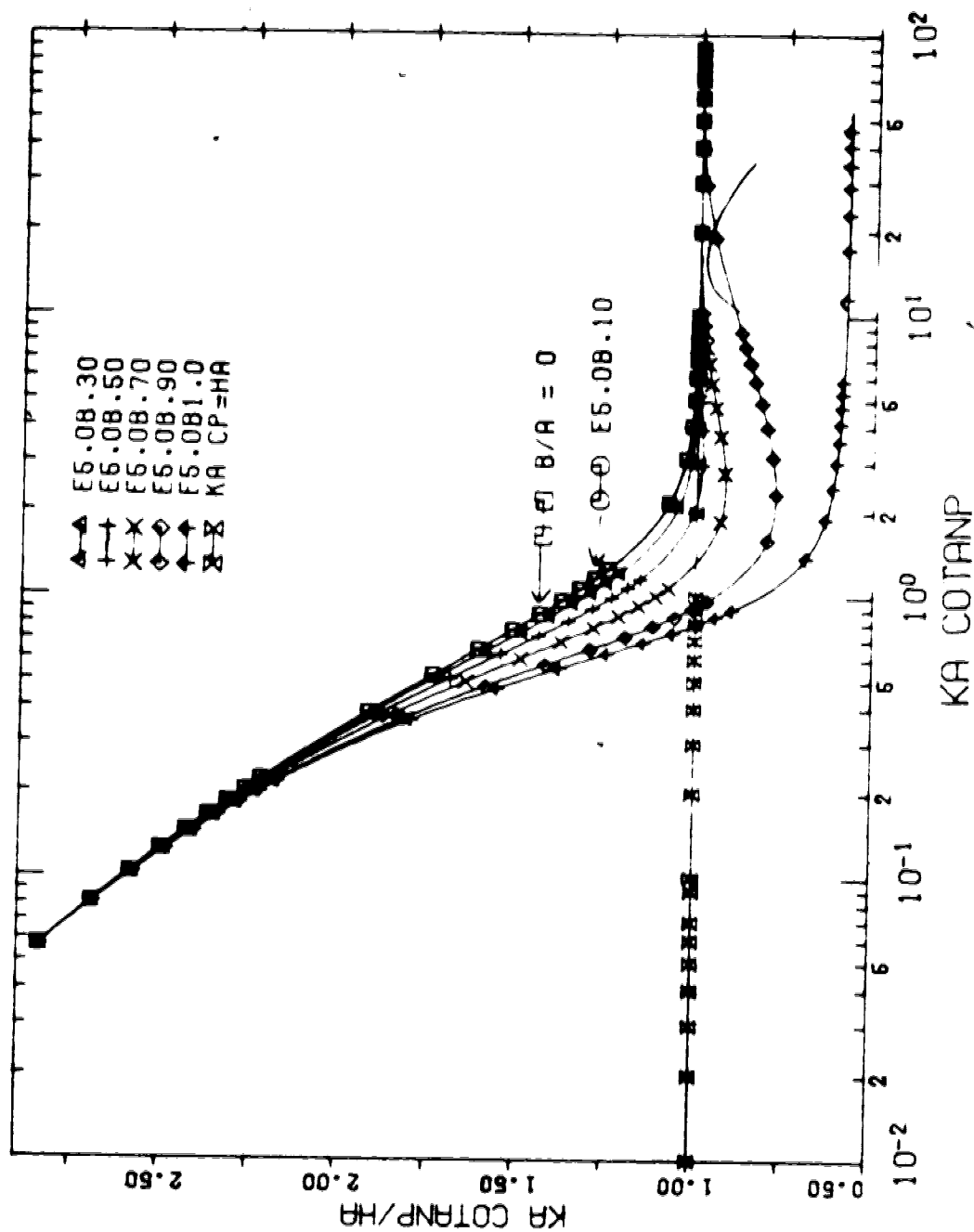
Figure D.5   Graph of ka cotanψ/h^{d}a versus ka cotanψ based on equation D.41. Curves for ϵ_r = 5.00 and b/a = 0, 0.100, 0.300, 0.500, 0.700, 0.900, and 1.00 are shown. The curve for b/a = 0 is based on the dispersion equation for the empty sheath helix, equation B.13. The asymptote ka cotanψ/h^{d}a = 1.00 is presented. (Note that HA = h^{d}a and KA COTANP = ka cotanψ. E5.0B.90 means that the curve represents ϵ_r = 5.00 and b/a = 0.900.)

Figure D.6   Graph of ka cotanψ/h^{d}a versus ka cotanψ
based on equation D.41. Curves for ϵ_r = 1.00x10^3 and
b/a = 0, 0.100, 0.300, 0.500, 0.700, 0.900, and 1.00
are shown. The curve for b/a = 0 is based on the
dispersion equation for the empty sheath helix, equation
B.13. The asymptote ka cotanψ/h^{d}a = 1.00 is presented.
(Note that HA = h^{d}a and KA COTANP = ka cotanψ. E1E3B.70
means that the curve represents ϵ_r = 1.00x10^3 and b/a =
0.700.)

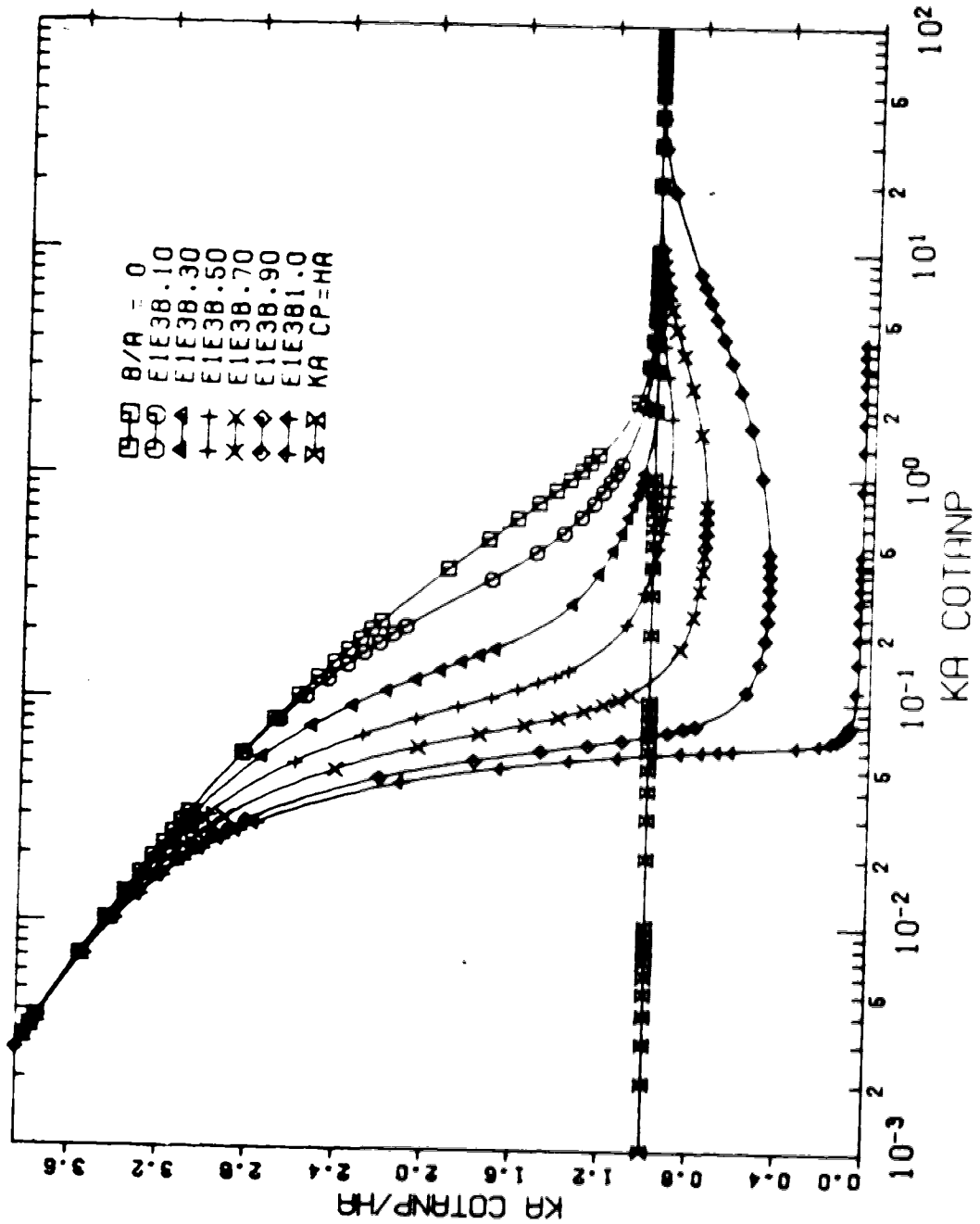sheath helix radius, the value of ϵ_r has a negligible effect on $_h{}^d{}_a$, and the dispersion curves are similar to the dispersion curve associated with the empty sheath helix. In addition, when the ideal dielectric rod permittivity is nearly unity, for both the two and three region configurations, the value of b/a has little effect on $_h{}^d{}_a$, and the dispersion curves are approximately that of the empty sheath helix. However, when ϵ_r is large, the value of b/a definitely affects $_h{}^d{}_a$ in the mid-region of $ka\ \cot an\psi$ values. Similarly, when the value of b/a is large, varying the value of ϵ_r has a great effect on $_h{}^d{}_a$ in the mid $ka\ \cot an\psi$ region. The phenomenon of negative dispersion is associated with the three region configuration and it is most pronounced when both b/a and ϵ_r are large. Even in this situation, however, for very small or very large values of $ka\ \cot an\psi$, the dispersion curves associated with the three region configuration are to a good approximation the same as that associated with the empty sheath helix. This is also true of the two region configuration for any value of ϵ_r, when $ka\ \cot an\psi$ becomes sufficiently small. However, for the two region configuration when $ka\ \cot an\psi$ is large, the dispersion curves will be different from the empty sheath helix dispersion curve.

Figure D.7 is a three dimensional plot of the quantity $ka\ \cot an\psi/_h{}^d{}_a$ as a function of both the variables $ka\ \cot an\psi$ and b/a. $\epsilon_r = 1.10$ is the relative permittivity characterizing the ideal dielectric rod. For this small value of the relative permittivity, the variable b/a has an insignificant effect. For some specified value of $ka\ \cot an\psi$, the quantity $ka\ \cot an\psi/_h{}^d{}_a$ is similar to the quantity $ka\ \cot an\psi/_h{}^a{}_a$, which is associated with the empty sheath helix.

Figure D.8 is a similar type of graph as the preceding figure, except that now a large relative permittivity, $\epsilon_r = 1.00 \times 10^3$, is used. When b/a is very small, the dependence of $ka\ \cot an\psi/_h{}^d{}_a$ on $ka\ \cot an\psi$ is approximately that of the empty sheath helix. Increasing b/a tends to emphasize the occurrence of negative dispersion. For the three region configuration, when b/a is large, this effect is great, but even here it clearly decreases as $ka\ \cot an\psi$ becomes large. For any fixed value of $ka\ \cot an\psi$, increasing b/a clearly makes the quantity $ka\ \cot an\psi/_h{}^d{}_a$ smaller, or, equivalently, $_h{}^d{}_a$ larger.
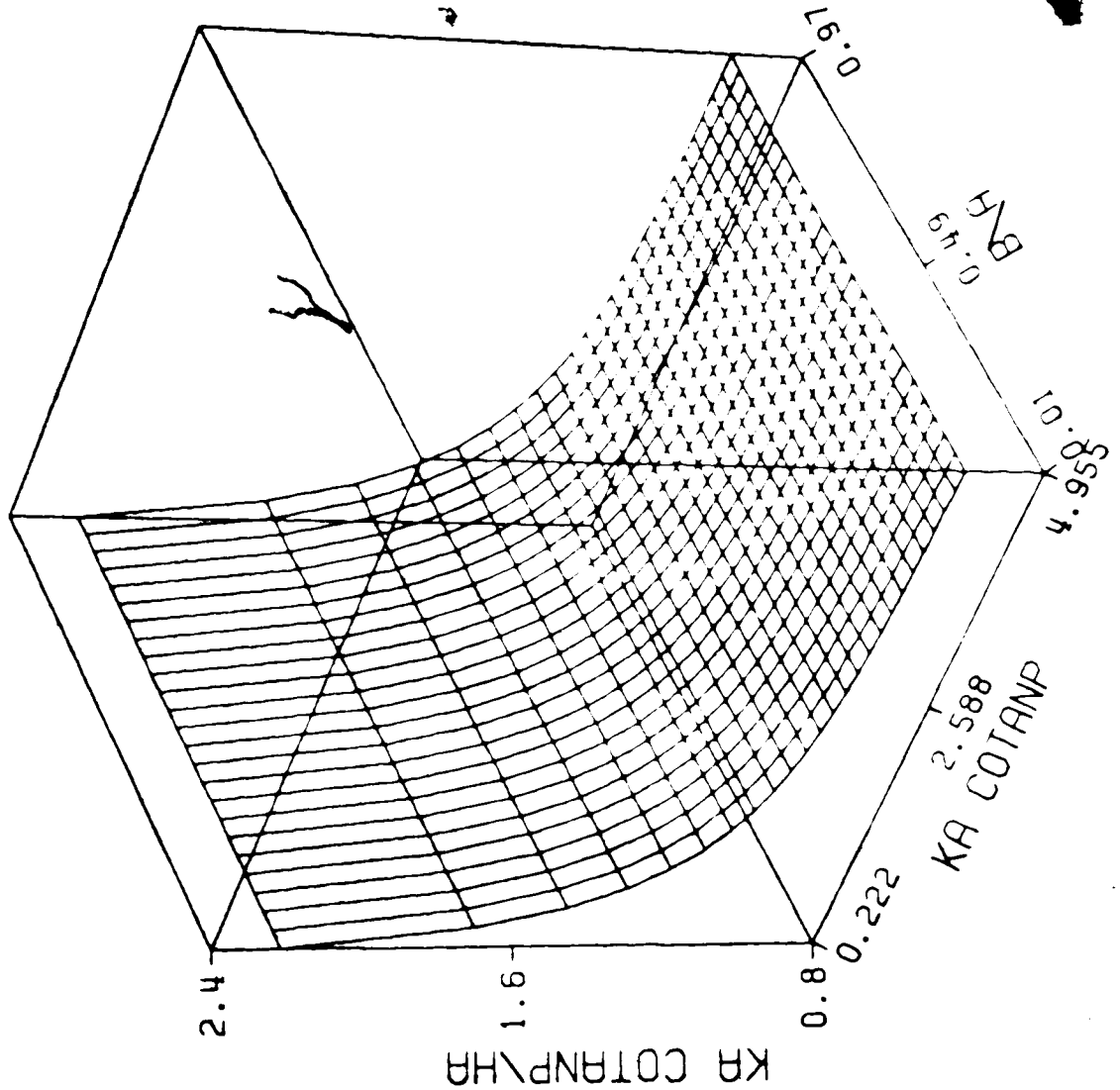
Figure D.7   Three dimensional graph of ka cotanψ/h^{d}a versus both ka cotanψ and b/a. ϵ_r = 1.10 is the relative permittivity which is used. The graph is based on equation D.41. (Note that HA = h^{d}a, KA COTANP = ka cotanψ, and B/A = b/a.)
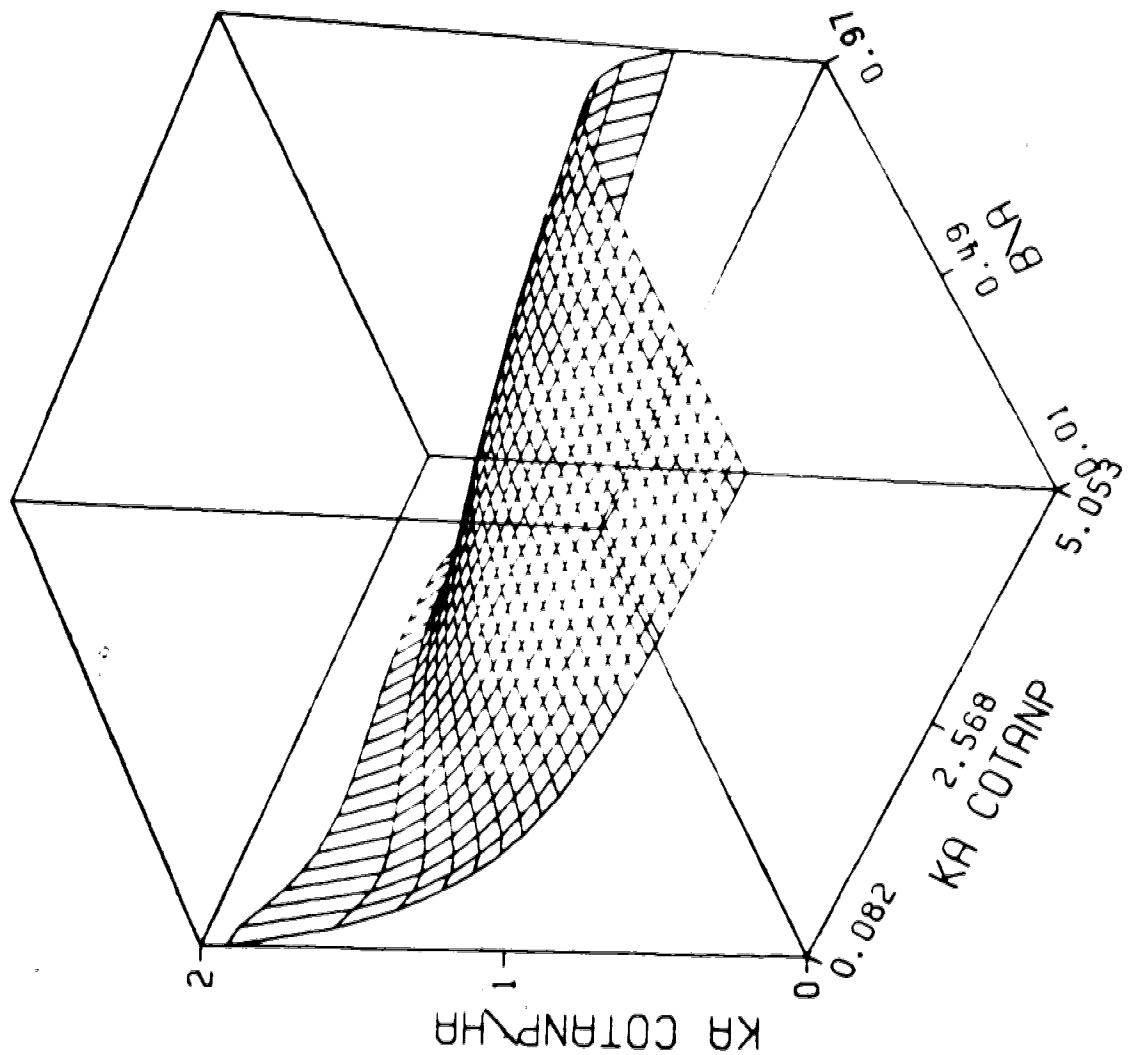
Figure D.8   Three dimensional graph of ka cotanψ/h^{d}a versus both ka cotanψ and b/a ϵ_r = 1.00x10^3 is the relative permittivity wh'ch is .sed. The graph is based on equation D.41. (Note that WA = h^{d}a, KA COTANP = ka cotanψ, and B/A = b/a.)

D.2.2 Discussion and Graphs of the Field Components

An investigation of the field components, equations D.23 – D.40, will be conducted in this part of the appendix. The pitch angle appears by itself in $E_{\theta n}^{\ d}$ and $H_{\theta n}^{\ d}$ (n = 1, 2, 3) as $\sin\psi$, while for all other field components, it appears by itself as $\cos\psi$. Decreasing the pitch angle in such a manner that the variable $ka\cot\psi$ remains constant, keeping in mind that the functional dependence of $h^d{}_a$ is given by equation D.47, the magnitudes of the angular fields are seen to be greatly reduced but the magnitudes of the radial and axial field components are approximately unchanged.

Assuming that the sheath helix is sufficiently tightly wound so that $\cos\psi \cong 1$, and making use of equation D.47, it is apparent what the approximate functional dependences of the field components are on the operating frequency, the ideal dielectric coaxial rod geometry, the dielectric material permittivity, the sheath helix geometry, and the sheath helix "windings'" current.

$$E_{\theta n}^{\ d} = L_n(\partial_{||}, ka\cot\psi, b/a, \epsilon_r, \psi), \qquad (D.61)$$

$$H_{\theta n}^{\ d} = S_n(\partial_{||}, ka\cot\psi, b/a, \epsilon_r, \psi), \qquad (D.62)$$

$$E_{rn}^{\ d} = Q_n(\partial_{||}, ka\cot\psi, b/a, \epsilon_r), \qquad (D.63)$$

$$E_{zn}^{\ d} = U_n(\partial_{||}, ka\cot\psi, b/a, \epsilon_r), \qquad (D.64)$$

$$H_{rn}^{\ d} = V_n(\partial_{||}, ka\cot\psi, b/a, \epsilon_r), \quad \text{and} \qquad (D.65)$$

$$H_{zn}^{\ d} = W_n(\partial_{||}, ka\cot\psi, b/a, \epsilon_r); \qquad (D.66)$$

where n = 1, 2, 3.

Region 1 $(0 \leq r \leq b)$ fields have a radial dependence described by either $I_0(h^d r)$ for the axial fields, or by $I_1(h^d r)$ for the radial and angular fields. Region 3 $(a \leq r < \infty)$ fields have a radial dependence described by either $K_0(h^d r)$ for the axial fields, or by $K_1(h^d r)$ for the radial and angular fields. The radial dependence of region 2 $(b \leq r \leq a)$ fields is more complicated. It is characterized by $I_0(h^d r)$ for the axial magnetic field, and by $I_1(h^d r)$ for the angular electric field and for the radial magnetic field. The radial dependence of the region 2 radial electric field and angular magnetic field is a linear combination of $I_1(h^d r)$ and $K_1(h^d r)$. Finally, the region 2 axial electric field has its radial dependence characterized by a linear combination of $I_0(h^d r)$ and $K_0(h^d r)$.

It was previously mentioned in part D.2.1 it is believed that the wave number $h^d a$ must be real positive for a free mode field solution to exist. Therefore, all the arguments of the Bessel functions mentioned in the previous paragraph are real positive. For one particular operating frequency, dielectric rod geometry, dielectric rod permittivity, and sheath helix geometry (which means that $h^d a$ has one particular value), as the radial distance normalized with respect to the sheath helix radius, r/a, increases, it must be true that the magnitude of any region 1 field always increases, while the magnitude of any region 3 field always decreases. (See Figure A.1. This is a graph of I_0, I_1, K_0, and K_1 for real positive arguments.) The behavior of the region 2 fields is more complicated. When r/a increases, the region 2 angular electric, radial magnetic, and axial magnetic fields always increase in magnitude. However, the region 2 radial electric, axial electric, and angular magnetic fields may either increase or decrease in magnitude, as the value of r/a increases.

A better understanding of the field components can be obtained by comparing them with the fields associated with the empty sheath helix, equations B.1 - B.12, for the special cases when $h^d a$ and $h^a a$ are either both large or are both small. First, assume that the two wave numbers are much smaller than unity, so that the small argument Bessel function representations can be used. Equations A.26 - A.29 were employed to approximate both the three region $(b < a)$ and the two region $(b = a)$ form of equations D.23 - D.40. The small argument Bessel function

representations were also employed to approximate equations B.1 – B.12. Use was made of the fact that $_h{}^d{}_a \simeq {}_h{}^a{}_a$, since the small argument approximations of the two dispersion equations, equations D.49 and B.21, are identical. It was discovered that the fields associated with both the three region and two region forms of the sheath helix surrounding an ideal dielectric coaxial rod configuration are usually similar to the corresponding empty sheath helix fields. The only exceptions occurred for $H_{\theta 1}{}^d$, $H_{\theta 2}{}^d$, and $E_{r2}{}^d$. They differed from the corresponding empty sheath helix fields, $H_{\theta 1}{}^a$ and $E_{r1}{}^a$, by an amount which is proportional to ϵ_r.

Values of $_h{}^d{}_a$ and $_h{}^a{}_a$ greater than unity are now considered, in order that the large argument Bessel function representations can be used. Just the first term of equations A.36 – A.39 was employed to approximate equations B.1 – B.12, and the three region form of equations D.23 – D.40. The approximations $_h{}^d{}_a \simeq {}_h{}^a{}_a \simeq$ $ka \cot an \psi$, which are simply statements of equations D.53 and B.20, are used. Comparison of the two sets of equations shows that the corresponding fields near $r = a$ are the same. As was previously explained in section B.3, the field components are now rapidly exponentially attenuated for increasing radial distances away from the sheath helix surface. Therefore, the dominant fields for the three region ideal dielectric coaxial rod configuration are the same as the corresponding ones associated with the empty sheath helix.

The procedure explained in the preceding paragraph was followed for the special case of the two region ideal dielectric coaxial rod configuration. Equations D.54 and B.20, the large argument approximations of the two dispersion equations, demonstrate that $_h{}^d{}_a > {}_h{}^a{}_a$. Making use of this fact and employing just the first term of equations A.36 – A.39 to approximate the two sets of field components, it is apparent that the dominant fields associated with the two region dielectric rod configuration are clearly different from the corresponding fields associated with the empty sheath helix.

A crude summary of the three previous paragraphs is now presented. *For small values of* $ka \cot an \psi$ *(which could be considered to mean low frequencies since*

$$ka \cot an \psi = 2\pi f \sqrt{\mu_0 \epsilon_0} \; a \cot an \psi),$$ *the wave number solution and most of the field components for both the two and three region ideal dielectric coaxial*

rod configurations are similar to the corresponding quantities associated with the empty sheath helix. Therefore, it can be said that the fields do not "see" the dielectric rod. When $ka \cot\psi$ *is large (which could be considered to mean high frequencies), the wave number solution and the dominant field components associated with the three region dielectric rod configuration are similar to the corresponding quantities of the empty sheath helix. Once again, the fields do not "see" the dielectric rod. However, for large values of* $ka \cot\psi$*, the wave number solution and the field components associated with the two region dielectric rod configuration are clearly different from the corresponding quantities associated with the empty sheath helix. In this case, the fields do "see" the dielectric rod.*

Equations D.23 – D.40 are lengthy and complicated expressions. In order to help understand how the field components behave at different points in space, graphs of their radial dependence have been prepared. All the electric fields were normalized from dividing them by an electric normalizing coefficient, $E_{z0}{}^d$. Furthermore, all the magnetic fields were normalized from dividing them by a magnetic normalizing coefficient, $H_{z0}{}^d$. The electric and magnetic normalizing coefficients are defined as.

$$E_{z0}{}^d = E_{z2}{}^d \bigg|_{\substack{z=0 \\ r=a}} = j \mathcal{B}_{11} \frac{120\pi}{ka \cot\psi} \cos\psi \, (h^d a)^2 \, K_0(h^d a) \cdot$$

$$[I_0(h^d a) - \frac{(\epsilon_r - 1) \, I_0(h^d b) \, I_1(h^d b) \, K_0(h^d a)}{(I_0(h^d b) \, K_1(h^d b) + \epsilon_r \, I_1(h^d b) \, K_0(h^d b))}]$$

$$\hspace{6cm} (D.67)$$

$$= j \mathcal{B}_{11} \, 120\pi \, ka \cot\psi \, \cos\psi \, I_1(h^d a) \, K_1(h^d a), \quad \text{and}$$

$$H_{z0}{}^d = H_{z2}{}^d \bigg|_{\substack{z=0 \\ r=a}} = \mathcal{B}_{11} \cos\psi \, h^d a \, I_0(h^d a) \, K_1(h^d a). \hspace{1cm} (D.68)$$

(The dispersion equation, equation D.41, was used for simplification in the derivation of

equations D.67.)

It is assumed for the radial dependence graphs that the axial coordinate is held constant. The transverse planes were chosen so that $\cos(h^d{}_a \cdot z/a) = +1$ for the angular and axial fields, and so that $\sin(h^d{}_a \cdot z/a) = +1$ for the radial fields.

Three different types of graphs are presented. These represent the "high frequency", "mid frequency", and "low frequency" cases. (The meanings of the terms in quotation marks is the same as it was when these expressions were previously used in section B.3.) For each of the three previously mentioned cases, both the three region and the two region ideal dielectric rod configurations are considered.

The procedure which was used to numerically evaluate the normalized fields is now explained. For the specified set of variables $ka\ \cot an\psi$, b/a, and ϵ_r, equation D.41 is solved to obtain the wave number $h^d{}_a$. (In fact, as was previously explained in part D.2.1, the method used to solve the dispersion equation is to first specify the quantities $h^d{}_a$, b/a, ϵ_r, and then directly calculate the corresponding value of $ka\ \cot an\psi$.) Next, equations D.67 and D.68 are computed to obtain the normalizing coefficients. Finally, the normalized field components are evaluated for several different values of the radial distance normalized with respect to the sheath helix radius, r/a. In order to directly evaluate the Bessel functions, the IMSL (43) software program library was used. It will be emphasized that all eighteen graphs of the normalized fields' radial dependence presented here are "exact" -- no approximations have been made to the dispersion equation, equation D.41, the field components, equations D.23 - D.40, and the normalizing coefficients, equations D.67 and D.68. Furthermore, it was ensured that the requirement mentioned in equation D.56 is always satisfied. This provides justification for using the approximations given in equations D.55, which is how equations D.23 - D.41 were obtained from equations D.1 - D.19.

Figures D.9 and D.10 show the absolute value of the (real valued) normalized electric and magnetic fields, respectively, as a function of r/a. The two vertical lines represent the surface of the ideal dielectric coaxial rod and the sheath helix surface. In all three regions, the algebraic sign of each normalized field component is indicated. The operating frequency, the ideal dielectric coaxial rod geometry, the rod permittivity, and
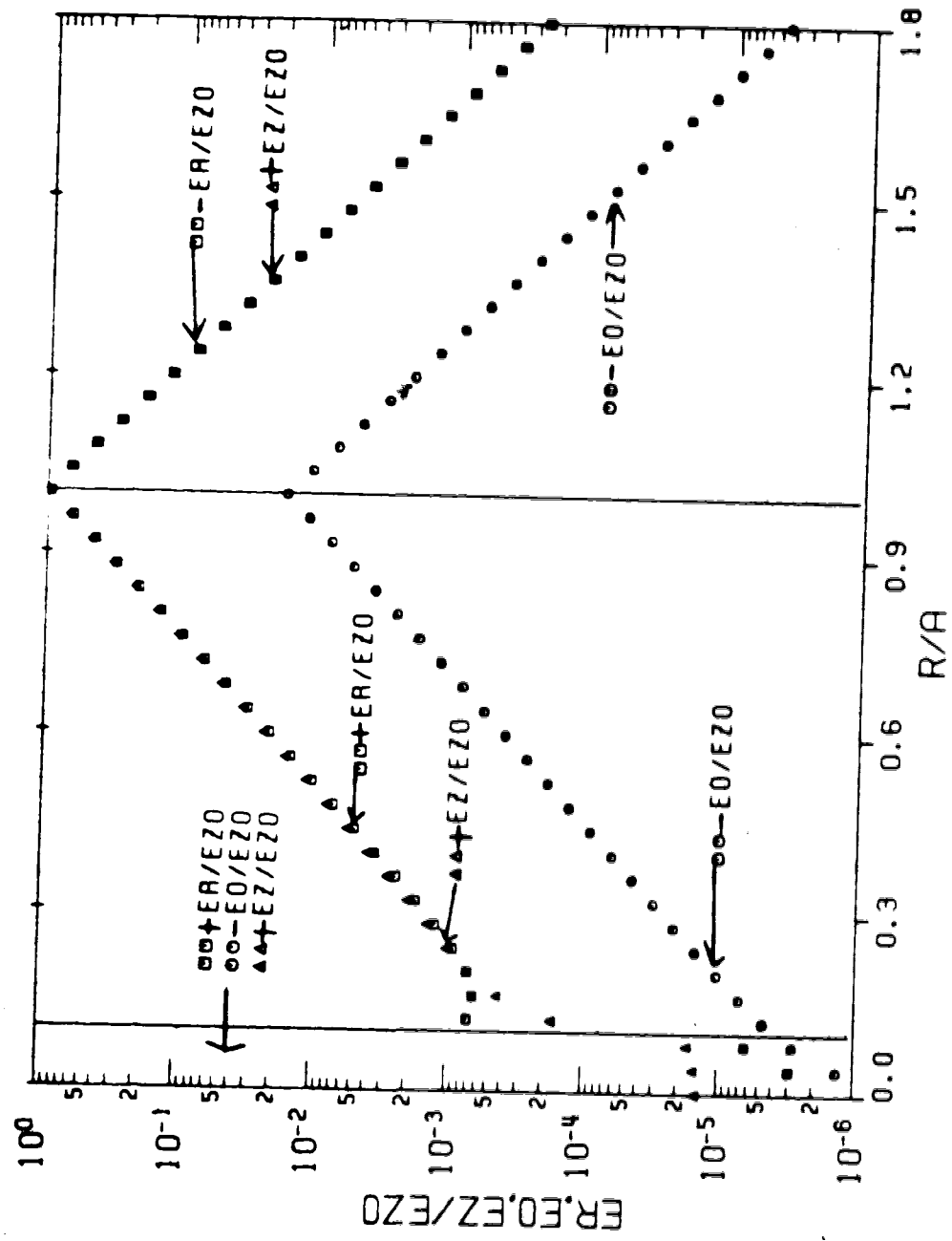
RADIAL DEPENDENCE OF ELECTRIC FIELDS

Figure D.9   Curves of the radial dependence associated with the normalized electric fields. The variables used are ka cotanψ = 10.0, b/a = 0.100, ε_r = 1.00x10^2, and ψ = 1.00°. They determine the wave number h^{d}a = 10.0 and the electric normalizing coefficient $E_{z0}{}^d$ = j $\}$₁₁ 188 (V/m). (Note that ER/EZO = $E_r{}^d/E_{z0}{}^d$, EO/EZO = $E_\theta{}^d/E_{z0}{}^d$, EZ/EZO = $E_z{}^d/E_{z0}{}^d$, and R/A = r/a.)
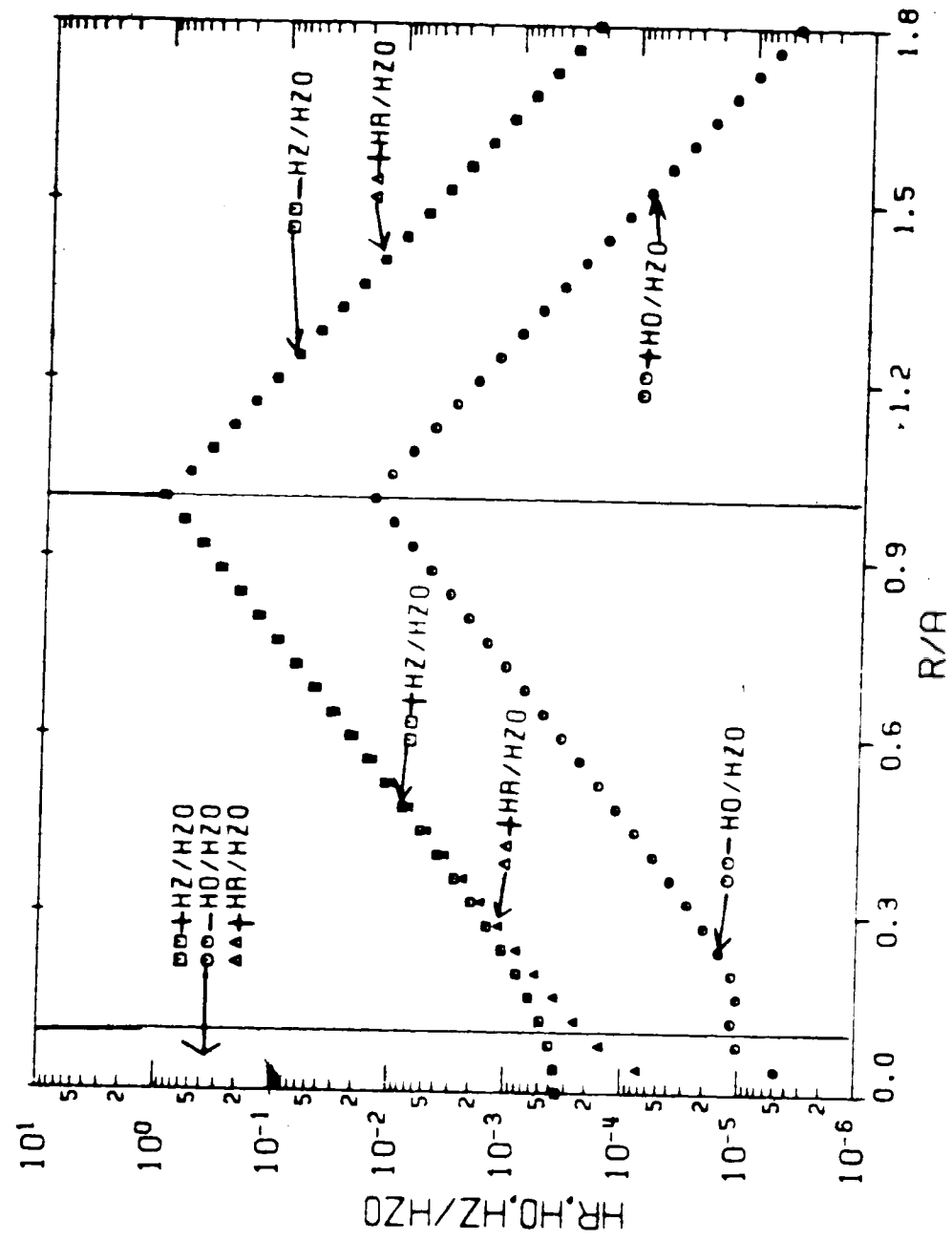
Figure D.10   Curves of the radial dependence associated with the normalized magnetic fields. The variables used are ka cotanψ = 10.0, b/a = 0.100, ε_r = 1.00x10^2, and ψ = 1.00°. They determine the wave number h^{d}a = 10.0 and the magnetic normalizing coefficient H$_{z0}$^{d} = $\S$$_{||}$ 0.525 (A/m). (Note that HR/HZO = H$_r$^{d}/H$_{z0}$^{d}, HO/HZO = H$_\theta$^{d}/H$_{z0}$^{d}, HZ/HZO = H$_z$^{d}/H$_{z0}$^{d}, and R/A = r/a.)

the sheath helix geometry are specified by the variables $ka \cot an\psi = 10.0$, $b/a = 0.100$, $\epsilon_r = 100$, and $\psi = 1.00°$. This is an example of the three region "high frequency" case. $h^d a = 10.0$ is the calculated value of the wave number.

$$E_{z0}^d = j \mathcal{Y}_{11} \; 188 \;\; (V/m) \quad \text{and} \quad H_{z0}^d = \mathcal{Y}_{11} \; 0.525 \;\; (A/m)$$

are the computed values of the normalizing coefficients.

Figures D.11 and D.12 are two additional graphs representing the three region "high frequency" case. The variables used are $ka \cot an\psi = 10.0$, $b/a = 0.900$, $\epsilon_r = 100$, and $\psi = 1.00°$. The calculated wave number is $h^d a = 10.5$, and the calculated normalizing coefficients are

$$E_{z0}^d = j \mathcal{Y}_{11} \; 176 \;\; (V/m) \quad \text{and} \quad H_{z0}^d = \mathcal{Y}_{11} \; 0.524 \;\; (A/m).$$

Two graphs representing the two region "high frequency" case are Figures D.13 and D.14. $ka \cot an\psi = 10.0$, $b/a = 1.00$, $\epsilon_r = 100$, and $\psi = 1.00°$ are the variables which are used. $h^d a = 71.1$ is the computed value of the wave number.

$$E_{z0}^d = j \mathcal{Y}_{11} \; 26.6 \;\; (V/m) \quad \text{and} \quad H_{z0}^d = \mathcal{Y}_{11} \; 0.503 \;\; (A/m)$$

are the computed values of the normalizing coefficients.

As expected, the wave number solution associated with Figures D.9 – D.12 approximately agrees with the large argument, three region, representation of the dispersion equation, equation D.53. Furthermore, the value of $h^d a$ associated with Figures D.13 and D.14 is in good agreement with the large argument, two region, approximation of the dispersion equation, equation D.54.

Figure D.11   Curves of the radial dependence associated
with the normalized electric fields. The variables used
are ka cotanψ = 10.0, b/a = 0.900, ϵ_r = 1.00x10^2, and
ψ = 1.00°. They determine the wave number h^{d}a = 10.5
and the electric normalizing coefficient E$_{z0}^d$ = j$\}_{11}$ 176
(V/m). (Note that ER/EZ0 = E$_r^d$/E$_{z0}^d$, E0/EZ0 = E$_\theta^d$/E$_{z0}^d$,
EZ/EZ0 = E$_z^d$/E$_{z0}^d$, and R/A = r/a.)

Figure D.12 Curves of the radial dependence associated with the normalized magnetic fields. The variables used are ka cotanψ = 10.0, b/a = 0.900, ϵ_r = 1.00x10^2, and ψ = 1.00°. They determine the wave number h^{d}a = 10.5 and the magnetic normalizing coefficient H$_{z0}^d$ = 0.524 (A/m). (Note that HR/HZO = H$_r^d$/H$_{z0}^d$, HO/HZO = H$_\theta^d$/H$_{z0}^d$, HZ/HZO = H$_z^d$/H$_{z0}^d$, and R/A = r/a.)

Figure D.13   Curves of the radial dependence associated
with the normalized electric fields. The variables used
are ka cotanψ = 10.0, b/a = 1.00, ϵ_r = 1.00x10^2, and
ψ = 1.00°. They determine the wave number h^{d}a = 71.1
and the electric normalizing coefficient E_{z0}^d = j$\mathfrak{I}_{11}$ 26.6
(V/m). (Note that ER/EZO = E_r^d/E_{z0}^d, EO/EZO = E_θ^d/E_{z0}^d,
EZ/EZO = E_z^d/E_{z0}^d, and R/A = r/a.)

Figure D.14   Curves of the radial dependence associated with the normalized magnetic fields. The variables used are ka cotanψ = 10.0, b/a = 1.00, ϵ_r = 1.00x10^2, and ψ = 1.00°. They determine the wave number h^{d}a = 71.1 and the magnetic normalizing coefficient H_{z0}^d = $\Omega_{||}$ 0.503 (A/m). (Note that HR/HZO = H_r^d/H_{z0}^d, HO/HZO = H_θ^d/H_{z0}^d, HZ/HZO = H_z^d/H_{z0}^d, and R/A = r/a.)

It is informative to compare Figures D.9 – D.14 with the "high frequency" case of the empty sheath helix, Figures B.3 and B.4. Examination of Figures D.9 – D.12 and Figures B.3 and B.4, keeping in mind the values of the normalizing coefficients and the fact that the same values of $ka\ cotan\psi$ and ψ are used, shows that near the sheath helix surface, the fields are similar. This agrees with the statement made earlier in part D.2.2 that for "high frequencies" the fields associated with the three region ideal dielectric coaxial rod configuration *do not "see" the dielectric rod*. However, comparing Figures D.13 and D.14 with Figures B.3 and B.4, it is clear that the fields for the two region dielectric rod configuration are quite different than the corresponding fields associated with the empty sheath helix. This provides support for the statement made previously in part D.2.2 that for "high frequencies" the fields associated with the two region ideal dielectric coaxial rod configuration *do "see" the dielectric rod*.

Figures D.15 and D.16 display the radial dependence of the normalized electric and magnetic fields, respectively, for the three region "mid frequency" case. $ka\ cotan\psi = 1.00$, $b/a = 0.100$, $\epsilon_r = 100$, and $\psi = 1.00°$ are the variables which are used. The wave number is calculated to be $h^d a = 0.80$.

$$E_{z0}{}^d = j\ \}_{||}\ 143\ (V/m)\quad and\quad H_{z0}{}^d = \}_{||}\ 0.804\ (A/m)$$

are the calculated values of the normalizing coefficients.

Two additional graphs associated with the three region "mid frequency" case are Figures D.17 and D.18. These illustrate the radial dependence of the normalized electric and magnetic fields, respectively. The variables employed are $ka\ cotan\psi = 1.00$, $b/a = 0.900$, $\epsilon_r = 100$, and $\psi = 1.00°$. $h^d a = 1.65$ is the computed value of the wave number. The calculated values of the normalizing coefficients are

$$E_{z0}{}^d = j\ \}_{||}\ 95.9\ (V/m)\quad and\quad H_{z0}{}^d = \}_{||}\ 0.668\ (A/m).$$
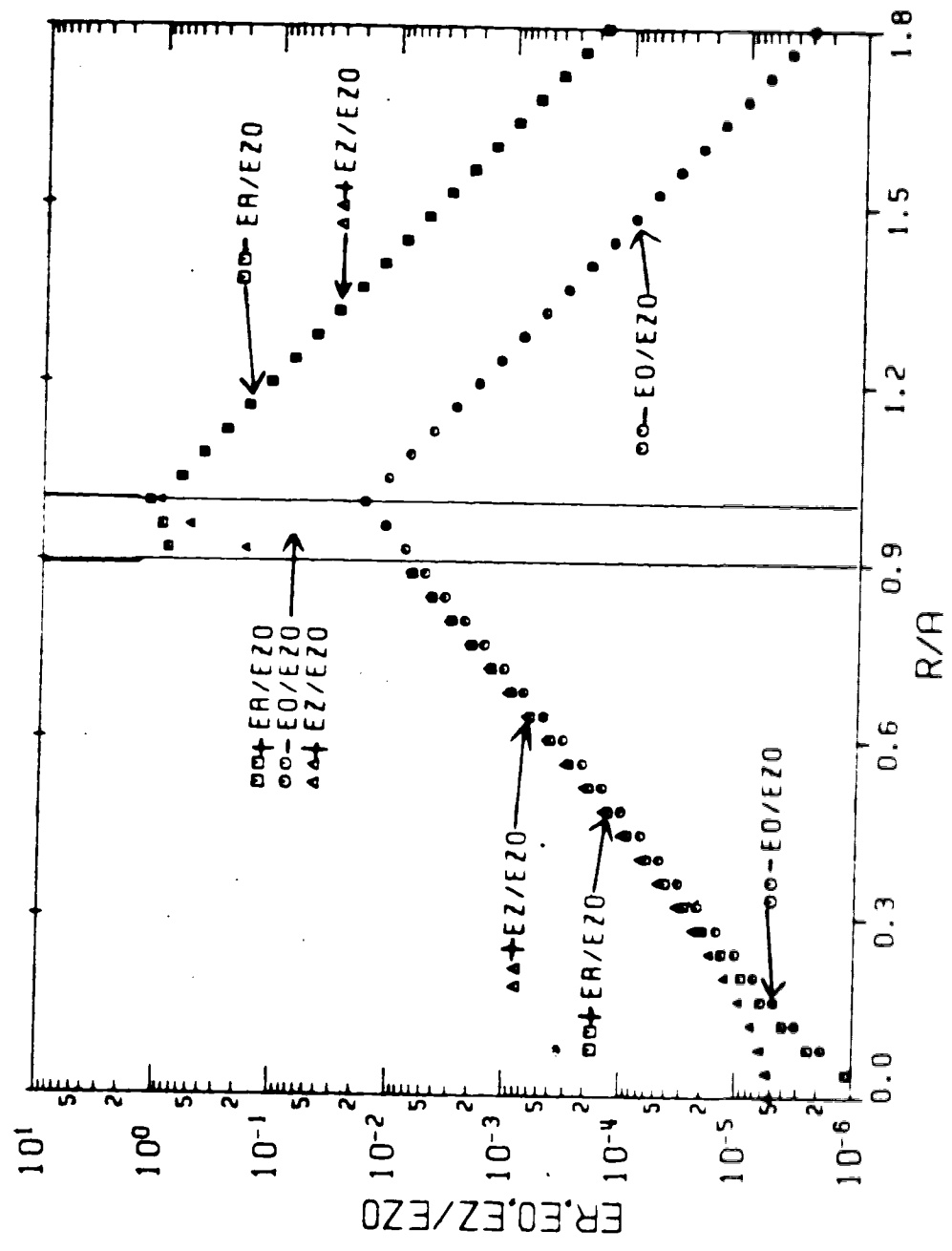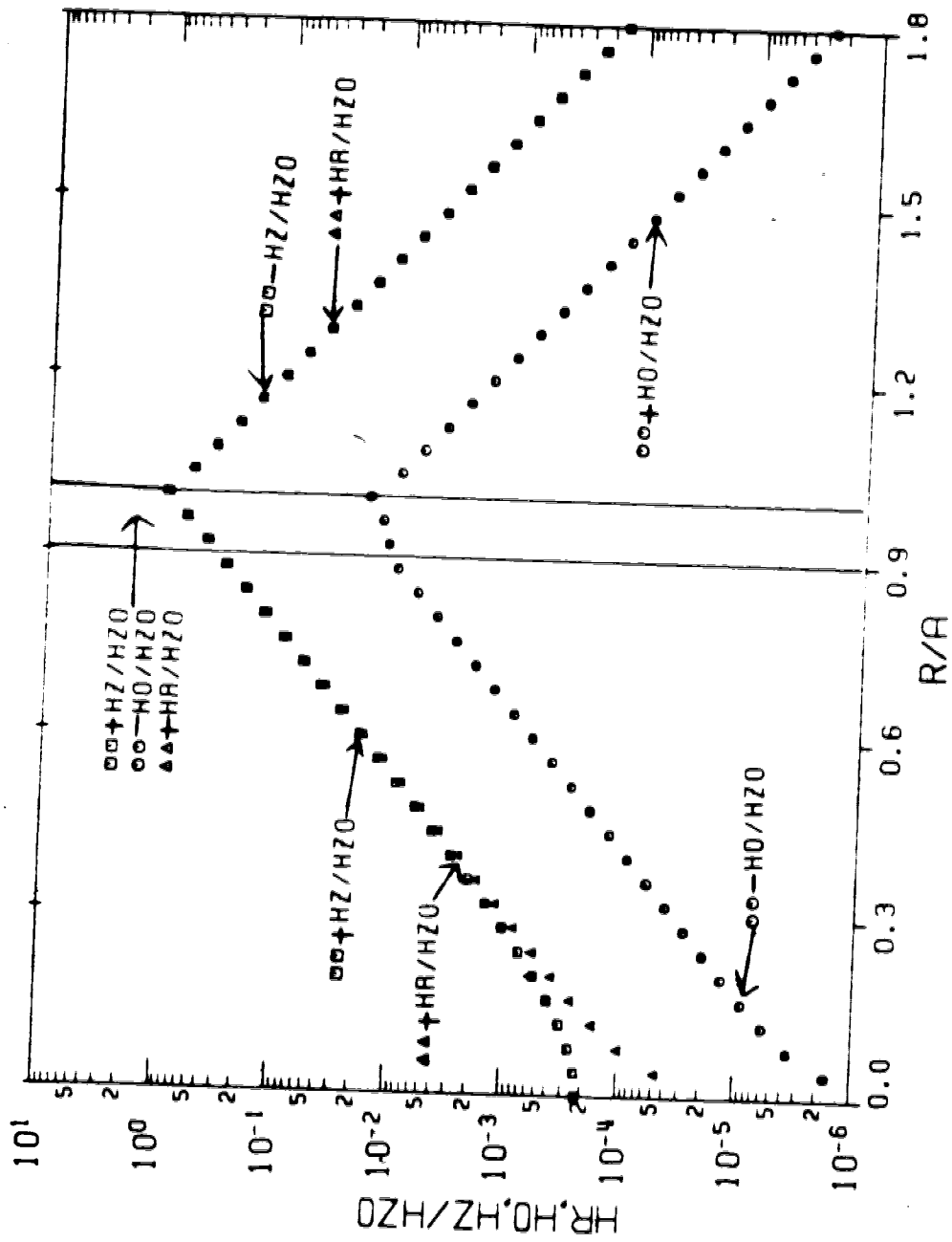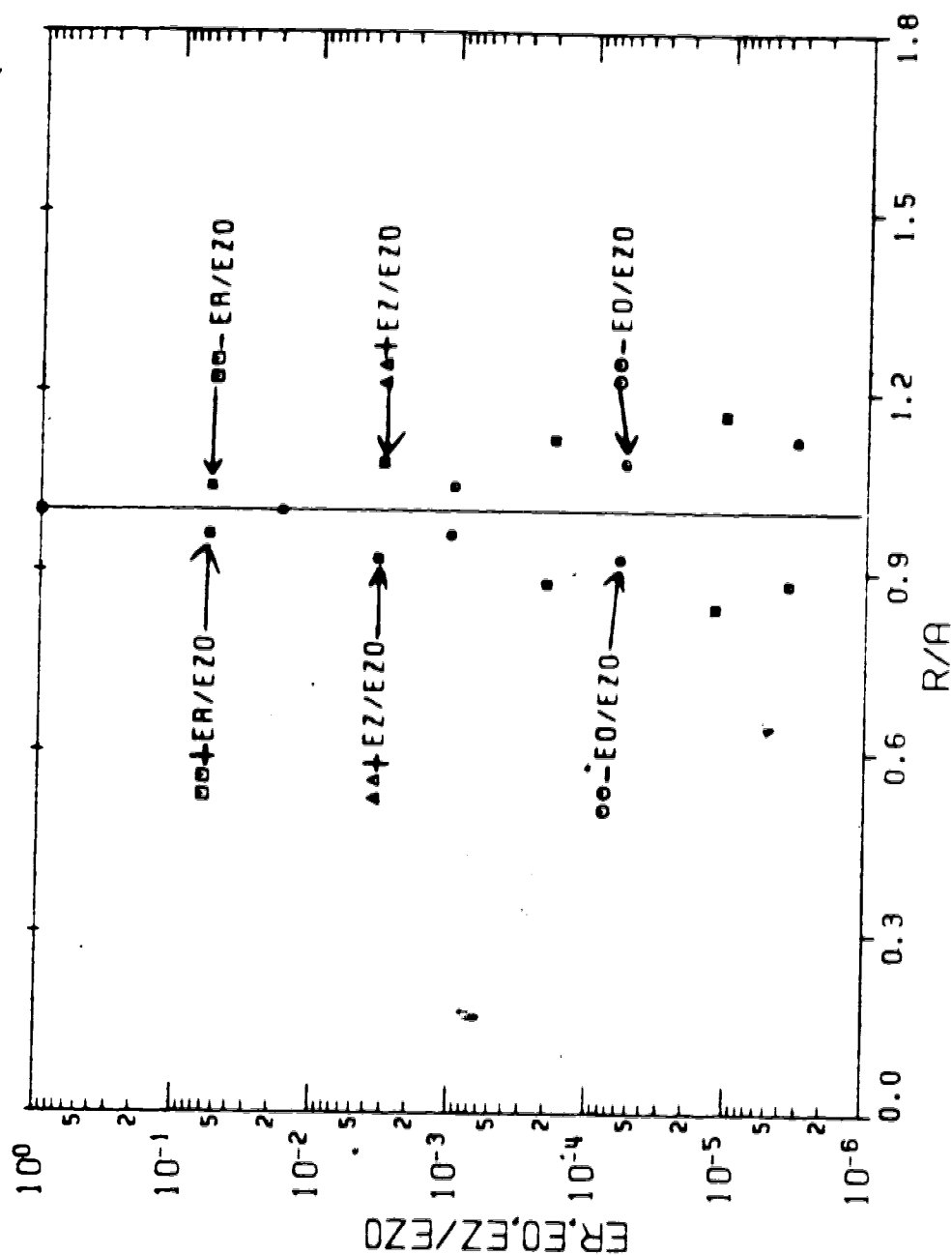
Figure D.15   Curves of the radial dependence associated with the normalized electric fields. The variables used are ka cotanψ = 1.00, b/a = 0.100, ϵ_r = 1.00x10^2, and ψ = 1.00°. They determine the wave number h^{d}a = 0.80 and the electric normalizing coefficient $E_{z0}{}^d$ = j $\}_{11}$ 143 (V/m). (Note that ER/EZO = $E_r{}^d/E_{z0}{}^d$, EO/EZO = $E_\theta{}^d/E_{z0}{}^d$, EZ/EZO = $E_z{}^d/E_{z0}{}^d$, and R/A = r/a.)

Figure D.16 Curves of the radial dependence associated with the normalized magnetic fields. The variables used are ka cotanψ = 1.00, b/a = 0.100, ϵ_r = 1.00x10^2, and ψ = 1.00°. They determine the wave number $h^d a$ = 0.80 and the magnetic normalizing coefficient H_{z0}^d = 0.804 (A/m). (Note that HR/HZO = H_r^d/H_{z0}^d, HO/HZO = H_θ^d/H_{z0}^d, HZ/HZO = H_z^d/H_{z0}^d, and R/A = r/a.)

Figure D.17   Curves of the radial dependence associated with the normalized electric fields. The variables used are ka cotanψ = 1.00, b/a = 0.900, ϵ_r = 1.00x10^2, and ψ = 1.00°.   They determine the wave number h^{d}a = 1.65 and the electric normalizing coefficient $E_{z0}{}^d$ = j $)$ 95.9 (V/m).   (Note that ER/EZO = $E_r{}^d/E_{z0}{}^d$, EO/EZO = $E_\theta{}^d/E_{z0}{}^d$, EZ/EZO = $E_z{}^d/E_{z0}{}^d$, and R/A = r/a.)

Figure D.18   Curves of the radial dependence associated with the normalized magnetic fields.   The variables used are ka cotanψ = 1.00, b/a = 0.900, ϵ_r = 1.00x10^2, and ψ = 1.00°. They determine the wave number h^{d}a = 1.65 and the magnetic normalizing coefficient H$_{zo}^d$ = 0.668 (A/m).   (Note that HR/HZ0 = H$_r^d$/H$_{z0}^d$, HO/HZ0 = H$_\theta^d$/H$_{z0}^d$, HZ/HZ0 = H$_z^d$/H$_{z0}^d$, and R/A = r/a.)

Figures D.19 and D.20 display the radial dependence of the normalized electric and magnetic fields, respectively, for the two region "mid frequency" case. $ka\ \cot\psi = 1.00$, $b/a = 1.00$, $\epsilon_r = 100$, and $\psi = 1.00°$ are used. The calculated value of the wave number is $h^d a = 7.30$, and the calculated values of the normalizing coefficients are

$$E_{z0}^d = j \mathcal{J}_{||}\ 27.4\ (V/m)\quad \text{and}\quad H_{z0}^d = \mathcal{J}_{||}\ 0.534\ (A/m).$$

It is informative to compare Figures D.15 – D.18 with Figures D.19 and D.20. Note that the same values of $ka\ \cot\psi$, ϵ_r, and ψ are used in all these graphs. For the two region configuration it is apparent that the fields are rapidly attenuated at increasing radial distances away from the sheath helix surface. However, the three region configuration shows that the fields change much more gradually as the radial distance is varied.

Figures D.21 and D.22 display the radial dependence of the normalized electric and magnetic fields, respectively, for the three region "low fequency" case. The variables used are $ka\ \cot\psi = 5.00\times10^{-2}$, $b/a = 0.100$, $\epsilon_r = 100$, and $\psi = 1.00°$. These variables determine the wave number solution $h^d a = 1.70\times10^{-2}$, and the normalizing coefficients

$$E_{z0}^d = j \mathcal{J}_{||}\ 9.52\ (V/m)\quad \text{and}\quad H_{z0}^d = \mathcal{J}_{||}\ 1.00\ (A/m).$$

Next, Figures D.23 and D.24 are two additional graphs illustrating the normalized electric and magnetic fields' radial dependence, respectively, for the three region "low frequency" case. $ka\ \cot\psi = 5.00\times10^{-2}$, $b/a = 0.900$, $\epsilon_r = 100$, and $\psi = 1.00°$ are used. The calculated wave number solution is $h^d a = 1.80\times10^{-2}$. The calculated values of the normalizing coefficients are

$$E_{z0}^d = j \mathcal{J}_{||}\ 9.51\ (V/m)\quad \text{and}\quad H_{z0}^d = \mathcal{J}_{||}\ 1.00\ (A/m).$$
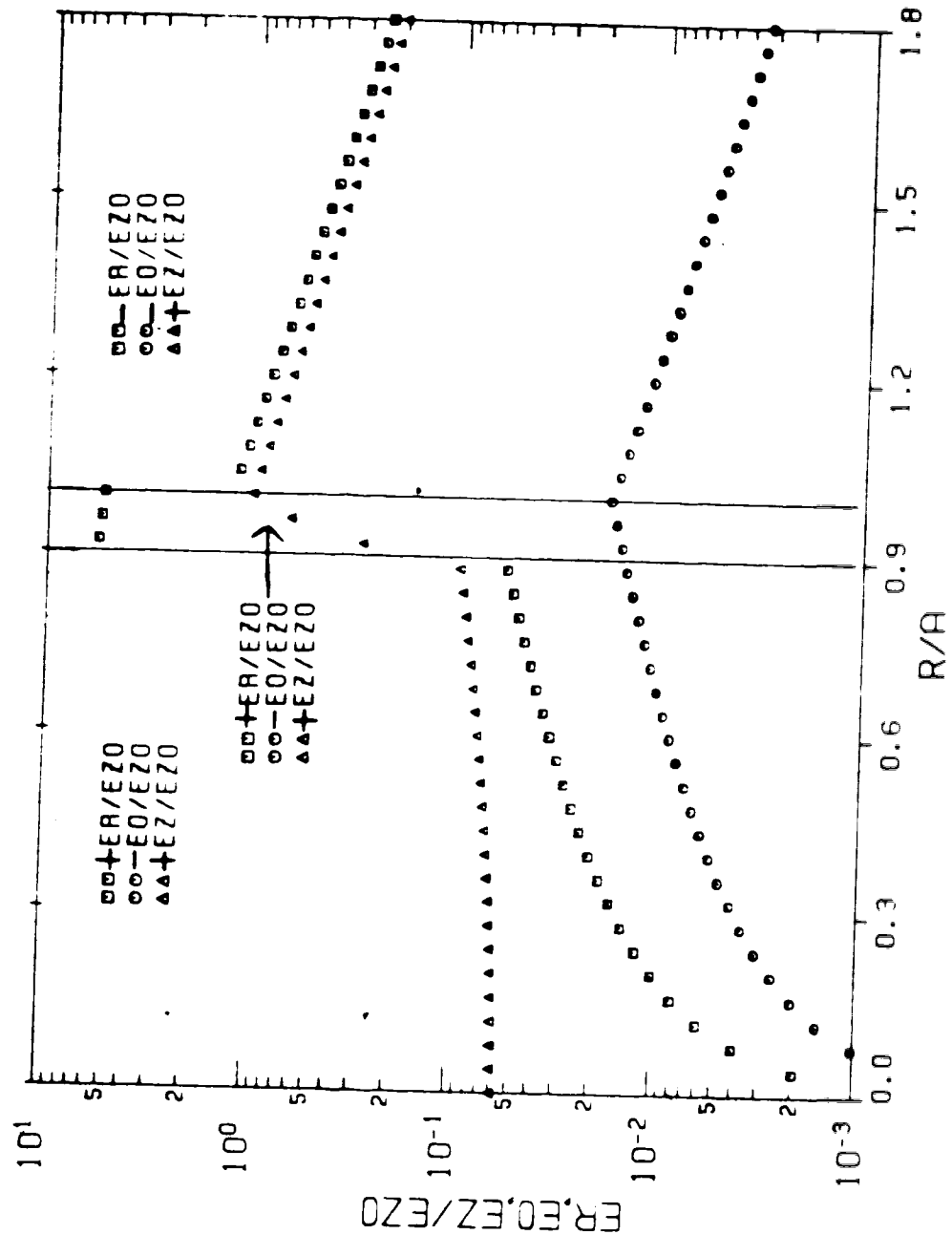
Figure D.19   Curves of the radial dependence associated with the normalized electric fields. The variables used are ka cotanψ = 1.00, b/a = 1.00, ϵ_r = 1.00x10^2, and ψ = 1.00°. They determine the wave number h^{d}a = 7.30 and the electric normalizing coefficient E_{z0}^d = j$\}$ 27.4 (V/m). (Note that ER/EZ0 = E_r^d/E_{z0}^d, E0/EZ0 = E_θ^d/E_{z0}^d, EZ/EZ0 = E_z^d/E_{z0}^d, and R/A = r/a.)
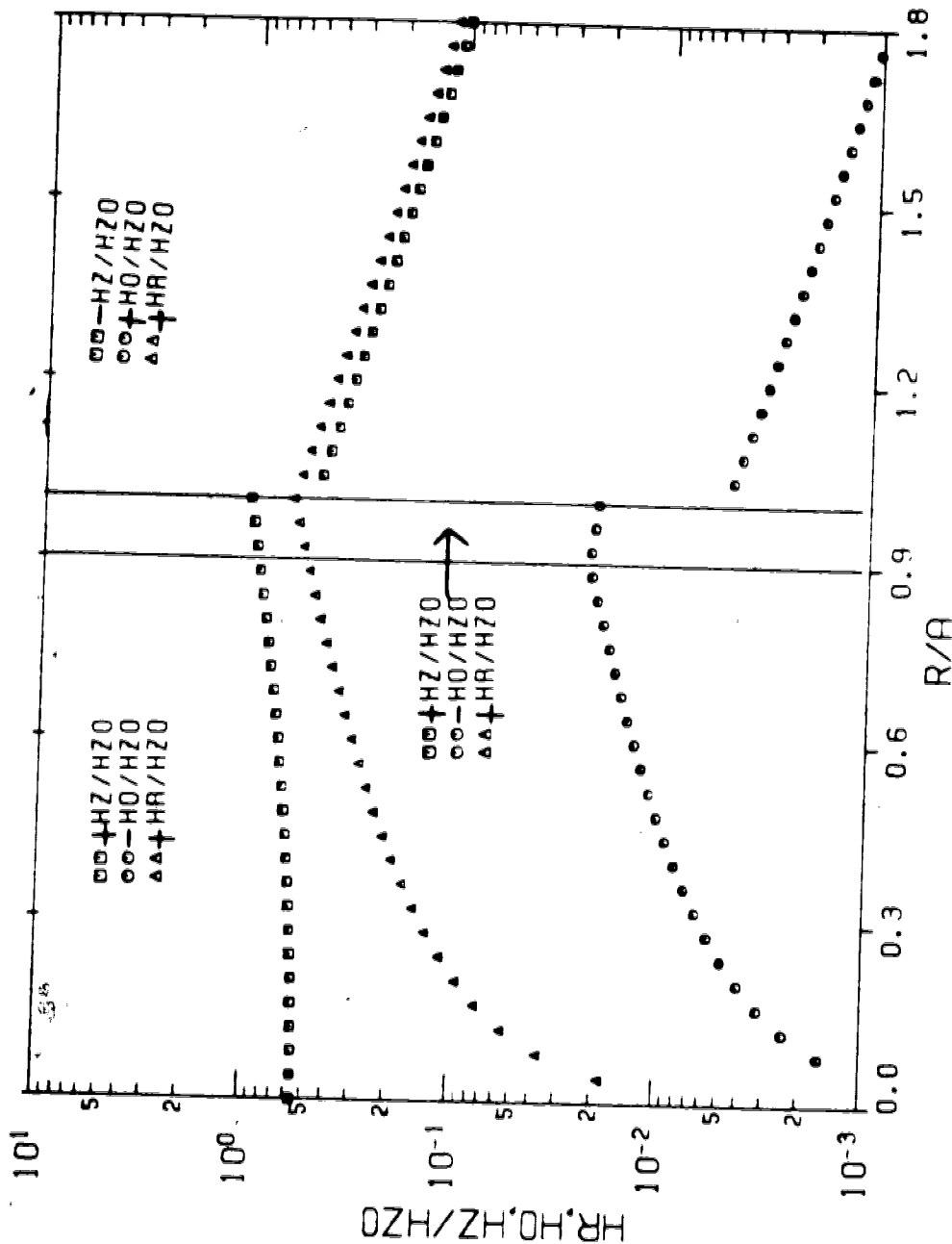
Figure D.20 Curves of the radial dependence associated with the normalized magnetic fields. The variables used are ka cotanψ = 1.00, b/a = 1.00, ϵ_r = 1.00x10^2, and ψ = 1.00°. They determine the wave number h^{d}a = 7.30 and the magnetic normalizing coefficient H$_{z0}$^{d} = 0.534 (A/m). (Note that HR/HZO = H$_r$^{d}/H$_{z0}$^{d}, HO/HZO = H$_\theta$^{d}/H$_{z0}$^{d}, HZ/HZO = H$_z$^{d}/H$_{z0}$^{d}, and R/A = r/a.)

RADIAL DEPENDENCE OF ELECTRIC FIELDS

Figure D.21 Curves of the radial dependence associated with the normalized electric fields. The variables used are ka cotanψ = 5.00x10^{-2}, b/a = 0.100, ϵ_r = 1.00x10^2, and ψ= 1.00°. They determine the wave number h^{d}a = 1.70x10^{-2} and the electric normalizing coefficient E_{z0}^d = j $\frac{\partial}{\partial\parallel}$ 9.52 (V/m). (Note that ER/EZO = E_r^d/E_{z0}^d, EO/EZO = E_θ^d/E_{z0}^d, EZ/EZO = E_z^d/E_{z0}^d, and R/A = r/a.)

Figure D.22 Curves of the radial dependence associated with the normalized magnetic fields. The variables used are ka cotanψ = 5.00x10^{-2}, b/a = 0.100, ε$_r$ = 1.00x10^2, and ψ = 1.00°. They determine the wave number h^{d}a = 1.70x10^{-2}, and the magnetic normalizing coefficient H$_{z0}^d$ = ℑ$_{II}$ 1.00 (A/m). (Note that HR/HZO = H$_r^d$/H$_{z0}^d$, HO/HZO = H$_\theta^d$/H$_{z0}^d$, HZ/HZO = H$_z^d$/H$_{z0}^d$, and R/A = r/a.)

Figure D.23   Curves of the radial dependence associated with the normalized electric fields. The variables used are ka cotanψ = 5.00x10^{-2}, b/a = 0.900, ϵ_r = 1.00x10^2, and ψ = 1.00°. They determine the wave number h^{d}a = 1.80x10^{-2} and the electric normalizing coefficient E$_{z0}^d$ = j 9.51 (V/m). (Note that ER/EZO = E_r^d/E_{z0}^d, EO/EZO = E_θ^d/E_{z0}^d, EZ/EZO = E_z^d/E_{z0}^d, and R/A = r/a.)

Figure D.24   Curves of the radial dependence associated
with the normalized magnetic fields. The variables used
are ka cotanψ = 5.00x10^{-2}, b/a = 0.900, ε_r = 1.00x10^2,
and ψ = 1.00°. They determine the wave number h^{d}a =
1.80x10^{-2} and the magnetic normalizing coefficient
H_{z0}^d = $\oint$|| 1.00 (A/m). (Note that HR/HZ0 = H_r^d/H_{z0}^d,
HO/HZ0 = H_θ^d/H_{z0}^d, HZ/HZ0 = H_z^d/H_{z0}^d, and R/A = r/a.)

Figures D.25 and D.26 are the final two graphs included in this appendix. They display the radial dependence of the normalized electric and magnetic fields, respectively, for the two region "low frequency" case. The variables used are $ka \cot an\psi = 5.00 \times 10^{-2}$, $b/a = 1.00$, $\epsilon_r = 100$, and $\psi = 1.00°$. $h^d a = 1.81 \times 10^{-2}$ is the computed wave number solution.

$$E_{z0}^d = j \, \}_{||} \, 9.45 \, (V/m) \quad and \quad H_{z0}^d = \}_{||} \, 1.00 \, (A/m)$$

are the computed normalizing coefficients.

As expected, the value of $h^d a$ associated with the six previously mentioned figures approximately agrees with equation D.49, the small argument representation of the dispersion equation, which is valid for both the two and three region configurations. A better understanding of the "low frequency" case can be obtained by comparing Figures D.21 - D.26 with Figures B.7 and B.8, which are associated with the empty sheath helix. It should be noted that the same values of $ka \cot an\psi$ and ψ are used in all these graphs. Keeping in mind the values of the normalizing coefficients, it can be seen that with the exception of $H_{\theta 1}^d$, $H_{\theta 2}^d$, and E_{r2}^d, the fields associated with both the two and three region dielectric rod configurations are similar to the corresponding fields of the empty sheath helix. This is in agreement with the discussion given earlier in part D.2.2. It provides support for the statement that at "low frequencies", the fields for both the two and three region ideal dielectric coaxial rod configurations *do not "see" the dielectric rod*.

Figures D.23 and D.24 provide a good illustration of the behavior of the fields at the sheath helix surface and at the surface of ideal dielectric coaxial rod. Since the field behavior at the sheath helix surface was previously discussed in section B.3, it will not be mentioned further here. Figure D.23 shows that the radial electric field is discontinuous at the rod surface. Indeed, evaluating equations D.23 and D.29 at $r = b$, it is easily shown that

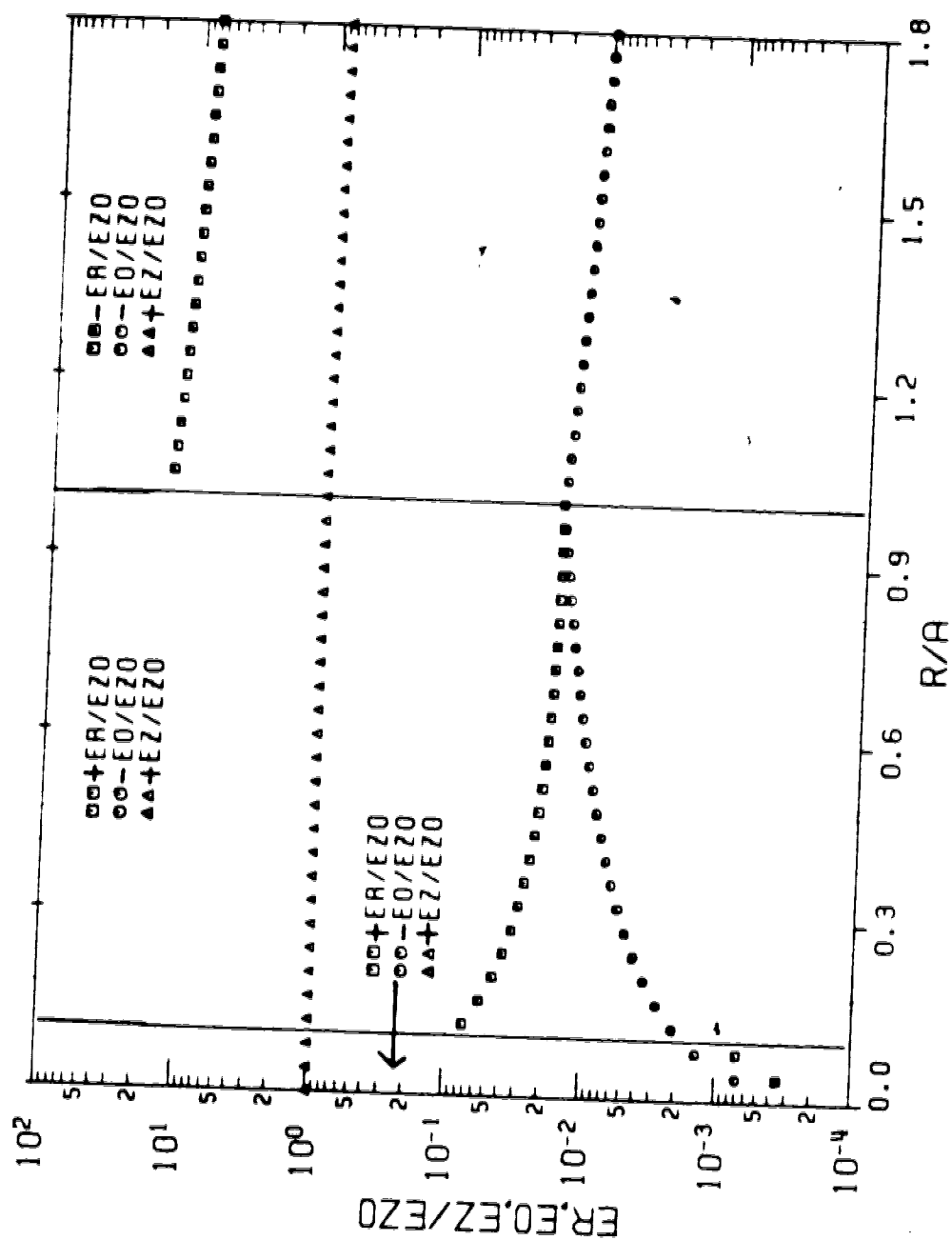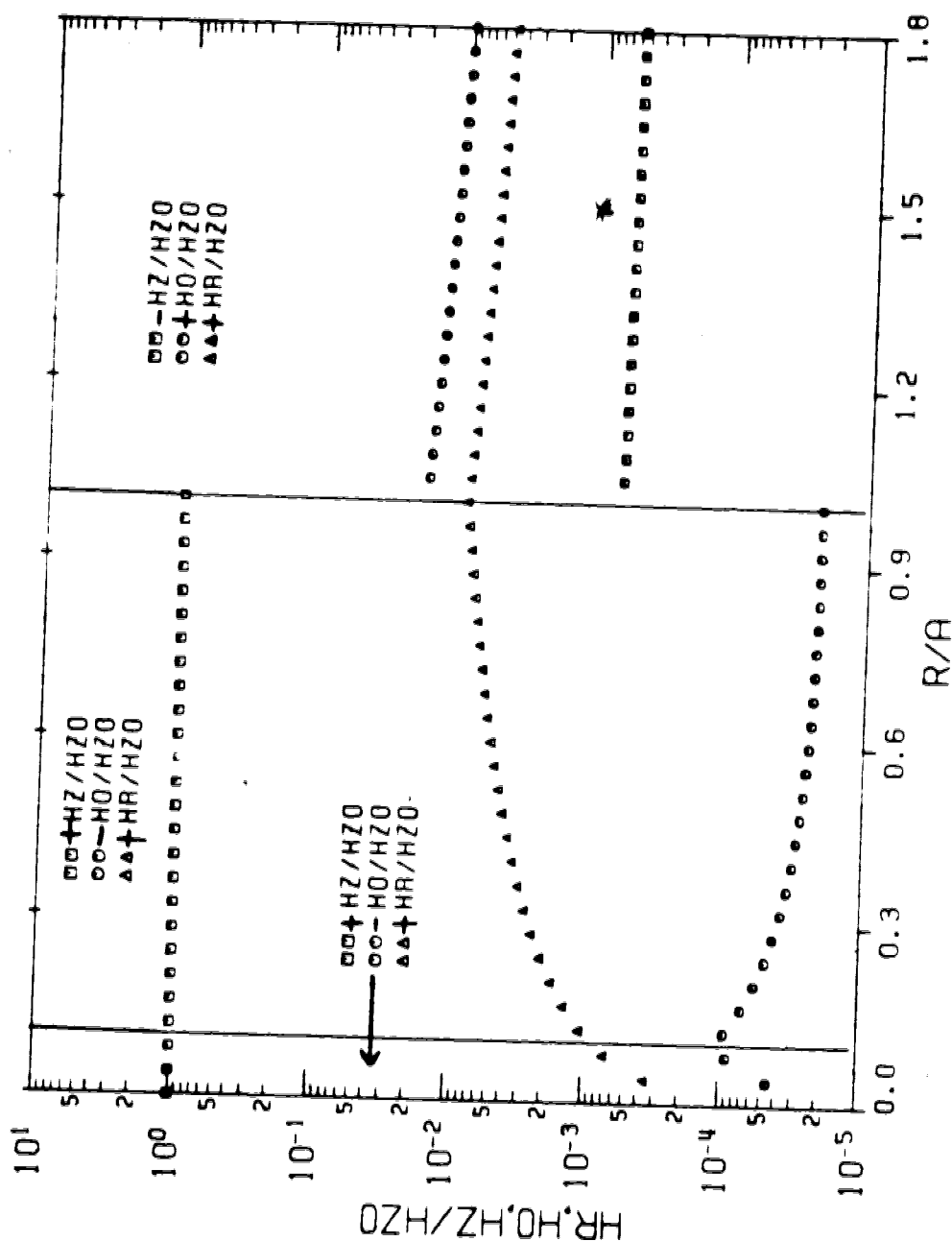$$\epsilon_r \, \epsilon_0 \, E_{r1}^d \Big|_{r=b} = \epsilon_0 \, E_{r2}^d \Big|_{r=b}. \qquad (D.69)$$
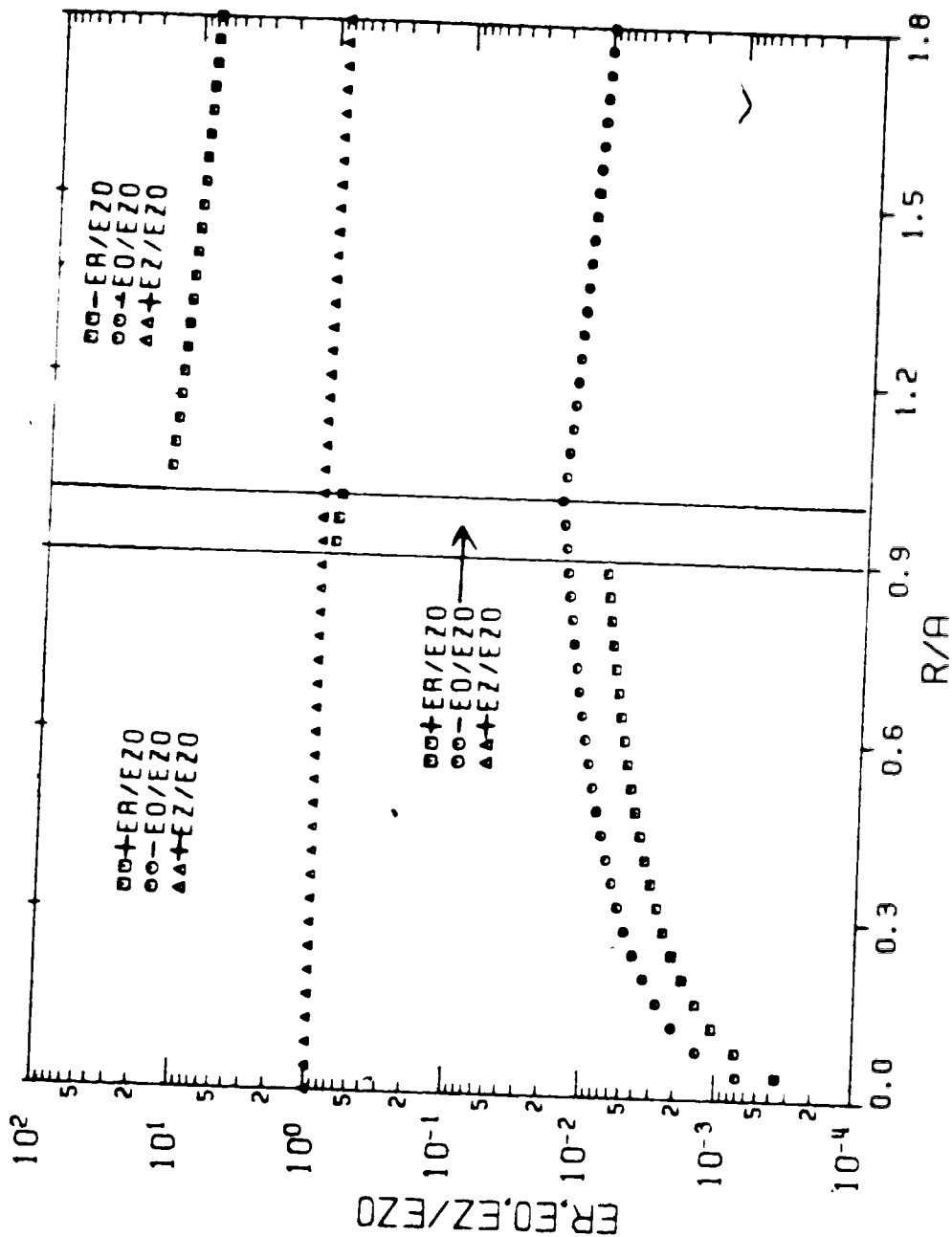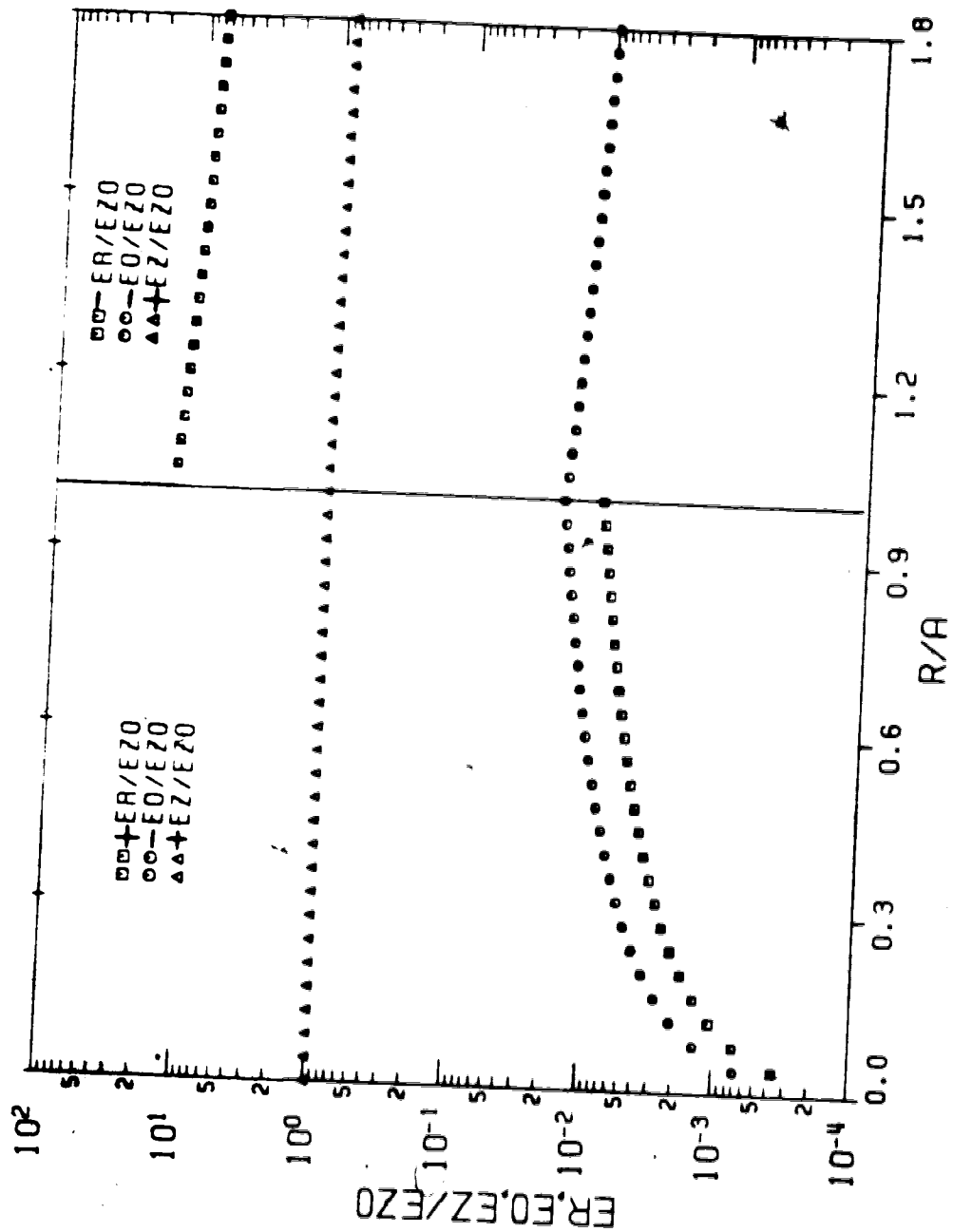
RADIAL DEPENDENCE OF ELECTRIC FIELDS

Figure D.25   Curves of the radial dependence associated with the normalized electric fields. The variables used are ka cotanψ = 5.00x10^{-2}, b/a = 1.00, ϵ_r = 1.00x10^2, and ψ = 1.00°. They determine the wave number h^d_a = 1.80x10^{-2} and the electric normalizing coefficient E_{z0}^d = j 9.45 (V/m). (Note that ER/EZO = E_r^d/E_{z0}^d, EO/EZO = E_θ^d/E_{z0}^d, EZ/EZO = E_z^d/E_{z0}^d, and R/A = r/a.)

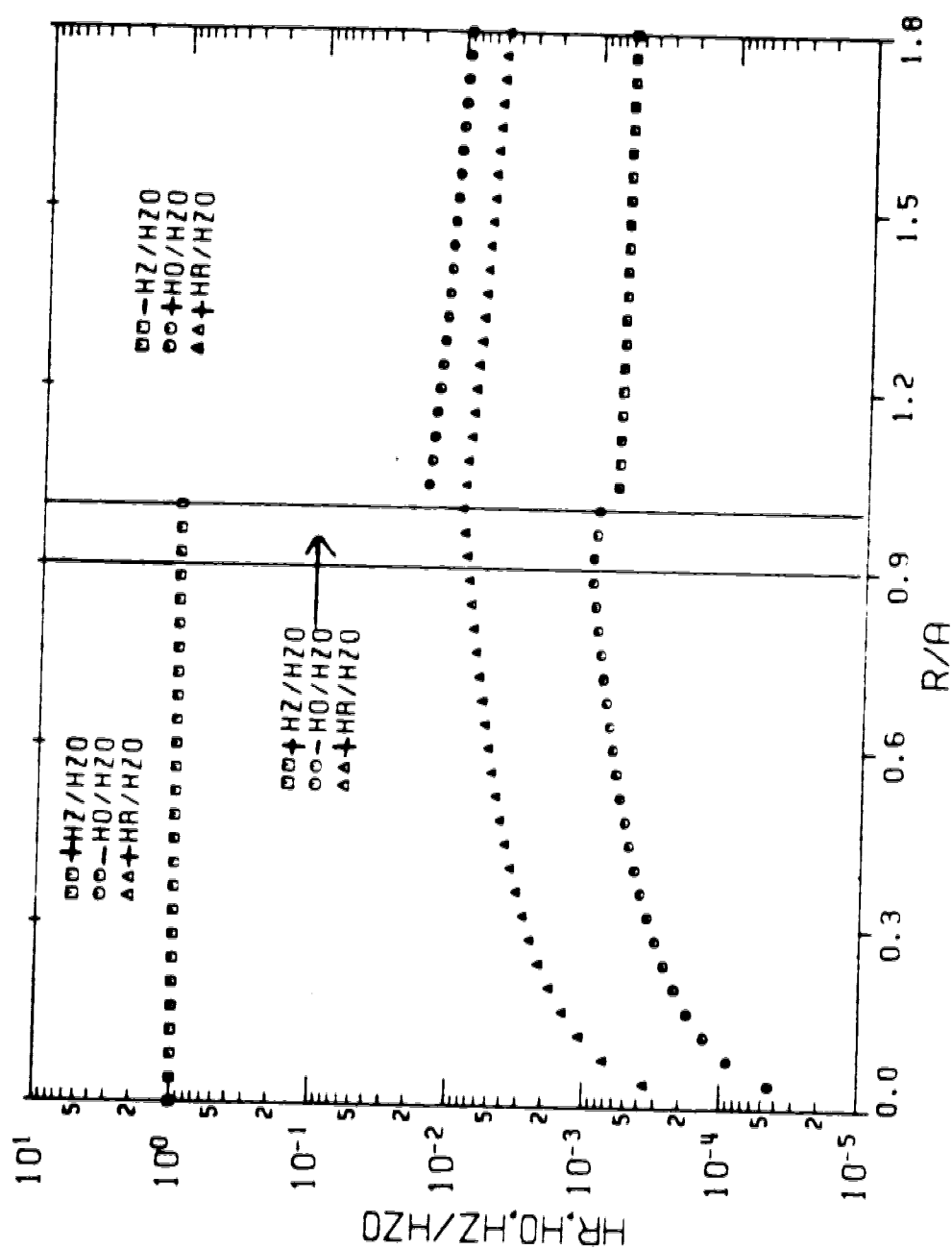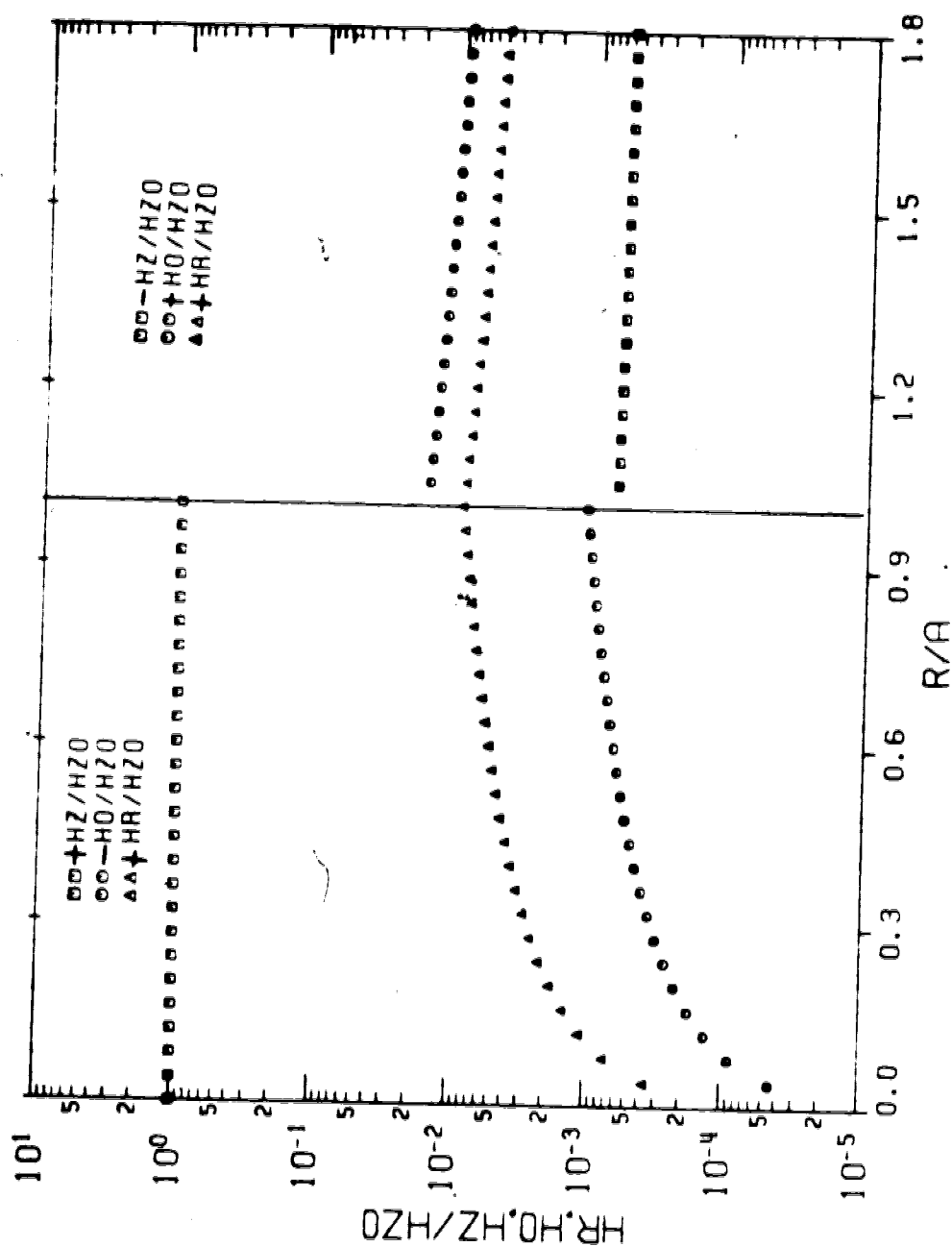Figure D.26   Curves of the radial dependence associated
with the normalized magnetic fields. The variables used
are ka cotanψ = 5.00x10^{-2}, b/a = 1.00, ε_r = 1.00x10^2,
and ψ = 1.00°. They determine the wave number h^{d}a =
1.80x10^{-2} and the magnetic normalizing coefficient
H$_{z0}^d$ = ∂ll 1.00 (A/m). (Note that HR/HZO = H$_r^d$/H$_{z0}^d$,
HO/HZO = H$_\theta^d$/H$_{z0}^d$, HZ/HZO = H$_z^d$/H$_{z0}^d$, and R/A = r/a.)

This is the correct statement of the discontinuity of the normal electric field at an interface associated with two regions having permittivities $\epsilon_r \epsilon_0$ and ϵ_0, when no free electric charge is present on the interface. In addition, the angular and axial electric fields are seen to be continuous at $r = b$. This is simply a statement of the fact that the electric fields tangential to an interface are continuous.

Figure D.24 clearly displays the behavior of the magnetic fields at the surface of the ideal dielectric coaxial rod. The angular and axial magnetic fields are seen to be continuous. Since the ideal dielectric rod is not perfectly conducting (in fact, it has a zero conductivity), it cannot possess an electrical surface current. Therefore, the magnetic fields tangential to the rod surface must be continuous. Furthermore, the radial magnetic field is shown to be continuous at $r = b$. This behavior is expected because free magnetic charge does not exist at the surface of the ideal dielectric rod.

E. Appendix E. Electrical Properties of Douglas Beech Wood, Steak Meat, Muscle Tissue, and Oil Sand

Four data tables are presented in this appendix. The electrical properties of Douglas Beech wood, steak meat, muscle tissue, and oil sand, all of which were previously used in part 3.2.3 of the thesis to make graphs of $P_{d\theta}/P_{dz}$ versus frequency, are listed. Each table shows the relative permittivity, ϵ_r, the conductivity, σ, and the loss tangent, $\sigma/\omega\epsilon_0$, as a function of frequency. The numerical values were obtained from reference 45 (pp. 268-271) and from reference 46 (Figure 2).

Table E.1   Electrical Properties of Douglas Beech
as a Function of Frequency at T=25°C.
(45, pp. 268.)

Frequency (Hz)	ϵ_r	σ (S/m)	$\sigma/\omega\epsilon_0$
1.0×10^3	2.0	8.9×10^{-10}	1.6×10^{-2}
1.0×10^4	2.0	1.4×10^{-8}	2.6×10^{-2}
1.0×10^5	2.0	2.1×10^{-7}	3.7×10^{-2}
1.0×10^6	1.9	2.8×10^{-6}	5.0×10^{-2}
1.0×10^7	1.9	3.3×10^{-5}	5.9×10^{-2}
1.0×10^8	1.9	3.4×10^{-4}	6.2×10^{-2}
3.0×10^8	1.9	9.9×10^{-4}	6.0×10^{-2}
3.0×10^9	1.8	8.2×10^{-3}	4.9×10^{-2}
1.0×10^{10}	1.8	2.9×10^{-2}	5.2×10^{-2}
2.5×10^{10}	1.8	7.9×10^{-2}	5.7×10^{-2}

Table E.2   Electrical Properties of Steak as a
Function of Frequency at T=25°C.
(45, pp. 270.)

Frequency (Hz)	ϵ_r	σ (S/m)	$\sigma/\omega\epsilon_0$
1.0×10^4	2.4×10^4	5.5×10^{-2}	9.9×10^4
1.0×10^6	2.0×10^2	0.67	1.2×10^4
1.0×10^7	50	0.72	1.3×10^3
3.0×10^8	50	0.65	39
3.0×10^9	40	2.0	12
1.0×10^{10}	30	6.1	11
2.5×10^{10}	15	8.3	6.0

Table E.3   Electrical Properties of Muscle Tissue
as a Function of Frequency at $T=25^\circ$C.
(45, pp. 271.)

Frequency (Hz)	ϵ_r	σ (S/m)	$\sigma/\omega\epsilon_0$
5.0×10^7	90	8.3×10^{-3}	3.0
2.0×10^8	56	1.0×10^{-2}	0.90
4.0×10^8	53	1.2×10^{-2}	0.52
7.0×10^8	53	1.3×10^{-2}	0.34
1.0×10^9	50	1.3×10^{-2}	0.23
3.0×10^9	46	2.2×10^{-2}	0.13
8.5×10^9	41	8.3×10^{-2}	0.18

Table E.4   Electrical Properties of Oil Sand as a Function of Frequency (46, Figure 2).

The oil sand has 5.8% water content by weight and is at a temperature of 25°C.

Frequency (Hz)	ϵ_r	σ (S/m)	$\sigma/\omega\epsilon_0$
1.0×10^1	2.0×10^5	2.0×10^{-2}	3.6×10^7
2.0×10^1	1.0×10^5	2.0×10^{-2}	1.8×10^7
3.0×10^1	7.0×10^4	2.0×10^{-2}	1.2×10^7
4.0×10^1	5.0×10^4	2.0×10^{-2}	9.0×10^6
5.0×10^1	4.0×10^4	2.0×10^{-2}	7.2×10^6
6.0×10^1	3.0×10^4	2.0×10^{-2}	6.0×10^6
7.0×10^1	2.5×10^4	2.0×10^{-2}	5.1×10^6
8.0×10^1	2.3×10^4	2.0×10^{-2}	4.5×10^6
9.0×10^1	2.1×10^4	2.0×10^{-2}	4.0×10^6
1.0×10^2	2.0×10^4	2.0×10^{-2}	3.6×10^6
2.0×10^2	1.0×10^4	2.0×10^{-2}	1.8×10^6
3.0×10^2	7.0×10^3	2.0×10^{-2}	1.2×10^6
4.0×10^2	5.0×10^3	2.0×10^{-2}	9.0×10^5
5.0×10^2	4.0×10^3	2.0×10^{-2}	7.2×10^5
6.0×10^2	3.5×10^3	2.0×10^{-2}	6.0×10^5
7.0×10^2	3.0×10^3	2.0×10^{-2}	5.1×10^5
8.0×10^2	2.5×10^3	2.0×10^{-2}	4.5×10^5
9.0×10^2	2.2×10^3	2.0×10^{-2}	4.0×10^5
1.0×10^3	2.0×10^3	2.0×10^{-2}	3.6×10^5
2.0×10^3	1.0×10^3	2.0×10^{-2}	1.8×10^5
3.0×10^3	7.0×10^2	2.0×10^{-2}	1.2×10^5

Table E.4 (continued)

Frequency (Hz)	ϵ_r	σ (S/m)	$\sigma/\omega\epsilon_0$
4.0×10^3	5.0×10^2	2.0×10^{-2}	9.0×10^4
5.0×10^3	4.0×10^2	2.0×10^{-2}	7.2×10^4
6.0×10^3	3.5×10^2	2.0×10^{-2}	6.0×10^4
7.0×10^3	3.0×10^2	2.0×10^{-2}	5.1×10^4
8.0×10^3	2.5×10^2	2.0×10^{-2}	4.5×10^4
9.0×10^3	2.2×10^2	2.0×10^{-2}	4.0×10^4
1.0×10^4	2.0×10^2	2.0×10^{-2}	3.6×10^4
2.0×10^4	1.5×10^2	2.0×10^{-2}	1.8×10^4
3.0×10^4	1.0×10^2	2.0×10^{-2}	1.2×10^4
4.0×10^4	8.0×10^1	2.0×10^{-2}	9.0×10^3
5.0×10^4	7.0×10^1	2.0×10^{-2}	7.2×10^3
6.0×10^4	6.5×10^1	2.0×10^{-2}	6.0×10^3
7.0×10^4	6.0×10^1	2.0×10^{-2}	5.1×10^3
8.0×10^4	5.5×10^1	2.0×10^{-2}	4.5×10^3
9.0×10^4	5.3×10^1	2.0×10^{-2}	4.0×10^3
1.0×10^5	5.0×10^1	2.0×10^{-2}	3.6×10^3
2.0×10^5	4.0×10^1	2.0×10^{-2}	1.8×10^3
3.0×10^5	3.5×10^1	2.0×10^{-2}	1.2×10^3
4.0×10^5	3.0×10^1	2.0×10^{-2}	9.0×10^2
5.0×10^5	2.7×10^1	2.0×10^{-2}	7.2×10^2
6.0×10^5	2.6×10^1	2.0×10^{-2}	6.0×10^2
7.0×10^5	2.5×10^1	2.0×10^{-2}	5.1×10^2
8.0×10^5	2.4×10^1	2.0×10^{-2}	4.5×10^2

Table E.4 (continued)

Frequency (Hz)	ϵ_r	σ (S/m)	$\sigma/\omega\epsilon_0$
9.0×10^5	2.3×10^1	2.0×10^{-2}	4.0×10^2
1.0×10^6	2.2×10^1	2.0×10^{-2}	3.6×10^2
2.0×10^6	1.8×10^1	2.5×10^{-2}	2.2×10^2
3.0×10^6	1.7×10^1	2.7×10^{-2}	1.6×10^2
4.0×10^6	1.6×10^1	2.8×10^{-2}	1.3×10^2
5.0×10^6	1.5×10^1	2.8×10^{-2}	1.0×10^2
6.0×10^6	1.4×10^1	2.9×10^{-2}	8.7×10^1
7.0×10^6	1.4×10^1	2.9×10^{-2}	7.5×10^1
8.0×10^6	1.4×10^1	3.0×10^{-2}	6.6×10^1
9.0×10^6	1.3×10^1	3.0×10^{-2}	6.0×10^1
1.0×10^7	1.3×10^1	3.0×10^{-2}	5.4×10^1
2.0×10^7	1.2×10^1	3.5×10^{-2}	3.1×10^1
3.0×10^7	1.2×10^1	3.8×10^{-2}	2.3×10^1
4.0×10^7	1.2×10^1	4.0×10^{-2}	1.8×10^1
5.0×10^7	1.1×10^1	4.2×10^{-2}	1.5×10^1
6.0×10^7	1.1×10^1	4.4×10^{-2}	1.3×10^1
7.0×10^7	1.1×10^1	4.6×10^{-2}	1.2×10^1
8.0×10^7	1.1×10^1	4.8×10^{-2}	1.1×10^1
9.0×10^7	1.1×10^1	4.9×10^{-2}	9.8
1.0×10^8	1.0×10^1	5.0×10^{-2}	9.0
2.0×10^8	1.0×10^1	6.0×10^{-2}	$5.$
3.0×10^8	1.0×10^1	7.0×10^{-2}	4.2

Table E.4 (continued)

Frequency (Hz)	ϵ_r	σ (S/m)	$\sigma/\omega\epsilon_0$
4.0×10^8	1.0×10^1	7.5×10^{-2}	3.4
5.0×10^8	1.0×10^1	7.8×10^{-2}	2.8
6.0×10^8	1.0×10^1	8.1×10^{-2}	2.4
7.0×10^8	1.0×10^1	8.4×10^{-2}	2.2
8.0×10^8	1.0×10^1	8.6×10^{-2}	1.9
9.0×10^8	1.0×10^1	8.8×10^{-2}	1.8
1.0×10^9	1.0×10^1	9.0×10^{-2}	1.6
2.0×10^9	9.8	1.1×10^{-1}	9.9×10^{-1}
3.0×10^9	9.7	1.3×10^{-1}	7.8×10^{-1}
4.0×10^9	9.6	1.4×10^{-1}	6.3×10^{-1}
5.0×10^9	9.5	1.5×10^{-1}	5.4×10^{-1}
6.0×10^9	9.4	1.6×10^{-1}	4.8×10^{-1}
7.0×10^9	9.3	1.7×10^{-1}	4.4×10^{-1}
8.0×10^9	9.2	1.8×10^{-1}	4.0×10^{-1}
9.0×10^9	9.1	1.9×10^{-1}	3.8×10^{-1}